europhysics
conference
abstracts

17th EPS Conference on

Controlled Fusion and Plasma Heating

Amsterdam, 25-29 June 1990

Editors: G. Briffod, Adri Nijsen-Vis, F.C. Schüller

Contributed Papers
Part II

Published by: European Physical Society

eries Editor: Prof. K. Bethge, Frankfurt/M.

anaging Editor: G. Thomas, Geneva

VOLUME 14 B Part II

XVII FUSION AMSTERDAM 1990

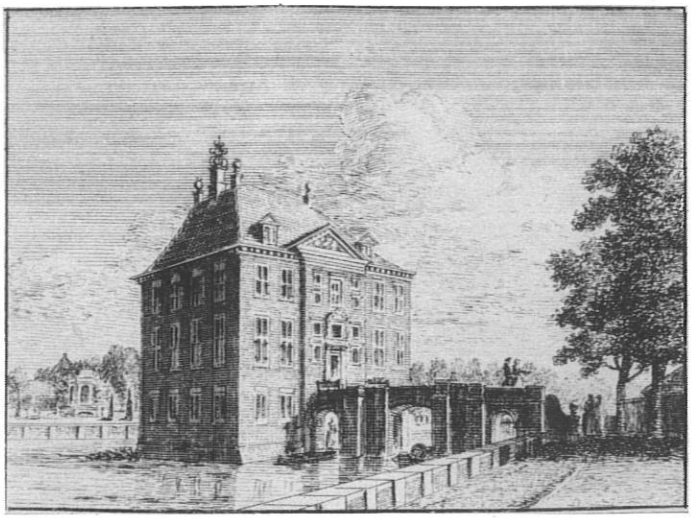

Het HUIS RYNHUIZEN.

17th
FUSION
AMSTERDAM
1990

B
C
D

17th European Conference on

Controlled Fusion and Plasma Heating

Amsterdam, 25-29 June 1990
Editors: G. Briffod, Adri Nijsen-Vis, F.C. Schüller

Contributed Papers
Part II

EUROPHYSICS CONFERENCE ABSTRACTS is published by the
European Physical Society, © 1990

PREFACE

The 17th European Conference on Controlled Fusion and Plasma Heating was held in Amsterdam, the Netherlands, from the 25th to the 29th of June 1990 by the Plasma Physics Division of the European Physical Society (EPS).

The Conference has been organized by the FOM-Instituut voor Plasmafysica Rijnhuizen, which is part of the Foundation for Fundamental Research on Matter (Stichting Fundamenteel Onderzoek der Materie). FOM is supported by the Dutch Research Organization NWO and Euratom.

The Conference has been sponsored by the Koninklijke Nederlandse Academie van Wetenschappen (KNAW) and by the Foundation Physica.

The programme, format and schedule of the Conference are determined by the International Programme Committee appointed by the Plasma Physics Division of the EPS.

The programme included 18 invited lectures; from the contributed papers 24 were selected for oral presentation and 470 for poster presentation.

This 4-volume publication is published in the Europhysics Conference Abstract Series and contains all accepted contributed papers received in due time by the organizers. The 4-page extended abstracts were reproduced photographically using the manuscripts submitted by the authors. The invited papers will be published in a special issue of the journal "Plasma Physics and Controlled Fusion" and sent free of charge to each registered participant.

The editors would like to acknowledge the skillful and dedicated support given by Laura van Veenendaal - van Uden, Rosa Tenge - Tjon A Tham and Cora de Bruijne in preparing the manuscripts for reproduction in these four volumes.

May 1990

The Editors

INTERNATIONAL PROGRAMME COMMITTEE

G. Briffod, Chairman, CEN, Grenoble, France
K. Appert, CRPP, Lausanne, Switzerland
R. Balescu, Université Libre de Bruxelles, Belgium
F. De Marco, Euratom-ENEA, Frascati, Italy
C. Gormezano, JET Joint Undertaking, Abingdon, United Kingdom
L. Laurent, Association Euratom-CEN, St. Paul-lez-Durance, France
S. Ortolani, Association Euratom-CNR, Padova, Italy
D.D. Ryutov, Academy of Sciences, Novosibirsk, USSR
F.C. Schüller, FOM-Rijnhuizen, Nieuwegein, The Netherlands
S.E. Segre, Euratom-ENEA, Frascati, Italy
P.E. Stott, JET Joint Undertaking, Abingdon, United Kingdom
H. Wobig, Max-Planck-Institut für Plasmaphysik, Garching bei München, FRG

LOCAL ORGANIZING COMMITTEE

M.J. van der Wiel, Chairman, FOM-Rijnhuizen, Nieuwegein
F.C. Schüller, Vice-Chairman, FOM-Rijnhuizen, Nieuwegein
A. Nijsen-Vis, Scientific Secretary, FOM-Rijnhuizen, Nieuwegein
J.T. van den Hout, Treasurer, FOM-Rijnhuizen, Nieuwegein
A.J.H. Donné, FOM-Rijnhuizen, Nieuwegein
N.J. Lopes Cardozo, FOM-Rijnhuizen, Nieuwegein
J. Rem, FOM-Rijnhuizen, Nieuwegein
H. Hopman, FOM-AMOLF, Amsterdam
D.C. Schram, Technical University, Eindhoven

CONTENTS

PAPER IDENTIFICATION

All contributed papers are listed with their title and responsible author. In those cases where no author was underlined the first author mentioned was taken. The day of the poster presentation of each paper, followed by the number of the poster board, is given under the title in the list of contributed papers. The four poster sessions will be held on:

Monday afternoon indicated as Mo,
Tuesday afternoon indicated as Tu,
Thursday afternoon indicated as Th,
Friday afternoon indicated as Fr.

The poster boards are numbered from 1 to 130. From the 494 contributed papers, 24 were selected for oral presentation. The authors of those orally presented papers were requested to give also a poster presentation. Most of them confirmed that they were prepared to do so.

TITLE LIST OF CONTRIBUTED PAPERS

A. TOKAMAKS

* This paper will also be presented orally on Friday 29 June at 9.40 hrs.

* This paper will also be presented orally on Tuesday 26 June at 14.30 hrs.

* This paper will also be presented orally on Tuesday 26 June at 14.10 hrs.
** This paper will also be presented orally on Tuesday 26 June at 13.30 hrs.
*** This paper will also be presented orally on Tuesday 26 June at 13.50 hrs.

* This paper will also be presented orally on Friday 29 June at 9.00 hrs.
** This paper will also be presented orally on Friday 29 June at 9.20 hrs.

B. STELLARATORS

* This paper will also be presented orally on Tuesday 26 June at 14.

* This paper will also be presented orally on Tuesday 26 June at 15.10 hrs.

C. ALTERNATIVE MAGNETIC CONFINEMENT SCHEMES

---

* This paper will also be presented orally on Thursday 28 June at 13.30 hrs.
** This paper will also be presented orally on Thursday 28 June at 13.50 hrs.

D. MAGNETIC CONFINEMENT THEORY AND MODELLING

* This paper will also be presented orally on Thursday 28 June at 14.10 hrs.

---

* This paper will also be presented orally on Thursday 28 June at 14.50 hrs.
** This paper will also be presented orally on Thursday 28 June at 15.10 hrs.

* This paper will also be presented orally on Thursday 28 June at 14.30 hrs.

E. HEATING BY NEUTRAL BEAM INJECTION

F. RF HEATING

* This paper will also be presented orally on Monday 25 June at 13.45 hrs.

* This paper will also be presented orally on Monday 25 June at 14.05 hrs.

G. CURRENT DRIVE AND PROFILE CONTROL

* This paper will also be presented orally on Monday 25 June at 14.25 hrs.

* This paper will also be presented orally on Monday 25 June at 14.45 hrs.
** This paper will also be presented orally on Monday 25 June at 15.05 hrs.

H. IMPURITY AND EDGE PHYSICS

---

* This paper will also be presented orally on Friday 29 June at 11.00 hrs.

* This paper will also be presented orally on Friday 29 June at 11.20 hrs.

I. DIAGNOSTICS

* This paper will also be presented orally on Friday 29 June at 10.00 hrs.

Project of magnetic fluctuation measurement by cross polarization scattering in the TORE SUPRA tokamak.
First author: M. Paume et al.

Fr 40 I 62 IV-1721

J. BASIC COLLISIONLESS PLASMA PHYSICS

* This paper will also be presented orally on Monday 25 June at 16.00 hrs.

K. INERTIAL CONFINEMENT FUSION

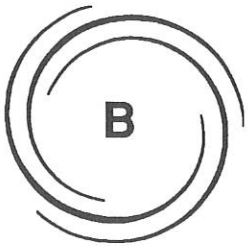

STELLARATORS

B1 EXPERIMENTS

ELECTRON-CYCLOTRON RADIATION (ECR) ASYMMETRY MEASUREMENTS AT 2 ω_{He} IN THE L-2 STELLARATOR

D.K. Akulina

General Physics Insitute, Moscow, USSR

ABSTRACT

The measurements of electron cyclotron radiation (ECR) at the second cyclotron harmonic (2 ω_{He}) both from the inner (HFS) and outer (LFS) side of the plasma vessel ("High" and "Low" magnetic Field Side) in the equatorial plane of the L-2 stellarator are presented. The asymmetry of radiation for an extraordinary wave (e-mode) ($\vec{E} \perp \vec{H} \perp (\vec{k})$ in the case of current-free plasma production and heating by a fundamental EC ordinary mode (0-mode) (n=1) is shown.

INTRODUCTION

The investigation of ECR at the second cyclotron harmonic $I_{2\omega He}$ is now routinely used to obtain the spatial profile of the temperature $T_e(r)$ [1, 2].

The emission intensity is determined by Rayleigh-Jeans Law and for the second harmonic an extraordinary mode is:

$$I^e_{2\omega He} = \frac{\omega^2 k T_e(r)}{8\pi^3 c^2} \left(\frac{1-e^{-\tau(r)}}{1-\rho e^{-\tau(r)}} \right) \qquad (1)$$

where τ is the optical thickness, ρ is the reflectivity of metallic walls.

In the case of optically thick lines ($\tau > 1$), $I^e \equiv T_e(r)$. However, the formula (1) is valid for thermal plasma radiation only, when the velocity distribution function is a Maxwellian one. If superthermal electrons are present in the plasma then the radiation temperature T_r can be much higher than the thermal one, T_e, and occurs at lower frequencies due to the relativistic shift. A nonthermal plasma radiation takes place in a low-density current plasma when the electric inductive field in the plasma is equal to ~ 0.1 E_c (where E_c is the Dricer's field) or in the experiments with plasma heating by microwave at ECRH conditions.

It is important to know from the methodical point of view from what side of the toroidal magnetic field ("low" or "high" field side) the measurements are performed since the measured radiation intensity may be different and this phenomenon is associated with the nonequal bulk-plasma absorption of a nonthermal radiation component.Theoretically this phenomenon was described in Ref. [4]. It was shown that for the intensity I^e_{HFS} at $2f_{He}$ in the e-mode one can use:

$$I^e_{HFS} = I_O(1-e^{-\tau}) \cdot e^{-\tau_{st}} + I_{ST}(1-e^{-\tau_{st}}) \quad (2)$$

and for I^e_{LFS}:

$$I^e_{LFS} = I_O(1-e^{-\tau}) + I_{ST}(1-e^{-\tau})e^{-\tau} \quad (3)$$

where I_O, I_{ST} are the intensities of the bulk and nonthermal component, respectively; τ is the optical thickness. Thus, making simultaneous measurements from HFS and LFS of the torus, one can get information about the plasma optical thickness and intensity of a nonthermal radiation component. The experiments at the first cyclotron harmonic have been described in Ref. [5].

EXPERIMENTAL RESULTS

In the L-2 experiments, a current-free plasma was produced and heated by an ECRH wave with a gyrotron power P = 200 kW at the fundamental 0-mode. The plasma parameters were: plasma density $N_e = 7 \cdot 10^{12}$ cm^{-3}, electron temperature T_e = (0.5-0.9) keV, magnetic field strength H = 1.35 T. Plasma radiation at $2f_{He}$ was received along the main torus radius (see Fig. 1). The LFS horn can receive both 0- and e-mode polarization whereas HFS horn - e-mode only. The radiation was analized by a superheterodyne receiver in the 70-80 GHz band corresponding to the second cyclotron harmonic frequency at H(0) = 1.35 tesla. The emission profile was measured shot by shot by varying the local oscillator frequency. The frequency resolution was determined by an IF amplifier and was equal to 400 MHz that corresponds to the space resolution 0.5-1 cm.

Plasma density was changed by the initial gas pressure and was either constant or slightly enhanced during 7-10 ms of the heating pulse. Figure 2 shows oscillograms of the signals received at different frequencies in the measurements from the "low" (I_{LFS}) and "high" (I_{HFS}) magnetic field sides. One can see that for f = 77 GHz there is observed an equality of signals $I^e_{HFS} = I^e_{LFS}$, corresponding to the layer radiation from r = -2 cm; but for f = 73 GHz the ratio of signals $I^e_{HFS}/I^e_{LFS} \sim 2$ times. The note should be made that the f = 73 GHz radiation is

nonthermal in nature [3] and exceeds essentially the thermal level (as compared to the radiation and Thomson scattering laser method of temperature measurements). In this series of experiments, the laser measured temperature was at r = -1 cm equal to 650 eV and at r = -4 cm is 300 eV. Note that laser measurements are performed along the vertical axis (Fig. 1).

If one supposes that the general electron interaction with a plasma took place at the frequency f = 37.5 GHz (at the optimum magnetic field) in the plasma center and that nonthermal electrons are produced at the same place, then the appearance of additional nonthermal radiation at f = 73 GHz can be related to the relativistic frequency shift. The estimation made on the basis of Ref. [1] shows that the shift mentioned above can be associated with the electrons up to 5 keV.

Taking into account formulas (2, 3) one can see that $\tau = 2$ and $\tau_{ST} = 0.3$ are the best fit to the experimental results for $T_e \sim 0.5$ keV and $T_{ST} \sim 5$ keV. Note that for $\tau(r)$ the calculations and measurements performed earlier [6] by microwave transmission in a current plasma of the L-2 with similar parameters have shown τ (r=0) ~ 4 and τ (r = 4 cm) ~ 1. The number of nonthermal particles is not high and is in the range of 10^{11} cm^{-3} > n_{ST} > 10^{10} cm^{-3}.

According to the theory of plasma radiation at 2 f_{He} [1], the intensity of an 0-mode should be in $(v_t/v_c)^2$ times less than that in a e-mode. In the experiment, the measured I_{LFS} was almost the same as I^e_{HFS} (Fig. 2"B"). The enhancement of the 0-mode radiation at 2 f_{He}, compared to the theory, was mentioned for the other machines too, and was explained both by wall reflection and loss of polarization [1,2,7]. Thus, making measurements in an 0-mode from LFS at different frequencies one can estimate a nonthermal component and by comparison of I^e_{LFS} and I^e_{HFS} the optical thickness, since the latter is absorbed by the bulk plasma and depends on τ.

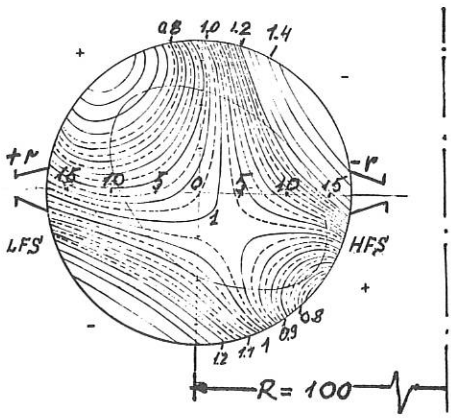

Fig. 1. The L-2 torus cross-section and /H/ = const. lines.

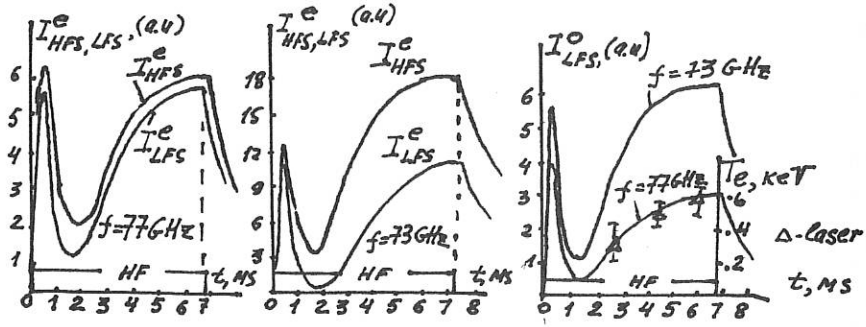

Fig. 2. Oscillograms of radiation intensity $I^{e,o}_{HFS,LFS}$ for different frequencies.

REFERENCES

[1] F. Engelmann, M. Curatolo, Nuclear Fusion, **13** (1973), 497.
C. Celata, D. Boyd, Nuclear Fusion, **17** (1977), 455.
M. Bornatici, R. Cano, O. De Barbieri, F. Engelmann, Nuclear Fusion **29** (1983), 1153.

[2] A. Costley, R. Hastie, J. Paul, J. Chamberlain, J. Phys. Lett., **33** (1974), 758.
D. Akulina, Yu. Khol'nov, Fizika Plazmy, 1978, n.5, p. 1015-1020.
D. Akulina, Proc. of Course and Workshop "Diagnostic technique for fusion plasma", Varenna, v. 1, p. 139-154; E. Suvorov, ibid, p. 155-168.

[3] H. Hartfuss, M. Tutter, W-7 team, Proc. EC-5 Workshop, San Diego, 1985; p. 37-44.
D. Akulina Proc. of 16 Europ. Conf. on CTR, Venice, 1989, p. 643-648.

[4] M. Lontano, R. Pozzoli, E. Suvorov, J. Nuovo Cimento, v.63, N.2 (1981) p. 529–540.

[5] F. Fidone, TFR Groupe, Rep. EUR-CEA 1091 Fontenay-aux-Roses, 1981.

[6] D. Akulina, O. Smoliakova, E. Suvorov, S. Fedorenko, O. Fedyanin, Proc. of EC-6 Workshop, Oxford, 1987.

[7] D. Campbell, A. Eberhagen, S. Kissel, Nuclear Fusion, 24, 3 (1984).

CONFINEMENT STUDIES OF ECRH PLASMAS IN A TOROIDAL HELIAC

G.D.CONWAY & B.D.BLACKWELL

Plasma Research Laboratory
Research School of Physical Sciences
Australian National University
Canberra, ACT 2601, Australia

The SHEILA heliac [1] is a toroidal device of major radius R_o = 18.75cm and mean minor radius a (last closed flux surface) of about 3.1cm. 24 toroidal field coils displaced 2.5 cm about a poloidal ring coil (radius R_o) form a N = 3 period helical axis stellarator. SHEILA has been converted to a flexible heliac by an additional l = 1 helical winding about the ring coil. Considerable variation in the magnetic geometry can be obtained by adjusting the current ratio C = I_h/I_r between -0.16 to +0.25, equivalent to the range $0.55 \geq \iota(0) \geq 1.86$, where I_h and I_r are the currents in the helical winding and poloidal ring.

The vacuum flux surfaces are generally bean-shaped in cross section, but change considerably with variations in the helical current (fig. 3 top). The |B| surfaces however remain roughly circular, concentric with the poloidal ring coil. Plasma formation by electron cyclotron resonance (ECR) depends critically on the position of the fundamental resonance surface, and also the second harmonic surface at low field strengths, relative to the plasma column and the launching antenna.

In this paper we investigate the particle confinement properties of the heliac geometry as the rotational transform is varied using up to 2.5kW peak 10ms wide pulses of microwave ECR power at 2.45GHz. Cool ($T_e \approx$ 6 - 10eV) but highly ionized argon plasmas with very reproducible characteristics are generated by discrete dipole/monopole or helical antennae positioned close to the plasma surface. Depending on the magnetic geometry and field strength the antennae can launch either from the high field side (HFS) or the low field side (LFS) of the fundamental resonance surface.

For a LFS launch geometry plasma densities up to 3 to 4 times the fundamental O-mode cutoff density (n_{co} = 7.4×10^{16}m^{-3}) are readily obtainable. With HFS geometry the central plasma becomes highly overdense, up to 4×10^{18}m^{-3}. Plasma density and electron temperature radial profiles are measured by a scanning Langmuir probe at ϕ = 0°. The density profiles change between a narrow strongly peaked profile for a HFS launch to a flat broad profile for a LFS launch. When the resonance layer is close to the magnetic axis at the toroidal position of

the antenna the LFS profile can become significantly hollow. Fig.1 shows four radial profiles at $\phi = 0°$ for different magnetic field strengths (B_m) using a quarter wavelength monopole antenna at $\phi = 75°$ with C = 0.02. Increasing the magnetic field strength moves the resonance field layer past the fixed antenna changing the geometry from a LFS to a HFS launch. This is more clearly seen in figs.2 & 4 where the central density is plotted as a function of B_m for two values of C. The upper and lower field limits coincide with the resonance layer leaving the outside and inside edge of the enclosed volume of the respective last closed flux surfaces. Both the HFS and LFS profiles depart from the 'parabolic' pressure profiles observed with an RF ohmic plasma (400W at 96kHz). The discrepancies appear to result from an enhancement in particle confinement at the plasma centre for the HFS launch and a deterioration for the LFS launch [2].

Fig.3 shows the central plasma density as a function of C for different field strengths B_m (ie LFS & HFS launch). The highest density case is similar to the curve obtained with the RF ohmic system. Around C = 0 ($\iota(0) \approx 1.19$: the standard heliac) the enclosed plasma volume is greatest and the central density highest. The toroidal variation in the flux surfaces is also at its minimum. With increasing C the rotational transform approaches the low order resonance 3/2 ($0.05 < C < 0.11$) which causes the flux surfaces to break up into islands. Consequently the radial density profiles are seen to flatten. As $C \rightarrow +0.16$ the nested flux surfaces reform and the profiles separate out into the peaked and hollow profiles of the HFS and LFS geometries. The LFS curve is much less sensitive to variations in the rotational transform.

Reversing the current ratio decreases $\iota(0)$ and the volume of the closed surfaces. At $C = -0.075$ the flux surfaces break up again as the $\iota(0) = 1$ rational surface and the 3/3 field harmonic resonate. Beyond $C < -0.10$ the surfaces reform with a reduced toroidal variation, but with only $\approx 25\%$ of the plasma volume of the standard case. The central density however fails to recover, and is notably insensitive to the launch geometry or the microwave power. The radial density profiles vary little with B_m and display several peaks (fig. 5). Most of the plasma is confined close to the poloidal ring coil. With the RF ohmic system alone it was not possible to produce breakdown for $C \approx -0.08$ or $C < -0.14$ [3].

For magnetic geometries with well-formed closed flux surfaces the confinement of ECR plasmas is generally good, except for large reverse helical currents (small rotational transform). The deterioration in central confinement for LFS launch geometries which was seen at moderate and high rotational transforms may be associated with the phenomenon of 'density pump-out' [2].

REFERENCES

[1] B.D.Blackwell *et al.* (1989), Aust. J. Phys. 42, 73.

[2] G.D.Conway & B.D.Blackwell (1990), 'Plasma production by first and second harmonic ECR in a heliac geometry', ANU-PRL-PP 89/9 (To be submitted to Plasma Phys. & Contr. Fusion).

[3] X.H.Shi *et al.* (1988), Nucl. Fusion 28, 859

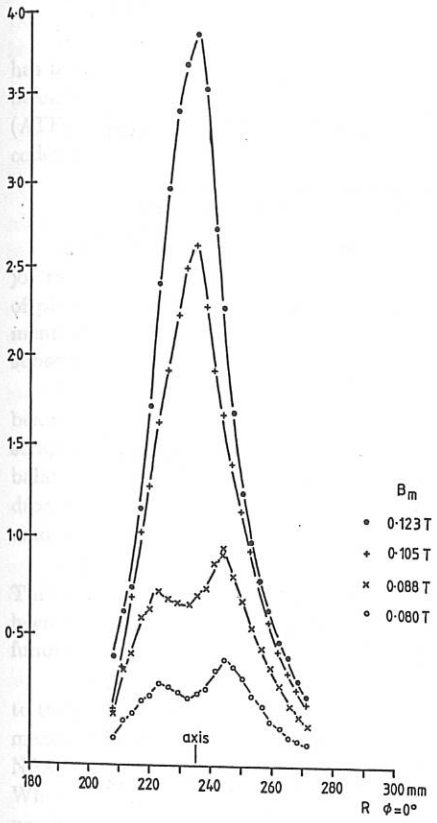

Fig. 1: Radial density profiles for four magnetic field strengths with C = 0.02

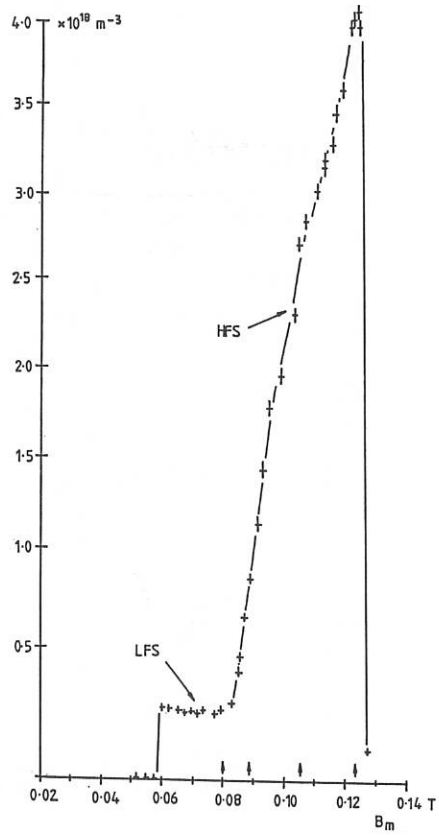

Fig. 2: Central density v. magnetic field strength with C = 0.02

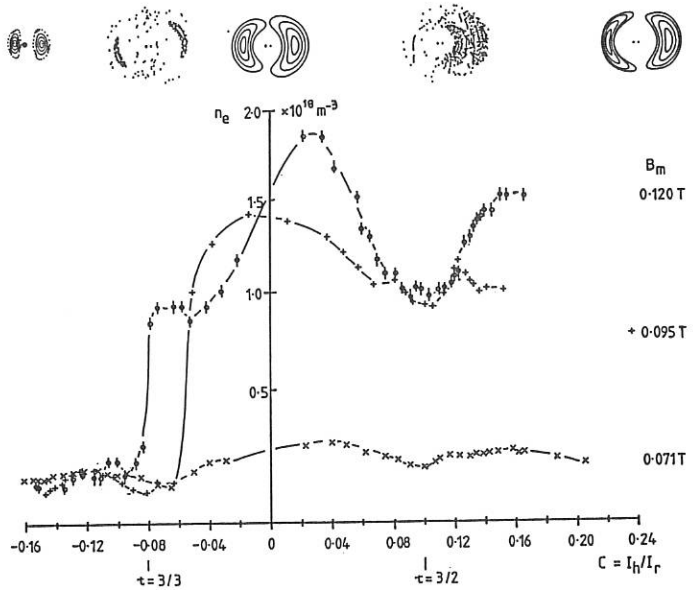

Fig. 3: Central density v. current ratio for 3 field strengths

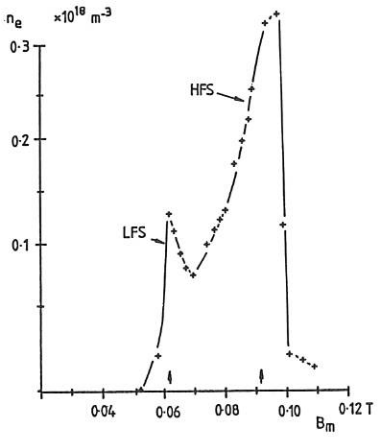

Fig. 4: Density v. field for C=-0.16

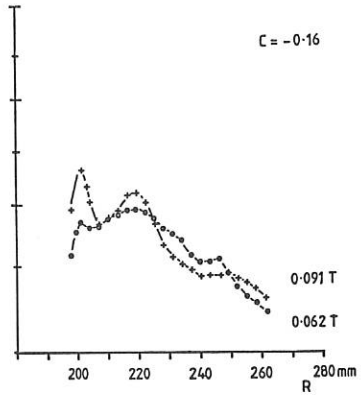

Fig. 5: Radial density profiles for 2 field strengths with C=-0.16

MEASUREMENTS OF THE FAST ION DISTRIBUTION DURING NEUTRAL BEAM INJECTION AND ION CYCLOTRON HEATING IN ATF *

M. R. Wade,[a] R. J. Colchin, G. L. Bell,[b] A. C. England, R. H. Fowler,[c] J. M. Gossett, L. D. Horton, R. C. Isler, M. Kwon,[a] J. F. Lyon, R. N. Morris,[c] D. A. Rasmussen, T. M. Rayburn, T. D. Shepard, and C. E. Thomas[a]

Fusion Energy Division, Oak Ridge National Laboratory, Oak Ridge, Tennessee
United States of America

A neutral particle analyzer (NPA) with horizontal and vertical scanning capability has been used to make initial measurements of the fast ion distribution during neutral beam injection (NBI) and ion cyclotron heating (ICH) on the Advanced Toroidal Facility (ATF). These measurements are presented and compared with the results of modeling codes that predict the analyzer signals during these heating processes.

Experimental Setup

ATF[1] is an $l = 2$, $m = 12$ torsatron with a moderate plasma aspect ratio (major radius $R_o = 2.10$ m, average plasma radius $\bar{a} = 0.27$ m). ATF has three forms of plasma heating: electron cyclotron heating (ECH), NBI, and ICH. For the experiments discussed here, target plasmas were produced using 400-kW, 53-GHz ECH with subsequent heating provided by $\simeq 1.7$ MW of NBI and $\simeq 0.2$ MW of ICH.

The orientation of the neutral beam injectors on ATF is shown in Fig. 1. These beam lines are aimed tangentially, 13 cm inside the magnetic axis to minimize beam scrape-off on the vacuum vessel walls. The opposing orientation of the injectors allows balanced injection with no net momentum input or net beam-driven current. Fast hydrogen neutrals are injected at energies up to 35 keV; the delivered power is distributed among the three energy components in the ratio 75:18:7.

Initial ICH experiments have been carried out using a fast-wave ICH antenna.[2] This antenna is tunable over the 10- to 30-MHz frequency range. Experiments have been conducted with D(H) and D(He^3) plasmas with the frequency adjusted to obtain fundamental resonance with the minority species of interest.

The NPA used on ATF is an $E \| B$ mass- and energy-analyzing spectrometer[3] similar to that used on TFTR. This analyzer has two mass columns (allowing for simultaneous measurements of H and D) with an energy range $0.5 \leq A(amu) \cdot E(keV) \leq 600$. The NPA is mounted on a carriage that allows it to be horizontally and vertically scanned. When the analyzer is scanned horizontally, its viewing angle can be changed from perpendicular to tangential (in both directions) to the axial magnetic field. The vertical

*Work sponsored by the Office of Fusion Energy, U.S. Department of Energy, under contract DE-AC05-84OR21400 with Martin Marietta Energy Systems, Inc.

[a]Georgia Institute of Technology, Atlanta, Georgia
[b]Auburn University, Auburn, Alabama
[c]Computing and Telecommunications Division Martin Marietta Energy Systems, Inc.

scanning capability allows the analyzer to scan from below to above the plasma column in ATF. The location of the NPA and its orientation relative to the neutral beam injectors are shown in Fig. 1.

Neutral Beam Injection

Several horizontal scans of the NPA have been performed during NBI at various densities. These experiments were performed by injecting hydrogen beams ($\simeq$ 35 keV) into a deuterium plasma, thus allowing the NPA to obtain simultaneous measurements of the thermal and fast ion distributions. The hydrogen spectra measured by the NPA at three horizontal angles during a low-density discharge ($\bar{n}_e = 8 \times 10^{12}$ cm^{-3}) are shown as the solid lines in Fig. 2. The three peaks seen in the spectra for angles near tangential ($\phi \simeq 50°$) correspond to the full-, half-, and third-energy components of the injected beam.

In an attempt to understand the fast ion slowing-down processes associated with these measured spectra, a modeling code has been developed that is based on the Fokker-Planck equation for a homogeneous magnetic field and uses the FIFPC code developed at ORNL.[4] This model (1) calculates the fast ion source distribution using appropriate plasma conditions; (2) computes the neutral density profile using a neutrals transport code; (3) uses FIFPC to solve for the ion distribution, given this source function and plasma conditions; and (4) calculates the signal expected to be measured by the NPA by integrating the charge-exchange contributions along the analyzer chord. To simulate the experiment, input parameters to the code were based on experimentally measured values. The electron temperature and density profile were measured at several different times during the NBI portion of the discharge by a 15-channel Thomson scattering system[5]; the temporal evolution of the central electron temperature was monitored by the central channel of a 16-channel electron cyclotron emission system.[6] The central ion temperature was obtained from Doppler broadening of central impurity lines.

The results of this calculation are shown as dashed lines in Fig. 2 along with the measured spectra for three horizontal viewing angles. The agreement is quite good considering that the error bars associated with the calculation are fairly large since several of the input parameters (especially the neutral density profile) are not very well known. The spectra shown in Fig. 2 were obtained 12 ms after initiation of NBI. The agreement between the model and the data is not nearly as good for later times in the beam portion of the discharge. This probably results from the model's inadequacy in handling finite orbit effects (including losses) and radial diffusion of these fast ions.

ICH Experiments

To assess the potential of ICH as an auxiliary heating method for ATF, various measurements were made by the NPA to examine the production of a high-energy tail during ICH and the confinement and thermalization of this tail. The results presented here for the NPA scans were obtained with a D(H) plasma with an on-axis magnetic field of 0.95 T. The ion cyclotron resonance frequency was adjusted to 14.4 MHz so that the fundamental resonance of the hydrogen minority intersected the center of the

plasma.

During these experiments, a high-energy hydrogen tail up to 50 keV was observed by the NPA (see Fig. 3) without any significant bulk heating being observed. The hydrogen concentration in this discharge—as determined from the ratio of the measured line intensities of the Balmer alpha transitions of hydrogen and deuterium—was found to be $\leq 2\%$. The magnitude of the high-energy tail was found to be very dependent on the hydrogen concentration in the plasma. Figure 4 shows the variation of the measured spectra with the measured hydrogen concentration.

The measured spectra were also found to vary as the analyzer viewing orientation was changed. This variation is shown in Fig. 5, where contours of measured flux are plotted versus energy and horizontal viewing angle. Two slightly asymmetric peaks near the perpendicular (90°) are evident. At present, this angular distribution is suspected to be the result of orbit effects associated with the location of the resonance layer. Recent horizontal scans have been made with the frequency changed to 12.8 and 16.0 MHz. There is a clear difference between the angular distributions of the NPA measured flux in these cases.

The existence of a 50-keV ICH-induced tail suggests that there is a class of particles in ATF that can gain energy from the launched wave and still be confined up to fairly high energies. Since the electron density ($\bar{n}_e = 5 \times 10^{12}$ cm^{-3}) and temperature ($T_e = 800$ eV) are fairly low, these particles not only transfer energy to the plasma slowly but also suffer little pitch angle scattering as they slow down. From a heating efficiency point of view, these effects are undesirable, since only a small amount of power is transferred to the plasma; however, from a physics point of view these effects are advantageous, since collisionless orbit calculations can be used. Such calculations are now in progress to determine if orbit effects can explain the observed angular distribution in Fig. 5.

REFERENCES

[1] J. F. Lyon et al., Fusion Technol. **10**, 179 (1986).

[2] F. W. Baity, D. J. Hoffman, and T. L. Owens, AIP Conf. Proc. **129**, 32 (1985).

[3] M. R. Wade et al., "ATF Neutral Particle Analysis System", accepted for publication, Rev. Sci. Instrum. (1990).

[4] R. H. Fowler, J. Smith, and J. A. Rome, Comput. Phys. Comm. **13**, 323 (1978).

[5] R. R. Kindsfather et al., Rev. Sci. Instrum. **57**, 1816 (1986).

[6] G. L. Bell et al., Rev. Sci. Instrum **59**, 1614 (1988).

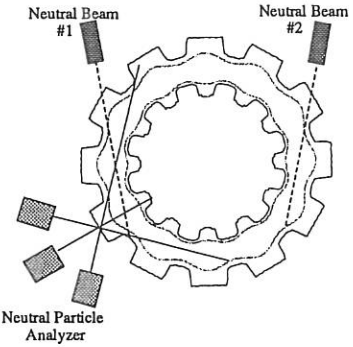

FIG. 1: Orientation of the two neutral beam injectors and the NPA on ATF. Three possible horizontal orientations of the NPA are shown.

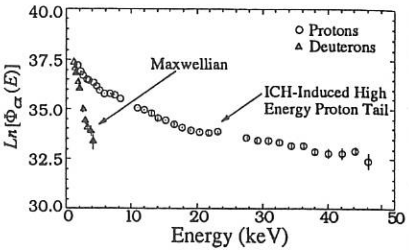

FIG. 3: High-energy proton tail measured by the NPA during ICH in a D(H) plasma ($\eta_H \leq 2\%$).

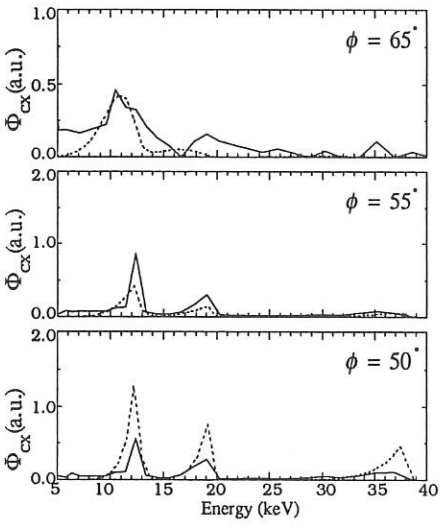

FIG. 2: Measured (solid lines) and modeled (dashed lines) NPA spectra at three horizontal viewing angles 12 ms after beginning of NBI. The horizontal viewing angle, ϕ, is defined such that 90° is perpendicular to the magnetic axis.

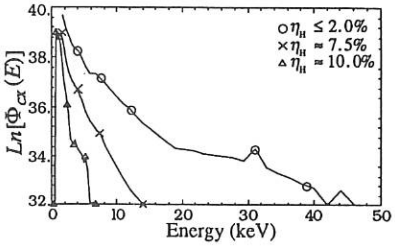

FIG. 4: Variation of the measured high-energy tail with the hydrogen concentration.

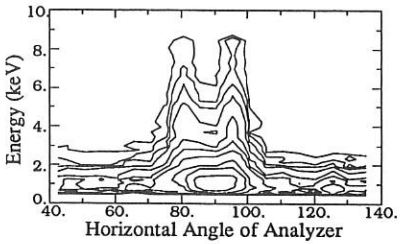

FIG. 5: Contour plot of the flux measured by the NPA versus horizontal viewing angle and particle energy.

BOOTSTRAP CURRENT STUDIES IN THE ADVANCED TOROIDAL FACILITY

M. Murakami, B. A. Carreras, G. L. Bell[1], T. S. Bigelow, G. R. Dyer, A. C. England, J. C. Glowienka, S. Hiroe, H. C. Howe, T. C. Jernigan, D. K. Lee[2], V. E. Lynch[2], S. Morita[3], D. A. Rasmussen, J. S. Tolliver[2], M. R. Wade[4], J. B. Wilgen, W. R. Wing, and the ATF Group

Oak Ridge National Laboratory, Oak Ridge, Tennessee 37831-8072, U.S.A.

ABSTRACT

The toroidal current observed during electron cyclotron heating (ECH) in the Advanced Toroidal Facility (ATF) torsatron is identified as bootstrap current. The observed current ranges between +3 kA and –1 kA with negligible Ohmic heating (OH) and ECH-driven currents. The observed currents agree well with predictions of neoclassical theory in magnitude (to within 30%) and parametric dependence (including the reversal of the current), as determined by systematic scans of quadrupole (shaping) and dipole (vacuum axis shift) moments of the vertical field. These results show that the current flow in ATF is well described by the neoclassical theory of bootstrap current despite the presence of anomalies in particle and heat flows. In addition, the results demonstrate the ability to control the toroidal current with the vertical field for currentless operation in stellarators.

INTRODUCTION

The bootstrap current has attracted substantial attention in toroidal confinement research. In tokamak reactors, it is desirable to maximize the magnitude of the bootstrap current for steady-state operation. In stellarators, it is desirable to achieve currentless operation. Bootstrap currents have been measured in several toroidal devices [1]. In contrast to the previous observations of bootstrap current, the present ATF experiments are aimed at testing the neoclassical theory through direct measurements (in the absence of other current sources) and through scans of controllable machine parameters (in particular, those for the magnetic configuration).

Bootstrap current is driven by viscous drag force between circulating and trapped electrons in a toroidal plasma. Neoclassical theory [2] predicts that, in the low-collisionality limit, the bootstrap current density is given by $j_b = -3(f_t/f_c)\, G_b\, B_P^{-1}\, \nabla p$, where f_t (f_c) is the fraction of trapped (circulating) particles, p is the plasma pressure, and B_P is the poloidal field. The magnetic geometry factor G_b depends on the magnetic field structure, in particular, on harmonic contents of the mod-B (|B|), and it is normalized to that in the axisymmetric tokamak ($G_b = 1$). In a stellarator, the magnetic field contains not only the axisymmetric harmonics, but also helical, and mixed symmetry harmonics. By varying the |B| harmonics, the bootstrap current can be externally controlled. In a plasma of finite collisionality, the bootstrap current decreases with increasing collision frequency. However, the collisionless regime for the locally trapped particles is more easily accessible than that for toroidally trapped particles because of shorter connection lengths (by factor of 1/M, where M is number of field periods). In this regime, the direction of the bootstrap current is opposite

---

[1]Auburn University, Auburn, AL, U.S.A.

[2]Computing and Telecommunications Division, Martin Marietta Energy Systems, Inc.

[3]National Institute for Fusion Science, Nagoya, Japan.

[4]Georgia Institute of Technology, Atlanta, GA, U.S.A.

to that of the usual bootstrap current, since the viscous force with helically trapped particles is relaxed by a flow in the poloidal (rather than toroidal) direction. The reversal of the current direction has been observed in the experiment described below.

EXPERIMENTAL RESULTS AND COMPARISONS WITH THEORY

The ATF device is a moderate-aspect-ratio torsatron with two continuous helical winding, M=12, major radius $R_0 = 2.1$ m, average minor radius $\bar{a} = 0.27$ m, and magnetic field on axis $B_0 \leq 2$ T. In the standard configuration, the rotational transform ι varies radially from 0.3 to ≈1.0. The magnetic configuration can be controlled by three sets of axisymmetric poloidal coils ("vertical" field coils). Variations of the dipole ($\Delta\hat{Q}_{10}$) and quadrupole ($\Delta\hat{Q}_{20}$) moments [3] of the vertical field change the flux surface position and shape, respectively. This occurs in a nearly fixed magnetic field which is primarily determined by the helical field coils, thereby changing the |B| harmonic contents on a flux surface. The present studies are carried out with ECH only in order to avoid the uncertainties resulting from beam-driven current with neutral beam injection. Up to 0.4 MW of ECH power from two 53.2-GHz gyrotrons is used for initiation and heating of the hydrogen plasma.

Figure 1 shows the time evolution of plasma parameters in two discharges with different quadrupole moments of the vertical field. Both the helical and vertical field coil currents reach flat-top >0.5 s before the ECH plasma is formed. The discharge becomes quasi-stationary, at which time the measurements are made. The total toroidal current is measured by a Rogowski coil wound on the inner wall of the vacuum vessel. There is negligible OH loop voltage (average resistive voltage less than 0.01 V). Furthermore, ECH

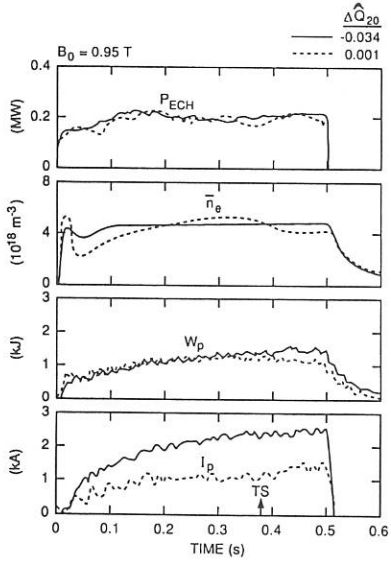

Figure 1. Time histories of plasma parameters in discharges with different quadrupole moments and one gyrotron ($P_{ECH} = 0.2$ MW).

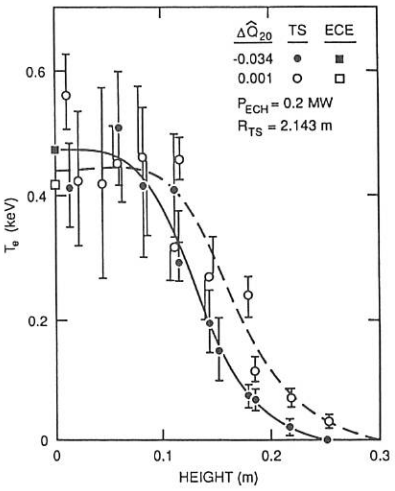

Figure 2. Electron temperature profiles measured with Thomson scattering along a vertical chord at two different quadrupole moments ($P_{ECH} = 0.2$ MW).

current drive is negligible because (1) the microwave power is launched perpendicular to the magnetic field, and (2) the observed current responds to reversal of the helical coil current and to changes in $\bar{n}_e$ in a manner opposite to expectations for an ECH-driven current. More importantly, the results described below confirm the parametric dependences on the vertical field that are expected from the neoclassical theory. The electron temperature profiles shown in Figure 2 are measured from Thomson scattering along a vertical chord in a toroidal plane ($\phi = 0°$) and demonstrate that the vertical elongation of the plasma is indeed decreased with a negative quadrupole moment, as indicated by vacuum flux surfaces calculated from coil currents.

Figure 3 shows the toroidal currents measured (shown by open points) as a function of the quadrupole moment while the dipole moment is kept constant (with the value corresponding to a vacuum axis shift of –2 cm). The observed current changes systematically from positive to negative values, as the quadrupole moment changes from negative to positive values (toward increasing vertical elongation). The theoretical predictions (shown by closed points) are calculated with experimental pressure profiles inferred from Thomson scattering and third harmonic electron cyclotron emission (ECE) measurements. The geometry factor G_b is calculated as in Ref. [2]. An analytical expression for the finite collisionality corrections was obtained by interpolating different collisionality limits and was shown to agree well with numerical results of DKES [4]. The error bars on the theoretical predictions correspond to an uncertainty in effective charge Z_{eff}, which is assumed to be 2.0 ± 0.5. The agreement between experiment and theory is good in magnitude (to within ±30%) and in the dependence on the quadrupole moment, including the reversal of the current.

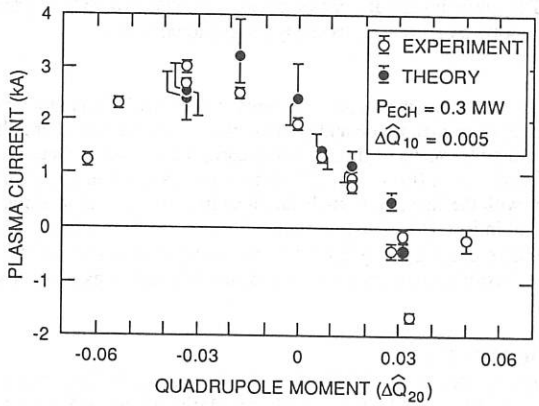

Figure 3. Measured toroidal currents and neoclassical predictions for the bootstrap current as functions of the quadrupole moment (P_{ECH} = 0.3 MW).

Figure 4 shows the bootstrap current measured in a dipole field scan with a fixed quadrupole moment. The results are also consistent with neoclassical predictions. The current increases as the vacuum axis is shifted inward ($\Delta_v < 0$), until it eventually decreases owing to reduction of plasma pressure caused by confinement deterioration. To account for the variation of the plasma pressure, we take a ratio of toroidal current to stored energy (or total plasma pressure). Such ratios are plotted in Figure 5 as functions of the vacuum axis shift for different quadrupole moments and field intensities. The normalized current for

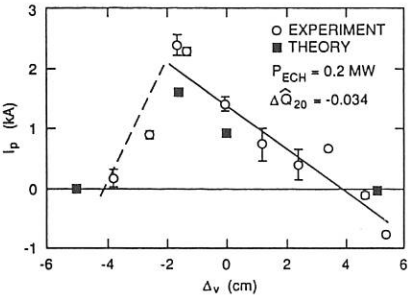

Figure 4. Measured toroidal currents and neoclassical predictions for bootstrap current as functions of vacuum axis shift in the dipole field scan (P_{ECH} = 0.2 MW).

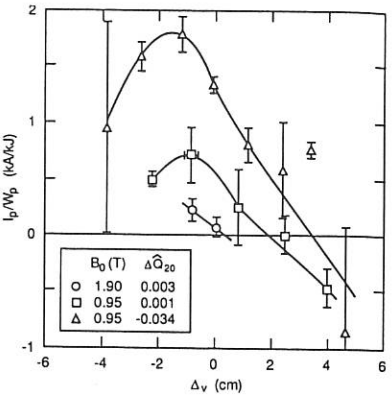

Figure 5. Bootstrap current normalized to plasma stored energy (or total pressure) as a function of vacuum axis shift for different quadrupole moments and helical field intensities (P_{ECH} = 0.2 MW).

operation at 1.9 T is lower by about a factor of two than that at 0.95 T, supporting the assertion that the bootstrap current is inversely proportional to B_0.

CONCLUSIONS

These results show that the toroidal currents in ATF with ECH alone agree well with neoclassical predictions in magnitude and parameter dependence (including the reversal of the current), as determined by scans of dipole and quadrupole moments, field intensity, and total pressure. There is still room (to within 30%) for an anomaly in the bootstrap current. This is not inconsistent with the fact that particle and heat transport are anomalous by larger factors, as predicted in Ref. [5]. The present results also verify the ability to reduce the bootstrap current to zero using the quadrupole and dipole components of the vertical field, demonstrating the feasibility of currentless operation of stellaratores in the low-collisionality regime.

ACKNOWLEDGMENTS

Research sponsored by the Office of Fusion Energy, U.S. Department of Energy, under contract DE-AC05-84OR21400 with Martin Marietta Energy Systems, Inc.

REFERENCES

[1] See, e.g., M. C. Zarnstorff and S. C. Prager, *Phys. Rev. Lett.* **53**, 454 (1984); J. D. Treffert et al., *Phys. Rev. Lett.* **53**, 2409 (1984); S. Besshou et al., *Plasma Phys. Controlled Fusion* **26**, 565 (1984); M. C. Zarnstorff et al., *Phys. Rev. Lett.* **60**, 1306 (1988); U. Gasparino et al., *Plasma Phys. Controlled Fusion* **30**, 283 (1988); M. Kikuchi et al., *Nucl. Fusion* **30**, 343 (1990).
[2] K. C. Shaing et al., *Phys. Fluids B* **1**, 1663 (1989).
[3] G. H. Neilson and J. H. Harris, *Nucl. Fusion* **27**, 711 (1987).
[4] K. C. Shaing (private communication, 1989).
[5] K. C. Shaing, *Phys. Fluids* **31**, 2249 (1988).

IMPURITY TRANSPORT IN ATF AND THE EFFECT OF CONTROLLED IMPURITY INJECTION*

L. D. Horton, R. C. Isler, E. C. Crume, Jr., T. C. Jernigan, and S. Morita†

Fusion Energy Division, Oak Ridge National Laboratory, Oak Ridge, Tennessee
United States of America

The operating window in the Advanced Toroidal Facility (ATF) is limited by the occurrence of a sudden decrease in energy confinement. Although it is clear that the final loss of confinement is due to thermal instability at low temperature, the cause of the initial degradation that reduces the plasma temperature to this low range is not clear. A series of experiments using impurities injected either by a fast gas puffing system or by a laser ablation system has been carried out to study the role of impurities in initiating these collapses of energy confinement.

In the early operation of ATF all discharges that were heated by neutral beams evolved irreversibly towards a loss of confinement. These plasmas can be modeled [1] by postulating an increasing impurity source generated at the time of beam turn-on by fast ion losses, beam scrape-off, or some other mechanism. However, some degradation in energy confinement must be assumed to properly follow the plasma stored energy in theoretical simulations. More recently, with the implementation of strong titanium gettering, it has been possible to generate neutral-beam-injected (NBI) plasmas that achieve an essentially stationary phase and last until the end of beam pulse. This type of plasma is obtained when a large gas puff is applied at the time of the beam turn-on. The line-integrated density and global stored energy are shown for one such shot in Figure 1. The density that can be obtained in these discharges is still limited by the occurrence of rapid losses of confinement. The difficulty in understanding the role of impurities in this process lies in separating the effects of possible changes in the source terms from the effects of changes in the transport coefficients themselves. Injecting impurities using the laser ablation technique provides a known, reproducible source and allows direct measurement of the impurity transport coefficients. For the experiments described here the injected impurities were aluminum and scandium.

The results of these laser ablation experiments have been modeled with the one-dimensional PROCTR transport code [2], which has been modified to solve the full multi-charge-state impurity equations. Presently, the code solves for impurity transport in the proper stellarator geometry using arbitrary values of the diffusion coefficient D and of the convective velocity v, both of which can be functions of the reduced minor radius. To model the electron-cyclotron-heated (ECH) plasmas it was necessary to employ a diffusion coefficient that increased with minor radius. The best fit was obtained with $D = 1000 + 4000\rho^2$ cm^2/s and with $v = 0$. The results of this fit are shown in Figure 2a for aluminum.

*Work sponsored by the Office of Fusion Energy, U.S. Department of Energy, under contract DE-AC05-84OR21400 with Martin Marietta Energy Systems, Inc.

†Permanent address: National Institute for Fusion Science, Nagoya 464-01, Japan.

If the global impurity particle confinement time is defined as the exponential decay time of the total injected impurity density, then for ECH plasmas the simulation gives a global impurity particle confinement time $\tau_p^z = 65$ ms. This is significantly longer than the global energy confinement time, which was approximately 5 ms for these discharges. The results of the fit to the scandium data from NBI plasmas are shown in Figure 2b. For these plasmas it was necessary to employ a centrally peaked diffusion coefficient. In this case the best fit was obtained with $D = 5000 - 4500\rho^2$ cm^2/s. Again, the convective velocity was set to zero. In this case, $\tau_p^z = 40$ ms, which is also longer than the energy confinement time. We emphasize that an impurity particle confinement time deduced from the decay time of central impurity radiation such as Sc XIII would be about twice as long as that defined by global losses.

The difference in the diffusion coefficients deduced for ECH and NBI plasmas is striking. This type of increased transport in the center of NBI plasmas has been deduced previously from measurements of charge exchange emission from helium-like ions of light impurities [3]. Such increased transport substantially alters the ionization balance, especially of light impurity species, and contributes to higher radiation levels. Nevertheless, the total radiated power from both spectroscopic and bolometric measurements is only about 25% of the input power for these beam-heated discharges, which are near the effective density limit.

It is difficult in the simulation to reproduce the absolute levels of radiation from ionization stages in the plasma edge (see Figure 2). Applying a pinch term to lower the edge radiation to a level more in line with the data does not reproduce the observed time behavior of the more central emission. In ATF the edge rotational transform is unity, in contrast to most tokamaks where $q = 3$ at the edge. By the definition of q, poloidal spreading of edge impurities will be smaller in ATF for each toroidal transit. Since the transit time for these impurities is of the order of 1 ms, poloidal asymmetries may be the cause of the overestimates shown in Figure 2 for the emissions from low ionization stages.

In another set of experiments designed to explore the role of impurity radiation in global energy confinement, neon was injected into both ECH and NBI plasmas. The amount of neon was increased in both cases until collapses occurred and then decreased slightly so that the plasma response to a significant perturbation in impurity content could be observed. In the experiment with ECH plasmas, the plasma temperature profile narrows significantly after the neon puff. The radiation from the injected neon is monitored using resonance lines from several different ionization states. The total radiation from the neon increases to about 30% of the input power and remains at that level until, approximately 150 ms after the neon puff, the plasma rapidly returns to its initial, broader temperature profile. This transition results in roughly a factor of two decrease in the neon radiation. The radiation from metallic impurities behaves in just the opposite manner to the neon radiation and to some extent compensates for the increased radiative losses. When the plasma column narrows and the edge temperature decreases the losses resulting from iron and titanium decrease dramatically. This is presumably due to decreased sputtering of metals from the wall owing to a cooler edge plasma. The total radiative losses due to both the neon and the intrinsic impurities are approximately 45% of the input power 150 ms after the neon puff. Slightly greater amounts of injected neon cause the plasma to collapse. It appears that local power balances in the plasma edge

that lead to shrinking of the plasma column can trigger rapid losses of stored energy even in situations where the global power balance, by tokamak standards, is acceptable. Very similar results were found for neon injection into NBI plasmas. Again, the increase in radiation due to the neon is offset by decreasing metal radiation due to the plasma edge cooling. The total radiated power in this experiment was about 25% of the input power.

It is clear from the neon injection experiments that thermal collapses can be generated in ATF by excessive impurity radiation. However, the measured low level of radiated power in beam-heated discharges suggests that impurity radiation does not initiate the confinement degradation that leads to radiative collapse during injection into low-density plasmas. The improvement in performance since the implementation of titanium gettering is thought to result from improved particle control, which allows the specially tailored gas puffing programs required to achieve stationary plasmas. Without such gas puffing programs, discharges heated with neutral beams continue to collapse. The cause or causes remain uncertain, but MHD instabilities and fast ion losses are possible candidates and could lead to the larger impurity transport coefficients required to model the NBI plasmas.

References

[1] HOWE, H.C., HORTON, L.D., CRUME, E.C., HARRIS, J.H., ISLER, R.C., MURAKAMI, M., RASMUSSEN, D., WILGEN, J.B., WING, W.R., Transport modeling of ECH and neutral-beam-heated plasmas in the Advanced Toroidal Facility, in Controlled Fusion and Plasma Physics (Proc. 16th Eur. Conf. Venice, 1989), Vol. 13B, Part II, European Physical Society (1989) 683.

[2] HOWE, H.C., Physics Models in the Tokamak Transport Code PROCTR, Technical Memo ORNL/TM-9537, Oak Ridge National Laboratory (1985).

[3] ISLER, R.C., CRUME, E.C., HORTON, L.D., HOWE, H.C., VORONOV, G.S., Nucl. Fusion **29** (1989) 1384.

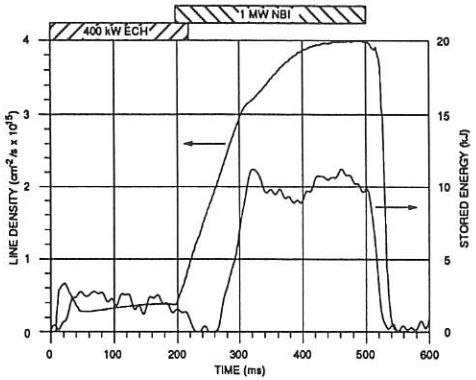

Figure 1: Line-integrated electron density and plasma stored energy as measured by a diamagnetic loop for a quasi-stationary NBI discharge.

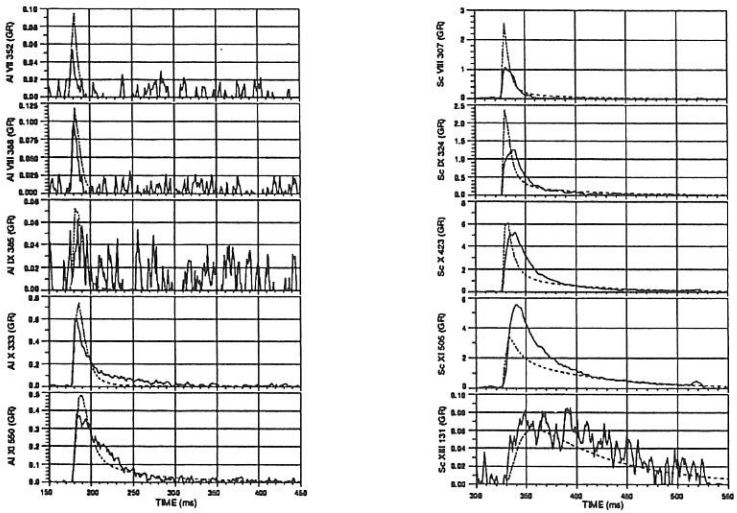

Figure 2: (a) Comparison of measured (solid lines) and simulated (dashed lines) line-integrated emissivities for Al injection into ECH plasmas. The simulation was done with $D = 1000 + 4000\rho^2$ cm^2/s and $v = 0$. (b) Comparison of measured and simulated line-integrated emissivities for Sc injection into NBI plasmas. The simulation was done with $D = 5000 - 4500\rho^2$ cm^2/s and $v = 0$.

TRANSPORT STUDY ON ECH- AND NBI- HEATED PLASMAS IN THE LOW-ASPECT-RATIO HELICAL SYSTEM CHS

H. Iguchi, M. Hosokawa, H. C. Howe[a], K. Ida, H. Idei, O. Kaneko, S. Kubo, K. Masai, K. Matsuoka, S. Morita, K. Nishimura, N. Noda, S. Okamura, T. Ozaki, A. Sagara, H. Sanuki, T. Shoji[b], S. Sobhanian[c], C. Takahashi, Y. Takeiri, Y. Takita, K. Tsuzuki, H. Yamada, T. Amano, M. Fujiwara

National Institute for Fusion Science, Nagoya 464-01, Japan
a) Oak Ridge National Laboratory, Oak Ridge TN#37831, U.S.A.
b) Plasma Science Center, Nagoya University, Nagoya 464-01, Japan
c) University of Tabriz, Tabriz, Iran

INTRODUCTION

Low-aspect-ratio helical systems are attractive due to their potential for high beta operation. However, enhanced neoclassical transport due to strong helical asymmetry is presumed, which might limit the possibility as a reactor-oriented confinement device. Experimental study on the transport in such magnetic configuration is necessary. The Compact Helical System (CHS) [1] is an *l=2, m=8* helical device with an aspect ratio A_p=5 (major radius R=1m, average plasma radius a=0.2m). The plasma is produced and heated by ECH (28GHz/120kW, 53GHz/150kW), ICRF (7.5-18MHz/150kW), and NBI (40kV/1.1MW).

In order to study the radial energy transport, diagnostics for profile measurements with high spatial resolution were prepared. These include Thomson scattering (single point, spatially scannable) for electron density and temperature profiles, visible charge-exchange recombination spectroscopy (34 ch) for ion temperature and poloidal rotation profiles. Radiation loss profiles are measured by a pyroelectric detector array (11ch), which are normalized by a total radiation monitor (a 2π pyroelectric detector). The experiments are carried out mainly with the magnetic axis position at R_{ax} = 94.9 cm, where the magnetic field ripple on axis vanishes[2] and the plasma performance is close to the optimum position around R_{ax} = 92cm. Transport analysis has been carried out using the ORNL PROCTR-mod code with the help of the finite β equilibrium code VMEC [3]. The operational regimes are ranging from a low density, high temperature ECH-heated plasma to a high density NBI-heated plasma.

ECH-HEATED PLASMA

Electron cyclotron heating is applied in three different modes, that is, 28GHz ECH (0.95T/90kW), 53GHz 2nd harmonic ECH (0.90T/150 kW) and simultaneous injection of 28GHz and 53 GHz (0.90T/90kW/150kW). The electron densities are from 0.2 to 2 x 10^{13} cm^{-3}. The highest central electron temperature above 1 keV is obtained in the combined heating with low density operation, where the electrons are in the low collisional $1/\nu$ regime. For the steady state transport analysis, ECH power deposition profiles are necessary. In low density operations, single path

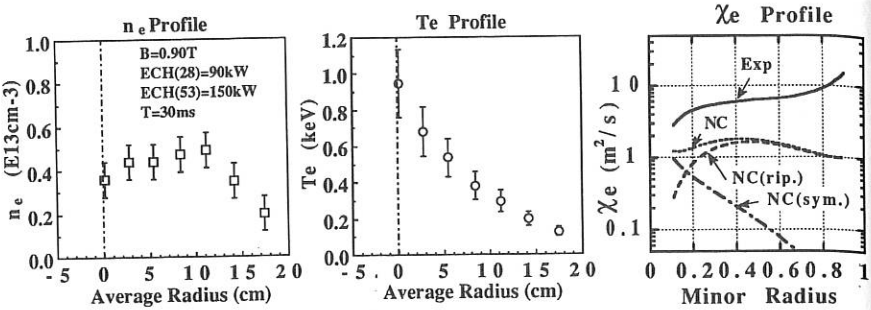

Fig. 1 (a) The electron density and temperature profiles and the electron thermal conductivity in an 1/ν regime of ECH plasma.

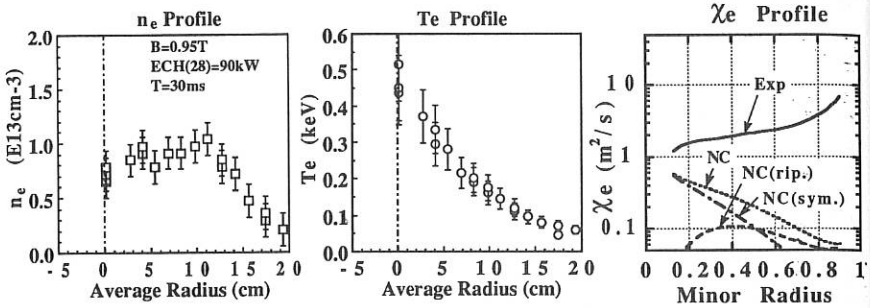

Fig. 1 (b) The electron density and temperature profiles and the electron thermal conductivity in a plateau regime of ECH plasma.

absorption is so low that we assume that the power absorption on magnetic surfaces is proportional to the volume of electron cyclotron resonance layer on those surfaces [4], and a total power absorption is estimated to be 70 % of the port-through power. As for the second harmonic heating, further assumption is added that the heating efficiency is proportional to n_eT_e. This model gives fairly peaked power deposition profile near the center, which is supported by the measurement of the electron temperature decay after ECH turn-off at the center and 1/3 a. A fast decay within 0.2 ms followed by a slow decay with the time scale of the energy confinement time was observed only at the center, which suggests the power absorption to be localized within 1/3 a.

The electron density and temperature profiles and the calculated electron thermal conductivity $\chi_e(r)$ are shown in Fig. 1 (a) and 1(b) for two different operational regimes. One is in 1/ν regime ($\nu^* \leq 1$) with the combined heating and the other is in the plateau regime ($\nu^* \sim 5$) with 28 GHz heating only. A significant similarity in the electron density and temperature profiles is seen in spite of the different collisionality regimes. The neoclassical values are calculated in the code,

which includes only a single helicity helical ripple transport as a non-axisymmetric part. It is shown that χ_e is larger in 1/ν regime and is about 7 m²/sec at 1/2 a. It is about 4 times as large as the neoclassical value. The difference may come from the simplistic ripple transport model in the code and the effect of the drift motion across the magnetic surfaces as is indicated in off-axis electron cyclotron heating [5] which enhances the neoclassical transport in the low aspect ratio magnetic configuration. On the other hand, an anomalous transport dominates at an outer half plasma radius, and χ_e increases gradually towards the edge. In the plateau regime, χ_e profile is similar but the anomalous transport covers all over the plasma radius. The anomaly factor is about 10 at the half plasma radius.

NBI-HEATED PLASMAS

Neutral beam up to 1.1 MW with a single beam line is injected tangentially into the target plasmas produced by ECH or ICH. The experiments are carried out in different toroidal field strength from 0.46 T to 1.5 T. Plasma parameters cover the range of the average electron density of $1 \sim 10 \times 10^{13}$ cm^{-3} and the central electron temperature of 100 ~ 600 eV. Thus the plasmas are all in the plateau regime. The toroidal current in the beam direction up to 15 kA is observed at low density operation, which increases the central rotational transform. While at high density operation the current direction reverses, which is considered to be a bootstrap current [6]. The modification of the rotational transform is not negligible at high current case, but the change in the global confinement is not observed. The effect is neglected in the present analysis. The ion temperature profile and the poloidal rotation profile are available with CXRS using the heating beam. A preliminary analysis on the latter suggests the negative electric field in NBI plasmas, which also is not included in the analysis.

An example of the analysis for 1.5 T is shown in Fig. 2. The power deposition profile in this case is approximated by the birth profile of the fast ions which is calculated in the code. In the co-injection of the beam in CHS, the drift axis of the fast ions shifts outward and the deviation from the magnetic axis is about 6 cm for 40 keV beam at 1.5 T. The broadening of the power deposition profile seems to be significant. The χ_e profile in the core region would be modified when the Monte Carlo simulation gives more reliable power deposition profiles, which is underway. Thus we evaluate the electron thermal conductivity at 2/3 a, which is about 3 m²/sec and is about 20 times larger than the neoclassical prediction. The anomaly in the electron transport is examined in a higher density regime ($n_e(0) = 7 \times 10^{13}$ cm^{-3}, $T_e(0) = 200$ eV, 1.05 T). The results are similar but the anomaly factor appears to be increasing as the electron density increases. On the χ_i profile, the lack of accurate Z_{eff} measurement makes the estimate of the power deposition to the ions more difficult, and the error is larger than that for electrons. However, the calculated χ_i assuming $Z_{eff} = 2$ is the same order as χ_e, and the anomaly in the ion transport is less than that in electron transport.

The experiments are extended to the low field operation at 0.46 T. The electron thermal conductivity evaluated at 2/3 a increases with reducing the magnetic field strength, although the error is larger in low field cases. The volume

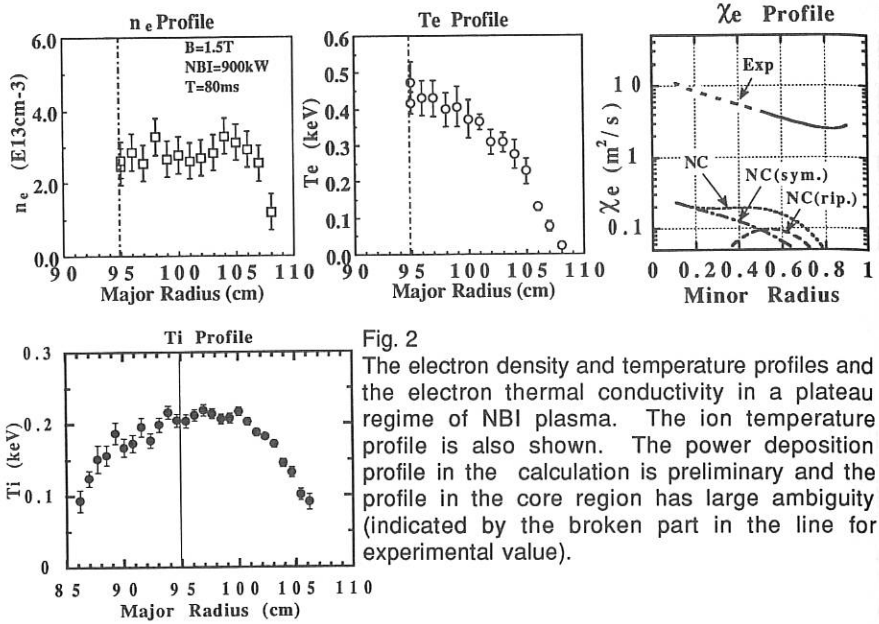

Fig. 2
The electron density and temperature profiles and the electron thermal conductivity in a plateau regime of NBI plasma. The ion temperature profile is also shown. The power deposition profile in the calculation is preliminary and the profile in the core region has large ambiguity (indicated by the broken part in the line for experimental value).

averaged beta value reaches 1.5 % and consistent Shafranov shift is observed. However, the fixed boundary equilibrium calculation is not necessarily agreeable with the measured pressure profile. The orbit shift for the fast ions becomes also larger. Improvements in the calculation are underway.

CONCLUSION

The electron heat transport is studied in the low-aspect-ratio helical system CHS. It is found that the anomalous transport is dominant in both ECH and NBI heated plasmas. However, the anomaly factor is reduced in 1/ν regime of ECH plasma below the factor 4 within a half plasma radius, while in the plateau regime it is about 10 at 1/2 a. The anomaly factor in the plateau regime in high power NBI plasma appears to be larger than that in ECH plasma. For more accurate comparison we must wait for a detailed power deposition calculation for NBI.

REFERENCES

[1] K. Matsuoka et al., Proc.12th IAEA Conf., Nice, 1988, Vol.2, 411.
[2] S. Okamura et al., Proc. 16th EPS Conf., Venice, 1989, part II 571.
[3] H. Yamada et al., to be published in Proc. 1st Toki Conf., Toki, 1989.
[4] S. Kubo et al., ibid.
[5] H. Iguchi et al., to be published in Proc. 7th Intern. Stellarator Workshop, OakRidge, 1989.
[6] O. Kaneko, et. al., to be published in Proc. 1st Toki Conf., Toki, 1989.

CLEANUP AND IMPROVEMENT OF OPERATIONAL PERFORMANCE OF ATF BY CHROMIUM AND TITANIUM GETTERING

R. C. Isler, G. L. Bell, T. S. Bigelow, E. C. Crume, A. C. England, J. C. Glowienka, L. D. Horton, T. C. Jernigan, R. A. Langley, J. F. Lyon, P. K. Mioduszewski, S. Morita†, M. Murakami, D. A. Rasmussen, J. E. Simpkins, J. B. Wilgen, and W. R. Wing.

Fusion Energy Division, Oak Ridge National Laboratory

Introduction

Several improvements have been realized recently in the performance of the Advanced Toroidal Facility (ATF). These have been achieved largely because of expanded employment of chromium and titanium gettering, as opposed to the earliest wall conditioning efforts that relied solely on glow discharge cleaning and baking. Spectroscopic analysis indicates that radiation decreases from as much as 75% to about 25% of the input power between nongettered operation and operation when approximately 70% of the vacuum vessel walls are covered with titanium. Nevertheless, the most important contribution of gettering appears to be the reduction of recycling and of hydrogen evolved from the walls during a discharge, thereby permiting better control of the gas fueling rate. As a result, operational procedures have been developed that allow much higher densities to be obtained than those reached without gettering. The maximum stored energy, confinement time, and line averaged density obtained in ATF to date are: 28 kJ, 25 ms, and 1.2×10^{14} cm^{-3}. In addition, quasisteady operation during neutral beam injection (NBI) into high-density plasmas has been achieved without the evolution to collapse which characterizes the low-density discharges. This paper describes the changes of impurity radiation effected by gettering and compares the behavior of low-density and high-density plasmas when titanium films are deposited over 50% or more of the vacuum vessel walls.

Impurity Radiation

Typical emission rates for strong lines of the major impurities are listed in Table I together with estimates of the total radiated power derived from analysis of the spectroscopic data. Results are shown for a nongettered sequence of discharges in a poorly conditioned vacuum vessel and for four sequences in which chromium and titanium were evaporated with different fractions of wall coverage. The radiation from the low ionization stages of carbon, nitrogen, and oxygen was reduced by factors of 40 to 60 between the nongettered experiment and the experiment in which approximately 70% of the wall was covered with titanium. This result does not indicate that the influx of low-Z ions is reduced by the same factor owing to the nonlinear response of peripheral emissions to changes of plasma conditions.

---

†National Institute for Fusion Science, Nagoya 464-01, Japan.

Charge exchange excitation (CXE) signals, which provide a direct measure of the impurity content in the interior of plasmas, indicated changes of less than 30% of the densities of carbon, oxygen, and nitrogen after the initial gettering with chromium that covered approximately 30% of the wall, although the emissions of the edge ions decreased by factors of 2-5. Titanium gettering, however, reduced the interior carbon and oxygen densities by factors of 2-3. The increase of edge temperature with the reduction of the peripheral radiation from the low-Z impurities is apparent in the concomitant rise of the emissions from the metallic ions to the point where they account for as much as 80% of the radiated power. In these low-density ECH discharges, radiated power scales approximately as $\bar{n}_e$, so that the results shown in Table I imply that chromium and titanium gettering respectively reduce the total radiation at a given density by factors of 1.4 and 2.5.

Table I. Typical radiation (gigarayleighs) from strong spectral lines of several impurities emitted from plasmas heated by 200 kW of ECH after various gettering procedures. Units of $\bar{n}_e$ are $10^{12}/cm^3$, and P_{rad}^{spect} is expressed in kW. Uncertainties in the spectroscopic estimates of total radiated power are ± 25%.

		Coverage			
Parameter	Non-gettered	30% Cr	50 % Cr	50% Ti	70% Ti
$\bar{n}_e$	7.5	4.6	9.2	4.9	6.5
O VI 1032 Å	50	25	42	2.2	1.3
C III 977 Å	12	2.5	10	0.5	0.22
N IV 765 Å	4.5	1.6	1.0	0.05	0.07
Fe XVI 360 Å	0.5	0.8	3.2	1.3	1.2
Cr XIII 328 Å	0.3	1.5	1.3	1.0	0.8
Ti XII 461 Å	-	-	-	2.5	2.5
P_{rad}^{spect}	148	69	116	45	40

Plasma Performance

Figures 1 and 2 illustrate several characteristics for low-density and high-density titanium-gettered plasmas respectively. No additional gas is added during NBI in the low-density case. In fact, the gas puff declines throughout the NBI phase, and any increase in n_e comes from beam fueling or from particles released from the walls. Such plasmas manifest the typical evolution reported previously for nongettered or

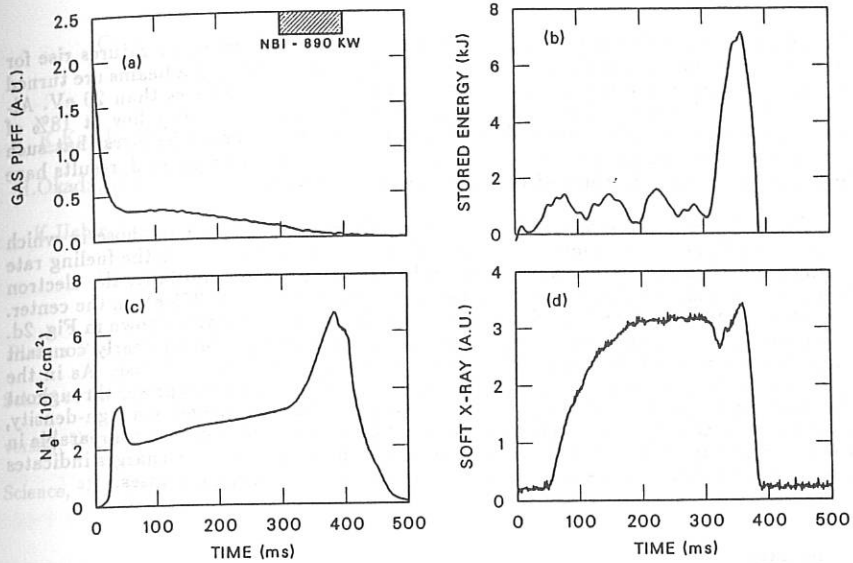

Fig. 1. Typical behavior of several plasma parameters in low-density titanium-gettered discharges. The stored energy begins to collapse at 60 ms after the start of injection. ECH power of 200 kW is applied from 0 to 400 ms.

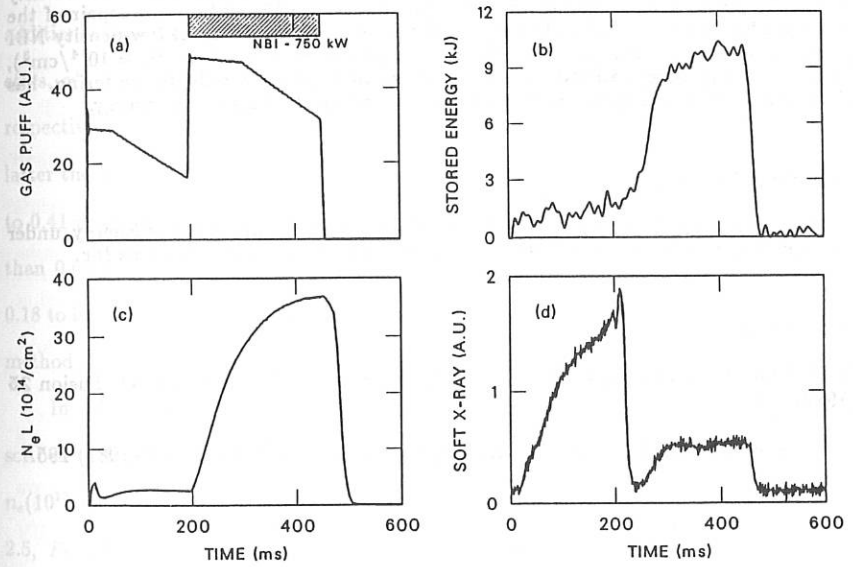

Fig. 2. Behavior of high-density titanium-gettered plasmas fueled by a gas puff at the time of injection. ECH power of 400 kW is applied from 0 to 215 ms.

chromium-gettered plasmas in which the stored energy and ion temperatures rise for about 60 ms after injection begins, but then decay rapidly.[1] After the beams are turned on, the electron temperature falls monotonically from 500 eV to less than 20 eV. Although these plasmas collapse, the radiation level remains relatively low at 18% of the input power up to the peak of the stored energy. Previous conjectures that such behavior resulted partially from field errors[1] have not been substantiated; results have been fundamentally the same after correction of the errors.

The high density discharges have a much different evolution than those in which no additional gas puff is added during injection. Figure 2a shows that the fueling rate is increased strongly at the same time the beams are injected. Initially, the electron temperature cools rapidly, but in the following 50 ms it reheats to 275 eV in the center. The electron temperature behavior is reflected in the soft x-ray signal shown in Fig. 2d. After the reheat, the electron temperature and stored energy remain nearly constant until the end of the NBI pulse with no sign of evolving toward a collapse. As in the low-density case, radiated power remains modest at 25% of the input power throughout the discharges. Without gettering, it has not been possible to achieve such high-density, quasisteady discharges. The fact that the fraction of radiated power is comparable in the neutral-beam phase of both the transient and the quasisteady discharges indicates that global radiation losses are not a primary factor in initiating collapses.

Summary

The total radiated power from ATF has been reduced substantially by gettering. Chromium was not found to be as effective as expected from previous work in the ISX-B tokamak[2], but the use of titanium has led to reductions of the total radiated power by factors of 2.5-3 from the nongettered cases when discharges of similar density and input power are compared. Neither this reduction of radiation nor repair of the magnetic field errors has, by themselves, eliminated the tendency of low-density NBI plasmas to collapse. However, the ability to operate at high densities ($\bar{n}_e \approx 10^{14}/\mathrm{cm}^3$), without unduly large radiative losses, a situation achievable only by gettering, has allowed production of quasisteady plasmas with relatively high stored energy.

Acknowledgement

Work sponsored by the Office of Fusion Energy, U. S. Department of Energy, under contract No. DE-AC05-84OR21400 with Martin Marietta Energy Systems Inc.

References

[1] R. C. Isler, E. C. Crume, L. D. Horton, H. C. Howe, G. S. Voronov, Nucl. Fusion **25** (1989) 1384.

[2] P. K. Mioduszewski, R. C. Isler, J. E. Simpkins, *et al.*, Nucl. Fusion **27** (1987) 195.

CONFINEMENT AND STABILITY ON HELIOTRON E PLASMA

K.Kondo, F.Sano, S.Sudo, M.Sato, M.Nakasuga, H.Zushi, T.Mizuuchi, S.Besshou H.Okada, K.Hanatani, Y.Nakamura, H.Sugama, M.Harada, K.Ichiguchi, K.Muraoka[1)], K.Uchino[1)], K.Matsuo[1)], T.Kajiwara[1)], A.Komori[1)], T.Yamashina[2)], H.Minagawa[2)] H.Matsuura[3)], N.Noda[4)], H.Kaneko[4)], T.Oda[5)], M.Wakatani, T.Obiki

Plasma Physics Laboratory, Kyoto University, Uji, Kyoto, Japan, [1)] Interdisciplinary Graduate School of Engineering, Kyushu University, [2)] Department of Nuclear Engineering, Hokkaido University, [3)] College of Engineering, University of Osaka Prefecture, [4)] National Institute for Fusion Science, [5)] Department of Applied Physics, Hiroshima University

I. Introduction

Heliotron E is an ℓ=2/m=19 helical system and the rotational transform, shear, average plasma radius a_p, and hill or well configuration are controlled by applying the additional toroidal field B_t and vertical field B_v on the helical field B_h [1]. The two parameters, $\alpha^*(= B_t/B_h)$ and $\beta^*(= B_v/B_h)$, change from -0.1 to 0.15, and -0.198 to -0.172, respectively. The former concerns mainly to the size of the magnetic surfaces and the latter the shift of the magnetic axis. The central rotational transform decreases from 0.63 to 0.41 as $\iota(\alpha^*) = \iota(0)/(1+\alpha^*)^2$. The magnetic hill turns to well as α^* increases larger than 0.05 at β^* =-0.185 in the plasma center. The average minor radius is varied from 0.18 to 0.23 m. The change of the magnetic surface was confirmed by the beam-impedance method, Langmuir probes and the thermal Li-beam probe[2].

In this report α^* dependence of the gross confinement property and stability is described. The range of plasma parameters used in the experiment is $0.94 \leq B(T) \leq 1.9$, $1 \leq n_e(10^{13}\mathrm{cm}^{-3}) \leq 10$, $0.3 \leq T_e(keV) \leq 1$, $0.2 \leq T_i(keV) \leq 0.9$, $\langle\beta\rangle(\%) < 1$, $P_{NBI}(MW) \leq 2.5$, $P_{ECH}(MW) \leq 0.6$, $2.14 \leq R(m) \leq 2.24$, $0.18 \leq a(m) \leq 0.23$.

II. Confinement

The dependence of the gross energy confinement time τ_E^G, on α^* and β^* has been analyzed by a 1-D profile analysis/transport-code (Proctor-Mod) with spatially resolved electron density, temperature and ion temperature data[3]. These profiles were measured by a laser Thomson scattering, FIR interferometer and CXRS. In the case of α^*=0, a good confinement region has been already found in 2 cm inward shift of the magnetic axis ($\beta^* = -0.192$) [4]. In this configuration, the deviation of the deeply trapped fast ion orbit from the magnetic flux surface is minimum[5]. Figure 1 shows the dependences of τ_E^G and plasma internal energy W_p on α^* for NBI plasmas at 2 cm inward shift of the magnetic axis. The plasma was produced by 53.2 GHz ECH and further heated by NBI of 2.2 MW port-through power. The magnetic field was 1.76 T for $\alpha^* < 0$ and 1.9 T for $\alpha^* \geq 0$. Increasing α^* from -0.1 to 0.15, the electron density increased from $2 \times 10^{13}\mathrm{cm}^{-3}$ to $6 \times 10^{13}\mathrm{cm}^{-3}$, and profile turned from peaked to broad one, while gas-puff condition was not changed. The electron temperature ($T_e(0) \simeq 500$ eV) and its profile were almost the same in the α^*-scan. The ion temperature decreased from 700 eV to 500 eV. The maximum values : W_p=16 kJ, τ_E^G=9 ms and $n_e(0)\tau_E^G Ti(0) = 3.5 \times 10^{14}\mathrm{cm}^{-3}$ sec eV were obtained at α^*=0.05 and β^*=-0.192.

The particle confinement time τ_p estimated by the laser induced H_α fluorescence and the emission spectroscopy has also revealed the same trend as τ_E^G. The average plasma radius changed as α^* increasing, and it was found that the size scaling of τ_E^G was consistent with the a^2 dependence. The electron thermal conductivity χ_e at $2/3a_p$ decreased at $\alpha^* \simeq 0.05$ and β^*=-0.192. The empirical scaling is very similar to "gyro-reduced Bohm" scaling based on the saturated drift wave turbulence [6], but the radial dependence is different. As α^* increases larger than $\simeq 0.08$ the plasma-wall interaction becomes strong, and emissions of metallic impurities, such as iron, nickel and chromium, increased as shown in Fig.2. The density ratio of iron to oxygen was estimated as 1/50~1/100 by the VUV spectroscopy.

III. Stability

Fluctuations are observed by multi-chord soft X-ray detectors, magnetic probes, FIR interferometer, and Fraunhofer diffraction of CO_2 laser. On the soft X-ray signals, internal disruptions appeared with $\Delta I_{SX}/I_{SX}$ of 60 % at maximum. Figure 3 shows the temporal evolution of the soft X-ray signals along the central chord for various α^* at 2 cm inward shift of the magnetic axis. The inversion radius was close to t=2/3 at α^*=-0.1, and t=1/2 for $\alpha^* \geq 0$. The m=2/n=1 oscillations were found during two successive internal disruptions. For $\alpha^* \simeq 0.03 \sim 0.08$, these internal disruptions were stabilized[7]. Low frequency (8~20 kHz) m/n=1/1, 2/1, 2/3 fluctuations, which are considered as resistive interchange modes, were observed by magnetic probes. These instabilities were also stabilized at $\alpha^* \simeq 0.05$ [8]. Figure 4 shows the amplitude of $\tilde{B}_\theta$ (1/1) at the $\iota = 1$ surface. Density fluctuation with frequency of 20~400 kHz and wave vector of 0.13~1.5 mm^{-1} were measured by Fraunhofer diffraction of CO_2 laser[8]. The observed density fluctuation has a dispersion relation of drift wave type. The low frequency component less than 100 kHz became weak in the range of $\alpha^* \simeq 0.05 \sim 0.1$.

IV. Summary

The optimum confinement region has been found on applying the additional toroidal field ($\alpha^* = 0.05$) and vertical field ($\beta^* = -0.192$), where the m/n=2/1 and 1/1 pressure driven interchange modes were also stabilized.

References

[1] T.Obiki et al., Fusion Technology 17(1990) 101.

[2] T.Mizuuchi et al., 1st Int. Toki Conf. on Plasma Physics and Controlled Nuclear Fusion, Toki, Japan, (1989), VII-29.

[3] F.Sano et al., Nuclear Fusion 30(1990) 81.

[4] H.Zushi et al., 7th Int. Workshop on Stellarators, Oak Ridge, USA, (1989), 03-3.

[5] K.Hanatani, 1st Int. Toki Conf. on Plasma Physics and Controlled Nuclear Fusion,

Toki, Japan, (1989), III-1.

[6] R.Goldston et al., Bull.Am.Phys.Soc. 34 (1989) 1964.

[7] H.Zushi et al., ibid., VII-31.

[8] M.Harada et al., ibid., VII-32.

[9] S.Sudo et al., This Conference.

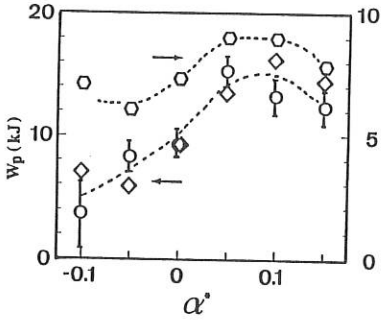

Fig.1 The dependence of plasma internal energy W_p (○: diamag, ◇: kinetic) and τ_E^G (○) on α^*.

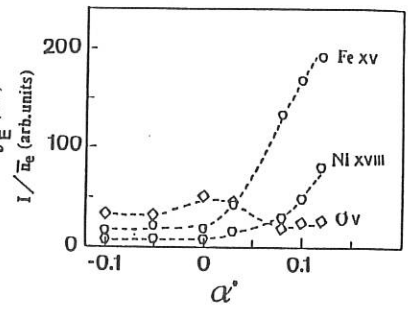

Fig.2 The α^* dependence of impurity line intensities normalized to the average electron density.

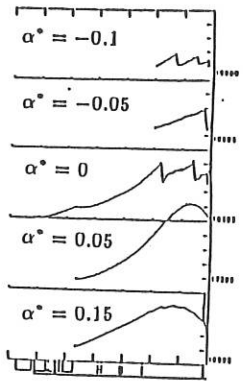

Fig.3 Temporal evolution of the soft X-ray along the central chord for various α^*.

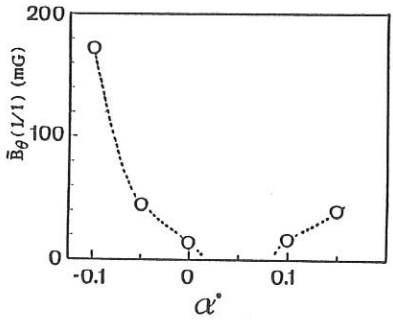

Fig.4 The α^* dependence of the amplitude of $\tilde{B}_\theta$ (1/1) at the $\iota = 1$ surface.

Efficiency of electron-cyclotron plasma heating in the L-2 stellarator.

Andryukhina Eh.D., Dyabilin K.S., Fedyanin O.I.

General Physics Institute , Moscow , USSR

Introduction.

Experiments on ECR heating of a current-free plasma in the L-2 stellarator have shown that this technique makes it possible to produce a plasma with $Te(o)=1keV$, $n<2*10^{13} cm^{-3}$, $Ti(o)=0.1keV$, $\beta(0)=0.5\%$, $\tau_E=3ms$. According to calculations, the absorption of microwave power for such a plasma amounts to approximately 90%, whereas the absorbed power P_{ab} measured from the jump of the diamagnetic derivative did not exceed 50- 60%. The measurements of microwave absorption have shown that the damping length does not exceed 10% of the device perimeter and in the resonance conditions all the power is absorbed. Such an anomalously low absorption of microwave power according to diamagnetic measurements was observed in the case of two different types of microwaves : the ordinary wave at the fundamental harmonic ($\Omega=\Omega ce$) and at the second harmonic of the extraordinary wave ($\Omega=2*\Omega ce$).

In this paper the method for the absorbed power measurements from the plasma diamagnetism is analised. It is well known that this method is based on the energy balance equation

$$dW/dt = P_{ab} - P_c - P_{rad} - P_{cx}$$

where W is the total plasma energy, P_c is the thermal conductivity flux, P_{rad} , P_{cx} - radiative and charge-exchange losses. When the microwave power is terminated , assuming all the losses to remain constant at this moment of switching off, the change of the plasma energy derivative amounts to P_{ab}. The assumption of constant P_{rad}, P_{cx} is clear from direct measurements of these magnitudes and that of constant P_c follows from the measurements of the plasma boundary parameters which is heated by thermal conductivity. The dynamics of W was determined by diamagnetic loops .

Experimental results.

To determine correctly the derivative of diamagnetic flux it is necessary to take into account the effect of the conducting vacuum chamber. In our case this can be done by simple correction formula

$$\left(d\Phi/dt \right)_{true} = \left(1 + \tau_{chamber} * d/dt \right) * (d\Phi/dt)_{measured}$$

which allows to find true magnetic flux time derivative when we know the measured one , $\tau_{chamber}$ - chamber time constant.The importance of incorporation of an auxiliary term

$$\tau_{chamber} * \frac{d}{dt}(d\Phi/dt)measured$$

for determining the absolute magnitude of the derivative jump we are going to illustrate using as example the experiments on plasma heating at the second harmonic (Ω =75 GHz ,B=1.34 T, P_o=200 kW).

After breakdown plasma density becames quasistationary up to the time less then 1ms and electron temperature and plasma energy up to 4-5 ms . The conventional diamagnetic measurements showed that at the beginning of the discharge the magnitude P_{ab} is noticeably higher than in the stationary phase. This peculiarity in the behaviour of P_{ab} is typical for almost all of the heating regimes which differ from each other by the magnitudes of plasma density, the levels of introduced power, the types of waves applyed for heating. Fig. 1 shows the time evolution of the derivative of diamagnetic signal close to the moment of microwave power switching off (the decay time of the power is up to 50 μs). In the same figure there are given the results of processing of this signal incorporating the effect of the conducting chamber*). It is seen that the true magnitude of the derivative jump (it is P_{ab}^{*} in figure) is in this case by 40% higher then measured one. What does this difference mean ?. Such a picture should be observed in the case when there is a certain fraction of plasma with a rather small its life time energy value (less or comparable with $\tau_{chamber}$ value). Let us call this fraction as a short-living component. Namely due to this component there exists the fast decay phase , which can not be detected because of the conducting chamber integration effect. The

*) Time constant $\tau_{chamber}$ is in our case 105-110 μs. It was evaluated both experimentally and theoretically .

energy lossed from the plasma during the fast decay phase does not , as a rule , exceed 5-7% of the whole plasma energy. However the gain P_f of the absorbed power with taking this phase into accoount could, in some cases, be fairly noticeable. As a rule , an essential difference between Pab and $Pab^* = P_{ab}+P_f$ is observed in a quasistationary phase of the discharge only, that is illustrated in Fig. 2. This Fig. shows the time evolution of magnitudes P_{ab} and P_f during the heating pulse when the launched power was P_o=200kW. It is seen that P_f (the microwave power absorbed by a short-living plasma component) at the end of the HF pulse amounts to 30 kW. It is of interest to note that the total absorbed power remains practically constant throughout the heating. This maybe because of the processes of power absorption by thermal and short-living components are competing. The role of this component in the total plasma energy balance is the higher , the the higher is the level of the launched power and the lower is the plasma density. Fig. 3a shows the dependence of P_{ab} and P_f on density at P_o=200 kW , and Fig. 3b shows their dependence on input power at $n = 1*10^{13}$ om^{-3}. Fig. 3c gives the dependence of absorption coefficient $\eta = P^*_{ab}/P_o$ on the magnitude of the input power. This dependence is seen to be week and the absolute magnitude η does not exceed 60 %.

Thus , we have a substantional discrepancy in the absolute values of absorbed power being measured from the microwave damping and diamagnetism. To understand this discrepancy we may assume the following picture. Fast energy decay phase could be accociated with the fast and trapped electrons being localliesed mainly in the region of microwave injection , rapidly escaping this region. Whereas the diamagnetic loops are nonuniformly situated along the perimeter of the torus and in the nearest vicinity of microwave injection these loops do not exist at all. It may be thus expected that the measured energy derivative jump may not include all the power absorbed by these trapped electrons .

Conclusion.

The analysis of diamagnetic measurements during microwave plasma heating in the L-2 stellarator allowed us to discover the existance of a short living plasma component which can absorb a noticeable fraction of the input power . The energy stored in this component is fairly low part of all the plasma energy . This analysis indicates also that for the diamagnetic measurements of fast processes it is necessary to take into account the effect of the conducting chamber which may distort essentially the measured signals.

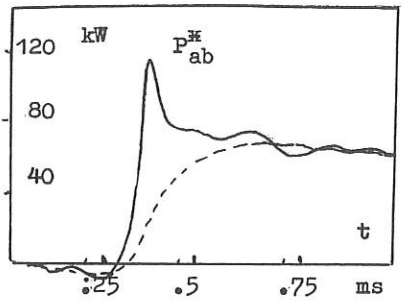

Fig.1

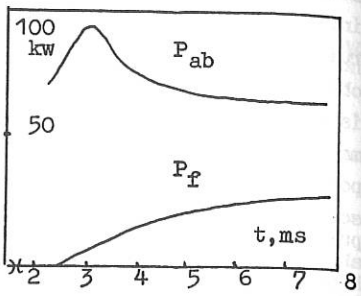

Fig.2

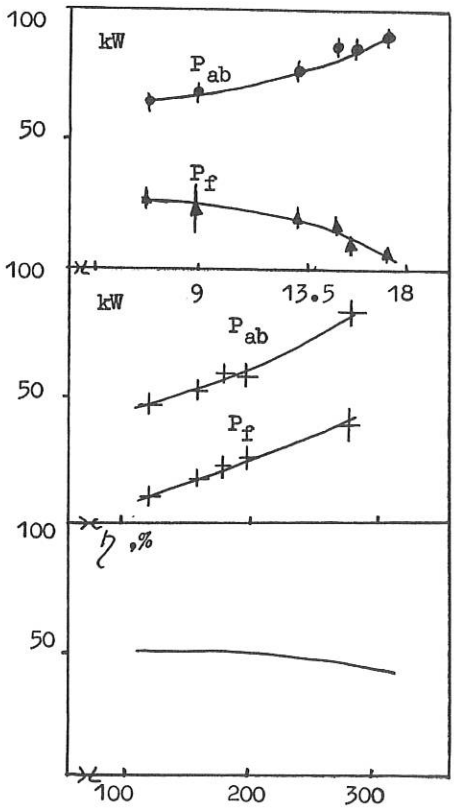

Fig.3

RAY TRACING DURING ECRH BY X-WAVE ON THE SECOND HARMONIC OF ω_{ce} IN L-2 STELLARATOR.

Likin K.M., Ochirov B.D.*

Institute of General Physics, Academy of Sciences
Vavilov street, 38, Moscow 117942, USSR

*Institute of Automation and Electrometry
Siberian Branch of Academy of Sciences
Novosibirsk 630090, USSR

Ray trajectories and absorption of the extraordinary wave on the second harmonic of the electron gyrofrequency ω_{ce} during ECRH were found from well known geometrical optic's equations [1], such that the dispersion expression for a "cold" plasma was used in the ray traccing and the electron temperature took into account in the calculation of absorption coefficient. X-wave on the frequency 75 GHz was launching perpendicular to the toroidal direction ($\bar{k} \perp \bar{B}$) into L-2 chamber from low magnetic field side as Gaussian beam ($E=E\exp(-\rho^2/w_0^2)$, where $w_0=2.75$ cm)

The calculations were carried out under the following plasma parameters: $B(0)=1.26-1.43$ T (Fig.1), $n_e(0)=(1.3-3.5)*10^{13}$ cm^{-3} (Fig.2), $T_e=400$ eV. Profiles of $T_e(r)$ and $n_e(r)$ were taken as parabolic: $T_e(r), n_e(r) \sim [1-(r/a_p)^2]$, where $a_p=11.5$ cm - mean plasma radius. To compare the results of both simulations the absorption coefficient of O-mode on the fundamental harmonic of ω_{ce} depending on a magnetic field and a plasma density are presented in Fig.1,2. The absorption coefficient of X-wave on $\omega=2\cdot\omega_{ce}$ practically is constant in the magnetic field band 1.32-1.36 T and in the plasma density range $(2-3.4)*10^{13}$ cm^{-3} but the maximum of absorption profile is shifted along plasma radius and the absorption power in the centre is changed. On ECRH experiences this finding may be helpful for an investigations of a transport phenomena and a plasma confinement as well as quasi-linear relaxation of

electron distribution function. The central heating (Fig.3) occurs under following plasma parameters: B(0)=1.33-1.34 T, n_e= =2*10^{13} cm^{-3}, $T_e(0)$=400 eV. In this case the absorption profile of X-wave on $\omega = 2 \cdot \omega_{ce}$ is more narrow (characteristic size r_x= =0.2*a_p) than the absorption profile of O-mode on $\omega = \omega_{ce}$ (r_0= =0.5*a_p) [2] and accodingly the absorption in the plasma centre increases from 2-2.5 W/cm^3 (O-mode) up to 18 W/cm^3 (X-mode).

Thus, this simulation is shown the high efficiency of X-wave absorption on the second harmonic of ω_{ce} in the wide ranges of the plasma densities and magnetic fields with posibility to change a location of the heating and the absorption power distribution.

References.

1. Alikaev V.V., Litvak A.G., Suvorov Ye.V., Fraiman A.A. Electron-cyclotron plasma heating in toroidal systems. Proc. of All-Union meeting "High-frequency plasma heating". Gorky. 1983.

2. Likin K.M., Ochirov B.D., Skvortsova N.N. Enegry deposition profiles of simulation of ECRH in L-2 stellarator. Proc. of 15-th Europ. Conf. on Contr. Fusion and Plasma Heat. Dubrovnik, 1988. V.2, p.451.

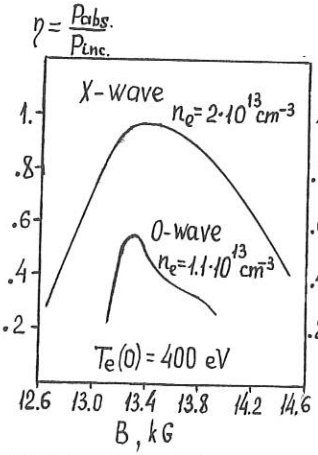

Fig.1 Absorption coefficient via magnetic field.

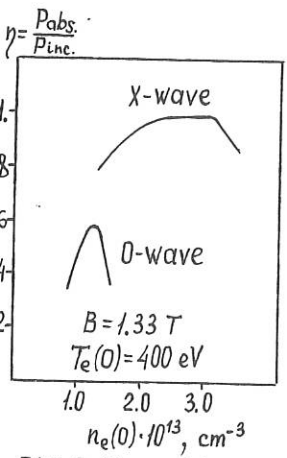

Fig.2 Absorption coefficient via plasma density.

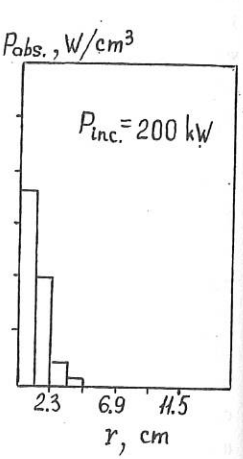

Fig.3 X-wave absorption profile.

ABSORPTION EFFICIENCY OF X-WAVE DURING ECRH ON THE SECOND HARMONIC OF ω_{ce} IN L-2 STELLARATOR.

Likin K.M., Batanov G.M., Kolik L.V., Petrov A.Ye., Sapozhnikov A.V., Sarksyan K.A., Shats M.G.

Institute of General Physics, Academy of Sciences
Vavilov street, 38, Moscow 117942, USSR

Experiences on the electron cyclotron heating of OH plasma by the extraordinary wave on the second harmonic of electron gyrofrequency ω_{ce} ($\omega_0 = 2 \cdot \omega_{ce}$, ω_0 – frequency of heating generator) have been carried out in L-2 stellarator. The current plasma parameters were as following: I_p = 17 kA, $T_e(0)$=300-350 eV, $\bar{n}_e = (0.9\text{-}1.8) \cdot 10^{13}$ cm^{-3} ($\bar{n}_e$ – line average density), B=1.1-1.39 T. The linear polarized wave ($\bar{E} \perp \bar{B}$) with microwave power up to 280 kW was launching from low magnetic field into L-2 chamber.

For the measurements of a single-pass absorption coefficient the one antenna to the inner window as well as the three receiving antennae at the opposite side from the microwave power launching into L-2 chamber were installed. To determine the single-pass absorption coefficient it is necessary to measure an intensities of the pass waves through a plasma column with ECRH (i.e. under those values of magnetic fields when EC resonance is inside a plasma) and without ECRH (i.e. when the resonance is outside a plasma) provided that a profiles and a magnitudes of a plasma densities are the same during the both regimes. The plasma density measurements as well as the measurements of single pass absorption coefficients were made in these experiences. The density profiles in the experiences on ECRH of the current plasma were the same at the magnetic fields from 1.1 T up to 1.39 T and had no change during a microwave pulse. The single-pass absorption coefficients as a function of the magnetic field are represented (Fig.1) for some plasma densities with the incident power 240 kW at the two instants: 1-the beginning of microwave pulse; 2-the pulse end. In the OH plasma the single-pass absorption coefficient on the resonance ($B(0)$=1.33-1.34 T) is equal to 0.8 at the beginning of ECRH and increases up to 0.9-0.95 at the pulse end. The growth of the absorption is connected with the heating of the plasma during a microwave pulse.

An another parameter characterized the absorption of microwave power in a plasma is the damping length of a heating

wave along a torus. A damping length is a distance along a torus on which microwave power decreases at e times. For measurements of a damping length the two receiving antannae were placed in the nearest ports. The X-wave damping length ($l_{damp.}$) on the second harmonic of ω_{ce} is less than 20 cm at B(0)=1.33-1.34 T (resonance) and $l_{damp.}$=150-200 cm at B(0)=1.16 T (nonresonance). The O-mode damping length on the fundamental harmonic is 50-80 cm (the single-pass absorption coefficient doesn't exceed 0.55) on the resonance and $l_{damp.}$=150-200 cm in the nonresonace case.

Thus, the measured single-pass absorption coefficients on the second harmonic of ω_{ce} is close to magnitudes obtained from the ray traccing code [3]. The measurements of damping length are in accordance with measurements of single pass absorption coefficients and show that the total absorption of X-wave on the second harmonic of ω_{ce} takes place near the microwave launching.

References.

1. Erkmann V., Janzen G., Kasparek et.al. Wave absorption and transport studies on ECR heated stellarator plasmas in W VII-A. 10-th Int. Conf. on Plasma Phys. and Contr. Nucl. Fus. Research. London, 1984. IAEA-CN-44/D-I-5.

2. Borshchegovskii A.A., Likin K.M. Location of microwave absorption during ECRH in T-10 plasma. Preprint IAE-4537/7. Moscow, 1987.

3. Likin K.M., Ochirov B.D. Ray traccing during ECRH by X-wave on the second harmonic of ω_{ce} in L-2 stellarator. This conference.

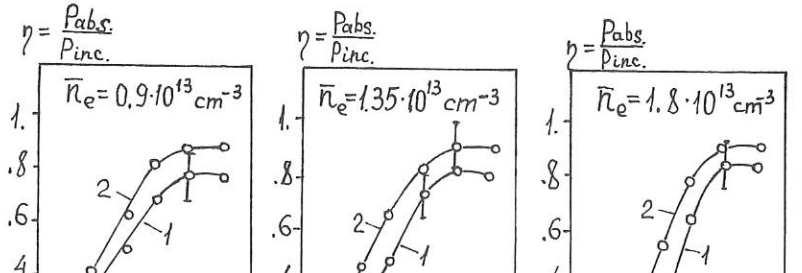

Fig.1 Single pass absorption coefficients.

PARTICLE TRANSPORT AND RECYCLING STUDIES ON THE WVII-AS STELLARATOR

F. Sardei, H. Ringler, A. Dodhy, G. Kühner
and WVII-AS Team
Max-Planck-Institut für Plasmaphysik, EURATOM Ass.
Garching bei München, FRG

ECRH Group
Institut für Plasmaforschung der Universität Stuttgart, FRG

To Professor Rudolf Wienecke on his 65th Birthday

INTRODUCTION

In WVII-AS, ECRH plasmas with central deposition are characterized by peaked temperature profiles but flat or slightly hollow density profiles up to $10 - 12\ cm$, which is more than half of the plasma radius (see Fig. 1). This difference is mainly due to the different radial location and extent of the energy and particle deposition zones, the first being narrow ($1 - 2\ cm$) and peaked at the center, the second broad ($5 - 10\ cm$) and peaked near the edge. In contrast to the energy source, the particle source strength is experimentally unknown, since it is dominated by toroidally and poloidally asymmetric recycling processes. However, the particle deposition profile can be determined by 3D neutral gas transport modelling and the source strength by calibrating the calculations with H_α measurements. Radially resolved particle fluxes and diffusivities can then be obtained from the particle sources and the measured density profiles.

RESULTS FOR 1.25 T DISCHARGES

In order to get information about ion production rates, particle confinement and neutral density distributions, several ECRH discharges at 1.25 T (2^{nd} harmonic X-mode) were analyzed by coupling DEGAS code /1/ simulations with H_α emissions obtained at different toroidal positions. For each discharge, with given Thomson temperature and density profiles at stationary conditions, three simulations were performed according to the three most relevant sources of neutrals (limiter recycling, wall recycling, external gas release). The magnetic-surface-averaged ion production rates, as obtained from the neutral densities and the Thomson profiles, were integrated to give the radially resolved ion fluxes. The electron fluxes were derived from the ion fluxes by adding estimated contributions due to the impurities, for which comparable confinement times as for the background ions were assumed. Neoclassical fluxes, as predicted by the DKES code, were used for comparison.

The radial profiles of the ion and electron fluxes and of the particle confinement time are shown in Fig. 2 for a 1.25 T discharge heated by 350 kW ECRH power (2 gyrotrons). In the central part of the plasma, the deduced electron fluxes are close to neoclassical values, whereas they become strongly anomalous towards the plasma edge. The ion particle confinement time has a maximum of 11 ms in the bulk of the plasma and drops to about 2 ms at the plasma edge, indicating strong recycling in front of the limiters. A comparison of this discharge with a similar one (same $\bar{n}$, same limiter position and comparable plasma density), but with only half of the ECRH power, shows an increase

of τ_p by a factor of two over the whole plasma radius. This is consistent with a similar ECRH power scaling of τ_E found for the same discharges.

The sensitivity of the limiter and wall recycling to the radial position of the limiters was also investigated by comparing two discharges with the limiters placed at the two extreme positions $z = 22$ and $31.5\ cm$ from the equatorial plane (see Fig. 3). If the limiter is fully retracted to the wall, the dominant refuelling (45%) is provided by wall recycling, the limiter contribution being only 20%, which is even less than that of the external gas feed (Fig. 3b). If, however, the limiter is moved deeply into the vacuum vessel, then it accounts for 80% of the ion production (Fig. 3a). In this case, the limiter effectively screens the wall from ion impact. Impact by high energetic CX neutrals, however, is not directly affected by the limiter position. The radial range of the ion production (between 12 and 18 cm, see Fig. 3c,d) is almost the same for the three sources and for the 2 limiter positions. This indicates that the refuelling profiles are mainly affected by the electron density and temperature profiles and only slightly by the limiter position. Between the plasma edge and the wall the electron density and temperature are very small ($n_e \simeq 10^{11}\ cm^{-3}, T_e \simeq 15eV$ from probe measurements) and the ion production is negligible.

For five typical ECRH discharges with r close to 0.5 and with fully retracted limiter, diffusivity profiles were calculated from particle fluxes and density gradients. D was found to range between 3×10^3 and $5\times10^4\ cm^2s^{-1}$. Fig. 4 shows diffusivities for various heating powers, with 1, 2 and 4 gyrotrons as indicated by the index. The strong increase of D towards the plasma edge is similar to that observed for χ_e. In the flat density region up to $r \simeq 10\ cm$, D is undetermined. At larger radii, the density profiles can be explained by diffusive transport only, without the need of an additional "inward drift". At moderate line averaged densities, $\bar{n} \simeq 10^{13}cm^{-3}$, there is a clear deterioration of the particle confinement with increasing ECRH power, a_2 vs. a_1. The same behaviour was found for the electron energy confinement and for the decay time of laser-ablated aluminum. If one compares diffusivities for constant heating power (4 gyrotrons) at low and high line densities ($\bar{n} = 8.5\times10^{12}cm^{-3}$, case b_{4low}, as compared to 1.8×10^{13}, case b_4), there is a clear decrease of D with increasing electron density. A similar improvement of the confinement was found from the decay time of laser-ablated titanium radiation, which could be simulated by diffusivities of 5×10^3 and $8\times10^3\ cm^2s^{-1}$ for high ($\bar{n} = 1.2\times10^{13}cm^{-3}$) and low ($\bar{n} = 7.3\times10^{12}cm^{-3}$) density, respectively.

RESULTS FOR 2.5 T DISCHARGES

The presented 1.25 T results can be compared with those obtained from recent ECRH discharges operated at the full field of 2.5 T (1^{th} harmonic O-mode). Fig.5 shows the diffusivities in the density gradient region $10 < r < 18\ cm$ for 4 Thomson series at full field, heated by 1,2,3,4 gyrotrons, respectively, with average absorbed power of 175 kW each. The bootstrap current was compensated by the OH transformer to a net current of $\simeq 200\ A$. The central electron density was $\simeq 4\times10^{13}\ cm^{-3}$ for all discharges, T_e increased with heating power from 1.4 to 2.4 keV. The density profiles were very similar, but in the 1 gyrotron case the profile was narrower by $\simeq 4\ cm$, which implies smaller densities at equivalent radial positions. As in the 1.25 T discharges, the diffusivities strongly increase from $r = 12\ cm$ up to the edge, suggesting an inverse scaling with the plasma density, as it was found for the thermal diffusivity /2/. A degradation with increasing ECRH power is also found except in the 1 gyrotron case (Fig. 5a), for which a reduction of D due to the small heating power seems to be overcompensated by an enhancement due to the smaller densities in the gradient region. The global particle confinement time at the plasma edge drops from 25 to 5 ms over the given ECRH power scan. A comparison with the 1.25 T

discharges shows a clear improvement of the particle confinement with the magnetic field throughout the gradient region, the average D being about 1/3 of the value in the half field case.

Finally, D is found to be smaller than χ_e (D/χ_e between 1/3 and 1/10) for the analyzed discharges both at 1.25 and 2.5 T.

Concerning the accuracy of the presented results, it should be noted that radially constant Z_{eff} values (increasing from 3 to 6 over the ECRH power scan), as estimated from X-ray continuum measurements, were used to determine the ion densities from the Thomson profiles. This may be a poor approximation of the actual Z_{eff} profiles. Furthermore, the wall recycling sources, as monitored by the H_α emission at the "undisturbed" triangular plasma cross section, may not represent a good average of the global recycling from the entire torus wall. Additional diagnostics are being installed to improve the experimental basis for both estimates.

REFERENCES

/1/ D.B. Heifetz et al., J. Comput. Phys. 46 (1982), 309

/2/ G.Kühner et al., see these proceedings

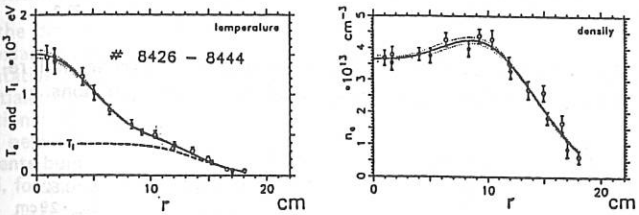

Fig. 1: Typical electron temperature and density profiles for ECRH discharges with central power deposition.

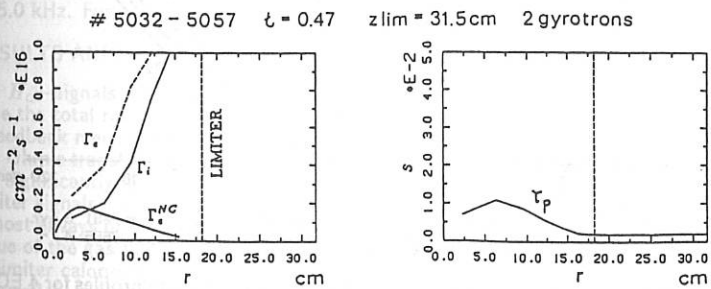

Fig. 2: Ion and electron fluxes and particle confinement time for a typical 1.25 T discharge heated by 2 gyrotrons. Γ_e^{NC}: neoclassical electron flux as obtained by DKES code.

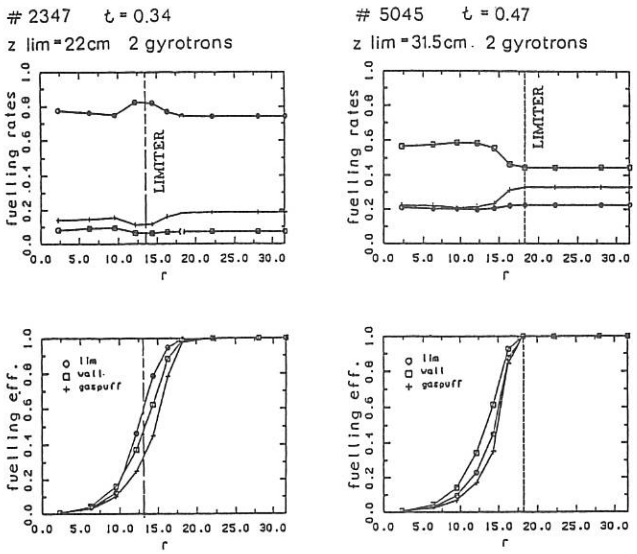

Fig. 3: Fuelling rates and fuelling efficiencies of limiter recycling, wall recycling and external gas feed for 2 different limiter positions.

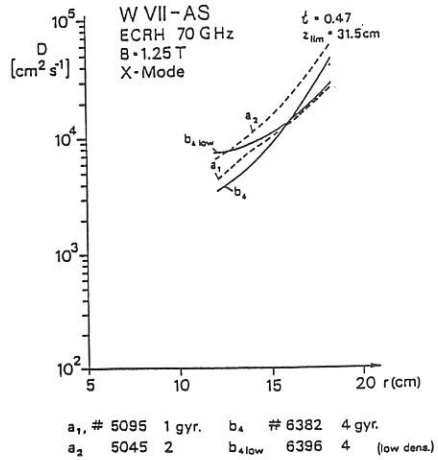

Fig. 4: Dependence of ion diffusivity profiles on ECRH power and electron density for 4 typical ECRH discharges at 1.25 T.

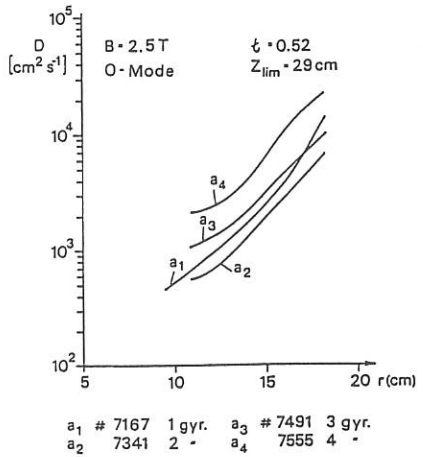

Fig. 5: Ion diffusivity profiles for 4 ECRH discharges at 2.5 T, heated by 1, 2, 3, 4 gyrotrons, respectively, with same central densities.

H_α–SPECTROSCOPY ON WVII-AS

A. Dodhy, G. Kühner, H. Ringler, F. Sardei
and the WVII-AS Team
Max-Planck-Institut für Plasmaphysik, EURATOM Ass.
D-8046 Garching, FRG

ECRH Group
Institut für Plasmaforschung der Universität Stuttgart
D-7000 Stuttgart, FRG

INTRODUCTION

The poloidal and the toroidal distributions of the neutrals were studied for ECR-heated plasmas at magnetic fields of 1.25 and 2.5 Tesla in WVII-AS using H_α–spectroscopy. In this paper the dependence of the plasma confinement on various plasma parameters such as magnetic configuration, heating and density will be presented relating it to H_α–fluxes and fluctuations of the H_α–signal. The H_α–detection system was calibrated absolutely so that the H_α–fluxes could be used directly in a 3D neutral particle transport code for evaluation of the absolute neutral particle densities.

EXPERIMENTAL

As the distribution of the neutrals is generally asymmetric in both the toroidal and the poloidal directions, observations at an arbitrary position could not be assumed to be representative of the entire machine. Consequently, the H_α–measurements on WVII-AS were initially carried out at five positions distributed around the torus for the following observations: (i) top limiter (ii) bottom limiter (iii) the wall between the limiters (iv) the wall near the gas inlet and (v) the wall far from the gas inlet and not disturbed by components built in the machine. The plasma cross-section for observations (i) and (ii) is elliptical, for (iii) a tilted ellipse and for (iv) and (v) a triangle.

The detection system used for the H_α–emission is similar to the one employed at TEXTOR [1]. It consists of the light filtering (transmission maximum at 656.3 nm, bandwidth = 4 nm) and imaging optics, a silicon photodiode and a signal amplifier (gain factor 10). The dynamic range of the detector was 0 - 15 V. The H_α–detector was absolutely calibrated by means of a tungsten filament lamp and the typical calibration factors were $1.0 \cdot 10^{12}$ photons/Volt-sec. The data sampling frequency was generally 2.5 or 5.0 kHz. For several cases 25 kHz was also used.

RESULTS AND DISCUSSION

H_α–signals for an ECR-heated plasma (two gyrotrons) are shown in Fig.1. In this case the total rotational transform, ι, was 0.48, the electron line density was controlled by a feedback mechanism to the gas puffing and the plasma current was kept constant using the Ohmic transformer. From these signals, it is seen that the H_α–fluxes from the limiters are significantly larger than those from the torus wall. Furthermore, the asymmetry of the limiter signals grows as a function of time. With a few exceptions, these asymmetries were almost always present and were dependent on the discharge conditions such as the absolute value of the gas flux. The limiter asymmetries seen in the H_α–signals were also observed in limiter calorimetry measurements [2]. Note, that the difference in the signals between the wall (undisturbed) and those from the wall near the gas puff gives the contribution of the external gasflux to the H_α–signal. Finally, the increase in the H_α–signal at 610 ms at all toroidal positions corresponds to the switching-on of the second gyrotron. As

the H_α−emission is sensitive to fast changes in the particle confinement, this increase is an indication of the deterioration of the particle confinement with increasing heating power although the electron density was decreasing during this phase.

Using signals similar to the ones discussed above, the global particle confinement time, τ_p , was investigated as a function of the magnetic configuration, especially the rotational transform. If the electron line density, $\int ndl$, is taken as a measure for the total number of particles and the H_α−signal for the number of ionization processes in the plasma, then $\int ndl/H_\alpha$−is a relative measure for τ_p. In this case, the ionization of hydrogen is assumed to be the dominating particle source. Figure 2a shows a case where $1/\tau_p$ is plotted for the bottom limiter as a function of ι. The signals are averaged over a time window of 30ms. Results show that the H_α−signal increases as ι approaches the rational value of $1/3$ thus indicating a deterioration of the particle confinement. This supports the well-known result that the plasma energy reaches a minimum at the rational values of ι (see Fig. 2b). Similar results were found at all the other toroidal positions. This behaviour is also found near the rational value $1/2$ of ι.

Another indication for the poor particle confinement was the increase in the fluctuations of the H_α−signal during the transition through the rational values of ι. This is demonstrated by the example in Fig. 3 in which the plasma was heated using one gyrotron (200 kW). Because the electron density approaches the cut-off density for X-mode ECR power launch, the discharge collapses and ι drops very fast below $1/2$ (Fig. 3a). Total energy (Fig. 3b) and density (Fig. 3c) recover again after a slow transition through $\iota = 1/2$. A strong increase of H_α−and an onset of oscillations of the H_α−signal (Fig. 3d) is typical for this phase. The range of ι, where this transition takes place is indicated in Fig. 3. The finite range of ι may be due to a small shear and the apparent shift of the ι scale is attributed to uncertainty in the determination of the absolute ι values.

A Fourier analysis of the fluctuations was made and frequencies up to 2.5 kHz were found. Higher frequencies could not be analyzed due to the sampling frequency used during this discharge. In addition to some low frequency fluctuations (50 - 400 Hz), strong fluctuations were found between 1.8 - 2.5 kHz. Time dependence of the individual frequencies showed maximum fluctuation amplitudes during poor confinement (see Fig. 3e for 2.3 kHz).

A possible explanation for these fluctuations are MHD activities present in the plasma which make themselves visible at the plasma edge when the latter is unstable. In order to pin point the source of these fluctuations, efforts are underway to increase the sampling frequency and to make toroidal correlations.

It should be mentioned that for other discharges investigated in WVII-AS, low frequency fluctuations around 300 Hz were dominant. These are attributed to the ripple on Ohmic transformer and toroidal field used by WVII-AS. Interestingly enough it was observed that the low frequency fluctuations like their high frequency counterparts were also maximum during phases when confinement at the plasma edge was poor owing to the presence of a rational surface.

Other studies included the dependence of the global particle confinement time on the ECR-heating power for various discharge conditions. For all cases, it was seen that τ_p decreases with increasing heating power. Calculations performed for the ion diffusion rates [3] and for the energy confinement times [4] support this result.

Furthermore, the global particle confinement time increases as a function of the electron density. This was investigated for an ECR-heated plasma (750 kW) at 1.25 Tesla and $\iota = 0.31$. As $\int ndl$ was increased from $3.5 \cdot 10^{18}$ to $7.5 \cdot 10^{18}/\mathrm{m}^2$, τ_p increased at least by a factor 1.5 at all the toroidal positions of H_α−observation.

REFERENCES

[1] T.Uckan, ORNL Report, TM-10698, May 1988.

[2] P. Grigull et al., To be published in the Proceedings of the ninth PSI Conference, 21.-25. May, 1990, in Bournemouth, U. K.

[3] F.Sardei et al., see these proceedings.

[4] G.Kühner et al., see these proceedings.

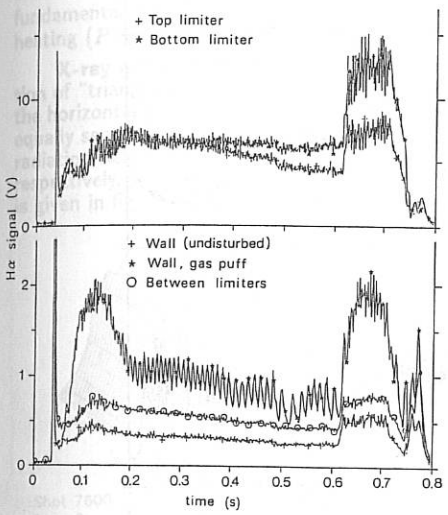

Fig. 1. H_α–signals at five toroidal positions for an ECR- heated plasma. The second gyrotron was switched on at 610 ms.

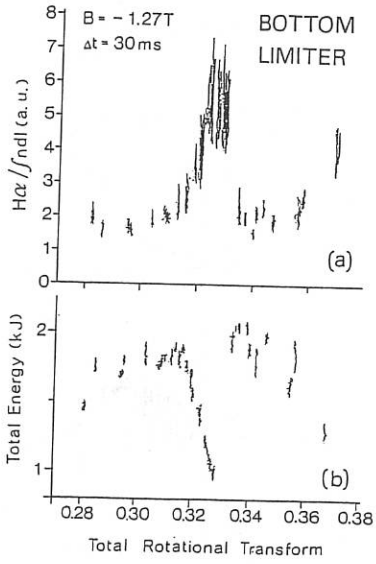

Fig. 2. a) H_α–signal normalized to the electron line density for the bottom limiter as a function of the total rotational transform. The H_α–signal increases as the rotational transform approaches the rational value 1/3, indicating a deterioration of the particle confinement. b) The corresponding deterioration of the energy confinement.

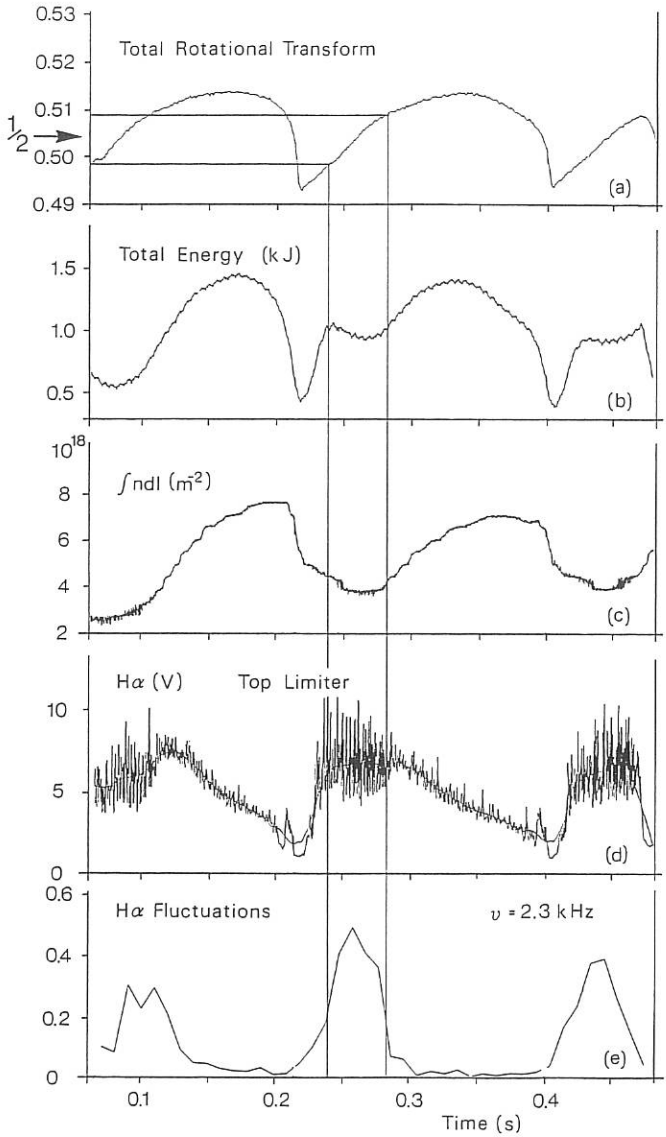

Fig. 3. Global plasma parameters and the H_α−signal as a function of time for an ECR-heated plasma. a) Total rotational transform b) the plasma energy c) the electron line density d) the H_α−signal for the top limiter e) the fluctuations at a frequency of 2.3 kHz.

RESULTS FROM X-RAY MEASUREMENTS ON THE WENDELSTEIN W7-AS STELLARATOR

A. Weller, R. Brakel, R. Burhenn, H. Hacker, A. Lazaros
W7-AS Team, ECRH Group, ICRH Group, NI Group, Pellet Injection Group

Max-Planck-Institut für Plasmaphysik, EURATOM Ass.
Garching bei München, FRG

Introduction - X-ray imaging measurements have contributed to studies of the plasma equilibrium, plasma fluctuations, impurity radiation and impurity transport effects in the advanced stellarator WENDELSTEIN W7-AS (R = 2 m, a = 17 cm). In addition, time resolved electron temperature profiles are deduced from X-ray intensity ratios according to the two absorber foil method. The plasma is generated and heated by fundamental and 2nd harmonic ECRH ($P \leq 800\ kW$ at $70\ GHz$). Neutral beam injection heating ($P \leq 1.5\ MW$) was applied also, assisted by D_2 pellet injection.

X-ray measurements - Two X-ray imaging arrays are installed at the toroidal location of "triangular" flux surfaces. They are inclined by an angle of $\pm 37.4^o$ with respect to the horizontal midplane. Each of the X-ray cameras is viewing the entire plasma along 36 equally spaced lines of sight. A variety of X-ray absorber foils (Be) can be used to suppress radiation below the filter cut off energies or outside the hot central core of the plasma, respectively. An illustration of X-ray intensity profiles and the effect of the absorber foils is given in fig. 1 (data from upper camera).

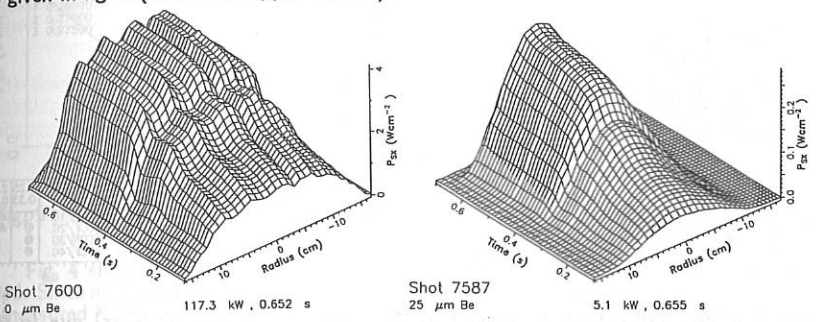

Fig. 1 : *Comparison of X-ray intensity profiles obtained without filter (left) and with 25 μm Be-foil (ECRH at $B_T = 2.5\ T$, $\iota \simeq 0.52$).*

For the electron temperature evaluation another soft X-ray camera system is used, which views the plasma at a toroidal location, where the flux surfaces are elongated in the direction of the observation (almost vertical). The measurements are made at 12 radial positions by a set of 24 large detectors arranged in pairs for intensity ratio determination with foils of different thicknesses.

Equilibrium studies - Generally the X-Ray profiles are consistent with equilibrium calculations based on the GOURDON -, KW - and TRANS - Codes [1,2], if the emissivity is assumed to be constant on magnetic surfaces. Smooth triangular flux surfaces are predicted for the low ι case, whereas at higher ι a clear ripple structure appears on the outer flux surfaces with the formation of a separatrix. This structure is observed in the steady state profiles, if no filter for the radiation is used and most of the intensity is due to very soft radiation ($300\ eV \lesssim E \lesssim 800\ eV$) from the outer part of the plasma. Figure 2 illustrates the agreement between the observed line integrated X-ray intensity profiles

and simulations by assuming constant emissivity profiles on the calculated flux surfaces (fig. 2, right).

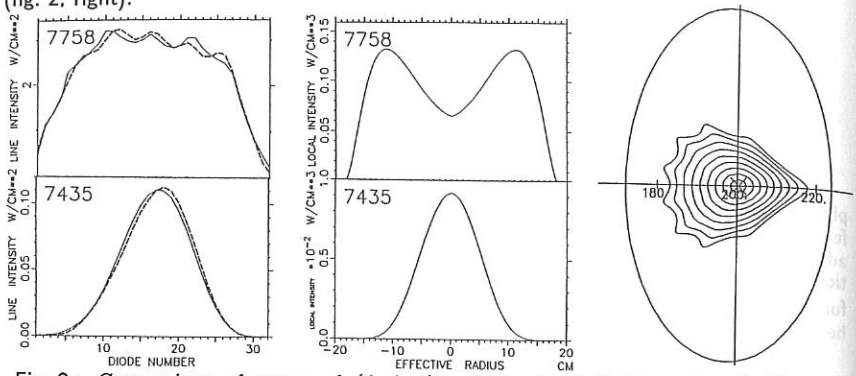

Fig. 2 : *Comparison of measured (dashed) and simulated (full) profiles (left) using a hollow (no filter, top) and a peaked (50 μm Be-filter, bottom) emissivity (middle), constant on flux surfaces (right); ECRH, $\iota(a) = 0.52$.*

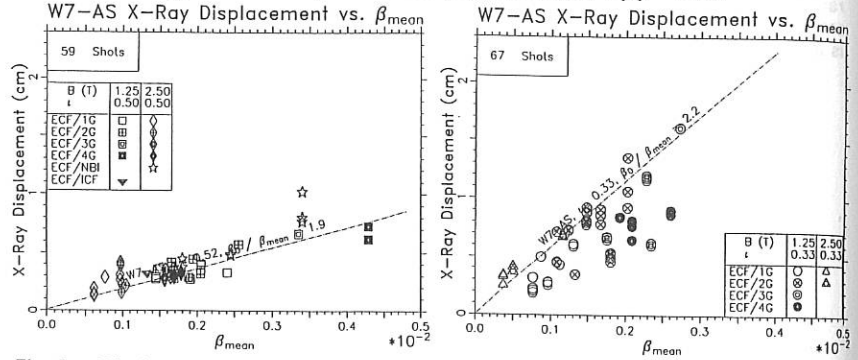

Fig. 3 : *Displacement of X-ray profiles (T_e camera, 125 μm Be-filter) due to the Shafranov shift as a function of $\langle\beta\rangle$. Left: data with $\iota \simeq 0.5$, right: $\iota \simeq 0.33$. Comparison with predictions for W7-AS.*

For W7-AS a reduced Shafranov shift is expected (factor $\simeq 2$) compared with a conventional l=2 stellarator [3]. In agreement with first magnetic measurements a shift of the X-ray profiles depending on β and ι was found as can be seen from fig. 3. The statistical analysis was done using the X-ray temperature camera (125 μm Be filter data) and selecting series of shots for which Thomson profiles were available. The displacement was determined by taking the 1^{st} moment of the profile data at the time of the Thomson measurements subtracting the value obtained at very low plasma energy in the same shot. Fig. 3 also contains the predicted curves for the axis shift for W7-AS.

Impurity studies - X-ray intensity profiles obtained using various absorber foils have been incorporated in the impurity analysis. The code IONEQ [4] calculates the radiation of the main impurities C,O,Fe,Ti including transport, which was modelled based on the STRAHL code [5]. The diffusion coefficients were determined by Al-injection ($D = 1000-2000\, cm^2 s^{-1}$ for ECRH at 2.5 T). The impurity concentrations were evaluated finally by a

least square fit of individual line intensities (SPRED-,Bragg-spectrometers), total radiation (bolometer system) and the X-ray data (central chord and integrated intensities) with the code simulations.

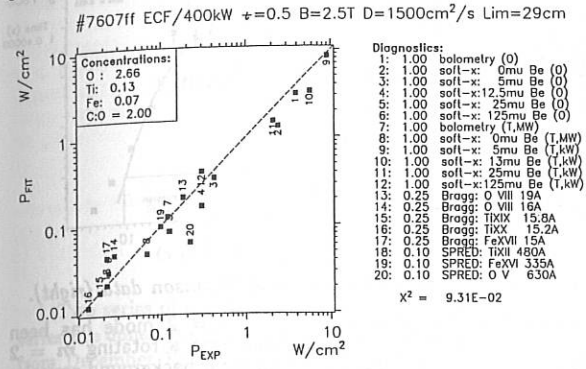

Fig. 4 : *Impurity concentrations obtained from fitting a variety of radiation measurements with code calculations.*

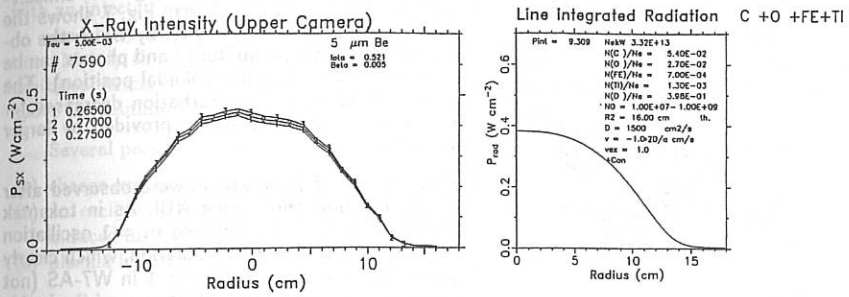

Fig. 5 : *Comparison of measured X-ray profiles (5 μm Be-filter, left) with impurity radiation calculation using the impurity composition as derived in fig. 4.*

Fig. 4 shows the result of this analysis, where 20 different experimental data were used. Since no quantitative measurement for C could be used, a ratio C:O=2 was assumed. A measured X-ray profile is compared in fig. 5 with a simulation taking the fitted impurity composition, which corresponds to $Z_{eff} \simeq 5$. The impurity level increases with the applied heating power and decreases with density. The radiated power is well below the heating power in ECRH plasmas but in high density NBI discharges radiation cooling effects are observed.

Temperature analysis - The electron temperature is derived from comparing the observed intensity ratios (2 different Be-filters) with values calculated by IONEQ. Impurity radiation of C,O,Fe and Ti (including line radiation) are taken into account. At $T_e \gtrsim 1\,keV$ the relative contribution of metals has to be known, since high energy lines become important. Fig. 6 shows the evolution of the T_e profile, which agrees well with the Thomson data, if the metals are included in the calculation.

Fluctuations - Optimized discharges are very quiescent due to the absence of large currents, but mode activity was observed, when the net toroidal current exceeds $\simeq 2\,kA$ and rational surfaces are created inside the plasma.

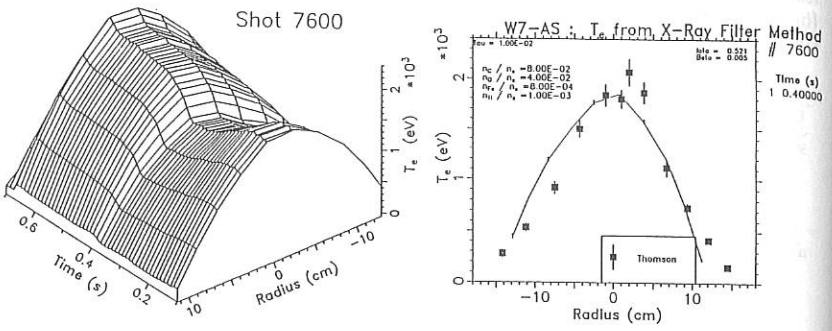

Fig. 6 : *T_e profiles from the 2 foil method, comparison with Thomson data (right).*

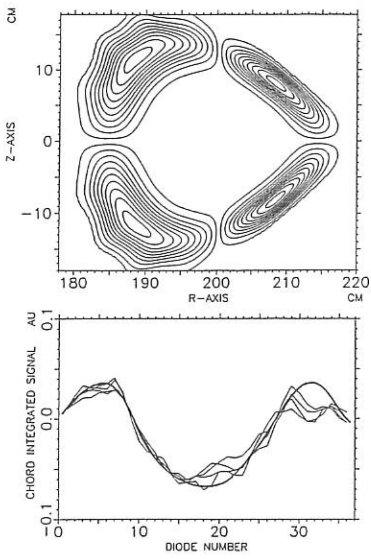

The structure of the $m = 2$ mode has been simulated by superimposing a rotating $m = 2$ component on the constant background emissivity following the flux surfaces. Fig. 7 shows the rotating part of the emissivity, by which the observed modulation amplitudes and phases can be explained (one particular poloidal position). The width of the $m = 2$ perturbation decreases for cases where higher shear is provided by larger currents.

Other types of fluctuations were observed after pellet injection and during NBI. As in tokamak experiments [6,7,8] a damped $m = 1$ oscillation was found just after pellet ablation, which clearly cannot be correlated with $q = 1$ in W7-AS (not existing). In ref. 6 this effect was seen outside or during non-existence of the $q = 1$ surface and attributed to pellet induced density oscillations.

Fig. 7 : *$m = 2$ mode simulation (fluctuating part of profile). Simulated and measured line integrated profiles (bottom).*

References

[1] Kisslinger, J., Wobig, H., in Controlled Fusion and Plasma Physics (Proc. 12th Europ. Conf. Budapest, 1985), Part I (1985) 453.
[2] Sardei, F., Richter-Gloetzl, M., private communication.
[3] Herrnegger, F., 5th Intern. Workshop on Stellarators, (Proc. of the IAEA Technical Committee Meeting on Plasma Confinement and Heating in Stellarators, Schloss Ringberg (FRG), 1984), Vol. 1, CEC, Brussels (1984) 401.
[4] Weller, A. et al., JET-IR-(87)10 (1987).
[5] Behringer, K., JET-R-(87)08 (1987).
[6] Parker, R. et al., Nucl. Fus. 27 (1987) 853.
[7] Kornherr et al., in Controlled Fusion and Plasma Physics (Proc. 14th Europ. Conf. Madrid, 1987), Part I (1987) 323.
[8] Weller, A. et al., Phys. Rev. Lett. 59 (1987) 2303.

FIRST RESULTS WITH NEUTRAL INJECTION INTO W7AS STELLARATOR

W. Ott, F.-P. Penningsfeld, W7AS Team,
ECRH Group, NI Group, Pellet Injection Group

Max-Planck-Institut für Plasmaphysik, Euratom Association
D-8046 Garching bei München

Two series of experiments have sofar been run with the stellarator W7AS. The first series was done with half the magnetic field strength (1.25 T). Neutral injection was applied from December 1988 until May 1989. The maximum plasma energy obtained was 4 kJ with an injected power of 1.5 MW at 45 kV and with pellet injection.

An unexpected phenomenon occurred with discharges carried solely by neutral injection. Mainly the plasma energy, but also the plasma density and the impurity radiation exhibited strong oscillations. The maxima of the plasma energy were up to a factor of 4 above the minima. The frequency was in the range of 10 to 20 Hz.

Several possible causes for these oscillations will be discussed including

(1) charge exchange losses of the injected fast ions,
(2) an oscillating confinement quality of the magnetic field structure due to currents induced in the plasma,
(3) plasma impurity radiation.

In February 1990, the second experimental campaign has begun, now with full field (2.5 T). First short-pulse injections with full power gave a maximum plasma energy of 13 kJ (with strong plasma impurity radiation). One important new experimental degree of freedom is the possibility of injecting helium beams instead of hydrogen beams. Helium beams, injected into a helium or a hydrogen plasma, suffer much less charge exchange losses than hydrogen beams when injected into a hydrogen (deuterium) plasma. In this way, it will be possible to support or exclude the first of the different explanations discussed sofar for the oscillations observed.

Statistical Analysis of Electron Heat Conduction on W7-AS

G.Kühner, H.Maaßberg, H.Ringler
W7-AS Team, ECRH-Group

Max-Planck Institut für Plasmaphysik
Association EURATOM-IPP, D-8046 Garching, FRG

INTRODUCTION

During the first two periods of plasma operation in the Wendelstein 7–AS stellarator most of the discharges were built up and sustained by ECRH at 70 GHz with up to 800 kW input power. Since in the earlier one the magnetic field strength was restricted to 1.25 T, 2^{nd} harmonic heating (x-mode launching) with average densities between $7 \cdot 10^{18}$ and $2 \cdot 10^{19}\ m^{-3}$ was extensively investigated. The more recent experiments were performed using 1^{st} harmonic heating at 2.5 T (o-mode) with densities up to $4 \cdot 10^{19}\ m^{-3}$.

Within the experimental range of the plasma parameters (heating power P_{ECF}, electron density n_e and temperature T_e, rotational transform ι and toroidal magnetic field B_0), a statistical description of the local electron heat conductivity, $\chi_e(r)$, resulting from the energy balance analysis is given by regression methods. Such formulae are used as a basis for model calculations, but they reveal also global parameter dependences and may give some insight into the mechanism of the enhanced electron energy transport. Additionally, these local χ_e formulae can be converted to global energy confinement times, τ_E. If a sufficient database is available, the statistical analysis of local transport is much more powerful than the usual global scaling of energy confinement times. Furthermore, for comparing present stellarator (W7-AS, ATF, Heliotron-E) and tokamak experiments of quite different size, a statistical formulation of the electron heat conductivity is very useful.

DATA ANALYSIS

About 30 series of discharges with 2^{nd} harmonic ECRH as well as about 20 series of 1^{st} harmonic ECRH are included in the database for the statistical analysis. The electron heat conduction was determined by a direct fit of the electron energy balance equation to electron temperature and density profiles measured by Thomson scattering (see Fig.1). For these discharges, electron heat conduction was the major loss channel, radiation and electron-ion coupling played only a minor role.

The χ_e, T_e, n_e profiles as well as global parameters like P_{ECF}, B_0, ι_a at the plasma edge were stored in a database system. Only discharges with central ECF power deposition which is highly localized were taken into account since the database for off-axis heating is not sufficient. For each profile a radial range of confidence was specified to avoid the influence of uncertainties at the profile boundaries. Nonlinear regression was employed for the determination of the parameter dependences. Using this method correlations between regression coefficients can be kept under control and also complicated parameter expressions can be tested.

The regression was tested for different intervals in minor radius and it turned out that a simple regression ansatz was inadequate for the central plasma interval with $r < 5\ cm$. In this region, two types of discharges were distinguished: a) discharges at very low collisionalities (with peaked T_e) which are dominated by neoclassical transport (high ripple losses in the $1/\nu$-regime), b) discharges at higher collisionalities for which no central

peaking in χ_e was found and for which the neoclassical χ_e was small compared to the experimental one over the whole plasma radius. As the neoclassical T_e-dependence is very strong, these two types of discharges could not be treated by a an unique regression ansatz indicating a quite different parameter dependence for χ_e in the central region. For the gradient region with $r > 5\ cm$ where all neoclassical χ_e are small compared to the experimental ones, the analysis gives reasonable results, therefore, the plasma center with $r < 5\ cm$ was excluded from the statistical analysis. The most significant parameters turned out to be $n_e(r)$, P_{ECF} and B_0, as the corresponding regression coefficients were large compared to their variances. This parameter combination was chosen to be the "best fit", the resulting formula is given below:

$$\chi_e{}^r = (0.79 \pm 0.07) \cdot P_{ECF}^{0.685\pm0.03} \cdot n_e{}^{-1.05\pm0.03} \cdot B_0{}^{-0.71\pm0.13}$$

(with T_e in keV, n_e in $10^{20}m^{-3}$, P_{ECF} in MW, B_0 in T). The quality of this regression result is demonstrated as a $\chi_e{}^r$ vs $\chi_e{}^{exp}$ plot in Figure 2. Including the electron temperature $T_e(r)$ and the edge value of the rotational transform, ι_a, improved the χ^2 of the fits only slightly. The corresponding regression coefficients were rather small and comparable to their variances while the other regression coefficients for $n_e(r)$, P_{ECF} and B_0 remain nearly unchanged.

The most remarkable effect was that $\chi_e(r)$ is better described by the global parameter P_{ECF} than by the local one, $T_e(r)$, the latter having a nearly vanishing regression coefficient. So the local heat conductivity seems to be determined by the global heating and not by only local effects.

In the same way experimental χ_e-scalings (e.g. W7-A: $\chi_e \sim n_e{}^{-1}T_e{}^{-2/3}$ for OH discharges and $\chi_e \sim n_e{}^{-1.7}T_e{}^{0.6}$ for ECRH) as well as theoretical approaches (see e.g. [1]) were tested. The results, however, were negative; none of the quoted formulae is capable of describing the electron heat conductivity found in W7-AS .

This analysis would be incomplete without a cross check of the χ_e formula for consistency with the global energy confinement time, τ_E. Therefore, τ_E was estimated by solving the electron energy balance equation for each regression ansatz, the results were related to the experimental τ_E. This cross check is shown in Figure 3 for the regression based on the combination of $n_e(r)$, P_{ECF} and B_0. The energy content based on the χ_e-regressions depends sensitively on deviations to the experimental χ_e at outer radii which may be influenced by the topology of magnetic surfaces at values of the rotational transform close to low order rational numbers. Nevertheless, the regressions excluding the heating power dependence underestimate the energy content typically by a factor of 2, while the other regressions result in a very reasonable agreement.

A similar analysis can be done by deriving analytical expressions for τ_E . Solving the energy balance equation for χ_e^r in an approximative way, one obtains:

$$\tau_E^r \approx \frac{3 \cdot a^2}{8 \cdot 0.79} < n_e >^{1.05} \cdot B_0^{0.71} \cdot P_{ECF}^{-0.685}$$

The parameter dependences are similar as in the formula of the LHS group [2] which was already anticipated by a direct comparison of the experimental τ_E to the latter relation.

DISCUSSION

The heating power dependence of χ_e can be qualitatively understood from the energy balance equation where radiation and ion heating is neglected for the discharges with

dominant electron heat conduction

$$-n_e \chi_e \left(\frac{\partial T_e}{\partial r} \right) \approx \frac{1}{r} \int_0^r S_{ECF}\, r\, dr$$

with S_{ECF} being the ECF power deposition profile. Typically, the density profiles were flat and very broad. The shape of the T_e profiles did not change very much on variation of external plasma parameters (see Figure 1), the temperature gradient was only little affected by the heating power. These experimental findings reflect the basic physics of the electron energy transport, the parameter dependence of $\chi_e(r)$ follows directly from the energy balance equation: the strong relation of $n_e \cdot \chi_e$ to the heating power becomes obvious. The statistical significance shows this to be a general trend in all ECF heated discharges where electron heat conduction is the dominant loss channel.

The observations just made can not be done by a study of the energy confinement time. As the analytical expression for τ_E above shows, the information on the temperature profile shape gets lost as only the global parameter dependencies remain.

CONCLUSIONS

Formulae of the electron heat conductivity for ECF heated discharges in W7-AS were derived based on statistical regression methods. They differ markedly from a parametrization found for W7-A for Ohmic discharges. The explicitly found ECF heating power dependence may be understood as owing to a roughly constant temperature gradient. Future work should answer the question whether this effect can also be found at higher densities using different heating methods.

The resulting energy confinement times are rather insensitive to the regression model used for the electron heat conductivity. Consequently, the statistical analysis of local electron heat conduction is much more significant than global scalings of energy confinement time.

REFERENCES

[1] W. Horton et al., IAEA-CN-50, Paper DIV-3, IAEA Conference (Nice), 1989
[2] S. Sudo et al., Nucl. Fusion **30**, p. 11, 1990

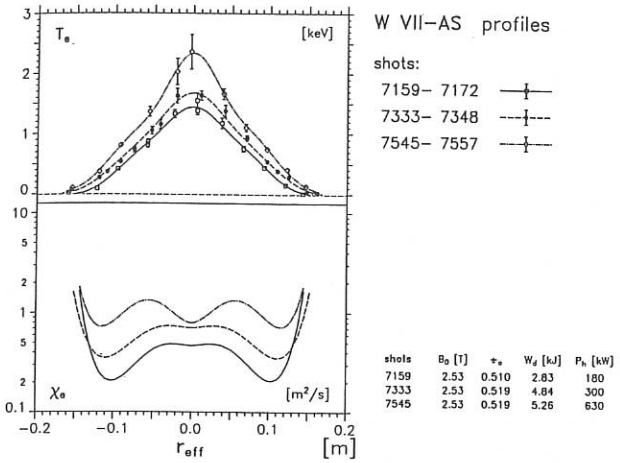

Fig. 1: Electron temperature profiles and heat conductivities, χ_e, for a power scan (1, 2 and 4 gyrotrons) at equivalent densities.

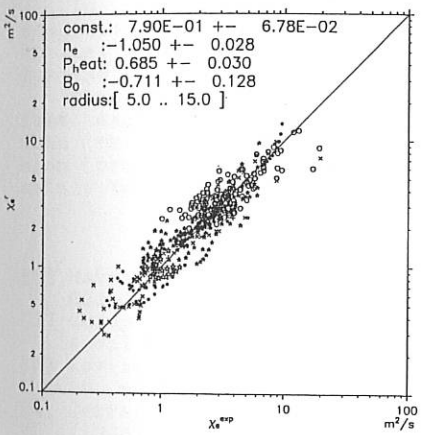

Fig. 2: $\chi_e{}^r$ vs $\chi_e{}^{exp}$ plot as a significance test of the $\chi_e{}^r$-regression ansatz with $n_e(r)$, P_{ECF} and B_0.

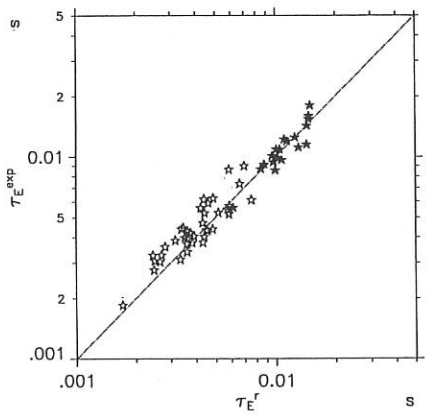

Fig. 3: Test of the global energy confinement time, τ_E^r obtained from the χ_e-regression with $n_e(r)$, P_{ECF} and B_0. Black and white symbols correspond to B_0=2.5T and 1.25T.

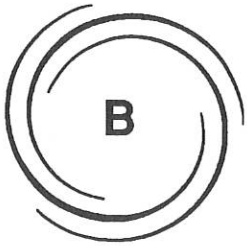

STELLARATORS

B2 THEORY

TWO-ION ICRH HEATING IN THE FLEXIBLE HELIAC TJ-II

Miramar Blázquez José Félix.
Area de Ingeniería Nuclear. Escuela Técnica Superior de Ingenieros Industriales.Universidad de Zaragoza. 50015 Zaragoza.

The object of this work consist of the determination of the power RF by volume unity that is necessary for the ICRH plasma heating in a Stellarator of the Flexible Heliac TJ-II type [1]. This dispositive is being built at the CIEMAT (Madrid, Spain) [2].

The ICRH heating corresponding to the Stellarator has been studied recently in some works [3], [4], in which a significant heating has been verified. This heating can be obtained by using the fast magnetosonic wave.

Starting of the components of a hot plasma dielectric tensor [5], the plasma dispersion equation is solved. The components of plasma refraction index and the local components of the wave vector are calculated. From recent works [6] about local dissipation of the wave power in an inhomogeneous plasma, the energy absortions of ions at cyclotron resonance and at first harmonic have been calculated. The absorbed energy by the electrons which is due to the Landau and the Transit Time effects has been calculated too.

In order to perform the calculations we need to know an adecuate expession about the static field of the Stellarator. At last we can obtain the RF power by volume unity necessary for the ICRH heating.

When the concentration of minority ions is high [7] the fast magnetosonic wave is converted into an Bernstein wave. When this one is low the absortion of energy in the conversion process is negligible and the absortion energy is due mainly to cyclotron damping of minority ions [8].

REFERENCES

[1] Harris, J.H. et al. Nucl. Fusion. Vol. 25, nº5, (1985),pp 623-629.
[2] Guasp, J. Association JEN/EURATOM. CIEMAT. Madrid. Spain. April 1986.
[3] Kovrizhnykh, L.M. Plasma Phis. and Contr. Fusion. Vol. 30, nº2, (1988).
[4] Carreras, B.A. et al. Nucl. Fusion. Vol. 28, nº 9. (1988), pp. 1657-1659.
[5] Alejaldre, C. and Guasp, J. Nucl. Fusion. Vol. 27. nº 12. (1987), pp. 2153-2160.
[6] Brambilla, M. and Krücken, T. Plasma Phys. and Contr. Fusion. Vol 30, nº8. (1988),pp 1083-1092.
[7] Hwang, D., Colestock, P., Phillips, C. "The Theory of minority species fast magnetosonic wave heating in a Tokamak Plasma". Ed. Gordon and Breach. New York. (1985) pp. 1-55.
[8] Tennfors, E. Plasma Phys. and Contr. Fusion. Vol. 28, nº9B. (1988). pp. 1483-1498.

INFLUENCE OF TJ-II FLEXIBILITY UPON ECRH

F. Castejón, C. Alejaldre and A. L. Fraguas

Asociación EURATOM/CIEMAT para Fusión.
28040, Madrid. Spain.

THE TJ-II FLEXIBILITY

The TJ-II is a l =1, m=4 stellarator. One of the main properties of this shearless device is its flexibility: Changing the currents in the circular and helical coils which form its hard core, the value of the vacuum magnetic field will vary and, hence, the properties of the magnetic configuration obtained will be very different [1]. In fact, the rotational transform per period can vary in a wide interval: $0.22 < \iota(0)/4 < 0.628$. The range of magnetic configurations achievable in this machine is presented in the flexibility diagram (see figure 1). The lines of constant rotational transform are plotted. As we go to the origin following a line, we obtain a configuration with deeper magnetic well and with less average minor radius. The depth of the magnetic well can reach the 6 %.

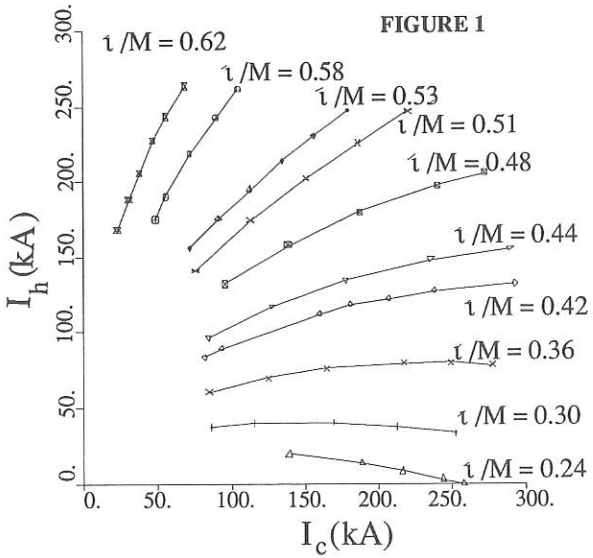

The relevant geometrical properties of the plasma are indeed changed. The average minor radius vary in the range of $10 < a < 25$ cm, the plasma position and the indentation of the magnetic surfaces are very different from a magnetic configuration to another. Besides, the resonance position in the plasma, which corresponds to the B=1 T line, changes. The

value of the magnetic flux and, so, the electron density and temperature are different. Then, it is clear that any calculation which lays on the plasma geometrical properties, like ECRH computation by ray tracing, should take into account this fact and so, any study should be extended to all the configurations.

In this paper, we present the ECRH calculations for two configurations. The first one is the "reference case", which corresponds to a rotational transform per period $\iota(0)/4=0.37$, an average minor radius a=20 cm. As can be seen in figure 2, the magnetic surfaces have a small indentation. The second case is characterized by its high rotational transform $\iota(0)/4=0.55$, its average minor radius is a=17 cm and, as it can be seen in figure 4, its magnetic surfaces have a bigger indentation.

THE RAY TRACING CALCULATIONS

The wave injection conditions considered are the same for both cases: X mode waves at second harmonic (f=53.2 GHz) are launched. The electron density and temperature at the magnetic axis are $n_0=1.4 \times 10^{19}$ m^{-3} and $T_0=0.8$ keV.

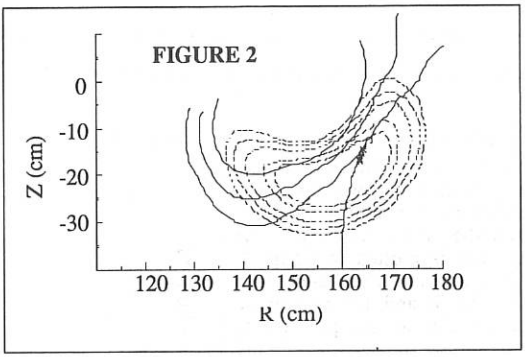

The VMEC equilibrium code has been adapted to the TJ-II device and its results are used as input to obtain the plasma characteristics [2]. Each magnetic surface is calculated using its Fourier representation.

The absorbed power is computed following the eikonal theory and using a weakly relativistic model for the dielectric tensor, which has been adapted to the ray tracing code RAYS [3]. The dispersion relation used to calculate the ray path is the cold plasma one.

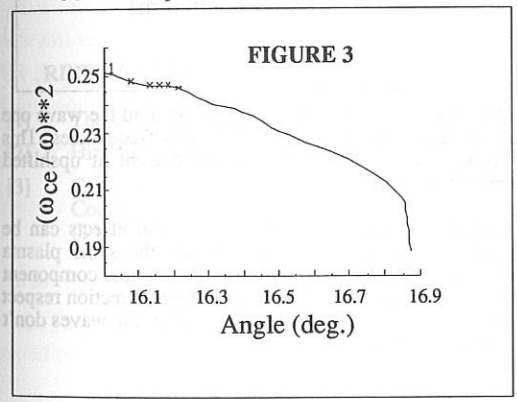

Up to now all the ECRH calculations for TJ-II have been performed for the "reference case" and we have obtained an optimal injection position. This corresponds to a toroidal angle of 16.8 deg. and wave launching from low filed side, in an interval of poloidal angles between 0 and –100 deg. approximately.

The results presented in figure 2 correspond to the -90 deg. poloidal angle in which the injected power is fully absorbed.

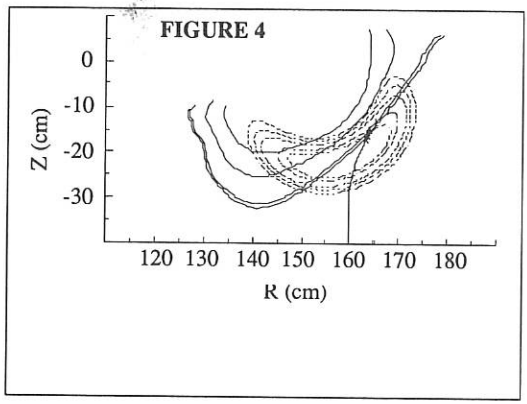

This launching situation has the advantage that the wave vector is almost perpendicular to the magnetic surfaces and that the toroidal component of the magnetic field is much bigger than the poloidal one. Hence, the refraction effects are not very important, as can be seen in figure 2. The ratio between the resonant frequency and the injection frequency is shown in figure 3, where it can be seen that absorption happens at upshifted frequencies. The power is absorbed in oblique regime for $N_{||}$ about 0.2 and the absorption takes place in an area in the plasma where the density is maximum, so the absorption coefficient is quite big.

We consider now the high rotational transform case and the same launching conditions. The results don't change very much from the "reference case". The ray path is plotted in figure 4. The absorbed power reaches also the 100 % and the absorption occurs also at oblique regime ($N_{||}$ varies between 0.17 and 0.22). In this case, the resonance takes place in an area where the plasma density is not maximum and so, the absorption index is smaller than in the "reference case". This makes the resonant area be wider.

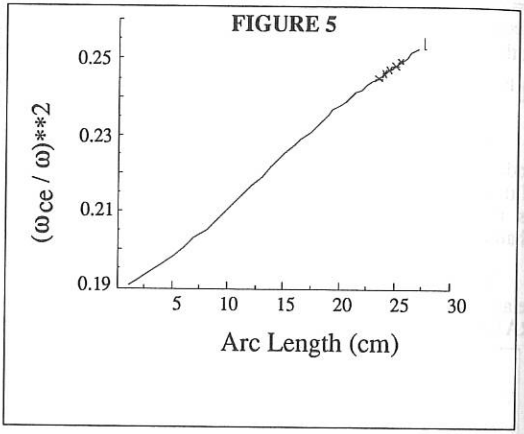

As can be seen in figure 5, where the ratio of the resonant frequency and the wave one is plotted, the absorption takes place at both upshifted and downshifted frequencies. This result has some repercussions for current drive, since the induced current at upshifted frequencies are opposite to the induced at downshifted ones.

An important property of this new configuration is that the refraction effects can be much more important. We have plotted in figure 6 the ray path for the same plasma parameters and for poloidal injection angle of 0 degrees. In this case the poloidal component of the magnetic field is important and we are launching waves in an oblique direction respect to the magnetic surfaces. The result is that the ray path deviates as much as the waves don't reach the resonance layer and the obtained absorption is 0 %.

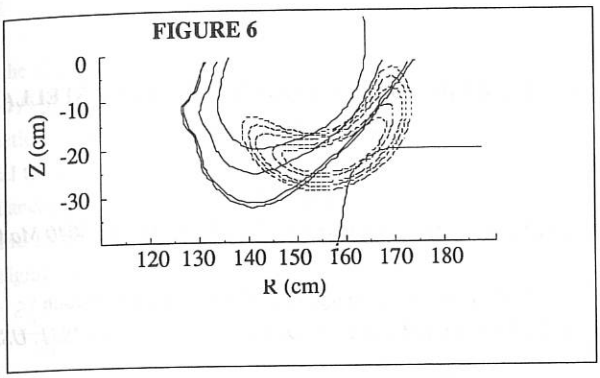

CONCLUSIONS

Unpleasant surprises can come from the flexibility properties of TJ-II. The plasma characteristics can change drastically from a configuration to another. The most important being the position of the resonance layer, the plasma size, the shape of the magnetic surfaces and even the plasma position. The magnetic field is also very different and, particularly, the poloidal component can be important in some cases. Indeed, all this things modify the wave propagation and absorption properties.

In order to keep good ECRH results along all the flexibility diagram it is necessary to choose an injection position which depends as less as possible on the plasma modifications. The refraction effects should be minimized to ensure that the waves always reach the the resonance layer.

In this work it has be shown that the launching situation corresponding to a toroidal angle of 16.8 deg. and a poloidal angle of -90 deg. (or its mirror symmetric situation at a toroidal angle of 73. 2 deg.) satisfies these conditions.

REFERENCES

[1] The TJ-II Team. IAEA Workshop in Stellarators. Oak Ridge, Tennessee (1989)

[2] Hirshman et al., Comput. Phys. Comm. 43 (1986) 143.

[3] C. Alejaldre, F. Castejón and M. J. Taboada. Proceedings of the 17th European Conference on Controlled Fusion and Plasma Physics. EPS, part III, 1115. Venice (1989)

IDEAL INTERCHANGE STABILITY BOUNDARIES FOR STELLARATOR CONFIGURATIONS

L. Garcia
Universidad Complutense and Association CIEMAT-EURATOM. 28040 Madrid, SPAIN

B.A. Carreras, N. Dominguez, J.N. Leboeuf, V.E. Lynch
Oak Ridge National Laboratory. Oak Ridge, Tennessee 37831, USA.*

The dominant fixed boundary instability in stellarator configurations is the interchange mode. Since this instability is localized in radius even for low-n modes, the Mercier criterion [1] has been the main practical approach for studying the stability properties of three-dimensional systems. An alternative way of calculating the stability properties of low-n modes is the use of the stellarator expansion technique [2, 3]. It has been shown that the low-n modes with resonant surfaces lying in a Mercier unstable region are unstable most of the times for configurations with moderate and high aspect ratio [4]. The critical beta given by the Mercier criterion is always lower than the critical beta for the lowest-n unstable mode.

Recently, we have derived a set of reduced MHD equations to study linear stability in general toroidal configurations by applying the averaging method to an equilibrium represented in a straight field line coordinate system [5]. The flux coordinates used are those described by Boozer [6]. We take the exact 3-D equilibrium as the lowest order of the expansion, being the toroidal curvature exact to all orders. To carry out the stellarator expansion, we assume the standard ordering of the basic stellarator parameters: $\beta \sim \varepsilon \sim 1/M \sim \delta^2 \ll 1$, where $\varepsilon = a/R_0$ is the inverse aspect ratio, M is the number of toroidal field periods, and δ measures the strength of the helical field relative to the toroidal field. For the derivation of the equations, we do a multiple scale expansion. The perturbed quantities can be considered as functions of ρ, θ, ϕ, t, and $M\phi \equiv y$. We can separate them in terms of slowly and rapidly varying parts in ϕ, $A = \langle A \rangle_1 + \left(\tilde{A}\right)_1$, where the slowly varying term in ϕ is given by

$$\langle A \rangle_1 = \frac{M}{2\pi} \int_0^{2\pi/M} A\left(\rho, \theta, \phi, t, y\right) dy$$

In order to reduce the MHD equations to a readily tractable set, we eliminate the fast MHD

* Operated by Martin Marietta Energy Systems, Inc., under contract DE-AC05-84OR21400 with the U.S. Department of Energy.

scale [3], i.e., the time scale for the propagation of the Alfvén waves across the magnetic field, namely, $\tau_A = a/V_A$, where V_A is the Alfvén speed. Consequently, the perturbation in the toroidal magnetic field will be neglected, and Faraday's law reduces to an evolution equation for the poloidal flux. The fluid velocity can be written in terms of a stream function and the momentum balance equation can be reduced to an equation for the vorticity.

Taking the toroidal average in y, we obtain the reduced set of MHD equations for stellarator configurations expressed in terms of the equilibrium flux coordinates:

$$\frac{\partial \langle \tilde{\Psi} \rangle_1}{\partial t} = -B_0 \left(\mp \frac{\partial \langle \Phi \rangle_1}{\partial \theta} + \frac{\partial \langle \Phi \rangle_1}{\partial \phi} \right)$$

$$\rho_m \frac{\partial \langle U^\phi \rangle_1}{\partial t} = -\frac{1}{\rho} \frac{\partial \langle \tilde{\Psi} \rangle_1}{\partial \theta} \frac{\partial}{\partial \rho} \left\langle \frac{J^\phi}{D} \right\rangle_0 + \frac{1}{\rho} \frac{\partial \langle \tilde{\Psi} \rangle_1}{\partial \rho} \frac{\partial}{\partial \theta} \left\langle \frac{J^\phi}{D} \right\rangle_0$$
$$+ \frac{B_0}{R_0} \left(\mp \frac{\partial}{\partial \theta} \left\langle \frac{\tilde{J}^\phi}{D} \right\rangle_1 + \frac{\partial}{\partial \phi} \left\langle \frac{\tilde{J}^\phi}{D} \right\rangle_1 \right)$$
$$- \frac{1}{\rho} \frac{\partial \langle p \rangle_1}{\partial \theta} \frac{\partial}{\partial \rho} \left\langle \frac{R_0}{D} \right\rangle_0 + \frac{1}{\rho} \frac{\partial \langle p \rangle_1}{\partial \rho} \frac{\partial}{\partial \theta} \left\langle \frac{R_0}{D} \right\rangle_0$$

$$\frac{\partial \langle p \rangle_1}{\partial t} = -\frac{1}{B_0} \frac{1}{\rho} \frac{\partial \langle \Phi \rangle_1}{\partial \theta} \frac{\partial \langle p_{eq} \rangle_0}{\partial \rho}$$

Here $\tilde{\Psi}$ is the poloidal flux perturbation, Φ is the electrostatic potential, with Φ/B_0 being the velocity stream function,

$$V = \frac{1}{DB_0} \left(\nabla \Phi \times e^\phi + v^\phi B \right).$$

D is the inverse Jacobian which is proportional to B^2, J^ϕ is the toroidal current density, U^ϕ the vorticity, p the pressure, and ρ_m is the mass density which we have assumed to be constant. The angle brackets $\langle \ \rangle_0$ denote average over the toroidal angle for an equilibrium quantity.

The radial derivative of $\langle 1/D \rangle_0$ is the average curvature term, and it is related to the specific volume by

$$V' \equiv \frac{dV}{d\psi} = 2\pi \frac{R_0}{B_0} \int_0^{2\pi} \left\langle \frac{1}{D} \right\rangle_0 d\theta$$

This reduced set of MHD equations has been implemented in the CHAFAR code, a modified version of the ideal MHD stability code FAR [7]. The equations are solved by a full

implicit scheme which allows a very fast determination of the linear growth rate. The equilibrium input is taken from the three dimensional equilibrium code VMEC [8].

To compare the results of the method described here with the stability results based on average method equilibria and the Mercier criterion, we use a configuration that models the Heliotron E device. We study a sequence of zero-current equilibria with $p \alpha (1-\Psi)^2$, where Ψ is the poloidal flux normalized to 1 at the edge. The linear growth rates of the $n=1$ mode obtained by this method are lower than those obtained by the stellarator expansion. The differences are consistent with the dependence of the interchange mode growth rate, γ (for $\gamma \ll 1$) on curvature [5]. However, the marginal stability beta is practically the same for both methods, and it agrees with the stability beta limit from the Mercier criterion at the radial position of the $\iota = 1$ surface [4].

The linear growth rates of the $n=4$ mode calculated with CHAFAR are plotted in Fig. 1. The dominant poloidal component is $m=6$ for $\beta_0 = 1.5\%$ and 3%, and $m=4$ for $\beta_0 = 4.6\%$ and 6.2%. The modes for the higher values of beta have the signature of ideal interchange modes, being very localized around the rational surface. However, for the lower beta values, the behavior is infernal-mode-like [9,10]: the value of the rotational transform at the origin is close to a rational number, the local shear is very low, and there is a strong effect of the toroidal coupling on the stability properties. The main poloidal components of the velocity stream function Φ for the $\beta_0 = 3\%$ case are plotted in Fig. 2. The scale is different for each component, and the vertical lines show the position of the $\iota = 2/3$ surface. The results are again in agreement with the Mercier criterion. This is not the case when the growth rates are obtained using the stellarator expansion approach, since the $n=4$ mode appears to be stable for $\beta_0 = 1.5\%$ and 3%.

REFERENCES

[1] C. Mercier, *Nucl. Fusion* **1** (1960) 47.
[2] J.M. Greene and J.L. Johnson, *Phys. Fluids* 4 (1961) 875.
[3] H. Strauss, *Plasma Phys.* **22** (1980) 733.
[4] N. Dominguez et al., *Nucl. Fusion* **29** (1989) 2079.
[5] L. Garcia et al., ORNL/P-89/4090, October 1989.
[6] A.H. Boozer, *Phys. Fluids* **25** (1982) 520.
[7] L.A. Charlton et al., *J. Comput. Phys.* **63** (1986) 107.
[8] S.P. Hirshman, W. Van Rij, P. Merkel, *Comput. Phys. Commun.* **43** (1986) 143.
[9] L.E. Zakharov, *Nucl. Fusion* **18** (1978) 335.
[10] J. Manickam, N. Pomphrey, A.M.M. Todd, *Nucl. Fusion* **27** (1987) 1461.

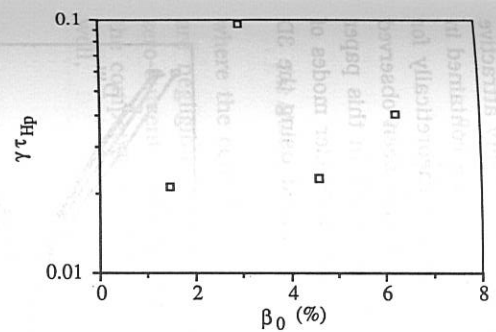

FIG. 1. Linear growth rate of the $n = 4$ mode versus β

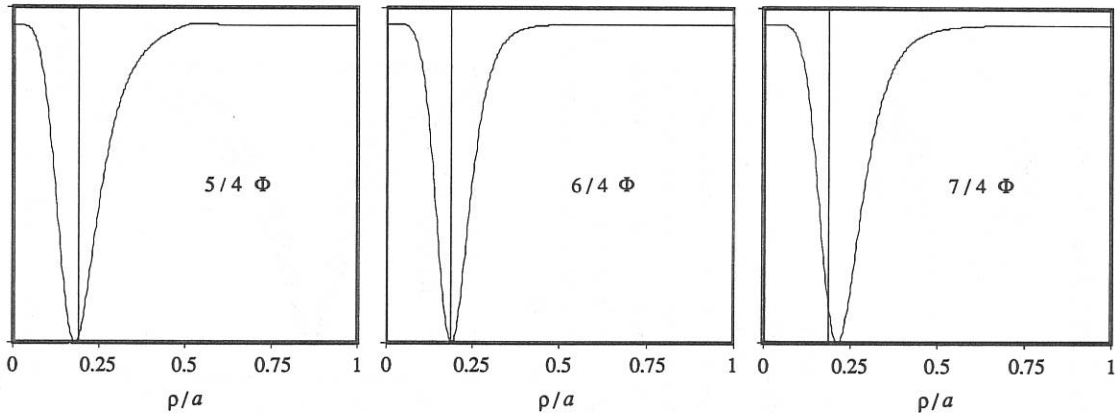

FIG. 2. Dominant components of the electrostatic potential eigenmode versus radius for $\beta_0 = 3\%$

Self-Stabilization of Ideal Modes in a Heliac

C. Alejaldre , A. Varias and A.L. Fraguas
Asociación EURATOM-CIEMAT para fusión
Av. Complutense 22, 28040 Madrid, Spain

B. Carreras, N. Dominguez and V. Lynch
Oak Ridge National Laboratory
Oak Ridge, Tennessee, U.S.A.

Introduction

Fusion devices operating in the second stability regime are very attractive because there is no limit to the amount of plasma pressure contained in the device. Second stability regime has been predicted theoretically for tokamaks and stellarators; moreover self-stabilization has been observed experimentally in the first operation of the ATF device [1]. In this paper we try to understand the self-stabilization behavior to Mercier modes of some TJ-II configurations whose equilibria were obtained using the 3D VMEC code [2].

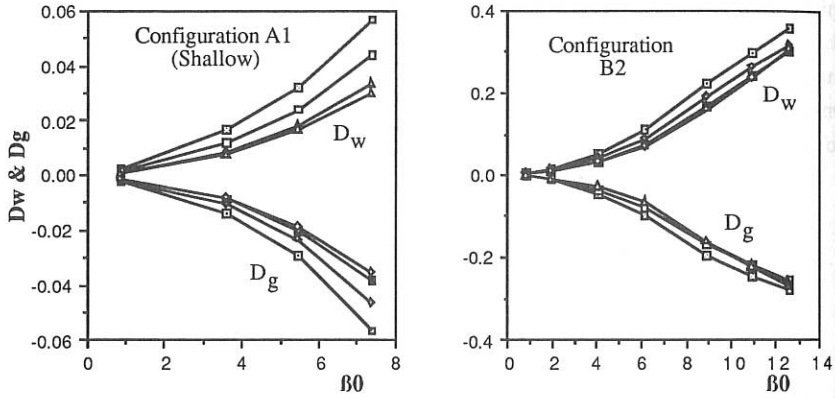

Figure 1

The Flexible Heliac TJ-II [3], under construction in Spain is characterized by a high degree of flexibility: changing the ratio of currents in its two central coils, different magnetic configurations can be achieved with a wide range of parameters ($0.22 \leq \iota/4 \leq 0.628$, $-1\% \leq$ magnetic well $\leq 6\%$). We studied the behavior of three configurations to Mercier modes belong-

ing to two different rotational transform "families", with characteristics summarized in Table I.

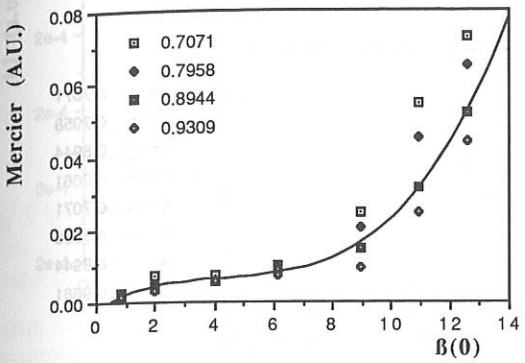

Figure 2

The Mercier criterion for several radii. Configuration B2

Ideal Mercier Stability

We have analyzed the stability of the three configurations using the Mercier criterion that can be written for closed magnetic flux surfaces as:

$$D_M = D_S + D_I + D_W + D_G > 0 \quad (1)$$

where the contributions due to the shear, D_S, and the net currents, D_I, are negligible since the equilibria considered are essentially shearless, zero-current equilibria. The stability properties of TJ-II are then given by the competitive effect between the positive contribution of the magnetic well,

$$D_W = \left\langle \frac{gB^2}{g^{ss}} \right\rangle P'V'' - \left(P'\right)^2 \left\langle \frac{g}{B^2} \right\rangle \left\langle \frac{B^2 g}{g^{ss}} \right\rangle \quad (2)$$

and the negative contribution of the geodesic curvature,

$$D_G = -\left\langle \frac{\left(\vec{J}\cdot\vec{B}\right)^2}{B^2} \frac{g}{g^{ss}} \right\rangle \left\langle \frac{gB^2}{g^{ss}} \right\rangle + \left\langle \frac{g\vec{J}\cdot\vec{B}}{g^{ss}} \right\rangle^2 \approx -c\beta^2 \quad (3)$$

The different behavior of the configuration B2 to Mercier analysis is not clear when one looks into the individual contributions to the Mercier criterion (see figure 1). Both D_W and D_g have similar beta dependance for the three configurations, but still A1 and A2 do not stabilize for increasing β (see ref. [4], where it is shown that A1 is unstable for essentially any value

of the pressure and A2 is stable up to a value of $\langle\beta\rangle \approx 2\%$), and on the contrary B2 shows a clear self-stabilization behavior (see figure 2. and ref [5]).

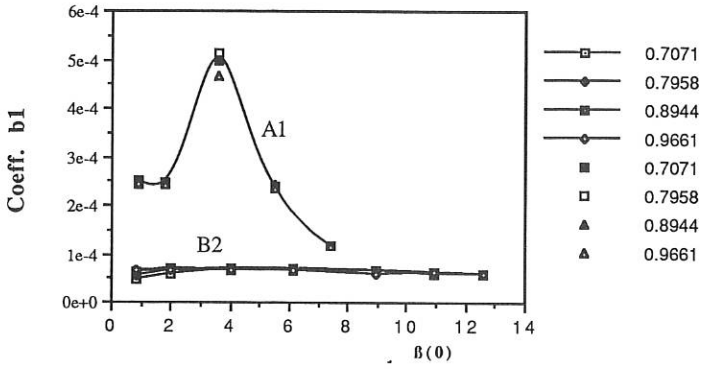

Figure 3

To understand the differences in the configurations, we have further analyzed the D_w term that can be written as:

$$D_w \approx \beta b_0 + b_1\beta^2 - b_2\beta^2 = \beta V''_{vaccum} + \left(\frac{V'' - V''_{vacuum}}{\beta}\right)\beta^2 - (\text{Diagm.})\beta^2$$

where b_1 represents the contribution to the term due to the existing vacuum magnetic well of the configuration, b_2 is the positive contribution of the deepening of the magnetic well with increasing pressure and b_2 the negative diamagnetic contribution. Figure 3 shows the term b_1 for the configurations A1 and B2. Only the configuration with self-stabilization effects has b_1 constant, allowing the magnetic well contribution to grow quadratically overcoming the negative increase of the curvature term and therefore explaining why this behavior was obtained. For the configuration A1, the term has a clear $1/\beta$ dependence for all values of the normalized radius, and therefore the stabilization due to the well cannot compensate the β^2 dependence of the geodesic term. Figure 4 shows in detail the term b_1 for the configuration A2, showing the change in the dependence with β of b_1 as we move from the inner to the outside of the plasma, or in

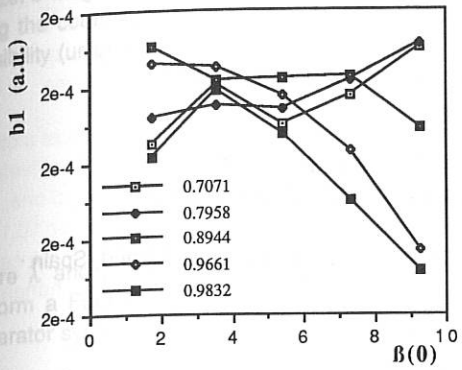

Figure 4

other words when we move from the Mercier stable part of the configuration to the unstable part, as was obtained in ref. [4].

Conclusion

Self-stabilization effects are observed in configurations for which the magnetic well contribution is quadratic in ß over the whole normalized radius.

Configuration	Iota/Period	Magnetic Well	Average radius	<ß> limit (Mercier)
A1	0.36	1%	16 cm	0%
A2	0.36	2%	15 cm	2%
B2	0.30	1%	8 cm	Self-Stable

Table I

Summary of configurations parameters

Acknowledgment

The authors want to thank Steve Hirshman for allowing us to use DESCUR and VMEC codes for these studies and for many useful discussions.

References

[1] J. Harris, et al., Phys. Rev. Lett. 1989.

[2] Hirshman et al., Comput. Phys. Comm. **43** (1986) 143.

[3] The TJ-II Team, Fus. Tech. **17** (1990) 131.

[4] A. Varias et al., submitted to Nucl. Fus.

[5] C. Alejaldre, et al. 1st International Toki Conference, Japan Dec. 1989.

DETERMINATION OF BOOZER MAGNETIC COORDINATES

A. López Fraguas, L. García* and A. Salas

Asociación EURATOM/CIEMAT
Avda. Complutense 22, 28040 Madrid, Spain

* Depto. de Física Teórica, Univ. Complutense, 28040 Madrid, Spain

For many problems in MHD and in transport theory the system of magnetic coordinates described by Boozer [1] is particularly convenient. Unfortunately, finding the correspondence between these magnetic coordinates and the Cartesian system is not easy. Some of the existing techniques follow field lines and give good results with reasonably simple magnetic surfaces, but run into problems when these surfaces are strongly indented, as in the case of the TJ-II heliac or similar machines. Here we use a simple algorithm [2] which does not directly follow field lines, but uses as input the equations of the magnetic surfaces in some given coordinate system, as well as the components of the magnetic field in some regular grid for the given coordinates. Specifically, we have used as input the output of the DESCUR code of Hirshman and Meier [3], which gives optimized Fourier representations for the magnetic surfaces.

The algorithm

We consider a plasma in MHD equilibrium ($\nabla p=\mathbf{j}\times\mathbf{B}$, $\nabla\times\mathbf{B}=\mu_0\mathbf{j}$, $\nabla\cdot\mathbf{B}=0$) whose magnetic surfaces constitute a set of nested topological torii. The initial coordinate system is (ρ,θ,ϕ), where ρ is constant on each magnetic surface, θ is a poloidal angle and ϕ is a toroidal angle. Then there exist functions λ, β and χ such that the magnetic field can be written in the following two forms:

$$\mathbf{B}=\nabla\rho\times\nabla\lambda \qquad \text{with} \quad \lambda=\Psi_t'(\rho)\theta+\Psi_p'(\rho)\phi+\tilde{\lambda}(\rho,\theta,\phi),$$

$$\mathbf{B}=\beta\nabla\rho+\nabla\chi \qquad \text{with} \quad \chi=I(\rho)\theta+g(\rho)\phi+\tilde{\chi}(\rho,\theta,\phi).$$

$\tilde{\lambda}$ and $\tilde{\chi}$, unlike λ and χ, are periodic functions of θ, ϕ, with periods 2π. Ψ_t and Ψ_p are the toroidal and the poloidal fluxes divided by 2π, and I and g are the toroidal and the poloidal currents multiplied by $\mu_0/(2\pi)$.

Boozer's magnetic coordinates are poloidal and toroidal angles θ_B, ϕ_B such that, using the coordinate system (ρ,θ_B,ϕ_B), the periodic parts of λ and χ are zero. One possibility (unique if we assume stellarator symmetry) is [2]

$$\theta_B = \theta + \tilde{\theta}_B \quad \text{with} \quad \tilde{\theta}_B = \frac{g\tilde{\lambda} - \Psi_p'\tilde{\chi}}{g\Psi_t' - I\Psi_p'},$$

$$\phi_B = \phi + \tilde{\phi}_B \quad \text{with} \quad \tilde{\phi}_B = \frac{\Psi_t'\tilde{\chi} - I\tilde{\lambda}}{g\Psi_t' - I\Psi_p'},$$

where $\tilde{\lambda}$ and $\tilde{\chi}$ are those corresponding to the original coordinates. If now we perform a Fourier expansion in θ and ϕ we get terms in $\sin(m\theta - n\phi)$ (assuming stellarator symmetry), and for their Fourier coefficients we have

$$\theta_B^{mn} = \frac{g\lambda^{mn} - \Psi_p'\chi^{mn}}{g\Psi_t' - I\Psi_p'}, \qquad \phi_B^{mn} = \frac{\Psi_t'\chi^{mn} - I\lambda^{mn}}{g\Psi_t' - I\Psi_p'}.$$

In order to make use of these formulae we need to calculate I, g, Ψ_t', Ψ_p', λ^{mn} and χ^{mn}. These are given by the Fourier coefficients of the covariant components of the magnetic field and of the contravariant components multiplied by the Jacobian $(J = (\nabla\rho \times \nabla\theta \cdot \nabla\phi)^{-1})$:

$$I = \mathbf{B}_\theta^{00}, \qquad g = \mathbf{B}_\phi^{00}, \qquad \Psi_t' = \left(J\mathbf{B}^\phi\right)^{00}, \qquad \Psi_p' = -\left(J\mathbf{B}^\theta\right)^{00},$$

$$\lambda^{mn} = \frac{\left(J\mathbf{B}^\theta\right)^{mn}}{n} = \frac{\left(J\mathbf{B}^\phi\right)^{mn}}{m}, \qquad \chi^{mn} = \frac{\mathbf{B}_\theta^{mn}}{m} = -\frac{\mathbf{B}_\phi^{mn}}{m}.$$

The hardest part is the computation of the needed components of the magnetic field. For the vacuum, which is the only case we have considered for the moment (except for tests with exact analytical solutions, such as those with helical symmetry described in [4]), the magnetic field is derived from the currents in the coils, and the metric tensor from the equations of the magnetic surfaces.

Results

We have run our code in combination with DESCUR, which gives the equations of the magnetic surfaces. The results turn out to be rather sensitive to the accuracy with which the magnetic surfaces are given. This is confirmed by the analytical tests with known analytical solutions, where these magnetic surfaces are perfectly known and the accuracy of the resulting Boozer coordinates is only limited by the rounding errors. More specifically, the largest source of error is the computation of the radial derivatives needed for the calculation of the metric tensor. These radial

derivatives affect the calculation of JB^{θ} and JB^{ϕ} but not that of B_{θ} and B_{ϕ}. Fortunately we have a test to obtain a qualitative estimate of the errors, which is the comparison of the two expressions given above for λ^{mn} and χ_{mn} when m and n are not both zero simultaneously. As expected, in the case of χ_{mn} both expressions give results very similar, since they do not depend on the radial derivatives.

The results obtained for the TJ-II [5,6] are best described with a few typical plots. In figs 1 and 2 we show the results obtained for λ^{11}/ρ and for $\lambda^{1\,-2}/\rho$ respectively, in each case using either the first formula above , with JB^{θ} (1), or the second one, with JB^{ϕ} (2), and also using maximum values of m and n per period of either 10,12 or 6,6. These modes have been chosen because they are more or less worst cases. Increasing the number of modes above 10,12 does not appear to change the results significantly.

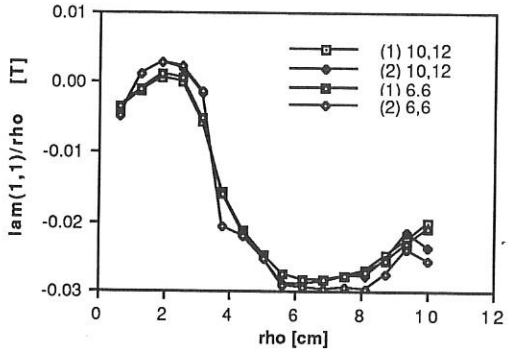

Fig.1. λ^{11}/ρ

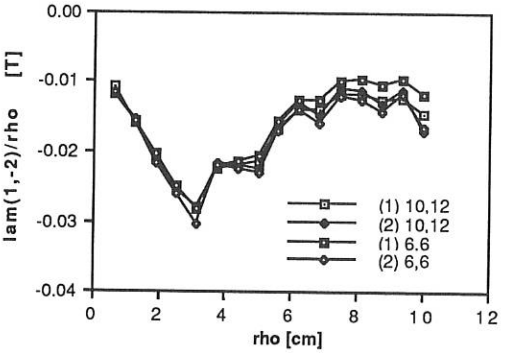

Fig.2. $\lambda^{1\,-2}/\rho$

As an example of the results for other number of modes, in fig. 3 we show $\lambda^{2\,-2}/\rho^2$, for 8,10 modes.

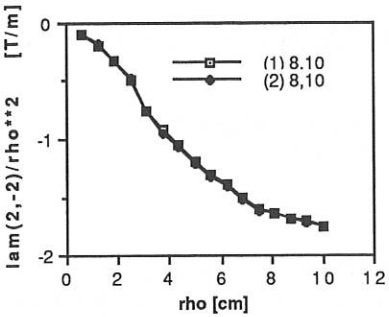

Fig.3. $\lambda^{2\,-2}/\rho^{**2}$

Finally, in fig.4 we compare the expression obtained for ι from our code with that given by DESCUR directly.

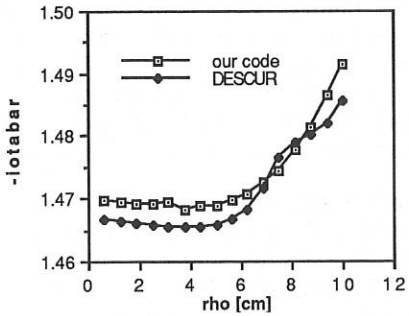

Fig.4. ι

References

[1] A.H.Boozer, Phys. Fluids **23**, 904 (1980); Phys. Fluids **24**, 1999 (1981)
[2] J. Nührenberg and R. Zille, in Theory of Fusion Plasmas, ed. by A.Bondeson, E. Sindoni and F. Troyon (Ed Compositori Bologna, Italy, 1988), p. 3
[3] S.P. Hirshman and H.K. Meier, Phys. Fluids **28**, 1387 (1985)
[4] P. Merkel and J. Nührenberg, IkComp. Phys. Comm. **31**, 115 (1984)
[5] T. C. Hender *et al.*, Fusion Technology **13**, 521 (1988)
[6] C. Alejaldre *et al.*, Fusion Technology **17**, 131 (1990)

BOOTSTRAP CURRENTS IN HELIAC TJ-II CONFIGURATIONS.

A. Rodríguez Yunta*, W.I van Rij#, S.P.Hirshman#.

* Asociación EURATOM-CIEMAT para Fusión. Madrid. Spain
# ORNL. Oak Ridge. USA

The bootstrap current is an important subject in stellarators since it causes a modification of the rotational transform profile when the plasma pressure is increased. Because stellarator reactors are ideally operated in the currentless mode, it is desirable to minimize the magnitude of the bootstrap current. Bootstrap currents have been identified in several stellarator devices and the measured values were found in close agreement with the neoclassical predictions .

In neoclassical theory the bootstrap current magnitude is determined by the pressure profile and the variation of the magnetic field strength on the magnetic surfaces. As TJ-II is a flexible heliac with capability to produce a large set of different magnetic configurations [1], it could be a useful device to make a more complete test of the neoclassical predictions for bootstrap currents and ways to control them.

In this work neoclassical estimations of Bootstrap currents are obtained from analytical formulae for plateau [2] and low collisionality [3] regimes and by numeric solution of the drift kinetic equation using the DKES code [4]. It is found that the magnitude of the current in TJ-II changes with the magnetic configuration and it can reverse its sign depending on the configuration, the radius of the magnetic surface, the collision frequency and the radial electric field.

In figure 1 it is shown the bootstrap geometrical factor, whose value for an equivalent axisymetric device is the unity, for several magnetic configurations as a function of average minor radius. The magnetic field structure was obtained from the 3D equilibrium code VMEC for a plasma pressure $<\beta>=1\%$ and different values for the hard core currents. In figure 2 it is shown the integrated currents for parabolic profiles of density and temperatures. As can be seen it is possible to find configurations with very low bootstrap current. From the comparison of two cases with similar value of rotational transform close to 1.5, it is

found that the bootstrap current is lower for the configuration with deeper magnetic well.

Figure 3 shows the bootstrap coefficient obtained from DKES versus collisionality for various radial electric fields. The calculations were made on the half radius magnetic surface for the configuration with $\iota = 1.5$ and deep magnetic well. The bootstrap current shows reversal of sign with the collisionality and the radial electric field. The change with radial electric field is mainly related to resonances between parallel velocity and poloidal rotation due to the electric field. The variation of bootstrap coefficient versus electric field for a fixed collisionality is shown in figure 4.

The obtained results show a rich variety of Bootstrap current profiles, with and without changes of sign inside the plasma, and very different magnitude. This variety can allow in the future a complete experimental test of the currents predicted by the neoclassical theory and also the ways of controlling them in order to obtain very low currents.

References

1. C.Alejaldre et al. Fusion Technology **17**, 131 (1990)
2. E.R.Solano, K.C.Shaing. Phys. Fluids **30**, 462 (1987)
3. K.C.Shaing, B.A.Carreras, N.Dominguez, V.E.Lynch, J.S.Tolliver. Phys.Fluids **B1**, 1663 (1989).
4. W.I.van Rij, S.P.Hirshman. Phys.Fluids **B1**, 563 (1989)

Figure 1. Bootstrap geometric factor in TJ-II

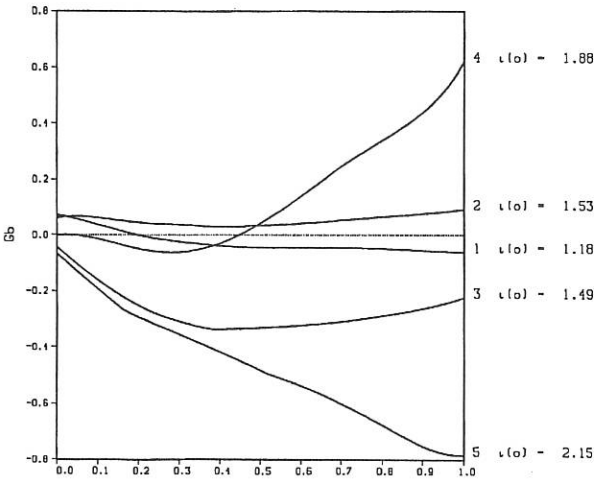

Figure 2. Integrated bootstrap current in TJ-II

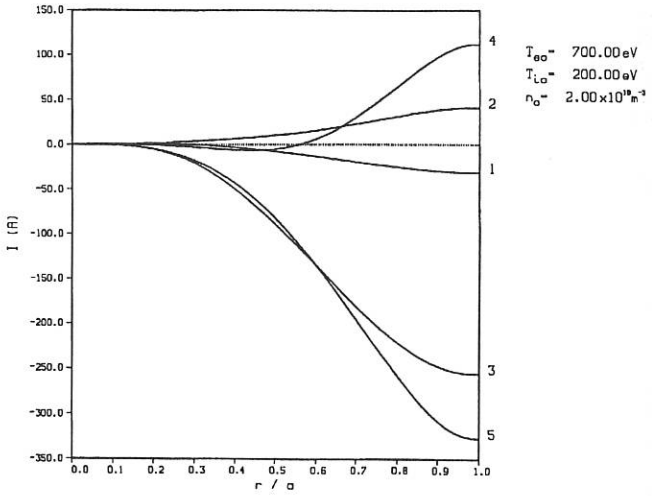

Figure 3. Bootstrap coefficient versus collisionality in TJ-II (magnetic surface r=a/2)

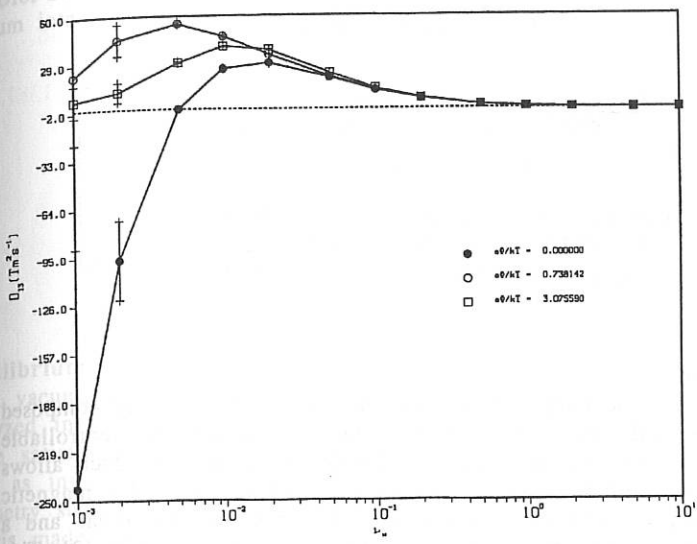

Figure 4. Bootstrap coefficient versus radial electric field in TJ-II

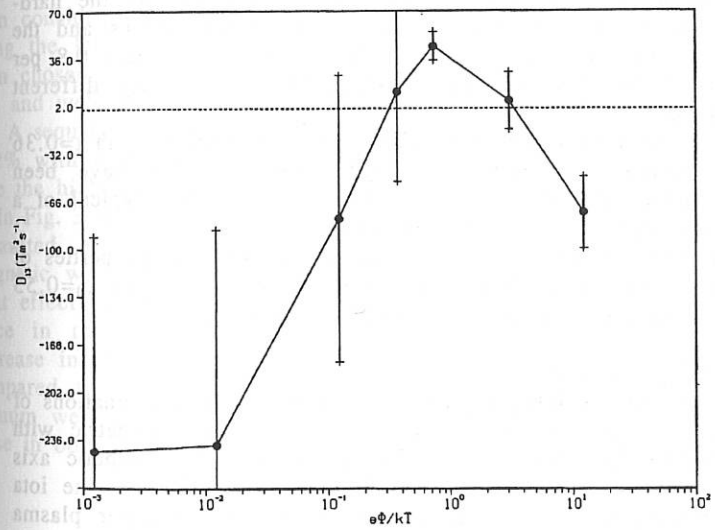

EQUILIBRIUM AND STABILITY OF HIGH ι TJ-II CONFIGURATIONS

A. L. Fraguas, A. Varias and C. Alejaldre
CIEMAT-EURATOM Association
E-28040 Madrid, Spain

B.A. Carreras, N. Domínguez and V.E. Lynch
Oak Ridge National Laboratory
Oak Ridge, Tennessee 37831, U.S.A.

Introduction

The hard-core winding of the four period heliac TJ-II is composed of a circular coil and a helical winding with separately controllable currents. This feature gives a great flexibility to the device which allows an independent control of the rotational transform and the magnetic well [1]. Heliacs have in common high iota values, low shear and a vacuum magnetic well, providing a potential for high β limits [2]. This potential can be endangered by magnetic islands induced by low order rational values of the transform [3]. The iota control through the hard-core currents is a very effective way to avoid rational values and the large range of iota available in TJ-II, going from 0.15 to near 0.8 per period, makes it possible to obtain configurations with very different MHD properties.

Previously we have studied the stability of configurations with $\iota=0.36$ and 0.30 per period [4]. Beta limits higher than $<\beta>\approx 6\%$ have been obtained and in the case of lower ι self-stabilization effects typical of a second stability regime have been observed.

In this work we explore the equilibrium and stability properties of configurations having higher transforms, selecting a case having $\iota_0=0.55$ in vacuum and comparing it with the lower transform cases.

Vacuum configurations

Table I shows the iota values obtained with several combinations of the hard-core currents. Magnetic surfaces more or less symmetric with respect to the toroidal angle can be obtained shifting the magnetic axis position with the vertical field, resulting in very little effect on the iota value. The most symmetric geometries have in general a larger plasma radius and make the three dimensional MHD calculations more tractable.

For this reason a posterior scan is made on the axis position to select surfaces not far from symmetry. A field line following code (FL) using the Biot-Savart law is employed to obtain the Poincaré Map and the vacuum iota and well profiles.

I_{cc} (kA)	I_{hc} (kA)	ι_0
250	80	1.467
131	146	1.894
100	207	2.204
39	261	2.640

TABLE I

Equilibrium and Stability

A vacuum magnetic surface, selected as plasma boundary, is Fourier analyzed in two angles: the geometrical toroidal angle and a poloidal angle satisfying the constraint of "Minimum spectral width" [5], and used as input to the VMEC 3D equilibrium code [6]. For a complex geometry such that of TJ-II a high number of modes is required and a test is made on the accuracy of the boundary representation comparing the iota and magnetic well profiles in vacuum between VMEC and the FL code [7]. Two set of Fourier components, with 138 and 202 modes, have been considered. As the agreement is good enough with 138 modes and using the larger set does not improve the result, the 138 mode set has been chosen for the equilibrium calculations. Figs. 1 and 2 compares the iota and well profiles in vacuum between FL and VMEC results.

A sequence of equilibria has been generated, with beta going up to $\langle\beta\rangle$ = 2% with linear pressure profiles in the toroidal flux, as these profiles give the higher beta limits in the standard iota cases, $\iota_0/M=0.36$.

In Fig. 3 we show the flux surfaces for $\langle\beta\rangle$ =2% at two toroidal sections separated by half a period. Figure 4 shows the deepening of the magnetic well with $\langle\beta\rangle$, less pronounced than in the lower iota cases. That effect can reduce the beta limits attainable with this configuration, since in the TJ-II stability is provided by the magnetic well. The decrease in well depth has a corresponding decrease in the toroidal shift compared to the Deeper Well case of Ref. [4], which has a similar vacuum well, as shown in Fig. 5. Conversely, the helical shifts are very close in both cases.

References

[1] T. C. Hender et al., Fus. Tech. **13** (1988), 521.
[2] D. A. Monticello et al., Phys. Fluids **27** (1984), 1248.
[3] A. Reiman and A. H. Boozer., Phys. Fluids **27** (1984), 2446.
[4] C. Alejaldre et al. Fus.Tech.,**17** (1990), 131.
[5] S. P. Hirshman and H. K. Meier., Phys. Fluids **28** (1985), 1387.
[6] S. P. Hirshman et al., Comp. Phys. Comm. **43** (1986), 143.
[7] A. Varias et al., Bull. Am. Phys. Soc. **33** (1988), 3S11.

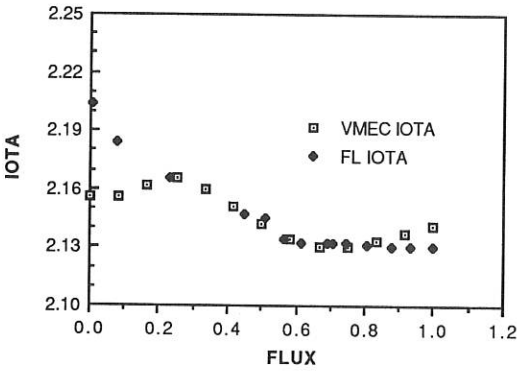

Fig. 1: Comparison of FL and VMEC iota profiles

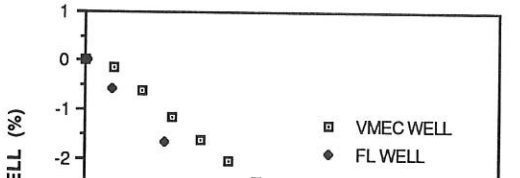

Fig. 2: Comparison of FL and VMEC well profiles

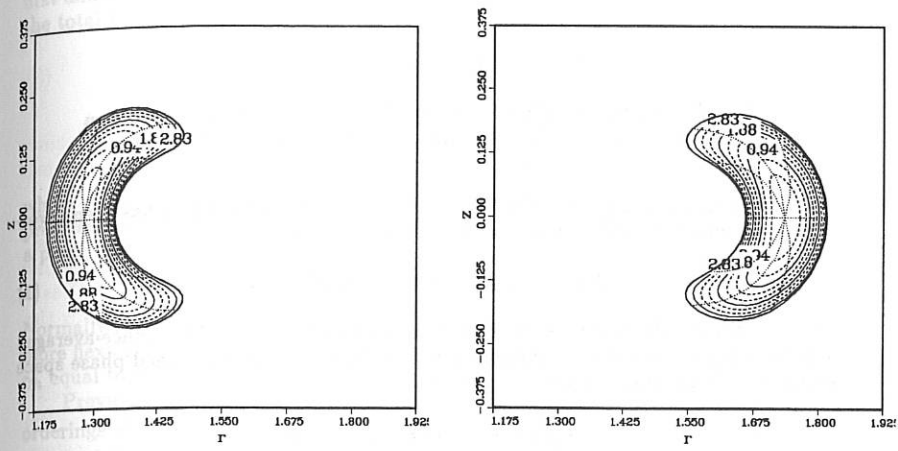

Fig. 3: Flux surfaces and theta contours at φ=0º and φ=45º

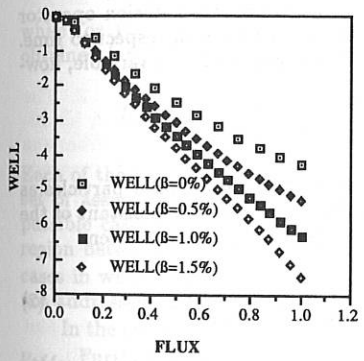

Fig.4: Well depth as function of <ß>

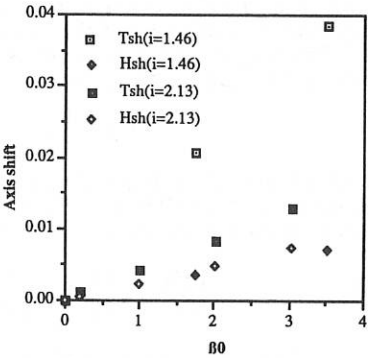

Fig. 5: Toroidal and helical axis shifts for the two iota cases

A GENERAL THEORY OF *LMFP* NEOCLASSICAL TRANSPORT IN STELLARATORS

C.D. Beidler

Max-Planck-Institut für Plasmaphysik, IPP-EURATOM Association
D-8046 Garching bei München, Federal Republic of Germany

Neoclassical transport in the long-mean-free-path (*lmfp*) regime has been investigated by many authors for the model stellarator field

$$B/B_0 = 1 - \epsilon_t \cos\theta - \epsilon_h \cos(\ell\theta - p\phi). \tag{1}$$

Most of these calculations have been based on solutions of the bounce-averaged kinetic equation in various asymptotic limits. In the bounce-averaged phase space $(r,\theta;\kappa,\mu)$ this equation may be expressed as

$$\dot{r}(\partial F/\partial r) + \dot{\theta}(\partial F/\partial\theta) = C_\mu F\ .$$

In the above, $\epsilon_t = r/R_0$ is the inverse aspect ratio, ϵ_h is the magnitude of the stellarator's *helical* ripple (it is particles which are localized in this helical ripple which give rise to the dominant transport processes in the *lmfp* regime), θ is the poloidal angle, ϕ is the toroidal angle, ℓ is the multipolarity of the stellarator windings, p is the number of field periods, r is a flux surface label related to the toroidal flux through the expression $\psi = B_0 r^2/2$, κ is the kinetic energy, μ is the magnetic moment, F is the distribution function, C_μ represents the Lorentz collision operator expressed in terms of μ and the dots indicate total derivatives with respect to time.

The magnetic momemt is not usually favored as the pitch-angle variable, however, and instead the "well-depth parameter"

$$k^2 = (\kappa/\mu B_0 - 1 + \epsilon_t\cos\theta + \epsilon_h)/(2\epsilon_h)$$

is introduced. Using k^2 greatly simplifies the classification of localized particles as all such particles satisfy $0 \le k^2 < 1$. However, unlike μ, k^2 is not a constant of the particle's motion and the bounce-averaged kinetic equation must be written

$$\dot{r}\frac{\partial F_m}{\partial r} + \dot{\theta}\frac{\partial f}{\partial\theta} + \dot{k}^2\frac{\partial f}{\partial k^2} = \frac{\nu_{eff}}{A'(k^2)}\frac{\partial}{\partial k^2}\left(A(k^2)\frac{\partial f}{\partial k^2}\right)\ . \tag{2}$$

The *collisionless* variation of k^2 represented by the additional term has not previously been accounted for in analytical calculations although its significance has been recognized in one numerical solution of Equation (2) [1].

In Equation (2) the distribution function has been assumed to be of the form $F = F_m + f$, i.e. to be the sum of a Maxwellian and a small perturbation. The usual transport ordering $\dot{\theta}, \nu_{eff} >> \dot{r}/\delta r$, where δr is the radial scale length of the plasma,

has also been assumed. The "effective" collision frequency is defined by $\nu_{eff} = \nu/2\epsilon_h$, where ν is the 90 degree scattering frequency; $A(k^2) = 8(E(k) - (1-k^2)K(k))$ and $A'(k^2) = 4K(k)$, where $K(k)$ and $E(k)$ are the complete elliptic integrals of the first and second kinds, respectively. Given the model magnetic field of Equation (1), the total time derivatives are

$$\dot{r} = v_d \sin\theta \qquad\qquad \dot{k}^2 = -\frac{v_d \sin\theta}{2\epsilon_h}\frac{\partial \epsilon_h}{\partial r}\frac{A(k^2)}{A'(k^2)}$$

$$\dot{\theta} = \Omega_E + \frac{v_d}{\epsilon_t}\left(\frac{\partial \epsilon_t}{\partial r}\cos\theta + \frac{\partial \epsilon_h}{\partial r}\left(\frac{2E(k)}{K(k)} - 1\right)\right)$$

where $v_d = T/R_0 B_0$ with T the particle's kinetic energy in eV, Ω_E is the $\mathbf{E}\times\mathbf{B}$ precessional frequency and the radial dependences of ϵ_t and ϵ_h are assumed to obey a power law, i.e.

$$\partial\epsilon_t/\partial r = \gamma_t \epsilon_t / r \qquad\qquad \partial\epsilon_h/\partial r = \gamma_h \epsilon_h / r\,.$$

Normally one would take $\gamma_t = 1$ and $\gamma_h = \ell$, however the current formulation offers more flexibility since it allows the suppression of various terms by setting γ_t and/or γ_h equal to zero.

Previous analytical solutions of Equation (2) have been obtained for various orderings of the characteristic frequencies ν_{eff} and $\dot{\theta}$ in the limits of large radial electric field ($\dot{\theta} = \Omega_E$) and in the limit $\Omega_E = 0$. The results of these calculations may be summarized by the expected scaling of the diffusion coefficient with parameters of interest. In the large Ω_E limit the so-called ν^{-1}, $\nu^{1/2}$ and ν regimes have been identified (from highest to lowest collision frequency, respectively)

$$D_{\nu^{-1}} \propto \frac{\epsilon_h^{3/2}\epsilon_t^{\,2}T^2}{r^2 B_0^{\,2}\nu}, \qquad D_{\nu^{1/2}} \propto \frac{\epsilon_t^{\,2}T^2\nu^{1/2}}{r^2 B_0^{\,2}\Omega_E^{\,3/2}}, \qquad D_{\nu} \propto \frac{\epsilon_h^{1/2}\epsilon_t T^2 \nu}{r^2 B_0^{\,2}\Omega_E^{\,2}},$$

while for $\Omega_E = 0$ the ν^{-1}, superbanana plateau and superbanana regimes are obtained (again from highest to lowest collision frequency)

$$D_{\nu^{-1}} \propto \frac{\epsilon_h^{3/2}\epsilon_t^{\,2}T^2}{r^2 B_0^{\,2}\nu}, \qquad D_{SP} \propto \frac{\epsilon_t^{\,2}T}{\epsilon_h^{1/2}B_0}, \qquad D_S \propto \frac{\epsilon_t^{1/2} r^2 \nu}{\epsilon_h}.$$

Each of these results represents the solution of the kinetic equation for a particular set of assumptions; even taken as a whole these six expressions do not cover all possible cases for which Equation (2) is valid. For example, in the transitionary region between two regimes the assumptions of neither are appropriate. Moreover, cases in which Ω_E and the remaining terms in $\dot{\theta}$ are of comparable magnitude are not addressed at all by these results.

In the current work no assumptions will be made as to the relative sizes of $\dot{\theta}$ and ν_{eff}. Furthermore, the full expression for $\dot{\theta}$ will be retained with no assumptions as to the relative sizes of its component terms. Instead, it will be assumed that the perturbed distribution function may be written

$$f = \frac{\partial F_m}{\partial r}\Big(Z(k^2) + Y(k^2)\sin\theta + X(k^2)\cos\theta\Big)\,.$$

Inserting this expression into Equation (2), the kinetic equation separates into three coupled differential equations. These are then solved by expanding Z, Y and X as infinite series in powers of k^2 with the approximations $A(k^2)/A'(k^2) = k^2 - k^2/4$, $2E(k)/K(k) = 2 - k^2 - k^2/4$ and the boundary conditions

$$Z(k^2=1) = 0\,, \qquad Y(k^2=1) = 0\,, \qquad X(k^2=1) = -\frac{\epsilon_t}{2\epsilon_h}\left.\frac{\partial X}{\partial k^2}\right|_{k^2=1}\,. \tag{3}$$

Because of the complexity of the recursion relationships which result and also because a large number of terms is often required for convergence, the solution is implemented numerically.

As an example, this general solution of the bounce-averaged kinetic equation is used to investigate neoclassical transport in a stellarator for which $R_0 = 20$ m, $B_0 = 4$ T, $\epsilon_h = 0.15$ and $T = 7$ keV. The flux surface corresponding to $r = 1$ m has been chosen for the results presented in the sequence of figures. A plot of D as a function of ν is given in the upper-left-hand figure; the remaining figures show the scaling of D with the various parameters of interest. This latter group of figures has been obtained by independently varying each parameter by 1% and comparing the result with the base case. Results given by the solid lines are for $\dot{\theta} = \Omega_E = -800$; the remaining terms in $\dot{\theta}$ have been suppressed by setting $\gamma_t = \gamma_h = 0$. Ignoring the additional terms in $\dot{\theta}$ is not a good assumption for this set of simulation parameters, it has been done here for purposes of comparison with the $\dot{\theta} = \Omega_E$ limit. For large values of ν the expected parameter scalings of the ν^{-1} regime are obtained. A $\nu^{1/2}$ regime of significant extent is predicted to exist for this set of simulation parameters, however the results illustrated here do not show a distinct range of collisionality where $\nu^{1/2}$ parameter scalings hold. The expected $\nu^{1/2}$ regime scalings are recovered, however, if one replaces the boundary conditions of Equation (3) with $Z(1) = Y(1) = X(1) = 0$. These boundary conditions have often been used in analytic calculations, however numerical solutions of the kinetic equation have shown that they are rarely appropriate [1,2] and that those of Equation (3) are much more consistent with reality.

Results shown by broken lines are for $\Omega_E = 0$ with $\gamma_t = 0$ and $\gamma_h = 2$. The expected scalings in the ν^{-1} and superbanana plateau regimes may be clearly identified in the figures. Furthermore, between the superbanana plateau and superbanana regimes, a previously unreported set of scalings is observed, constituting the presence of an additional regime. In the $\Omega_E = 0$ limit the presence of the $\dot{k}^2(\partial f/\partial k^2)$ term in the kinetic equation is of critical importance; if $\dot{k}^2$ is independently set to zero neither the additional or superbanana regime is found. It should also be noted that these results are insensitive to the choice of boundary conditions. Finally, results given by the dotted lines are for $\Omega_E = -800$, $\gamma_t = 1$, $\gamma_h = 2$ and show how important it is for this set of simulation parameters to retain all terms in $\dot{\theta}$; although the plot of D vs. ν is not significantly different than that obtained in the $\dot{\theta} = \Omega_E$ limit, the parameter scalings are seen to be radically altered.

[1] H.E. Mynick, W.N.G. Hitchon, **Nucl. Fusion 26**, (1986) 425.

[2] S.P. Hirshman, K.C. Shaing, W.I. van Rij, C.O. Beasley, Jr., E.C. Crume, Jr., Phys. Fluids 29, (1986) 2951.

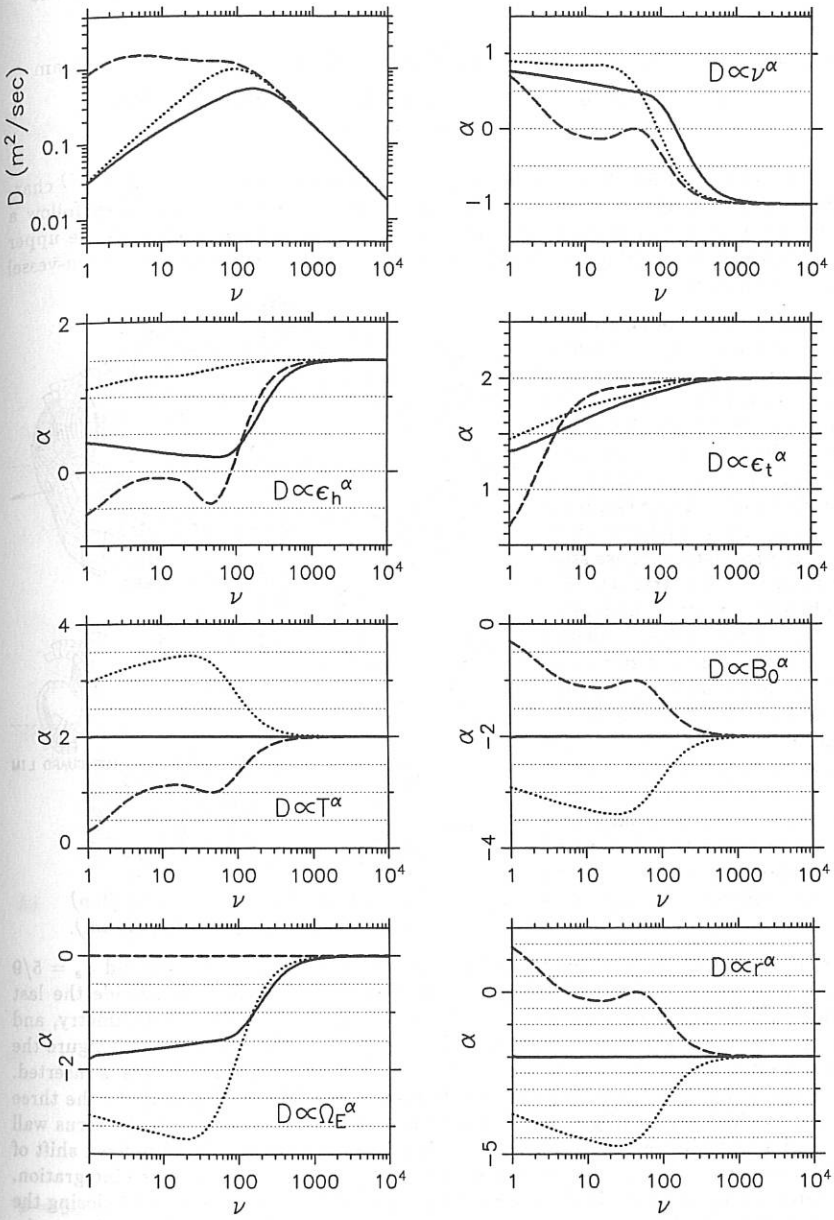
D (m²/sec)
1
0.1
0.01
1
10
100
1000
10⁴
ν
D∝ν^α
α
D∝ε_h^α
D∝ε_t^α
D∝T^α
D∝B_0^α
D∝Ω_E^α
D∝r^α

ON THE EDGE STRUCTURE OF THE W VII-AS STELLARATOR

C. Beidler, E. Harmeyer, J. Kißlinger, F. Rau , H. Wobig, and W VII-AS Team

Max-Planck Institut für Plasmaphysik, D-8046 Garching, FRG
EURATOM-Association.

Wendelstein VII-AS showed after one year of operation - mainly at 1.25 T - [1] characteristic stripes due to plasma-wall interaction along the torus wall. They follow a helical contour from the lower torus apex along the radial outside towards the upper apex, through each field period [2]. The pattern is modified by the limiters and in-vessel components, Fig. 1.

This paper aims to clarify the origin of these stripes by following numerically the behaviour of vacuum field lines and guiding center orbits (Monte Carlo code, using pitch angle scattering of H^+ ions with 50 eV energy, no electric field) . Monte Carlo calculations are considered to be more appropriate for these studies than field line tracing. The guiding center orbits are started at random toroidal and poloidal points, at a small distance inside the edge radius. Field lines started not too far outside the edge give similar results. The influence of the limiter position and of the value of the rotational transform ι are investigated for limiter or separatrix dominated configurations, at irrational or rational values of the edge rotational transform.

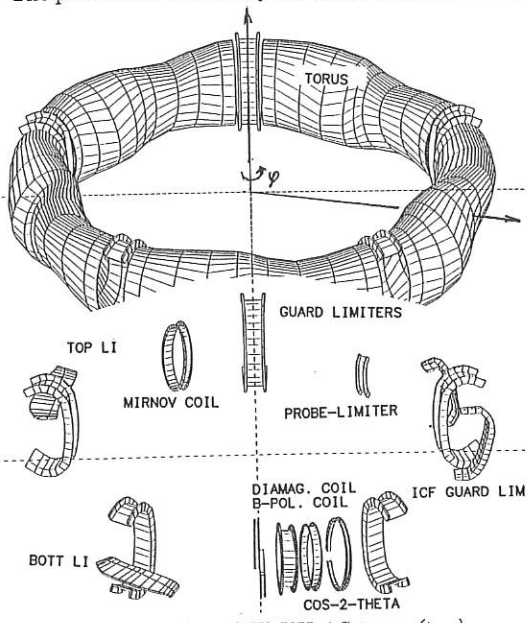

Fig. 1: Perspective of W VII-AS torus (top) and in-vessel components (bottom).

A separatrix-dominated configuration is present for $\iota = 0.53$ on axis and $\iota_s = 5/9$ at the separatrix, if the limiters are placed at $Z_L = \pm 31.5$ cm, just outside the last closed surface of the vacuum field. Its shape is influenced by the 5/9 symmetry, and shows 9 tips along the minor circumference, Fig. 2 a . In the left part of the figure the probe limiter with a number of intersection points of guiding center orbits is inserted. More complete guiding center puncture plots are shown in Fig. 2 b to d for the three typical toroidal angles. Fig. 2 e is the helical intersection pattern with the torus wall in a radial outside view at $\varphi = 0$. The slope is nearly constant. The up-down shift of the traces corresponds to the toroidal direction of particle flow or field line integration. An intensified picture is obtained when removing the in-vessel objects, and closing the 8° gaps of the module separation near $\varphi = 36°$. About 13 % of the orbits end near the

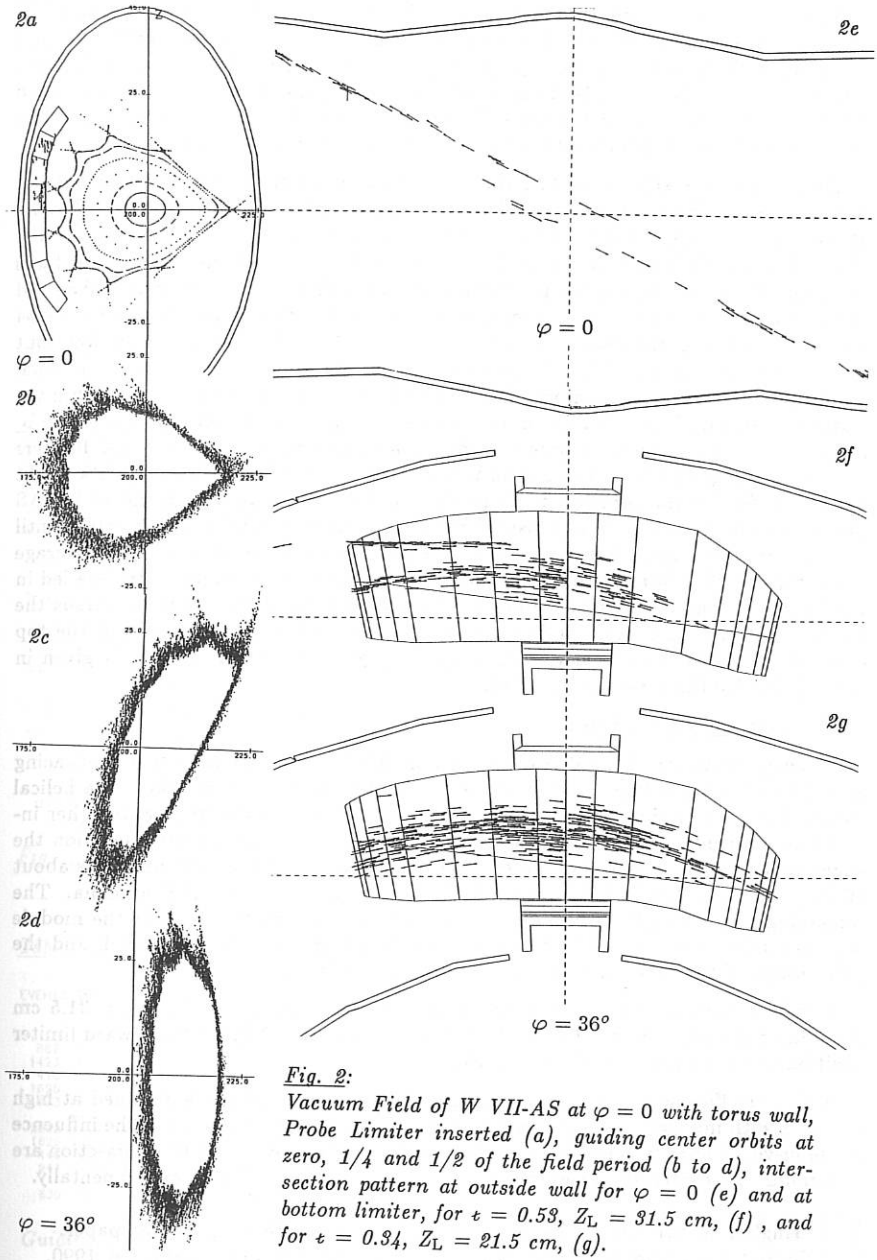

Fig. 2:
Vacuum Field of W VII-AS at $\varphi = 0$ with torus wall, Probe Limiter inserted (a), guiding center orbits at zero, 1/4 and 1/2 of the field period (b to d), intersection pattern at outside wall for $\varphi = 0$ (e) and at bottom limiter, for $\iota = 0.53$, $Z_L = 31.5$ cm, (f) , and for $\iota = 0.34$, $Z_L = 21.5$ cm, (g).

torus apeces, slightly more than the relative toroidal gap width. At $\varphi \approx 0$, about 3 % of the orbits end near the mid-plane radially inside. Such intersection points have not been seen with in-vessel objects. Fig. 2 f and g are intersection patterns at the bottom limiter for $\iota = 0.53$ and 0.34, respectively, i.e. for separatrix and limiter dominated cases. At $\iota = 0.53$ two intersection stripes develop near the limiter edge and continue at the torus apex. A similar structure is seen without the in-vessel objects.

For all ι-values studied so far, the intersection numbers at the top and bottom limiter differ in the computer jobs. This up-down asymmetry is reversed by reversing all velocities, or changing the charge of the particles and thus the direction of the $\vec{B} \times \nabla B$-drift. Drift surfaces of guiding center orbits deviate from magnetic surfaces by order of ρ/ι, where ρ is the Larmor radius. This offset is reduced in the advanced stellarator W VII-AS by a factor of about two. In our calculations a number of 64 orbits is followed in the code simultaneously. The initial velocities are at random, but not completely balanced. Therefore we always use both velocity directions for the final evaluation. This results in comparable loading of the top and bottom limiter, within the statistical spread of the data. Examples of local 'hot spots' are given in Fig. 3 a and b for $\iota = 0.53$, in perspective views of the region near one of the ICF guard limiters and the diamagnetic coil. The gap in the pattern of torus intersections points might be the 'shadow' of the adjacent diamagnetic coil. The photo taken from the W VII-AS torus shows no gap. Fig. 4 is a histogram of the lengths of guiding center orbits until intersection. They range between 1 and 100 transits around the machine at an average of 25 transits. The intersection numbers of the various in-vessel objects are detailed in the insert. In Fig. 5 the relative loads of in-vessel components are shown versus the limiter position. At outside limiter position the two ICF guard limiters and the top and bottom limiters are nearly equally loaded. Quantitative information is given in Table I for the three ι-values studied.

Summary and conclusions :

The edge structure of the W VII-AS vacuum field is investigated by field line tracing and Monte Carlo guiding center orbits with similar results for $\iota = 0.53$. The helical shape of the interaction stripe at the wall and 'hot spots' at the limiters or other in-vessel components are recovered in essential details. At outward limiter position the edge topology is separatrix dominated. The efficiency of the two main limiters is about 40 % , while another 35 % are seen at the guard limiters of the ICF antenna. The remaining guiding center orbits end at the diamagnetic coil, the torus or the module separation limiters. For $Z_L \lesssim 28$ cm the configuration is limiter dominated, and the percentages of the other in-vessel objects drop below 10 % .

Configurations at low $\iota = 0.34$ are always limiter dominated. For $Z_L = 31.5$ cm the limiter efficiency is only 66 % . It increases to about 100 % for the inward limiter position; then the aspect ratio is $A \approx 16$.

A limiter efficiency $\gtrsim 90\%$ in a separatrix dominated topology is obtained at high $\iota = 0.71$ with inward limiter position, at increased aspect ratio $A \approx 20$. The influence of the in-vessel objects is negligible, and the average orbit lengths until intersection are maximum. This interesting case remains to be studied in W VII-AS experimentally.

---

1) H. Ringler, W VII-AS-, ECH-, and NBI-Teams, this conference, Invited paper.
2) P. Grigull et al., and W VII-AS Team, paper at PSI-9, Bournemouth, UK 1990.

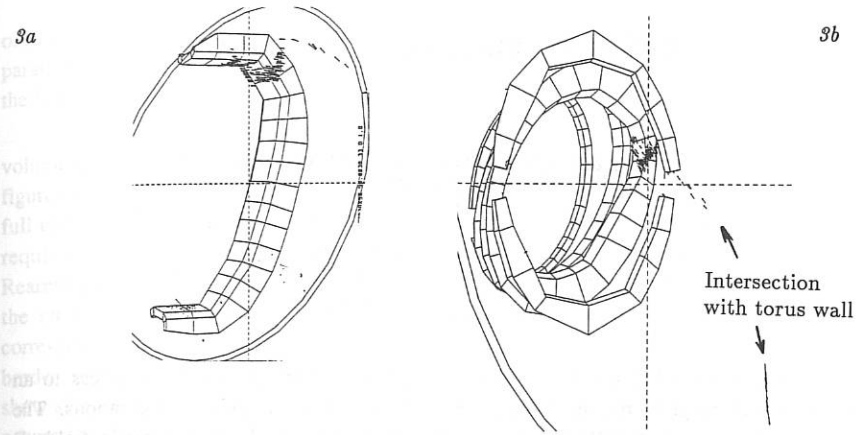

Fig. 3: Perspective views; $\iota = 0.53$.
Vicinity of one of the ICF guard limiters (a) and of diamagnetic coil (b).

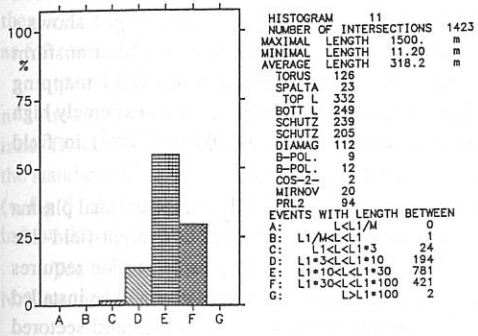

Fig. 4: Histogram of the guiding center orbits.

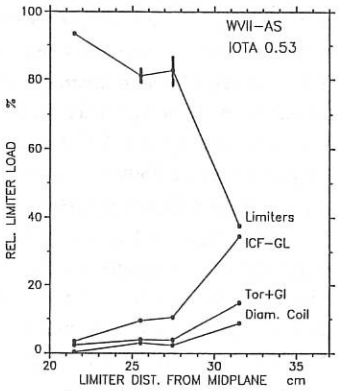

Fig. 5: Relative loads of in-vessel components.

Table I:

EVENTS	IOTA	ZLim	Reff (cm)	AVERAGE LENGTH OF GUIDING CENTER ORBITS (m) TOR+GL	LIMITERS	ICF-GL	DIAM.	ALL	PERCENTAGES OF EVENTS TOR+GL	LIMITERS	ICF-GL	DIAM	OTHERS	PRL2
887	0.53	31.5	15.4	421.0	278.6	383.4	408.3	356.7	14.8	37.7	34.5	8.9	4.1	–
1423	PRL2			403.8	266.0	326.4	335.7	318.2	10.5	40.8	31.2	7.9	3.0	6.6
410		27.5	15.0	301.4	128.3	268.9	255.9	153.8	3.9	82.7	10.5	2.4	0.5	–
1626		25.5	14.0	554.8	175.5	487.8	508.5	239.6	4.0	81.0	9.8	3.0	2.2	–
773		21.5	12.1	789.6	233.0	806.5	591.3	270.0	2.3	93.3	3.4	0.4	0.6	–
	start													
2262	outs.	31.5	17.9	258.0	105.5	137.5	219.3	121.2	0.4	65.0	31.9	0.9	0.4	1.4
1626	inside limiter			470.7	205.1	305.4	359.8	241.6	0.7	66.2	30.5	1.0	0.3	1.3
449	0.34	21.5	12.5	–	260.0	826.4	–	268.8	0	98.4	1.6	0	0	0.0
941	more data			–	244.6	725.5	–	255.5	0	97.8	2.0	0	0	0.2
639	0.71	21.5	10.2	1037.0	517.6	1133.0	1218.0	565.5	0.8	92.4	5.0	1.7	0.1	0

Guiding center orbits : H^+ at 52 eV, normalized mean free path $L^* = \lambda\iota/\pi R = 0.1$.

PHYSICS STUDIES FOR THE H-1 HELIAC

B.D.Blackwell, G.D.Conway, R.L.Dewar, H.J.Gardner,
S.M.Hamberger, J.Howard, and L.E.Sharp

Plasma Research Laboratory
Research School of Physical Sciences
The Australian National University
Canberra, Australia

The H-1 heliac[1], which is nearing completion, offers experimental access to an unusually wide range of 'plasma-current-free', low-shear, low-q toroidal configurations. The plasma dimensions ($\bar{a} \leq 0.22$ m, $V_p \sim 1$ m^3) and operational modes (steady fields B ≤ 0.25 T, 1 second pulse ≤ 1 T) are appropriate to detailed basic plasma physics studies, while the versatile coil arrangement allows rotational transforms to be readily varied between 0.6 and 1.95, e.g. to control the position of most low order rational surfaces. Fig. 1 shows a typical set of flux-surface cross-sections, and Fig. 2 illustrates some accessible transform profiles. Successful demonstrations of new low energy electron-beam field mapping techniques on the prototype heliac SHEILA indicate good possibilities to obtain extremely high spatial resolution ($\Delta r/\bar{a} < 0.5\%$) and rotational transform accuracy ($\Delta\iota/\iota \leq 10^{-3}$) in field mapping and error field studies on the much larger machine, H-1[2].

Experience with SHEILA [4] has shown that problems associated with the unusual plasma shape can be greatly reduced by referring all observations to appropriate straight-field-line magnetic, rather than geometric, coordinates. The strongly-indented plasma-section requires special diagnostic techniques. For example, a fast-scanning FIR interferometer will be installed to allow tomographic reconstructions of the 2-D density contours[3]. A rotating multi-sectored wheel rapidly scans the probing laser beam to give ~15 channels in each of four fan views of the poloidal cross-section (fig 3). The phase-shift information in each view is bandlimited by diffraction and Nyquist sampled to allow unambiguous recovery of the low order structure of the plasma distribution. The instrument should therefore be capable of sensing the slow changes in the density profile caused by plasma pressure effects, and can in principle recover the structure of low m-number density fluctuations. A 10.6μm scintillation interferometer is also being constructed for the observation of small-wavelength, high frequency fluctuations.

The coil arrangement also allows a variety of different combinations of magnetic well and shear profiles to be obtained. Some of these are being examined for equilibrium and both global and Mercier stability, using the BETA and VMEC 3D-MHD codes, to guide future experimental work on finite beta studies.

Studies with the BETA code have been undertaken with a view to examining the correlation between Mercier stability and non-linear global stability. Initial results were

obtained for an inner flux tube represented by a simple form (corresponding to the BETA parameterization NGEOM=5). (A more accurate surface representation is being developed for the VMEC code using DESCUR.)

The BETA code shows (Fig 4) the configuration to be Mercier stable for an equivalent volume average beta for the full plasma of 1% ($p=p_0(1-\psi)$, finest mesh $12 \times 36 \times 36$). The figure shows that stability improves at the edge of this model geometry, but an analysis of the full configuration with the VMEC code (to overcome the star-like domain requirement) is required. The axis region first becomes unstable, as shown by the case for ß=1.2%. Rearrangement of the pressure profile to reduce the pressure gradients near the axis improves the stability. Mercier stability decreases as the magnetic well is decreased (□ fig 4), corresponding to increased vertical field. Thus it is hoped that H1 can be tuned to explore the border of absolute Mercier instability ($\Omega_M<0$). Although the BETA code and field line tracing show similar limits for the well depth (–1 to +6%), better agreement with field line tracing occurs for slightly different surface coefficients than those for the best surface match. We expect that the more accurate surface fit obtained with DESCUR/VMEC may resolve this. It has been suggested that the Mercier criterion is a pessimistic indicator of stability[5]. Under these assumptions ($\Omega_M>-.02$) we estimate that a practical Mercier stability limit may be as high as 5% average beta.

Non-linear stability studies by the method of second minimization[5] indicate that the n=1,m=1 global mode appears to be stable at values much higher than this (<ß>=10%), for an inner flux tube, with a fixed boundary. Fig.5 shows the stability margin increasing with ß for the standard H-1 case. This stability is apparently improved by the indentation of the surfaces, (•, fig 5) where the same analysis is performed for configurations with a greatly reduced indentation but a similar rotational transform.

We gratefully acknowledge valuable discussions with, and advice from, B.A. Carreras, N. Dominguez, P.Garabedian, and V.Lynch.

References

[1] S.M. Hamberger, B.D.Blackwell, L.E.Sharp and D.B.Shenton, Fusion Technol. **17** ,123 1990.

[2] T.Y.Tou, B.D.Blackwell and L.E.Sharp, "An Image Intensifiying probe for Magnetic Surface Mapping", submitted to Rev. Sci. Instrum.

[3] J. Howard *"Novel Scanning Interferometer for 2-D Plasma Density Measurements"* Rev. Sci. Instrum. (in press)

[4] X.H. Shi, B.D.Blackwell and S.M.Hamberger, Plasma Phys. Contr. Fusion 31, 2011 1989

[5] F. Bauer, O. Betancourt, P. Garabedian, M. Wakatani, "The BETA Equilibrium Stability and Transprt Codes", Acad. Press, Orlando 1987.

[6] Hirshman, S.P., Betancourt, O., *"Preconditioned Descent algorithm for Rapid Calculations of Magnetohydrodynamic Equilibria"*, to be publ. J. Comput. Phys.

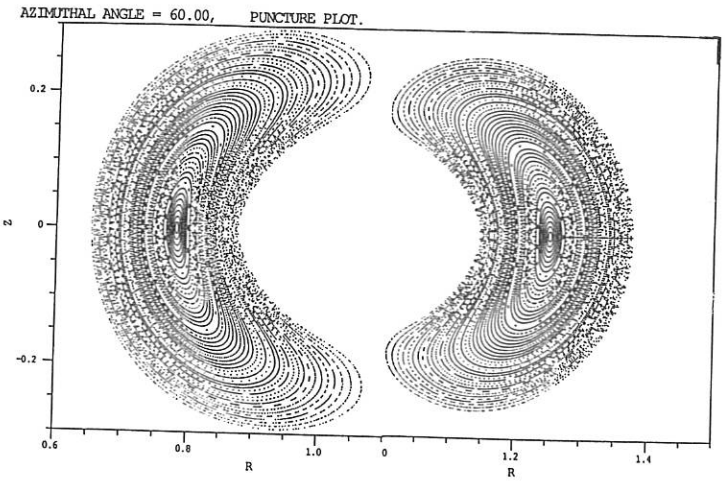

Fig. 1: Set of flux surfaces for low-shear magnetic configuration, I_h/I_r = 0.09: Inside & Outside.

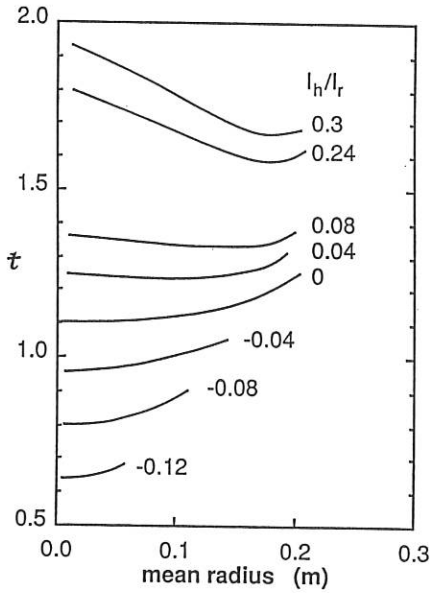

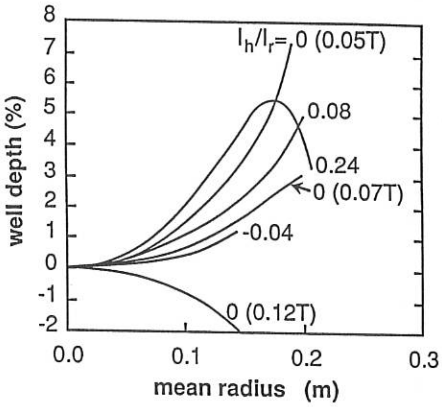

Fig. 2: (a) Rotational transform and (b) magnetic well profiles, for various current ratios I_h/I_r. For I_h/I_r = 0, the vertical field is given in parenthesis.

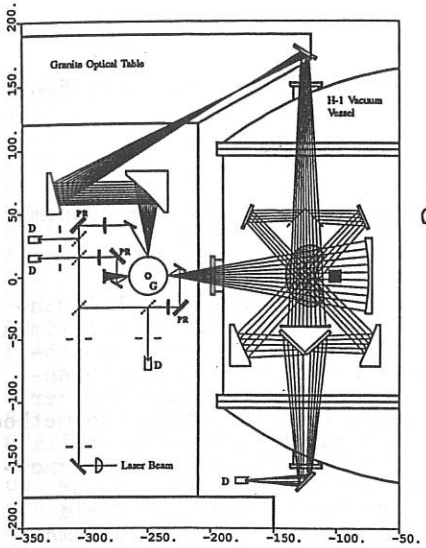

Fig. 3: Proposed interferometer arrangement for the H-1 heliac. Key: D-detectors; PR-polarization transforming reflectors; G-rotating scanning grating. Axes are marked in centimetres, origin is centre of vacuum vessel.

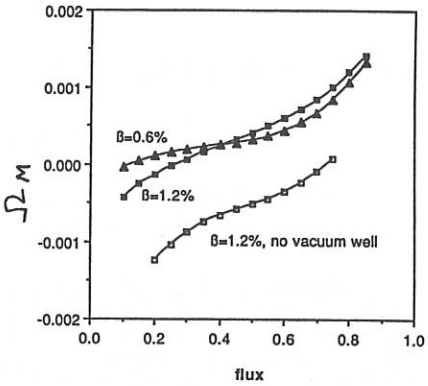

Fig. 4: Radial profile of mercier criterion for the inner flux tube with a vacuum well of 4%. A case with no well is shown for comparison.

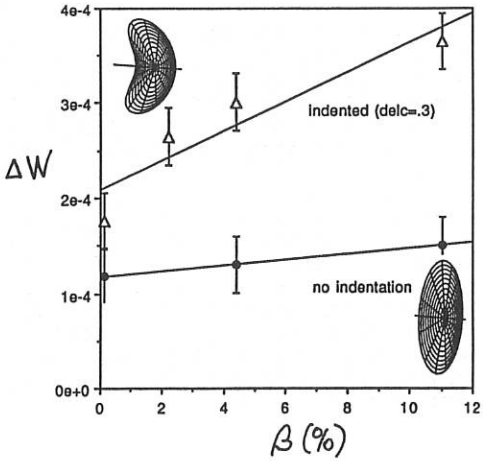

Fig. 5: Energy difference for second minimization for two configurations.

STUDY OF PLASMA EQUILIBRIUM CURRENTS IN AN l=3 TORSATRON

V.N.Kalyuzhnyj, V.V.Nemov

Institute of Physics and Technology, Ukrainian SSR Academy of Sciences, 310108 Kharkov, USSR

Investigation of plasma equilibrium currents (Pfirsch-Schluter currents) is of interest when searching for optimum schemes of stellarator systems /1/. In this paper equilibrium currents for magnetic configurations of an l=3 torsatron are investigated as a function of the homogeneous vertical magnetic field value. For the investigation, the method discussed in /2/ is used, allowing one to calculate equilibrium currents in real magnetic configurations, whose magnetic surfaces are determined only numerically. The case of small β (β is the plasma pressure-to-the magnetic field pressure ratio) is considered. Possible effects of plasma pressure on both the magnetic configuration and the equilibrium currents are estimated. The torsatron was considered with the following parameters that are close to those of the Uragan-3 device:

$$R = 100 \text{ cm}, \quad r_0 = 26.2 \text{ cm}, \quad m = 9 \qquad (1)$$

The model of the helical coil with filament-like conductors was used with the following winding law

$$(m/\ell)(\varphi - \varphi_{01,2,3}) = \vartheta - \alpha \frac{r_0}{R} \sin\vartheta, \quad \varphi_{01} = 0, \quad \varphi_{02,3} = \pm 2\pi/m \qquad (2)$$

Here R and r_0 are the major and minor radii of the torus, on which the helical coil is placed, m is the number of helical field periods on the torus length, ϑ is the angle in the meridional section of the torus counted from the direction of the normal to the circular axis of the torus, α is the modulation coefficient of the winding angle for the helical coil.

The case of exact compensation of the axially symmetric component of the poloidal magnetic field of the helical coil has been considered. There was a small vertical homogeneous magnetic field $B_\perp$ on the value of which the equilibrium current dependence was investigated.

The calculation was performed numerically using the method given in /2/. The distributions of $\nabla\psi$ along the magnetic line of force (ψ is the magnetic surface function) as well as of h, determining the density of the longitudinal equilibrium current

$$\vec{j}_{\parallel} = c \frac{dp}{d\psi} h \vec{B} \qquad (3)$$

were calculated ($p=p(\psi)$ is the plasma pressure). In accordance with the discussed case of small β, the vacuum magnetic field is used in the appropriate equations. For calculations this field was presented in the form of expansion in series over toroidal harmonic functions /3,4/. Calculations were performed in the cylindrical system of coordinates ρ, φ, z with the z-axis coinciding with the main axis of the torus. As starting points of integration (see /2/), the points on the ρ-axis (i.e., z=0) in the meridional plane $\varphi = 0$ were chosen (in this plane the cross sections of the magnetic surfaces are symmetric with respect to ρ-axis). At starting points $|\nabla\psi| = 1$.

Fig. 1 shows the cross sections of several magnetic surfaces in the $\varphi = 0$ plane (in coordinates $(\rho - R)/r_0$ and z/r_0) and also at the half period of the magnetic field. They were obtained for $\alpha = -1$ and for $B_\perp = 0$ and $B_\perp/B_0 = 2\%$ (the winding law with $\alpha = -1$ is often used and is rather close to the optimum law /5/). For every $B_\perp$ value two magnetic surfaces are presented. One from each pair of the surfaces was taken near the boundary of the confinement volume. Fig. 2 shows the distribution over magnetic surface cross sections (given in Fig. 1) of the quantities $|\nabla\psi|$ and g characterizing the distribution of the plasma pressure gradient $\nabla p = (dp/d\psi)\nabla\psi$ and the longitudinal current density $j_{\parallel}$

$$j_{\parallel} = \frac{2c}{\iota B_0} \frac{dp}{d\psi} g \quad , \quad g = 0.5\, \iota B_0 B h \qquad (4)$$

as functions of $\gamma = \omega/2\pi$. Here ι is the rotational transform (in 2π-units), B_0 is the longitudinal field on the circular axis of the torus, ω is the angle counted around the centre of the magnetic surface section from the direction of the normal to the circular axis. The g distributions shown correspond to $h_0 = 0$, where h_0 is the starting value for h.

Apart from $j_{\parallel}$, it is of interest to consider also the ratio $j_{\parallel}/j_\perp$ /1/, where $j_\perp = c\,|\nabla p|/B$. Through $j_{\parallel}/j_\perp$ one may express the surface current density i, which is equivalent to the $j_{\parallel}$ distribution between two close magnetic surfaces

$$i = j_{\parallel} d = \frac{j_{\parallel}}{j_\perp} \cdot \frac{c\,\Delta p}{B} \qquad (5)$$

where d and Δp are the distance and the pressure drop between these surfaces. Table 1 lists approximate values of g, $j_{\parallel}/j_\perp$ and $\lambda = 0.5\, \iota\, j_{\parallel}/j_\perp$ distribution amplitudes (g_m, $(j_{\parallel}/j_\perp)_m$ and λ_m, respectively) obtained over the cross sections of outer surfaces of Fig. 1 versus $B_\perp/B_0$. These results correspond to such a choice of $h_0 \neq 0$ when the total longitudinal current between infinitely close surfaces equals zero.

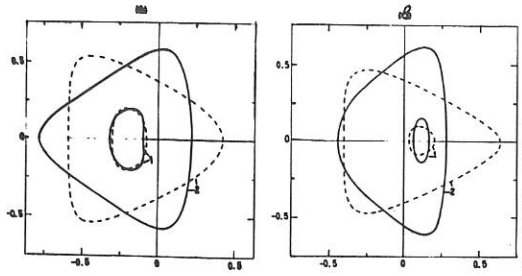

Fig. 1
Cross sections of the magnetic surfaces with the plane $\varphi = 0$ (solid lines) and $\varphi = \pi/m$ (dashed lines) for: a) $B_\perp/B_0 = 0$ (1: $\iota = 0.41$, 2: $\iota = 0.67$), and b) $B_\perp/B_0 = 2\%$ (1: $\iota = 0.44$, 2: $\iota = 0.54$) in coordinates $(\rho - R)/r_0$ and z/r_0.

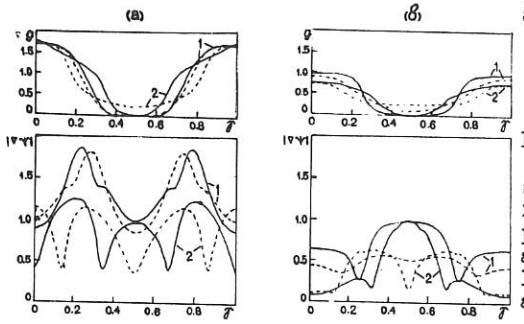

Fig. 2
Distribution of g and $|\nabla\psi|$ over the cross section of the magnetic surfaces in the planes $\varphi = 0$ (solid lines) and $\varphi = \pi/m$ (dashed lines) for: a) $B_\perp/B_0 = 0$ and b) $B_\perp/B_0 = 2\%$.

Table 1

$B_\perp/B_0$	0	0.66%	1.32%	2%
ι	0.665	0.667	0.8	0.54
g_m	0.85	0.65	0.63	0.35
$(j_\parallel/j_\perp)_m$	4.2	4.2	3.5	4.4
λ_m	1.4	1.4	1.4	1.2
β	0	0.63%	1.5%	1.8%

It follows from the table that, when $B_\perp/B_0$ changes from 0 to 2% (with the $B_\perp$ direction causing outward shift of the magnetic axis), the $j_\parallel/j_\perp$ value for outer surfaces is somewhat larger than it follows from the well-known approximate Pfirsch-Schluter current formula (for which $\lambda_m = 1$).

The results obtained may be used to estimate the possible effect of plasma pressure on the magnetic configuration and equilibrium currents. As is known, in the magnetic field excited in the toroidal plasma by plasma equilibrium currents, the homogeneous vertical component of this field plays an important role. Here we try to estimate the plasma pressure effect on plasma equilibrium currents, judging on the value of the homogeneous component of its magnetic field.

Let the plasma be limited by outer magnetic surfaces of Fig. 1 and have a sharp boundary. Then the homogeneous vertical magnetic field generated inside the plasma by the surface equilibrium current may be evaluated as

$$B_\perp \sim 2\pi i_m/c \qquad (6)$$

where i_m is the amplitude of the surface current distribution. Using (5) we obtain

$$B_\perp \sim \frac{1}{4}\beta\left(\frac{j_\parallel}{j_\perp}\right)_m B_0 = \frac{1}{2}\beta B_0 \lambda_m/t \qquad (7)$$

where $\beta = 8\pi p/B_0^2$ and it is assumed that $\Delta p = p$ (the sharp boundary). If one considers the transverse field $B_\perp$ employed in our calculations of magnetic configurations and equilibrium currents as a field (7) generated by equilibrium currents, then one may define the plasma β equivalent to it, viz.,

$$\beta \sim 4\frac{B_\perp}{B_0}\cdot\frac{1}{(j_\parallel/j_\perp)_m} = 2\frac{B_\perp}{B_0}\cdot\frac{t}{\lambda_m} \qquad (8)$$

The β values calculated by formula (8) are listed in Table 1 (the last line). In accordance with these estimates, we may consider the magnetic configurations in Fig. 1 and Table 1 at $B_\perp/B_0 \neq 0$ as configurations without the additional vertical field (i.e., at $B_\perp = 0$) but with the presence of a plasma having β up to $\beta \approx 2\%$.

REFERENCES

1. Chodure R., Dommaschk W., Herrnegger F. et al., IEEE Trans. Plasma Sci. PS-9 (1981) 221.
2. Nemov V.V. Nucl. Fusion 28 (1988) 1727.
3. Kovrizhnykh L.M. Zh.Tekh. Fiz. 33 (1963) 377 (In Russ.).
4. Kalyuzhnyj V.N., Nemov V.V. Voprosy atom. nauki i tekhniki, ser. Termoyadernyj sintez N2 (1985) 35 (In Russian).
5. Hanson J.D., Cary J.R. Phys. Fluids 27 (1984) 767.

IMPURITY FLUX REVERSAL IN l=2 TORSATRONS USING RF HEATING

D. L. Grekov, A. V. Zolotukhin, A. A. Shishkin

Kharkov Institute of Physics & Technology, Ukrainian SSR Academy of Sciences, Kharkov, 310108, USSR

We have studied the influence of local heating on the impurity flows in the Pfirsch-Schluter regime. If the effect of the thermoforce on the impurity ions is included the impurity flux can be reversed by heating the impurities. This concept can be realized in torsatron experiment using RF heating. We present estimates of the power required, and describe the design of the RF launch system,

Experimentally discovered degrading of plasma parameters due to impurity ions stimulates the search for diverse techniques of plasma cleaning. Passive (divertors) and active methods can possibly be used to act on impurity ions. Active methods may involve the bulk component puffing (particle source), bulk plasma heating (heat source) and momentum transfer e.g. due to high energy particle injection. These methods were studied for tokamaks theoretically and experimentally. Present paper deals with studying the RF heating action on heavy impurity flux in the Pfirsch-Schluter regime in the torsatrons and the condition of the impurity flux reversal is found.

Following the papers [1,2] where the heavy impurity behaviour in tokamaks is considered write the MHD equations for bulk plasma ions (i) and impurity ions (I) in the form

$$\nabla p_i = n_i e(\underline{E} + \underline{v}_i \times \underline{B}) + \underline{R}_\parallel$$
$$\nabla p_I = n_I Z_I e(\underline{E} + \underline{v}_I \times \underline{B}) - \underline{R}_\parallel \qquad (1)$$

where

$$\underline{R}_\parallel = - C_1 \frac{m_i n_i}{\tau_{iI}} \underline{u}_\parallel - C_2 n_i \nabla_\parallel T_i \qquad (2)$$

Here p_α is the pressure, $\underline{v}_\alpha$ is the velocity, n_α is the particle density, $Z_\alpha e$ is the charge, m_α is the mass, T_α is the temperature of α-species ions (α=i,I), τ_{iI} is the time of scattering ions off impurities, $\underline{u}_\parallel = \underline{v}_i - \underline{v}_I$, $\underline{R}_\parallel$ is the friction force. When the sources of heat and particles are present the radial flux of impurity ions, averaged over the tokamak

magnetic surface, has the form

$$\Gamma_I = -\Gamma_i/Z_I = \frac{n_i q^2 \rho_i^2}{Z_I \tau_{iI} T_i}\left[\left(C_1 + \frac{C_2^2}{C_3}\right)\left(\frac{1}{n_i}\frac{\partial p_i}{\partial r} - \frac{1}{Z_I n_I}\frac{\partial p_I}{\partial r}\right) - \frac{5C_2}{2C_3}\frac{\partial T_i}{\partial r}\right] -$$

$$\frac{n_i q^2 \rho_i^2}{Z_I \tau_{iI} T_i}\frac{eB_T R}{n_i}\left[\left(C_1 + \frac{C_2^2}{C_3}\right)a_{\tau 1} - \frac{C_2}{C_3}\frac{a_{Q1}}{T_i}\right] \qquad (3)$$

Here $q = rB_T/RB_p$, r,R are the small and large radii of the torus B_T and B_p are the toroidal and poloidal components of the tokamak magnetic field, ρ_i is the ion Larmor radius, $a_{Q1}(r)$, $a_{\tau 1}(r)$ are the amplitudes of the $\sin\vartheta$ components in the Fourier series of heat $Q_i(r,\vartheta)$ and bulk ion $\tau_i(r,\vartheta)$ sources. To neutralize the first term in (3) and nullify Γ_I it is necessary that $\mathrm{sgn}(a_{\tau 1}) = -\mathrm{sgn}(B_T)$ and $\mathrm{sgn}(a_{Q1}) = \mathrm{sgn}(B_T)$.

Considering the possibility of applying asymmetric heat source created by RF heating to reverse the impurity flux in torsatrons two points should be noted: first, it is difficult to create with RF means the heat source having the necessary between top and bottom asymmetry; second, one obtains too large a_{Q1} values when heating bulk ions asymmetrically. Therefore in the following consideration we'll take into account the thermoforce which is due to the impurity temperature gradient along the magnetic field lines $R_T^I \propto n_I|\nabla_\parallel T_I|\tau_{II}/(\tau_{II}+\tau_{Ii})$. This friction force is considerably less then the thermoforce due to the temperature gradient of bulk ions $R_T^i \propto n_i|\nabla_\parallel T_i|\tau_{ii}/(\tau_{ii}+\tau_{iI})$ ($\tau_{\alpha\beta}$ is the collision time): R_T^i/R_T^I changes from $Z_I^2 \gg 1$ to $Z_I^2(m_I/m_i)^{1/2}$ on increasing n_I from $n_I \le (m_i/m_I)^{1/2} n_i/Z_I$ to $n_I \ge n_i/Z_I$. Nevertheless the account of R_T^I allows one to include into consideration the heat source acting on impurities. To find $\nabla_\parallel T_{i,I}$ use the expressions for heat fluxes

$$q_{\parallel i} = C_2 n_i T_i u_\parallel - C_3 \frac{n_i T_i}{m_i}\frac{\tau_{ii}\tau_{iI}}{\tau_{ii}+\tau_{iI}}\nabla_\parallel T_i$$

$$q_{\parallel I} = -C_3 \frac{n_I T_I}{m_I}\frac{\tau_{II}\tau_{Ii}}{\tau_{II}+\tau_{Ii}}\nabla_\parallel T_I \qquad (4)$$

Inserting $\nabla_\parallel T_\alpha$ from (4) to (2) with the account of R_T^I yields

$$\underline{R}_{\parallel} = - C_1 \frac{m_i n_i}{\tau_{iI}} \underline{u}_{\parallel} - C_2 n_i \nabla_{\parallel} T_i + C_2' n_I \nabla_{\parallel} T_I \qquad (5)$$

The further calculation of Γ_I we perform in the 'straight stellarator' approximation. This allows one to account for the action of the helical heat source of the form $Q_\alpha = l\varepsilon_l Q_\alpha'(r)\sin l\zeta$ Here $\zeta = \vartheta - m\varphi/l$, ϑ, φ are the poloidal and toroidal angles respectively m is the number of field periods over the torus lenght $\varepsilon_l = b_l/B_0$, b_l, B_0 are the magnitudes of the helical and toroidal fields. Note that other components of the Q_α Fourier series expansions over $\sin(p\zeta)$, $\cos(p\zeta)$ do not influence Γ_I in this approximation. After averaging over the helical magnetic surface one obtains

$$\Gamma_I = \Gamma_{IH} + \frac{n_i m_i}{\tau_{iI}} \frac{l\varepsilon_l^2 I_l(l\alpha\bar{r})}{2Z_I e^2 B_0 \alpha^2 \bar{r}^2} \left[- \frac{C_2}{C_3} \frac{eB_0}{l\alpha} \frac{Q_i'(\bar{r})}{n_i T_i} + \frac{4}{3\sqrt{\pi}} \frac{C_2'}{C_3'} \frac{eB_0}{l\alpha} \frac{Q_I'(\bar{r})}{n_I T_I} \right] \qquad (6)$$

where Γ_{IH} are the small corrections to first terms in (3) appearing due to the account of the helical nonuniformity of plasma parameters and of the magnetic field, $\alpha = m/lR$, $I_l(l\alpha\bar{r})$ is the Bessel function.

Thus with the corresponding sign of $B_0 Q_i'(\bar{r})$ or $B_0 Q_I'(\bar{r})$ one may reverse the impurity flux using the helical heat sourse acting on basic ions or on impurities. The estimates for Uragan-2M torsatron with the parameters $n_e(0) = 10^{13} cm^{-3}$, $T_i(0) = 1keV$, $\iota/2\pi = 0.5$, $m = 4$, $B_0 = 1T$, $T_i(\bar{r}) = 50 \div 100eV$, $\bar{r} = 22cm$ give for Q_i' too large value: $Q_i' = 100\ W/cm^3$. Besides the quite appreciable value for Q_I' is obtained at $n_I/n_i = 10^{-3}$: $Q_I' = 0.1\ W/cm^3$. To create the helical heat source Q_I we suggest using the cyclotron absorption of fast magnetosonic waves (FMSW) by impurity ions. Choosing, e.g., FMSW with the frequency $\omega = 0.11\omega_{ci}(0)$ (ω_{ci} is the cyclotron frequency of bulk ions) one may simultaneously influence the ions Cr^6_{52}, Mn^6_{55}, Fe^6_{56}, Ni^7_{59}, Cu^7_{63} and Cu^7_{64} at $\bar{r}$: $T_e(\bar{r}) = 50eV$ and Mo^{11}_{96} at $\bar{r}$: $T_e(\bar{r}) = 100eV$. At $\omega = 0.16\omega_{ci}(0)$ one may influence Cr^8_{52}, Mn^9_{55}, Fe^9_{56}, Ni^9_{59}, Cu^{10}_{63} at $\bar{r}$: $T_e(\bar{r}) = 100eV$ and C^2_{12} at $\bar{r}$: $T_e(\bar{r}) = 10eV$. Besides it must be the preferential absorption along one of two helical surfaces of the resonance $\omega = \omega_{cI}$. It may be provided by using the antenna system consisting of two (four) pairs of loop antennas located in the small cross-section of

the torus, as shown in Fig.1 and distanced by $\Delta\varphi=\pi$ ($\Delta\varphi=\pi/2$) along the large circumference of the torus. Put RF field in the form $\underline{E}=\underline{E}(r)\exp[i(M\vartheta+k_{\parallel}z-\omega t)]$, ($z=R\varphi$). The suggested system allows one to excite waves with $M=1,3$ and $k_{\parallel}=m(1+2k)/2R$ ($k=0,1,\ldots$), which will be strongly absorbed ($\gamma \sim \omega$) in the narrow zone $r\Delta\vartheta \cong m(1+2k)\rho_i/R$ along the chosen helical surface. The part of the RF energy that goes to the 'necessary' part of the spectrum, is determined by the formula

$$\kappa_u = \frac{4\Delta z}{\pi R}\sum_{k=0}^{k_{\parallel max}} A_k^2 \qquad (7)$$

Here the summation is performed over the spectrum part for which $k_{\parallel}=m(1+2k)/2R$, $k_{\parallel max}=k_A(0)$, $k_A=\omega/v_A$, v_A is the Alfven velocity, Δz is the antenna dimension in the z-axis direction. The estimates show that κ_u changes from $\kappa_u=0.05$ for $\Delta z=4$cm, the system consists of two pairs of loops to $\kappa_u=0.3$ for $\Delta z=16$cm, four pairs of loops. The total RF power necessary to reverse the impurity flux is determined by the expression

$$P_{tot} = 2\pi Ra\Delta r\kappa_u Q_I' \qquad (8)$$

where Δr is the radial dimension of the impurity location zone that interact with the RF field (in the estimates $\Delta r=5$cm). For the Uragan-2M and antenna system parameters given above one obtains $P_{tot} \sim 200$ kW.

Thus there exists an effective RF method for reversing the flux of heavy impurities in l=2 torsatrons.

REFERENCES

1. P.H.Rutherford The Physics of Fluids, v.17, p.1782, 1974.
2. K.T.Burrell The Physics of Fluids, v.19, p.401, 1976.

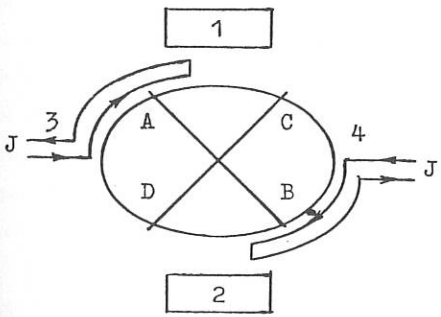

Fig.1 The small cross-section of the torsatron. 1,2 are helical conductors 3,4 is the antenna system. AB is the line $\omega=\omega_{cI}$ on which the absorption is at maximum (the absolute value of RF field is at maximum). CD is the line $\omega=\omega_{cI}$ on which the absolute value of RF field is at minimum

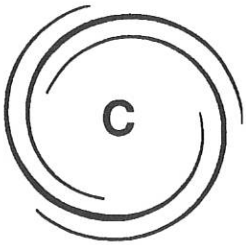

ALTERNATIVE MAGNETIC CONFINEMENT SCHEMES

C1 REVERSED FIELD PINCHES

ION TEMPERATURE MEASUREMENTS ON THE ETA-BETA II RFP

Carraro,L.,Innocente,P.,Martini,S.,Ortolani,S.,Puiatti,M.E.,Scarin,P.,Valisa,M.
Istituto Gas Ionizzati del C.N.R.
EURATOM-ENEA-C.N.R. Association-Padova Italy

Ion temperature values Ti ≥Te are a common feature of ohmically heated RFP [1,2,3] indicating the presence of a significant non-ohmic ion heating mechanism. The increase with fluctuations of the ratio Ti/Te [4] has suggested a direct coupling between ion heating mechanism and the power associated with the fluctuations which drive the dynamo electric field required to sustain the RFP configuration [3,5].

In this paper are presented results on the ion temperature in ETA-BETA II, obtained from CV 2271 Å line Doppler broadening measurements , together with the electron temperature time evolution from Si(Li) detector and electron density from a two colour CO_2 interferometer.

The temporal behaviours of Te from Si(Li) detector and of Ti from CV 2271 Å spectral profile, are reported in Fig.1; the corresponding evolution of the electron line density is shown in Fig.2.

Measurements of CV 2271 Å line along different chords in the plasma and simulations of the CV profile time evolution with a 1D impurity transport code [6] indicate that the ion temperature deduced from CV is representative of the centre of the plasma provided the ion temperature profile is not much more peaked than the electron temperature profile. However, the measured Ti values are always greater than Te, with a more pronounced difference between the two temperatures in the early phase of the discharge.

Evaluating β_θ and $<\beta>$ from the previous Te, Ti and n_e data, with parabolic profiles, gives $\beta_\theta \geq 10\%$ and $<\beta> \geq 5\%$ at the early times (Fig.3).

The time variation of the resistivity anomaly factor Z_{eff}^*, defined as the ratio between the resistivity from Ohm's law on axis, $\eta^*(0) = V_{loop}/(2\Pi R J_\Phi(0))$ and the on axis Spitzer's resistivity with Z=1, is shown in Fig.4. In the early phase of the

discharge the resistivity remains close to classical, while later on, higher values are observed which could be due both to an increase of the ion effective charge and to a change in the profile of Z_{eff} , Te and current density [7,8]. The values of Z_{eff}^* and β_θ combine into the energy confinement time $\tau_E \propto \beta_\theta Te^{3/2}/Z_{eff}^*$ which, as shown in Fig. 4, at the beginning of the discharge is about 100 μs and 1.4 ms later decreases to about 40 μs.

The decrease of β_θ to about 5% , of $<\beta>$ to about 2% and of τ_E to 40 μs at late times seem to be essentially due to the decrease of the electron density. However, sustaining the density, e.g. by pellet injection, has proven to allow to maintain in time electron β and Z_{eff}^* close to those at early times [9], which gives a significant improvement in the energy confinement time. The possibility of obtaining the same results for the total β will remain an open question until Ti measurements with pellet injection are done.

The experimental evidence that Ti≥Te can be discussed in terms of magnetic and helicity balance equations. It is known that the input power P_W, necessary to maintain the total energy content of a steady-state RFP as evaluated from the energy balance equation, is less than the input power P_K, evaluated from the helicity balance equation, which better describes the experimentally measured power input. Typically the excess power is comparable to the ohmic term, i.e. $(P_k - P_w) \sim P_w$ [10]. Moreover, it has also been noted elsewhere [11] that this excess power input, necessary to maintain the helicity of a relaxing system, represents the fraction of the ohmic power absorbed by fluctuations and that plasma instabilities and fluctuations could be directly coupled with an anomalous ion heating mechanism [3]. On this basis comparable ion and electron temperatures would indeed be expected.

Furthermore the excess of energy may be thought as stored in the magnetic field and then dissipated into plasma heating during reconnection processes [10]. In particular, during the relaxation phase the configuration evolves towards lower energy states; if all of the energy released during this process ($\Delta W_M/W_M \sim 10\% \sim \beta$) goes into ions through viscous dissipation, a significant increase of the ion energy content is obtained. In this simple model the ratio Ti/Te increases with Θ [12] as experimentally observed [13].

ACKNOLEDGMENTS

The authors wish to thank the technical support of Mr. E. Baseggio.

[1]Howell R.B.,Nagayama Y., Phys. Fluids 28 ,743 (1985)

[2]Ogawa K., MaejimaY., Nucl. Fusion 25,1295(1985)

[3]Carolan P.G. et al., 14th Europ. Conf. on Contr. Fus. and Pl. Phys. Madrid 1987,II , p.469

[4]Wurden G.et al., 15th Europ. Conf. on Contr. Fus. and Pl. Phys. Dubrovnik 1988,II,p.533

[5]Ortolani.S., Plasma Phys. Contr. Fusion 31,10,1665 (1989)

[6]Carraro L. et al, this Conference

[7]Alper B. et al. Nucl. Fusion 26, 1256 (1986)

[8]Gabellieri L. et al. Nucl. Fusion 27, 863 (1987)

[9]Antoni V. et al. 14th Europ. Conf. on Contr. Fus. and Pl. Phys. Madrid 1987,II , p.532

[10]Giubbilei M.,Martin P., Ortolani S., to be published in Plasma Phys. Contr. Fusion

[11]Schoenberg K.F. et al. Phys. Fluids 27, 1671 (1984)

[12]Martin P., Ortolani S., New Delhi 1989 Int. Conf. on Pl. Phys., Vol.1,p.149

[13]Shimada T.et al, 12th Int. Conf. on Pl. Phys.. and Contr. Fus. Res.,Vol. 2,p.457,1989

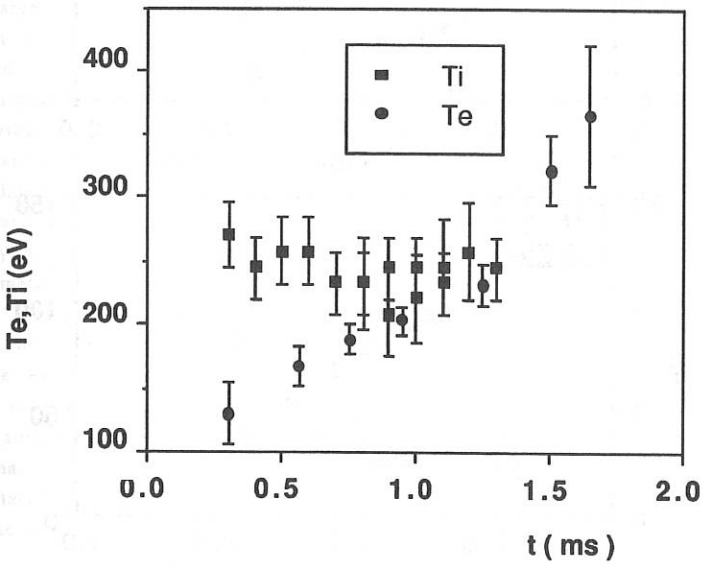

Fig. 1

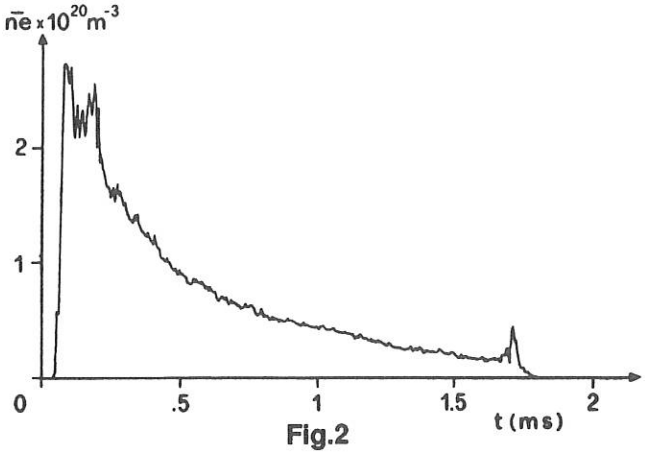

Fig.2

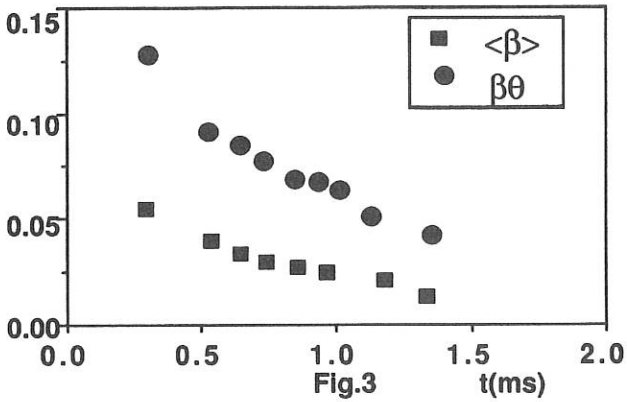

Fig.3

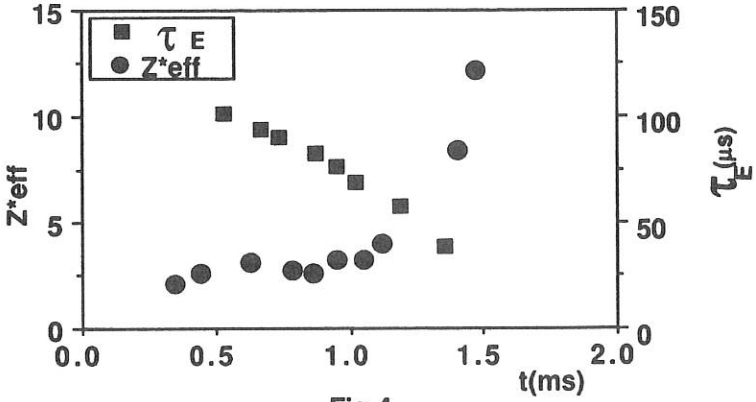

Fig.4

CARBON EMISSION MEASUREMENTS ON THE RFP DEVICE ETA-BETAII

Carraro,L., Muzzolon,A., Puiatti,M.E., Scarin,P., Valisa,M.
Istituto Gas Ionizzati del C.N.R.
EURATOM-ENEA-CNR Association - Padova, Italy

The emissivity of the CV 2271Å line has been measured on the RFP device Eta-BetaII along 7 plasma chords, using a 1-m Czerny-Turner spectrometer, equipped with a 2400g/mm grating. The spectrometer has been absolutely calibrated by a strip tungsten lamp to evaluate the carbon content in the discharge. The time-integrated spectrum measured along a diameter in the range 2250-2320Å by a photo-diode array is shown in fig.1. Due to the photo-diode array poor time resolution (compared with the pulse lenght of about 2ms), the emission along 7 plasma chords has been measured by a photomultiplier, to evaluate the time behaviour of the CV emission profile. The experimental data have been inverted by an asymmetric inversion technique. Fig. 2a shows the profiles obtained inverting the data at the maximum of carbon emission (300 μsec after the current start) and during the flat-top phase of the plasma current; the chordal re-integrated profiles and the experimental points are also shown, as a test of the error introduced with the inversion procedure (fig.2b). In the early phase of the discharge the carbon emission is peaked in the centre of the plasma, while later on it is hollow, reaching a quasi-steady profile, and showing a displacement towards the external region of the vacuum vessel.

An impurity transport model [1] has been modified to simulate the impurity lines behaviour: for each ion, the ground and metastable state population densities are separately calculated. Infact the intensity of many lines may not be properly calculated by a simple corona balance between excitation from ground state and spontaneous decay. This happens when, as in the case of OV, the metastable state is highly populated or when, as for the 2271Å line of CV, the excitation process from the metastable state has a very high probability compared with the excitation from ground state, and therefore may not be neglected even if the metastable is much less populated than the ground state. In particular, for the 2271Å line of CV, if the excitation from the metastable state is not considered, the corona balance leads to a value about 4 times lower.

The simulation of the experimental data cannot account for the asymmetry of the plasma, because the diffusion model is cylindrically symmetric. Therefore, only a qualitative comparison between the calculated and experimental time behaviour of the emission profiles may be obtained.

Fig.3 shows an example of the CV line profile simulation obtained from the model at two times, corresponding to the emission peak and to the flat-top phase of the plasma current. The time behaviour is consistent with the experimental observation: around the emission peak, in the early phase of the discharge, CV shows an emission profile essentially peaked at the centre, while the profile is more hollow at later times. The ion populations corresponding to these two times are shown in fig.4. The time evolution of the line integrated emissivity, calculated along two chords, corresponding to the plasma diameter and to the external experimental chord, is shown in fig.5, together with the experimental data: the model reproduces the slower dynamics of the external chord, due to the lower electron temperature and to the diffusion of CV. The discussed simulation has been obtained with electron temperature and density profiles parabolic in the early phase of the discharge and slightly flatter (quartic) during the flat-top. It has been assumed that the recycling coefficient at the wall increases from 0.8 to 0.95 ; the diffusion has been calculated by a classical transport model with the fluxes enhanced by a space-dependent coefficient, whose value is 10 on the axis and 100 at the wall. With the same values of the particle fluxes, the time behaviour of OIV,OV,OVI lines has been simulated ; the result for OIV and OV is drawn in fig.6. No emission line from OVII has been measured; however, from the spectrum measured by a Si-Li detector in the range 500-700eV, the intensity of OVII 21.6Å line has been estimated to be $\geq 100 watts/m^3$, corresponding to an OVII concentration less or equal than 0.1% of electron density. Comparing the line intensities obtained from the model with the measured emissivities, the carbon and oxygen content may be evaluated, leading to $n_C/n_e \approx n_{OX}/n_e \approx$ 0.5-1%.

Acknowledgement: the authors are grateful to E.Baseggio for the technical support.

[1] Carraro,L.,et al, in Controlled Fusion and Plasma Physics (Proc. 15th Europ. Conf. Dubrovnik 1988) Part II,p.561
[2] Ortolani, S., in Twenty Years in Plasma Physics, p.75 (1985)

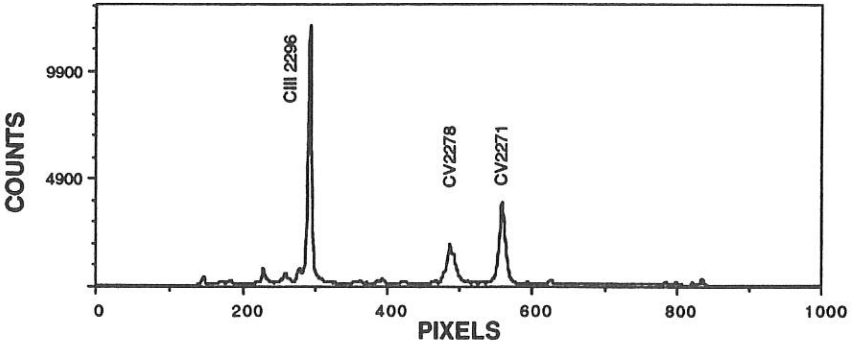

Fig. 1- Example of time integrated spectrum around the CV 2271 Å line

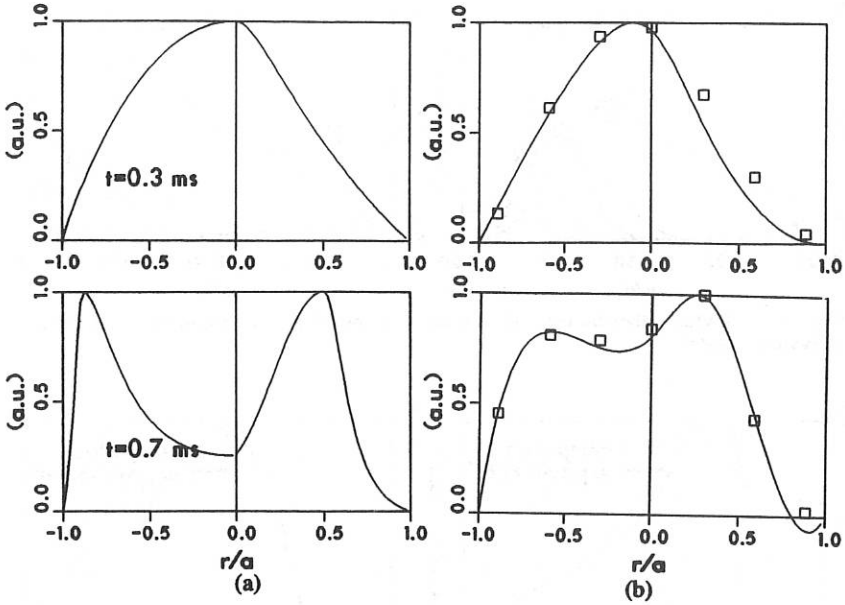

Fig. 2 - Radial CV profiles obtained from the inversion (a), and their chordal reconstruction(b); the squares represent the experimental points. The two times correspond to the emission peak (0.3ms) and to the flat-top phase of plasma current (0.7ms).

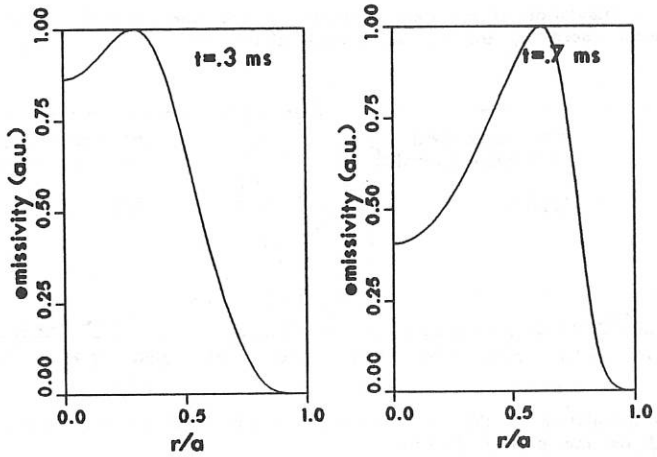

Fig. 3 - Radial CV profiles obtained from the diffusion model.

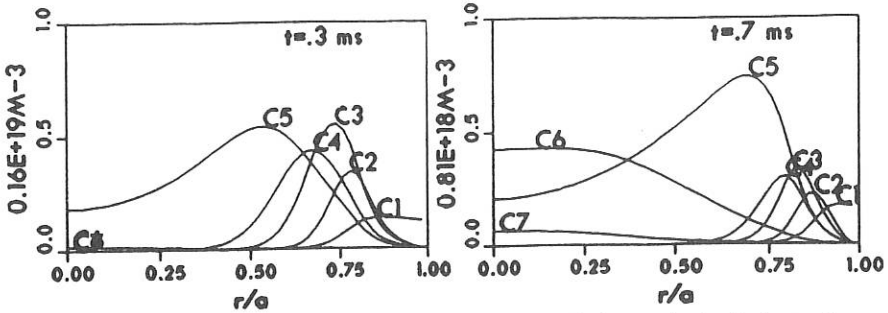

Fig. 4 - Radial distribution of carbon ion populations obtained from the diffusion model.

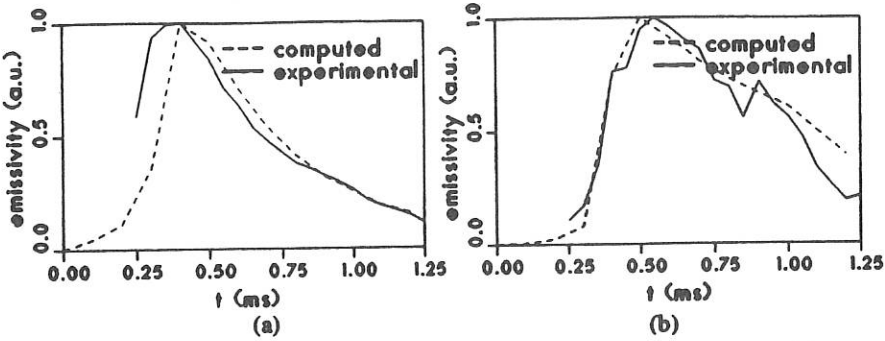

Fig. 5 - Simulation of the time behaviour of the line integrated emissivity on the central chord (a) and on the external chord (b)

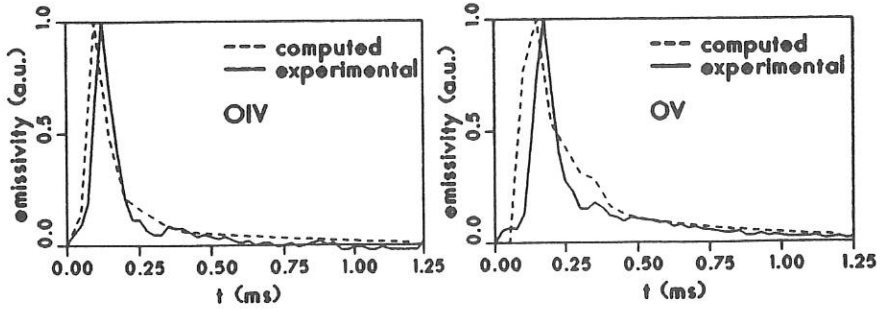

Fig. 6 - Simulation of the time behaviour of OIV and OV line emissivities, integrated on the plasma diameter.

SHELL GAP MODIFICATION AND LIMITER INSERTION IN THE REPUTE-1 RFP

S. Shinohara, I. Ueda, M. Awano, Y. Shimazu
A. Fujisawa, H. Ji, A. Ejiri, A. Shirai, S. Odachi
K. Mayanagi, K. Yamagishi, H. Toyama, K. Miyamoto

Department of Physics, Faculty of Science,
University of Tokyo, Bunkyo-ku, Tokyo 113, Japan

INTRODUCTION

In the previous papers [1,2] in the REPUTE-1, it was shown that the plasma resistance R_p at the current flat-topped phase decreased by 15 - 50 %, depending on conditions, with bypass plates due to a reduction of error fields near the port sections. In order to get the better plasma parameters, focusing on reducing error fields, shell gap modification was tried. For the study of plasma resistance and plasma response, we inserted a movable limiter with a negative bias voltage in the plasma. The correlation of the ion temperature with the plasma resistance was also investigated.

SHELL GAP MODIFICATION

We covered the shell gaps on two toroidal locations with Aluminum foils (effectively 10 layers of 80 μm thickness each). This cover extended to about 0.2 m and 1.1 m in the toroidal and poloidal directions (over 220° of the poloidal angle (outer side of the torus)), respectively. The minor radius of the cover normalized by the plasma radius is ~ 1.3, while ~ 1.1 of the stainless steel shell with 5 mm thickness. The expected skin time of the cover for the vertical field penetration is an order of 0.5 ms (1 ms for the shell case).

As is shown in Fig.1, the plasma resistance R_p decreased by about 12 % compared with that without the cover for the case of $R = 2$ and decoupling mode [1]. For comparison, the least square fitting curves for both cases are also shown. Here, R is a winding ratio of the step-down transformer of the ohmic power supply. This R_p scaled as $-(3/2)$ power law of the plasma current I_p, and did not show a saturation of R_p even at

the higher plasma current regime. At I_p = 390 kA, R_p of down to 0.25 mΩ was obtained, and in this current range, clear sawtooth oscillations (~ ± (10 − 20) % change of amplitude) such as soft X−ray, CV line emissions and $\dot{\Phi}$ (Φ: toroidal flux) were sometimes observed [3]. After this covering, the reproducibility of discharges became better without noticeable shift of plasma column. However, the plasma discharge duration time has not been changed (≤ 3.2 ms).

LIMITER INSERTION

In order to study the edge effects concerning dynamo electric field [4,5], a stainless steel limiter plate, 35 mm wide and 3 mm thick, was inserted into the plasma from the outer side of the torus. As is shown in Fig.2, a slight increase in the one turn loop voltage V_l (by ~ 10 V) was found with an advance in the movable limiter (inserted distance Δ) for I_p = 210 − 220 kA range (R = 4, $\Delta \leq$ 17.5 cm, plasma minor radius a = 22 cm). The charging voltage of the ohmic power supply must be increased by ~ 3 % for the deepest insertion case to maintain the same plasma current. There were not appreciable differences of loop voltage, changing the angle θ of the limiter plate. Here, the angles θ of 0° and 90° denote that the limiter surface is parallel with the toroidal and poloidal directions, respectively.

Preliminary experiment on biasing a negative voltage to the movable limiter with respect to a vacuum vessel was tried. This limiter was connected in series with a resistance of ~ 35 mΩ and an inductance of ~ 55 μH, and the vessel was shorted to the earth through a 2.5Ω resistance. For the case of several cm insertion of the limiter into the plasma with − (200 − 400) V bias by a capacitor bank, a slight decrease in the plasma resistance and slight increases in the discharge duration and plasma density were observed. Near the plasma current maximum phase, the limiter current was < 2 kA. These favorable effects were not found for the deep limiter insertion case.

ION TEMPERATURE AND PLASMA RESISTANCE

In the REPUTE−1, the ion temperature T_i from the Doppler broadening of CV line [6] was much higher than the electron temperature measured by the methods of the Thomson scattering and pulse height analysis of soft X−ray, especially for the low plasma density case. Even

with the same plasma density and the same plasma current, the obtained R_p and T_i were scattered from shot to shot, which indicates the different plasma performance relating MHD activities.

Figure 3 shows a relation between the ion temperature and plasma resistance for three different plasma density regimes with I_p = 300 kA and R = 4. This shows that the ion temperature was higher for the larger plasma resistance case. With a increase in R_p, the amplitude of m = 1 poloidal mode (toroidal field at the wall) as well as the soft X-ray fluctuation were enhanced. There seemed to have no correlation of T_i with m = 0 component.

The plasma resistance R_p was roughly proportional to $T_{e0}^{-3/2}$, *i. e.*, Spitzer formula (T_{e0}: the measured central electron temperature). When we used the helical factor ($\xi \sim 12$) and T_{e0}, $Z_{eff} \sim 2.3$ was obtained from the plasma resistance. As for the electron energy transport, an electromagnetic feature rather than an electrostatic one was suggested from the edge measurements using arrays of the magnetic and Langmuir probes.

CONCLUSIONS

After the covering of the shell gaps, plasma resistance R_p decreased by $\sim$ 12 % for the case of R = 2 and decoupling mode, and R_p obeyed $-(3/2)$ power law of I_p. Slight increase in the loop voltage was found when the limiter was inserted into the plasma, regardless of the angle of the limiter plate. A good correlation of the ion temperature with the plasma resistance and MHD activities was found.

REFERENCES

[1] S. Shinohara *et al.*: in *Proc. 16th Conf. on Contr. Fusion and Plasma Physics* 13B PART II (1989) 741.

[2] H. Toyama *et al.*: *ibid.* 13B PART II (1989) 737.

[3] Y. Shimazu *et al.*: this conference.

[4] P. G. Carolan *et al.*: in *Proc. 14th Conf. on Contr. Fusion and Plasma Physics* 11D PART II (1987) 469.

[5] G. A. Wurden *et al.*: in *Proc. 15th Conf. on Contr. Fusion and Plasma Heating* 12B PART II (1988) 533.

[6] A. Fujisawa *et al.*: *ibid.* 12B PART II (1988) 549.

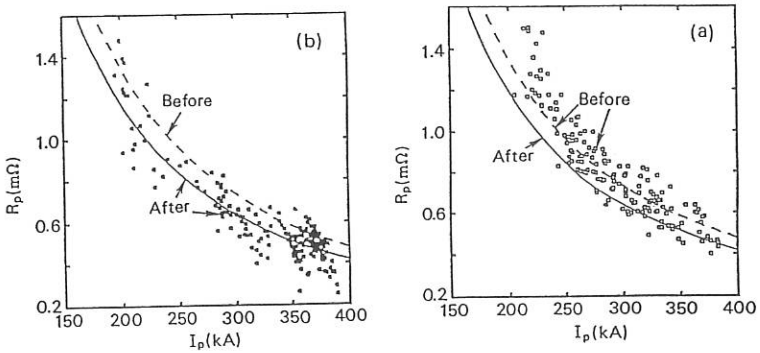

Fig.1 Plasma resistance R_p vs. plasma current I_p before (a) and after (b) the covering of shell gaps. Dotted and solid lines are the least square fitting curves (R_p scales as $-(3/2)$ power law of I_p) before and after the covering, respectively.

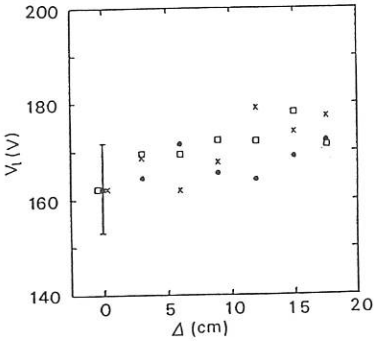

Fig.2 Relation between loop voltage V_l and limiter position (insertion) Δ for different angles of limiter plate. Here, □, ● and x show the angles θ of 0°, 45° and 90°, respectively.

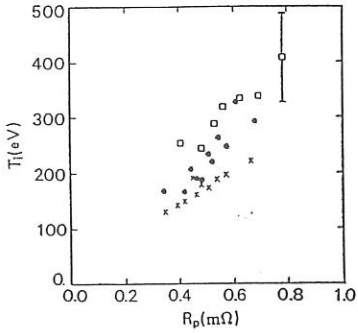

Fig.3 Dependence of ion temperature T_i on plasma resistance R_p for different regimes of line−averaged plasma density (□: 0.4 − 0.5, ●: 0.5 − 0.6, x: 0.6 − 0.7 (in 10^{14}cm^{-3} unit)).

OBSERVATIONS OF HIGH ENERGY ELECTRONS IN TPE-1RM15 REVERSED FIELD PINCH

Y.Yagi, T.Shimada, Y.Hirano, K.Hattori, Y.Maejima, I.Hirota,
K.Saito*, S.Shiina*
Electrotechnical Laboratory,
1-1-4 Umezono, Tsukuba-shi, Ibaraki, 305 Japan
*College of Science and Technology, Nihon University,
1-8 Kandasurugadai, Chiyodaku, Tokyo, 100 Japan

INTRODUCTION

In recent RFP plasma experiments, energetic electrons more than an order of magnitude higher than the local bulk electron temperature has been observed at the edge region by using Faraday cup [1], and it is discussed relating it to the Kinetic Dynamo Theory (KDT) [2]. In this paper we present the measurements related to the energetic electrons at the plasma edge of TPE-1RM15, mainly featuring its heat power flux loss fraction and estimation of the energy of the incident energetic electron. The latter was done by observing the soft X-ray emission from the fixed limiter and by inserted metal target material. These can give information about the energy distribution of the incident electron in the range over keV.

HEAT FLUX AND LOSS FRACTION

In TPE-1RM15, it was found by movable limiter insertion that energy flux onto the electron drift side was 3-5 times higher than that onto the ion drift side [3], indicating the anisotropic heat loss channel carried by electrons. The energy flux deposited onto the electron drift side of the limiter at the fixed limiter position, 135 mm from the center of the vacuum vessel, was typically about $2.2 - 2.3 MJ/m^2$ with the effective input time of about 4-5 ms at the plasma current, $I_p = 135$ kA, joule input power, $P_{oh} = 4.5 - 5.0 MW$. Thus the power flux was estimated to be about $440 - 580 MW/m^2$. The total power loss fraction by electrons onto the fixed limiters can be about 68-75 % at largest, if 3/4 to 5/6 of the non-radiative loss of about 90 % is due to the electron loss into the fixed limiters. This fraction corresponds to the effective number of 17-28 fixed limiters being exposed to the electron flow with 5 mm depth. Note that there are a total of 88 fixed limiters, 60 mm wide along the toroidal direction. This effective number of exposed limiters is slightly less than the case when the shadowing effect of a fixed limiter at the same toroidal straight section is considered, which yields effectively 32 fixed limiters to be exposed in the case of $\Theta = 1.55/F = -0.11$.

If the power flux is carried by mono-energetic electrons, the electron current density, j_e^H, and electron density, n_e^H, which are responsible for the power flux loss, can be estimated as a function of energy, E_e^H (fig.1). Since j_e^H should be less than the current density sustaining the RFP configuration, E_e^H should be higher than about 1 keV when the heat flux is $440 - 580 MW/m^2$. On the other hand, n_e^H should be less than a few times $10^{17} m^{-3}$ in the corresponding case, while the bulk electron density at the edge, n_e^b, is $0.6 - 1.0 \times 10^{19} m^{-3}$ and the bulk electron temperature, T_e^b, is $10 - 20$ eV. These estimates indicate that the electron heat flux is carried by energetic electrons, $E_e^H / T_e^b > 50 - 100$, of low density, $n_e^H / n_e^b < 2 - 5$ %.

SOFT X-RAYS FROM FIXED LIMITERS

One of the nine surface barrier diode (SBD) array channels looking at one of the fixed limiters on the inside wall of the vacuum vessel showed many spikes superposed on a slowly changing level from the plasma itself. These spikes were strongly related to the relative displacement of the plasma column to the fixed limiter (fig.2). When the plasma column was pushed inward to the center of the torus (B_{dcv} = 140 % of the optimum) so that the outermost flux surface was determined by the inside fixed limiters, many large spikes appeared, while the plasma column was pushed outward ($B_{dcv} = 0$), these spikes disappeared. The energy of these spikes was roughly estimated by the absorption method to be more than 1 keV in the case of graphite fixed limiters. In the case of S/S fixed limiters, the qualitative behavior was the same as the graphite limiter case but the energy from the absorption method was more than several keV which possibly was affected by characteristic X-ray lines from the metal limiter and by the difference of the plasma confinement properties between the two cases [4]. These spikes are usually observed to come in bursts coinciding with valleys of sawteeth seen in the near central chords of the SBD array.

SOFT X-RAYS FROM METAL TARGET MATERIAL

In order to have more accurate information about the energy distribution of the incident electrons, we have inserted the metal target which consists of Ti, Cr, Fe and Ni pure metal wafers into the plasma edge and observed the emission of soft X-rays by a Si(Li) detector (fig.3). Figure 4 shows typical wave forms of the plasma current and loop voltage, V_{loop}, of the reference discharge of TPE-1RM15 where I_p = 145 kA and V_{loop} = 30 volt at t=4.5 ms, and the equilibrium position of the plasma column is centered in the vacuum vessel and the error field at the poloidal shell cuts is minimized [5]. In these reference discharges, central electron temperature is typically about 440±60 eV and line averaged density is $2.2 \pm 0.2 \times 10^{19} m^{-3}$. Figure 4 shows the typical output signal from the Si(Li) detector, where only the data acquired in a CAMAC AD convertor with $0.2 \mu sec/sample$ and $32 ksamples/shot$ are displayed. Pulse height analysis was done by the computer program which can best fit the pulses to a series of Gaussians with adjustable height, width and position on an adjustable base line for an appropriately divided time window, in order to take into account some undershoot and recognizable overlap of pulses, which allows the pulse height analysis with higher pulse rate than using multi channel energy analyzer. Almost all the measurements were done with Be foil of $450 \mu m$ and solid angle of about 10^{-7} str. The energy resolution of the Si(Li) detector itself is 220 eV FWHM at a pulse shaping time of $1 \mu sec$ and the total resolution is determined by the accuracy of pulse shape fitting (2.0-2.5 % of the full scale pulse height) which results in 400-500 eV.

A typical result of the pulse height analysis for the reference discharge is shown in fig.5. Four K_α lines from Ti, Cr, Fe and Ni are clearly observed and also the continuum emission level is observed to decay as the energy increased, indicating that an incident electron energy of more than 8.3 keV (ionization energy of Ni K-shell) exists and the energy distribution seems not to be monoenergetic.

Generally speaking, the estimation of the energy distribution of the incident electrons from these results is not straightforward. In principal, there are two ways to

estimate it as follows. (1) The relative line intensity of each K_α line can give the best fit parameters as many as the number of K_α lines by using the empirical database about the line intensity as a function of Z and energy [6]. (2) The continuum emission level can be treated, in the first approximation, in the same way as is usually done for recombination or bremsstrahlung radiation from the plasma itself. Thus it can give a temperature of the incident electrons if it is well defined.

The estimation according to (1) has been found to be difficult because of non uniform solid angle for each material plate caused by the change of shape by melting. On the other hand, there remains the possibility of the estimation according to (2). After characteristic lines were subtracted from the data, the continuum level was treated as is written in (2). Thus, as a measure for energy distribution of the incident electrons, temperature of the energetic electrons, T_H, was deduced from the slope of the continuum level in the energy range of 4-8 keV. Figure 6 shows the temporal evolution of T_H accumulated from 1.6 ms time windows of 12 reference discharges. It reaches about 18 keV near the end of the current flat top, while the average T_H during 2.5-6.5 ms is about 7 keV. These values may be overestimated because of pulse pile up and the values may need further correction with a more accurate theory of X-ray emission from thick targets.

CONCLUSION

The energetic electrons observed at the edge region of TPE-1RM15 show qualitatively similar behavior to ref. [1]. Such electrons carry as high as 68-75 % power loss of the joule input power with less than a few % of the local electron density. The preliminary energy estimate from the target insertion experiment is about several keV. This energy is an order of magnitude higher than that obtained in [1], presumably because of the difference in observed energy region, the difference in plasma confinement properties and remaining uncertainties in estimating the correct energy information from the observed energy spectrum.

This work is supported by the Science and Technology Agency, Japan. The authors are grateful for the discussions on the interpretation of the target insertion experiment to Dr. B. Alper, Dr. P. G. Carolan and Dr. A. A. Newton in Culham Laboratory.

REFERENCES

[1] J C Ingraham et al: Phys Fluids B2 (1990) 143.
[2] R W Moses, K F Schoenberg and D A Baker: Phys Fluids 31 (1988) 3152.
[3] Y Yagi et al: J of Nucl Material 162-164 (1989) 702.
[4] T Shimada et al: 12th Int Conf on Plas Phys & Cont Nuc Fus Res, Nice (1988), IAEA-CN-50/C-II-4-2, Vol.2, p.457.
[5] T Shimada et al: 11th Int Conf on Plas Phys & Cont Nuc Fus Res, Kyoto (1986), IAEA-CN-47/D-II-6, Vol.2, p.453.
[6] M Green: Int Symp on X-ray and X-ray Microanalysis, Ed H H Pattee et al, New York, Academic Press, (1963) 185.

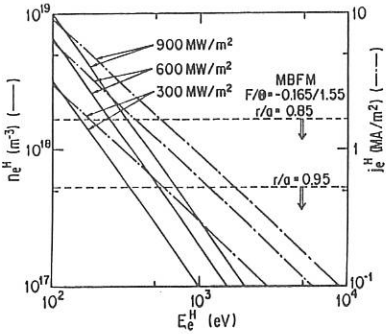

Figure 1: *Estimation of electron current density and electron density which are responsible for heat flux.*

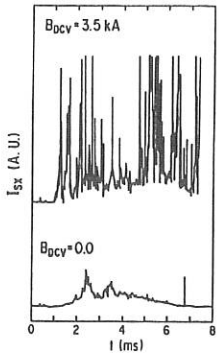

Figure 2: *Typical signals of the SBD looking at a fixed limiter.*

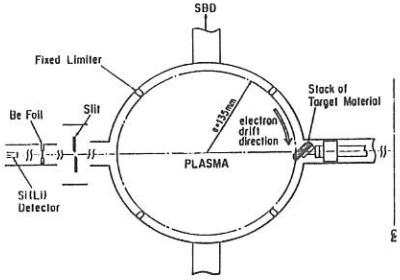

Figure 3: *Schematic figure of the measurement system of Si(Li) with metal target.*

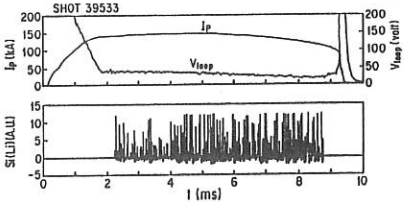

Figure 4: *Typical waveforms of plasma current, I_p, and loop voltage, V_{loop} with output signal from Si(Li)*

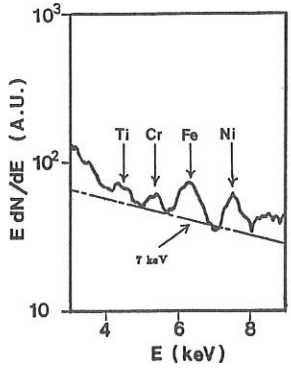

Figure 5: *Result of the pulse hight analysis of reference shots. t=2.5-6.5 ms.*

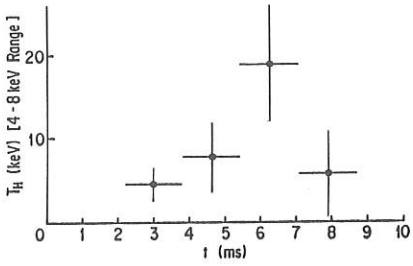

Figure 6: *Temporal evolution of the seeming temperature of the incident electron.*

COHERENT SOFT X-RAY OSCILLATIONS AND MAGNETIC FLUX REGENERATION IN THE REPUTE-1 RFP

Y. Shimazu, S. Shinohara, A. Fujisawa, H. Ji,
A. Ejiri, A. Shirai, K. Mayanagi, S. Ohdachi,
K. Yamagishi, H. Toyama, K. Miyamoto

Department of Physics, Faculty of Science,
University of Tokyo, Bunkyo-ku, Tokyo 113, Japan

1. Introduction

Oscillations of soft X-ray (SXR) emission which are accompanied by toroidal magnetic flux regeneration have been reported on many RFP machines (HBTX1B[1], ZT-40M[2] and so on), including REPUTE-1[3], in which the amplitude of the oscillations was small and correlations were not clear in its low current regime ($I_p < 250$ kA). In this paper we present large amplitude coherent oscillations of SXR emission in high current discharges of REPUTE-1 ($I_p > 350$ kA), and their strong correlations with other plasma parameters such as the field reversal ratio F and plasma resistance. The change of the radial profile during the oscillations and the correlation in the toroidal direction are shown.

2. Experimental results

The SXR emission is measured by surface barrier diodes (SBD), most of which are arranged in three arrays of totally 20 SBDs on top, side, and bottom ports at the same toroidal location. The other SBDs are installed at five different toroidal locations. Thus we can identify both toroidal and poloidal mode numbers. A 4 μm polypropylene film is used as a filter to cut VUV emission lower than about 100 eV. The intensity calibration is performed by using synchrotron radiation.

Large amplitude coherent oscillations shown in Fig. 1 were observed in the high current discharge with $I_p \simeq 360$ kA, $\bar{n}_e \simeq 2 \times 10^{19} m^{-3}$, $F \simeq -0.5$ and $\theta \simeq 2$. The typical peak-to-peak amplitude is 20 % of the signal, and the oscillations are

clearly seen on all chords of the SBD arrays. The SXR intensity profile exhibits peaking ones several times during the discharge as shown in Fig. 2. The carbon V impurity light emission (2271Å) from the plasma center oscillates in phase with SXR emission with a similar relative amplitude, although ion temperature obtained from the CV Doppler broadening does not show clear correlation with the intensity of SXR emission. The frequency of the oscillation is about 10 kHz, and the rise and fall periods are nearly equal. The SXR oscillations are in phase across the plasma minor cross section from $-0.65a$ to $+0.65a$ where a is the minor radius, and an inversion radius is not observed within this range.

Figure 3 shows SXR signals at different toroidal locations. Large amplitude oscillations are not clear at the toroidal locations more than 80 degrees apart from the SBD arrays. This suggests that the activity is localized in a particular toroidal location. Within the range of 20 degrees from the SBD arrays in the toroidal direction, the correlations are strong and the oscillation propagates in the opposite direction to the plasma current and toroidal field at the center. This direction of the propagation is the same as that of perturbation of toroidal flux reported before on REPUTE-1 [4].

High frequency fluctuations in SXR signal have a large m=1 component (about 70 % in power of total m components), where m is the poloidal mode number. Correlation analysis shows that a m=1 perturbation rotates poloidally in the ion diamagnetic direction with respect to the toroidal magnetic field at the plasma center, and the frequency of the rotation is approximately 30 kHz.

The time derivative of the toroidal flux $\dot{\Phi}$, which is measured by a flux loop 60 degrees apart from the SBD arrays, exhibits large amplitude oscillations corrrelated well with the SXR signals. In the crash phase of SXR emission profile, $\dot{\Phi}$ rises up to the positive maximal value, indicating large flux generation occurs. Associated with those oscillations, the field reversal ratio F and the edge toroidal field $B_\phi(a)$ oscillate significantly, because of oscillations of the poloidal liner current induced by change of the toroidal flux. The variation of F is from 0.1 to 0.2. The period of $B_\phi(a)$ rising is 7 to 10 times longer than the falling period, and in its rising phase, fast fluctuation which looks like a precursor of large relaxation is seen. The relative fluctuation of the toroidal flux $(\Delta\Phi/\Phi)$ is less than 1 %.

The F-θ trajectory during the SXR oscillations in this discharge is shown in Fig. 4. It oscillates mainly in the direction of F-axis. The pinch parameter θ decreases monotonously with time since toroidal flux keeps increasing while the plasma current

and thus poloidal magnetic field at the edge $B_\theta(a)$ are almost constant. Thus the F-θ trajectory does not describe a periodic circulation on the diagram.

3. Discussion

The change of SXR intensity reflects mainly fluctuation of the electron temperature T_e rather than that of the line averaged electron density $\bar{n}_e$, because $\bar{n}_e$ shows no oscillations correlated with SXR emission. This is supported by the observation that oscillations of plasma resistance, which is calculated from plasma current and loop voltage without correction for inductive effects, are almost in antiphase to the SXR emission as shown in Fig. 1.

The periodic oscillations of $B_\phi(a)$ and F indicating magnetic flux regeneration are observed in all discharges. However, coherent SXR oscillations shown in the present paper are not always observed clearly even in high current discharges. In the discharges with the strong coherent SXR oscillations, the SXR signals on all the chords ($r < 0.65a$) were observed with much higher level than those in other shots of similar plasma current, suggesting that the electron temperature is high.

4. Conclusion

In high current discharges of REPUTE-1 ($I_p > 350$ kA), large amplitude coherent oscillations in SXR emission were observed which were in phase across the poloidal cross section and accompanied by toroidal flux regeneration. Poloidal rotation of SXR fluctuation and its propagation in the toroidal direction were also found. The oscillation of SXR emission suggests the variation of electron temperature.

Acknowledgements

The authors are greatful to Dr. N. Asakura for helpful comments during the preparation of this manuscript.

References

[1] R. J. Hayden and B. Alper, Plasma Phys. Contr. Fusion **31**, 193 (1989)
[2] R.G. Watt and R. A. Nebel, Phys. Fluids **26**, 1168 (1983)
[3] N. Asakura *et al.*, Nucl. Fusion **29**, 893 (1989)
[4] K. Hattori *et al.*, J. Phys. Soc. Jpn. **58**, 565 (1989)

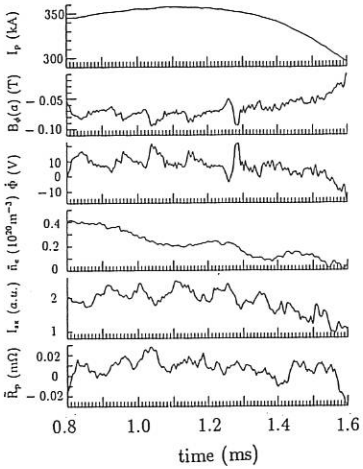

Fig. 1 : Time evolution of plasma current I_p, toroidal field at the wall $B_\phi(a)$, time derivative of toroidal flux $\dot{\Phi}$, line averaged electron density $\bar{n}_e$, soft X-ray intensity I_{sx}, fluctuation of plasma resistance (loop voltage divided by I_p) $\tilde{R}_p$ during SXR oscillations.

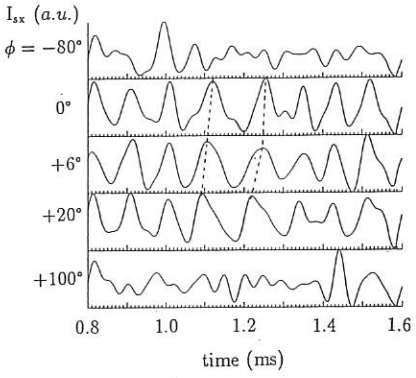

Fig. 3 : SXR signals at different toroidal locations. Toroidal angle is denoted by ϕ with plus sign for the direction of plasma current. The location of SBD arrays corresponds to $\phi = 0°$.

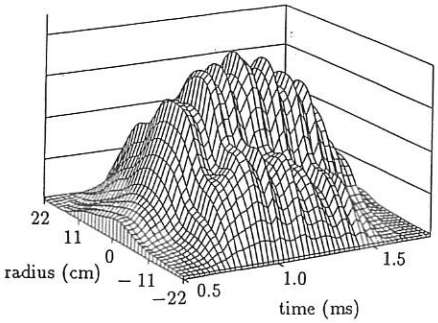

Fig. 2 : Chord integrated SXR profile as a function of radius and time for the discharge shown in Fig. 1.

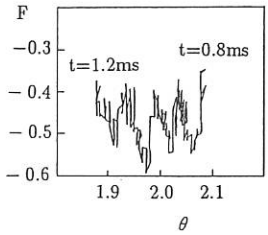

Fig. 4 : F-θ trajectory described during SXR oscillations from t=0.8ms to 1.2ms.

Impurity ion temperature and rotational velocity observations in the HBTXIC RFP

R. A. Bamford*, C. A. Bunting, P. G. Carolan, T. P. Hughes* and J. B. Sidle

AEA Fusion, Culham Laboratory, Abingdon, Oxon, OX14 3DB, UK
(UKAEA/Euratom Fusion Association)
* University of Essex, Wivenhoe Park, Colchester CO4 3SQ, UK

Introduction

There are various and conflicting observations in Reversed Field Pinches (RFPs) of the ion temperature (e.g. T_{imp}=T_i and $T_{imp} \gg T_i$) and rotational velocity (v_ϕ from $< 6 \times 10^3 \mathrm{ms}^{-1}$ to $2 \times 10^4 \mathrm{ms}^{-1}$) as deduced from the shape and position of impurity spectral lines. We report on results from HBTX-1C, using a high resolution grating spectrometer, with a CCD camera system, which show that caution must be exercised when applying a single Gaussian fit to the impurity spectral line profiles and interpreting the broadening as due to Doppler effects alone. The presence of anomalous features and deformations to the line shape can lead to a wider line profile and an apparently higher impurity temperature. Measurements of the impurity ion temperature and toroidal rotation velocities are given, at different times during the plasma discharge, and the affect of laser ablation[1] of carbon upon these temperatures. We also show spectra whose profiles are difficult to explain in terms of ion temperature.

Instrumentation

The spectrometer used is a 1.26m SPEX Czerney-Turner with 1mm diameter monofibres imaged at the input slit, one above the other. The quartz fibers view the plasma in (a) two opposing tangential directions and (b) three parallel vertical chords. A 3600 gr/mm grating in 1st order gives an inverse linear dispersion of 2.08Å/mm at the image plane, for the wavelength 2270.9Å of the helium-like carbon. A typical 250eV CV Doppler broadened linewidth would therefore give a FWHM of 0.38mm. Using a charged coupled device (CCD) detector with a 15μm channel width provides a large number of channels per spectral line ($\sim$ 30 for 250eV CV). The CCD, being a two dimensional array detector of 640 $\times$ 512 pixels, allows the simultaneous imaging of many fibres. The poor responsivity of the CCD detector to the UV is circumvented by the application of a gated microchannel plate image intensifier, which is coated with a UV-to-visible scintillator (TPB)[3], and placed at the image plane of the spectrometer.

The duration of the CCD camera exposure could be varied by gating the image intensifier between 210μs and 420μs. This allowed a time scan of the impurity ion temperature throughout the discharge with adequate time resolution for T_i variations[2].

Ion temperature and rotational observations

A typical spectrum in the 2780-2790Å region is shown in figure 1. The magnesium-II has a negligible width and can thus be used as an instrument function for the other (clearly broadened) oxygen-V triplet as well as for the carbon-V at 2270.9Å.

Spectra from opposing tangential views are shown in figure 2 for the CV 2270.9Å region. This illustrates the Doppler broadening of the spectral lines and the net Doppler shift due to the bulk toroidal plasma rotation. The wavelength separation gives the rotational velocity. The value of v_ϕ here is $2.7 \pm 0.6 \times 10^4$m/s and in the positive ion current direction.

The Doppler ion temperatures were extracted from the spectral profiles via a Gaussian fitting algorithm. Figure 3 shows the evolution of the impurity ion temperature with time. Laser ablation of carbon was used to enhance the CV intensity levels for times later than 2.0ms into the plasma. Temperatures at similar times but without laser ablation, were too low in signal intensity to be used for ion temperatures measurements.

The comparison between T_{CV} and T_i (as measured by a neutral particle analyser NPA) is given in figure 4.

Distorted spectral line profiles

When the line intensity from lowly ionized or neutral metals (e.g. FeII, CrI) was high, the CV 2271Å spectral region registered additional spectral lines (at present unidentified). These features distort the spectral line profile and give rise to an apparently broader spectral width to the CV 2271Å (figure 5).

Quantitive correlation between the metallic signal levels (as monitored by a 40 channel 600-4500Å Polychromator) and the appearance of features on CV, is made unreliable by the physical separation of the two diagnostics about the torus. This fact is particularly relevant since it was later discovered that there were protrusions of the stainless steel vacuum vessel around the area of the Doppler spectrometer. The obstructions were from damaged discrete coil covers.

Other observations worth noting include:

- Spectra taken under 1ms were relatively clear compared with exposures taken during the plasma current 'flat top' region of 2 to 4ms. At early times the temperatures are relatively low and the metallic influxes have not risen to significant levels.

- The affect of carbon laser ablation, on the degree of spectral purity of CV 2270.9Å , is to increase the CV signal by approximately an order of magnitude and so make insignificant the contribution from line blending.

Conclusions

The values ion temperature T_{CV} extracted from the Doppler broadening are observed to be between 80-800eV. No large increase in T_{CV} was seen with laser ablation of carbon, but an increase of ~200-300eV occured between plasma currents of 100 and 200kA. Initial results indicate the value of T_{CV}/T_i increases from 0.4 to about unity during the early part of the pulse (from 0.8 to 2.0ms). Values for v_ϕ ranged (irrespective of laser carbon ablation) from 1.0 to $2.9 \pm 0.6 \times 10^4$m/s in the positive ion current direction.

Acknowledgements

We would like to thank K. J. Gibson for providing the ion temperatures from the NPA and P. D. Wilcock for the information on the metallic obstructions from the vacuum vessel.

References

[1] Carolan P. G. ,Patel A. , Walsh M. J. , this conference.

[2] Bunting C. A. , Carolan P. G. , Gibson K. J. , Rusbridge M. G.; this conference.

[3] Carolan P. G. , Manley A. M. Rev. Sci. Instrum. , 57(8), 2038-2040, (1986).

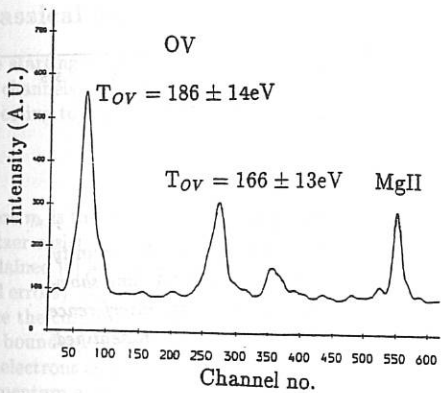

Figure 1:

A typical HBTX-1C spectrum showing the MgII 2795.5Å metallic impurity and the OV 2781.0Å, 2787.1 and 2789.9Å triplet.

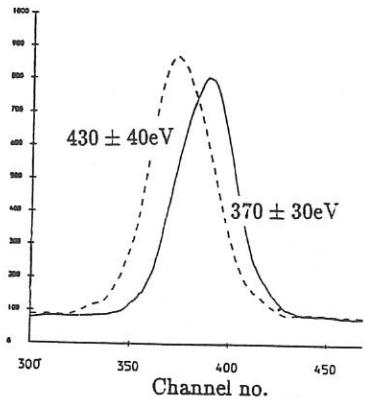

Figure 2: *CV 2270.9Å with opposing tangential spectra overlaid. The separation of the spectra due to Doppler shift rotation is of the order of 15 channels. and yields $v_\phi = 2.7 \pm 0.6 \times 10^4 m/s$ in the direction of the positive ion current. The instrument function separation correction is less than 10%.*

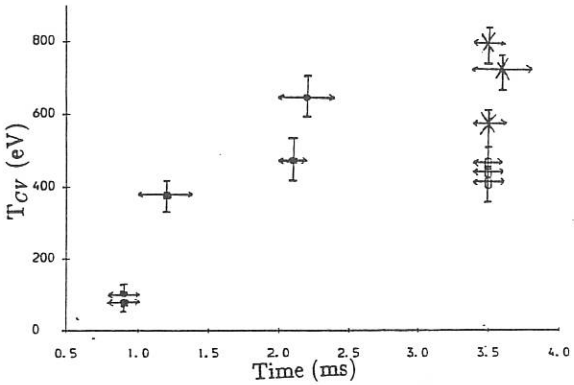

Figure 3: *Toroidal CV ion temperatures. The horizontal bar indicates the exposure duration. The symbols '■' are for 200kA plasma current pulses with no carbon ablation, '×' are those for with ablation at 200kA and '○' are for ablation at 100kA.*

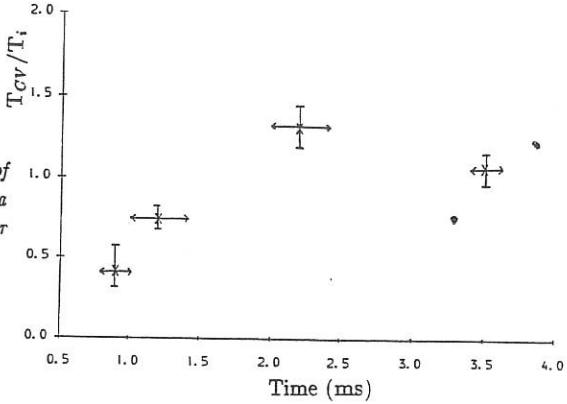

Figure 4: *The variation of T_{CV}/T_i with time. The data point at t=3.5ms is with laser carbon ablation.*

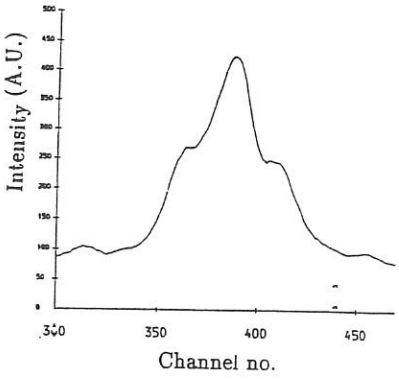

Figure 5:
The spectrum in the vicinity of the CV 2270.9Å line showing evidence of interference from other, as yet unidentified, spectral features.

Ion heating and confinement in the HBTX1C Reversed Field Pinch

P. G. Carolan, B. Alper, R. A. Bamford[1], C. A. Bunting, K. J. Gibson[2], A. Patel and M. J. Walsh[3]

AEA Fusion, Culham Laboratory, Abingdon, Oxon, OX14 3DB, UK
(UKAEA/Euratom Fusion Association)
[1]University of Essex, Wivenhoe park, Colchester, UK.
[2] UMIST. Manchester, UK.
[3]University College Cork, Ireland (supported by EURATOM)

Introduction.

A distinguishing feature of RFPs is that both the plasma resistance and ion heating are much higher than expected from classical, or collisional, considerations. Ion power balance models have been proposed elsewhere [1] which link these effects through magnetic helicity balance, including helicity losses at the edge. These models incorporate the MHD dynamo electric field, $\langle \tilde{v} \wedge \tilde{B} \rangle$, generated by the fluctuations in the fluid velocity, $\tilde{v}$, and the magnetic field, $\tilde{B}$.

Here we have conducted a series of experiments and measurements which focus separately on the various aspects of the ion dynamics in HBTX1C. These encompass (i) altering the ohmic input power by impurity injection [2] ; (ii) measuring the particle confinement time by the laser ablation method [3]; (iii) measurements of the ion power loss [4] and (iv) measuring the temperature and rotational velocities, of impurities [5].

Classical and anomolous loop voltage.

The starting point, in determining the sharing of input power, $I_\phi V_\phi$, between the electron and ion channels, is to first account for the observed loop voltage, V_ϕ. A general expression for V_ϕ, appealing to global magnetic helicity, is given by:

$$V_\phi = \frac{1}{\Phi} \int \eta_k j.B dx^3 + \Delta V_\phi \qquad (1)$$

where η_k is the resistivity appropriate to the helicity dissipation in the plasma. If the measured Spitzer resistivity, η_S, is assigned to η_k then the change in V_ϕ with I_ϕ can be quantitatively explained [6] leaving a constant ΔV_ϕ which depends only on the plasma boundary (e.g. tiles, field errors). An alternative explanation from Kinetic Dynamo Theory (KDT) [7] is that $\eta_k \neq \eta_S$ since the current density, or electron momentum, is deemed to diffuse from the plasma core to the boundary in times comparable to the local collisional momentum exchange time between the electrons and ions (+impurities). In this case [8] $\eta_k = \eta_S(1+\tau_{ei}/\tau_e)$ where τ_{ei} is the electron momentum exchange time with the ions and τ_e is the electron non-collisional momentum loss time. The local electric field is given by $E = \eta_S j + E_a$ where

$$E_a = -\langle \tilde{v} \wedge \tilde{B} \rangle \qquad (2)$$

for the pure MHD dynamo field (MDF) model, or, $E_a = \eta_S \tau_{ei}/\tau_e$ in the pure KDT model.

In both cases the local resistive heating of the electrons is pure Spitzer ($\eta_S j^2$) but in the MDF model the residual power, $E.j - \eta_S j^2$, is available to heat the ions, and possibly the

electrons. In the KDT model this power energises non-thermal electrons which escape to the plasma boundary in times of the order of, or less than, τ_{ei}(few μsec), and no power is available for the ion heating. Since the energy confinement time of the electrons, τ_{Ee}, is at least $100\mu sec$, the density of fast electrons, which are calculated [7] and measured [9] to have energies at the edge comparable to the central thermal energies, must be of the order of 1% of the axial density. The application in isolation, of either of these descriptions of the electric field and magnetic helicity dissipation, cannot account for both observations of non-collisional ion heating and the substantial power in the fast electrons at the edge. These are observed [9] to be directed along the magnetic field lines and opposing the applied electric field as expected in the KDT model.

Effects of changing the classical loop voltage.

Previously in HBTX1B the validity of using $\eta_k = \eta_S$ and appealing to the presence of ΔV_ϕ in Eqn. 1 was tested by keeping η_S constant while altering V_ϕ by the introduction of limiters into the plasma [6]. Here we take the opposite approach by altering η_S while keeping the same plasma configuration (F, Θ, no additional obstructions). According to Eqn. 1, increasing η_S by $\delta\eta_S$ should increase V_ϕ by

$$\delta V_\phi = \frac{1}{\Phi} \int \delta\eta_S j.B dx^3 \qquad (3)$$

provided ΔV_ϕ is not affected. The application of 'heavy' laser ablation [2] has the required features of increasing the Z_{eff} and decreasing T_e, (both enhancing η_S) and the observed increase in V_ϕ can be accounted for using Spitzer effects alone. According to Tsui [10] it is unlikely that an increase in ΔV_ϕ occurred to account for the results, since in his model $\Delta V_\phi \propto T_{e,edge}$ and so ΔV_ϕ is more likely to decrease if a reduction in $T_{e,edge}$ accompanies the drop in $T_{e,axis}$.

The effects on T_e and T_i can be seen in Fig 1. showing that there is no detectable increase in ion heating as expected when the increase in loop voltage is interpreted as due largely to the increased η_S . When account is taken of the contribution from the ionised impurity densities, as estimated from measurements using a VUV Polychromator and an absolutely calibrated bolometer, the plasma ion density is found to be largely unaffected by the laser ablation.

The products of density and temperature, nT, for electrons and ions are shown in Fig. 2, showing contrary behaviour after ablation but the sum $n_eT_e + n_iT_i$ looks reasonably constant. This opposing behaviour of ion and electron energy densities has also been observed in other conditions in the HBTX experiments [8] [11] and in other experiments [12] and suggests that β_Θ may be playing some role.

Power balance and T_i scaling.

Determining the input power to, and loss of, the electrons, presents problems in RFPs. In HBTX1B satisfactory agreement is obtained between predictions of T_i/T_e, from a power balance model [1] and experimental results in standard conditions ($I_\phi \sim 200kA$) but the agreement is less favourable at low currents when the edge tiles were removed. Plotting the electron energy density on axis against the Spitzer power, $\eta_{S,axis}j^2_{axis}$, for HBTX1B [1] and HBTX1C shows an energy intercept at zero Spitzer power which suggests some of the residual power, $E_\phi j_\phi - \eta_S j^2$, is being deposited in the thermal electrons. This additional electron heating is of the order of 1 MWm^{-3} on axis and not accounted for in existing applications of RFP plasma heating descriptions. When account is taken of radiation losses, which are $\sim$ 50% of the total Spitzer

power, $\int \eta s j^2 dx^3$, it is clear that more investigation is required to elucidate the heating and power loss of the electrons.

On the other hand, charge exchange losses are not important for the ions and convective losses appear to dominate [4]. The latter is supported by recent results from laser ablation [3] which gives diffusion coefficients close to those predicted earlier [1]. Thus, treating the ions in isolation of the electrons may be more fruitful. According to Robinson [13] the energy confinement time, τ_E, for turbulent convection is described by $\tau_E \propto \rho^{\frac{1}{2}} \tilde{B}^{-1}$, where ρ is the mass density. It was suggested that $\tilde{B}/B \propto S^{-\frac{1}{2}}$ where S is the magnetic Reynolds number. Here we explore the possibility that $\tilde{B}$ is related to the MDF. In the HBTX experiments the loop voltage $V_\phi \gg 2\pi R \eta s j_\phi$ so that, from the MDF description, it is reasonable to assume that $\langle \tilde{v} \wedge \tilde{B} \rangle \propto \Delta V_\phi$. This suggests that $\tilde{P} \tilde{\propto} \Delta V_\phi^{\frac{1}{2}}$ (cf. Eqn. 2). Considering the ion power balance in isolation of the electron power channel we assume, as previously [1], that the power $I_\phi \Delta V_\phi$ provides the ion heating. The ion energy confinement time, τ_{Ei}, should scale as $\tau_{Ei} \propto n_i^{\frac{1}{2}} \Delta V_\phi^{-\frac{1}{2}}$, resulting in $T_i \propto I_\phi \Delta V_\phi^{\frac{1}{2}} n_i^{-\frac{1}{2}}$. A comparison of measured ion temperatures with the calculated scaling is shown in Fig. 3. Results from both HBTX1C and HBTX1B (w/o edge tiles) are shown as the ΔV_ϕ is quite different in the two machines ($\sim 50V$ and $\sim 10V$ respectively). Reasonable agreement is seen between measured and calculated scaled T_i's, with the HBTX1B results overlapping those of HBTX1C.

Conclusions.

A simple scaling of T_i with n_i, I_ϕ and V_ϕ is observed. This scaling is found from a description of the ion power balance, which assumes that the non-Spitzer input power provides the ion heating and that turbulent convection, which incorporates the $\tilde{B}$ scaling expected for the MHD dynamo field, dominates the ion losses.

References.

[1] P. G. Carolan et al. Culham Laboratory Preprint CLM-P852 (1989)
[2] B. Alper, et al. , this Conference.
[3] P. G. Carolan, et al. , this Conference.
[4] C. A. Bunting, et al. , this Conference.
[5] R. A. Bamford, et al. , this Conference.
[6] B. Alper, et al. Plasma Physics and Controlled Fusion 30, 843 (1988).
[7] R. W. Moses, et al. Physics of Fluids 31 3152. (1988)
[8] P. G. Carolan, et al. to be published in Plasma Physics and Controlled Fusion (1990)
[9] C. Ingraham, et al. Physics of Fluids B2(1) 143 (1990).
[10] H. Y. W. Tsui, Nuclear Fusion 28, 1543 (1988).
[11] R. J. Hayden, et al. Plasma Physics and Controlled Fusion 31, 193 (1989).
[12] G. A. Wurden et al. Proc of 15th European Conference on Controlled fusion and Plasma Heating II 533 (1988).
[13] D. C. Robinson, Pulsed High Beta Plasmas, 273, Pergamon Press (1977).

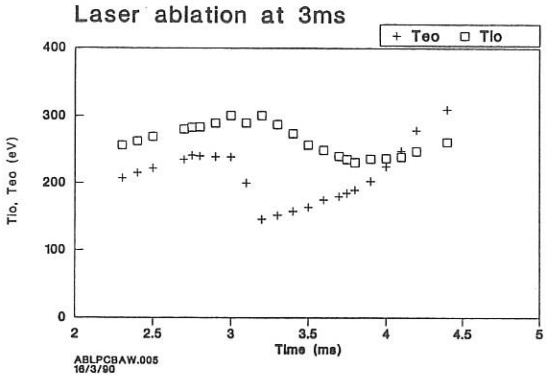

Fig 1. *Temporal evolution of T_{e0} and T_{i0} preceding and during laser ablation of carbon which doubled the density at $t = 3$ ms.*

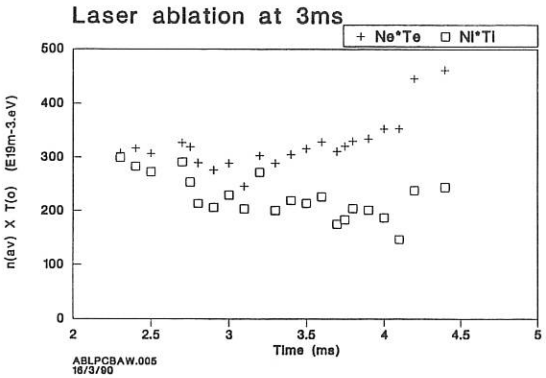

Fig 2. *The behaviour of ion and electron energies, preceding and during laser ablation.*

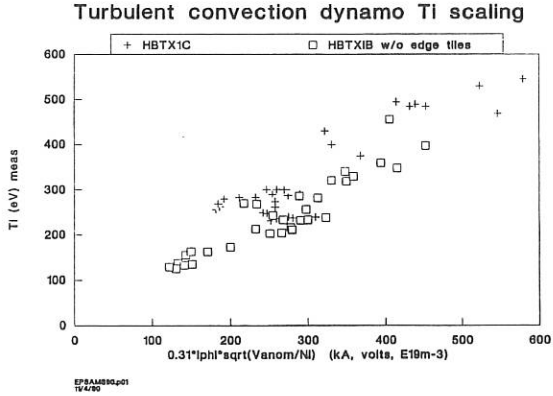

Fig 3. *Comparison between the measured ion temperature, using an NPA, and that calculated ($T_i \propto I\Delta V_\phi^{\frac{1}{2}} n_i^{-\frac{1}{2}}$) based on turbulent convection losses, non-Spitzer power heating the ions and a scaling of $\tilde{B} \propto \Delta V_\phi^{\frac{1}{2}}$, as expected from an MHD dynamo field.*

Ion Power Loss in the HBTX1C Reversed Field Pinch

C. A. Bunting, P. G. Carolan, K. J. Gibson† and M. G. Rusbridge†

AEA Fusion, Culham Laboratory, Abingdon, Oxon, OX14 3DB, UK
(UKAEA/Euratom Fusion Association)
† UMIST, Manchester, UK.

Introduction

The problem of ion power balance in RFPs is typically characterised by anomalously high temperatures, short confinement times and high input powers. The source of ion heating is essentially non-collisional (the energy confinement times are much less than the ion-electron equipartition times with T_i often exceeding T_e) and is apparently connected with the anomalously high loop voltages found on RFPs.

An ion power balance model has been developed [1] in which it is assumed that all the power associated with the anomalous loop voltage ΔV_ϕ (where $V_{loop} = V_{spitz} + \Delta V_\phi$ [2]) is coupled to the ions. This power typically represents 75-90 % of the total power input to the plasma, and so ion power losses in this description dominate the total energy confinement in an RFP.

In this paper we report on attempts to determine the relative importance of different ion power loss channels. To date the investigations have centred on studying those of charge exchange (proposed to be significant in RFPs and spheromaks e.g. [3]) and convective losses (sufficient to account for all the ion power loss in some models [1]).

Charge Exchange Losses

A neutral particle analyser (NPA) has been used to obtain the central ion temperature and to infer the core neutral density of the plasma.

Neutral particle energy spectra are routinely obtained over 1ms in the flat top phase of a standard discharge (I_ϕ = 175kA, $n_e \simeq 1.8 \times 10^{19}\mathrm{m}^{-3}, T_e$ = 300eV, T_i = 450eV). In the absence of multichord measurements it has been necessary to extract the ion temperature profile by Monte-Carlo modelling of the curvature of the spectrum obtained. A reasonable fit to the data has been obtained by assuming a peaked profile of the form $T_i(r) = T_{io}(1-(r/a)^2)^2$. This is in agreement with previous measurements of the neutral temperature profile by fluorescent scattering [4] and similar analyses of NPA spectra in HBTX1B [1] and ZT40M [5]. The absolute magnitude of the signal has been found to correspond to a core neutral density of between $2 - 6 \times 10^9\mathrm{cm}^{-3}$. Further accuracy is not possible with the present calibration, though it should be noted that the values obtained are not dissimilar to those obtained by Evans et al. [6] using fluorescent scattering on HBTX1A ($6.0 \times 10^9\mathrm{cm}^{-3}$, 8cm from axis).

The global charge exchange losses can be calculated by the expression:

$$P_{cx} = \frac{3}{2}k \int_0^a n_i(r) n_o(r) < \sigma v >_{cx} T_i(r) \alpha dr$$

where α is a factor describing the attenuation of outgoing neutrals due to ionisation or re-charge exchange. For the conditions found on HBTX we have computed $\alpha \simeq 0.3$ for central (i.e. within 5cms of axis) regions of the plasma whilst $\alpha \simeq 0.6$ volume averaged over a simplified spherical topology. We may estimate therefore that the charge exchange losses globally are of the order of 1 $\mathrm{MWm^{-3}}$. Given an ion input power (assuming all the anomalous voltage is coupled to the ions) of $\sim$ 10 $\mathrm{MWm^{-3}}$ it appears that charge exchange losses are not globally important. This estimate represents an upper limit to charge exchange losses, since the inclusion of a fully toroidal geometry further increases the attenuation of outgoing neutrals.

More qualitative evidence that charge exchange plays only a limited role in determining the peak ion temperature comes from correlation of the measured charge exchange flux and the ion temperature. There are many conditions in which order of magnitude changes of neutral flux have been shown to have little effect on the ion temperature (or the ion energy density in cases where the ion particle density varies). Examples of this sort of behavior have been observed in a wide range of conditions, such as pellet injection in ZT40M [7], laser ablation of impurities in HBTX1C [8] as well as being sometimes observed in standard discharges. Figure 1 shows an example of the latter where no significant change in temperature or density (i.e. $\leq 5\%$) accompanies the large changes in neutral outflux. That these changes in flux are simply local wall interactions has been shown to be unlikely by cross correlation of the neutral flux with a D_α monitor viewing along the flight tube of the NPA. It is found that the detected neutral flux is not correlated with the local release of neutrals from the wall, indicating that the observed variations are related to global changes in the neutral density.

Convective Losses

A model [1] describing the balance of power in the RFP has shown that convection of particles alone may be sufficient to describe the ion energy loss without resort to ion conduction terms. Under this model ion energy transport may be represented by the equation:

$$\Gamma_{E_i} = D \frac{dU_i(r)}{dr}$$

where D is a diffusion coefficient assumed to describe the transport of both particles *and* energy and $U_i(r)$ is the ion energy at radius r. By using the profiles of ion temperature and density it is possible to obtain from this expression a relationship between the ion energy confinement time and D. From the NPA results and assuming a parabolic density profile:

$$\tau_{E_i} = \frac{a^2}{12D}$$

whereas :

$$\tau_p = \frac{a^2}{4D} \text{ indicating that } \tau_p \simeq 3\tau_{E_i}$$

On HBTX1C it has been possible to evaluate the particle confinement time by the use of laser ablation of carbon [8]. Thus it has been possible to directly compare the ion energy confinement time with the particle confinement time. Figure 2 shows the relationship between the measured decay rate of the injected carbon signal (which represents a minimum possible confinement time) and the ion energy confinement time.The values of τ_{E_i} obtained are in the range 100-200μs compared with the total confinement time of around 300μs. The results indicate that a possible relationship exists between the particle and energy confinement times of the form $\tau_p \geq 5\tau_{E_i}$. More direct measurements of density and temperature profiles are needed before the apparent quantitative disagreements between the experimental and predicted results can be accounted for.

In evaluating the energy confinement time it has been assumed that all of the extra input power associated with the anomalous loop voltage is dissipated in ion heating. There are indications [1], however, that some of the anomalous power is heating the electrons, implying that the ion energy confinement is greater than has been calculated. Such uncertainties in the ion power input, although unlikely to explain the discrepancy between the predicted and experimental results, warrant further investigation in future ion heating studies.

Conclusions

Charge exchange losses have been shown to be insignificant in determining central ion temperatures. Some correlation between the measured decay time of an injected impurity and ion energy confinement time has been found, indicating that $\tau_p \geq 5\tau_{E_i}$. The work has highlighted the need for a better description of the partition of the anomalous power between ions and electrons.

References

[1] P. G. Carolan, A. Lazaros, M. G. Rusbridge and J. W. Long, Culham Laboratory Report, CLM-P-852.

[2] T. R. Jarboe, B. Alper, Physics Fluids, **30**, 1177, (1987).

[3] J. C. Fernández *et al.* Nucl. Fusion **28**, 1555, (1988).

[4] M. J. Forrest, D. L. Trotman, R. A. Bamford, Rev. Sci. Instrum. **59**, 1461, (1988)

[5] G. A. Wurden *et al.*, in 15^{th} Conference on Controlled Fusion and Plasma Heating, Vol.12B, Pt II p533 (1988).

[6] D. A. Evans, M. J. Forrest, M. G. Nicholson, D. D. Burgess, P. G. Carolan and P. Gohill, Rev. Sci. Instrum. **56**, 1012,(1984).

[7] G. A. Wurden *et al.* IAEA Technical Committee Meeting on Pellet Injection and Toroidal Confinement, Gut Ising, Bavaria, FRG (1988)

[8] P. G. Carolan, A. Patel, M. J. Walsh, This Conference.

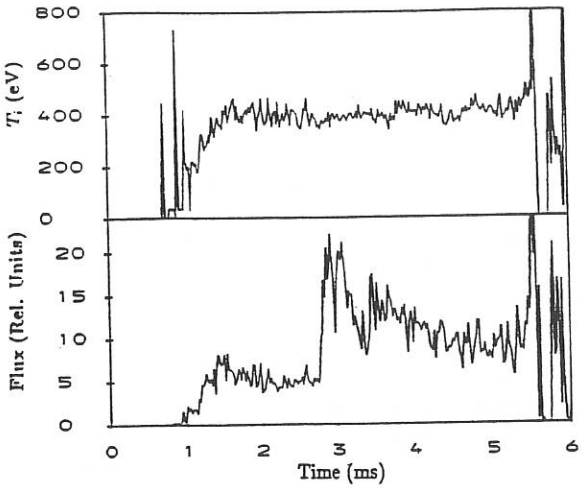

Figure 1 Ion Temperature (top) and Neutral Flux (bottom) during shot # D0111062.

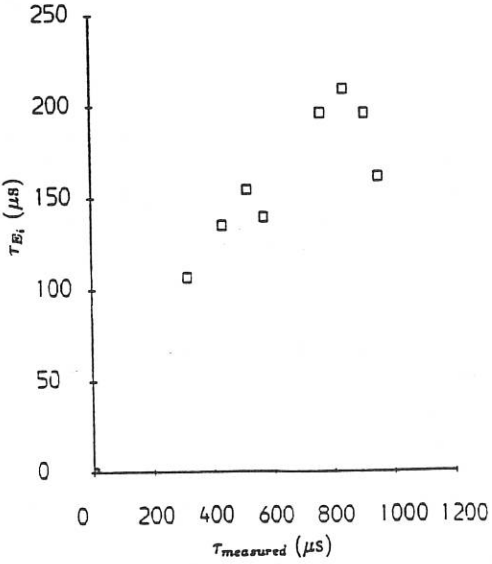

Figure 2 Ion energy confinement time against decay time of carbon signal.

RFP Plasma Resistance Following Laser Ablation Of Carbon

B Alper, C A Bunting, P G Carolan, A Patel, M J Walsh*

AEA Fusion, Culham Laboratory, Abingdon, Oxon, OX14 3DB, UK
(UKAEA/Euratom Fusion Association)
*University College Cork, Ireland (supported by Euratom)

1 Introduction

Models based on the conservation of magnetic helicity in RFP discharges [1,2] suggest that the observed loop voltage, V_ϕ, on HBTX can be represented in the form

$$V_\phi = \Delta V_\phi + I_\phi \Omega_c \tag{1}$$

Here Ω_c is the classsical or Spitzer resistance and ΔV_ϕ is a non-Spitzer component of the loop voltage which is shown to be dependant on the quantity of magnetic flux which intercepts the plasma–first wall boundary. This representation has worked well in accounting for the observed loop voltage over a range of plasma conditions and machine configurations [3], with the dominant contribution to variations in the measured loop voltage attributed to changes in ΔV_ϕ. The 'paddle' experiment results [4] were, however, complicated by a combination of effects from increases in ΔV_ϕ dominant early in the discharge to an increase in the Spitzer contribution from radiation enhanced sputtering of carbon from the paddle [5] later in the discharge. Experiments have recently been carried out on HBTX1C using laser ablation of controlled amounts of impurities into the plasma to study particle confinement and ion heating [6,7,8]. A preliminary analysis of a subset of those experiments, in which large amounts of carbon were ablated into HBTX1C, are presented here. Under these conditions rapid changes were observed in both effective charge, Z_{eff}, and electron temperature, T_e. This led to a rise in Ω_c in times ($\sim 200\mu s$) which were short compared to changes in plasma equilibrium or the growth of magnetic modes. Thus such a technique has allowed us to study changes in Spitzer resistance, in a controlled way, over times short compared to expected variations in the contribution from edge helicity loss.

2 Carbon ablation experiments

The carbon ablation experiments were carried out on HBTX1C when operated with a combined close-fitting resistive shell and distant secondary shell [9], on RFP discharges of $\sim 7ms$ duration with plasma currents, I_ϕ, rising from $\sim 75kA$ to $\sim 120kA$ over the reversal period. Carbon was ablated into the plasma using a pulsed ruby laser at

$3ms$ into the discharge. Figure 1 shows the time variation of the line-averaged electron density, n_e, for one of these discharges and figure 2 shows the corresponding CV line emission at 2271Å for the same discharge. The interferometer and spectrometer were displaced 180° toroidally with respect to the ablation unit. The electron density, in the example shown, rises from $\sim 10^{19}$ to $\sim 2 \times 10^{19} m^{-3}$ following the ablation of carbon into the plasma. Although there is some shot-to-shot variation in n_e prior to ablation, the rise of $\sim 10^{19} m^{-3}$ was fairly reproduceable. For the analysis presented here we have assumed that the rise in electron density is entirely attributable to the carbon influx and that the background composition of the plasma remains unchanged over the 1–$2ms$ before and after ablation. Furthermore, with CV as the dominant core ionization state we have assumed that each carbon atom contributes 4 electrons to n_e. The total radiation averaged over 6 discharges with carbon ablation rose from $\sim 0.4MW$ just before ablation to $\sim 1.2MW$ just after ablation. From studies of impurity radiation emitted from HBTX1C, the plasma was assumed to be composed of 2–4% oxygen, 1–3% carbon and 0.1–0.3% metals (mainly iron), prior to ablation. Calculations consistent with the variations in: electron density, CV emissions and total radiation, indicate that the effective charge of the plasma rose from $Z_{eff} = 2.3 \pm 0.3$ before ablation to $Z_{eff} = 3 \pm 0.4$ just after ablation. Further, Z_{eff} was assumed to fall to its value before ablation over the subsequent 1–$1.5ms$ in line with the fall in n_e and CV radiation. The time variation in electron temperature, T_e, is shown in figure 3 averaged over all discharges. The figure shows a fall in T_e from 240 ± 20 eV before ablation to 164 $\pm$ 15 eV just after. The value of T_e subsequently rises to over $300eV$ over the following millisecond reaching, at those times, values obtained in discharges without ablation.

3 Plasma resistance and loop voltage

The Spitzer resistance is calculated using helicity balance from the values of Z_{eff} and T_e presented above with similar assumptions to those made in previous analyses on HBTX [3], namely: a temperature profile of the form $T_e = T_{eo}[1 - (r/a)^4]$ and a current profile derived from a Modified Bessel Function Model and corrected for finite beta. Figure 4 shows the variation in time of the measured plasma resistance (corrected for inductive effects) compared to the calculated values of the Spitzer component. Two features are of note from this figure. Firstly, there is a brief rise in measured plasma resistance attributed to the carbon ablation which is well matched by the calculated rise in the values of the Spitzer component and secondly, the Spitzer values at times unaffected by the ablation, account for less than 25% of the measured values. These features are highlighted in figure 5 where the difference between the measured and Spitzer resistance is displayed. No evidence of an excursion in the non-Spitzer component is observed. Further, these values agree with those obtained in discharges without ablation. Also shown in figure 5 is the corresponding value of the non-Spitzer loop voltage ΔV_ϕ, determined from the product of the anomalous resistance and the measured plasma current. Since the current was ramping in these discharges, the value of ΔV_ϕ rises with time. Non-zero values of ΔV_ϕ are attributed to edge helicity loss in the RFP where flux lines inter-

cept the wall. In HBTX1C, which has resistive shells, the presence of thin shell modes leads to a flux interception of the wall [4] which increases in magnitude throughout the discharge. The rise with time in ΔV_ϕ , as seen in figure 5, (similar to values found in comparable discharges without ablation), may be related to the growth of the thin shell modes during the discharge.

4 Conclusions

The carbon ablation experiments on HBTX1C have provided an ideal opportunity to test the concept that the measured loop voltage or plasma resistance in RFP discharges can be separated into a classical component, dependant on electron temperature and Z_{eff}, and a non-classical component, dependant on flux penetration of the first wall. The results of this preliminary analysis provide clear support in that variations in plasma resistance from the ablation of carbon are accounted for classically, as expected, with a large (>75%) fraction of the total value attributed to non-classical effects from the growth of thin shell modes.

[1] *T R Jarboe and B Alper, Physics Fluids 30, p1177 (1987).*

[2] *H Y W Tsui, Nuclear Fusion 28, p1543 (1988).*

[3] *B Alper, H A B Bodin, C A Bunting et al, Plasma Physics Controlled Fusion 30, p843 (1988).*

[4] *B Alper and H Y W Tsui in Physics of Mirrors, Reversed Field Pinches and Compact Tori, Varenna (1987), Vol.III, p1095.*

[5] *A Patel and P G Carolan, ibid, Vol.III, p1103.*

[6] *P G Carolan, et al., this conference.*

[7] *C A Bunting, et al., this conference.*

[8] *R A Bamford, et al., this conference.*

[9] *B Alper, M K Bevir, H A B Bodin et al, in Proceedings of 16th European Conference on Controlled Fusion and Plasma Physics (1989), Vol. 13B, Part II, p705.*

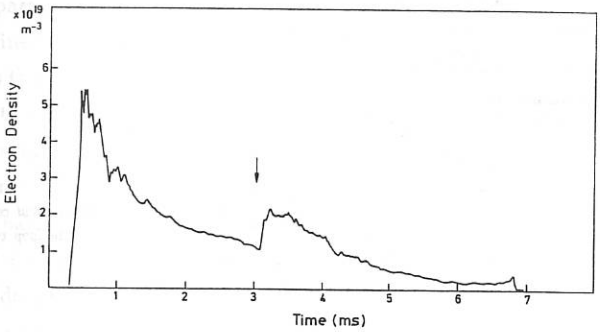

Figure 1: *Electron density showing a rise after carbon ablation at 3ms.*

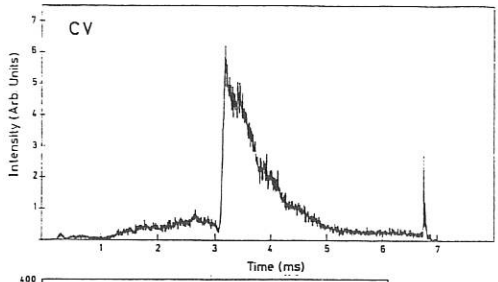

Figure 2: *CV (2271Å) emission during the same discharge as Figure 1.*

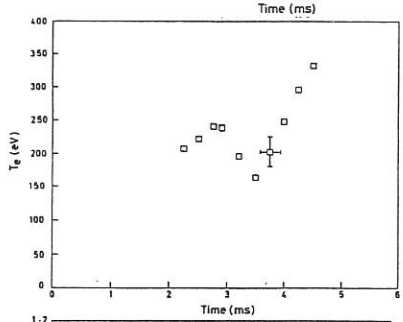

Figure 3: *Electron temperature averaged over several discharges with carbon ablation.*

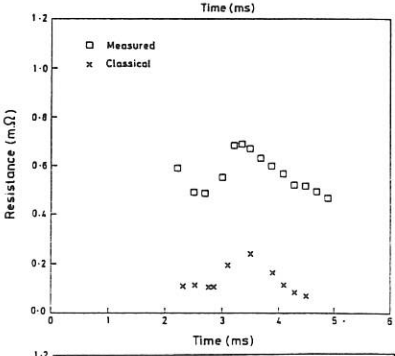

Figure 4: *Comparison of the measured resistance and calculated Spitzer component.*

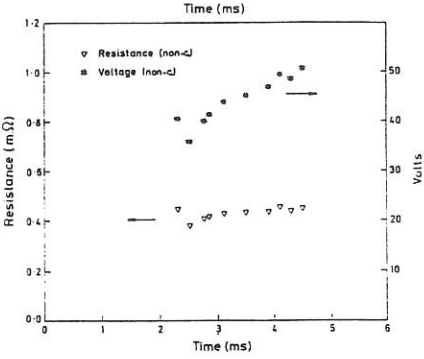

Figure 5: *The non-classical components of resistance and loop voltage.*

Particle Confinement in the HBTX1C Reversed Field Pinch

P. G. Carolan, A. Patel and M. J. Walsh*

AEA Fusion, Culham Laboratory, Abingdon, Oxon, OX14 3DB, UK
(UKAEA/Euratom Fusion Association)
*University College Cork, Ireland (supported by EURATOM)

Introduction

The dominance of non-collisional ion heating in current Reversed Field Pinch (RFP) plasmas is now well established. As a first step in understanding the underlying physics, reliable measurements of the ion heating, or loss, rates are required. Previous estimates of these rates relied on the observation of a non-Spitzer component to the resistance whose corresponding ohmic power was assumed to provide the ion heating. Now, a more direct method of measuring particle confinement, or transport, is used. This involves the laser ablation of small quantities (a few percent of n_e) of an appropriate impurity into the plasma and monitoring the line-radiation time histories. These time histories are interpreted by using zero and one dimensional models.

Experiment

Typical parameters for HBTX1C are $T_e(\approx 200eV)$, $n_e(\approx 1.5\times 10^{19} m^{-3})$ and global energy confinement time, $\tau_E \approx 200\mu s$. To decide on which impurity to use, a first approximation is to assume that the particle confinement time, τ_p, is equal to τ_E. Confinement times of this order means that low Z impurities (i.e. such as those from boron to fluorine) are far from coronal equilibrium and are not completely ionised in the core. Ionisation rates from the helium-like states of these elements are sufficiently long to measure particle confinement times from line intensity decay rates. We monitor the near UV transitions (1s2s–1s2p) to obtain spatially resolved measurements in both the poloidal and toroidal directions using multichord spectrometers. A range of these elements were injected, but the results discussed here are from carbon only.

In the HBTX1C RFP [1], the carbon concentration is typically a few percent of n_e, hence the injected concentration must be at least of this order but not so high that

the plasma is perturbed (e.g. less than $\approx 10\%$ change in n_e or in the radiated power). The CV emissions (with wavelengths 2270.9Å, 2277.2Å and 2277.96Å) are monitored using (i) a polychromator, (ii) a visible spectrometer, and (iii) multichord spectrometer, which are respectively located, 180°, 90° and 0° toroidally from the ablation port.

The temporal behaviour of the line intensity of carbon is shown in figure 1 for two different plasma currents. The burn-through of the pre-helium-like states and the fast transport of the impurities around the torus is evident from the sharp rise time of the signals to a maximum. Here we are more interested in the line intensity decay rate and how it relates to the particle confinement time.

Data Interpretation

We have constructed a simple zero dimensional model which treats the ionisation and loss of impurities [2]. Recombination and recycling is neglected. Sample simulations of the evolution of the CV ionisation state in time is shown in figure 2 for n_e of $1.5\times10^{19}\mathrm{m}^{-3}$ and T_e=200eV and different particle confinement times. Comparing these with the raw data for the same conditions, (I_ϕ=100kA) we get τ_p=1.0ms$^{+0.7ms}_{-0.1ms}$. Applying the same approach to data for I_ϕ=200kA, we get τ_p=0.5ms$^{+0.6ms}_{-0.1ms}$. The main uncertainty comes about because we allow an error of $\pm15\%$ in electron temperature.

By assuming a relationship between the minor radius of the plasma, a (0.255m), the diffusion coefficient D and the particle confinement time is related by $\tau_p = a^2/4D$. Using a τ_p of 1.0ms, this yields an on-axis diffusion coefficient of $\approx 15\mathrm{m}^2\mathrm{s}^{-1}$.

Whereas a zero dimensional approach is useful as a first approximation, a more realistic approach will include profile information. By considering a cylindrical model of the magnetic flux surfaces, the impurity density can be assumed to satisfy the following set of coupled equations:

$$\frac{\partial n_i}{\partial t} = \frac{1}{r}\frac{\partial}{\partial r}\left(rD(r)\frac{\partial n_i}{\partial r}\right) + \xi_{\mathrm{source}} - \xi_{\mathrm{sink}} \qquad (1)$$

where the source and sink terms include ionisation and recombination etc., no pinching term, vn_i, is included at this stage. This equation can be solved by using the impurity transport code "STRAHL" [3]. To simulate the measured data, the diffusion coefficient profile is expressed as a function of α as:

$$D(r,\alpha) = D(0)\left\{1 + \alpha\left(\frac{r}{a}\right)^5\right\} \qquad (2)$$

where the fifth power is used for comparison with other results [4]. By varying α a range of $D(0)$ values can be found that suit the experimental data above. This is represented in figure 3, where the curves are chosen to match the measured data for two different particle confinement times (τ_p=1ms and 0.5ms). In order to determine accurately which value of α and $D(0)$ are appropriate to our conditions, we have to appeal to multichord data. If we assume that the diffusion coefficient at the wall is not more, or less, than a few times $D(0)$, then a useful value of $D(0)$ can be found. For a flat profile this would be $D(0)$=14m^{2}s^{-1}, even for an α of 3 the diffusion coefficient only changes by a factor of two. A flat diffusion profile produces results that corroborate the zero dimensional treatment for both cases of τ_p.

It should be noted that the data above are for (a) I_ϕ=100kA, n_e=1.5×10^{19}m^{-3}, T_e=200eV, (b) I_ϕ=200kA, n_e=1.5×10^{19}m^{-3}, T_e=300eV. This indicates that increasing the plasma current results in a reduction of the particle confinement time.

Conclusion

We have shown that laser ablation of low-Z impurities can be usefully applied to the study of transport in Reverse Field Pinch plasmas. Particle confinement times of about 1ms are obtained in the HBTX1C experiment at conditions of, 100kA plasma current and T_e=200eV, and n_e=1.5×10^{19}m^{-3}. These confinement times are much longer than the global energy confinement times and ion energy confinement times of a few hundred microseconds.

References

[1] B. Alper, M. K. Bevir, H. A. B. Bodin *et al.*, Proc. EPS, 16th European conf. on Controlled Fusion and Plasma Physics(Venice), II, 705, (1989).

[2] P. G. Carolan, A. Patel, M. C. Sexton, M. J. Walsh, "First measurements of particle confinement in a Reversed Field Pinch by the laser ablation method", Culham report CLM-P-890 (1990), submitted to Nuclear Fusion.

[3] K. Behringer, "Description of the impurity transport code "STRAHL"", Jet report, JET-R(87)08.

[4] P. G. Carolan, A. Lazaros, M. G. Rusbridge, J. W. Long, "Ion heating and power balance in the reversed field pinch", Culham report CLM-P-852 (1989), submitted to physical review A.

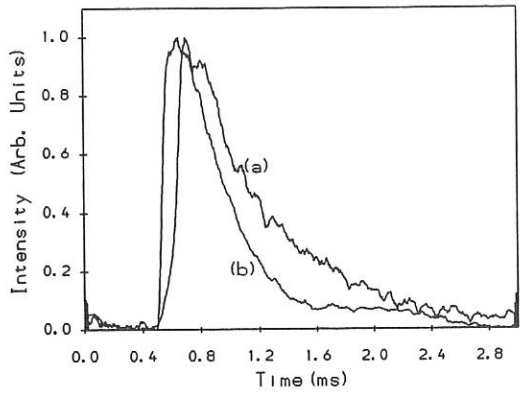

Figure 1: *Temporal behaviour of CV line intensity for (a) 100kA, (b) 200kA plasma current, n_e is $1.5\times10^{19}m^{-3}$ for both cases.*

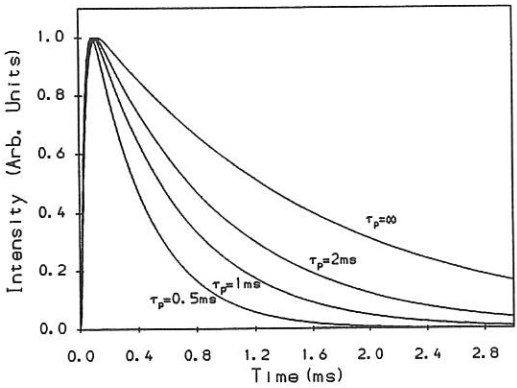

Figure 2: *Calculated evolution of CV line intensity for a range of particle confinement times using a zero dimensional model.*

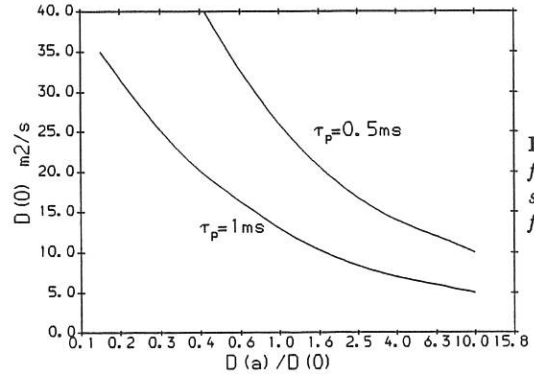

Figure 3: *Diffusion coefficient on axis, $D(0)$, versus normalised diffusion coefficient at the wall $D(a)/D(0)$.*

HIGH CURRENT DENSITY TOROIDAL PINCH DISCHARGES WITH WEAK TOROIDAL FIELDS

P.Brunsell, J. Brzozowski, C. Bunting*, J.R.Drake,
G. Hellblom, E. Källne, S. Mazur, P. Nordlund

Royal Institute of Technology, Fusion Research, S-100 44 Stockholm
*Culham Laboratory, Abingdon, Oxon OX14 3DB

Abstract. Toroidal discharges in the ultralow q regime (ULQ) have been studied in the rebuilt Extrap T1 device. ULQ discharges are sustained for pulse lengths exceeding 1 ms, which corresponds to more than 10 resistive shell times. Values for the safety factor at the vacuum vessel wall are between rational values; $1/(n+1) < q(a) < 1/n$, $n = 1,2,3$ and 4. The device has a high aspect ratio, 8.8, and a high current density, up to 5 MA m^{-2}. The magnetic fluctuation level increases during the transition between rational values of q(a). For very low values of q(a), the loop voltage increases and the toroidal field development in the discharge exhibits the characteristic behaviour of the setting-up phase of a field reversed pinch.

Introduction. The ULQ configuration has been described as a self-organized equilibrium which is an intermediate state between the Tokamak and the RFP [1]. The equilibrium profiles develop through the combined action of resistive diffusion, producing the tokamak type profile, and the MHD relaxation process, leading to the Taylor state of the RFP. These self-organized ULQ profiles may be stable against $m = 1$ modes if q(a) is sustained between two rational $m = 1$ surfaces.

The ULQ experiments have been carried out in the rebuilt T1 device shown in Fig. 1. Parameters for the device are presented in Table I. The vacuum vessel is now a stainless-steel liner, manufactured from bellows, with a perpendicular magnetic field penetration time of 3 μs and a toroidal field penetration time of about 50 μs. This liner is surrounded by a stainless steel shell, with poloidal and toroidal gaps, which has perpendicular magnetic field penetration time of about 100 μs.

The Ohmic heating circuit (OHC) includes a 0.4-V·s iron core transformer and a 3 stage capacitor bank power supply. The primary turns are distributed on the outboard side and the inboard side of the torus to provide the necessary equilibrium vertical field for discharges with pulse lengths longer than the shell penetration time. The primary windings can be connected to give a four-turn or an eight-turn primary.

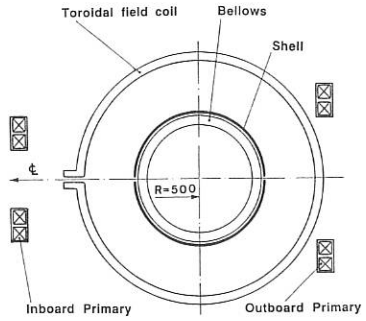

Fig. 1. Extrap T1 device. The parameters of the device are presented in Table I.

Table I. Parameters of the T1 device.

Vacuum Vessel		
	major radius (m)	0.5
	inside minor radius (m)	0.057
	bellows wall thickness (mm)	0.25
	bellows material	316L stainless steel
Shell		
	inside minor radius (m)	0.068 m
	shell wall thickness (mm)	2.5
	number of poloidal gaps	12
	number of toroidal gaps	2
	shell material	stainless steel
	perpendicular field penetration time (μs)	100
Ohmic Heating Circuit		
	number of primary turns	4 or 8
	number of capacitor bank stages	3
	maximum initial loop voltage (kV)	3
	maximum sustainment loop voltage (kV)	1.5

Discharge pulse parameters. Pulse shapes for various parameters are shown in Fig. 2 for two discharges with different filling pressures. Discharge a) shows a typical step transition between the windows $1/4 < q(a) < 1/3$ and $1/3 < q(a) < 1/2$. After the transition, the discharge

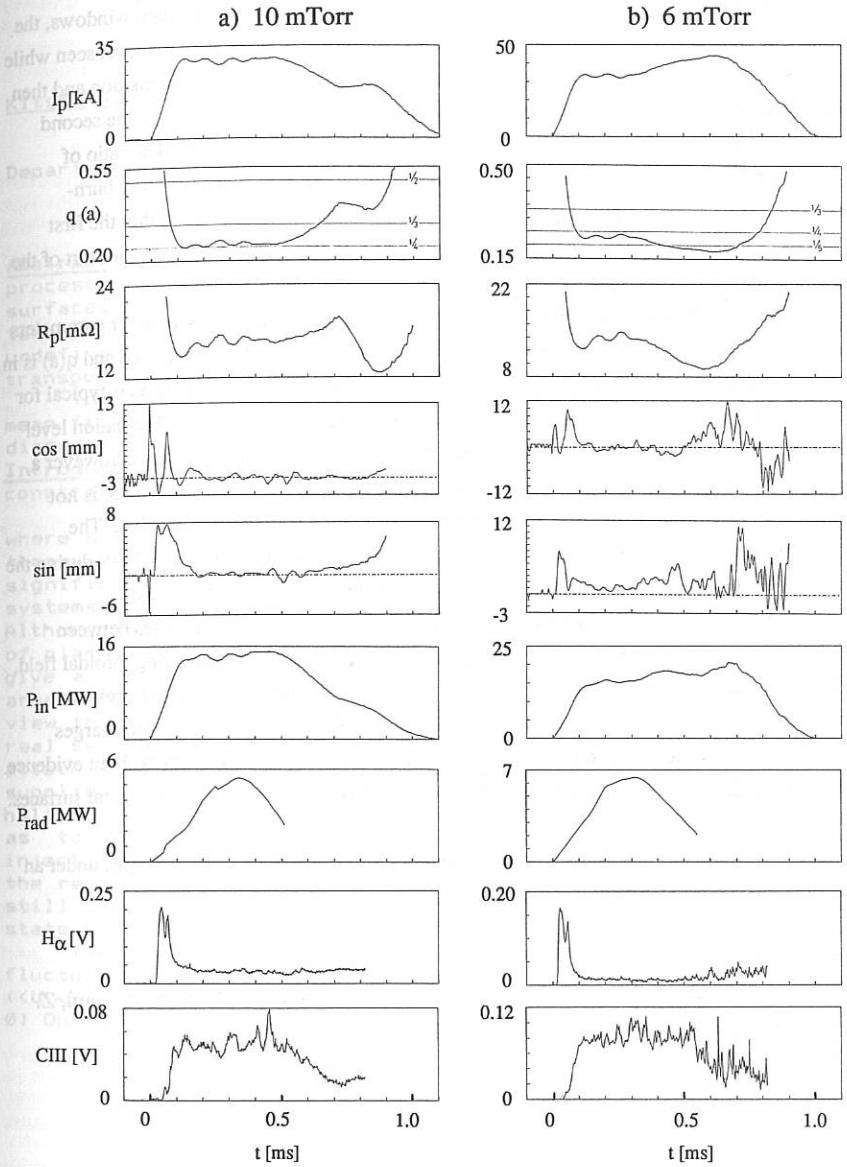

Fig. 2 Pulse forms for two discharges with different filling pressures.

is sustained until the iron core saturates. During the transition of q(a) between windows, the magnetic fluctuation level, seen on the cosine and sine coils, is larger than the level seen while q(a) is sustained in a window. The plasma resistance increases during the transition and then decreases to a lower level during the second q(a) window. The power input at the second window is reduced. The radiated power was monitored with a bolometer. The ratio of radiated power to input power decreases substantially during the pulse indicating burn-through. A monitor of the H-alpha radiation shows that ionization occurs within the first 100 μs of the pulse while the current is rising. The C-III radiation increases at the start of the pulse and then decreases later as burn-through is achieved.

Discharge b), which was initiated with a lower filling pressure but with other parameters unchanged, exhibits a different development. A larger discharge current resulted and q(a) is in the range $1/5 < q(a) < 1/4$ for about 300 μs. The resistance decreases in time as is typical for burn-through, and the current increases resulting in a decrease in q(a). The fluctuation level increases at the same time, as is characteristic for a transition between windows, however a new quiescent period, corresponding to operation in the window, $1/6 < q(a) < 1/5$, is not achieved. Operation with $q(a) \approx 1/6$ corresponds to a pinch parameter of $\theta \approx 0.6$. The fluctuation level is higher and toroidal flux is generated as is characteristic for RFPs during the set-up phase. The plasma resistance increases as the fluctuation level increases.

The development of ULQ discharges, with q(a) sustained within windows between rational values, is dependent on the initial parameters of the discharge including toroidal field, filling pressure and OHC bank voltages. For the same toroidal field and filling pressure parameters as for discharge a) above, a decrease in the OHC voltages leads to discharges where the plasma current decreases smoothly and the resulting q(a) increases without evidence that the discharge development is dependent on the relation between q(a) and rational surfaces.

Acknowledgements. This work has been supported by the European Communities under an association contract between Euratom and Sweden.

References.

[1] Y. Kamada, T. Fujita, Y. Murakami, T. Ohira, K. Saitoh, Y. Fuke, M. Utsumi, Z. Yoshida, N. Inoue, Nucl. Fusion 29 (1989) 713.

Relaxation, Reconnection and the MHD Dynamo

Kitson D.A. and Browning P.K.

Department of Pure & Applied Physics, UMIST, Manchester, UK.

Abstract: By considering a turbulence driven reconnection process we calculate the helicity transport across flux surfaces to produce a mean field representation of the turbulent dynamo ($\mathcal{E} = \langle \mathbf{U}_1 \wedge \mathbf{B}_1 \rangle$) with no free or physically undefined parameters. This model shows that in order to transport helicity, energy must be anomalously dissipated.

The implications and results of this model with respect to mean field profiles, anomalous ion heating and edge effects are discussed.

Introduction. Minimizing the magnetic energy with the constraint that the global helicity is conserved leads to

$$\nabla \wedge \mathbf{B} = \mu \mathbf{B} , \qquad (1)$$

where μ ($=\mathbf{J}\circ\mathbf{B}/(\mathbf{B}\circ\mathbf{B})$) is constant everywhere. Taylor's [1], [2] theory agrees well with experimental results, however significant deviations have been found in steady state driven systems such as Reversed Field Pinches and Spheromaks [3], [4]. Although magnetic helicity has shown to be a better invariant of plasma motion than magnetic energy, Taylor's theory does not give a mechanism for the relaxation phenomenom or explain the anomalous dissipation of energy. In this note we advance the view that deviations from the Taylor state occur because in a real system the plasma has a finite resistivity and in order to attain a steady state equilibrum helicity and energy must be supplied. The systems under consideration exhibit unequal local helicity injection and decay rates, thus the dynamo must act so as to redistribute helicity from places where the local injection is greater than the local dissipation to places where the reverse is true. In the limit of zero dissipation ($\eta \to 0$, still allowing reconnection) and so zero injection, the Taylor state would be attained.

The electromotive force ($\mathcal{E}$) generated by the turbulent fluctuating (subscript 1) magnetic and velocity fields ($\langle \mathbf{U}_1 \wedge \mathbf{B}_1 \rangle$) produces an extra term in the mean field (subscript 0) Ohm's law, helicity and energy balances (assuming $\mathbf{U}_0 = 0$),

$$\mathbf{E}_0 + \mathcal{E} = \eta \mathbf{J}_0 \qquad (2)$$

$$\frac{\partial K}{\partial t} = 2V\psi - 2\int \eta \, \mathbf{J}_0\circ\mathbf{B}_0 \, \partial\tau + 2\int \mathcal{E}\circ\mathbf{B}_0 \, \partial\tau, \qquad (3)$$

$$\frac{\partial W}{\partial t} = VI - \int \eta \, \mathbf{J}_0\circ\mathbf{J}_0 \, \partial\tau + \int \mathcal{E}\circ\mathbf{J}_0 \, \partial\tau. \qquad (4)$$

Derivation. Considering only axisymmetric systems, helicity can be defined solely as the amount of flux linkage, considering a 1D slab model (see fig. 1) then if we choose the poloidal (ψ) and toroidal (ϕ) flux gauges so

$$\psi(x=Lo) = \phi(x=0) = 0 \qquad (5)$$

then the helicity content of a flux tube (per unit length, unit depth) contained by Δx at x_1 is

$$k(x_1) = (By\ \phi + Bz\ \psi)\ \Delta x \qquad (6)$$

thus the total helicity in the volume is

$$K = 2\int_0^{Lo} (By\phi + Bz\psi)\ \partial x = 4\int_0^{Lo} By\phi\ \partial x = 4\int_0^{Lo} Bz\psi\ \partial x \qquad (7)$$

Although we may define an helicity density from equation (2), helicity which is resistively dissipated locally does not reduce the helicity density locally. η only dissipates the local current density **Jo** as the local magnetic field **Bo** is produced by the linear superposition of the fields produced by currents throughout the plasma. In the context of the 1D slab model, we consider a flux tube at x_1 of width Δx containing poloidal flux $\Delta\psi_1$ ($By\Delta x$) and toroidal flux $\Delta\phi_1$ ($Bz\Delta x$) carrying a total current ΔI_1. The effect of local helicity dissipation (injection) is to decrease (increase) the current ΔI_1. Thus we consider the effect of a small peturbation (∂I_1) on the current flowing in the flux tube at x_1,

$$\Delta I_1 \Rightarrow \Delta I_1 + \partial I_1 \qquad (8)$$

As μ is constant on field lines, the fractional increase in the current components must alter accordingly. If the current changes at x_1 then this effects the magnetic fields and hence the fluxes <u>everywhere</u> in the plasma and from equation (6) this will decrease the helicity density everwhere in the plasma. This exemplifies the global nature of helicity and shows that it is not possible to simply consider local conditions; global variables also have to be taken into consideration. <u>The helicity we must consider in order to obtain a local balance is not the local helicity density, but is the effective helicity change in the volume due to the change in current in the flux tube under consideration.</u> Thus the effective helicity change in the total volume due to the current peturbation (equation (8)) to a first order can be shown to be

$$\Delta K_{eff} \approx 4\ \Delta\mu\ \Delta x\ G \quad , \quad G = \frac{Bo^2\ Lo^2}{\lambda_o^2} \qquad (9)$$

where λ_o is the characteristic eigenvalue dependent upon the geometry of the system (eg. $\pi/2$ for a slab). From the reconnection mechanism depicted in figure 2, the effective rate of helicity transfer from region (1) to region (2) in a time Δt ($=l_t/U_r$, where l_t is the perpendicular reconnection length and U_r is the reconnection velocity) can be shown to be

$$\frac{\partial K}{\partial t} = \gamma\ \frac{\partial \mu}{\partial x} \quad , \quad \text{where} \quad \gamma = \frac{2\ l_t\ U_r\ Bo^2\ Lo^2}{\lambda_o^2} \qquad (10)$$

note that γ is always positive and zero at a solid boundary where l_t and U_r are zero. Balancing the local helicity dissipation and injection rate with the effective helicity flux, we can produce a mean field approximation of the dynamo, thus Ohm's law becomes,

$$E_A + \frac{Bo}{|Bo|^2}\ \nabla_o(\gamma\nabla\mu) = \eta\ Jo \qquad (11)$$

where E_A is the applied electric field. Note that this is the form postulated by Boozer [5], however we have given a physical

interpretation to γ and shown that it is always positive and zero at the boundary. Substituting equation (11) into the global helicity balance (eq.(3)) shows that the dynamo term disappears and helicity is globally classically conserved as assumed. However in the energy equation the dynamo term does not disappear and equation (4) becomes

$$\frac{\partial W}{\partial t} = VI - \int \eta \, \mathbf{Jo} \cdot \mathbf{Jo} \, \partial\tau - \int \gamma |\nabla\mu|^2 \, \partial\tau \qquad (12)$$

as $\gamma > 0$ in the volume then equation (12) shows the important result that in order to transport helicity, energy must be anomalously dissipated and presumably goes into ion heating.

Results and Discussion. By specifying the perpendicular reconnection length and the reconnection velocity (and hence the relaxation time $\tau_R = L_0/U_R$), then equations (1) (with $\mu \neq$ constant) and (11) form a closed set of equations, which we solve in a cylinder (infinite aspect ratio rfp). Normalising (indicated by) with respect to the values on axis (subsript a) or the radius of the cylinder leads to

$$\gamma \frac{\partial^2 \mu}{\partial r^2} + \left[\frac{\gamma}{r} + \frac{\partial \gamma}{\partial r} \right] \frac{\partial \mu}{\partial r} - \frac{1}{R_{mt}} \eta \mu \, \mathbf{Bo} \cdot \mathbf{Bo} + F_R \, \mathbf{E_A} \cdot \mathbf{Bo} = 0 \, . \qquad (13)$$

Two non-dimensional numbers classify the solution, the Magnetic Reynolds number based on turbulent parameters ($R_{mt} = \mu_0 U_R l_t / \eta_\alpha$) and F_R the ratio of the applied to the dynamo electric field. The two limiting cases are $R_{mt} = \infty$ in which case there is no driving and no dissipation and the Taylor State is attained and $R_{mt} = 0$ where no helicity can be transfered so the Paramagnetic Force-Free solutions are obtained. In this limit the dynamo electric field is zero ($F_R = \infty$) and so reversal is impossible. Fig 3 shows these two limiting cases on an F/θ plot, note that all finite values of R_{mt} and experimental points lie between these two limits.

For a flat resistivity profile the anomalous energy dissipation rate is only a few percent of the total energy injection rate (Fig. 4 solid line). However experimental evidence suggests that the classical resistivity at the edge is greatly increased through the field lines intersecting the wall, this dramatically increases the amount of energy injection needed in order to sustain the plasma. This effect can be enhanced by inserting carbon tiles into the plasma [6]. The model mirrors this effect, the dotted line in fig. 4 shows that the anomalous energy dissipation rate is dramatically increased if the edge resitivity is increased.

Conclusions. Considering only a dynamic helicity balance we have formulated a mean field representation of the dynamo in terms of the turbulent Magnetic Reynolds number, thus producing a simple 1 or 2D model of a turbulent plasma. This model shows that in order to conserve helicity, energy must be anomalously dissipated. The two limiting cases give the Taylor state ($R_{mt} = \infty$) and the Paramagnetic force free solution ($R_{mt} = 0$), finite values of R_{mt} link these two limiting cases. Solving the equations in cylindrical geometry gives realistic mean field profiles for an rfp and also mirrors the experimentally observed effect of increased fields errors dramatically increasing the anomalous energy dissipation rate.

References

[1] Taylor J.B., 1974, Phys. Rev. Lett., 33, 1139
[2] Taylor J.B., 1986, Rev. Mod. Phys., 58, 741
[3] Browning et al, 1990 This conference.
[4] Bodin H.A. and Newton A.A, 1980, Nucl. Fusion 20, 1255
[5] Boozer A.H., J. Plasma Physics, 35, 133
[6] Alper B. and Tsui H.Y., 1987, Proc. 14th Eur. Conf. Madrid, vol 11D, Part II, p469

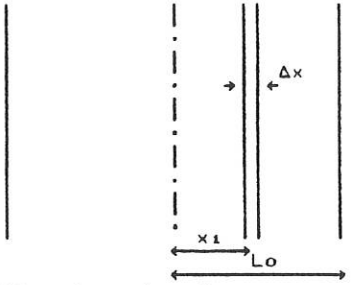

Fig. 1 $\phi = 0$ $x = 0$ $\psi = 0$ $x = L_0$

1D Slab Model

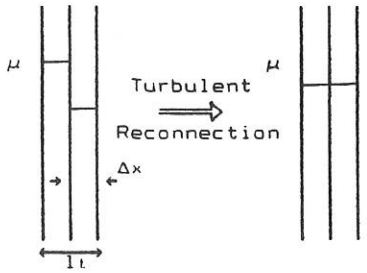

Fig. 2

Turbulence driven reconnection locally flattens μ over a perpendicular scale length l_τ.

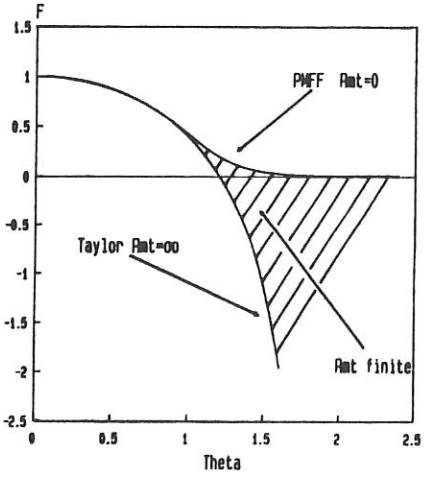

Fig 3
F/θ plot for rfp in dynamic equilibria, shows the two limiting cases $R_{mt}=\infty$ (Taylor State) and $R_{mt}=0$ (Paramagnetic Force Free). All finite values of R_{mt} lie between these two cases.

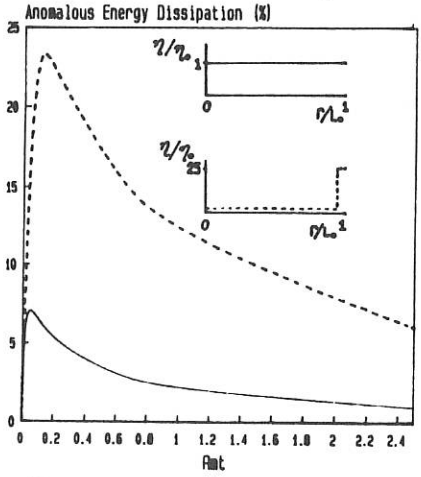

Fig. 4
Anomalous energy dissipation rate (% of injection rate) against turbulent Magnetic Reynolds no. (θ=1.5), the effect of high edge resistivety (dotted line) dramatically increases the anomalous energy dissipation

MAGNETIC AND ELECTROSTATIC FLUCTUATION MEASUREMENTS ON THE ZT-40M REVERSED FIELD PINCH

G. Miller, J. C. Ingraham, C. P. Munson, K. F. Schoenberg, and P. G. Weber
Los Alamos National Laboratory, Los Alamos, NM 87545, USA

H. Y. W. Tsui and Ch. P. Ritz
Fusion Research Center, University of Texas, Austin TX 78712, USA

INTRODUCTION It is presently unknown whether anomalous transport in toroidal, magnetically confined plasma systems, if fluctuation induced, is dominated by electrostatic or magnetic turbulence. We are participating in a joint study of the edge plasmas of tokamak, stellarator, and RFP in an attempt to elucidate this issue. We measure magnetic and electrostatic fields using probes inserted into the edge of the ZT-40M RFP.[1] Using the present technique, with stationary probes, these measurements can be done without damaging the probes only for low current discharges ($60\,kA$). In this initial study, we find that both turbulent magnetic and electrostatic transport are of importance.

MAGNETIC FLUCTUATIONS The magnetic probe measurements utilized a square, four-fingered vector B probe array ($3.5\,cm$ spacing). For some of the measurements a fifth probe was used, located across a minor diameter from the four-probe array. The magnetic probes were typically inserted $1\,cm$ into the plasma ($a = 20\,cm$).

The most accurate method of obtaining the spatial mode spectrum of the fluctuations is to make measurements of correlations as a function of spatial separation. We used instead a simpler technique discussed in Ref. 2. With probes separated by a fixed amount in the θ (poloidal) and ϕ (toroidal) directions, one uses the measured phase shift as a function of frequency to determine the mode numbers m and n. The fluctuations are found to be mostly $m = 1$. By using the fifth probe and looking at the correlation across a minor diameter, we find that there is a small $m = 0$ component. A fit to the dominant part of the spectrum ($-50 < n < 20$) is given by the analytic form

$$|b_{mn}|^2 = \langle(\tilde{B}_r)^2\rangle \frac{\sigma}{\sqrt{2\pi}}\{\epsilon\delta_{m,0}\, exp[-\frac{\sigma^2 n^2}{2}] + (1-\epsilon)\delta_{m,1}\, exp[-\frac{\sigma^2(n-N)^2}{2}]\},$$

where the width of the n-number spectrum is determined by the parameter σ, equal to 0.1, the $m = 0$ amplitude ϵ is equal to 0.1, and N, the peak n number for $m = 1$, is equal to -15 (corresponding to resonance inside the reversal surface). For $1\,cm$ ($0.05\,a$) probe insertion, $\sqrt{\langle(\tilde{B}_r)^2\rangle}/B = 0.015$.

To extrapolate $b_{mn}(r)$ into the plasma, the quasi-static equation for $b_{mn}(r)$ was used,[3] assuming zero-pressure equilibrium current profiles consistent with the experimental constraints (F and Θ). Generally $b_{mn}(r)$ satisfies only one of the two required boundary conditions at the outer conducting wall and at the origin, so the two solutions obtained by

integrating out from the origin and in from the wall join with some discontinuity in derivative. The point where the two solutions was brought together was the singular surface, if one existed for the particular mode, or $r = a/2$, where a is the minor radius, if there was no singular surface. Figure 1 shows the resultant value of $\tilde{B}_r/B$ as a function of r, obtained by summing over all modes.

Using the mode amplitudes $b_{mn}(r)$ obtained in this way, we calculate several quantities of interest: 1) the Chirikov parameter (island width/distance between islands), given by

$$S = 4|\frac{b_{1n}}{B_z} R \frac{n(dq/dr)}{q}|^{1/2},$$

where q is the safety factor and R is the major radius; 2) the quasi-linear magnetic field line diffusivity,[4] given by

$$D_m = \frac{2\pi R}{B|B_z|}|b_{1n}(r)|^2;$$

and 3) the Kolmogorov (field line divergence) scale length, given by[5]

$$\frac{L_K}{a} = 2.75(\frac{L_s}{a})^{2/3}(\frac{D_m}{a})^{-1/3},$$

with shear length $L_s = Bq/(B_\theta dq/dr)$. These are shown in Figure 2.

The quantities $S(r)$, $D_m(r)$, and $L_K(r)$ depend on magnetic fluctuation amplitudes resonant at a particular radius r. Resonant $b_{mn}(r)$ is best determined in the core region because the dominant modes, which are the best measured ones, are resonant in the core. Edge-resonant modes have very high n numbers and small amplitudes. It is questionable whether subdominant mode amplitudes can be measured using our present technique. Consequently, Fig. 2 includes only the region where resonant n is less than 40.

In the core region S is larger than 1, indicating stochasticity, and D_m/a is in the range 10^{-3} to 10^{-4}. Suprathermal electrons are known to be present in ZT-40M.[6] For these electrons the mean free path satisfies $\lambda/a = 1900$ ($T_e = 500\,eV$, $n_e = 8 \times 10^{12}\,cm^{-3}$). From Fig. 2c the collisionless criterion[7] $\lambda >> L_K$ is well satisfied. An estimate of the global confinement time $\tau = a^2/(D_m v_e)$, where v_e is the electron velocity, is the right order of magnitude to account for the observed energy confinement time for these low current discharges. However, the actual confinement mechanism may well be more complicated, involving high n-number edge-resonant, pressure-driven modes, which could give the observed β-limited confinement. The core stochasticity observed here accounts for the Taylor-like flattened j/B profiles observed and the observed relatively poor central confinement (flat central T_e profiles).

ELECTROSTATIC FLUCTUATIONS The electrostatic probe, supplied by the University of Texas, consisted of an array of four single Langmuir probes. Two of the probes, separated by $\Delta z = R\Delta\phi = 1\,cm$, were used to measure the floating potential Φ_f and the electric field $E_\phi = \Delta\Phi_f/\Delta z$. The other two probes were operated as a double probe with $\approx 150\,V$ bias. Nominally, the difference between the potential of the positively biased double probe and the floating potential gives the electron temperature T_e (by multiplying by $1/log\,2$) and the double probe current, I_{sat} (ion saturation current), gives the electron density n_e. However, fast electrons are also present in the edge plasma, and these electrons are very

efficient at ejecting secondary electrons from surfaces, with a secondary emission coefficient δ of order 1 for Molybdenum[6] (the probe tip material). If $\delta > 1$, as seems to be the case, the floating potential is driven in the positive direction from its value in the absence of fast electrons to minus a few tens of volts (as observed) and the apparant ion saturation current is increased, leading to a several times overestimate of n_e and an underestimate of T_e by as much as 15%. Furthermore, the large power flux parallel to B carried by the fast electrons can heat the probe tips sufficiently to cause thermionic emission of electrons and evaporation of probe material. Evidence of some melting of the probe tips was seen. Clearly such effects complicate the interpretation of the electrostatic probe measurements in this case. Nevertheless, a simple interpretation of the measurements may have some validity as a rough estimate. Electrostatic probe measured fluctuations are included in Table I.

The observed phase difference between the floating potential probes implies a linear k versus ω dispersion relation for $\tilde{\Phi}_f$ corresponding to a drift $v_\phi = (3 \pm 1) \times 10^6\, cm/s$, approximately equal in sign and magnitude to the electron diamagnetic drift given by $v_\phi = T'/(eB)(1/a_{n_e} + 1/a_{T_e}) \approx 2.5 \times 10^6\, cm/s$, where the a's are measured radial gradient scale lengths. This implies that radial electric field does not dominate the drift. The observed correlation between $\tilde{I}_{sat}$ and $\tilde{E}_\phi$ implies an outward flux $\Gamma = \langle \tilde{n}\tilde{v} \rangle = C\langle \tilde{I}_{sat}\tilde{E}_\phi \rangle / B$ of about $10^{18}\, cm^{-2}s^{-1}$, where C is an empirical constant relating n and I_{sat}. The particle confinement time $na/(2\Gamma)$ is about $100\,\mu s$, comparable to that expected from other measurements for these conditions.[8] However, $\langle \tilde{p}\tilde{v} \rangle$, where p is the pressure, seems too small to account for transport of energy, consistent with the hypothesis that suprathermal electrons are a dominant energy loss channel.[9] A clear correlation between $\tilde{B}_r$ and $\tilde{I}_{sat}$ was observed, as expected from earlier observation of a correlation between $\tilde{B}_r$ and the hot electron current measured with an electrostatic energy analyzer.[10] The model for this correlation is the relation $\tilde{n} = (dn/dr)\xi$, where dn/dr is the gradient of the mean density profile and $\xi = rB_r/(mB_\theta + krB_z) \approx rB_r/B_\theta$ is the plasma displacement. The measured quantity $\langle \tilde{I}_{sat}\tilde{B}_r \rangle / \langle (\tilde{B}_r)^2 \rangle$, agreed within about 35% with the model result $I_{sat}a/(a_{I_{sat}}B_\theta)$.

CONCLUSIONS For $60\,kA$ discharges in ZT-40M we have found direct evidence for magnetic stochasticity in the core. The magnetic diffusivity and Kolmogorov scale length have been determined. Electrostatic fluctuations in the edge have been roughly characterized. Most of the density fluctuation $\tilde{n}$ is accounted for by $\tilde{B}_r$. Tentatively, it seems that $\langle \tilde{n}\tilde{v} \rangle$ explains edge particle transport, while $\langle \tilde{p}\tilde{v} \rangle$ is too small to acount for energy transport.

REFERENCES

1. R. S. Massey *et. al.*, Fusion Technol. 8, 1571 (1985).
2. Ch. P. Ritz *et. al.*, Rev. Sci. Instrum. 59, 1739 (1988).
3. G. Miller, Phys. Fluids 28, 560 (1985).
4. M. N. Rosenbluth *et. al.*, Nucl. Fusion 6, 297 (1966).
5. A. B. Rechester *et. al.*, Phys. Rev. Lett. 42, 1247 (1979).
6. J. C. Ingraham *et. al.*, Phys. Fluids B2, 142 (1990).
7. A. B. Rechester and M. N. Rosenbluth, Phys. Rev. Lett., 40, 38 (1978).
8. P. G. Weber. Phys. Fluids 28, 3136 (1985).
9. K. F. Schoenberg *et. al.*, Plasma Physics and Controlled Nuclear Fusion Research 1988 (IAEA, Nice 1988), Vol. II, p. 419.
10. G. Miller, Bull. Am. Phys. Soc. 34, 2105 (1989).

TABLE I—Fluctuations measured in the edge ($r/a = 0.95$) for $60\,kA$ discharges in ZT-40M (edge parameters: $T_e \approx 15\,eV$, $a_{T_e} = T_e/(dT_e/dr) \geq 2.5\,cm$, $n_e \approx 5 \times 10^{12}\,cm^{-3}$, $a_{n_e} \approx 1.3\,cm$)

quantity	rms amplitude	frequency (kHz)*
$\tilde{B}_r/B$	0.015	50
$\tilde{n}/n$	0.5	100
$\tilde{\Phi}_f$	$25\,V$	100
$\tilde{T}_e/T_e$	0.5	100
$\tilde{E}_\phi$	$10\,V/cm$	150

* frequency at which normalized power spectrum equals mean square power

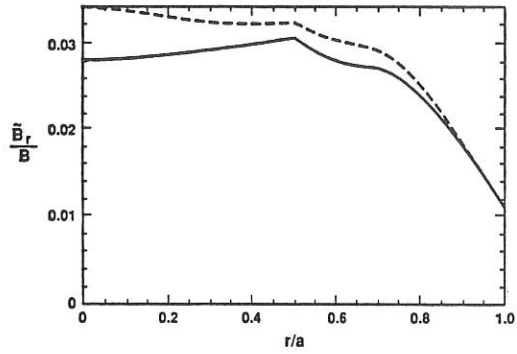

Fig. 1
Magnetic fluctuation $\tilde{B}_r/B$ extrapolated into the plasma from probe measurements at $r/a = 0.95$. The effective conducting wall is at $r/a = 1.12$. The two curves are for two different equilibrium profiles consistent with experimental constraints. The derivative discontinuity at $r/a = 0.5$ is an artifact of the extrapolation method.

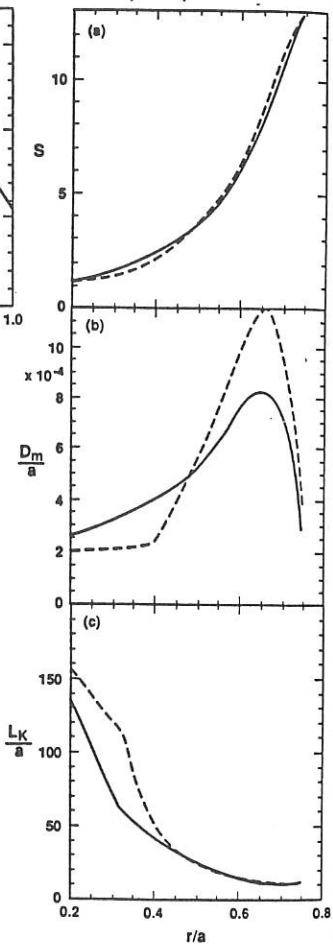

Fig. 2
(a) Chirikov (island overlap) parameter, (b) magnetic field line diffusivity, and (c) Kolmogorov (field line divergence) scale length for the two assumed equilibrium profiles.

FINITE ELEMENT ANALYSIS OF HELICALLY SYMMETRIC EQUILIBRIA

H. Igarashi and T. Honma

Department of Electrical Engineering, Faculty of Engineering,
Hokkaido University, Kita 13, Nishi 8, Kita-ku, Sapporo, 060 Japan

INTRODUCTION

It is well-known that Taylor's force-free states, which satisfy the relation $\nabla\times B=\mu B$, can exist only for discrete values of μ when the mode number m is grater than zero and when the solution to the above equation has the lowest energy, the constant μ also takes the smallest value 3.11 for $m=1$, $h \simeq 1.25$ (where h is the helical pitch) under the condition that a plasma is enclosed by a straight perfectly conducting shell with a circular cross-section [1]. However, the dependence of the minimum-μ states on the shape of a shell still remains unclear.

In this report, a finite element analysis of $m = 1$ helically symmetric Taylor's force-free states is presented. In particular, we study the dependence of those states on the shape of perfectly conducting shells enclosing plasmas using the present scheme.

FORMULATION

The MHD equilibrium equation is given by [2]

$$\nabla\cdot(\kappa\nabla\Psi) = -\frac{2\kappa^2}{h}g(\Psi) - \kappa g(\Psi)g'(\Psi) - \mu_0 p'(\Psi) \tag{1}$$

where $\kappa\equiv h^2/(1+h^2r^2)$, p is the plasma pressure, μ_0 is the permeability of the free space, Ψ is the magnetic stream function, $g(\Psi)$ is the current potential and h is the helical pitch. When $p'=0$, $g'=-\mu$ and μ is a constant, the solution to eq. (1) corresponds to Taylor's state $\nabla\times B=\mu B$ to be calculated here [3].

We choose the following boundary condition for Ψ.

$$\Psi = 0 \qquad \text{on the boundary} \tag{2}$$

We introduce the twisted coordinates (X, Y, Z), which is used in the analysis of the propagation of electromagnetic waves in twisted waveguides [4], defined by

$$X=x\cos(hz) + y\sin(hz),\ Y=y\cos(hz) - x\sin(hz),\ Z = z \tag{3}$$

From eqs. (1), (2) and (3), we can obtain a variational form of eq. (3) in the twisted coordinates as follows :

$$\frac{\delta}{2}\int\int \kappa\left\{(1+h^2Y^2)\left(\frac{\partial\Psi}{\partial X}\right)^2 - 2XYh^2\left(\frac{\partial\Psi}{\partial X}\right)\left(\frac{\partial\Psi}{\partial Y}\right)+(1+h^2X^2)\left(\frac{\partial\Psi}{\partial Y}\right)^2\right\}dXdY$$

$$= \frac{\delta}{2}\int\int \mu\left(\frac{2\kappa^2}{h}-\mu\kappa\right)\Psi^2\, dXdY \tag{4}$$

To numerically solve eq. (4), the domain is subdivided into small triangle elements $\triangle_k$ with nodes i, j and k and the stream function Ψ is linearly interpolated in $\triangle_k$ as follows :

$$\Psi = [N_i\ N_j\ N_k]\begin{bmatrix}\Psi_i\\ \Psi_i\\ \Psi_i\end{bmatrix}$$

$$\equiv \mathbf{H}^T\boldsymbol{\Psi}^e \tag{5}$$

where N_i, N_j and N_k are the area coordinates and Ψ_i, Ψ_j and Ψ_k are the values of Ψ at the nodes i, j and k. The element matrices for an element $\triangle_k$ are derived from eqs. (4), (5) as follows :

$$\mathbf{A}_k^e = \int\int_{\triangle_k} \kappa\left\{(1+h^2Y^2)\frac{\partial\mathbf{H}}{\partial X}\frac{\partial\mathbf{H}^T}{\partial X} - 2XYh^2\left(\frac{\partial\mathbf{H}}{\partial X}\frac{\partial\mathbf{H}^T}{\partial Y}+\frac{\partial\mathbf{H}}{\partial Y}\frac{\partial\mathbf{H}^T}{\partial X}\right)\right.$$

$$\left. + (1+h^2X^2)\frac{\partial\mathbf{H}}{\partial Y}\frac{\partial\mathbf{H}^T}{\partial Y}\right\}dXdY$$

$$\mathbf{B}_k^e = \int\int_{\triangle_k}\frac{2\kappa^2}{h}\mathbf{H}\,\mathbf{H}^T\,dXdY,\quad \mathbf{C}_k^e = \int\int_{\triangle_k}\kappa\,\mathbf{H}\,\mathbf{H}^T\,dXdY \tag{6}$$

From eq. (6), we can derive the following the eigen equation to be numerically solved.

$$\mathbf{A}\boldsymbol{\Psi} = \mu\,\mathbf{B}\boldsymbol{\Psi} - \mu^2\mathbf{C}\boldsymbol{\Psi} \tag{7}$$

NUMERICAL RESULTS

We study $m=1$ Taylor's force-free states inside two types of shells : (a) circular cross-section helical shells, area π, displacement S from the origin, pitch h and (b) elliptic cross-section straight shells, area π, displacement zero, pitch h, eccentricity e.

Figure 1 shows the dependences of μ on the pitch h in the case of (a). As shown this figure, the helical pitch h which minimizes the value of μ decreases with an increase in the displacement S.

Figure 2 shows the dependences of μ on the eccentricity e in the case of (b). From Fig. 2, we can see that the helical pitch h which minimizes the value of μ increases as the shape of the cross-section comes to be circular. On the other hand, the value of minimum-μ does not monotoniously depend on e. This suggests that

the value of minimum-μ has its minimum at a certain e. To study this point, we calculate the minimum-μ values as a function of (h, e). The resultant contor lines of minimum-μ are illustrated in Fig. 3. The contor lines are approximately drawn using the values of μ at finite points (h, e) by the least squares method. From Fig. 3, we can see that those contor lines are elliptic and the value of minimum-μ has its minimum at (0.68, 1.10).

Figures 4, 5 show magnetic surfaces for $S=0.6$, $h=-1$, $e=0$, $\mu=3.38$ and $S=0$, $h=-1.1$, $e=0.68$, $\mu=3.0$, respectively.

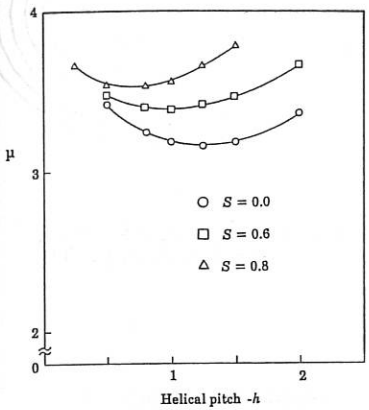

Fig. 1 Dependence of μ on the displacement

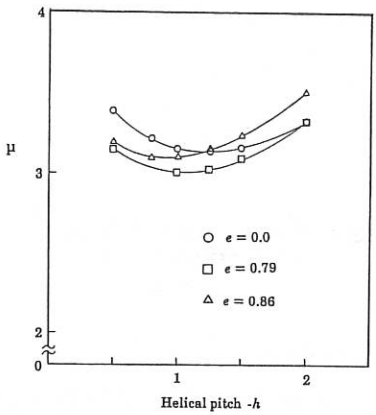

Fig. 2 Dependence of μ on the eccentricity

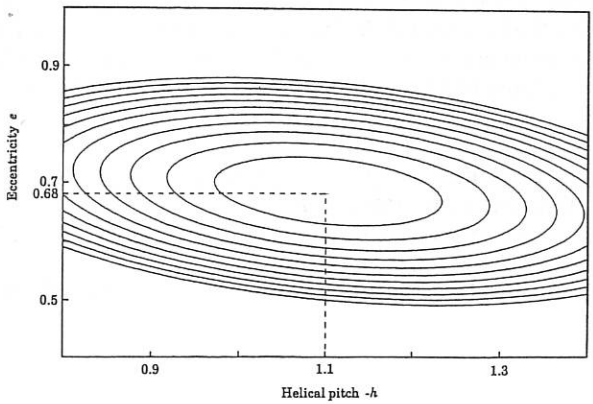

Fig.3 The minimum-μ values as a function of (h, e)

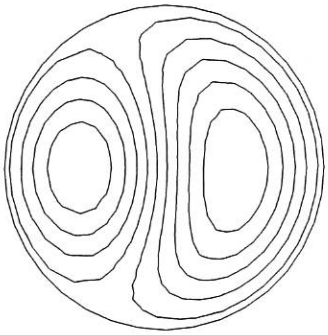

Fig. 4 Contor lines of Ψ : $S=0.6$, $h=-1$, $e=0$, $\mu=3.38$

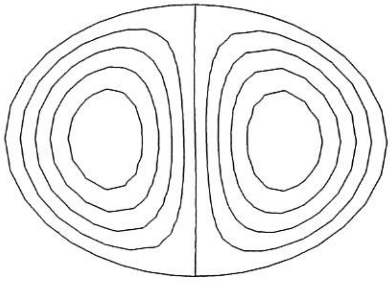

Fig. 5 Contor lines of Ψ : $S=0$, $h=-1.1$, $e=0.68$, $\mu=3.0$

CONCLUSIONS

Numerical results obtained in this report are summerized as follows :

(1) When plasmas are enclosed by helical shells with circular cross-section of displacement S from the origin, the helical pitch h which minimizes the value of μ decreases with an increase in the displacement S.

(2) When plasmas are enclosed by helical shells with elliptic cross-section of eccentricity e, the helical pitch h which minimizes the value of μ increases as the shape of the cross-section comes to be circular. In addition, the value of minimum-μ approximately has its minimum at $(e, h) \simeq (0.68, 1.10)$.

REFERECES

[1] Taylor, J. B., Phys. Rev. Lett. **33**, 1139, (1974).

[2] Grad, H., Phys. Fluids, **10**, 137, (1967).

[3] Chu, C., Schaffer, M. J., La Haye, R. J. and Ohkawa, T., IEEE Trans. Plasma Science, **PS-9**, No. 4, 187, (1981)

[4] Lewin, L., "Theory of Waveguides", Newnes-Butherworths, 96-101, (1975)

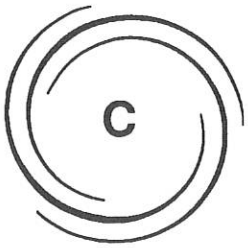

ALTERNATIVE MAGNETIC CONFINEMENT SCHEMES

C2 OTHER MAGNETIC CONFINEMENT SCHEMES

MHD STABILITY OF A PLASMA WITH ANISOTROPIC COMPONENT IN THE RIPPLED MAGNETIC FIELD

V.V.Arsenin
I.V.Kurchatov Institute of Atomic Energy, Moscow, USSR

Abstract. It is shown that there are straight rippled configurations in which a low-pressure plasma with anisotropic population is stable against the flute perturbations.

In a straight paraxial trap with the rippled magnetic field the plasma with isotropic pressure is unstable against the flute perturbations /1/. The addition of an anisotropic component with $p_\perp > p_\parallel$ aggravates the instability within a paraxial geometry, since this component is trapped within the zones with reduced field, where the field line curvature is unfavorable. However, at a nonparaxial ripple, when the field variation length is comparable with a distance to the axis, the stability situation can be changed. Below one can see that 1) there are axisymmetric rippled configurations in which the local field attenuations (local traps for anisotropic populations) along the field lines passing at the radial periphery have place not in the convex parts only but in the concave ones too (due to the fact that the extreme periphery field lines are drawn off from the axis, Fig.1); 2) the ratio of the curvature on the inner (facing the axis) side of these traps to that on the outer one can be such that the plasma stability with $\beta \ll 1$ according to the principle of an average minimum-B is reached at the suitable pressure ratio of anisotropic populations inhabiting them. One should emphasize the fact that the MHD-stabilization is meant: azimuthal magnetic drift frequency, ω_d, is much lower than that of the flute motion, ω (in difference from systems of the bumpy torus type, where $\omega_d \gg |\omega|$ in the stabilizing rings).

Let us consider a periodic system (Fig.1), for certainty. Let us assume, for simplicity, that B has the symmetry planes z=Ø and z=L. Let us designate the quantities related to the circular traps of anisotropic plasma with the indices 1,2; let us refer the index 3 to the isotropic component. Now let us find the conditions under which the contribution of an anisotropic component, $W_1 + W_2$, into the potential energy (per one period 2L) of flute perturbation, W, is positive. As for an isotropic component, it plays the role of a linking plasma providing the equalizing the perturbation of a potential φ along the field line. The pressure p_3 is constrained from above by the stability condition $|W_3| < W_1 + W_2$.

Let us limit ourselves by the case $p_\perp \gg p_\parallel$ when the populations 1,2 are concentrated nearby the field minima along the field lines. In this case /2,3/

$$W_{1,2} = - C\int \left(\frac{\partial B}{\partial \bar{\psi}} \right)_{1,2} \frac{dP_{1,2}}{d\bar{\psi}} |\varphi(\psi)|^2 \, d\psi, \qquad (1)$$

where C is a positive constant, ψ is the flux coordinate, $P_{1,2} = \int (p_{1,2}/B^2) ds$, ds is the field line length element.

Let $P_{1,2}(\psi)$ have maxima at $\psi = \psi_\varnothing$ and monotonously decay to the boundaries of the layer occupied by anisotropic plasma, $\Delta\psi$ (Fig.2). Taking account of the fact that $\partial B/\partial\psi = (\partial B/\partial\psi)_{\psi=\psi_\varnothing} + (\partial^2 B/\partial\psi^2)_{\psi=\psi_\varnothing} (\psi - \psi_\varnothing) + \ldots$ and $(\psi - \psi_\varnothing) dP_{1,2}/d\psi \leq \varnothing$, one find that for a positive sign of $W_1 + W_2$ it is sufficient to have

$$P_1 (\partial B/\partial\psi)_{1\ \psi=\psi_\varnothing} + P_2 (\partial B/\partial\psi)_{2\ \psi=\psi_\varnothing} = \varnothing \qquad (2)$$

(with an accuracy better than $(|æ|r + 1)\Delta\psi/Br^2$, where $æ = r\partial B/\partial\psi$ is the field line curvature) , and in both traps (nearby the planes z =Ø and z=L)

$$\frac{\partial^2 B}{\partial \psi^2}\Big|_{\psi=\psi_\varnothing} > \varnothing. \qquad (3)$$

This inequality can be rewritten in the form

$$\frac{\partial^2 B}{\partial r^2} > \frac{1}{B}\left(\frac{\partial B}{\partial r}\right)^2 + \frac{1}{r}\frac{\partial B}{\partial r} . \qquad (4)$$

The requirement of existence of the field minima along the field line on the planes z = Ø,L is reduced /3,4/ to the condition at this line

$$\frac{\partial^2 B}{\partial r^2} < \frac{2}{B}\left(\frac{\partial B}{\partial r}\right)^2 - \frac{1}{r}\frac{\partial B}{\partial r} \qquad (5)$$

at z =Ø,L.

Since $\partial B/\partial\psi$ has different signs in the traps 1,2, the equality (2) is satisfied at the suitable ratio P_1/P_2. Let us show that there are configurations $B = \nabla\Phi = \nabla(B_Ø z + \sum_{n>Ø}(nk)^{-1}B_n \cdot I_Ø(nkr)\cdot\sin(nkz))$, $k = \pi/L$, produced by an external winding, for which the conditions (4),(5) (at z =Ø,L) are satisfied on the surface $\psi = \psi_Ø$ and in its vicinity (of course, at z =Ø there is a field minimum along the field line not at any ψ). Let us limit ourselves by the case $B_n/B_Ø \lesssim \varepsilon \ll 1$. For representation brevity, let us assume that $r \gg (\varepsilon k)^{-1}$, so that $|æ|r \gg 1$. This corresponds to the transition to the plane geometry, replacing the radial variable by the rectangular x, and $I_Ø$ by exp(nkx); the terms with 1/r in (4) being small. Let us count off x from the surface position $\psi = \psi_Ø$ at z = Ø and introduce the dimensionless coordinates X = πx/L and Z = πz/L. It is easy to see that the conditions (4),(5) are satisfied, e.g., for the field including three harmonics

$$\Phi = B_Ø\Big[Z + \Big(\frac{3}{2}\varepsilon - \Big(\frac{9}{4} - \alpha\Big)\varepsilon^2\Big) e^X \sin Z + \frac{1}{16}\Big(3 - 2\alpha\Big)\varepsilon^2 e^{2X}\sin 2Z - \frac{1}{18}\Big(\varepsilon - \frac{3}{2}\varepsilon^2\Big) e^{3X}\sin 3Z \Big]. \qquad (6)$$

Here $\alpha = \varepsilon^{-2}(\partial^3 B/\partial X^3)_{X=Ø,\,Z=\pi}\cdot\xi$; the quantities ξ, field line position at $\psi = \psi_Ø$, $Z = \pi$, and $\partial^3 B/\partial X^3$ are taken at the lowest ε-order ($\xi = \frac{26}{9}\varepsilon$, $(\partial^3 B/\partial X^3)_{X=Ø,\,Z=\pi} = 3\varepsilon$). Indeed, for this field

$$(\partial B/\partial X)_{X=\emptyset,\,Z=\emptyset} = \varepsilon + O(\varepsilon^2), \quad (\partial B/\partial X)_{X=\xi,\,Z=\pi} = -\varepsilon + \dots ,$$

$$(\partial^2 B/\partial X^2)_{X=\emptyset,\,Z=\emptyset} = \frac{3}{2}\,\varepsilon^2 + \dots , \quad (\partial^2 B/\partial X^2)_{X=\xi,\,Z=\pi} = \frac{3}{2}\,\varepsilon^2 + \dots$$

The MHD stabilization in the presence of the anisotropic plasma concentrated in the rippled layer can occur in the case, when there is an additional field line curvature not related with the ripple ,e.g., in a long closed system, too.

References

1. Rosenbluth M.N., Longmire C.L. Ann. Phys., 1957,1,12Ø.
2. Arsenin V.V. Pis´ma JETPh, 1986,43,27Ø.
3. Ryutov D.D., Stupakov G.V. Fizika plasmy, 1986,12,1411.
4. Arsenin V.V. Intern. Conf. on Plasma Phys.1984 (Lausanne). Contrib. papers, v.1,p.2Ø6.

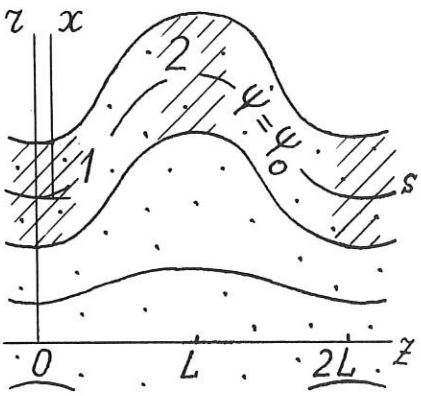

Fig. 1

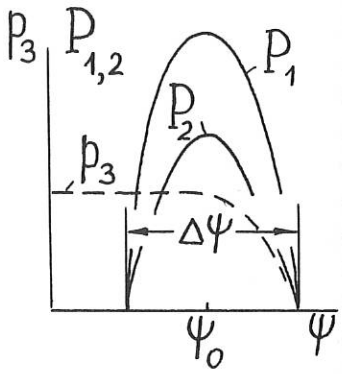

Fig.2

Fig.1. Element of a periodic system. Dots are an isotropic plasma, shadowed areas are filled with an anisotropic component

Fig.2. Pressure profiles

HOT ELECTRON PLASMAS INSTABILITIES IN OPEN TRAPS OGRA-4 AND OGRA-4K.

BELAVIN M.I., ZHIL'TSOV V.A. AND SKOVORODA A.A.
I.V.KURCHATOV INSTITUTE OF ATOMIC ENERGY, MOSCOW, USSR.

ABSTRACT An experimental study of the instabilities in ECR heated mirror (cusp and baseball) plasma is presented.

Experiments were performed in two open traps of different magnetic field geometries. OGRA-4 is a baseball type trap [1], OGRA-4K is the axially-symmetric single cusp [2]. Hydrogen ECRH hot-electron plasma (β=3-10%) in both installations have shown many common features not only in the parameters but in instabilities too. However, there is an essential difference.

As a rule, fluctuating signals from various diagnostics on both facilities are regularly observed.

Typical OGRA-4 data are presented in Fig.1 (electron flux, unintegrated diamagnetic signal, H_α)The data on cusp are similar. The pulsed or burst-type structure of oscillations [5] is clearly seen. SHF plasma radiation are observed as a bursts, correlating with the enhancement of the longitudinal warm electrons flow, bursts of X-ray radiation and low-frequency oscillations in other signals. The frequency of SHF oscillations is lower then the gyrotron frequency,. (ECR-fundamental frequency). These results, identical to the observation [3-5] on the other facilities, confirm the development of the electromagnetic anisotropic electron cyclotron instability (EAECI).

This instability doesn't result in an essential effect on the plasma parameters. The superhot electron (100 keV) stability perhaps is related with the relativistic effects on the EAECI [3,6].

As for difference of the baseball plasma we observe global instability in the cusp, which can limit plasma pressure.

Fig.2 show typical data from cusp plasma during the global instability (disruptions),when a high-power burst of X-ray and microwave radiation is observed, (nl - line density, H_α -

intensity of H_α radiation, D - diamagnetic signal, J_i - ion current along the magnetic field).

Features of disruptions. 1.the disruptions occur simultaneously in both semi-cusps. But the hot electron populations in semi-cusps are noticeably separated in space (by 3-6 cm) so that the introduction of a movable probe between them only slightly changes the plasma parameters. The rings of hot electrons do not have a common magnetic flux that excludes the natural perturbation transfer along the magnetic field lines. At the time of disruption a change in the ratio of signals from the diamagnetic coils located along the field lines takes place. This confirms the existence of a change in the spatial plasma distribution under disruption.

2.The disruptions may be suppressed or shifted towards the gyrotron pulse end by a small increase in the gas influx (Fig.3).

3.The disruption may be observed at the quit stage of decay (in some msec after the end of gyrotron pulse).

4.During the disruption high energy ions (>300 eV) is observed in the plasma fluxes during the disruption.

Two horns oriented in parallel to the cusp axis, so that the line connecting them cross both hot electron rings is used to measure transparency η for diagnostic microwave ray (f=41 GHz). The results are shown in Fig. 4. One can see that an enhanced passage occurs before the disruption and a maximal absorption is observed after the disruption.

Similar disruption in a diamagnetic signal were observed in numerous experiments with a hot electron plasma.

For example such phenomenon was observed in a simple mirror [5] and was explained on the basis of an electrostatic anisotropic electron-cyclotron instability.

In bumpy-torus [7] that was explained as a MHD-instability in the rings of hot electrons with a warm plasma. Disruptions were observed in the end quadruple plugs in tandem trap TMX-U [4] and were explained on the basis of a

relativistic upper hybrid loss cone instability.

As seen, this phenomenon was ambiguously explained. We also haven't come to an adequate explanation but have managed (as we hope) to limit the choice by two opportunities.

The first one is related with the development of an absolute EAECI [6]. The arguments in favor of this explanation are as follows, as shown above, we always observe the EAECI in a convective form (wave amplitude increases in the process of propagation along the field line). The boundary of a transition to the absolute instability depends on the cool plasma component density which is changed by gas puffing [6]. This can explain the observed stabilization and the simultaneous disruptions in both semi cusps(cusps are connected by means of a cool plasma through a non-adiabatic zone).The experiments with the microwave probing (see Fig.4) show that the plasma absorption drops before disruption (anisotropy rises) and then, in spite of a reduction in density, it abruptly rises (anisotropy decreases).

The counter-argument. We do not observe disruptions in OGRA-4 (baseball) at the same plasma parameters. It is hard to explain the presence of disruptions at the stage of decay.

The second opportunity is related with the MHD-instability at the inner cusp boundary. Preliminary measurements show that the density of hot electrons have strong gradient from the cusp center.

The slab geometry approximation for one of bumpy torus trap with hot electrons in warm plasma [8] allowed us to obtain frequency of MHD-oscillation and threshold for cool plasma stabilization correlated with the experimental results. But the microwave burst during the disruption, the enhanced longitudinal plasma fluxes and the absorption of probing microwave signal are not explained by this way.

1.Belavin M.I., Zhil'tsov V.A., Kosarev P.M. et al. //Voprosi Atomnoi Nauki i Tekh. Ser. Termojad. Sintez. 1988, V.1.,p.51.
2.Belavin M.I., Golovin I.N., Zhil'tsov V.A. et al.in Pl. Phys. and Contr. Nucl. Fus. Res. (Proc.12th Int.Conf.Nice,1988) v.2. p.691 .
3.Garner R.C.//MIT Pl. Fus. Center report PFC/RR-86-23, 1986.
4.TMX - U final report // LLNL, UCID - 20981, 1988, p.696.
5.Alikaev V.V., Glagolev V.M., Morosov S.A. // Pl.Phys. 1968, v.10, p.753.
6.Gladd N.T. // Phys. Fl. 1983, v.26, p.974.
7.Hiroe S., Wilgen J.b., Baity F.W. et al. // Phys.Fl. 1984, v.27, p.1019.
8.El-Nadi // Phys.Fl. 1982, v.25, p.2019 .

Fig. 1.

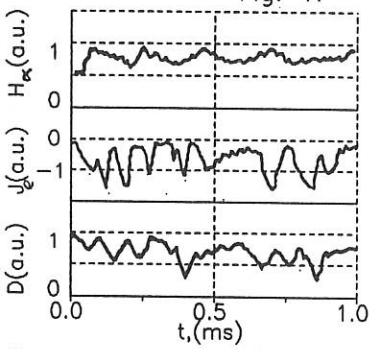

Fig. 2.

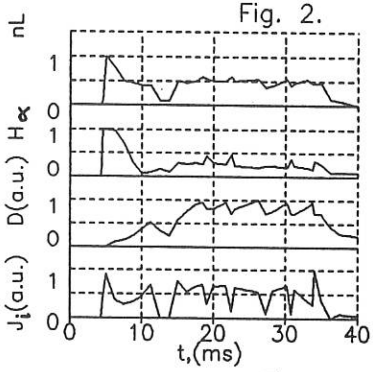

Fig.3.

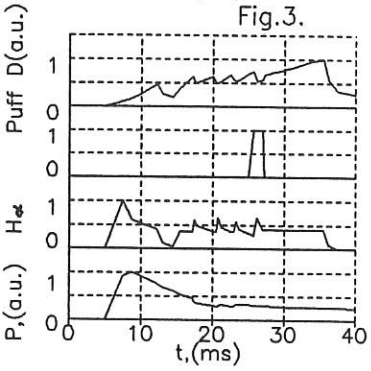

Fig. 4.

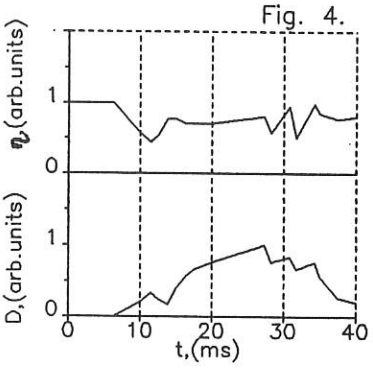

SELF ORGANIZATION OF WAVE COUPLING AT SK/CG-1 MACHINE AND CONCEPTUAL DESIGN OF SK/CG-2

S. Sinman and A. Sinman *

Plasma Engineering Laboratory, Electrical and Electronic Engineering Department, Middle East Technical University

* Nuclear Fusion Laboratory, Nuclear Research and Training Center, Turkish Atomic Energy Authority

Ankara - Turkey

INTRODUCTION

In magnetic confinement systems, the self organization process can generally be defined by the important mechanism which develops the variation of controlled and programmable system parameters impressed by the principal plasma parameters.

The role of the self organization process may be seen in the examples such as the change of q profiles at high beta systems /1/; the sensitivity of magnetic Reynolds number S at RFP schemes /2/; the influence of F-θ field reversal ratio and pinch parameter /3/ and the tokamak formation in circular cross section from a cylindrical transverse plasma sheet in the DC helicity driven tokamak /4/.

Previously, at the SK/CG-1 device (World Survey of Activities in Controlled Fusion Research, 1986 Edition, IAEA Vienna, p. 197) by means of the C-Gun located directly inside the flux conserver, the non inductive helicity injection with high efficiency has been determined. Although the operating period of the C-gun is only a few microseconds depending on the used gas pressure in the range of 30-50 mTorr, in SK/CG-1 device the low frequency drift waves continuing up to 5-20 ms or more have been observed /5/.

This interesting result has caused to reexamine the drift wave mode in SK/CG-1 by the concept of helicity transfer from the wave to plasma including the self organization process.

SK/CG-1 DEVICE

The C-gun is a noval and alternative version of conventional magnetically driven plasma gun. The vertical two electrodes at the toroidal plane of flux conserver are the main structure of the C-gun.

The electrical charactristics of the gun conforms with the Critical Damping and Under Damping Modes (CDM and UDM) of operation depending upon the back ground gas pressure ranges of 40-70 mTorr and 75-250 mTorr respectively. The operating period of the C-gun at UDM is about 10-12 us. But at the CDM this is only 2-3 us. Without using crowbaring technique, the operational regime of this gun can be transformed from UDM scheme into CDM. For this purpose, it has been sufficient only to be changed the

back ground gas pressure. The working voltage range of the C-gun is 10-15 KV and maximum operating loop current is 150 kA. The logaritmic decrement is about 0.58 at the UDM.

The vertical electrodes of the C-gun are in the plasma slab where it extends from the center of octagonally shaped flux conserver up to the vertical surface of conserver which is inductively coupled to the back strap. The cross section of this plasma slab is the poloidal frame of the C-gun. The boundaries of the poloidal frame is defined by the surfaces of flux conserver and the passive rod located across the top and bottom walls of conserver at the center. Thus the poloidal frame is a closed loop. On the construction of flux conserver there exist two symmetrical poloidal frames at an angular distance of 180 degrees.

The main diagnostic techniques used are: the Langmuir and the floating surface electrical probes; the magnetic probes and the paramagnetic loops including the L-R fast operational integrators; the charge exchange cell and lastly the visible light and high frequency spectrum analyzers. In addition, for data recording and processing the fast analog and digital storage oscilloscopes have been used.

Due to the inductive coupling between the back strap and the vertical surface of conserver and the eddy currents on it during the operational phase of the C-gun, the conserver becomes active. By the calculations using data measured, the following typical results have been obtained. The minimum energy storage time is 288 ns; The characteristic impedance is 106 Ohms; The LC time constant is 2.12 ns (471 MHz); The storage energy is 23.4 Joule for a gun current of 150 KA; The L/R time constant of conserver with decaying flux density is 28-30 ms for I/e.

By the experiments made using a practical network model of flux conserver, it has been understood that the eddy currents on the conserver can produce a multi pole toroidal cusped type of magnetic field which affects to the plasma directly.

OPERATIONAL PROCEDURE

Taking into account the electrical characteristics of C-gun, it has been understood that the discharge starts between vertical electrodes by the critical damping mode and after 0.35 us, the discharge goes on with the gun current through upper electrode and the wall changing its direction. Here, a process similar to the crowbaring occurs and the poloidal frame generates a toroidal field lasting 28-30 ms depending on the L/R time constant of flux conserver. The current on the external circuit of the gun at the on-set phase, transforms into closed loop current and so the gun current fed by capacitor bank circuit suddenly breaks. At this moment between the gun electrodes the potenial differences up to 70 KV comes into existance and it decays exponantially in 2 us down to 12 KV. Consequently, depending upon the discharging time constant of the capacitor bank circuit of 500 ms, the C-gun is impressed under this potential difference passively and quasi steadily.

INSTABILITIES AND WAVE COUPLING

Specifically, the drift wave generation and its coupling phases in poloidal frame has not been possible to observe experimentally by above mentioned diagnostic techniques. But nevertheless the scenario at on-set phase has indirectly been observed. In fact, by means of the time evaluation of the data obtained from the electrical and magnetic probes placed at the angular distances of 135 and 45 degrees from the C-gun and the correlation of electrical characteristics of the gun, all of the mechanisms such as the drift wave generation, instability and coupling have separately been explained.

In the first 500 ns, C-gun operating at CDM, generates the ion cyclotron waves having 30 MW pulse power in the frequency range of 10-15 MHz and it damps in 1-2 us. The hot electrons at that of plasma belt produced by the gun, interacting with toroidal magnetic field, the beam plasma instabilities are generated. In this content, ion cyclotron and ion accoustic waves and electron pressure gradient along azimuthal direction come into existance. At the end of the resonance of low frequency drift wave with ion acoustic wave and the dissipation of back ground plasma in the conserver, the drift wave instabilities start and the density gradient decreases.

CONCEPTUAL DESIGN OF SK/CG-2

The SK/CG-2 machine is a new developed version of the SK/CG-1 and instead of only one C-gun two identical C guns located inside the flux conserver with an angular distance of 180 degree facing each other are used.

The aim of this study is to determine and optimize the helicity injection condition and Taylor's minimum energy state at that of spheromak scheme of the SK/CG-2. For this purpose, for the SK/CG-2 a special numerical scheme has been developed.

In general, taking into account the electrical characteristics of two C guns and the b/a form factor of eliptical plasma, some computational experiments have been carried out.

In conculusion, in accordance with the minimum energy state and the helicity injection rate; the increase of the energy confinement time, the variations of volume avaraged beta and safety factors indicated by q(0), q(r), q(a) and q(1), the range of Troyon Gruber constants and other standart plasma parameters such as density and temperature have been determined.

CONCLUSIONS

The analysis and correlation of electric and magnetic probe signals have shown that the instabilities are in hybrid character. The recombination time corresponding to the pressure range of 30-50 mTorr is almost 607 us. Whereas at the same range, the duration of ion acoustic waves are about 5-20 ms. Thus, it has exactly been understood that this mechanism is not an afterglow.

The sustainment phenomenon is independent of the recombination of three body collision scheme. The sustainment period can be controlled and it has been found as 100-150 ms for the optimum conditions. The equibrium condition is depend upon the quasi steady state self organizing wave coupling.

The time and frequency domain analysis of ion acoustic wave oscillograms have shown that the electron temperatures of 25-30 eV at that of the beginning are about 2-5 eV near the damping case.This characteristic result is not varying in the sustainment period of 5-25 ms. It has been observed that the sustainment period depends on the onset gas pressure and the electric field strength in poloidal frame. An average electron density of about 10^14 cm-3 has been found. The maximum diffusion rate is limited by the initial electron density and the critical value of toroidal magnetic flux density in time at poloidal frame.

SK/CG-2 device has been scaled by using the experimental data obtained from SK/CG-1. The capacitance of the capacitor bank of two symmetrical C guns being 10 uF and changing the charge voltage in the range of 10-15 kV, it has been seen that the Taylor's minimum energy state can realize in SK/CG-2. Here, gas pressure has been accepted to be in the range of 100-200 mTorr. Besides, in this version too, mode conversion is possible. For instance, in spherical torus scheme of SK/CG-2, they have been found the following computational results of design parameters: The maximum electron density is 5x10^15 cm-3; the average electron temperature is 40-60 eV depending on the pressure; the volume averaged beta is approximately 12-15 % ; the form factor of elliptical plasma is 1.24; the safety factor q(o) is 0.6; the Troyon-Gruber constant is 3.2 and the energy confinement time is 400-600 us.

ACKNOWLEDGEMENT

This work was performed under a co-operative agreement between the Turkish Atomic Energy Authority and the International Atomic Energy Agency, Vienna, Contract No.: 3823/R4/RB.

REFERENCES

/1/ KIYAMA,H., et al., in Proc. 12th Int. Conf. Nice, 1988,IAEA, CN-50, Vienna, Vol.I (1989) 437.
/2/ SATO,K., et al., in Proc. 11th Int. Conf. Kyoto, 1986, IAEA, CN-47, Vienna, Vol.II (1987) 413.
/3/ YAMADA,S., et al., Nucl. Fusion 29 (1989) 316.
/4/ ONO,M., et al., in Proc. 12th Int. Conf. Nice, 1988, IAEA, CN-50, Vienna, Vol.III (1989) 479.
/5/ SINMAN,A., SINMAN,S.,in Proc. Tech. Comm. Meeting on Research Using Small Tokamaks, Nice, 1988, IAEA-TECDOC-519 (1989) 185.

FRC: TC-I MACHINE RESULTS

M. Machida[1], R.Y. Honda[2], E.A. Aramaki[3], P. Porto, L. Berni

[1]Instituto de Física, Universidade de Campinas, SP, Brazil
[1]Instituto de Física, Universidade de São Paulo, SP, Brazil
[2]Instituto de Física, Universidade Federal Fluminense, RJ, Brazil
[3]Faculdade de Engenharia Guaratinguetá, SP, Brazil

Field reversed configuration TC-I device is 16 cm diameter, 1 meter long with two mirror coils and 30 kJ field reversed theta pinch working for over two years at University of Campinas. Its implosion dynamics and field reversal parameters have been studied using flux excluded loops, internal magnetic probe, visible spectroscopy, photodiode array and image converter camera. The vacuum vessel is a pyrex tube of 14,5 cm diameter pumped with a liquid nitrogen cooled diffusion pump to a base pressure of 6×10^{-7} Torr. The schematic view of the machine and experimental set up are shown in fig. 1.

As first step, the implosion phase of the FRC formation was studied by the analysis of light emission and electromagnetic probe signals. In the fig. 2 we show the influence of the internal probe for separatrix radius measurements. In the case of absence of internal probe the pinch effect is faster and is more stable towards the end of implosion phase. The influence of the probe seems to start at about 2 μsec after the main bank discharge start. The internal probe influence can also be seen by end-on framing image converter camera in the fig. 3 where the light emission region is stronger and broadened for the presence of internal magnetic probe. The internal magnetic probe has been inserted in order to check the field reversal existency where after it's confirmation it has been taken out for furhter studies.

While the best pressure operation for He gas was determined to be 10 m Torr with ion temperature reaching 70 eV as been reported previously[1], for the hidrogen the best pressure operation is 3mTorr and the ion temperature was measured by taking the Doppler broadening of Hα and CII line giving 28.3 eV: (fig. 4). This lower temperature is due to the cold border plasma emission.

The three photodiode set up for plasma rotation measurements did not show any onset of n=2 instability during the implosion phase and also the change of rise time from 4.5 μsec to 3.8 μsec did not give appreciable modification on the plasma parameters.

An interesting result which we observe is the appearence of cusp type plasma during the formation phase[2] when a strong bias field of 0.25 B_T is applied, as can be seen on fig. 5. Further analysis of this plasma shape which we get without use of any auxiliary coil system is under work at this time.

Another result which we get is the appearence of halo plasma, where near the end of first implosion a second layer of plasma appears forming a halo shape plasma which can be seen on fig. 6. This effect can also be observed in magnetic field mapping by internal probe measurements which presents two magnetic field peaks, at r=1.5 cm and r=4.0 cm.

REFERENCES

[1] E.A. Aramaki et al, Nuclear Inst. and Methods in Phys. Res. A280, 597 (1989).

[2] D.S. Harned, Phys. Fluids 26, 1320 (1983).

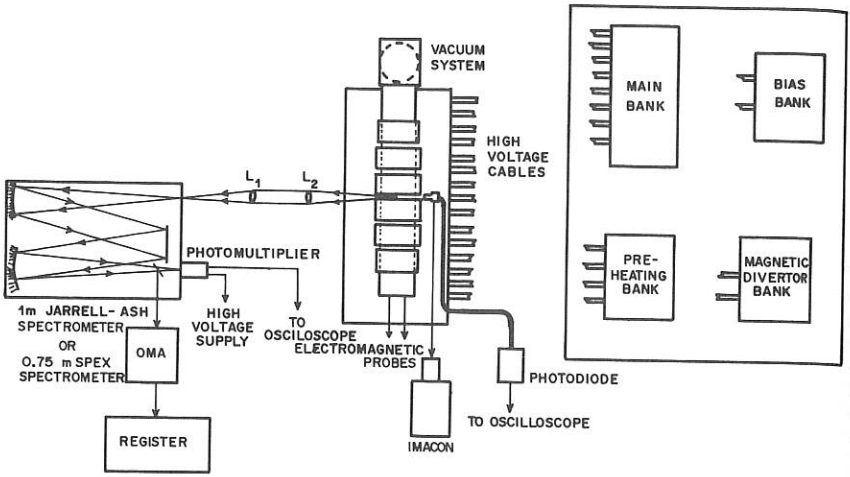

Fig. 1 - Schematic view of TC-I FRC device.

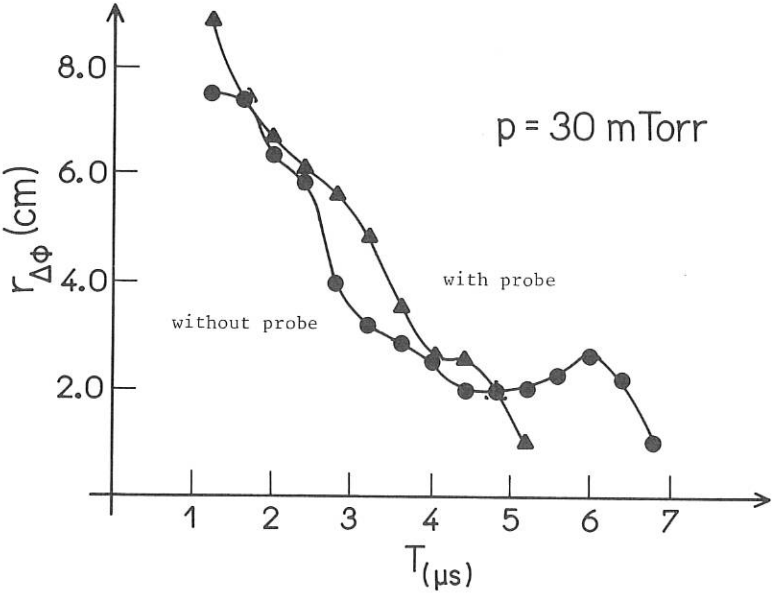

Fig. 2 - Flux excluded signals with and without internal magnetic probe.

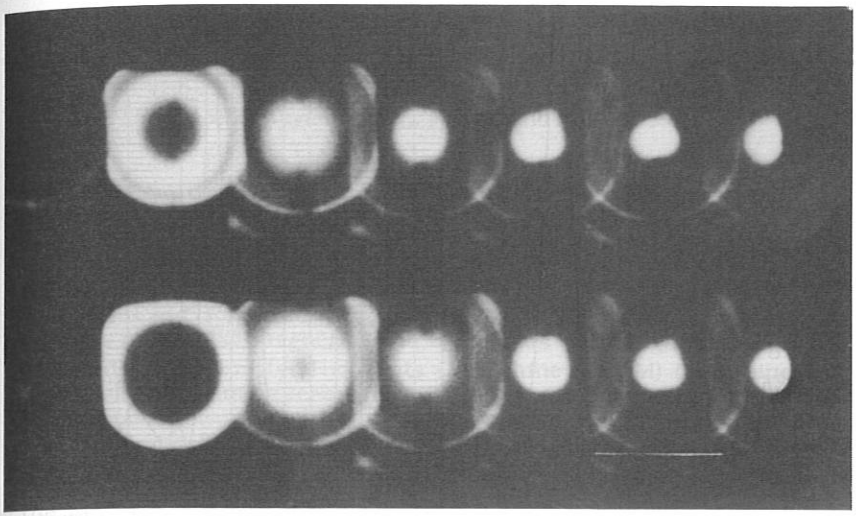

Fig. 3a - End on framing picture, with internal probe case, start from bottom to up and left to right with Δt of 0.5 μs for each frame.

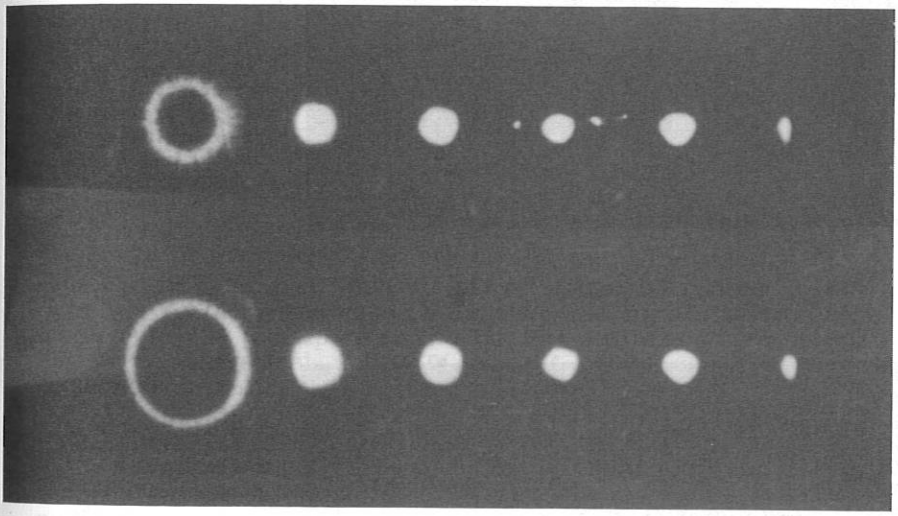

Fig. 3b - End on framing picture, without internal probe. Same speed as above.

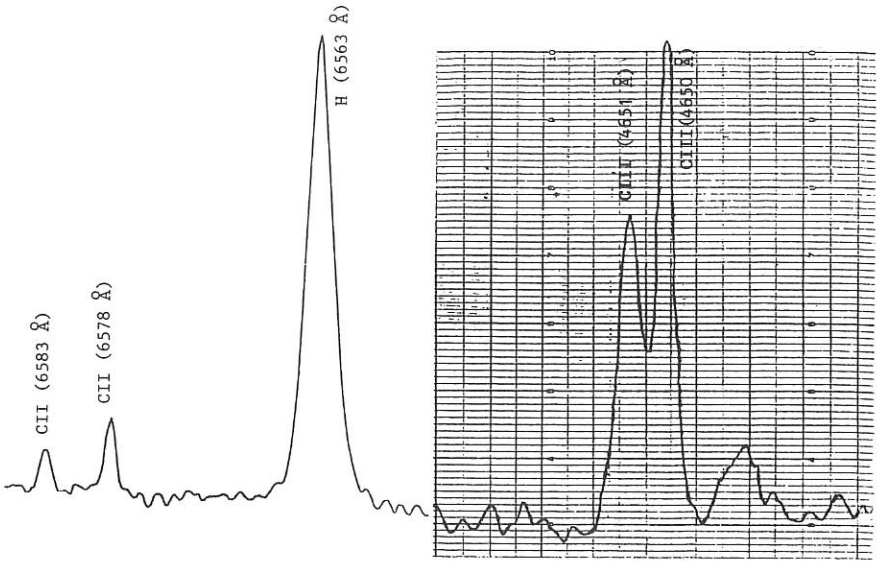

Fig. 4 - Doppler broadening of Hα (6563Å), CII (6578 Å), CII (6583 Å) and CIII duplet (4651 and 4650 Å).

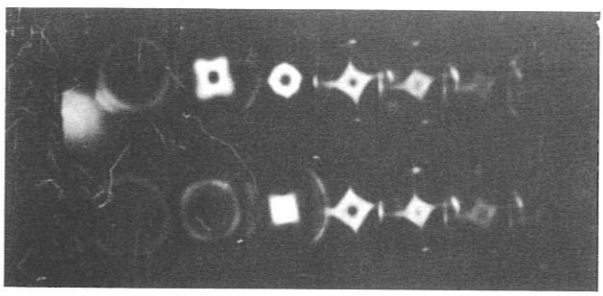

Fig. 5.

High mode n=4 formation obtained by high bias and fill pressure of hydrogen plasma (same time internal as fig.3)

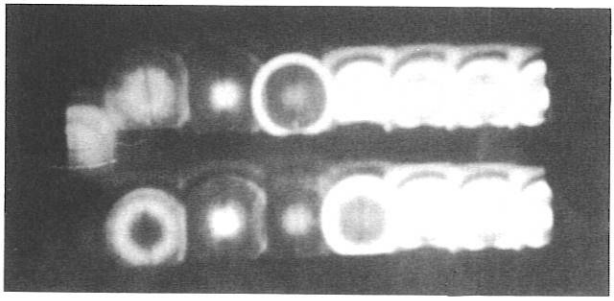

Fig. 6.

Halo plasma type plasma obtained in the helium and hydrogen gas. The picture is for the hydrogen gas case. (same time internal figure 3).

STUDY OF AN FRC WITH n=1 EXTERNAL PERTURBATIONS†

M.E. Kayama*, B.A. Nelson and F.L. Ribe

University of Washington, Seattle WA, USA

Introduction

The Field Reversed Configuration (FRC) is a Compact Toroid without a toroidal magnetic field. Plasmas with high beta can be obtained in the 3-meter High Beta Q Machine (HBQM) theta pinch[1] using relatively simple techniques. Two macroscopic instability modes have been shown to be highly dangerous to FRCs: the rotational instability and the internal tilt mode. These modes are described by the Lagrangian displacement $\xi = \xi_0 \exp[i(\omega t - n\theta)]$, where $\omega_r = \mathrm{Re}(\omega)$ is the modal frequency, $d\theta/dt = \omega_r/n$ is the rotational frequency of the plasma and $\gamma = \mathrm{Im}(\omega)$ is the growth rate of the instability. The rotational mode n=2 is observed in many machines and is presently suppressed by poloidal multipole fields. However, the predicted n=1 (m=1) internal tilt mode has not yet been observed. The growth rate of this mode is given by:

$$\gamma_{tilt} \approx v_A/l_s$$

where v_A is the Alfvén speed and l_s the separatrix half length. This growth rate is very rapid, but FRCs have exhibited configuration lifetimes of 30-50 times the MHD growth time. This discrepancy is attributed to finite-orbit, kinetic effects.[2] The objective of this experiment is to study this mode in an FRC when its equilibrium is perturbed by external n=1 coils.

Experiment

The experiment was performed on the HBQM with an FRC having the length of the compression coil (l=180 cm). The external n=1 coils (torque coils, $B_z \propto \sin\theta$) are placed at the end regions;[3] the ratio between the perturbing axial magnetic field and the equilibrium magnetic field at the separatrix is 0.18. The perturbation is a single half-period sinusoidal pulse ($T_{1/2}$ = 3.4 μsec). The maximum equilibrium magnetic field is 3.2 kG.

The FRC is formed in 4 μsec, with low radial compression. A large transient toroidal field attributed to the Hall effect is observed at the end region during this phase.[4] The excluded flux radius is 6.5 cm. The electron density of the hydrogen plasma at the null point is $n_e \cong 0.7 \times 10^{15}$ cm^{-3}. The temperature is $\langle T_i + T_e \rangle \cong 315$ eV (from pressure balance). The predicted real tilt period is 50 μsec.[2]

Results and Discussion

The magnetic field was measured by small internal magnetic probes in a quartz jacket (o.d. 0.54 cm). Figure 1 shows the local magnetic field at r=2.6 and 5.8 cm at the n=1 coil position. The magnetic field bump observed at r=5.8 cm is due to the n=1 coil perturbation. The inner probe, at r=2.6 cm, shows a fast rise of the local magnetic field relative to the external axial field when the torque coil is applied. This indicates the plasma moving away from the torque coil, where the magnetic pressure is raised by the perturbing coil.

The diagnostics were extended to non-perturbing methods: Axial dual-beam and radial IR laser quadrature interferometry were applied for integrated electron line density measurement. The axial beams were at the same radial position and 90 degrees apart in the r-θ plane. Measurements were made at different radii and also close to the axis with a beam tilted relative to the main axis. Figure 2 shows a typical density waveform at r=1.0 cm. The small differences between the signals are within the fluctuations of the discharges. This axial measurement shows a high density in the open field line region (Fig. 3). Also, an axisymmetric equilibrium is observed. The radial interferometer was operated close to the tilt coil at z=71.0 cm (10.3 cm from the n=1 coil, where z=0 is the midplane). The radially integrated density was measured crossing the main axis and off-axis. Figure 4 shows a typical signal on the axis. The small difference in the signals is within the fluctuations of the discharges, even when the perturbation pulse is applied at different times. No violent disruption of the FRC is observed.

Conclusion

An FRC, formed without axial contraction, is perturbed by external n=1 coils. Extensive measurements were made with axial and cross-tube interferometers and small internal magnetic probes. A high electron density in the open field line region is observed. Magnetic field measurements indicate an axial shift of the configuration. Radial interferometry at the end region could not show this effect (inside the separatrix) because of the almost flat density profile throughout the discharge tube. No disruption of the FRC associated with the perturbation is observed.

[1] E. Sevillano and F.L. Ribe, Physics of Fluids **28**:3142 (1985).
[2] D.C. Barnes, J.L. Scharzmeier, H.R. Lewis, and C.E. Seyler, Physics of Fluids **29**:3379 (1986); D.C. Barnes, private communication.
[3] M.E. Kayama, B.A. Nelson, F.L. Ribe and D.C. Barnes, Proceedings of the Ninth U.S. Compact Toroid Symposium, 142 (l989).
[4] M.E. Kayama, B.A. Nelson, F.L. Ribe, and D.C. Barnes, Bulletin of the American Physical Society **34**(9):2053 (1989).

†Work supported by U.S. DOE.

*Universidade Estadual de Campinas, Brasil.

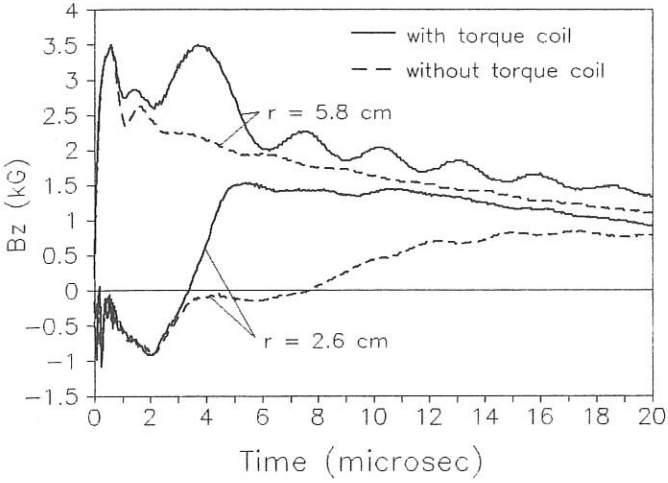

Fig. 1. Axial magnetic field at r=2.6 and 5.8 cm, with and without the torque coil (z=81.3 cm).

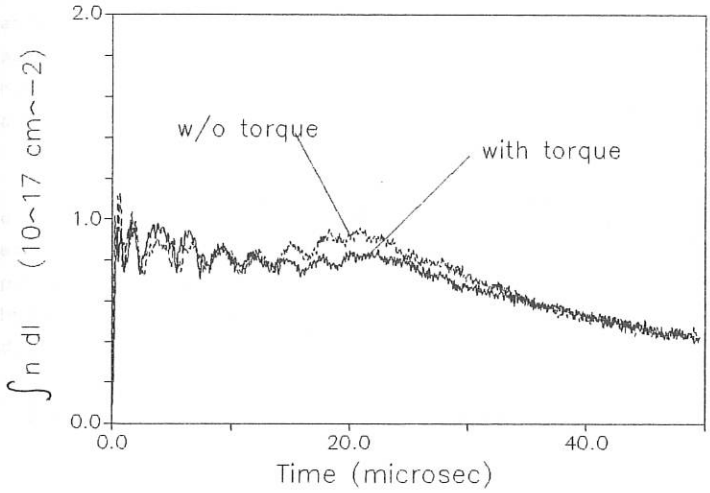

Fig. 2. Axially integrated electron line density at r=1.0 cm with and without the torque coils.

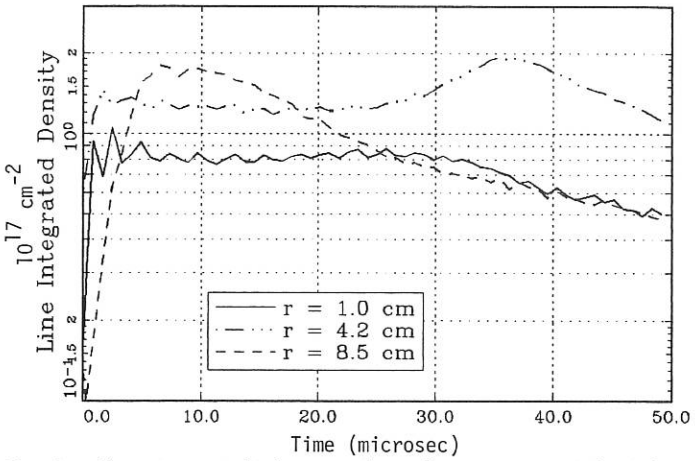

Fig. 3. Axially integrated electron line density at r=1.0, 4.2, and 8.5 cm.

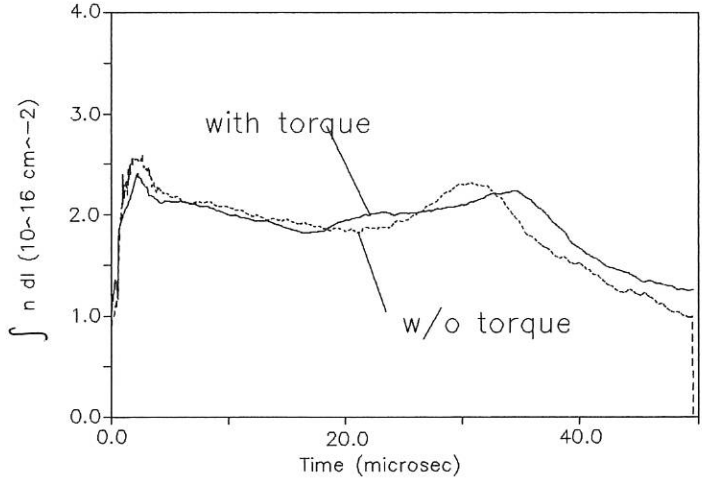

Fig. 4. Radially integrated electron line density with and without the torque coils (z=71.0 cm).

Optimization of Pulse Plasma Production in Z-pinch Systems

Rudakov L.I., Bogolyubskii S.L., Dan'ko S.A., Gordeev E.M., Kalinin Yu.G., Korolev V.D., Kuksov P.V., Lukin A.A., Smirnova E.A., Shashkov A.Yu.

I.V.Kurchatov Institute of Atomic Energy,
123182, Moscow, USSR

The possibility of the production of hot dense plasma which is obtained due to its compression by plasma shell stabilized by axial magnetic field is investigated in the paper. In the experiments being held on "Module-A-5" installation the cylindrical shell with the mass ~10^{-4} g/cm and the radius 1.5-2 cm is accelerated by the magnetic pressure of the current 2-3 MA. In previous experiments the high Z gas shell is imploded to the axis to convert the kinetic energy into line radiation. As distinct from these experiments we form and accelerate low Z gas shells with a goal to realize the shell kinetic energy in the heat of compressed plasma. However the heat maintenance of plasma magnetized by B_z is restricted by the longitudinal heat conductivity. Thus the plasma will be heated and energy will be realized in the form of radiation.

The instability of the thin shell leads to the disruption of current shell as well as to the current penetration towards the axis and results in bad plasma compression conditions. Freezed B_z field in the shell prevents its break. Some experimental results concerning the realization of the suggested scheme as well as the ways of the dense hot plasma and pulse radiation production will be introduced in the paper.

EXTRAP L-1 EXPERIMENTAL STABILITY

P. Brunsell, G. Hellblom, P. Karlsson, S. Mazur, P. Nordlund and J. Scheffel

Plasma Physics and Fusion Research
Royal Institute of Technology, S-100 44 Stockholm, Sweden

Introduction

In the Extrap scheme a Z-pinch is stabilized by imposing a strongly inhomogeneous octupole magnetic field. This field is generated by four conductor rods, each carrying equal currents I_v antiparallel to the plasma current I_p itself. The cross-section geometry is given in Fig.1. Theoretically, interchange stability is improved by the magnetic field, as well as long-wavelength kinks due to induced currents in the plasma and in the rods. Short wavelength kinks are, as in the 1-D pinch, stabilized by FLR and viscous-resistive effects.

We have performed a set of experiments in the linear Extrap L-1 device (length 40 cm, plasma radius a 2 cm, rod distance 3 cm) in order to determine optimal performance in terms of confined current (5-20 kA) and stability during the discharge length (80 μs; of the order 100 Alfven times). In this paper we summarize our results from two types of experiments; with and without external axial magnetic field. The results are compared with theory in the final paragraph.

Extrap mode; no B_z

Without octupole field the pinch is strongly unstable, as measured from flux loops and Rogowski coils. In Fig.2 we show measurements of the fluctuation level of the induced axial magnetic field δB_z, as the octupole field has been varied. Measurements have been made at three different values of plasma current. δB_z has been normalized to I_{inner}, the current that flows inside a Rogowski coil situated just inside the octupole rods. The graph clearly indicates that a weak octupole field ($I_v < I_p$) causes strong fluctuations.

For given I_p we find an optimum ratio $I_v/I_p \approx 1$ away from which part of the plasma current is carried outside the octupole rods, see Fig.3. Here the current I_{loss}, flowing outside a Rogowski coil with radius 19.5 mm, is measured. I_v is varied for three different values of I_p. Clearly, for too small values of I_v/I_p, the octupole field is not sufficient for stability, and for too large values, the plasma radius is forced outside the limiting magnetic separatrix, as will be shown below.

It might be expected , that as long as I_v/I_p is kept of order unity, I_p could be continously increased. Experiments, however, surprisingly feature an upper limit for I_p of about 5kA. This maximum attainable I_p has been found to be insensitive to filling pressure in the interval 10-100 mTorr.

Since we expected the current limit to be related to the value of the pinch radius, we have devised a new method for measuring the latter. By simply tilting the Rogowski coil into succesively larger angles, we could measure the angle at which some plasma current passed outside of it. This angle corresponded to the estimated pinch radius. In Fig.4 a case where the pinch radius was well inside the separatrix is shown.

Extrap with applied axial magnetic field

With an applied B_z, larger currents could be stably confined. For sufficiently high B_z, I_p was only limited by the external circuit resistance (0.5 Ω) , thus having a linear

dependence on the applied discharge bank voltage. Defining the safety factor as $q = 4\pi^2 a^2 B_z/(\mu_0 L I_p)$, where L is the the discharge length, this operating regime was characterized by $q > 1/2$. Equivalently, the ratio of B_z to I_p had to exceed 0.015T/kA. For lower B_z or alternatively higher discharge bank voltages, giving initial current amplitudes corresponding to $q < 1/2$, part of the plasma current was quickly lost from the region inside the rods. The remaining current settled into lower, discrete levels. The discharges had the typical behaviour seen in ULQ experiments; the unstable setting up phase, the stepwise decay of the current and the stable current levels corresponding to q slightly larger than rational values.

For an intermediate range of discharge bank voltages giving $q \leq 1/2$, the plasma current settled, after the initial stage, into an apparently stable level, which lasted throughout the rest of the discharge. For a given bank voltage, the observed current levels had a linear dependence on axial magnetic field strength, corresponding roughly to $q = 1/2$. Evidently, the plasma produced naturally an equilibrium with q near, or slightly larger than, the rational value.

We have especially investigated the effect of the separatrix boundary on the stable current levels by gradually increasing the current in the octupole field conductors. No change in plasma current level was observed for conductor currents up to $I_v = 2I_p$, corresponding to a separatrix radius of about half the metal limiter radius. For higher octupole field, the plasma current dropped during the initial stage of the discharge to a lower level in a a similar manner as with weak B_z.

For high discharge bank voltages, giving initial current amplitudes corresponding to $q << 1/2$, we observed a stepwise decay of I_p into succesively lower levels, as shown in Fig.5. The current levels, which were dependent on the discharge bank voltage, correspond in the present shot to $q = 1/2$ and $q = 2/3$. In this type of discharges, the ultimate lowest current levels generally gave q values slightly above the rational values 1/2, 2/3 and 1. The selected current levels were somewhat different in cases with and without the octupole field. The levels were unchanged, though, for a certain range of discharge bank voltages, which indicates that the resulting equilibria to some extent are independent of initial conditions. This is consistent with the apparent self organizing property of ULQ plasmas.

For $q \geq 1/2$, $I_p$as measured inside the Rogowski coil, could exceed the externally fed current by up to 30%, indicating that current drive was obtained through the $\mathbf{v} \times \mathbf{B}$ electric field, arising through radial particle flux near the boundary.

We can also report that Thomson scattering measurements of temperature and density establish that the plasma was in this mode driven *into the collisionless regime.* As an example we mention a shot with the parameters I_p=10kA, I_v=22kA, B_z=0.22T, $n=3\cdot10^{20}$ m^{-3}, T=27eV the collision parameter becomes $\omega_{ii}\tau_i=14$ and the magnetic Reynolds number R_m= 580.

Theoretical interpretation

The reason for the current limit in Extrap L1 can be understood by comparing theoretical values for the pinch radius with the radial distance to the separatrix. If the pinch radius, as determined by Bennett's relation and transport, exceeds the separatrix radius, current will be lost from within the separatrix region. This certainly is a plausible model for the Extrap mode. When an axial field is added, however, we can formulate necessary conditions for the pinch radius, but here stability requirements put further restrictions on the range of I_p.

By assuming the radial profiles $p(r)=p_0(1-\gamma r^2/a^2)$ and $B_z(r)=B_{z0}(1-\lambda r^2/a^2)$, we can solve the Bennett relation for the pinch radius;

$$a^2 = \frac{\mu_0 I_p^2}{4\pi^2 p_0 \left[\gamma + \frac{8\lambda(1.5-\lambda)}{3\beta_z}\right]}$$

in which expression $\beta_z = 2\mu_0 p_0 / B_{z0}^2$. The on-axis pressure $p_0 = 3.2 \cdot 10^{-19} nT[eV]$. Obviously, large on-axis pressure implies small plasma radius. Note that the case $\gamma = 0$, i.e. constant pressure, corresponds to a force-free configuration with the pinch radius determined by the inhomogeneity of the axial field. In the case $B_{z0} = 0$, γ must be finite to maintain force balance.

Estimating the pinch radius in the pure Extrap mode we have $B_z = 0$, $I_p = 5$kA, T = 10eV, $n = 1.0 \cdot 10^{21}$ m^{-3} and $\gamma = 0.9$. These are approximately the parameters at the observed current limit in Extrap-L1. In a 1-D Z-pinch $\gamma < 1$ is necessary (but not sufficient) for stability of m = 0 modes. Extrap can, however, allow for values of γ near unity. The result is a = 0.017m. This value should be compared to the distance to the magnetic separatrix.

For anti-parallel plasma and octupole rod currents, the radial distance to the X-points is $r_x = A[\, \kappa/(4-\kappa)\,]^{1/4}$ where $\kappa \equiv I_p/I_v$ and A is the radial distance to the rods. A more relevant distance is the azimuthally averaged separatrix distance $d_x = (2/\pi)^{1/2} r_x$. For $\kappa = 1$ we have $d_x = 0.018$ m since A = 0.03 m. Obviously, for $\gamma < 1$ or $\kappa < 1$ we have $a \geq d_x$, which implies loss of current. *The experimental parameters of L1 are such that the plasma radius is critically large for* $I_p = 5$*kA*. When the plasma current is raised further, the pinch radius cannot be accomodated inside the separatrix. Obviously this can be viewed as a pressure limit, since an increase in I_p does not increase p sufficiently. This has also been noted by B. Lehnert. For times $t \geq \tau_{res} = \mu_0 a^2 \sigma$, the equilibrium becomes markedly time-dependent and more elaborate analysis is required.

We now turn to $B_z \neq 0$ operation. For $I_p = 5$kA we would require $B_{z0} \approx 0.08$ T to reach the current limit. We use the values $\lambda = 0.3$, $\gamma = 0.9$ and the same pressure as above in the expression for the pinch radius. For this case we find $a(B_z=0.08) \,/\, a(B_z=0) = 0.74$. The ratio for $\lambda = 0.1$ becomes 0.91. *The paramagnetic axial field may strongly decrease the pinch radius*. Since the $B_z(r)$ profile is unknown, the theory is so far not conclusive, however.

When B_z becomes too weak, the effect becomes too small. In one shot $B_z = 0.22$T, $I_p =$ 22 kA, and $I_v = 22$ kA. In this discharge about a fourth of the plasma current was lost from the central channel within 10 μs. Choosing the same pressure as before, $\gamma = 0.9$ and $\lambda = 0.3$ we get a = 0.022m, whereas $d_x = 0.023$m in this case. Another shot featured a fully contained plasma current, but of the value $I_p = 10$ kA. This gives a = 0.012m and $d_x =$ 0.018m, consistent with our theory. For the last two shots all relevant physical parameters were measured, except the profile factors γ and λ.

Conclusions

Stable modes of operation of the linear Z-pinch Extrap L-1 has been reported. In the Extrap mode, i.e. without external axial magnetic field, a limit in plasma current $I_p \leq 5$ kA was found. This limit has been interpreted as a maximum allowable pinch radius, due to the presence of the magnetic separatrix. Clearly, if the pinch could accomodate larger plasma pressure, the current limit would be passed. The discharges in this mode are stable for at least 100 Alfvén times, however in the collision dominated regime.

When an axial magnetic field was applied, higher plasma currents could be stably confined if the field were strong enough. Theoretically, paramagnetism can strongly decrease the pinch radius, enabling operation with higher currents in this mode. These discharges were predominantly collisionless and lasted at least as many Alfvén times, which is encouraging for future operation further into the collisionless regime.

In this latter mode, ULQ performance was established. As the discharge bank voltage was increased, the plasma current settled into levels corresponding to values of the safety factor q near rational numbers like 1/2 , 2/3 and 1.

The authors wish to thank Prof J. Drake for discussions and for letting them proceed far outside projected time limits and Mr R. Landberg for his skilful technical assistance. This work has been supported by the European Communities under an association contract between Euratom and Sweden.

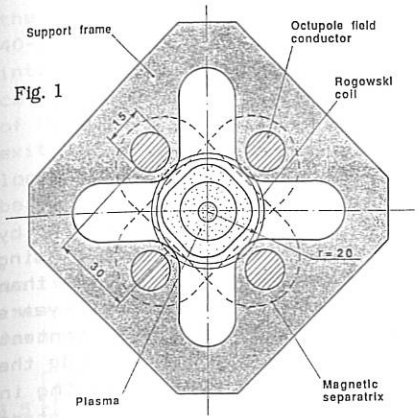

Fig. 1

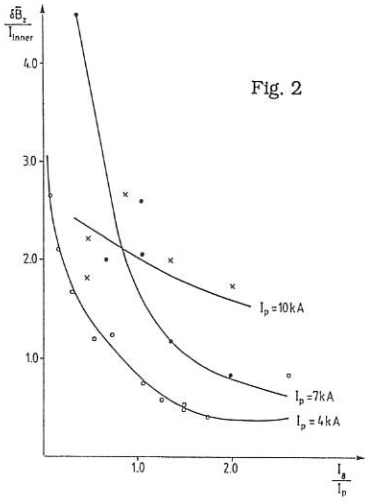

Fig. 2

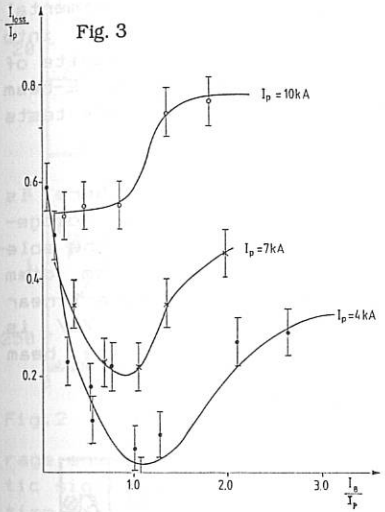

Fig. 3

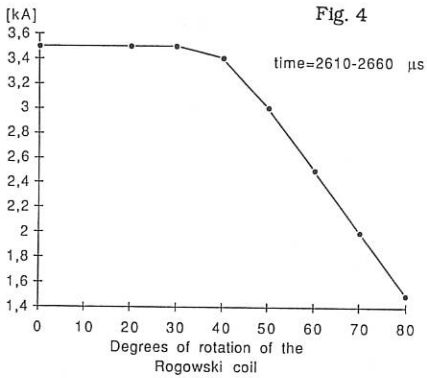

Fig. 4

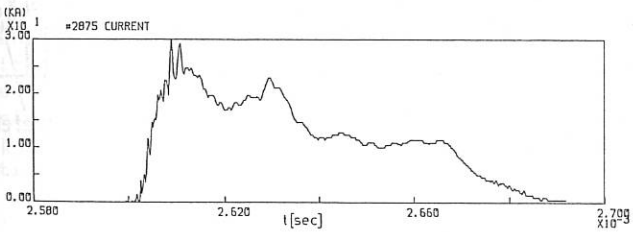

Fig. 5

DENSE PLASMA HEATING IN A MIRROR TRAP DURING INJECTION OF 100 kJ MICROSECOND ELECTRON BEAM

A.V.Burdakov, A.V.Karyukin, V.S.Koidan,
V.V.Konyukhov, S.V.Lebedev, K.I.Mekler,
V.V.Postupaev, M.A.Shcheglov, S.G.Voropaev

Institute of Nuclear Physics, 630090 Novosibirsk, USSR

1. INTRODUCTION. The studies of the fast plasma heating by high-power E-beams have until recently been performed using nanosecond beams with a total energy content not higher than several kilogoules (see, e.g. /1/). But during last years high-power microsecond REB generators with beam energy content of about 100 kJ have been developed /2/. This has been made the basis for performing the experiment on dense plasma heating in an open trap at a new level. For this purpose the first stage GOL-3 device was put into operation /3/. The first experimental results on the injection of a 100 kJ microsecond beam into a plasma were presented in /4/. In present paper the results of new experiments on plasma heating at the injection of E-beam into a neutral gas are presented, as well as the validty tests of the "two-stage" plasma heating are described.

2. DEVICE. The GOL-3-1 device is shown in Fig.1. There is a 7 m-long solenoid with a 6 T magnetic field in its homogeneous section and a 12 T one in mirrors at the ends of the solenoid. The plasma chamber inside the solenoid is a 10 cm diam SS tube. An initial hydrogen plasma can be produced by a linear discharge /5/. The beam produced by the generator U-3 /6/ is injected into the chamber through one of the mirrors. The beam

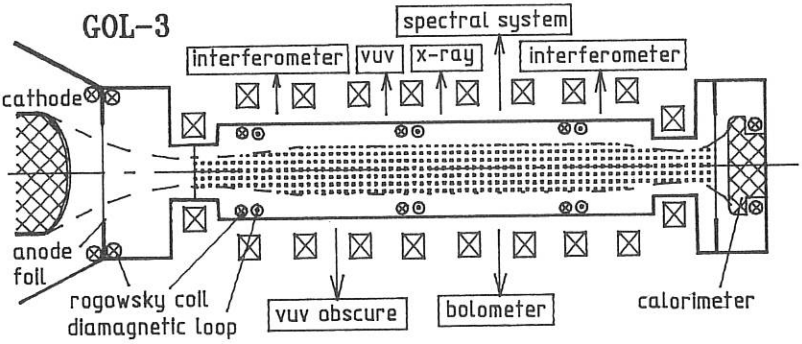

diameter is 6 cm in the homogeneous section of the solenoid, the current density is 1-2 kA/cm^2, the beam energy content is 40-100 kJ. Here we describe experiments on the beam injection into neutral hydrogen with a density ranged from 10^{14} to 10^{16} cm^{-3}. The diagnostic system (60 channels) comprises detectors of beam parameters (voltage, current, total current in plasma, exit current), 3.39 μm Michelson interferometers, diamagnetic loops, a calorimeter for measuring the total energy of the beam, X-ray and VUV detectors /7/, fast bolometers, etc.

3. BEAM INJECTION IN A GAS. First of all, it should be mentioned that in the case of a similar density, the beam-gas interaction seems not to differ essentially from the beam-plasma one under our conditions. The typical signals are given in Fig.2. In this shot: $n=8\cdot10^{14}$ cm^{-3}, B=5.5 T, Q=50 kJ. The growth of diamagnetic signals is shown to start with some time delay, nevertheless the beginning of heating never exceeding 1 μs in the given pressure range. The plasma production is mainly not the result of a direct gas ionization by beam electrons, but is accounted for by secondary effects, i.e. a breakdown of the gas due to voltage produced at the beam injection in the chamber, a plasma heating due to a collective REB-plasma interaction and by a return current in a plasma column. For the conditions shown in Fig.2 the average energy of an electron-ion pair, calculated from diamagnetic signals, is 1-2 keV. The maximum amplitude, as well as the time of the diamagnetic signal decay after the beam injection is over, depends on the location of diamagnetic loops along the chamber and on the regime of the device operation. The decay of a heated plasma can result from the thermal conductivity to the ends with a characteristic time $\sim L^2/v\lambda$. By this estimate T_e ~0.5 keV. Another mechanism of the plasma energy loss is a scattering of "hot" electrons into the loss cone. In this case $\tau \sim \ell_n R/\nu_{ei}$, where R is the mirror ratio. The characteristic decay time corresponds to the energy of electrons of 1-10 keV.

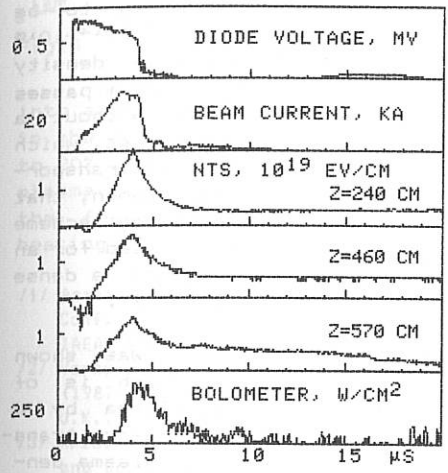

Fig.2

Note, that transverse losses from the trap are negligibly small, which is proved by bolometric measurements (see Fig.2).

The above estimates show that there might appear a case, when the time of escape of heated electrons from the trap is less than the time of beam injection. Then the beam energy loss should exceed the energy content of plasma, which fact was recorded in the experiment (see /4/ for the case of a beam injection in a preliminary plasma). Thus, the beam energy loss can make about 10 kJ for a density of $5 \cdot 10^{14}$ cm^{-3}, while in plasma remained 1-2 kJ. The efficiency of the beam-to-plasma energy transfer depends on the density (Fig.3) (see, also /4,8/). The efficiency of plasma heating is seen to be high for a density of 10^{14}-10^{15} cm^{-3}, meanwhile for a density of $\sim 10^{14}$ cm^{-3} the beam passes through the system without a noticeable energy loss, which corresponds to a good transportation. It is well known, that the "two-stage" heating scheme is supposed to be used for an effective heating of a dense plasma (see, e.g., /1/).

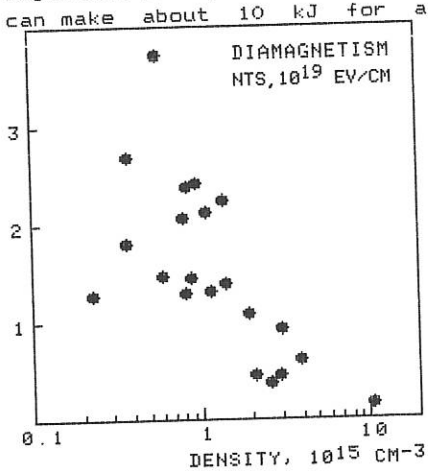

Fig.3

4. SIMULATION OF THE "TWO-STAGE" HEATING. As was shown above, in the case of a high-density plasma, which is of practical importance, there is no heating of the plasma by a beam. At the same time, the efficiency of the beam energy transfer to "hot" plasma electrons is very high for a plasma density of 10^{14}-10^{15} cm^{-3}. If in such a plasma one produces a high density region with a length exceeding the free path length of "hot" electrons, then the dense plasma will be heated by these electrons due to binary collisions. As to its technical realization, it can be performed either with a pulsed gas filling or by placing a solid target in the plasma /9/.

For realizing this scheme of plasma heating a special experiment was carried out. A thin organic film, used as "dense" target, could be placed transverse to the plasma column cross section in different points along the chamber length. Fig.4 shows, for example, the diamagnetic signals for the case, when the foil was placed near the end of the device (Z=580 cm from the entrance). The signal near the foil are shown to be

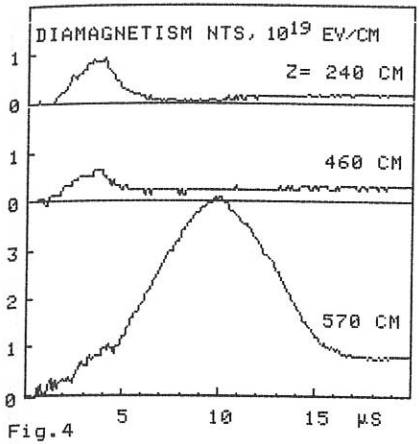

Fig.4

3-8 times higher compared to the case when this foil is absent. It means that the material of the foil is heated and ionized by the fast electrons produced as a result of the background plasma heating. The experiment shows an expansion of the dense plasma both from the diamagnetic signals and as a result of the VUV radiation observated by the obscure chamber. The radiation and expansion of this plasma were also observed in visible spectrum.

5. CONCLUSION. The experiments on the injection of a REB into a gas, performed on the GOL-3 device, have shown that like in the case of its injection in a plasma, the beam can loose up to 20% of its energy. Some part of this energy remains in the plasma after the beam injection. The experiments have proved the feasibility of the "two-stage" scheme of dense plasma heating with a relativistic electron beam.

/1/ Arzhannikov A.V., Astrelin A.V., Avrorov A.P. et al. Proc. 11th Intern. Conf. on Plasma Physics and Contr. Nucl. Fusion Res., 1986, Kyoto. IAEA, Vienna, v.2, p.323 (1987).

/2/ Voropaev S.G., Knyasev B.A., Koidan V.S. et al. Pis'ma v ZhTF, 7, p.431 (1987), Proc. 18th Intern.Conf. on Phenomena in Ionized Gases, Swansea, U.K., v.1, p.204 (1987).

/3/ Arzhannikov A.V., Burdakov A.V., Kapitonov V.A. et al. Plasma Physics and Contr. Fusion (Proc. 15th Europ. Conf., Dubrovnik, 1988), v.30, N 11, p.1571 (1988).

/4/ Burdakov A.V., Kapitonov V.A., Koidan V.S. et al. Proc. 1989 Intern. Conf. on Plasma Physics, New Delhi, v.3, p.973 (1989).
Burdakov A.V., Kapitonov V.A., Koidan V.S. et al. ibid, p.969.

/5/ Burdakov A.V., Deulin Yu.I., Kapitonov V.A. et al. Proc. 19th Intern. Conf. on Phenomena in Ionized Gases, Belgrade, v.1, p.252 (1989).

/6/ Voropaev S.G., Konyukhov V.V., Lebedev S.V., Shcheglov M.A. Voprosy Atomnoj Nauki i Tekhniki, ser. Termojadernyj sintez, v.3, p.26 (1988).

/7/ Burdakov A.V., Koidan V.S., Piffl V. et al. Proc. 19th Intern. Conf. on Phenomena in Ionized Gases, Belgrade, v.2, p.318 (1989).

/8/ Chikunov V.V., Knyasev B.A., Melnikov P.I. Proc. 13th Intern. Symp. on Discharge and Electrical Insulation in Vacuum, Paris, v.2, p.436 (1988).

/9/ Burdakov A.V., Koidan V.S., Postupaev V.V. Fizika Plasmy, 11, 944 (1985)

ON POSSIBILITY OF CREATING MHD-STABLE PLASMA DISTRIBUTION IN AXISYMMETRIC PARAXIAL MIRROR

Kuz'min S.V., Lysyansky P.B.
USSR, 630090, Novosibirsk, Institute of Nuclear Physics

A lot of works (see, for example, [1]) is devoted to the problem of creating the MHD-stable axisymmetric open plasma trap. Their authors emphasize especially an issue of finding such geometry of the trap's magnetic field which ensures plasma MHD stability. As a rule, the simplest models are considered, where plasma pressure decreases along the mirror's magnetic lines in direction to magnetic throats, as well as in transverse direction to walls of a vacuum chamber or a limiter. The plasma pressure profile along magnetic lines is determined usually as the same for all the trap's lines, i.e. not depending on a transverse coordinate. However, investigations of the MHD plasma stability in axisymmetric traps with a high curvature, for example in a cusp [2] and other nonparaxial geometries [3-5], show that it is impossible to obtain the same pressure distribution along all magnetic lines. Firstly, this is connected with a limited length of plasma hot components due to nonadiabatical effects of particle motion [6], and also with different maximum and minimum values of magnetic field on force line, as well as with different dispositions of these points on different lines [5]. Also the conditions of creating plasma, i.e. injection and particle heating may be here of importance.

It seems important to draw attention to taking into account such effects not only for analyzing the MHD stability, but to their possible use to obtain stable plasma in simple mirror with the help of special distribution of plasma pressure there. In particular, consider a clear example of the single paraxial axisymmetrical trap with

mirror ratio $R = B_{max}/B_{min} = 4.0$ and with a magnetic field value distribution along the axis $B(r=0,z)$, as shown in Fig.1. For simplicity let us consider only potential flute disturbances for the small plasma pressure case $\beta \ll 1$. Plasma pressure distribution is assumed to be described by following model functions:

$p = p_{\parallel} + p_{\perp} = p_o(\psi)\cdot\hat{p}(B)$, where $p_o(\psi) = \exp(-\psi/\psi_*)$;

$$\hat{p}(B) = \left[\frac{B_{min}}{B}\cdot\frac{B_{max}-B}{B_{max}-B_{min}}\right]^n\cdot\left[\frac{B_{max}-B}{B_{max}-B_{min}}\right]^{1/2}\cdot\frac{2(n+2)B_{max}-B}{2(n+2)B_{max}-B_{min}};$$

$\psi = B\cdot r^2/2$ - a magnetic flux; n - a parameter describing the plasma length along a magnetic line (see Fig.1). Let a parameter n be a function of the transverse coordinate ψ. The flute disturbance energy for the paraxial mirror may be written as follows: $W = \frac{1}{2}\cdot\int d\psi\cdot\varphi^2\cdot w$, where φ is perturbed electrostatic potential. The disturbance energy density $w = -\int ds\cdot\frac{\partial p}{\partial\psi}\cdot\frac{\varkappa}{rB^2}$, $\varkappa = r\cdot(\partial B/\partial\psi)$ - a curvature of force line, in our case may be written as follows:

$$w = -(\partial p_o/\partial\psi)\cdot I - (\partial n/\partial\psi)\cdot p_o\cdot I_1,$$

where $I = \int ds\cdot\hat{p}\cdot(\varkappa/rB^2)$; $I_1 = \int ds\cdot(\partial\hat{p}/\partial n)\cdot(\varkappa/rB^2)$.

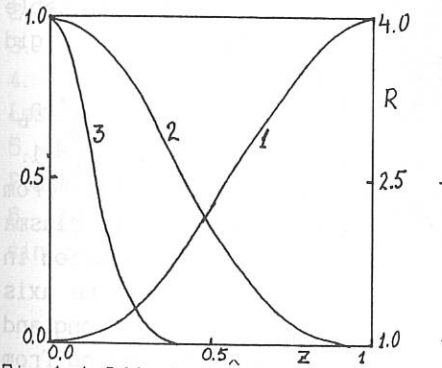

Fig.1 1-$B(0,z)$; 2-$\hat{p}(B)$ for n=1; 3-$\hat{p}(B)$ for n=20.

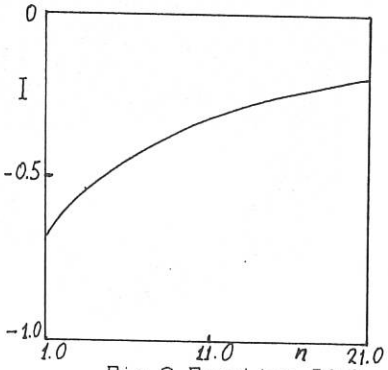

Fig.2 Function I(n) in arbitrary units

Evidently for $p(\psi = \psi_{boundary}) = p_b \neq 0$ and under

condition $\partial n/\partial\psi > \frac{1}{p_o}\cdot\frac{\partial p_o}{\partial\psi}\cdot\frac{I}{I_1}$ it turns out that for every ψ $w > 0$, i.e. plasma is stable relatively to all modes of MHD-disturbances. But estimates show that $n(0) \geq 500$ is needed to obtain this, that corresponds practically to disk-shaped plasma on the trap axis. Another situation takes place under consideration of the hot ion plasma case, when the FLR effects stabilize the all small-scale MHD modes and only rigid mode m= 1 remains unstable. Here $\varphi^2 \sim \psi$ and $W = A\cdot\int d\psi\cdot\psi\cdot w = -\psi_b\cdot p_b\cdot I(\psi=\psi_b) + \int p_o I\cdot d\psi$. Consequently, for stabilizing the rigid mode it is necessary to fulfil the condition $(p_b/p_{max}) > (\int (p_o/p_{max})\cdot I\cdot d\psi\ ) / (\ \psi_b\cdot I(\psi_b)\ )$. From the dependence $I(n)$ (see Fig.2) one can conclude, that the more difference of values of n on the axis and on the border of plasma, the less the relation p_b/p_{max}, guaranteeing the rigid mode to remain stable.

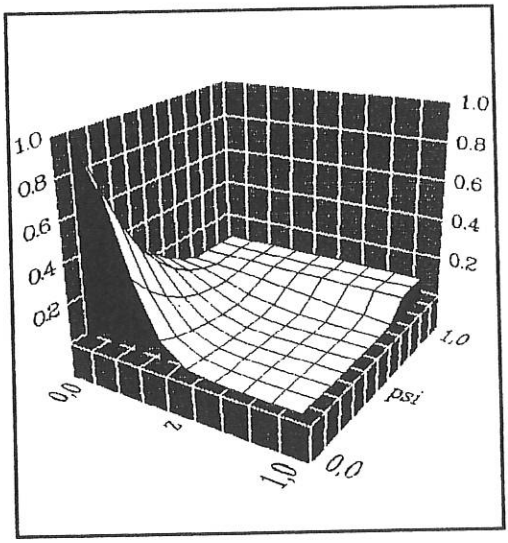

Fig. 3.

In the Fig.3 the two-dimensional plasma pressure profile in the paraxial mirror is given, being MHD stable relatively to the rigid mode $n(\psi)=(n_{max}-n_b)(1-\frac{\psi}{\psi_b})^4+n_b$, where $n_{max}= 21$, $n_b= 1$. As one can see from Fig.1 and Fig.3, plasma pressure distribution in the trap along the axis is sufficiently long and smoothly decreasing from the center to the periphery, and does not seem to be exotic.

Stability is obtained with the help of small pressure variations in the vicinity of the edge of plasma. Physically the stabilization effect is explained by creating plasma pressure distribution being inverse "in average". Just due to this reason it is necessary to have the non-zero plasma pressure near a chamber wall. Analogously to the "average min B" principle, we can name the describe above method of stabilization as the "average min P" principle.

As to the possibility of the technical realization of the effect, the related problem of plasma finite pressure at the device wall, naturally existed in the form of plasma halo, should be studied separately for hot plasma in the case of reactor. For creating the special profile in the paraxial trap several methods could be suggested, in particular:

- application of mechanical constructions;
- special injection of neutral beams, fuel pellets and gas;
- impact of different types of ERF waves.

REFERENCES:

1. Ryutov D.D. Plasma Phys. and Contr. Fus., 1986, v.28, p.191.
2. Nagorny V.P., Stupakov G.V. Phyz. Plazmy, 1984, т.10, с.476.
3. Ruytov D.D., Stupakov G.V. Phyz. Plazmy, 1986, т.12, с.1411.
4. Arsenin V.V. In: Proc. Int. Conf. on Plasma Phys., Losanna, 1984, v.1, p.206.
5. Kuz'min S.V., Lysyansky P.B. In: Proc. Int. Conf. on Plasma Phys., Kiev, 1987, v.3, p.257.
6. Kuz'min S.V., Stupakov G.V. VANT. Ser.: Termoyaderny sintez, 1989, issue 1, p. 40.

MAGNETIC AND LANGMUIR PROBE MEASUREMENTS IN THE SPHEX SPHEROMAK

P.K.Browning, B.Browning, G.Cunningham, P.J.Dooling,
S.J.Gee, D.A.Kitson, M.G.Rusbridge

Department of Pure & Applied Physics, UMIST, Manchester M60 1QD, U.K.

Abstract: We present measurements of the magnetic field configuration in the SPHEX spheromak, together with measurements of the field components at the wall and the fields in the "entry region" which links the gun with the spheromak.

We also present measurements of the potential, density and temperature distributions obtained with Langmuir probes inserted both at the "equator" and at the "pole" of the device. The temperature increases inwards from the wall, but the density shows a hollow profile; the electric field is about 600 V/m in the central column but very small elsewhere.

The implications of these results are discussed.

Introduction. SPHEX is a gun-injected spheromak similar in concept to the CTX device at Los Alamos National Laboratory [1]; it has been described by Browning et al. [2]. In this paper we present results from magnetic and Langmuir probe measurements, both at the edge and inserted into the plasma. These results confirm that the current and magnetic flux injected through the gun is amplified in the flux-conserver, and that the magnetic configuration is partially relaxed; they largely complete the initial characterisation of the plasma, and open the way for an investigation of the relaxation process.

Description and Plasma Formation. The flux-conserver is a 5mm thick shell of copper, 0.95m in diameter and 0.48m deep; the entry region is 0.23m long and tapers in diameter from 0.54m at the gun to 0.44m at the junction with the flux-conserver. The device is powered from an 8 mF capacitor bank storing up to 250 kJ, with a 40 μH inductor as an intermediate energy store. In normal operation the gun current is typically 60 kA and the current pulse lasts for 2-3 msec. The spheromak plasma is formed for only part of each pulse, starting when the current I_G is large enough to eject the plasma from the gun against the magnetic field of the gun solenoid, and finishing when $\mu_G = \mu_0 I_G/\Psi_G$ falls below the spheromak eigenvalue μ_e = 11.1m^{-1} [3] (Ψ_G is the flux in the gun solenoid); the plasma lasts typically for about 1 msec. The experimental results on plasma ejection, described in [4], fit a simple model based on force-balance at the mouth of the gun; details will be published elsewhere.

Magnetic Probe Measurements. The insertable magnetic probe comprises 8 orthogonal coil pairs spaced at 3.3 cm; each coil spans 12mm along the probe axis, and the pairs are interlinked so that their centres are 6mm apart. This whole assembly, contained within a quartz sleeve 15mm in diameter, has been inserted both at the "equator" of the flux-conserver, where it reaches to just beyond the magnetic axis, and into the entry

region between the gun and the flux-conserver. At the equator, the probe is mounted on a rack-and-pinion motion which allows it to be moved between shots, so that the resolution of the mean field measurements can be improved; at the entry region, however, only one position is available, in which the probe penetrates to just beyond the geometric axis of the machine.

Results from the equatorial position confirm that the configuration has the qualitative form expected for a relaxed state, with a magnetic axis at 30 cm from the geometric axis. The most important results obtained from this position are measurements of the μ-profile and the poloidal flux. The spatial variation of $\mu = \mu_0 j_{//}/B$ is shown in fig.(1); its form is similar in all conditions studied and is also similar to that seen in CTX [5]. It can to a good approximation be represented as a linear function of the poloidal flux coordinate. It also satisfies the condition derived by Kitson and Browning [3] that the range of μ should span the spheromak eigenvalue for significant flux amplification.

The poloidal flux measurements show that this quantity is almost independent of the gun current, provided that the plasma ejects; the maximum flux is always about $3.5\,\Psi_G$. Fig.(2) shows measurements of the equatorial poloidal field as a function of the solenoid flux for different gun currents, confirming its independance of I_G. A corollary of this is that for a given gun current the toroidal current I_T in the spheromak has its maximum value when the plasma has only just ejected; in this "optimum" condition $I_T \approx 2I_G$, i.e. up to about 150 kA. As Ψ_G is reduced, I_T is reduced in proportion but the plasma lasts longer.

The main result from the insertable probe in the entry region is that the current from the gun flows in a column of about the same diameter as the central electrode, but this is surrounded by a near-vacuum field. Thus the return current in the plasma is virtually zero, i.e. the current returns through the wall rather than through the plasma. This again is confirmed by the edge coils, which show that the toroidal field does not vanish at the wall as expected, so that there must be a net longitudinal current in the plasma. An analysis of the edge coil results [4] shows that the current reaches the wall in two zones: about 60% at the outer edge of the front or polar face of the flux conserver, and the remainder around the junction with the entry region. Some loss of current to the wall is expected as field lines diffuse into the wall, but this should amount to no more than a few kA, and should have a different distribution both in space and time from the observed current flow. We are so far unable to account for this massive flow of current across the confining magnetic field.

Langmuir Probe Measurements. We use double Langmuir probes, with tungsten tips 1mm long by 1mm in diameter, separated by 3 mm, and mounted on a ceramic stem. The probe is driven by a 5 kHz A.C. supply giving up to 0.5 amp at 100 V. Thus the complete probe characteristic is scanned about 10 times during a pulse; reliable probe characteristics are obtained by averaging over 2 cycles in 3 successive pulses. A typical current trace and its corresponding probe characteristic, taken near the magnetic axis, are shown in fig.(3), corresponding to $T_e \approx 11$ eV and $n \approx 2\times10^{19}$ m^{-3}. Similar measurements using a D.C. bias give the saturation current profile along an equatorial radius shown in fig.(4): the density profile is hollow. The average density agrees well with the line-of-sight average obtained from an interferometer. The temperature is about 6 eV near the wall, increasing to about 10 eV over the bulk of the plasma as far as the magnetic axis.

The equatorial probe has also been used to measure the floating potential; this is small near the wall but increases negatively to about

-50 V. However, when the result is corrected for the sheath potential we find that the space potential is within 10-20 V of earth. This contrasts with the results obtained when the probe is inserted at the pole and along the geometric axis: the potential rises steadily through the flux-conserver to flatten off at a value of 250 V in the entry region (fig. 5). The temperature is about 13 eV and the density 4×10^{19} m^{-3} in the flux-conserver, but the density falls and the temperature rises in the entry region.

Discussion. The voltage on the gun is typically 300 V, which with a solenoid flux of 2.4 mWb gives a helicity injection rate of 1.4 Wb^2/sec. From estimates of the total helicity we then find a helicity-based resistivity temperature [6] of 11 eV (for $Z_{eff} = 1.2$). This agrees well with the observed value. We believe that this low value arises from the very low gun impedance of about 5 mΩ, which gives very poor energy transfer from the power supply. Results from CTX [7] suggest that by changing the power supply circuit it may be possible to force the gun to operate at a higher impedance; preliminary results from SPHEX seem to confirm this.

The measured electric field along the geometric axis of 600 V/m is considerably larger than the estimated Spitzer value of about 30 V/m, and we suggest that the field must represent the loading due to the relaxation process which maintains the current on the closed flux lines. However, the observation of a hollow density profile and the low, perhaps negative, space potential of the closed flux region suggest that this region is isolated from the central plasma column. There is then a problem of power transfer; the estimated dissipation in the closed flux is 10 MW, comparable to the power of 12.5 MW deposited ohmically in the central column. One possibility is that the power flow may be associated with the large-scale n = 1 magnetic field oscillations [2]. In contrast to observations of large-scale magnetic fluctuations in RFP's [8], this is a radially propagating mode with the edge leading the magnetic axis in phase by about a radian; it can therefore carry an inward flux of energy. This mode is also seen by Knox et al.[4], who show that it is predicted to be unstable for the observed μ-profile.

Conclusions. The SPHEX plasma exhibits an unexpected structure in which the energy is deposited on a central column of plasma which carries the bulk of the gun current; this current flows to the wall of the flux-conserver rather than to the outer gun electrode as expected. The region of closed flux appears to be isolated from the central column; a prominent 25 kHz oscillation may be responsible for transferring energy from the column to the closed flux.

References

[1] T.R.Jarboe et al., Phys.Rev.Lett.51,39(1983)
[2] P.K.Browning et al., 16th Euro.Conf.Cont.Fus.Plas.Phys., Venice; Europhysics Conference Abstracts 13B, part II, p.787(1989)
[3] D.Kitson and P.K.Browning, submitted to Plas.Phys.Cont.Fus.
[4] P.K.Browning et al., 11th US-Japan Workshop on Compact Toroids (1989)
[5] S.O.Knox et al., Phys.Rev.Lett.56,842(1986)
[6] K.F.Schoenberg, R.W.Moses, R.L.Hagenson, Phys.Fluids 27,1671(1984)
[7] C.W.Barnes et al., 11th US-Japan Workshop on Compact Toroids (1989); Los Alamos report LA-UR-89-909 (1989)
[8] I.H.Hutchinson et al., Nuc.Fusion 25, 59 (1984)

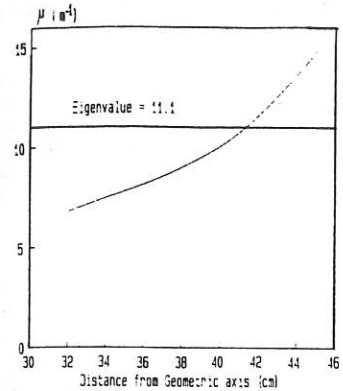

Fig.1 μ profile compared with eigenvalue

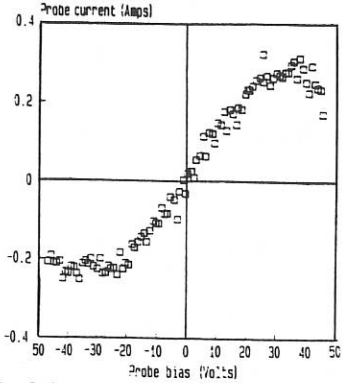

Fig.3.2 Corresponding characteristic

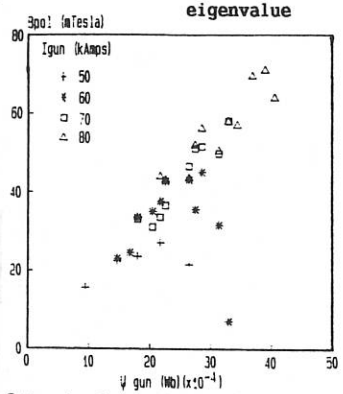

Fig.2 Equatorial poloidal field dependence

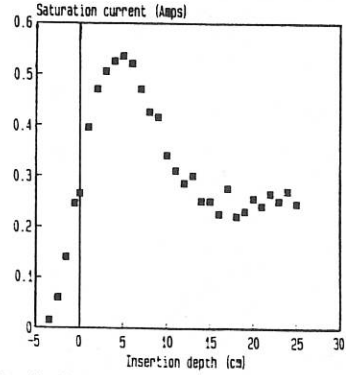

Fig.4 Saturation current along equatorial radius

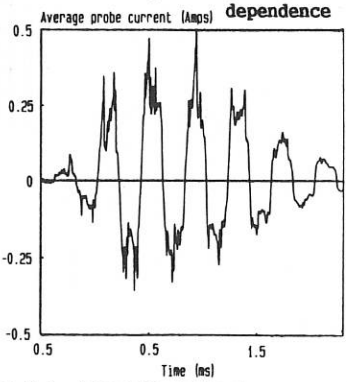

Fig.3.1 Langmuir probe trace

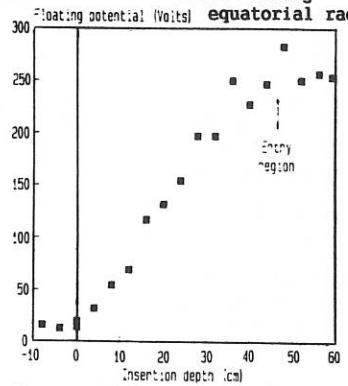

Fig.5 Potential variation along geometric axis

MAGNETIC FIELD CONFIGURATION OF FBX-II SPHERICAL TORUS

Masaru IRIE, Hideaki KUSAMA, Norio SAITOU

Hiroshi YOSHIKAWA, Hiroshi ABE, Yuuji ISHIHARA, Hajime SONEHARA

WASEDA UNIVERSITY

OHKUBO,SHINJUKU,TOKYO, 160, JAPAN

1. Main Object of the Project

FBX (Free Boundary Experiment) scheme is introduced and deviced
1. to study transport mechanism
2. to find out the condition to activate flux conversion, if any,
3. to check the capability of helicity injection,

in ultra-law aspect ratio plasma, Spherical Torus , produced by specially designed " Split Ohmic Heating Coil " system.

2. Basic Design of FBX-II

The current device in a series of experiment is FBX-II. In Fig.1a, schematic cross sectional view, in holizontal plane , with experimentally obtained poloidal magnetic field lines is presented.

An "upright"plasma is formed in ordinally tokamak sence. A ultra-low aspect ratio plasma normally 0.3m in minor and 0.5m in major radius is produced.

This plasma dimension is vertually the same as other largest spheromaks up to now, S1 in Princeton University and CTX in Los Alamos National Laboratory.

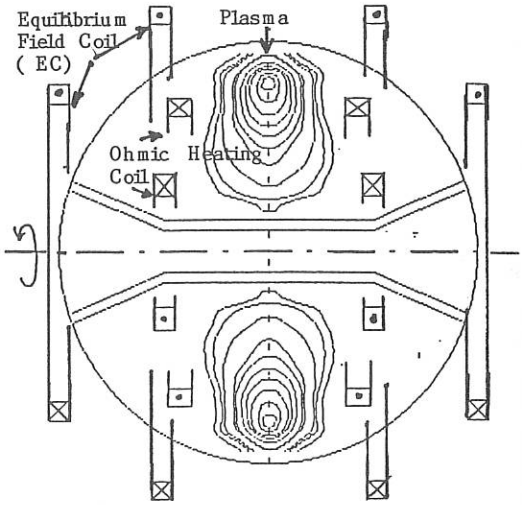

Fig.1. Cross Sectional View and Measured Poloidal Field of FBX-II Plasma

a. Shell/vacuum vessel

The shell/ vacuum vessel is made of SUS 304 stainless steel sphere with 1.6 m in diameter. FBX-II is equipped with a 20 inch Cryo-pump and a 10 inch turbo molecular pump.

b. Toroidal Magnetic Field and Poloidal Plasma Current (Ipp) Drive

Toroidal magnetic field is supplied by six-sectional rod coils. They are linked in series with 12 sectional external return conductors to decrease field ripple on the magnetic axes. Rod coils are covered with 0.4 mm thick stainless steel liners welded to the spherical vessel to form poloidal shell. This has a effect to supress plasma deformation faster than about 10 kHz but still allows low frequency e.m.f. injection to drive poloidal component of plasma current(Ipp).

c. Poloidal Magnetic Field and Toroidal Plasma Current (Ipt)Drive

The poloidal magnetic field is constructed both by a plasma and 8 section poloidal field coils, square with current direction indicator , x or dot, in Fig.1. Four coils inside the shell behave as ohmic heating coils (OHC) to drive toroidal component of plasma current (Ipt). By this " Split Ohmic Heating Coil System ", with sacrificing operational simplicity, further engineering simplification and reliability is expected. Four external coils act as equilibrium field coils (EC). OHC and EC are set on vertual mirror simmetry positions against the shell. These coils have external terminals to increase flexibility in field control.

d. Operational senario of poloidal field

Basic plasma production senario is shown schematically in Fig. 2 a-c without field lines looping around OHC. In order to keep control over a plasma with Ipt, the EC is over-activated to produce fluxes crossing the shell to get line tying effect. The inclusion of even small toloidal field grately enhance the effect of local average minimum-B ring zone (Min-B), shown in black dots in Fig.2a.

A plasma with small Ipt or one injected by a helicity injector falls into this Min-B and settles there. The shell problems originated from skin time can be compensated by EC current control, because of the coil and shell position. The poloidal field near the equator can be vertually steady for both fast and slow OHC activation.

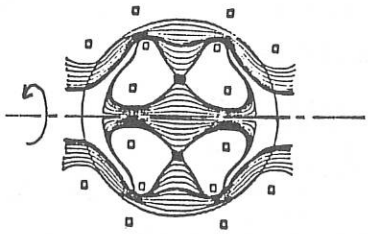

Fig.2a Poloidal Vacuum Field

When the current in OHC starts changing rapidly after this time, an electrical breakdown is initiated along the seed plasma on the Min-B ring.

By activating toloidal coils at the same time, a main plasma with helical current can be produced. Because magnetic coupling between OHC and a plasma is tighter than that between the toroidal coils and the plasma, Ipt drive is far efficient in plasma formation stage and Ipp drive become efficient

when the minor radius of the plasma is near at its peak, Fig 2.b. This poloidal field configuration is similar to the standard operation of PDX (Poloidal Divertor Experiment) tokamak studied in Princeton University in early 1980's, even though the latter is believed to to have no Ipp. From this configuration the OHC current decreases by transferring the flux to the plasma.

Fig.2 c. shows a poloidal field with zero OHC current.

This is a common poloidal profile of spheromak just like Hill's vortex with center flux hole. By adjusting the EC current, the main plasma is controlled not to touch OHC by keeping the separatrix between vacuum region and the main plasma inside. After then an OHC current changes its direction. A plasma is compressed and stablised with this reverse current-fed OHC and forms " Extrap-like " field configuration as is shown by experiment, Fig.1.

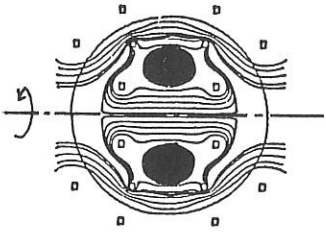

Fig.2b Poloidal Field with Largest Plasma

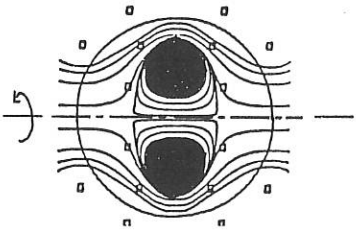

Fig.2c Poloidal Field with Zero OHC Current

3. Experimental Results

In the beginning, fast time scale plasma production with low frequency toroidal field is conducted. The OHC activation frequency is 1.5 kHz, shorter than the skin time, and faster than toroidal field variation with 300 Hz. As is expected, the most efficient plasma current drive is attained if the OHC activation is initiated at the peak of toroidal field. When the toroidal field decays to zero, toroidal plasma current is extinguished. This is similar to the tokamak operation.

However even though very critical, there is a small operation window around the toroidal field zero period that the plasma can be initiated efficiently for the second half cycle of the toloidal field. This is because of the poloidal multipole field to keep the seed plasma even in zero toroidal field period. By utilizing this feature , it is possible to inject arbitrary helicity as the initial condition.

In the following step, the current waveforms and the phase difference in both toroidal and poloidal coils are altered and scanned. Through this experiment, the

optimum condition is obtained with crawbarred or reverse-crawbarred current.

In Fig.3. time history of the toroidal magnetic field profile is presented, which is obtained with 13 channel search coil system set on the equator crossing both the center of the toroid and the magnetic axis. On 15 cm position just outside the rod coil, toroidal field follows the current. However in the main plasma region (25 - 75 cm) the toroidal field is vertually independent of the coil current, and show slower transition.

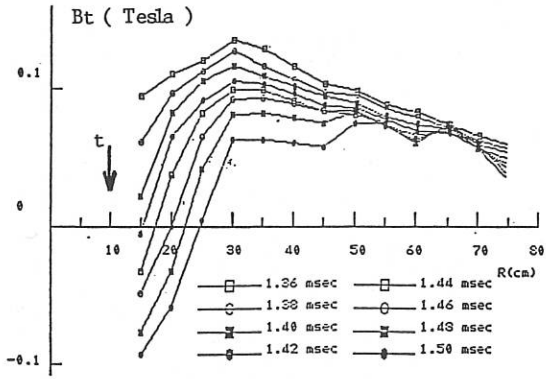

Fig.3. Time History of the Toroidal Field

This profile indicates induced diamagnetic poloidal current in the plasma.

This profile is similar to the initiation stage of the RFP forced reversal operation, but FBX plasma has ultra-low aspect ratio and out of ordinary linear plasma approximation. The plasma decays gradually after this stage.

If the toroidal coil current is interrupted within current zero period, the plasma configuration becomes spheromak type. Because of the existance of toroidal rod coils near the torus major axis, the plasma has a flux hole and is passvely controlled against major spheromak instabilities.

In the first figure of this presentation, Fig.1, the field profile obtained with search coils are presented. The field lines shows that the magnetic axis of the plasma is shifted further outside from the Min - B in vacuum field and plasma decays gradually by major radius expansion. As in this stage the profile is in good agreement with our computer simulation, we expect to extend this decay time constant with faster field control.

Acknowledgements

We are grateful to Prof. S.Yoshikawa, Dr. D.M.Meade and former PDX group , Dr. M.Yamada and former S1 group, Profs. M.Katsurai and T.Sato for comments on the FBX concepts in the initial stage and to Prof. A.Iiyoshi and K. Watanabe and former Japanese Compact Torous Project for the comments in the developping stage.

This work is partially supported by the following organizations.
Ministory of Education (Grant in aid for science and engineering),
Institute of Electromagnetic Aplication Research,
Science and Engineering Research Institute, Waseda University

CORRELATION BETWEEN MAGNETIC TEARING AND X-RAY EMISSION IN COAXIAL DISCHARGES

H.M. Soliman and M.M. Masoud

Plasma Physics and Nuclear Fusion Department,
Nuclear Research Centre, Cairo 13759, Egypt

Introduction:

Previous study of the X-ray emission from a coaxial discharge of 6 KJ has been shown that [1] a very localized X-ray sources, dots or rod shaped with diameter ~ 0.2 mm, were located far from the coaxial region at a distance of upt to 1-2 cm from the axis. An off-axis, X-ray sources were observed [1] in 10-15% of the X-ray photographs recorded outside the axial pinch in region of the current sheath that carries filament even during the focus stage of the discharge [1]. In small plasma focus device performed with 1 KJ facility, X-ray hot spots appear not only on the axis of coaxial elelctrodes muzzle but also considerably off-it [2]. It has been observed in Mather-type plasma focus 18 KJ [3] that after the current sheath collapses radially and forms the plasma column, the length of the plasma column extended axially in time. the column was disrupted later by the growth of the m = 0 instabilities and after thd disruption an X-ray was observed [3]. It has been found that, magnetic field tearing and instabilities occur within the plasma current sheath [4].

The present study investigates the correlation between X-ray emission and magnetic reconnection in coaxial discharges and the influence of applied external axial magnetic field on these correlation processes.

Experimental Set-up

Investigations have been carried out in a coaxial electrodes discharge of the Mather geometry, Fig. (1), the diameter of the outer electrode is 6.6 cm and that of inner electrode is 3.2 cm. The length of two stainless-steel electrode is 31.5 cm. The discharge is energized by a condenser bank charged to 11 KV, which yields a stored energy of 10 KJ. The peak discharge current reached 115 KA. The device is filled with hydrogen gas with a pressure of 0.9 Torr. An externally excited magnetic field (B_z) of intensity 2.4 KG is introduced in the plasma sheath axial region along the coaxial electrodes.

Experimental Results and Discussion:

The time resolved soft X-ray emission from coaxial discharge has been measured by plastic scintillator, light guid and photomultiplier detectors. The scintillator detector was placed on the axis and at 3 cm from the muzzle, and off - the axis in the annular space between the coaxial electrodes at the distance approaches to muzzle. Fig. (2) shows the time structure of the soft X-ray emission from the axis and off-axis, in the free magnetic field region and presence of external axial magnetic.

The electron temperature for plasma emitted from coaxial discharge was determined by measuring the X-ray intensity as a function of absorbers thickness placed on front of plastic scintillator. This detector was positioned at axial distance of 3 cm from the coaxial electrodes muzzle. Fig. (3) shows the calculatd values [5] of X-ray intensity as a function of aluminum absorber with different thickness and for different electron temperatures, solid curves. The experimental points are presented on the same figure, dotted line, for the presence and absence of the external axial magnetic field. The results illustrate that, the electron plasma temperature is 2.7 KeV which increased with the application of the axial magnetic field to 5 KeV.

The axial magnetic field intensity vairation was measured by a magnetic probe of 2 mm diameter located along the axial position at mid-distance of the annular space between the coaxial electrodes. Fig. (4) shows the axial magnetic field intensity versus the axial distance. The experimental observations indicated that the presence of external (B_z) caused a reduction in the induced axial magnetic field of about 35%.

Time distribution of axial magnetic field in case of the applied external axial magnetic field (B_z), at 28 cm from the coaxial electrodes breech, Fig. (5), this figure showed that, the reversed magnetic field intensity increased in the presence of external axial magnetic field.

Conclusion:

the experimental results indicated that, the X-ray emitted from the annular space between the coaxial electrodes was less intense than those of the focused region. The intensity of the X-ray emitted from both focused region and annular space increased with the application of external axial magnetic field (B_z). Moreover the X-ray energy from focused region was found to be increased by a factor of ~ 2 from its initial value, when (B_z) was applied on the plasma sheath. This attributed to the increased of acceleration mechanism of the electrons which initiated from the tearing and reconnection of internal axial magnetic field lines. magnetic field intensity measurements along the coaxial elecrtodes, illustrated that partial diamagnetic effect of the plasma sheath increased with the application of (B_z). This result indicated that the main cause of the X-ray emitted from annular space, as well as the increase in the X-ray energy and intensity, were due to tearing and reconnection of internal magnetic field lines

References:

(1) Bostick, W.H., Nardi, V. and Prior, W. J. Plasma Phys., Vol 8 (1972) 7.

(2) Schonbach, K.H., Michel, L., and Fischer, H., Appl. Phys. Lett. 25 (1974) 547.

(3) Hirano, K., Yamamoto, T., Shimoda, K., Okabe, Y. and Wakabayashi, K., International Conf. on Plasma Phys. and Controlled Nucl. Fusion Research, CN. 47/D-IV-5-1 (1986) 583.

(4) Masoud, M.M., Soliman, H.M. and El-Khalafawy, T.A., 15th European Conf. on Controlled Fusion and Plasma Heating, Vol. 12 B part 1 (1988) 1275.

(5) Alexin, V.S., Souprunenko, V.A., soukhomlin, E.A. and Reva, N.I., Soviet Phys. Tech. Phys. 36 (1965) 620.

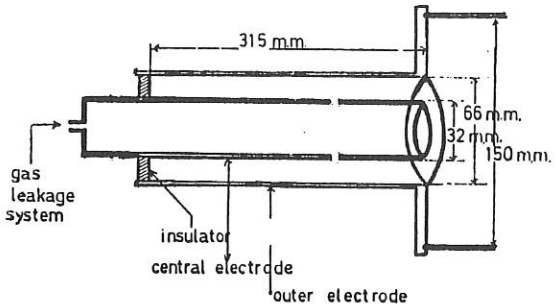

Figure (1) Schematic diagram of the experiment

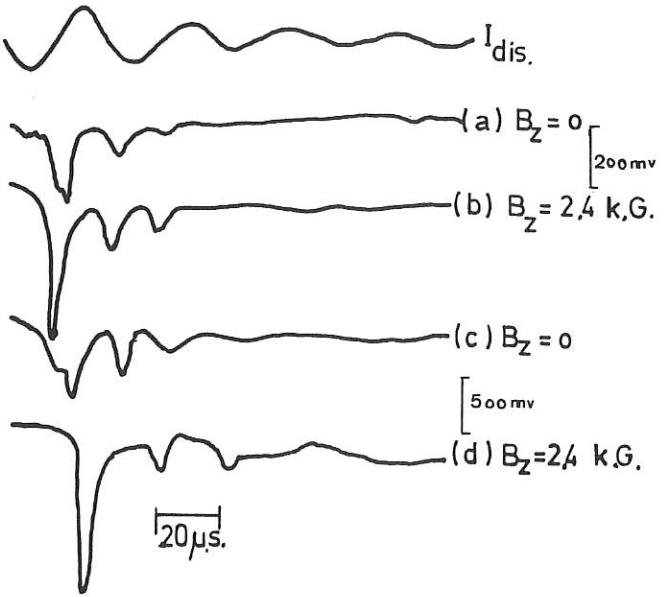

Figure (2) X-ray probe out'put signals,
(a)& (b) off-axis , (c) & (d) on-axis

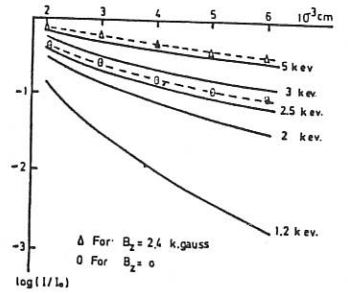

Figure (3) X-ray intensity as a function of absorber thickness, calculated values are solid curves, measured are dashed.

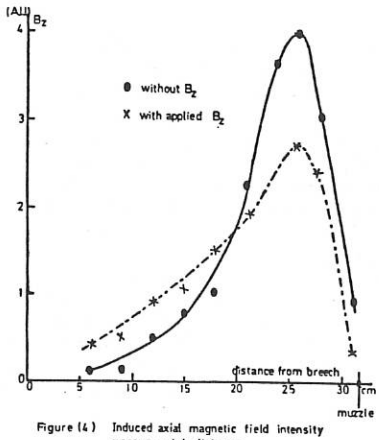

Figure (4) Induced axial magnetic field intensity versus axial distance

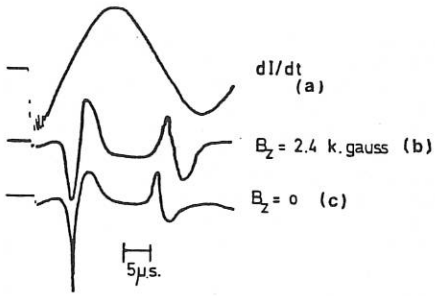

Figure (5) Axial magnetic field traces (b) & (c), tearing and reconnection case, (a) is dI/dt trace.

SPECIFIC OPERATIONAL MODES OF HIGH-CURRENT PINCH DISCHARGES

M.Sadowski, A.Szydłowski, and J.Żebrowski

Soltan Institute for Nuclear Studies
05-400 Otwock-Świerk, Poland

Abstract: The paper reports on experimental studies of the pinch formation and emission characteristics of the plasma-focus (PF) discharges performed under different operating conditions.

Introduction

Numerous experiments carried out with high-current pinches of different types have demonstrated that some physical phenomena appearing in such discharges have not been investigated enough.

With an increase in energy supplied to Z-pinch devices, one can observe an evident decrease in pinch stability and a lack of the neutron production scaling [1-2]. For large plasma-focus (PF) facilities one also finds that the neutron yield saturates or even decreases when the initial energy input is increased above certain limits [3]. It is usually observed that the larger is nominal energy stored in a condenser bank, the smaller is a fraction of a discharge current flowing through a plasma sheath accelerated within an interelectrode region [1-3].

Varying experimental conditions, e.g., changing the working gas pressure, one can realize different operational modes of high-current pinch discharges. The main aim of this paper has been to study characteristics of some selected specific modes, and in particular to investigate the pinch formation in PF discharges under various operating conditions.

Experimental setup

The studies have been carried out with the MAJA-PF facility [4] modified in order to enable different experimental conditions to be realized. The facility has been equipped with a 72-mm-dia. inner electrode made of the copper tubing, and a 124-mm-dia. outer electrode of the squirrel-cage type, which consisted of 16 copper rods of 10 mm in diameter. The two electrodes were 298 mm long. The main insulator, embracing the beginning of the inner electrode,was initially made of a pyrex tube of 75 mm in length. In a modified version that insulator has been replaced by a ceramic tubing equipped with a collar mounted in contact with the main insulation of the collector plates, and the inner electrode has been plugged with a tungsten insert.

Static initial gas conditions have been realized by filling the whole experimental chamber with pure deuterium under pressure ranging from 0.8 to 4.0 Torr. In order to form dynamic initial gas conditions, use has been made of a fast-acting electromagnetic valve placed inside the inner

electrode. The gas streams injected into the interelectrode gap have been formed by special nozzles and an additional gas reflector made of a glass tubing outside the outer electrode. Two different versions of the nozzles have been applied. In version A the nozzles directed deuterium streams towards the insulator, and in version B - those streams were injected far away from the insulator surface.

Experimental results

In all the experiments under consideration the main discharge has been supplied directly from a 96 μF condenser bank charged up to 35 kV. For the gas-puffed mode, before the main discharge, the electromagnetic gas valve has been powered by an auxiliary condenser bank through a pulsed transformer.

A comparative analysis of discharge voltage and current-waveforms, as registered for different PF shots, has shown that for the static initial gas conditions (at pressures 0.8 - 4.0 Tr D_2) those waveforms have been similar to typical traces observed for other PF facilities. Only at lower values of the initial pressure, for so-called ionic operational mode, more distinct spikes have been observed within voltage pulses accompanying the current pecularity.

For the gas-puffed operation, with the injection of about 1 cm^3 of deuterium at pressure of 1.8 MPa, the voltage- and current traces have not discerned far from those observed for standard PF-discharges. It has however been found that for such an operational mode the voltage spikes are considerably higher, and the insulator is sometimes broken by several discharges.

Observations of the X-ray emission, as performed with pinholes cameras, have shown that under optimized experimental conditions the pinches are symmetric and reproducible from the macroscopic point of view.

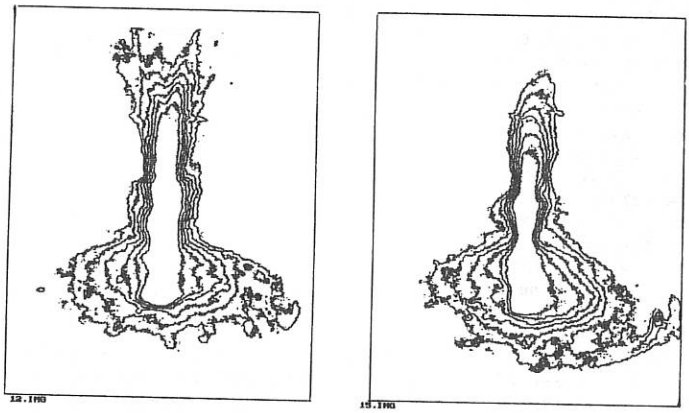

Fig.1. Contours of the soft X-ray emissivity from a pinch column, as observed for regular PF-discharges at p_o=1.5 Tr D_2. Bottom parts show the emission from the front surface of the inner electrode.

An analysis of the emissivity contours demonstrates however distinct irregularities and microscopic irreproducibility, as shown in Fig.1. It can also be noted that the X-radiation emitted from the insert plugging the inner electrode shows sometimes radial tracks of the current filaments.

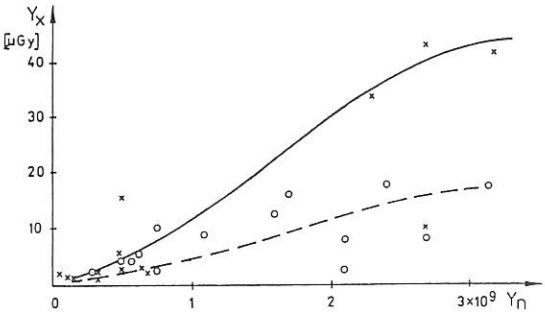

Fig.2. X-ray emission vs. neutron yield for PF shots under static (o) and dynamic (x) initial gas conditions.

Simultaneous measurements of X-rays and neutrons have demonstrated that for the gas-puffed mode the X-ray emission is considerably higher than that for shots under static initial gas conditions, as shown in Fig.2.

Detailed measurements of the neutron emission for the gas-puffed mode have shown that for the system in question one can find the optimum time delay between the firing of the fast gas valve and the triggering of the main discharge. The results of such measurements have been presented in Fig.3.

During recent experiments with MAJA-facility particular attention has been paid to the studies on a fine structure of the pinches. Numerous observations of hot-spots and quasi-axial filaments inside a dense plasma region have been performed. An example of a double structure of the pinch has been shown in Fig.4. It has been observed that such filamentary pinches are characterized by evidently higher X-ray and neutron emission.

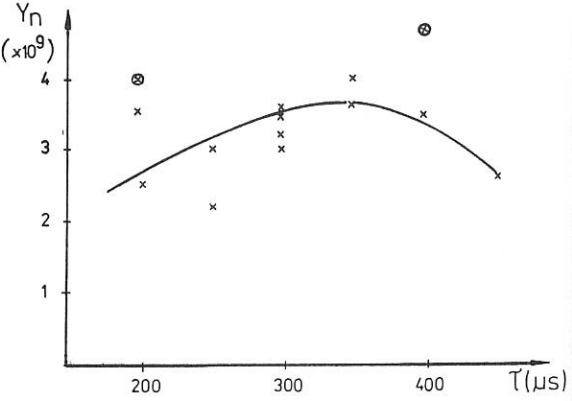

Fig.3. Neutron yield vs. time delay for the gas-puffed operational mode at initial background pressure p_o=0.8 Tr D_2 and charging voltage U_o=35 kV (x) or 37.5 kV (o).

Results of the ion emission measurements, as performed with MAJA facility at lower energetics as well as those obtained recently, demonstrate that deuteron energy spectra observed for various operational modes, are different with regard to the range and slope. Taking into account also the neutron emission characteristics mentioned above, one can conclude about differences in the ion acceleration mechanisms.

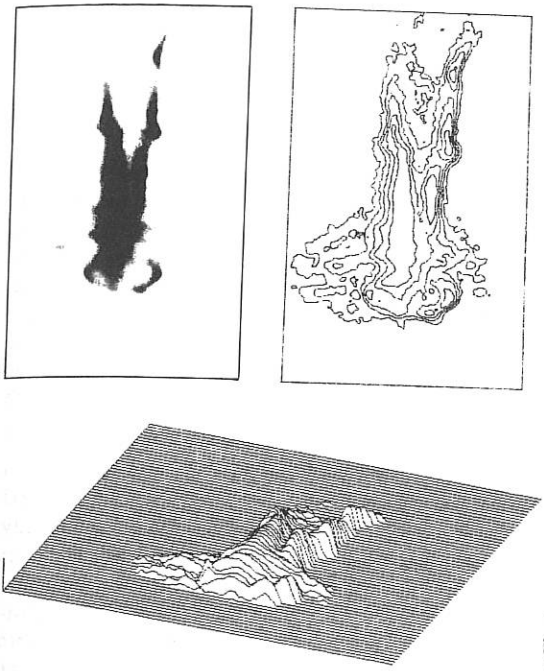

Fig.4. Double structure of a pinch column shown by the soft X-ray pinhole picture, and by corresponding contours of the emissivity and profiles of that.

Conclusions

From the experiments described above one can formulate the following conclusions:

1. Changing the initial gas conditions in the PF-type facility, one can realize operational modes characterized by a quasi-radial filamentation of the current sheath and/or a quasi-axial filamentation of the pinch column, which can be accompanied by an increase in the X-ray and neutron emission.
2. Measurements of X-rays, neutrons, and ions emitted from high-current pinches, as observed in the PF-type discharges, suggest that in various specific operational modes there are dominating different ion acceleration and neutron production mechanisms.
3. Studies of the pinch formation in the gas-puffed mode should be continued, in particular with large-scale PF-facilities and fast-acting high-pressure valves enabling the production of dense gas curtains before the breakdown.

Acknowledgements

The authors wish to thank Mr. E.Rydygier and Mr. P.Karpiński for technical assistance in running the experiments and in completion of the data.

References

1. Proc. 1987 Workshop on Plasma-Focus and Z-Pinch (Edit. Imperial College of Science & Technology, London 1988).
2. Proc. 1988 Z-Pinch & Plasma-Focus Workshop (Edit. Ecole Polytechnique, Nice 1988).
3. H.Herold, A.Jerzykiewicz, M.Sadowski, H.Schmidt; Nuclear Fusion 29 (1989) 1255.
4. M.Sadowski, J.Baranowski, L.Jakubowski et al.; Proc. 16th European Conf. Contr. Fusion & Plasma Phys.(Venice 1989), ECA Vol. 13B, Part II, p.779.

FIELD-REVERSED CONFIGURATIONS: A SEARCH FOR A VIABLE REACTOR OPTION

Manfred Heindler and Winfried Kernbichler
Graz University of Technology, Petersgasse 16, A-8010 Graz, Austria

Recent studies of Field-Reversed Configurations (FRC) with β-values in the range of 50 to 100% lead to several optimistic conclusions regarding the reactor potential of this alternative magnetic confinement concept. A comparison between the features related to D-T and to D-^{3}He as the primary reactor fuel, respectively, clearly indicates the avantages of D-^{3}He over D-T. A similar comparison between steady state vs. pulsed operation emphasizes the need for a steady-state concept. Frequent start-up procedures would be particularly detrimental for D-^{3}He as long as they rely on a transition from D-T to D-^{3}He, with the pertinent tritium contamination which would abolish most of the benefits of the "clean" fuel alternative.

Such a field reversed configuration does not only offer the potential for a compact fusion device with high power density, but also several additional benefits, e.g. the cylindrical geometry of the concept, the divertor action of the open field lines and the possibility for direct energy conversion of the charged particle flow. An evaluation of the difficulties related to the realization of these potential benefits is therefore required, in partiuclar because many vital questions need to be answered. The answer to open questions regarding the stability of large-S devices, the transport mechanisms , the start-up scenarios etc will require further theoretical research in this field combined with an experimental "next step" in the direction of a steady-state FRC.

Our investigation uses a profile-averaged computer model to simulate steady-state operation of an FRC. In this context much care is given to radiation losses, confinement expressions, fusion reactions among the fast and thermal plasma constituents, and to loss and slowing-down of fast fusion products. Our computations reveal the basic properties of fusion plasmas in an FRC. The identification of ignition windows in the temperature-density space and of upper and lower bounds of power densities, neutron production, tritium inventory, wall loading and current requirement is among the results that will be presented. The sensitivities of these results to changes in size, magnetic field strength, reversal factor, confinement properties and the fuel mix rate will be discussed in order to clarify the influence of parameter assumptions. This is particularly important in the context of FRCs since reactor studies based on this alternative concept necessarily rely on extensive extrapolations from the present state of the art.

SELF-SIMILAR DYNAMICS OF FIBER INITIATED HIGH-DENSITY Z-PINCH

M.A.Liberman, A.B.Bud'ko, F.F.Kamenets

Institute for Physical Problems
ul.Kosygina, 2. Moscow 117334, USSR

The general interest to the fiber-initiated high-density Z pinches after the first successful experiments [1-3] stimulated active studies of structure,dynamics and stability of dense Z pinches.The most intriguing feature of these experiments is the observed remarkable stability of the Z pinch plasma.To study the stability at least 1D fluid model is needed.According to [1-3] the pinches are stable and plasma slowly expands as current increases.The velocity of the plasma expansion increase rapidly beginning from the instant when dI/dt=0,and pinch became unstable.As these pinches appear to be stable for many Alfven transit times τ_a ,they represent essentially subsonic plasma flows.The first step to study the dynamics of dense pinches is the adequate description of the unperturbed plasma motions.The required fluid model of the pinch plasma should take into account dissipations because the time variation of the pinch flow is comparable to the Ohmic heating time.Hence,we use the full system of one-fluid two-temperature MHD,neglecting inertia and viscosity,but retain the other dissipative terms that is the terms describing the transverse heat conductivity,the thermogalvanomagnetic effects,called Nernst and Ettingshausen effects,and electron-ion temperature relaxation,all of them being of the same order.

The dense high temperature plasma produced at the developed stage of the fiber initiated Z pinch is expected to be fully magnetized,with both $\Omega_e\tau_e$ and $\Omega_i\tau_i$ much greater than unity [2].For a cylindrical symmetric motion of a fully magnetized plasma the full system takes the following form:

$$\frac{\partial \rho}{\partial t} + \frac{\partial (r\rho u)}{r\partial r} = 0 , \tag{1}$$

$$\frac{\partial}{\partial r}(nT_i + nT_e) - \frac{B_\varphi}{4\pi r}\frac{\partial rB_\varphi}{\partial r} \tag{2}$$

$$\frac{\partial B_\varphi}{\partial t} + \frac{\partial}{\partial r}(uB_\varphi) = \frac{\partial}{\partial r}\left\{\upsilon_m\left[\frac{1}{r}\frac{\partial (rB_\varphi)}{\partial r} + \frac{3\beta_e B_\varphi}{4T_e}\frac{\partial T_e}{\partial r}\right]\right\} , \tag{3}$$

$$\frac{3}{2} n \left(\frac{\partial T_i}{\partial t} + u \frac{\partial T_i}{\partial r} \right) + \frac{nT_i}{r}\frac{\partial (ru)}{\partial r} \tag{4}$$

$$= \upsilon_m \left\{ \frac{1}{r}\frac{\partial}{\partial r}\left[\frac{n\beta_i}{\delta}\left(T_e/T_i\right)^{3/2} r \frac{\partial T_i}{\partial r} \right] + 3\Pi\,(n/R^2)\,(T_e - T_i) \right\},$$

$$\frac{3}{2} n \left[\frac{\partial}{\partial t}(T_e + T_i) + u \frac{\partial}{\partial r}(T_e + T_i) \right] + \frac{n(T_e + T_i)}{r}\frac{\partial (ru)}{\partial r}$$

$$= \upsilon_m \left\{ \frac{1}{r}\frac{\partial}{\partial r}\left[\frac{n\beta_i}{\delta}\left(T_e/T_i\right)^{3/2} r \frac{\partial T_i}{\partial r} + 2.33\, n\beta_e r \frac{\partial T_e}{\partial r} \right.\right. \tag{5}$$

$$\left.\left. + \frac{3\beta_e B_\varphi}{16\pi}\frac{\partial (rB_\varphi)}{\partial r} \right] + \frac{1}{4\pi r^2}\left[\frac{\partial (rB_\varphi)}{\partial r} \right]^2 + \frac{3\beta_e B_\varphi}{16\pi T_e r}\frac{\partial (rB_\varphi)}{\partial r}\frac{\partial T_e}{\partial r} \right\} .$$

Here $\upsilon_m = c^2/4\pi\sigma_\perp$, $\beta_{e,i} = 8\pi n T_{e,i}/B_\varphi^2$, $\delta = (2m_e/m_i)^{1/2}$, $\Pi = 4e^2N/(m_i c^2)$, where N is linear density. The electron heat conductivity term in Eq.(5) is retained because of sharper gradient of electron temperature near the boundary.

Solutions of Eqs.(1)-(5) can be presented as separable functions of time and self-similar coordinate $\xi = r/R(t)$:

$$\begin{aligned} u(r,t) &= \frac{dR}{dt}\,\xi , \\ n(r,t) &= n_0\,\alpha^{-2}(t)\,N(\xi), \\ T_{e,i}(r,t) &= T_0\,\alpha^{-2\varkappa}(t)\,\theta(\xi), \\ B_\varphi(r,t) &= B_0\,\alpha^{-1-\varkappa}(t), \end{aligned} \tag{6}$$

where $\alpha(t) = R(t)/R_0 = (1+2\lambda^2 t/t_0)^{-1-3/2\varkappa}$, $\varkappa = (2\zeta+2)/(2\zeta+3)$, λ^2-the dimensionless parameter related to the magnetic Reynolds number Rm. The total current has also power-law time

dependence: $I(t) \simeq (1+2\lambda^2)^{(\zeta+1)/\zeta}$.

Comparing the expressions for $I(t)$ and $\alpha(t)$ one can obtain the relation

$$R(t) = R_0 \, (1+2\lambda^2 t/t_0)^{1/2} / I(t)^{3/2}.$$

This relation is independent of ζ and show the tendency for the radius increase when the current is decreasing.

From (6) it follows that, provided $\zeta > 0$ and $\zeta < -3/2$, the solutions correspond to the self-similar compression with the increasing current. The case $-3/2 < \zeta < 0$ corresponds to the self-similar pinch expansion with the increasing ($-3/2 < \zeta < 0$) and decreasing ($-1 < \zeta < 0$) current.

Here we consider the self-similar solutions corresponding to a stationary equilibrium ($\zeta = -3/2$). Depending on the value of $\lambda^2 = Rm$ there exists two types of solutions. Solutions corresponding to $Rm > 2.5$ are shown to correspond to a thermally isolated Z pinch with density and heat flux vanishing at the boundary [4] (fig.1). Lesser values $Rm < 2.5$ refer to solutions with non-vanishing density and heat flux, which can be interpreted as describing a gas embedded Z pinch [4] (fig.2).

From the inequality $Rm > 2.5$ we find for the constant radius of a Z pinch

$$R \geqslant R_{min} = 18.5 \, \frac{(N(10^{18} sm^{-3}))^{3/4}}{I(MA)\left[\dot{I}(MA/100ns)\right]^{1/2}} \, \mu m \qquad (7)$$

Therefore, substituting in Eq.(7) parameters of the NRL experiment [2] $N=5\cdot10^{18} sm^{-1}$, $I=0.5MA$, $\dot{I}=0.5MA/130ns$, we obtain the estimate for the minimal radius of the stationary pinch: $R_0 \simeq 200 \mu m$, which is approximately the value observed in [2].

The obtained self-similar solutions can be used as a zero-order approximation to calculate the growth rates the Rayleigh-Taylor and internal modes of instabilities. The most dangerous instabilities in pinches with a sharp edge are the surface RT modes [5]. The rapid growth of the instabilities starting from the moment $dI/dt=0$ as well as stability of an early stage of the motion can be related to the change of the sign of the particle acceleration near the pinch edge, resulting in the condition for RT instability: $\partial\rho/\partial r<0$, $a(r)<0$, a being acceleration of the particle.

1. Scudder D.W. Bull.Am.Phys.Soc. 30, 1408 (1985).
2. Sethian J.D. et.al. Phys.Rev.Lett. 59 , 892 (1987).
3. Hammel J.E. and Scudder D.W. Proc.14th Eur.Conf. on Contr.Fusion and Plasma Phys. (EPS,Budapest) part 2, 450 (1987).
4. Bud'ko A.B. et.al. Journ of Plasma Phys.and Contr.Fusion,in press.
5. Bud'ko A.B. et.al. Zh.Eks.Teor.Fiz. 96 , 140 (1989).

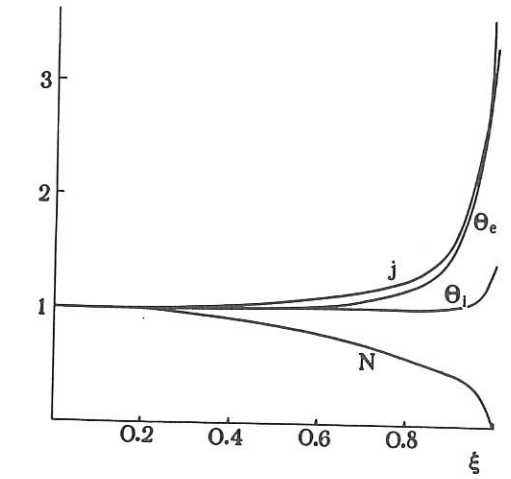

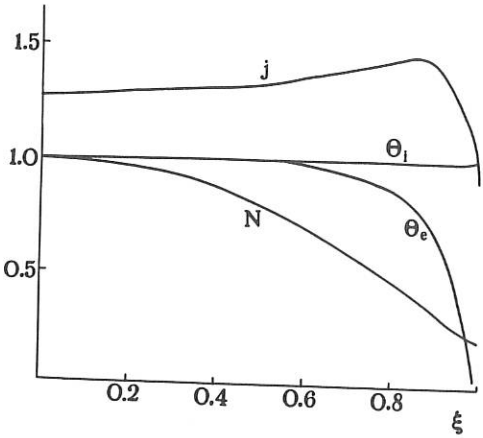

IMPROVED UNDERSTANDING OF CURRENT DRIVE AND CONFINEMENT IN SPHEROMAKS*

R. M. Mayo, F. J. Wysocki, J. C. Fernández, I. Henins, and G. J. Marklin

Los Alamos National Laboratory, Los Alamos, NM 87545

Typical spheromak parameters from the CTX 0.67m Mesh Flux Conserver (MFC) were $\tau_E \sim$ 0.017ms, $\tau_{B^2} \sim$ 0.66ms, and $T_e \sim$ 70eV, at 0.38T.[1] A reduction in field errors was achieved by replacing the MFC with a 0.60m solid wall flux conserver. The new configuration was not edge dominated (as evidenced by a positive scaling of τ_{B^2} with T_e). Confinement parameters increased to $\tau_E \sim$ 0.18ms, $\tau_{B^2} \sim$ 2ms, and $T_e \sim$ 150eV.[2] This dramatic improvement in confinement was a direct result of the reduction of field errors associated with the replacement of the MFC with the solid flux conserver, a change prompted by the edge helicity dissipation model of Jarboe and Alper.[3]

The edge helicity dissipation model,[3] in which most of the magnetic helicity is dissipated on open flux at the resistive plasma edge, has been successfully applied to the CTX-MFC,[1] other spheromaks,[4] and RPF's.[5] In the MFC, the neutral hydrogen fill pressure (used for refueling) accounts for the globally dominant edge plasma resistance (through the Paschen breakdown condition in H_2),[1] so that the plasma resistivity comes mainly from electron-neutral collisions.[1,4] In spheromaks, a plasma current-density relaxation mechanism attempts to maintain a minimum energy state[7] ($\lambda = \mu_o j / B$ = spatial constant). Relaxation current-drive is associated with the observed anomalously high T_i (often $T_i \gtrsim T_e$).[4,6] The high ion temperatures and the large inventory of neutrals at the edge suggest that charge exchange and the consequent escape of hot neutrals represents the greatest contribution to plasma energy dissipation.[1,4,6]

We intend to further explore the nature of this current-drive mechanism by employing the edge helicity dissipation model and the standard CTX–MFC equilibrium model[8] to decaying MFC discharges. We seek to predict the amount of current-drive attributable to the decay of magnetic flux and to relaxation currents. We will demonstrate that the term $\vec{v} \times \vec{B}$ in the generalized Ohm's law cannot contribute to parallel current drive making it necessary to invoke some other (non-single fluid MHD) effect to produce the observed spheromak current drive.

In warm ($T_e \gtrsim$ 50eV), non-radiation dominated spheromak discharges, deviations from minimum energy occur over long periods of time allowing relaxation current drive to provide flux sustainment. In this condition, a large classical resistivity gradient (small at the plasma center due to high T_e, and large at the edge due to electron neutral collisions)[1,4] results in a λ gradient. Since this situation represents a divergence from the state of minimum energy, one would expect the plasma to attempt to relax (flatten) the λ profile to again approach minimum energy. Spheromak experiments show evidence of such a continuous relaxation mechanism[1,4,6,9] in the form of current drive assist at the edge and anti-current drive at the center (*i.e.* anomalous loop voltage).

The magnitudes of anti-current drive and current drive assist, as well as their dependence on equilibrium parameters are under investigation here. In particular, we are interested in the contributions to the observed plasma current (inferred from the effective electric field, $\vec{E}_{eff} = \eta\vec{j}$) from the real electric field ($\vec{E}$) in the plasma and other components of Ohm's law

$$\vec{E} + \vec{v} \times \vec{B} + \vec{\varepsilon} = \eta\vec{j} \equiv \vec{E}_{eff} \tag{1}$$

where $\vec{\varepsilon}$ is the term that incorporates all other contributions to Ohm's law (*i.e.* $\vec{j} \times \vec{B}$, ∇p_e, ...).

*This work is supported by the Los Alamos National Laboratory Institutional Support Research fund.

The term $\vec{E}_{eff} = \eta\vec{j}$ in Eq. 1 represents the dissipation of magnetic helicity,[3] $\dot{K} = \frac{dK}{dt} \equiv -2\int \vec{E}\cdot\vec{B}\,dV$ where the integration is over the entire plasma volume. From Eq.(1), we get

$$\dot{K} = -2\int \eta\vec{j}\cdot\vec{B}\,dV + 2\int \vec{\varepsilon}\cdot\vec{B}\,dV \tag{2}$$

which indicates there can be no contribution to local parallel current drive from the $\vec{v}\times\vec{B}$ term. By Taylor's hypothesis,[10] it is assumed that $|\int \vec{\varepsilon}\cdot\vec{B}\,dV\,| (\sim 0) \ll |\int \eta\vec{j}\cdot\vec{B}\,dV|$, so that only "true (electron collisional) resistivity" dissipates helicity. (Note that only the total volume integral of the parallel component, $\varepsilon_{\|}$, vanishes; there may be non-vanishing local contributions.) This means that locally $\vec{E}\cdot\vec{B} \neq \eta\vec{j}\cdot\vec{B}$, in general. It is only these quantities integrated over the entire plasma volume that must balance. We can then reduce $\dot{K}$ to $\dot{K} = -2\int \vec{E}_{eff}\cdot\vec{B}\,dV$.

In the MFC, considering measured T_e profiles which are peaked near the magnetic axis and edge neutral densities which are large (and dominate edge resistivity), $\vec{E}_{eff}$ should be large at the plasma edge and small in the center plasma volume.[1,4,6] Now we can use the edge dominated helicity decay model to evaluate[1] $\langle\vec{E}_{eff}^{edge}\rangle_{pol} \equiv \frac{-\dot{K}}{2V_{edge}\langle B_{edge}\rangle} \simeq \frac{-\dot{K}}{2L\dot{\psi}_{edge}}$ which is strictly correct for small ψ_{edge}, the open flux. Here L is the edge poloidal path length. The notation $\langle\vec{E}_{eff}^{edge}\rangle_{pol}$ indicates an edge volume-average of $\vec{E}_{eff}$ which is parallel to the edge $\vec{B}$ and almost entirely in the poloidal direction. From Faraday's law, $\vec{\nabla}\times\vec{E} = -\partial\vec{B}/\partial t$, applied to the edge flux surface, to define $\langle\vec{E}_{\|}^{edge}\rangle_{pol} \equiv -\frac{1}{L}\dot{\phi}_{tor}$. The notation $\langle\vec{E}_{\|}^{edge}\rangle_{pol}$ denotes the edge surface average of $\vec{E}$ (the real electric field) which is approximately parallel to the edge $\vec{B}$ and entirely in the poloidal direction. The ratio,

$$\frac{\langle\vec{E}_{eff}^{edge}\rangle_{pol}}{\langle\vec{E}_{\|}^{edge}\rangle_{pol}} = \frac{\dot{K}}{2\psi_{edge}\dot{\phi}_{tor}} \tag{3}$$

only depends on functions of the plasma equilibrium and their time derivatives. Without loss of generality, we can write each of these in terms of the toroidal current, I_{tor}, and a function of a single profile parameter, α. The single parameter profile model has been seen to be a good one for the CTX–MFC spheromak.[8] The factors in Eq. (3) may be expanded in the following way

$$\begin{aligned} K = f(\alpha){I_{tor}}^2, \dot{K} &= 2f(\alpha)I_{tor}\dot{I}_{tor} + f'{I_{tor}}^2\dot{\alpha}, \psi_{edge} = p\psi_{pol} = pm(\alpha)I_{tor} \\ \phi_{tor} &= g(\alpha)I_{tor}, \dot{\phi}_{tor} = g(\alpha)\dot{I}_{tor} + g'I_{tor}\dot{\alpha} \end{aligned} \tag{4}$$

where p is the fraction of open (edge) poloidal flux, $p = \psi_{edge}/\psi_{pol}$, $\zeta' \equiv \frac{d\zeta}{d\alpha}$, and $\dot{\zeta} \equiv \frac{d\zeta}{dt}$. Note that the function $g(\alpha)$ is just $\mu_o/\langle\lambda\rangle(\alpha)$. p will be considered constant in time, which has been shown[1] to be a reasonable assumption for the CTX–MFC experiment. Eq. (3) then becomes

$$\frac{\langle\vec{E}_{eff}^{edge}\rangle_{pol}}{\langle\vec{E}_{\|}^{edge}\rangle_{pol}} = \frac{f(\alpha)}{pg(\alpha)\,m(\alpha)}\,\frac{(1+\frac{1}{2}\frac{f'(\alpha)}{f(\alpha)}\mathcal{T}_{I_{tor}}\dot{\alpha})}{(1+\frac{g'(\alpha)}{g(\alpha)}\mathcal{T}_{I_{tor}}\dot{\alpha})} \tag{5}$$

where $\mathcal{T}_{I_{tor}} = I_{tor}/(\dot{I}_{tor})$ (≤ 0 for a decaying plasma). For the CTX–MFC spheromak α is defined by the linear $\lambda(\psi)$ model,[8] $\bar{\lambda}(\psi) = \bar{\lambda}[1+\alpha(2\psi-1)]$ where ψ is the normalized flux function (1 at the magnetic axis and 0 at the separatrix). $\bar{\lambda}$ is the average of $\lambda(\psi)$. The difference between $\bar{\lambda}$ and $\langle\lambda\rangle$ is of order α^2 and quite small (cf: Ref. 1).

In the limit $\dot{\alpha} \ll |\,{\mathcal{T}_{I_{tor}}}^{-1}\,|$ (slow α evolution due to strong relaxation clamping the $\lambda(\psi)$ profile), and since $\frac{f'(\alpha)}{f(\alpha)}$ and $\frac{g'(\alpha)}{g(\alpha)}$ are of order 1, Eq. (5) reduces to

$$\left.\frac{\langle\vec{E}_{eff}^{edge}\rangle_{pol}}{\langle\vec{E}_{\|}^{edge}\rangle_{pol}}\right|_{\dot{\alpha}\sim 0} \sim \frac{f(\alpha)}{pg(\alpha)m(\alpha)} = \frac{1}{p}\frac{K}{\phi_{tor}\psi_{pol}} \quad . \tag{6}$$

The ratio $\frac{K}{\phi_{tor}\psi_{pol}}$ is numerically calculated to be between 1.04 and 1.08 for all positive α (*i.e.* during decay), thus a simple result is obtained; $\left.\frac{\langle \vec{E}_{eff}^{edge}\rangle_{pol}}{\langle \vec{E}_{\parallel}^{edge}\rangle_{pol}}\right|_{\dot{\alpha}\sim 0} \sim \frac{1}{p}$. For the 0.67m CTX mesh, $p \sim 0.25$, so $\left.\frac{\langle \vec{E}_{eff}^{edge}\rangle_{pol}}{\langle \vec{E}_{\parallel}^{edge}\rangle_{pol}}\right|_{\dot{\alpha}\sim 0} \sim 4$. Since this ratio is > 1, we conclude from Eq. (1) that there is a substantial contribution to parallel current drive from non-single fluid MHD effect(s). (*i.e.* $\vec{\varepsilon}$ must have a parallel component, and $\langle \vec{\varepsilon}_{\parallel}^{edge}\rangle_{pol} \gtrsim 3\langle \vec{E}_{\parallel}^{edge}\rangle_{pol}$ for the 0.67m CTX mesh.) The small $\dot{\alpha}$ case represents the strong relaxation limit. Since $f'/f > 0$ and $g'/g < 0$, $\langle \vec{E}_{eff}^{edge}\rangle_{pol}/\langle \vec{E}_{\parallel}^{edge}\rangle_{pol} \sim 4$ is an upper bound to this ratio.

Applying a similar formalism to $\dot{W}$ ($W = \frac{1}{2\mu_o}\int B^2\, dV$), we can make predictions regarding central electric fields and anti-current drive. We explicitly separate the edge and center contributions, $\dot{W} = -\int_{center} \vec{E}\cdot\vec{j}\, dV - \int_{edge} \vec{E}\cdot\vec{j}\, dV$. The only assumption here is that the Poynting flux through the separatrix is zero. For a plasma with an constant volume, this assumption is valid. Consistent with our previous integral approximations, defining $W = r(\alpha){I_{tor}}^2$ where $r(\alpha) = \frac{\langle\lambda(\alpha)\rangle}{2\mu_o} f(\alpha)$, and realizing $I_{pol_{edge}} = \frac{\langle\lambda\rangle_{edge}}{\mu_o}\psi_{edge}$, we arrive at the expression

$$\frac{\langle \vec{E}_{\parallel}^{center}\rangle_{tor}}{\langle \vec{E}_{\parallel}^{edge}\rangle_{pol}} = \frac{L}{\pi\mathcal{R}(1-p)}\frac{r}{g}\left[\frac{1+\frac{1}{2}\frac{r'}{r}\mathcal{T}_{I_{tor}}\dot{\alpha}+(\frac{3}{4}\alpha-1)\frac{pm}{2r}(1+\frac{g'}{g}\mathcal{T}_{I_{tor}}\dot{\alpha})}{1+\frac{g'}{g}\mathcal{T}_{I_{tor}}\dot{\alpha}}\right] \tag{7}$$

where $\mathcal{R}$ is the spheromak major radius. In obtaining Eq.(7) it was necessary to evaluate $\langle\lambda\rangle_{edge}$

$$\langle\lambda\rangle_{edge} = \frac{1}{\psi_{edge}}\int_o^p \lambda(\alpha)\, d\psi = 4\bar{\lambda}\int_o^{\frac{1}{4}}[1+\alpha(2\psi-1)]\, d\psi = \bar{\lambda}(1-\frac{3}{4}\alpha) \quad . \tag{8}$$

As an example, again take the $\dot{\alpha} = 0$ case (large relaxation) with $p = 1/4$, $L = 2.3$m, $\mathcal{R} = 0.5$m, and $\alpha = 0.5$ (nominal values for CTX 0.67m mesh[1]), then Eq.(7) gives $\langle \vec{E}_{\parallel}^{center}\rangle_{tor}/\langle \vec{E}_{\parallel}^{edge}\rangle_{pol}$ is 2.6. At the center $\eta\vec{j} \sim 0$ so from Eq.(1), $\langle \vec{\varepsilon}_{\parallel}^{center}\rangle_{tor}/\langle \vec{E}_{\parallel}^{edge}\rangle_{pol} = -\langle \vec{E}_{\parallel}^{center}\rangle_{tor}/\langle \vec{E}_{\parallel}^{edge}\rangle_{pol} = -2.6$ or

$$\frac{\langle \vec{\varepsilon}_{\parallel}^{center}\rangle_{tor}}{\langle \vec{E}_{eff}^{edge}\rangle_{pol}} = \frac{\langle \vec{\varepsilon}_{\parallel}^{center}\rangle_{tor}}{\langle \vec{E}_{\parallel}^{edge}\rangle_{pol}}\frac{\langle \vec{E}_{\parallel}^{edge}\rangle_{pol}}{\langle \vec{E}_{eff}^{edge}\rangle_{pol}} = -\frac{2.6}{4} = -0.65 \quad . \tag{9}$$

So, in magnitude, the $\vec{\varepsilon}$ contribution to anti-current-drive at the center is on the same order as $\eta\vec{j}$ at the edge.

With the results of the above formalism (Eq.(5)), we can begin to explore more realistic experimental conditions. It will suffice to summarize our comparison with experimental conditions by examining several of the CTX–MFC conditions presented in Fernández, *et al.*[1] These conditions will be distinguished by the starting discharge number of the set. For brevity we'll limit our discussion to conditions 13715, 14168, 15804, and 16024, since these conditions span a wide range of parameters.

The results from these conditions are summarized in Table 1. The quantities $\alpha, \dot{\alpha}$, and $\mathcal{T}_K(= K/\dot{K})$ are taken from the figures in Ref. 1 listed in Table 1. The quantity $\mathcal{T}_{I_{tor}}$ is calculated from $\mathcal{T}_K$ in the following way $\mathcal{T}_{I_{tor}} = \frac{2\mathcal{T}_K}{1-\frac{r'}{7}\mathcal{T}_K\dot{\alpha}}$ which results from Eq.(4) and the definition of $\mathcal{T}_K$. The remaining quantities are determined from Eq's.(5), (1), and (9), respectively.

The condition 14168 represents the limit where relaxation current drive is weak or almost non-existent. This is a very cold and radiation dominated discharge. Here $\dot{\alpha}$ is very large and $\langle \vec{E}_{eff}^{edge}\rangle_{pol}/\langle \vec{E}_{\parallel}^{edge}\rangle_{pol}$ is small (~ 1) as we would expect for this type of plasma. Conditions 16024

Table 1: Summary of Results from Experimental Conditions from the CTX–MFC During Decay.

condition	Fig. # in Ref. 1	α	$\dot{\alpha}(\mathrm{ms}^{-1})$	τ_K(ms)	$\frac{\langle \vec{E}_{eff}^{edge} \rangle_{pol}}{\langle \vec{E}_{\|}^{edge} \rangle_{pol}}$	$\frac{\langle \vec{\varepsilon}_{\|}^{edge} \rangle_{pol}}{\langle \vec{E}_{\|}^{edge} \rangle_{pol}}$	$\frac{\langle \vec{\varepsilon}_{\|}^{center} \rangle_{tor}}{\langle \vec{E}_{\|}^{edge} \rangle_{pol}}$
14168	4	0.4–0.8	4.5	-0.45	1.2	0.2	-0.08
16024	3	0.4–0.8	0.85	-0.46	3	2	-1.5
13715	2	0.3–0.7	0.75	-0.7	2.8	1.8	-1.2
15804	12	0.4–0.6	0.43	-0.37	4	3	-2

and 13715 are quite similar to each other in $\dot{\alpha}$, but differ in τ_K by $\sim$ 50%. However, the ratio, $\langle \vec{E}_{eff}^{edge} \rangle_{pol} / \langle \vec{E}_{\|}^{edge} \rangle_{pol}$, for these two cases is nearly the same, indicating that τ_K does not influence the ratio as much as $\dot{\alpha}$ does. As well, these two conditions represent a significant relaxation effect in which the $\vec{\varepsilon}$ contribution to current drive is $\sim 2\langle \vec{E}_{\|}^{edge} \rangle_{pol}$. The condition 15804, with even smaller $\dot{\alpha}$, is more dominated by relaxation current drive. Notice here the τ_K is more like that of condition 16024, but $\dot{\alpha}$ is lower by a factor of two and the ratio, $\langle \vec{E}_{eff}^{edge} \rangle_{pol} / \langle \vec{E}_{\|}^{edge} \rangle_{pol}$, is larger. This again indicates a stronger $\dot{\alpha}$ than τ_K effect on the ratio.

Hence, we can see that for most experimental conditions, the $\vec{\varepsilon}$ contribution to current drive is significant and may even be dominant. The fact that $\dot{\alpha}$ effects are most important has physical interpretation. A large $\dot{\alpha}$ indicates a rapid deviation from the state of minimum energy. That $\dot{\alpha}$ is allowed to become large in any given discharge, is an indication that relaxation effects are not influencing the discharge progression. Discharges with smaller $\dot{\alpha}$ show significant relaxation current drive. We mean to suggest that these (small $\dot{\alpha}$) discharges do possess deviations from minimum energy; however, a relaxation mechanism is able to provide current drive with the appropriate profile dependence as to attempt a flattening of the λ profile. Though this mechanism does not succeed in returning the plasma to minimum energy ($\alpha = 0$), it does limit $\dot{\alpha}$ and, hence, the eventual α value.

As mentioned in Ref. 1, the edge helicity dissipation model also provides an estimate for the quantity of magnetic energy being dissipated by the relaxation mechanism, P_{relax}. As a fraction of the total magnetic energy decay rate, this is $\frac{|P_{relax}|}{|\dot{W}|} = 1 - \frac{|P_{ohm}|}{|\dot{W}|}$ where $W = \frac{1}{2\mu_o}\int B^2\, dV = \frac{\langle\lambda\rangle}{2\mu_o}K$ and $\dot{W} = \frac{\langle\lambda\rangle}{2\mu_o}\dot{K} + \frac{\langle\lambda\rangle'}{2\mu_o}K\dot{\alpha}$. The Ohmic dissipation is again limited to the edge where η is large so that $|\, P_{ohm}\,| = \int_{edge} \eta\vec{j}\cdot\vec{j}\, dV = \frac{\langle\lambda\rangle_{edge}}{2\mu_o}\dot{K}$. With $\langle\lambda\rangle/\bar{\lambda} = (1 + 0.23\alpha^2)/(1 + 0.15\alpha^2)$ and $\langle\lambda\rangle'/\langle\lambda\rangle = 0.46\alpha/(1 + 0.23\alpha^2)$, the result is

$$\frac{|\, P_{relax}\,|}{|\,\dot{W}\,|} = 1 - \frac{(1 - \frac{3}{4}\alpha)[\frac{1+0.15\alpha^2}{1+0.23\alpha^2}]}{1 + [\frac{0.46\alpha}{1+0.23\alpha^2}]\tau_K\dot{\alpha}} \quad . \tag{10}$$

Ignoring terms of order α^2 and taking $\dot{\alpha} = 0$ (strong relaxation), we find $\frac{|P_{relax}|}{|\dot{W}|} = \frac{3}{4}\alpha$, a slight modification to Eq.(10) of Ref. 1.

[1] J. C. Fernández *et al.*, Nucl. Fusion **28**, 1555 (1988).
[2] F. J. Wysocki *et al.*, submitted to Phys. Rev. Lett.
[3] T. R. Jarboe and B. Alper, Phys. Fluids **30**, 1177 (1987).
[4] R. M. Mayo *et al.*, Phys. Fluids B **2**, 115 (1990).
[5] B. Alper *et al.*, Plasma Physics and Controlled Fusion **30**, 843 (1988).
[6] J. C. Fernández *et al.*, Nucl. Fusion **30**, 67 (1990).
[7] J. B. Taylor, Reviews of Modern Physics **58**, 741 (1986).
[8] S. O. Knox *et al.*, Phys. Rev. Lett. **56**, 842 (1986).
[9] R. M. Mayo *et al.*, Nucl. Fusion **29**, 1493 (1989).
[10] J. B. Taylor, Phys. Rev. Lett. **33**, 1139 (1974).

DIFFUSION-DRIVEN CURRENTS IN A Z-PINCH

B. Lehnert

Royal Institute of Technology, S-10044 Stockholm, Sweden

Abstract In a Z-pinch plasma which is impermeable to neutral gas and sustained by an imposed axial electric field the recirculation of matter generates diffusion-driven toroidal (axial) and poloidal (transverse) "bootstrap-like" currents in the partially ionized boundary layer. This recirculation modifies the coupling between the magnetic field components which arises from anisotropic resistivity and the Taylor dynamo process.

Introduction Diffusion-driven "bootstrap-like" currents in the Z-pinch, including Extrap, have earlier been investigated for magnetically confined plasmas with internal particle and heat sources [1]. This paper considers a steady state being sustained by an imposed toroidal (axial) electric field, and by recirculation of plasma and neutral gas. There is a hot plasma core which is impermeable to neutral gas and surrounded by a partially ionized boundary layer, as shown in Fig.1. The radial diffusion across the magnetic field drives "bootstrap-like" currents. Here $r = a$ stands for the radius of the fully ionized core, ξ for the ionization rate, L_n for the penetration length of neutrals which is of the order of the thickness of the "ionization region", and x_b for the thickness of the "diffusion" region where $\xi \simeq 0$ [2].

Diffusion-Driven Currents A linear or large aspect ratio pinch is considered where a cylindrical frame (r,φ,z) is introduced with z along the pinch axis. The electric field $\underline{E} = (E_r,0,E_z)$ has an imposed axial component $E_z = E_o = \text{const}$. The current density $\underline{j} = (0,j_\varphi,j_z)$ and magnetic field $\underline{B} = (0,B_\varphi,B_z) = B\hat{\underline{B}}$ have components in the toroidal (axial) and poloidal (transverse) directions. Part of the component B_z consists of an axial field B_{za} being imposed by external sources. A plasma of electron density n and isotropic temperature T is assumed where the resistivity has the perpendicular and parallel components $\eta_\perp \simeq \eta$ and $\eta_\parallel \equiv \eta/f$ with respect to the unit vector $\hat{\underline{B}}$. In the partially ionized boundary layer there is neutral gas of density n_n, and temperature $T_n \simeq T$. Conventional MHD equations are used in this paper.

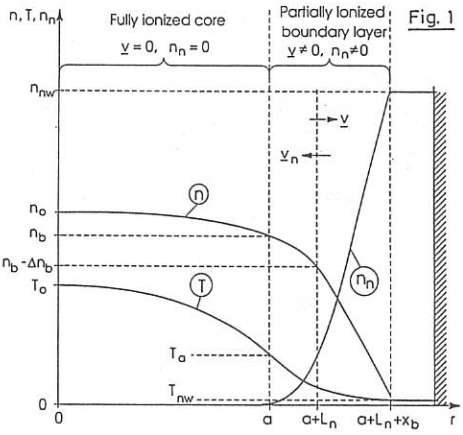

Fig. 1

The components of Ohm's law in the φ and z directions yield

$j_\varphi = j_{\varphi E} + j_{\varphi v}$ and

$j_z = j_{zE} + j_{zv}$ where

$$j_{\varphi E} = (f - 1)B_\varphi B_z E_o/\eta(B_\varphi^2 + B_z^2) \qquad j_{\varphi v} = - B_z v/\eta \tag{1}$$

$$j_{zE} = B_\varphi^2 + fB_z^2)E_o/\eta(B_\varphi^2 + B_z^2) \qquad j_{zv} = B_\varphi v/\eta \tag{2}$$

Here the contributions $j_{\varphi E}$ and j_{zE} are driven by the imposed electric field E_o, and the contributions $j_{\varphi v}$ and j_{zv} are the "bootstrap" currents driven by the radial diffusion velocity $\underline{v} = (v,0,0)$. The latter differs from zero only in the boundary layer where the plasma and neutral gas fluxes are related by $\Gamma \equiv nv = -n_n v_n$ with $\underline{v}_n = (v_n,0,0)$ standing for the radial diffusion velocity of the counter-stream of neutral gas.

We limit ourselves to a boundary layer thickness $L_n + x_b$ of Fig.1 which is much smaller than the radius $r = a$ of the fully ionized core. Then the toroidal (axial) bootstrap current becomes

$$J_{zb} = \mu_o F_b J_a \; ; \qquad F_b = \int_a^{a+L_n+x_b} (v/\eta)dr \tag{3}$$

provided that $J_{zb} \ll J_a$ where J_a is the total pinch current in the core $r \leqslant a$. Analogously the total poloidal (transverse) bootstrap current becomes

$$J_{\varphi b} = - B_{za} F_b/L = B_{zb} L/\mu_o \tag{4}$$

where $B_{za} = B_z(r = a)$, L is the axial pinch length, and B_{zb} the magnetic field due to the current $J_{\varphi b}$.

Combination of the plasma momentum balance equation with Ohm's law yields

$$-2kd(nT)/dr \simeq \left[m_i \xi_{in} n(n + n_n) + (B^2/\eta)\right]v \tag{5}$$

where $\xi_{in} = \sigma_{in}(3kT/m_i)^{1/2}$, σ_{in} stands for the ion-neutral collision rate, and we restrict ourselves to cases where the electron-ion collision frequency is much smaller than the electron gyro frequency. We assume the neutral density n_n to be negligible at the edge $r = a$, and the plasma density $n \simeq n_b \simeq n_o$ to be approximately constant within all parts of the boundary layer where the temperature T is high enough for v/η to give noticeable contributions to the bootstrap integral F_b. Then eqs. (3) and (5) result in

$$F_b \simeq - \int_a^{a+L_n+x_b} f(T) \frac{dT}{dr} dr = \int_{T_{nw}}^{T_a} f(T)dT \tag{6}$$

where $T_a = T(r = a)$, $T_{nw} = T(r = a + L_n + x_b)$,

$$f(T) = 2kn_o/(B_a^2 + m_i\xi_{in}n_o^2\eta) \equiv c_1T/(1 + c_2T) \tag{7}$$

$$c_1 = (2/\sigma_{in}k_\eta n_o)(k/3m_i)^{1/2} \tag{8}$$

$$c_2 = (B_a^2/\sigma_{in}n_o^2k_\eta)(1/3km_i)^{1/2} \tag{9}$$

with $k_\eta = \eta T^{3/2} = 129\ (\ell n\Lambda)$, and $B_a^2 = B_{\varphi a}^2 + B_{za}^2$ where $B_{\varphi a} = B_\varphi(r = a)$. When $T_{nw} \ll T_a$ eq. (6) yields

$$F_b \simeq (c_1/c_2)\left[T_a - (1/c_2)\ell n(1 + c_2T_a)\right] \tag{10}$$

The temperature at the interface between the plasma core and the boundary layer is expected to be in the range $5 \times 10^4 < T_a < 10^5$K [2].

Further, with a current density distribution

$$j_z = j_o - (j_o - j_a)(r/a)^\alpha \qquad (j_a \ll j_o) \tag{11}$$

in the core, the strength of the poloidal (transverse) magnetic field at the edge $r = a$ is given by [3]

$$B_{\varphi a}^2 = 2\mu_o k(\alpha + 1)n_oT_o/\bar{\beta}_\eta\ (\alpha + 3) \tag{12}$$

where

$$\bar{\beta}_\eta = (1/4)(1 - \beta_o) + \left[(1/16)(1 - \beta_o)^2 + 3(\beta_o/8)\right]^{1/2} \tag{13}$$

$$\beta_o = 2\mu_o kn_oT_o(\alpha + 1)/(\alpha + 3)B_{za}^2 \tag{14}$$

with $n_o = n(r = 0)$ and $T_o = T(r = 0)$.

Finally, it should be observed that for $E_o > 0$ and $f > 1$ we have $j_{zE} > 0$, $B_\varphi > 0$ and $j_{\varphi E} \cdot B_z > 0$. This implies that anisotropic resistivity, i.e. $f \neq 1$, gives rise to a "paramagnetic" effect.

Numerical Illustrations As a numerical illustration we choose the mass number A = 1, a parabolic current density profile with $\alpha = 2$, and $k_\eta = 10^3$. The quantity of eq. (13) varies slowly with β_o and we can put $\bar{\beta}_\eta \simeq 0.6$. The toroidal (axial) bootstrap current ratio J_{zb}/J_a is given in Fig.2 as a function of the axial density n_o for the two cases $T_a = 10^5$K, $T_o = 3 \times 10^5$K, $B_{za} = 0$ and $T_a = 5 \times 10^4$K, $T_o = 2 \times 10^5$K, $B_{za} = B_{\varphi a}$. For the latter case, and with $n_o = 10^{21}$ m^{-3}, eqs. (10) and (4) further yield a toroidal (axial) magnetic field ratio $B_{zb}/B_{za} = -0.082$. The broken parts of the curves in Fig.2 correspond to cases where the local penetration length $L_\eta(r = a)$ exceeds 0.01 m. At large L_η the plasma becomes permeable to neutral gas and the current densities $j_{\varphi v}$ and j_{zv} are distributed all over the plasma body.

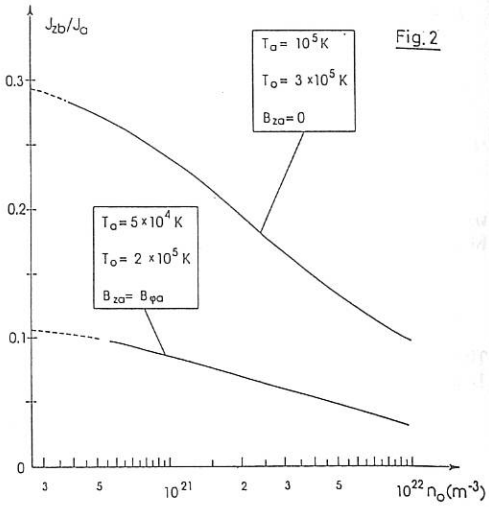

Fig. 2

Conclusions According to the present model, comparatively large toroidal (axial) and poloidal (transverse) bootstrap-like currents can arise in certain parameter ranges of the Z-pinch. The former reinforce the pinch current, and the latter produce a "diamagnetic" effect which counteracts the "paramagnetic" effect due to anisotropic resistivity. These bootstrap-like currents also give rise to a coupling between the toroidal and poloidal magnetic field components, in addition to that of the Taylor dynamo process.

References

[1] B. Lehnert, Fusion Technology 13(1988)87.

[2] B. Lehnert, Nuclear Fusion 8(1968)173.

[3] B. Lehnert, Royal Inst.Tech., Stockholm, TRITA-PFU-89-09(1989).

PASSAGE OF POWERFUL CURRENT PULSES THROUGH PLASMA LAYER

L.E.Aranchuk, V.M.Babykin, A.S.Chernenko, A.S.Chuvatin,
I.V.Kurchatov Institute of Atomic Energy
123182, Moscow, USSR

Not long ago a new element - Plasma Opening Switch (POS) - has appeared in the technique of powerful accelerators (0.1-1 MA current, 0.1-1 MV voltage). Plasma is injected into the load assembly area and at first provides a shorting of the facility. During the current flowing through POS its resistance increases abruptly and the current is switched to the load. From the point of view of the technique, POS is a nonlinear element which allows to influence the output characteristics of the installation. And besides by using the principle of energy storage in some intermediate inductance with following interrupting of the current in it one can increase 2-3 times the load power in comparison with matched load regime [1]. The further progress in powerful pulse generators technique development is connected with POS use. However physical mechanisms governing the process of powerful pulses passage through plasma layer and switching dynamics have not common understanding and remain the subject of further investigation. One of the most characteristic and surprising phenomena obtained in these investigations is the anomalous quick pulse propagation through plasma in POS region.

The experiments held on "MS" generator (2.3 Ohm wave impedance, ~200 kV incident wave amplitude). Inductive storage assembly ($L_1 \approx \rho\tau_{1/2} \approx 120$nH) is attached to the output of the installation (Fig.1). The terminal part of this inductance represents a strip line of 35cm length, 12.5cm width and with the gap between strip plates of 1cm. The line is loaded to the blade cathode diode. Plasma jet has 90mm diameter, $\sim 10^{13}$ cm^{-3} density, 5-10 eV temperature and $\sim 10^7$ cm/s directed velocity. It is injected through the grid in the center of the strip line at the distance of 17cm from the diode. The following

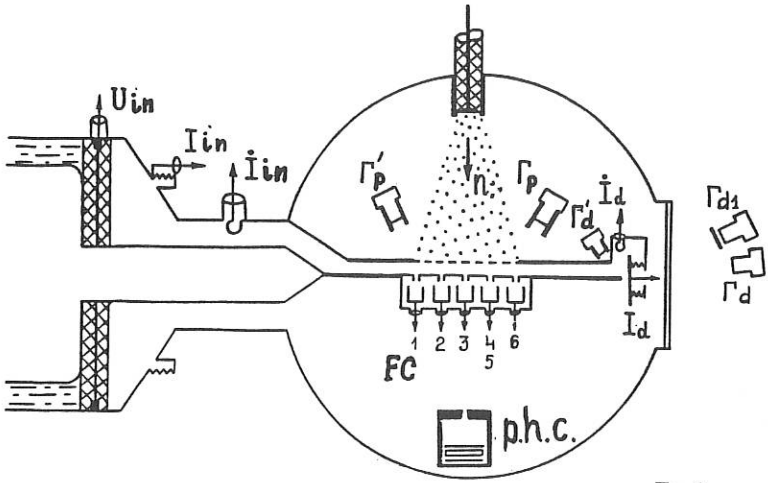

FIG.1

PARAMETERS WERE MEASURED IN THE EXPERIMENTS: INPUT AND OUTPUT CURRENTS (I_{IN}, I_D); THE VOLTAGE JUST BEFORE THE INDUCTIVE STORE (U_{IN}), WHILE THE LOAD VOLTAGE U_D IS CALCULATED); X-RAY RADIATION WITH THE ENERGY >30 KEV FROM THE LOAD (Γ_D) AND POS (Γ_P, Γ'_P). TIME INTEGRATED PICTURES WERE MADE BY THE PIN-HOLE CAMERA. THREE-FRAME IMAGE CONVERTER TUBE SYSTEM WITH EXPOSURE OF ~5 NS WAS USED TO OBTAIN PLASMA PICTURES OF THE LUMINOSITY IN THE VISIBLE RANGE. THE BLOCK OF SIX FARADAY CUPS WAS INSTALLED TO REGISTER THE ION LEAKAGES DYNAMICS IN POS REGION.

EXPERIMENTAL CURVES ARE SHOWN IN FIG.2 ($I_P=I_{IN}-I_D$ - PLASMA CURRENT, $R_D=U_D/I_D$ - LOAD RESISTANCE, U_D - LOAD VOLTAGE, DASHED CURVE - THE WORK WITHOUT POS, OTHER ITEMS ARE IN THE TEXT). THE LOAD CURRENT I_D IS τ_D ~ 50 NS DELAYED WITH REGARD TO THE INPUT CURRENT WHICH FLOWS AT FIRST ONLY IN PLASMA ($I_P=I_{IN}-I_D$). WHILE THE CALCULATED TIME OF THE DIFFUSIVE PENETRATION OF THE MAGNETIC FIELD IN PLASMA LAYER IS $\tau=4\pi\sigma L^2/c^2 \sim 2\cdot10^{-4}$ S, THAT IS 4 ORDERS OF MAGNITUDE HIGHER. IT WAS SHOWN IN [1] BY THE MAGNETIC PROBES THAT THE CURRENT MAGNETIC FIELD PROPAGATES ALMOST WITH CONSTANT VELOCITY IN PLASMA LAYER, AND THE LOAD CURRENT APPEARANCE CORRESPONDS TO

THE MAGNETIC FIELD WAVE COMING TO THE DIODE BORDER OF THE PLASMA. IN OUR CASE DURING THE CONDUCTION PHASE POINTED OUT ABOVE, I.E. WHEN ALL THE CURRENT IS SHORTED BY THE PLASMA, THE PROPAGATION VELOCITY IS $V=L/\tau_D \sim 2\cdot 10^8$ CM/S. THE PLASMA RESISTANCE DURING THE CONDUCTION PHASE $R_P=U_P/I_P$ IS SMALL, THERE IS A SMALL AMOUNT OF ENERGY EMITTED IN PLASMA, AND ONE COULD NOT MANAGED TO REGISTER ITS LUMINOSITY. IN THE LOAD CURRENT RISING PHASE WE REGISTERED THE SHINING AREA DISPLACEMENT ON THE CATHODE ELECTRODE SURFACE TOWARDS THE

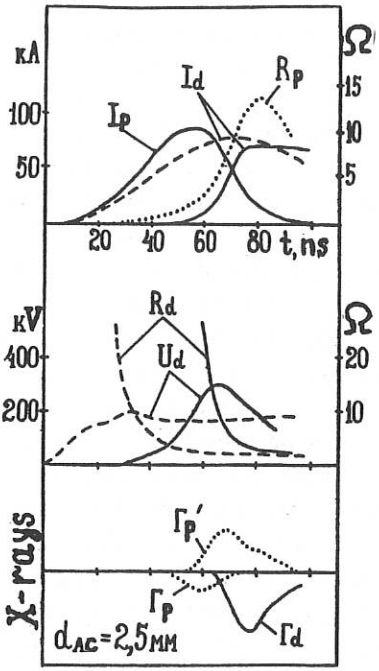

FIG.2

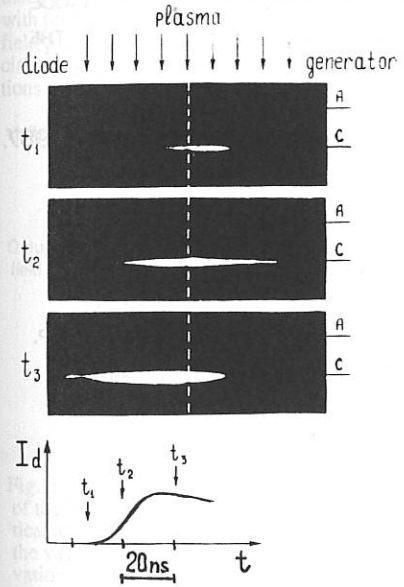

FIG.3

DIODE WITH THE VELOCITY OF $3\div 5\cdot 10^8$ CM/S (FIG.3), WHICH IS THOUGHT TO BE CONNECTED WITH THE ACCELERATED IN POS IONS BOMBARDMENT. IN THIS SWITCHING PHASE WITH THE HELP OF FARADAY CUPS BLOCK WE OBTAINED A SUCCESSIVE APPEARANCE OF SIGNALS AT THE SAME DIRECTION, WITH THE SAME VELOCITY. HENCE THE SWITCHING PROCESS, AS WELL AS THE CONDUCTION PHASE IS REVEALED IN THE FORM OF THE WAVE. ONE SHOULD POINT OUT THAT

THE VELOCITIES MENTIONED HAVE, MAYBE BY CHANCE, THE SCALE OF THE ALFVEN VELOCITY VALUE.

FROM THE DATA BEING PRESENT IT IS DIFFICULT TO PICK OUT THE DOMINATING ONE BETWEEN THE MECHANISMS WERE CONSIDERED IN SOME THEORETICAL PAPERS: ANOMALOUS CONDUCTIVITY, CONNECTED WITH MICRO-INSTABILITIES DEVELOPMENT [2]; NEAR ELECTRODE PHENOMENA [3]; MAGNETIC FIELD TRANSFER BY THE ELECTRON DRIFT MOTION [4]. ALL THE MENTIONED IS POSSIBLE IN OUR CONDITIONS. WE POINT OUT ONLY THE EXISTENCE OF THE PROCESSES IN POS LEADING TO SOME INSTABILITIES APPEARANCE.

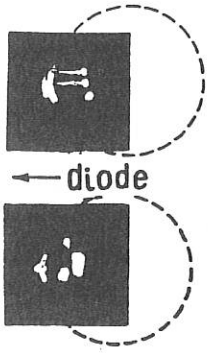

FIG.4

IT IS REVEALED ESPECIALLY IN THE PIN- HOLE PICTURES (FIG.4) AS SPOTS WITH THE DIMENSIONS OF THE ORDER OF THE INTERELECTRODE GAP (~1 CM). THERE ARE THE STRIPS FROM SOME OF THEM IN THE DIRECTION TO THE DIODE EDGE OF POS. THEIR SOURCE IS THOUGHT TO BE THE LOCAL BEAMS (PINCHES), WHICH ARE DISPLACED TO THE DIODE BORDER OF POS JUST AFTER THE PHASE OF THEIR FORMATION BY THE MAGNETIC PRESSURE.

[1] B.V.WEBER, ET AL., IEEE TRANS. PLASM SCI., PS-15, 635, 1987.
[2] R.M.KULSRUD, P.F.OTTINGER, J.M.GROSSMAN, PHYS. FLUIDS, 31(6), 1741, 1988.
[3] R.J.MASON, ET AL., PHYS. REV. LETT., 61(16), 1835, 1988.
[4] K.V.CHUKBAR, YANKOV V.V., J.TECH.PHYS.(SOV.), 58(11), 2130, 1988
L.E.ARANCHUK, V.M.BABYKIN, A.V.GORDEEV, ET AL, 13TH SYMP. ON DISCHARGES AND ELECTR. INSULATION IN VACUUM, PARIS, V.2,1988

NEW SPECTROSCOPIC RESULTS FROM EXTRAP-T1 PLASMA

J.H. Brzozowski, E. Källne* and K.-D. Zastrow*

Department of Plasma Physics and Fusion Research, * Department of Physics I
Royal Institute of Technology, S-100 44 Stockholm, Sweden.

INTRODUCTION

In this paper we present results of observations and analysis of vacuum ultraviolet (VUV) spectroscopy from a high-beta discharge experiment performed on the Extrap-T1 device. We describe the experiment and the spectroscopic observations of relevance for the characterization of the impurity behaviour in the discharge. Spectroscopic observations are performed both in the visible and the VUV wavelength regions. They show, that the main radiation comes from carbon and oxygen in their low ionization stages and no line radiation is observed for metals. Studies of the VUV spectrum indicate that ionization equilibrium is achieved during the peak current period of the discharge and that the energy balance is not dominated by radiation losses during that period. Some comparisons can be drawn with previous theta-pinch [1] and reversed field pinch [2] observations and with the special study [3] of impurity behaviour in conditions out of coronal equilibrium.

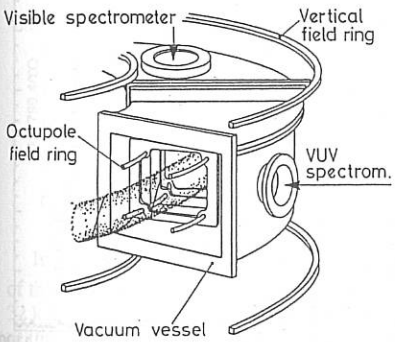

Fig.1: A schematic diagram of a quadrant of the Extrap-T1 experiment with the vertical and octupole field rings together with the vacuum vessel and the plasma. Observation windows for visible and VUV spectrometers are also shown.

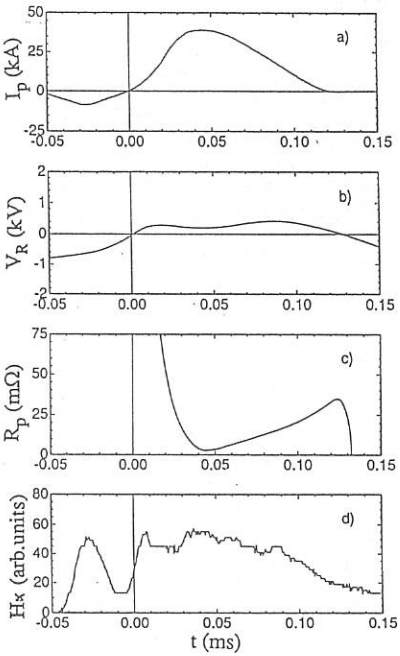

Fig.2: Typical Extrap-T1 discharge with filling pressure 4 mTorr, showing the time evolution of the plasma current (a), the resistive component of the loop voltage (b), the plasma resistance (c) and the time evolution of the line-of-sight integrated Balmer-α emission from hydrogen.

THE EXTRAP-T1 EXPERIMENT

Extrap T1 is a low-q, high-beta discharge bounded by a magnetic separatrix with four x-points in the poloidal field produced by currents in four toroidal rings placed outside the perimeter of the discharge cross section [4,5]. The device is a toroidal, high aspect ratio configuration with a major radius of 0.45 m and a week toroidal field $B \leq 0.3$ T.

A schematic of the Extrap-T1 geometry is shown in figure 1. In figure 2 we show the time evolution of the plasma discharge current, the resistive component of the loop voltage, the plasma resistance and the line-of-sight integrated Balmer-α emission from hydrogen. The resistive component of the loop voltage and resistance are evaluated from loop voltage and ring current measurements using a model that accounts for the inductive component of the loop voltage. The Ohmic power input P_{in} is derived from this resistive loop voltage evaluation.

In the experiments described here I_p was in the range 15-40 kA. The electron temperature T_e, estimated from the loop voltage and from Thomson scattering, was in the range 5-40 eV at the current maximum. The electron density n_e, from Thomson scattering, was in the range 0.3-$3.0 \cdot 10^{15}$ cm^{-3} [7,8].

VUV SPECTROSCOPY

The VUV spectrometer is a McPherson 251 grazing incidence instrument covering a spectral range of 100 to 1700 Å using two toroidal gratings (450 l/mm and 290 l/mm) which give a flat field focus. The detector consists of an open microchannel plate (MCP) with an image intensifier/converter which is optically coupled to a self-scanning photodiode array (PDA). The MCP is covered with a 1000 Å thick layer of CuI to enhance the photon sensitivity at longer wavelengths. The PDA is controlled and read out by an optical multichannel analyser (OMA) system. The PDA which is 2.5 mm high and 25 mm broad, consists of 1024 diodes and detects simultaneously a spectrum of 100-1100 Å with ≈ 3 Å resolution, alternatively 155-1700 Å with ≈ 4.5 Å resolution. Time resolution of 1μs on a shot-to-shot basis is obtained by gating the multichannel plate in the intensifier stage of the detector.

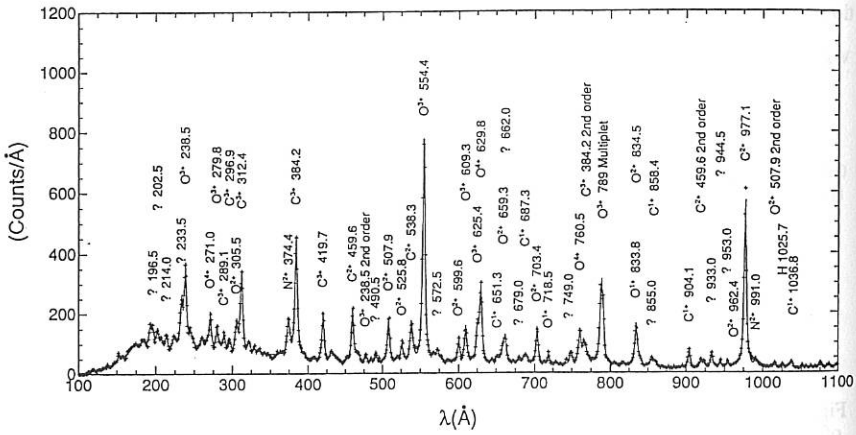

Fig.3: VUV spectrum acquired with the 450 l/mm grating during the equilibrium phase of a discharge with a peak plasma current of about 40 kA. The acquisition time of the signal is 10 μs. The crosses mark the actual number of counts/Å and the solid line is a result of the least squares fit.

A typical spectrum is shown in figure 3. The most prominent lines are originating from C^{+1}, C^{+2}, C^{+3} and O^{+1}, O^{+2}, O^{+3} and O^{+4}. An indication of presence of O^{+5} is also observed. The solid line is a least square fit through the full spectrum.

RESULTS

The spectra we have analysed here have been measured during a time interval around the current maximum when the plasma conditions are fairly constant. All results are based on spectra taken with the 450 l/mm grating. We present the spectroscopic results as a function of the average plasma current. Through the scaling of T_e with plasma current, which is about 1 eV/kA [6], these results can be related to the plasma temperature.

Figure 4 shows the time evolution of spectral line intensities of different ionization stages (IS) of oxygen. In order to get an idea of the relative importance of the different IS to the energy balance, the intensity from a spectral line representing a single IS is divided by the total normalised line-of-sight radiation from the representative spectral lines for all the observed oxygen ionisation stages Σ O. ($\Sigma O = O^{+1}(718.5) + O^{+2}(507.9) + O^{+3}(789.4) + O^{+4}(629.8)$) In this figure relative intensities and plasma current are normalised to an arbitrary value (set to 0.95 of the maximum value).

In figure 5 we show the fractional abundance (FA) of the oxygen IS as a function of I_p during the equilibrium phase of the discharge. The decreasing of FA with increasing I_p we interpret as an increase in the central electron temperature and consequent decrease of the width of the emission shell connected with the observed ionisation stage.

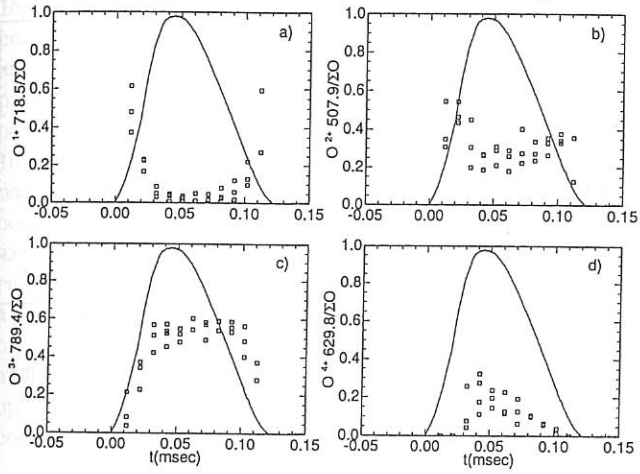

Fig.4: Time evolution of the measure for the fractional abundance of oxygen ionisation stages with time. The solid line represents the time evolution of the normalised plasma current for this series of plasma discharges.

In figure 6 the ratio E_{vuv}/P_{in} as a function of I_p is shown. E_{vuv} is the sum over all channels of the intensity in counts per Å times photon energy. The ratio shows its maximum at around 32 kA, where the normalised intensity of the O^{+3} line in figure 4c becomes constant and that of the O^{+4} line in figure 4d starts to appear. From the T_e scaling the central electron temperature at a plasma current of 30 kA is around 30 eV. Thus it follows that the impurity radiation is important for the energy balance only for plasma currents less then 30 kA. For higher values the radiation channel of the energy loss becomes less important. This means, that the width of the region in the plasma, where T_e is between 10 eV and 20 eV is decreased sufficiently, so that the ratio E_{vuv}/P_{in} starts to decrease. This is confirmed by the decrease of the relative inten-

sities from low ionization stages, which contribute most to the energy loss by radiation in this temperature region. Further details of the spectroscopic results are given in [9].

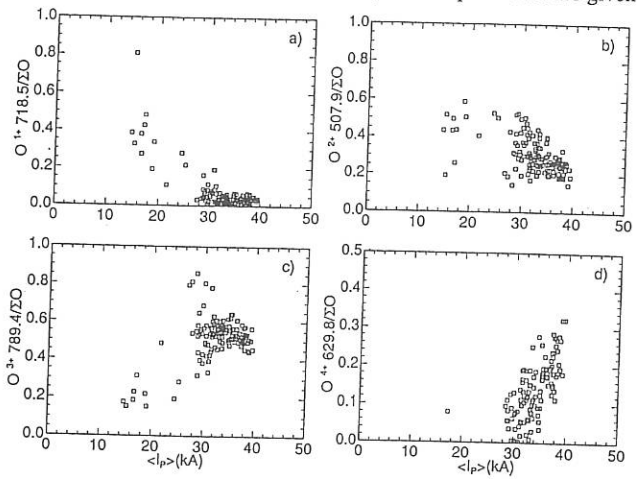

Fig.5: Scaling of the measure for fractional abundance of oxygen ionization stages with plasma current during the equilibrium phase.

CONCLUSIONS

Spectroscopic observations of the VUV line radiation from carbon and oxygen have been analysed for the Extrap-T1 experiment. It is observed that the temporal evolution of the line radiation can characterize the plasma discharge into three different phases. During the central part of the discharge and for the highest plasma currents in Extrap-T1, we conclude that burn-through is achieved and that the plasma impurity radiation has no major effect on the energy balance of the plasma.

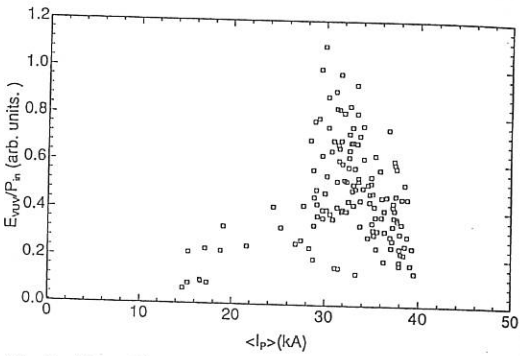

Fig.6: Normalised ratio of total detected energy in the VUV to the total input power as a function of plasma current during the equilibrium phase.

References

[1] Griem Hans R., J. Quant. Spectrosc. Radiat. Transfer 40 (1988) 403.
[2] Ortolani S. et al, Plasma Physics and Controlled Fusion 27 (1985) 69.
[3] Carolan P.G. and Piotrowicz V.A., Plasma Physics 25 (1983) 1065.
[4] Lehnert B. in "Unconventional approaches to fusion", p.135, Plenum Publ. Corp., New York, 1982, Eds. Brunelli P. and Leotta G.G.
[5] Lehnert B., Nucl. Instr. and Meth. 207 (1983) 223.
[6] Drake J.R. et al, RIT report TRITA-PFU-89-01 (1989).
[7] Brunsell P. and Tennfors E. RIT report TRITA-PFU-88-10 (1988).
[8] Karlsson P. RIT report TRITA-PFU-89-06 (1989).
[9] Brzozowski J.H., Källne E. and Zastrow K.-D., to appear in Plasma Physics and Controlled Fusion 1990, TRITA-PFU-89-08 (1989).

Compression, Heating and Fusion in Dynamic Pinches Stabilized by an Axial Magnetic Field

M.A.Liberman, S.M.Golberg, A.L.Velikovich

Institute for Physical Problems
ul. Kosygina, 2. Moscow 117334, USSR

The inertial confinement Z-pinch fusion systems have at least one advantage: there is no limitation on I like I_{PB}, the current can be as high as the pulsed power driver is capable to deliver. When a dynamic Z-pinch is treated as an ICF system, its most important characteristic is stability of compression. The idea of combining the advantages of inertial and magnetic approaches to controlled fusion in some hybrid scheme has been discussed for a long time [1 - 3]. It was shown that a sufficiently strong magnetic field in the ICF systems can localize the ignition by suppressing the electron thermal conductivity and diffusion of the α-particles, and also provide an initial preheating of the compressed plasma. It was also pointed out [4] that perhaps the most important is the possibility to inhibit the development of hydrodynamic instabilities in the course of compression with the aid of the magnetic field, thus increasing the degree of stable radial compression. It was shown [5, 6, 7] that a relatively small axial magnetic field can significantly improve the uniform radial compression by suppressing the most dangerous sausage and kink modes of RT instability associated with inward acceleration of an annular plasma by the azimuthal magnetic field. This allows one to obtain higher degrees of stable radial compression up to 22-fold compression achieved in [7] instead of conventional ~8.

The stabilizing effect of axial magnetic field on pinch implosions can be explained with the aid of an ideal MHD model [4]. Stability of an implosion can be expected if the final number of e-folding of the dominating perturbation modes n_{ef} is shown to be small or, at least, limited in comparison with the case when no axial magnetic field is present.

Explicit analytic expressions for the "instantaneous growth rates" $\Gamma_{m,k}(t)$ as functions of time and wave numbers are

obtained in WKB approximation, and the evolution of $\Gamma_{m,k}(t)$ spectra in the course of compression is studied. In the presence of a magnetic shear, the most dangerous local RT modes can be fully suppressed and the growth rates of the inertial modes substantially. For the simplest case supposing a power-low density profile near the boundary $\rho=\rho_0\left[r/L\right]^s$, the WKB approximation yields the following spectra for the n-th eigenvalue:

$$\sigma_n^2=|gk|\frac{s}{2n+1}$$

if it's possible to neglect the shear of the an perturbed magnetic field near the plasma boundary, because B_z^2 decrease faster then ρ as the boundary is approached. Otherwise

$$\sigma_n^2=|gk|\ 8\sqrt{2}\ s\ \chi\ \exp\left[-\frac{\pi}{2}\left(n+\frac{1}{2}\right)\right],\ \chi \gg 1$$

The parameter characterizing the magnetic shear is

$$\chi^2=\frac{2B^2}{8\pi\rho|g|Ls},\ \text{or}\ \ \chi^2\cong\frac{\min(B_z^2,\ B_\varphi^2)}{|B_z^2-B_\varphi^2|}$$

for a thin plasma shell, confining an axial magnetic field B_z inside and being accelerated by pressure of an azimuthal magnetic field B_φ outside.

If the shear becomes significant, then the growth rates of the most dangerous modes become exponentially small. Analysis of the perturbation growth in the WKB approximation allows one to make a conclusion that the instability growth is manageable for an initial axial field

$$B_{z0} \geq 10\ \text{kG}\ I\ (\text{MA})/R_0(\text{cm})$$

where I is the average current during the implosion. Such scaling law was confirmed by the experiments [5, 6, 7]. It's possible to organize the optimal compression in such a way that the parameters of plasma flow all the time remain within the "window of stability", i.e. the magnetic shear parameter χ is kept sufficiently high. It will be so, for a pinch current varying in time $I(t)$ as $R^{-1}(t)$, for example.

Two schemes of a Z pinch ICF system using an axial magnetic field were proposed recently. The first one (a Z-θ pinch) [8] suggests compression of a frozen DT fiber in a θ pinch geometry by a rapidly increasing axial magnetic field, which, in turn, is produced by magnetic flux compression with an imploding gas-puff Z pinch. An advantage of this scheme is that dynamics of

compression makes the magnetic pressure pulse acting on the fiber considerably shorter than the current pulse driving the puff. The other method is based on compression of a gaseous target by an annular liner in an axial magnetic field [9]. The following scaling was derived from the Lawson's criterion for the breakeven conditions:

$$I_m\ (\mathrm{MA}) = 550\ \left[m/M\right]^{1/4} \cdot \left[\frac{R_o\ (\mathrm{cm})}{(R_o/R_f)\ln(R_o/R_f)}\right]^{1/2}$$

where I_m is amplitude of a sinusoidal current pulse, m and M are masses of the compressed DT plasma and the liner, respectively, R_f is the final radius of the liner.

Our present estimates are based on the numerical results obtained with a 1D hydrodynamic code. Braginskii's fluid equations were solved for a DT plasma compressed in an axial magnetic field, with bremsstrahlung and synchrotron radiative energy losses taken into account. We simulated a 10-30-fold radial compression of a liner imploding onto an axial magnetic field B_{zo} = 80 to 300 kG with a cold solid-density plasma cylinder on the axis. The fiber radius was varied from 20 to 100 μm, the initial radius of the liner R_o from 1 to 2 cm, the axial current amplitude I_m from 7.5 to 50 MA. No one of the trials came close to the ignition conditions.

Compression of a plasma-filled liner in an axial magnetic field appears to be a more feasible approach to achieving the fusion conditions. The above scaling law for I_m is indeed confirmed by our numerical results, in particular, for I_m=20 MA, R_o= 3 mm, n_o=$2\cdot10^{21}$ cm^{-3} , M/m=5.5. The resulting compression was R_o/R_f=31. In agreement with the scaling law here we achieve just the breakeven threshold, see Fig. 1.

1. Dawson J.M. Phys. Fluids 7, 981 (1964).
2. Lindemuth I.R. and Kirkpatrick R.C. Nucl. Fusion 23, 263 (1983).
3. Liberman M.A. and Velikovich A.L. J. Plasma Phys. 31, 381 (1984).
4. Bud'ko A.B. et al., Phys. Fluids B 1, 598 (1989).
5. Baksht R.B et al., Sov. Phys. - Tech. Phys. 32, 145 (1987).
6. Felber F.S. et al., J. Appl. Phys. 64, 3831 (1988).
7. Felber F.S. et al., Phys Fluids 31, 2053 (1988).
8. Rahman H.U. et al., Bull. Am. Phys. Soc. 31, 1818 (1987).
9. S.M.Golberg et al., Plasma Phys. Contr. Fusion, in press.

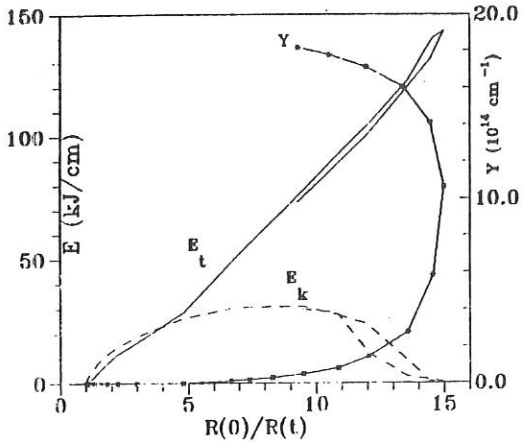
150
100
50
0
E (kJ/cm)
20.0
10.0
0.0
Y (10^{14} cm^{-1})
Y
E_t
E_k
0
5
10
15
R(0)/R(t)

THE DENSE Z-PINCH PROJECT AT IMPERIAL COLLEGE

M.G. Haines, A.E. Dangor, P. Choi, I. Mitchell, M. Coppins, J.P. Chittenden, I.D. Culverwell, J. Bayley, A. Power.

Blackett Laboratory, Imperial College, Prince Consort Road, London SW7 2BZ.

ABSTRACT

The Science and Engineering Research Council has recently awarded a grant of over £0.8M to build a large new Z-pinch driven by a high voltage pulsed power generator. The generator will be 4 Marx generators in parallel which together will supply up to 2MA at 2.85MV for 200ns. When the load is a frozen fibre of hydrogen, it is predicted that radiative collapse above the Pease-Braginskii current will lead to ultra high density (10^4 x solid density) at 10 to 20 KeV temperature. Deuterium-tritium fibres would lead to conditions close to thermonuclear breakeven. Scaled experiments at lower currents reveal anomalous stability due to finite Larmor radius effects in one case or to a low magnetic Lundquist number in another. The theory of stability has been extensively studied in many regimes, and it is found the ideal MHD occupies a small fraction of parameter space.

1. INTRODUCTION

The physical parameters, particularly the size (radius, length or major radius) of magnetically confined plasmas is generally determined by the maximum magnetic field that can be conveniently and practically generated using current-carrying field coils. A field of 5 tesla leads to a plasma radius of about 1 metre in order to satisfy Lawson condition when β limits are set by stability and the losses are diffusive, albeit anomalous. This results in very large reactor designs. In contrast, and alone in the field of magnetic confinement a Z-pinch (an unstabilised Z-pinch i.e. zero axial magnetic field in old fashioned terminology) has no such constraint on magnetic field and so a very compact fusion device is possible. The limitation is instead determined by constraints of pulsed power technology, as will be explained in Sec.2. Progress in understanding the many regimes for stability modelling is summarised in Sec.3. The possible attainments in radiative collapse are discussed in Sec.4 and the DZP project is outlined in Sec.5.

2. LAWSON CONDITIONS WITH END LOSSES

A theory of heat conduction to the electrodes of a Z-pinch satisfying the equilibrium Bennett relation reveals similar scaling laws for zero or infinite Hall parameter (HAINES, 1961). Imposing conditions for thermonuclear breakeven leads to the requirement of a current I of 10^6 A, a line density N of $6\times10^{18}m^{-1}$, and a steady voltage of 10^5V, implying an initial applied voltage in excess of 10 V. Immediately this dictates the employment of pulsed power technology, which will place a limit in the pulse length of about 200ns or so. With the confinement time fixed at 100ns the number density has to be $5\times10^{27}m^{-3}$, the pinch radius, a, 20 micron and the

length of the pinch 10 cm (HAINES, 1987). It is noticeable that these parameters are close to that of a hair, and the present trend in this field is to actually commence with a frozen fibre of deuterium.

3. STABILITY

It is well-known both experimentally and theoretically that Z-pinches are unstable by ideal MHD to m=1 (kink) and, if the current profiles are not centrally peaked (KADOMTSEV, 1966), also to m=0 (sausage) instabilities. However when resistivity, viscosity, anisotropy and finite ion Larmor radius effects are considered we find that ideal MHD assumptions apply only to a small part of parameter space. The various regimes are best described in a I a versus N plot, shown in fig.1. (HAINES, COPPINS and CULVERWELL, 1989).

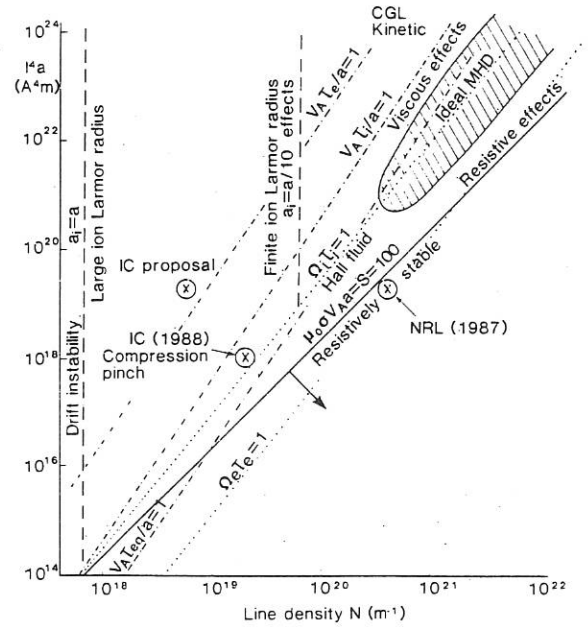

Resistive stabilisation is expected for a Lundquist number below about 100 (CULVERWELL and COPPINS, COCHRAN and ROBSON, 1990), and this is consistent with the onset of instability in the NRL fibre pinch. Large Larmor radius effects will be important under fusion conditions, and the compression Z-pinch at Imperial College has shown stability for at least 16 MHD growth times.

Fig.1 Stability regimes in the Z-pinch

4. RADIATIVE COLLAPSE

At currents above the Pease-Braginskii value of $0.433(\ln \Lambda)^{\nu} 2.10^6 A$ radiative collapse to about 10^4 x solid density is predicted to occur, as illustrated in fig.2 from HAINES, 1989. Recent work by CHITTENDEN et al 1989 has shown that the inclusion of electron degeneracy and radiation transport is necessary to limit compression when the variation of $\ln \Lambda$ both spatially and temporarily is included.

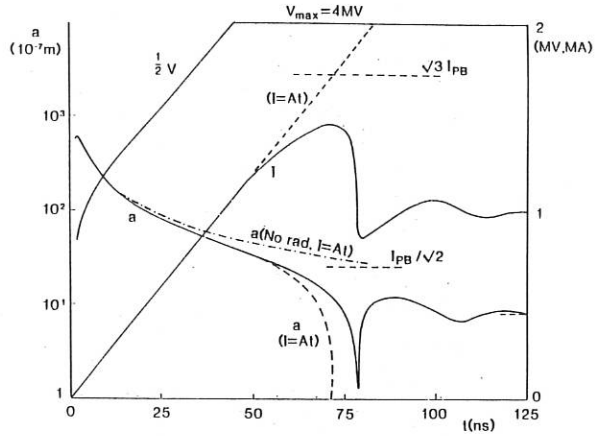

Fig.2 Current and pinch radius versus time for a simple model of radiative collapse

5. DZP PROJECT

The Science and Engineering Research Council has awarded a grant of £800K to allow the construction of a 2MA, 2.85MV, 336KJ generator for studying radiative collapse and the physics properties of a dense Z-pinch under fusion conditions. It has been designed in the form of four Marx generators and pulse forming lines as illustrated in fig.3 in order that the total line impedance is 1.25 ohm. Construction will take 3 years.

References

CHITTENDEN, J.P., POWER, A.J. and HAINES, M.G. (1989), Plasma Phys. Contr. Fusion, 31, 1813; also to be published.
COCHRAN, F.L. and ROBSON, A.E., (1990) Phys. Fluids B2, 123.
CULVERWELL, I.D. and COPPINS, M. (1990) Phys. Fluids B2, 129.
HAINES, M.G. (1961) Proc. Phys. Soc. 77, 643.
HAINES, M.G. (1978) J. Phys. D : Appl. Phys. 11, 1709.
HAINES, M.G., COPPINS, M. and CULVERWELL, I.D., (1989) AIP Conf. Proc. 195, p.203 (AIP, New York).
KADOMTSEV, B.B. (1966) in Reviews of Plasma Physics Vol.2, p.153. (Consultants Bureau, New York).

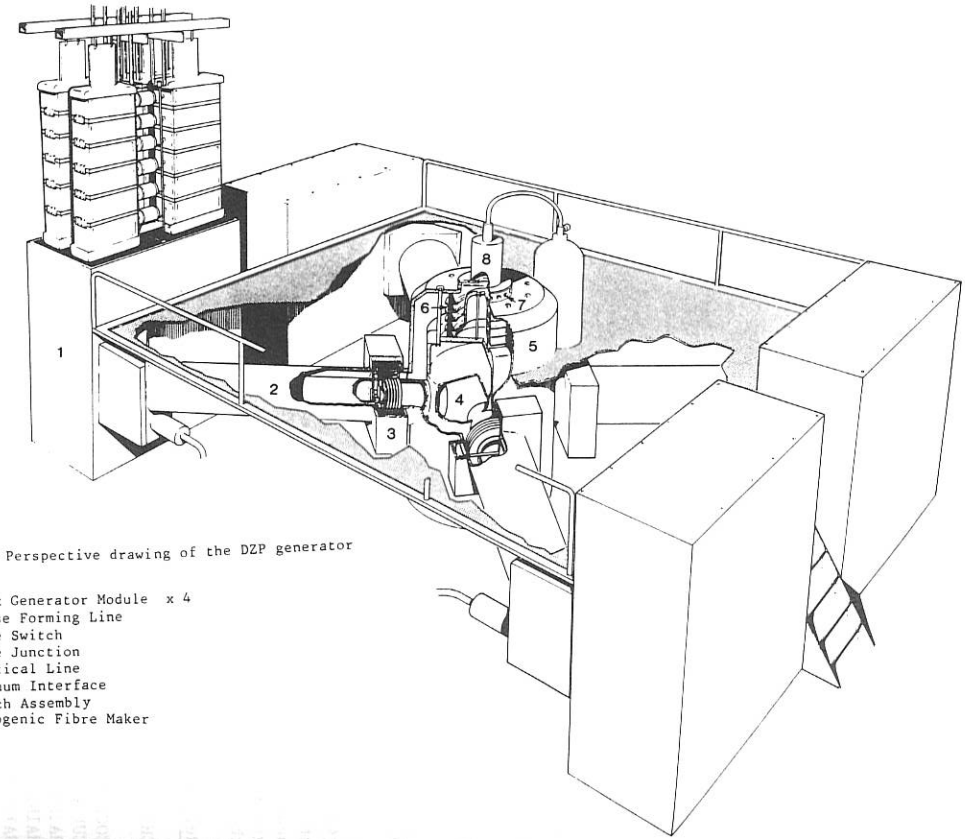

Fig.3 Perspective drawing of the DZP generator

1.Marx Generator Module x 4
2.Pulse Forming Line
3.Line Switch
4.Line Junction
5.Vertical Line
6.Vacuum Interface
7.Pinch Assembly
8.Cryogenic Fibre Maker

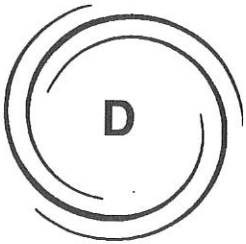

MAGNETIC CONFINEMENT THEORY AND MODELLING

D1

D1 MAGNETIC CONFINEMENT THEORY

TURBULENT DRIFT OF ELECTRONS ACROSS A MAGNETIC FIELD: THE EFFECT OF AN AVERAGE ELECTRIC FIELD

M.B.Isichenko and J.Kalda
I.V.Kurchatov Institute Of Atomic Energy, 123182 Moscow, USSR

The drift turbulence is believed to be one of the main reasons for the anomalous diffusion in high-temperature plasmas [1-3]. The turbulent diffusion of particles in magnetic confinement systems depends significantly upon the shape of drift trajectories. The latters are determined by the electric field geometry which is natural to be taken random for a turbulent plasma. In the present report we do not concern magnetic drifts which is justified for a sufficiently strong drift turbulence.

Let us introduce the local frame where z-axis represents the direction of the magnetic field $\vec{B}$, and y-axis lies in the magnetic surface. Suppose the perturbations of the electric field $\vec{E}=-\nabla\varphi$ to be strongly elongated in the direction of $\vec{B}$, and the electric potential φ to vary slowly compared to electron drift motion:

$$\omega \ll v_d/\lambda . \qquad (1)$$

Here ω is the characteristic frequency and $\lambda=2\pi/k_\perp$ is the characteristic wavelength of the drift turbulence. Under the condition (1) the drift flow

$$\vec{v}_d = c\hat{z}\times\vec{\nabla}\varphi/B \qquad (2)$$

is an incompressible one with the random stream-function $\psi=-(c/B)\cdot\varphi(x,y,t)$ which depends on time weakly.

In the absence of an average electric field the stream-function ψ can be considered limited. The passive transport problem for such a flow has been solved in the paper [4] where the following expression for the turbulent diffusion coefficient has been obtained:

$$D_T \approx \lambda v_d(\lambda\omega/v_d)^{1/(\nu+2)} . \qquad (3)$$

To the result (3) the main contribution is made by stream-lines with the characteristic diameter

$$a = a_T = \lambda(v_d/\lambda\omega)^{\nu/(\nu+2)} . \qquad (4)$$

The mixing length (4) is defined from the maximum orbit length L the particle has time to pass in the life-time of the orbit [4]

$$t_h = h/(\lambda\omega), \tag{5}$$

where h is the width of the convective cell consisting of stream-lines with the same order of diameter magnitude a. For a random 2D incompressible flow having the unique characteristic spatial scale λ, the quantities h and L are expressed through a as follows [4,5]:

$$h = \lambda(\lambda/a)^{1/\nu}, \tag{6}$$

$$L = \lambda(a/\lambda)^{(\nu+1)/\nu}, \tag{7}$$

where $\nu=4/3$ [6] is the correlation length exponent in the 2D percolation theory.

The subject of the present report will be to study the effect of a small uniform transverse electric field $E_x \ll E_d$, which is perpendicular to the magnetic flux surfaces (i.e. radial in the tokamak geometry). In hydrodynamic terms the presence of such a field means the perturbation of the flow (2) by a small average velocity $\vec{u}=(cE_x/B)\hat{y} \ll v_d$ or, in other words, the appearance of a small stream-function gradient.

Let us consider the isolines topology of such a function. (These isolines are also the stream-lines of the flow.) For a non-perturbed (limited) stream-function $\psi_o(x,y)$ every isoline is closed with the probability 1 [4]. After the perturbation $\psi(x,y)=\psi_o(x,y)-uy$ the most of isolines are modified negligibly. Consequently, the average flux $\vec{u}$ will be concentrated in narrow snaky channels [7] with characteristic width $\delta_\varepsilon \ll \lambda$ and distance $\Delta_\varepsilon \gg \lambda$ between them (see the figure). the quantity Δ_ε is also the width of the walk of every percolating (i.e. infinite in x-direction) stream-line. Since the flow velocity in the channels is of the order of v_d, while the plane average flux is $v_d\delta_\varepsilon/\Delta_\varepsilon=u$, we obtain

$$\delta_\varepsilon/\Delta_\varepsilon = u/v_d \equiv \varepsilon. \tag{8}$$

The second equation connecting the values δ_ε and Δ_ε can be derived from the following arguments. On scales $a \leq \Delta_\varepsilon$ the perturbed stream-

lines are qualitatively the same as non-perturbed ones. on the scale Δ_ε the percolating channel corresponds to the convective cell with the diameter $a=\Delta_\varepsilon$ and the width $h=\delta_\varepsilon$. Hence, the formula (6) supplies the additional link between δ_ε and Δ_ε: this results in

$$\delta_\varepsilon = \lambda(u/v_d)^{1/(\nu+1)}, \tag{9}$$

$$\Delta_\varepsilon = \lambda(u/v_d)^{-\nu/(\nu+1)}. \tag{10}$$

So, the small side flux $\vec{u}\parallel\hat{y}$ leads to the limitation of convective cells size along the x-axis by the quantity (10), which means the decrease of transport along $\hat{x}$. If one recollects the initial magnetic geometry, it is quite clear that this flux along $\hat{y}$ does not contribute to the average transport provided that magnetic surfaces are closed (periodic condition over y).

When the mixing length (4) is small in comparison with the distance between the channels (10), or $\varepsilon\ll\varepsilon_*$, where

$$\varepsilon_* = (\lambda\omega/v_d)^{(\nu+1)/(\nu+2)} \ll 1, \tag{11}$$

the effect of the average electric field is negligible. In the opposite limit, $\varepsilon\gg\varepsilon_*$, the main radial transport is produced by stream-lines having maximum spread along x-axis, equal to Δ_ε. Taking into account the life-time (5) of these lines, $t_\varepsilon=\delta_\varepsilon/(\lambda\omega)$, and the occupied area fraction, $f=\delta_\varepsilon L_\varepsilon/\Delta_\varepsilon^2$, with L_ε defined by (7), we obtain the following turbulent diffusion coefficient along x-axis:

$$D_T = f\Delta_\varepsilon^2/t_\varepsilon = \lambda^2\omega/\varepsilon, \quad \varepsilon>\varepsilon_*. \tag{12}$$

Thus, the effect of an ambipolar electric field in the low frequency limit (1) becomes significant when E_x exceeds very low threshold (11). The final result can be written in the form

$$D_T \approx \begin{cases} \lambda v_d(\omega\lambda/v_d)^{0.3}, & E_x/E_d<(\omega\lambda/v_d)^{0.7}, \\ \lambda^2\omega\cdot E_d/E_x, & E_x/E_d>(\omega\lambda/v_d)^{0.7}. \end{cases} \tag{13}$$

The non-stationarity of the drift flow (2) may be also caused by the finite longitudinal drift wave-length via electron motion along the magnetic field. In this case in all the formulae above we must substitute $\omega\to\max(\omega,k_\parallel v_{Te})$, provided that the condition (1)

still holds.

Note that besides transverse electric field effects, turbulent transport can be similarly modified by magnetic drifts, in particular, on account of the magnetic shear [3].

The assessments made should be regarded as preliminary, as we have assumed the only characteristic scale of potential drift perturbations, while usually a wide turbulent spectrum takes place [8]. The percolation approach to the spectral problem will be published elsewhere [9].

Acknowledgment. We are thankful to B.N.Kuvshinov for critical remarks.

REFERENCES:

1. Horton W. In: *Handbook of Plasma Physics* II, edited by M.N.Rosenbluth and R.Z.Sagdeev (North-Holland, Amsterdam, 1984), p. 383.
2. Liewer P.C. Nucl. Fusion, 1985, 25, 543.
3. Horton W., Choi D.-I., Yushmanov P.N. and Parail V.V. Plasma Phys. and Controlled Fusion, 1987, 29, 901.
4. Gruzinov A.V., Isichenko M.B. and Kalda J.L. Zh. Eksp. Teor. Fiz. (Sov. JETP), 1990, 97(2), 476.
5. Isichenko M.B., Kalda J.L., Tatarinova E.B., Tel´kovskaya O.V. and Yankov V.V. Zh. Eksp. Teor. Fiz., 1989, 96(9), 913.
6. Saleur H. and Duplantier B. Phys. Rev. Lett., 1987, 58, 2325.
7. Zel´dovich Ya.B. Pis´ma v Zh. Eksp. Teor. Fiz. (Sov. JETP Lett.), 1983, 38, 51.
8. Hasegawa A., Maclennan C.G. and Kodama Y. Phys. Fluids, 1979, 22, 2122.
9. Isichenko M.B. and Kalda J. To be submitted to *Physica D.*

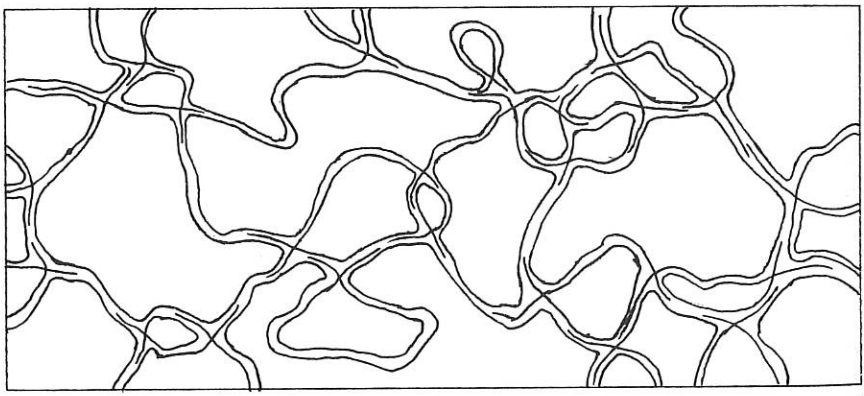

Figure. The stream-lines of the electric drifts

Anomal diffusion in plasmas across the magnetic field in approaching of strong turbulence

A.B.Arutiunov, S.I.Krasheninnikov

The problem of the impurities transfer in the strong-magnetized plasma is considered. The cross-section particles drift in the given approximations is of the Hamiltonian nature. The change of the Hamiltonian topology in time is defined by the cross-section drift that, in its turn, depends on the properties flow. It is shown by means of the theory of critical exponents that the impurities transport is of the diffusive nature for the slowly-changing structure drift of "general character".

1.The quasi-linear theory, the field of application of which in real experiments can be crashed, is often used to analyze the anomalous impurities transport in plasma across the magnetic field ($k_\perp u \ll \omega$, $k_z v_z$) (u - cross-section particle drift velocity in the fluctuations field, v_z - tangential particle drift velocity; ω, $k_\perp$, k_z - frequency, the cross-secional and tangential oscillation wave vectors.

In the given paper we shall study the particles drift of the magnetized plasma in the strong fluctuations fields $k_\perp u \gg \omega, k_z v_z$. on the basis of the percolation theory. Let us consider that the particles drift is described by the Hamiltonian $H(\vec{r}_\perp, t)$:

$$\frac{d\vec{r}_\perp}{dt} = [\nabla H, \vec{e}_z] \qquad (1)$$

We have chosen for the studythe analysis of the intensive fluctuations the characteristic drift time of which on a wave-length order distance is considerably less than that of the fluctuations amplitude change. Thus, one can assume in the null-approximation that the particles drift along the closed Hamiltonian equipotentials and their trajectories are defined by the equipotentials topology that can be rather complicated $H(\vec{r}_\perp, t)$ [1-3].

Suppose the function $H(\vec{r}_\perp)$ is the function of the "general positions". There is a number of trajectories with the lengths much more than $k_\perp^{-1}$. The connection between the trajectories lengths and their characteristic cross-sectional dimensions are defined by the relationships of the type [1]. It is natural that such an "ice-bounded" particles drift can be considered

only for some period of time that, in its turn, is defined by a characteristic Hamiltonian time change $H(\vec{r}_\perp, t)$. Gradually the particles get "defreezed" and stochastized.

We shall consider the Hamiltonians of two types:

$$H_1 = H_1(\vec{k}_\perp \vec{r}_\perp, \omega t) \tag{2}$$

$$H_2 = H_2'(\vec{k}_\perp \vec{r}_\perp) + \frac{v_z(t)}{v} H_2''(\vec{k}_\perp \vec{r}_\perp) \tag{3}$$

where $k_\perp^{-1}, \omega^{-1}$ -the characteristic correlational lengths of the fucntions H_1, H_2 в $\vec{r}_\perp$, t in space ; $\varepsilon = \bar{H}_2'' / \bar{H}_1' \ll 1$, $\bar{H} = \langle H^2 \rangle^{1/2}$.

The Hamiltonian (3) describes the electrons drift in the low-frequency electro-magnetic fluctuations fields [4], $\varepsilon \propto (c/\omega_{pe})^2 k_\perp^2$, the change $v_z(t)$ in a tokamak can be either connected with the baunce-oscillations of the trapped electrons or with the Coloumb collisions.

2. Let us first consider the particles drift in the field H_1. The effective coeficient with due regard to the long trajectories can be put in the form: (cf: see [3] where the particles behaviour in the field H_1 was considered but under [3], H_1, $\omega=0$ and small diffusion). $D\, k_\perp L \gg 1$

$$D = \int_0^\infty \frac{dh}{h} \left(\frac{L(h)\, \Delta(h)}{a^2(h)} \right) \frac{\delta^2(h)}{\tau_c(h)}, \tag{4}$$

where $h = H_1/\bar{H}_1$ - relative level of the equipotentials; H_1; $a(h)k_\perp \propto h^{-\nu}$; $L(h)k_\perp \propto (a(h)\, k_\perp)^d$ - characteristic space scale and the trajectories lengths; $\Delta(h)\, k_\perp \simeq h$ - characteristic width of the trajectories region at the level h; $\nu = 4/3$, $d=7/4$ [1] - critical exponents; $\tau_c(h)$ - particle drift correlation time along the equipotentials h ; $\delta(h)$ - particle displacement for the time τ_c. The term in brackets in (4) describes the relative number of the trajectories with the length L(h). The whole expression is a sum of partial contributions into the diffusion coefficient of the trajectories of various scales.

Unlike [3], where τ_c was defined by the particle departure from the equipotential for the distance $\Delta(h)$ at the expense of the seed diffusion in (2), τ_c will be defined by the equipotentials topology change time h, and, consequently, by the time of finding out of the separatrix which determines the topology in the 2D - space in the range $|H_1| \simeq h\, H_1'$: $\tau_x \simeq h/\omega$. Thus, $\tau_c \simeq \tau_x$. Substituting the expression for τ_c B in (4), it is simple to show that the trajectories $h_m^{(1)}$: $\delta(h_m^{(1)}) \simeq a(h_m^{(1)})$, contribute maximally into the diffusion coefficient. For these trajectories $L(h_m^{(1)})/ u_1 \simeq \tau_c(h_m^{(1)})$, where $u_1 = \bar{H}_1 k_\perp$, at this:

$$D \simeq \frac{\omega}{k_\perp^2}\left(\frac{k_\perp^2 \bar{H}_1}{\omega}\right)^{7/10} \qquad (5)$$

$$h_m^{(1)} \simeq \left(\frac{\omega}{k_\perp^2 \bar{H}_1}\right)^{3/10} \ll 1 \,, \qquad (6)$$

$$a(h_m^{(1)}) \simeq \left(\frac{k_\perp \bar{H}_1}{\omega}\right)^{2/5} \gg 1$$

3.Now we shall consider the particle drift in the potential H_2, bearing it in mind that $v_z(t)/v = \sin \omega_b t$, where ω_b - the baunce-frequency of trapped electrons . Under large enough values of ε : $\varepsilon > \varepsilon_* = (\omega_b / k_\perp^2 H_2)^{3/7}$ the value h_m appears to be less than ε. The results from section 2 are applicable. The effective diffuion coefficient is expressed by (5,6) with the replacement of $(\varepsilon\omega_b)$:

$$D \simeq \varepsilon^{3/10} \frac{\omega_b}{k_\perp^2}\left(\frac{k_\perp^2 \bar{H}_2}{\omega_b}\right)^{7/10} \,, (\varepsilon > \varepsilon_*) \qquad (7)$$

However, under $\varepsilon < \varepsilon_*$, $h_m^{(1)} > \varepsilon$; a considerable equipotentials topology change takes place in the region $\Delta h \simeq \varepsilon \ll h$. B In this case the value $\tau_c \simeq h^2/(\varepsilon^2 \omega_b)$, trajectories $h_m^{(2)}$:

$\delta(h_m^{(2)}) \simeq a(h_m^{(2)})$, for which $L(h_m^{(2)})/u_2 \simeq \tau_c(h_m^{(2)})$, where $u_2 = \bar{H}_2 k_\perp$,

$$D \simeq \varepsilon^{6/13} \frac{\omega_b}{k_\perp^2} \left(\frac{k_\perp^2 \bar{H}_2}{\omega_b} \right)^{10/13} \qquad (\varepsilon < \varepsilon_*) \tag{8}$$

$$h_m^{(2)} \simeq \varepsilon_* \, (\varepsilon/\varepsilon_*)^{6/13} \gg \varepsilon;$$

$$a(h_m^{(2)}) k_\perp \simeq \varepsilon_*^{-4/3} (\varepsilon_*/\varepsilon)^{8/13} \gg 1 \tag{9}$$

contribute maximally into D.

The case when the change $v_z(t)$ is connected with the Coloumb collisions is analogous to the case $\varepsilon < \varepsilon_*$ for $v_z \propto \sin(\omega_b t)$. Here $\tau_c \simeq h_*^2/\varepsilon\nu_e$, where: ν_e - the frequency of the Coloumb interaction.

$$D \simeq \varepsilon^{6/13} \frac{\nu_e}{k_\perp^2} \left(\frac{k_\perp^2 \bar{H}_2}{\nu_e} \right)^{10/13} \tag{10}$$

REFERENCES

1. Sokolov I.M.UPN, 1986, 150, 221.
2. Zeldovitch J.B.JETP Lett., 1983, 38, 51.
3. Isitchenko M.B.and oth. JETP, 1989, 96.
4. Parail V.V., Yushmanov P.N.JETP Lett., 1983, 42, 278.

Average Magnetic Surfaces in TBR-1 Tokamak *

S.J.Camargo, I.L.Caldas
Instituto de Física, Universidade de São Paulo
C.P. 20.516, 01498, São Paulo-SP Brazil

The equilibrium of a tokamak can be improved using resonant helical windings with the same helicity as the magnetic field [1]. These helical windings, however, spoil the symmetry of the system and may destroy the magnetic surfaces.

We consider a toroidal equilibrium of a tokamak modified by resonant helical windings, regarded as a perturbation, because the amplitude of the current in the helical windings is much smaller than that of the plasma current. The magnetic field is thus a superposition of the magnetic fields of the equilibrium and the helical windings.

A variational principle can describe the field lines, using the vector potential of the system [2]. The Noether's theorem can then be applied and one conclude that if all components of the vector potential are independent of one of the coordinates, the component of the vector potential corresponding to this coordinate is an invariant [2].

As the equilibrium has a toroidal symmetry and the windings depend on an helical variable, there is no symmetry . Then, the Noether's theorem cannot be applied directly, because there is a dependence on all three coordinates. An average vector potential is defined in order to obtain an average invariant, which describes approximately the problem [3].

The vector potential of the system $\mathbf{A}$ is the superposition of the vector potential of the equilibrium $\mathbf{A}^0$ and of the perturbation $\tilde{\mathbf{a}}$

$$\mathbf{A}(\rho,\theta,\phi) \simeq \mathbf{A}^0(\rho,\theta) + \tilde{\mathbf{a}}(\rho,\theta,\phi), \tag{1}$$

*Work partially supported by FAPESP and CNPq

where ρ, θ, ϕ are the local coordinates [4].

The average vector potential is defined as the average over the poloidal angle θ on a line where u, which describes the helical windings ($u = m\theta - n\phi$), is a constant [3, 4]. It is then natural to use the variable u instead of ϕ. As the vector potential does not depend on the poloidal angle θ, following Noether's theorem, the component θ of the average vector potential is an invariant [3, 4]

$$\Psi(\rho, u) = \overline{A}_\theta(\rho, u) + \frac{m}{n}\overline{A}_\phi(\rho, u) = constant. \tag{2}$$

Although Ψ is an exact invariant, it is not the exact invariant of the problem. The validity of the method derives from the fact that the average vector potential approximates the exact vector potential. The invariant of the approximate magnetic surface is thus an approximate invariant of the exact magnetic surface [3].

A plasma confined in a toroidal apparatus was described by Shafranov using toroidal coordinates [5], the resulting invariant ψ^0 can be expressed in local coordinates [6]. The resulting expression depends on λ defined by [7] $\lambda = \beta_p - 1 + l_i/2$, where β_p is the ratio between the kinetic pressure and the magnetic poloidal pressure of the plasma and l_i its internal induction.

The magnetic field can be obtained from ψ^o [4, 8] and the vector potential is then calculated through the expression [9]

$$\mathbf{A} = \chi\nabla\theta - \Gamma\nabla\phi, \tag{3}$$

where χ and Γ are the toroidal and the poloidal fluxes of the magnetic field [9, 4]. Using these expressions, it is possible to calculate the vector potential of the equilibrium up to the order of ρ^2/R_0^2 [4, 8], where R_0 is the major radius of the tokamak.

The scalar potential Φ of a number of equidistant thin conductors wound on a circular torus carrying currents I in alternating directions is known [10]. The magnetic field can then be obtained [4] and through the fluxes of the magnetic field we have the vector potential of the helical windings.

Applying the expressions of the vector potential of the equilibrium and of the helical windings in equation (1) and following the average method described, the approximate invariant Ψ of the system is obtained [4, 8].

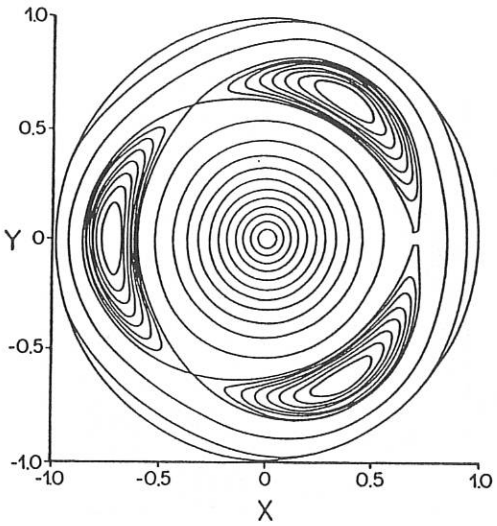

Figure 1: Surfaces of Ψ constant for $\lambda = 0.28$

Figures (1) and(2) show curves of constant Ψ using the parameters of the TBR-1 tokamak: $a = 8cm$ (minor radius of the plasma), $b = 11cm$ (minor radius of the tokamak), $R_0 = 30cm, I_p = 18kA$ (plasma current), $I_e = 600kA$ (current in the tokamak coils), $I = 100A$ (helical current) and $m = 3, n = 1$ (number of periods of the helical field in the toroidal and poloidal directions respectively). In figure (1) one uses $\lambda = 0.28$, a typical value for TBR-1 tokamak and in figure (2) $\lambda = -1$, which corresponds to the limit of a zero ratio between the kinetic and magnetic pressures of the plasma.The figures are normalized by a.

From the figures, it can be seen that in the limit of zero pressures, the average magnetic islands are bigger and are nearer of the plasma boundary. The effect of the pressure on the island can be verified by calculating the island width using usual expressions [8].

The same analysis was made using an expression for the helical windings without the toroidal effect [8]. It was concluded that the toroidal effect results in magnetic islands which are slightly smaller than that obtained from cylindrical approximation [8].The effect of the pressure was also noticed in this case.

It should be stated that considering the pressure of the plasma is equivalent to a displacement of the magnetic axis, because when the pressure is not considered the magnetic axis coincides with the geometric axis. The effect of the island width has already been observed by considering the

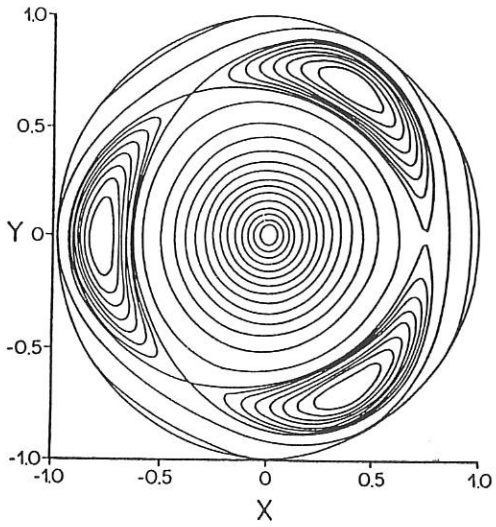

Figure 2: Surfaces of Ψ constant for $\lambda = -1$

displacement of the magnetic axis analytically and numerically [11].

References

[1] Pulsator Team, *Nucl. Fusion* 25, 1059 (1985).

[2] J.R. Cary, R.G. Littlejohn, *Ann. Phys.* 151, 1 (1982).

[3] J.R. Cary, *Phys. Fluids* 27, 119 (1984).

[4] S.J. Camargo, I.L. Caldas, submitted to *Phys. Scripta.*

[5] V.D. Shafranov, *Sov. Phys. JETP* 37, 775 (1960).

[6] V. Okano, Master of Science thesis, São Paulo University (1990).

[7] R.J. La Haye et al., *Nucl. Fusion* 21, 1235 (1981).

[8] S.J. Camargo, Master of Science thesis, São Paulo University (1989).

[9] A.H. Boozer, *Phys. Fluids* 29, 4123 (1986).

[10] M.Y. Kucinski, I.L. Caldas, *Z. Natur.*, 42a, 1124, (1987).

[11] S.B. Zheng, A.J. Wooton, *Report Tx 78712* Texas University (1987).

SUPPRESSING EFFECT OF ELECTROSTATIC WAVES ON DRIFT WAVE INSTABILITY

YIN Yongxiang
(Southwestern Institute of Physics, Leshan, Sichuan, China)

ABSTRACT

The trajectory of charge particles will be changed by electrostatic wave with a large amplitude in plasma. The dispersion relation of drift waves is derived with the help of integration along the changed trajectory. It shows that the drift wave instability can be suppressed by a so-called "quasi-Larmor radius effect" as long as the condition, $\vec{K}\cdot\vec{S}_e>\vec{K}\cdot\vec{S}_i$, is satisfied, where $\vec{K}$ is the wave number of drift wave, $\vec{S}_e$, $\vec{S}_i$, caused by electrostatic waves, are the amplitudes of shift of charge particles, respectively.

1. INTRODUCTION

It was reviewed in Ref. [1] that a high frequency electric field polarized in z direction has a stabilizing effect on drift instability, and the possibility of stabilization is due to an additional pressure from the external field. In this letter, we present a mechanism of suppressing drift instability, which is caused by an electrostatic wave with a large perpendicular component. This mechanism is named "quasi-Larmor radius effect".

Assuming that there is a monochromatic electrostatic wave with frequency, $|\Omega_i|\ll\omega_0\ll\Omega_e$, in plasma, its phase velocity parallel to fixed magnetic field satisfies $\omega_0/k_{0z}\gg V_e=\sqrt{T_e/m_e}$. Neglecting the effect of Landau interaction between particle and the wave, we consider $\vec{V}_{Ee}=\vec{E}\times\vec{B}_0/B_0^2$, and $d\vec{V}_{Ei}/dt=e\vec{E}/m_i$ as the responses of electrons and ions to the wave, respectively. The trajectory of particles will then be changed from the unperturbed one . Of course, the dispersion property of plasma will also be changed, which leads to the stabilization of drift instability.

2. INTEGRATION ALONG CHANGED TRAJECTORY

When an electrostatic wave

$$\vec{E}=\vec{E}_0\cos(K_0\cdot r-\omega_0 t) \qquad (1)$$

is in plasma if $K_{0\perp}V_t/|\Omega|\ll1$, the changed trajectory of particles with the initial condition $t'=t$, $\vec{r}'(t')=\vec{r}(t)$, $\vec{V}'(t')=\vec{V}(t)$, are [2]

$$\vec{V}'(t') = \vec{\vec{B}}_e(t'-t)\cdot\vec{V}+\vec{E}_0\times\vec{B}_0\cos\psi/B_0^2 - eE_z\sin\psi\,\vec{e}_z/(m_e(k_{0z}V_z-\omega_0)),$$

$$\vec{r}'(t')-\vec{r}(t)= \frac{\vec{\vec{H}}_e(t'-t)\cdot\vec{V}}{\Omega_e} + \frac{\vec{E}_0\times\vec{B}_0(\sin\psi-\sin\psi_0)}{B_0^2(k_{0z}V_z-\omega_0)} + \frac{eE_z(\cos\psi-\cos\psi_0)}{m_e(k_{0z}V_z-\omega_0)^2}\vec{e}_z \qquad (2)$$

for electrons; and

$$\vec{V}'(t') = \vec{\vec{B}}_i(t'-t)\cdot\vec{V} + e\vec{E}_0\sin\psi/(m_i(k_{0z}V_z-\omega_0)),$$

$$\vec{r}'(t')-\vec{r}(t)= \frac{\vec{\vec{H}}_i(t'-t)\cdot\vec{V}}{\Omega_i} - e\vec{E}_0(\cos\psi-\cos\psi_0)/(m_i(k_{0z}V_z-\omega_0)^2) \qquad (3)$$

for ions, where $\vec{V}=V_\perp\cos\theta\,\vec{e}_x+V_\perp\sin\theta\,\vec{e}_y+V_z\vec{e}_z$, $\psi_0=\vec{K}_0\cdot\vec{V}-\omega_0 t$, $\psi=\psi_0+(K_{0z}V_z-\omega_0)(t'-t)$, $\vec{\vec{H}}$, and $\vec{\vec{B}}$ are definied in Ref. [2]. $\vec{E}_0=E_x\vec{e}_x+E_y\vec{e}_y+E_z\vec{e}_z$, $\vec{K}_0=K_{0x}\vec{e}_x+K_{0y}\vec{e}_y+K_{0z}\vec{e}_z$, $\vec{r}=x\vec{e}_x+y\vec{e}_y+z\vec{e}_z$, and $V_\perp$, θ , V_z , x, y, z are constants that arise in the integration of equation of motion of particles. Usually, the zeroth distribution function of particles, f_0 , depends on these constants of integration. In our case, we choose

$$f_0 = f_0(V_\perp^2 \ , \ V_z \ , \ X) \ . \qquad (4)$$

where

$$V_\perp^2=(V_x' - \frac{E_y\cos\psi}{B_0})^2+(V_y'+ \frac{E_x\cos\psi}{B_0})^2 \ ,$$

$$V_z=V_z'+eE_z\sin\psi/(m_e(k_{0z}V_z-\omega_0)), \qquad (5)$$

$$X=x'- \frac{1}{\Omega_e}(V_y'+ \frac{E_x\cos\psi}{B_0})- \frac{E_y(\sin\psi-\sin\psi_0)}{m_i(k_{0z}V_z-\omega_0)}$$

for electrons, and

$$V_\perp^2=(V_x'- \frac{eE_x\sin\psi}{m_i(k_{0z}V_z-\omega_0)})^2+(V_y'- \frac{eE_y\sin\psi}{m_i(k_{0z}V_z-\omega_0)})^2 \ ,$$

$$V_z = V_y' - eE_z\sin\psi \ / \ (m_i(k_{0z}V_z - \omega_0)) \ , \qquad (6)$$

$$X=x'- \frac{1}{\Omega_i}(V_y'- \frac{eE_y\sin\psi}{m_i(k_{0z}V_z-\omega_0)})+ \frac{eE_x(\cos\psi-\cos\psi_0)}{m_i(k_{0z}V_z-\omega_0)^2}$$

for ions.

When there is a drift perturbation

$$\phi_k(r, t) = \phi(k)\exp[i(k_y y+k_z z-\omega t)] \qquad (7)$$

in the plasma, the perturbed distribution function can be found as following. [1]

$$\frac{m}{q}f_1(r, t)= \int_{-\infty}^{t}dt' \nabla_r\cdot\phi_k(r', t)\cdot\nabla_v\cdot f_0(V_\perp^2 \ , \ V_z \ , \ X) \ , \qquad (8)$$

where $f_1(r, t)=f_1(k)\exp[i(k_y y+k_z z-\omega t)]$. Making use of Eq.(2),(4),(5), we have

$$\frac{m}{q}f_{1e}(r, t) = 2\frac{\partial f_{0e}}{\partial V_\perp^2}\phi_k(r, t)+ \int_{-\infty}^{t}dt' [2i(\omega-k_z v_z)\frac{\partial f_{0e}}{\partial V_\perp^2} + i\frac{\partial f_{0e}}{\partial V_z}k_z-$$

$$-i\frac{\partial f_{0e}}{\partial X}\frac{k_y}{\Omega_e}+2i\frac{\partial f_{0e}}{\partial V_\perp^2}\left(\frac{k_y E_x\cos\psi}{B_0}+\frac{k_z eE_z\sin\psi}{m_e(k_{0z}V_z-\omega_0)}\right)]\phi_k(r',\ t'). \qquad (9)$$

After a heary derivation, we finally get

$$f_{1\sigma}(k)=\frac{q_\sigma}{m_\sigma}\sum(-2n\Omega_\sigma\frac{\partial f_{0\sigma}}{\partial V_\perp^2}+\frac{\partial f_{0\sigma}}{\partial V_z}k_z-\frac{\partial f_{0\sigma}}{\partial X}\frac{k_y}{\Omega_\sigma})\phi_k(k)\times$$

$$J_n^2\left(\frac{k_y V_\perp}{\Omega_\sigma}\right)J_s^2(\delta_\sigma)/(\omega_n-s(k_{0z}V_z-\omega_0)), \qquad (10)$$

where $\omega_n=-n\Omega_\sigma+k_zV_z-\omega$, σ denotes the kind of the particle . Thus,

$$\delta_e=[\left(\frac{k_yE_x}{B_0(k_{0z}V_z-\omega_0)}\right)^2+\left(\frac{k_zeE_z}{m_e(k_{0z}V_z-\omega_0)^2}\right)^2]^{1/2}, \qquad (11)$$

$$\delta_i=(k_yeE_y+k_zeE_z)/(m_i(k_{0z}V_z-\omega_0)^2) \qquad (12)$$

Recalling that $\omega\ll\Omega_i\ll\omega_i$ and $\omega/k_{\parallel}\gg V_e>V_i$, only the terms of n=0, s=0 in Eq.(10), are important in use. Therefore

$$f_{1\sigma}(k)=\frac{q_\sigma}{m_\sigma}\left(\frac{f_{0\sigma}}{V_z}k_z-\frac{k_y}{\Omega_\sigma}\frac{f_{0\sigma}}{X}\right)J_0^2\left(\frac{k_zV_\perp}{\Omega_\sigma}\right)J_0^2(\delta_\sigma)\phi(k)/(k_zV_z-\omega). \qquad (13)$$

Setting

$$f_{0\sigma}=n_\sigma(1-\varepsilon X)\exp(-(V_\perp^2+V_z^2)/2V_\sigma^2)/(\sqrt{2\pi}V_\sigma)^3, \qquad (14)$$

and substituting it into Eq.(13), integration in velocity space gives

$$n_{1\sigma}(k)=\frac{q_\sigma n_\sigma}{m_\sigma V_\sigma^2}\phi(k)I_0(b_\sigma)e^{-b\sigma}J_0^2(\delta_\sigma)[-1+\zeta_\sigma)Z(\zeta_\sigma)\left(\frac{\omega_e^*}{\omega}-1\right)]. \qquad (15)$$

where $b_\sigma=\left(\frac{k_yV_\sigma}{\Omega_\sigma}\right)^2$, $\zeta_\sigma=\omega/(\sqrt{2}k_zV_\sigma)$ and $Z(\zeta_\sigma)$ is plasma dispersion function.

3. DISPERSION RELATION AND RESULTS

Substituting Eq.(15) into Poisson equation, we finally get the dispersion relation of drift wave in an imhomogenous plasma with an electrostatic wave

$$(k_y^2+k_z^2)\lambda_D^2+\frac{T_e}{T_i}I_0(b_i)e^{-b_i}J_0^2(\delta_i)[1-\zeta_iZ(\zeta_i)\left(\frac{\omega_i^*}{\omega}-1\right)]+$$

$$J_0^2(\delta_e)[1-\zeta_eZ(\zeta_e)\left(\frac{\omega_e^*}{\omega}-1\right)]=0, \qquad (16)$$

where $\lambda_D^2=V_e^2/\omega_e^2$ is Debey length. For deriving Eq.(16), we make use of $b_e\ll1$, $I(b_e)e^{-b_e}=1$. Setting $\omega=\omega_r+i\gamma$, $\gamma\ll\omega_r$, and $\zeta z(\zeta)=\zeta z_r(\zeta)+i\sqrt{\pi}\zeta\exp(-\zeta^2)$, for the case of $V_i\ll\omega_r/k_z\ll V_e$, $\zeta_iZ_r(\zeta_i)=-1-1/2\zeta_i^2$, $\zeta_eZ_r(\zeta_e)=-2\zeta_e$, the roots of Eq.(16) are

$$\frac{\omega_e^x}{\omega_r} = J_0^2(\delta_e)/J_0^2(\delta_i)I_0e^{-b_i}\ , \tag{17}$$

$$\frac{\gamma}{\omega_r} = J_0^2(\delta_e)\sqrt{\pi}\,\zeta_e\exp(-\zeta_e^2)(1-J_0^2(\delta_i)I_0e^{-b_i}/J_0^2(\delta_e))/J_0^2(\delta_i)I_0e^{-b_i}\ . \tag{18}$$

It is clear from Eq(18) that the growth rate of drift instability γ increases as b_i increases. However, for arbitrary b_i , when

$$J_0^2(\delta_e) < I_0(\delta_i)I_0e^{-b_i}\ , \tag{19}$$

the unstable drift wave will be suppressed. As a example, we consider the case of lower hybrid wave in plasma. Where the components of electric field of LHW satisfy[3] $E_x \gg E_z > E_y$. Therefore, $\delta_e \approx K_y E_x / B_0\omega_0$, $\delta_i \approx 0$, inequality (19) becomes $J_0^2(\delta_e) < I_0(b_i)e^{-b_i}$. If $\rho_i \sim 10^{-3}m$, $\omega_0 \sim 10^8 S^{-1}$. We get $E_x > 1.2B_0 \times 10^6 v/m$ for $k_y \sim 10^3 m^{-1}$, and $E_x > 3B_0 \times 10^6 v/m$ for $K_y \sim 10^2 m^{-1}$. These values of electric field of LHW can be achieved in experiments. [4]

The fact of stabilization of the instability can be understood on the following consideration.

A requisite for inequality (19) is

$$J_0^2(\delta_e) < J_0^2(\delta_i)\ , \tag{20}$$

Our discussion about Eq.(20) is limited in the region of $0 \leqslant \delta_e < x_{01} \approx 2.4$, where x_{01} is the first root of zeroth Bessel function. In this region, $J_0(x)$ is a monotonously decreasing function. Inequality (20) implies that $\delta^2 < \delta^2$, from which we have

$$\vec{K}\cdot\vec{S}_e > \vec{K}\cdot\vec{S}_i\ . \tag{21}$$

where $\vec{K}$ is the wave number of drift wave. $\vec{S}_e \approx \vec{E}_0 \times \vec{B}_0 / (B_0^2(k_{0z}V_z - \omega_0))$, $\vec{S}_i = e\vec{E}_0/(m_i(k_{0z}V_z - \omega_0)^2)$ are the amplitudes of shift of electrons and ions from their original trajectory, respectively. Inequality (21) shows that when the shift of electrons, which is caused by electrostatic wave, in the direction of drift wave propagation, is greater than that of ions, drift instability may be suppressed.

In the integration along trajectory, there is a factor, $\exp(ik_y y') = \exp[ik_y(y+y_\Omega+y_{\omega_0})]$, where $y_\Omega = -(V_\perp/\Omega)[\cos(s+\Omega(t'-t)) - \cos\theta]$ is the projection of Larmoy motion of particle in direction y, which is equivalent to an oscillation with frequency Ω;

$y_{\omega_0} = \dfrac{E_x(\sin\psi - \sin\psi_0)}{B_0(k_{0z}V_z - \omega_0)}$ or $-\dfrac{eE_y(\cos\psi - \cos\psi_0)}{m_i(k_{0z}V_z - \omega_0)^2}$ is equivalent to an oscillation

with frequency ω_0 in direction y. Due to Larmo-motion, y_Ω has an effect on drift wave through $J_0^2(K_\perp V_\perp/\Omega)$; the shift, y_{ω_0} must influences drift wave in the same way. The oscillation of electrons in K direction has a stable effect on drift wave, but that of ions has the reverse effect. Because the mechnism of this effect is similar to that of Larmor motion in physical picture and mathmatic expression, we name it "quasi-Larmor radius effect".

4. CONCLUSION

We have shown that a large amplitude electrostatic wave leads to an additional shift of particles, which can suppress drift instability by quasi-Larmor radius effect. This mechanism is valid and obvious only under the following conditions. They are $|\Omega_i| \ll \omega_0 \ll \Omega_e$, $(\omega_0/K_{\theta i}) \gg V_e$, as well as inequality (19). The last condition, in fact, requires the power of electrostatic wave. As an example, in the present experiment of lower hybrid wave heating and current drive, it is not difficult to satisfy these conditions.

The author greatly thanks Din Houchang, Que Wenxiao and Wang Zhongtian for their helpful discussions and suggestions to this work.

References

[1] A.A.Ivanov. Review of Plasma Physics, New York-London, Consultanrs Bureau, V.6,(1975)161.

[2] S.Ichimaru. Basic Principles of Plasma Physics. W.A.Benjamin, INC.(1973)P.46.

[3] M.Brambilla, Nucl.Fusion, Vol.18, No.4,(1978)

[4] E.Barbato, A.Cardinal, Heating in Toroidal Plasma. Proceedings of the 4th International Symposium. Roma, March 21-28, 1984, Vol.Ⅱ, P.1353.

Drift dissipative instabilities in a two electron temperature plasma

M. Bose and S.K. Sharma
Physics Department
I.I.T. Hauz-Khas
New Delhi-110 016.

ABSTRACT

In this investigation the electron-acoustic and lower hybrid drift dissipative instabilities have been studied in the presence of two types of electrons i.e. hot and cold. Assuming the electrons to be magnetized and ions unmagnetized and using fluid equations we derive the expressionsfor growth rate of electron acoustic drift dissipative and lower hybrid drift dissipative waves. It is found that increase in cold electron changes the growth rate of the electron drift dissipative wave where as the lower hybrid dissipative wave remains nearly unchanged.

EFFECTS OF RIPPLE LOSSES ON FUSION ALPHA PARTICLE DISTRIBUTIONS

Gerald Kamelander*)
Austrian Research Center Seibersdorf, A-2444 Seibersdorf, Austria

The aim of the present paper consists in evaluating the fusion alpha particle distribution function taking account of the ripple induced losses. The consequence of alpha ripple losses for the performance of the next generation of TOKAMAK reactors is an important subjekt of TOKAMAK research.

The alpha particle distribution function is calculated by means of a bounce-averaged kinetic equation $f_\alpha(\rho,E)$ [1,2]

$$\frac{\partial f_\alpha}{\partial t} + \frac{\partial}{\partial E}(L.f_\alpha) - \frac{\partial}{\partial E^2}(Df_\alpha) = Q(\rho,E) \qquad (1)$$

where $L(E,\rho)$ and $D(E,\rho)$ are the usual FOKKER-PLANCK coefficients. The source term Q is the sum

$$Q(\rho,E) = Q_{ex} + Q_{in} \qquad (2)$$

of the extern fusion source Q_{ex} and of the inner source Q_{in} for transport processes. Equ.(1) is a model equation conserving particle number and energy and may be applied to all transport processes where the transport coefficients are known as recently done for semi-empiric transport laws [3]. The alpha energy deposition rates obtained from the distribution functions f_α as a solution of equ.(1) are to be used as an input for the plasma equations to simulate the dynamic behaviour of the plasma.

A generalized theory of ripple-banana transport in a TOKAMAK has been published by Ref. [4]. Basing on this theory expressions for particle- and heatfluxes have been derived andbuilt in into the inner source term of the kinetic equation (1).

Equ.(1) has been solved by a computer routine and linked to a simplified plasma simulation code. It is shown that the stochastic ripple transport may have the same order of magnitude as the semi-empiric anomalous transport [3]. It may give rise to distortions of the distribution function and therfore to instabilities.

References

[1] D.F. Düchs, D.Pfirsch, IAEA-CN-33/A17
[2] G. Kamelander, JET-IR(88)13, 1988
[3] G. Kamelander, IAEA, Alpha particle meeting, Kiev, Oct. 1989
[4] P.N. YUSHMANOV, Nuclear Fusion, Vol. 23, No.12 (1983)

STATIONARY SPECTRA OF SHORT-WAVE LOW-FREQUENCY FLUCTUATIONS IN A FINITE-BETA PLASMA

P.P.Sosenko, M.O.Vakulenko

Institute for Theoretical
Physics, Kiev 252130,
Ukrainian SSR (USSR)

It has been exhibited[1] that in the low-beta plasma the short-wave fluctuations of transverse magnetic field take place, with their spectral characteristics being determined by the nonlinear interaction with the convective fluctuations of the electric potential, and the stationary spectra of thermal convective and magnetostatic fluctuations in the short-wavelength range have been calculated for a strong nonlinear interaction.

We show that electromagnetic effects play an important role in the nonlinear interaction of low-frequency motions, in particular, transverse and longitudinal magnetic field fluctuations in the finite-beta plasma affect substantially the spectral characteristics of the short-wavelength convective fluctuations. Stationary spectra of strongly nonlinear thermal fluctuations of the potential and the magnetic field in the finite-beta plasma are calculated. Magnetic fluctuations are shown to produce an essential broadening of the convective-fluctuations spectrum.

1. Vakulenko M.O., Sosenko P.P. Stationary spectra of short-wave convective and magnetic fluctuations in a plasma //1989 ICPP Contr. papers v.III. New Delhi, 1989. P.905-907.

THE EFFECT OF MAGNETIC FIELD PERTURBATIONS ON THE NUMERICALLY DERIVED DIFFUSION COEFFICIENT FOR THE FAST ALPHA PARTICLES

Ezio BITTONI, Marcel HAEGI*

Centro Calcolo ENEA "Ezio Clementel"
Viale G.B.Ercolani,8, I-40138 Bologna
*Associazione EURATOM-ENEA
C.P. 65 I-00044 Frascati

Abstract

Numerically derived diffusion coefficients for the fast alpha transport in presence of magnetic ripple, due to the discrete toroidal field coils, for the NET benchmark parameters, have recently be published by the authors [1].

The present calculation extends the previous work, by taking account, in addition, of the level of the perturbations of the magnetic field produced by MHD activity. First results for m=n=1 modes are presented.

Introduction

The lack of axisymmetry of the magnetic field in a tokamak, is one of the main reasons of the loss of the fast alpha particles.

The effects of the ripple on the fast alpha confinement, due to the discrete toroidal magnetic coils, is still the object of a long-standing numerical effort, including three methods:

A) The guiding centre orbit numerical calculations, following the alphas up to theire critical energy [2][3][4], which results in very long computing time, and still presents some degree of uncertainty.

B) The mapping of the parameters of the orbits, which permits an evaluation of the stochastic regions [5][6][7], and gives a fair insight of the behaviour of these complicated trajectories, however a comprehensive evaluation of the losses is difficult.

C) Using a guiding centre orbit following code for only a few hundreds of orbits, it is possible to derive local numerical diffusion coefficients [1], which permit a faster evaluation of the losses than the full particle deceleration

calculation of A). The obtained local coefficients may then usefully be compared with the qualitative one of the mapping method.

The numerical diffusion coefficient is defined as:

$$D_k \equiv \frac{1}{i} \sum_i \frac{(r_{ik} - \bar{r})^2}{t_{ik}}$$

Where: i the total number of cases taken into account for the same particle (from 20 to 50)
k the total number of calculated orbits
r the maximum displacement of the orbits on the equatorial plane
t_{ik} the time at the orbit k for the case i
$\bar{r}$ mean position of the i particles after k orbits

Recently, the effects of the MHD perturbations on the fast alpha confinement have also been investigated by means of the mapping method [7][8][9].

In this paper, we give a first evaluation of the diffusion coefficient of the fast alphas in presence of a static magnetic perturbation, simulating MHD activity, as a function of the level of the perturbation, in presence of ripple and pitch angle scattering collisions.

It has to be stressed that these various diffusion mechanisms do not simply add up, but the may present substantial mutual enhancement and none linear effects.

The physical model

We simulate large scale quasi-static helical mode involving practically all the plasma column, by using the following perturbation:

$$\delta\vec{B} \equiv \vec{\nabla} \times a\vec{B}$$

$$a \equiv a_{nm} \sin(m\theta - n\varphi)$$

$$\delta_{MHD} \equiv \frac{|\delta\vec{B}|}{|\vec{B}|}$$

Where $\vec{B}$ is the total magnetic field, and δ_{MHD} the size of the perturbation.

This perturbation has been applied to the "NET Benchmark" , which corresponds to a circular section, low current, tokamak reactor: B=5.5T ; I_p=3MA ; R_o=5.3m ; a=1.2m ; $n=4*10^{20} m^{-3}$. The toroidal field coils are simulated by 12

closed polygons of current which produce a ripple, in the plasma, extending from a maximum of $\delta=10^{-2}$ to a minimum of $\delta=3.5*10^{-4}$ [1].

Because of the ripple alone, and in presence of collisions, this model loses about 15% of the fast alphas before they undergo thermalization.

Numerical results

The calculated numerical diffusion coefficient is shown, in Fig 1, as a function of the maximum pitch angle, for a maximum radius of the orbit of r/a=0.2 and an energy of the alpha of 3.5 MeV. The banana trajectories are represented by $\cos\chi \leq 0.2$, the circulating by $|\cos\chi| \geq 0.4$, and the mixed one by $0.2 \leq \cos\chi \leq 0.4$. Dashed levels indicate, from top to bottom, ripple-plateau, intermediate, neoclassical diffusion coefficient for the bananas, and classical coefficient for the circulating.

The dotted line is the calculated coefficient, in presence of the sole ripple of $\delta_r=10^{-2}$ and collisions.

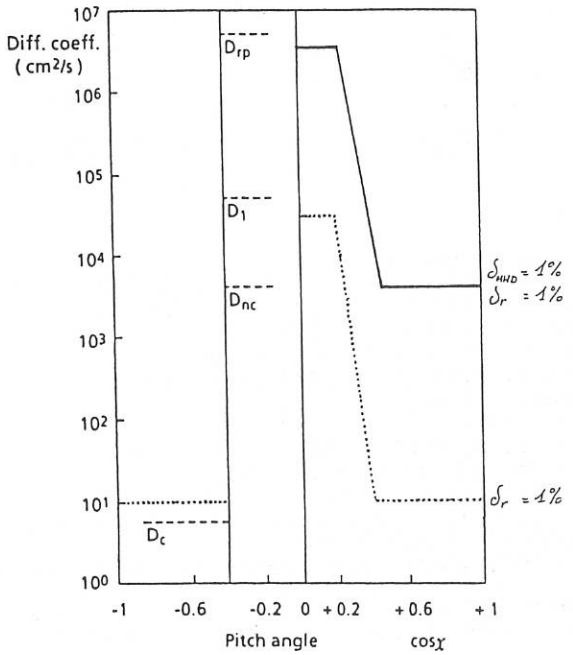

Figure 1

As we add the MHD helical $\delta_{MHD}=10^{-2}$ perturbation m=n=1, the calculated coefficient increases by several orders of magnitude, as the plain line shows.

The behaviour of this coefficient with the level of the MHD perturbation is shown in Fig 2, for typical co-streaming, counter-streaming and banana trajectories.

It results that if the level of the MHD perturbation reaches 1%, roughly 70% of the fast alpha are lost, only co-streaming circulating particles remain confined.

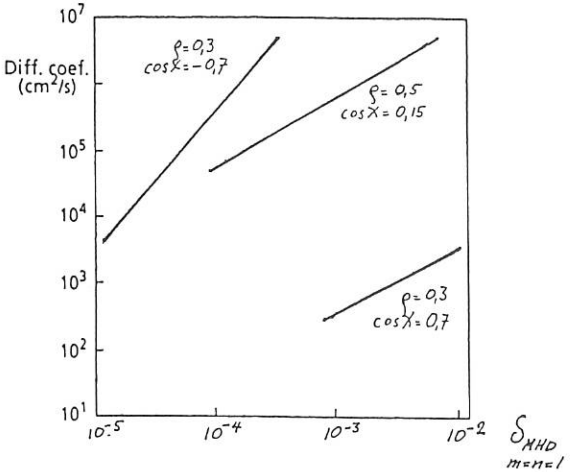

Figure 2

References

[1] E.BITTONI, M.HAEGI
Fusion Technology, Spec. Issue IAEA Kiev Meeting, 8/1990
[2] K.TANI, T.TAKIZUKA, M.AZUMI, H.KISHIMOTO
Nuclear Fusion 23 (83) 657
[3] L.HIVELY Nuclear Fusion 24 (84) 779
[4] E.BITTONI, M.HAEGI NET Report 1990
[5] R.GOLDSTON, R.WHITE, A.BOOZER
Physical Review Letters 47 (81) 647
[6] V.BELIKOV, Y.KOLESNICHENKO, V.YAVORSKIJ
Fusion Technology 15 (89) 1365
[7] S.KONOVALOV, S.PUTVINSKII
Soviet Journal of Plasma Physics 14 (88) 461
[8] S.KONOVALOV, S.PUTVINSKII
Fusion Technology, Spec. Issue IAEA Kiev Meeting, 8/1990
[9] R.WHITE, M.CHANCE, J.JOHNSON et al.
Proceeding of the 12th Inter.Conf. on Plasma Physics and Controlled Fusion Research. Nice 1988. Paper 50/D-2-4

ON DIFFUSION OF MAGNETIC FIELD LINES

D.F. Düchs, A. Montvai*, Ch. Sack

JET Joint Undertaking, Abingdon, Oxon., OX14 3EA, UK
*on leave from MTA KFKI Budapest, Hungary

The existence of magnetic flux surfaces is regarded as essential for magnetic confinement of fusion plasmas. The blurring or disintegration of these surfaces is quoted in the literature [e.g. 1-3] as cause for the observed anomalously high transport perpendicular to the (ideal) flux surfaces; mass and thermal energy are assumed to spread along magnetic field lines which fill certain volumes ergodically. Thus, the heat conductivity is composed of the radial (perpendicular) spread in space given by the field lines and the motion along these trajectories [1]

$$\chi_r = <(\Delta r)^2> /2\tau = D_{st}\ \upsilon \qquad (1)$$

with a mean free path denoted by $\lambda = \upsilon\tau$. The basic quantity in this hypothesis is, therefore, the "magnetic diffusion" coefficient D_{st}.

This coefficient is usually computed by overlaying a set of perturbations (islands) on an equilibrium field (e.g. solution of the Grad-Schlüter-Shafranov equation); the appearance and approximate size of the stochastic regions is quantified by resonance overlap criteria [4]. D_{st} is then determined with arguments of unlimited, Gaussian random walk of Markov type (called "Brownian process" in Ref. [1]).

Application of such theory to a more realistic (toroidal) tokamak plasma for a JET equilibrium [3] had shown reasonable agreement between the estimated and the observed confinement. However, the assumptions for the concept of diffusion have never been validated.

In this paper we have chosen the same case, i.e. the profile of the equilibrium safety factor

$$q_o(J) = 1 + 5J^2 \qquad (2)$$

with J ($0 \le J \le 1$) labelling the flux surfaces.

With an ansatz for the perturbation

$$\tilde{\psi} = \varepsilon \sum_{m=3}^{4} \frac{1}{(m+1)^2} \sin(m\vartheta - 2\phi) \qquad (3)$$

we obtain the magnetic field lines by solving a Hamiltonian system ($\psi = \psi_o + \tilde{\psi}$):

$$\frac{dJ}{d\phi} = -\frac{\partial\psi}{\partial\vartheta} \quad and \quad \frac{d\vartheta}{d\phi} = \frac{\partial\psi}{\partial J} \qquad (4)$$

with

$$\frac{\partial\psi_o}{\partial J} = 1/(1+5J^2)$$

The basic "resonances" in $\tilde{\psi}$ have (obviously) been imposed in the "confinement" region of q_0 at values:

$$m/n \equiv 3/2 \quad and \quad 4/2$$

As compared to [3] the numerical accuracy has been improved very considerably as well as the extent of the calculation with regard to number and length of computed field lines [5].

The perturbation amplitude ε in (3) has been varied in a large range: $0.05 \leq \varepsilon \leq 150$. A value of $\varepsilon \approx 0.01$ corresponds to observed magnetic field fluctuations $\delta B/B_0 \sim 10^{-3}$.

In order to check the assumption of "field line diffusion" we chose (arbitrarily) a number of flux labels around the resonances as starting points (typically $0.1 \leq J_{oj} \leq 0.7$), covering either sections or the full 2π of the poloidal angle, and followed the field lines usually several hundred times the long way around the torus (in ϕ).

Corresponding to a "Brownian diffusion" process the field lines would have to spread to neighbouring J's with a roughly Gaussian profile broadening with increasing number of revolutions (in ϕ)!

Figure 1 shows the distribution of field lines over J starting at $J_0 = 0.35$ for up to 100 revolutions.

Although this case is a most favourable one with respect to ergodicity, the actual distribution does not exhibit a diffusion behaviour. The profile is far from Gaussian, the broadening is much slower. Sometimes even contractions can be observed (see later).

In Fig. 2 the actual half width is plotted as function of ϕ and shows saturation with oscillating amplitude. A diffusive half width must increase monotonically ($\propto \sqrt{\phi}$).

Another method of checking diffusion is through correlation lengths of field lines. In a true diffusion process the field lines would "lose memory" exponentially after a typical correlation length.

$$2\pi R / L_c \equiv \ell n(\pi / 2s) \qquad (5)$$

with s ≡ stochasticity parameter [1].

In Fig. 3 several correlations are shown and compared with those for L_C. Clearly, the correlation is much stronger than for a Brownian behaviour.

With respect to the application of such field line properties to anomalous transport one should observe the following points:

a) In general it seems not possible to describe the spreading of the magnetic field lines through a diffusion process; any artificial "diffusive" approximation of the actual data yields coefficients (D_{St}) which are at least an order of magnitude smaller than previously [1-3] estimated.
b) For realistic perturbation levels ($0.005 < \varepsilon < 0.03$) most of the surfaces are only modified in shape but stay intact as shown in Fig. 4, where according to the present assumptions no anomalous transport would occur across J = 0.53, and J = 0.23.
c) For larger ε the expected evolution towards enhanced diffusivity does not occur [6]; instead a new (ordered) structure re-appears gradually.
d) Computing the magnetic field energy of the perturbed state in function of ε, at realistic levels one gets a growth of about one percent as compared to the unperturbed state. That is energy of the order of the plasma thermal energy is obviously needed to produce the perturbed fields; the corresponding (perpendicular) currents would have to be driven (in addition to the enhanced confinement losses).

REFERENCES

[1] A.B. Rechester, M.N. Rosenbluth, Phys. Rev. Letters (1978), 38.
[2] P.H. Rebut, M. Brusati, M. Hugon, P. Lallia, IAEA Plasma Physics and Controlled Nuclear Fusion Research, (1986), Vol. 2, 187
[3] K. Elsässer, D.F. Düchs, Ch. Sack, Physics Letters A, 120 (1987), 57.
[4] For example, A.B. Rechester, T.H. Stix, Phys. Rev. Lett. 36, 587 (1976).
[5] A. Montvai, IPP Report 2/299 (1989).
[6] A. Montvai, D.F. Düchs, JET-P(89)75

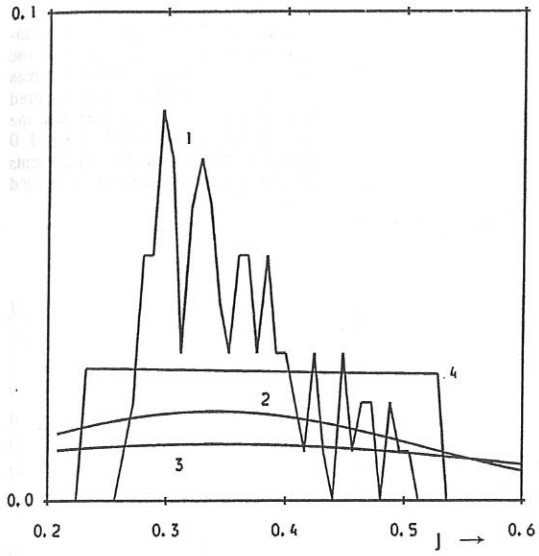

Fig.1 Distribution of the J_i coordinate values of one hundred field lines (started at $J_{0i}\equiv 0.35$, $0\leq\vartheta_{0i}\leq 2\pi$, i=1...100) after 100 toroidal revolutions.

1) Density function computed with Eq.4.
2) Density function of a hypothetical diffusion process with $D_{st}=\sigma^2$ of the actual distribution after five times around the torus.
3) as curve 2, but D_{st} is the one computed according to Ref [1].
4) as curve 3, but taking into account the presence of intact magnetic surfaces as reflecting barriers.

(Curves 1-4 are normalised to the same integral value ≠ 1!)

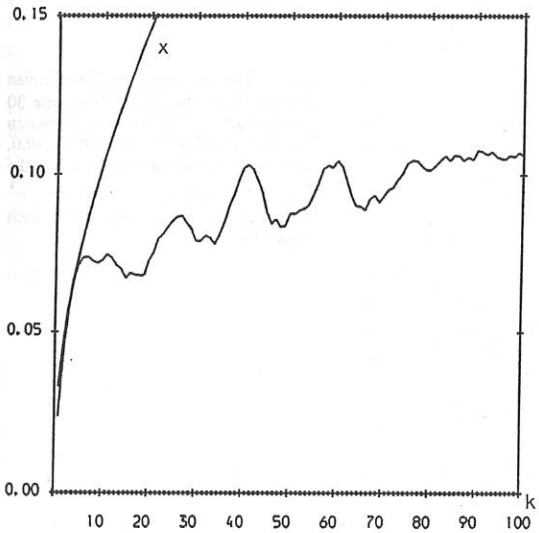

Fig.2 Half width of the Gaussian curves fitting the actual distributions of the J_i coordinate values of one hundred trajectories of Fig. 1 as function of the number of transitions (k) through the Poincaré section. Also shown is the expected evolution of a diffusion half width on the basis of the first five transitions (curve: x)

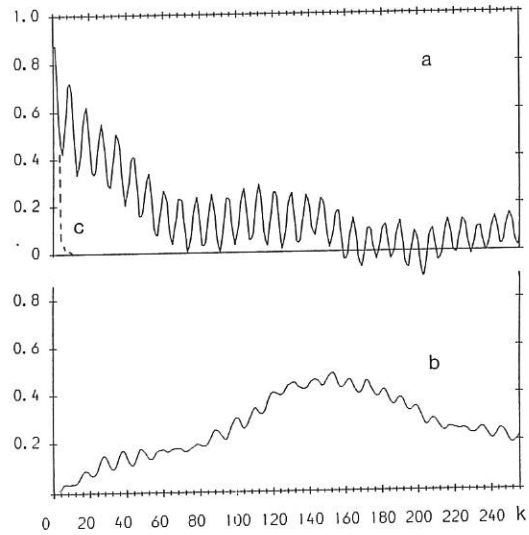

Fig.3 Auto (a) and cross-correlation (b) functions as functions of the number of toroidal revolutions (k). The auto-correlation is computed for the field line starting at J_{01}=0.43, ϑ_{01}=1.0. whereas the cross correlation is computed between the former trajectory and the one starting at J_{02}=0.33, ϑ_{02}=1.0 (ε=0.025). The dashed line (c) represents the autocorrelation function computed by using L_c in Eq.5.

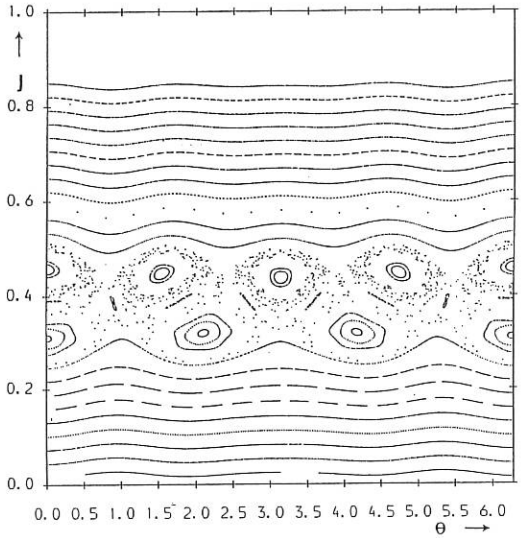

Fig.4 Poincaré plot of the Hamiltonian problem given by Eq.4. There are 30 equidistant trajectories between J_{01}=0.05 and J_{030}=0.85, with φ_{0i}=0.0, i=1...30. The perturbation level is the same as in Figs.1-3: ε=0.025. 10^3 transitions have been computed for each trajectory.

TOROIDAL ION TEMPERATURE GRADIENT DRIVEN WEAK TURBULENCE

Nathan Mattor* and J.W. Connor

Culham Laboratory, Abingdon, Oxfordshire OX14 3DB, England
(Euratom/UKAEA Fusion Association)

Introduction: The theory of ion temperature gradient driven turbulence ("η_i turbulence") is able to explain many *qualitative* features of tokamak transport, but there has not yet been accurate *quantitative* agreement with experimental measurements.[1] This is perhaps because no single theory to date has combined the complexities due both to geometry (*e.g.*, toroidicity or trapped particles) and to nonlinearity (*e.g.*, the effects of higher eigenmodes or kinetic vs. fluid saturation). This work is part of an attempt to obtain better agreement with experiments by extending certain nonlinear studies[2,3] from slab to toroidal geometry.

Here, we study toroidal η_i turbulence near the stability threshold (recently explored in sheared slab geometry[2]). The threshold regime is characterized by weak turbulence (since the growth rate, γ, is smaller than the frequency, ω_r) and strong ion resonances (both nonlinear, in the form of ion Compton scattering, and linear). Although this analysis is strictly valid only for a narrow range of η_i near the threshold, the results allow assumptions about the influence of Compton scattering over a wide range of η_i. (For example, in the slab model of the instability, it can be argued that the strong nonlinear damping from Compton scattering provides a cutoff for the higher radial eigenmodes, giving a significant correction to the transport coefficient at all η_i.[3])

Model and Linear Theory: We consider a toroidal geometry with circular concentric flux surfaces and radial gradients of density and ion temperature. Modes are described by the nonlinear ion gyrokinetic equation in ballooning representation,[4]

$$\left(\frac{\partial}{\partial t}+v_\parallel\nabla_\parallel+i\omega_{Di}\right)\hat{h}_{\vec{k}}\left(\hat{\theta},\vec{v},t\right)-F_M J_0\left(k_\perp v_\perp\right)\left(\frac{\partial}{\partial t}+i\omega_{*,i}^T\right)\hat{\phi}_{\vec{k}}\left(\hat{\theta},t\right)$$
$$=2\pi\sum_{p',p''}\sum_{\substack{n'+n''\\=n}}\sum_{\substack{k_r'+k_r''=\\k_r-2\pi p'k_\theta'\\-2\pi p''k_\theta''}}\hat{s}k_\theta'k_\theta''\left[\theta_{\vec{k}'}-\theta_{\vec{k}''}+2\pi\left(p'-p''\right)\right]J_0\left(k_\perp'v_\perp\right)\times$$
$$\times\,\hat{\phi}_{\vec{k}'}\left(\hat{\theta}-2\pi p',t\right)\hat{h}_{\vec{k}''}\left(\hat{\theta}-2\pi p'',\vec{v},t\right), \qquad (1)$$

* Permanent address: Center for Plasma Theory and Computation; University of Wisconsin; Madison WI 53706; United States

and the quasineutrality equation with adiabatic electrons:

$$(1+1/\tau)\,\hat{\phi}_{\vec{k}}\left(\hat{\theta},t\right)=\int d^3v\,J_0\left(k_\perp v_\perp\right)\hat{h}_{\vec{k}}\left(\hat{\theta},\vec{v},t\right). \tag{2}$$

Here $\hat{h}$ is the nonadiabatic part of the ion distribution function, $\hat{\phi}$ is the electrostatic potential normalized to e/T_i, $\hat{\theta}$ is the parallel co-ordinate in ballooning space, $k_\theta = nq/r$ is the poloidal wave vector, $k_r(\hat{\theta}) = k_\theta \hat{s}(\hat{\theta}-\theta_{\vec{k}})$ is the local radial wave vector, $\theta_{\vec{k}} = k_r/\hat{s}k_\theta$ represents the radial wave vector, F_M is a local Maxwellian with radial T_i and n gradients, J_0 is a Bessel function, $\omega_{Di} = \omega_{*i}\epsilon_n[\cos\hat{\theta}+\hat{s}(\hat{\theta}-\theta_{\vec{k}})\sin\hat{\theta}](v_\parallel^2+v_\perp^2/2)$, $\omega_{*i}^T = \omega_{*i}[1-\eta_i(3-v^2)/2]$, $\omega_{*i} = -k_\theta\rho_i^2\Omega_i/L_n$, $\eta_i = L_n/L_{T_i}$, $L_n^{-1} = -d\ln n/dr$, $L_T^{-1} = -d\ln T/dr$, $\hat{s} = d\ln q/d\ln r$, q is the safety factor, $\tau = T_e/T_i$, $\epsilon_n = L_n/R$, R is the major radius, $v_i^2 = T_i/m_i$, $\Omega_i = eB/mc$, $\rho_i = v_i/\Omega_i$ and distance and time have been undimensionalized to ρ_i and $1/\Omega_i$.

The linear analysis is performed by neglecting the right hand side of Eq. (1), approximating $\nabla_\parallel$ semilocally as $ik_\parallel(\hat{\theta})$ (consistent with a WKB representation of the modes), and substituting $\hat{h}_{\vec{k}}$ from Eq. (1) into Eq. (2). In order to perform the velocity space integral in the appropriate regime ($k_\perp\rho_i \gtrsim 1$, for which J_0 cannot be expanded), we make the "curvature approximation" by substituting $v_\perp^2 \to 2v_\parallel^2$ in ω_{Di}. The resulting equation admits a solution with the ordering scheme $\zeta \sim \sqrt{\epsilon_n}$; $\omega_i < \omega_r \sim \epsilon_n\omega_{*i}$; and $b_\theta \sim 1$ (verifiable a posteriori for η_i sufficiently close to the threshold). When $L_n \to \infty$, then $\epsilon_T = L_T/R \ll 1$ can replace ϵ_n. The linear equation then is

$$\frac{\partial^2}{\partial\theta^2}\hat{\phi}_{\vec{k}}+Q(\omega)\,\hat{\phi}_{\vec{k}}=0, \tag{3}$$

where,

$$Q(\omega)=-\frac{b_\theta q^2}{2\epsilon_n^2 p}\left[\eta_i A/2-\eta_i\omega/\omega_{*i}+i\frac{\sqrt{\pi}\omega}{\zeta\omega_{*i}}\left(\frac{\eta_i}{\eta_c}-1+\omega/\omega_{*i}-\eta_i\zeta^2\right)\right],$$

$A = 4\epsilon_n[\cos\hat{\theta}-\hat{s}(\hat{\theta}-\theta_{\vec{k}})\sin\hat{\theta}]$, $\zeta = \omega/\sqrt{2}k_\parallel$, $p = (1+1/\tau)/\Gamma_0$, $\eta_c^{-1} = 1/2 + b(1-\Gamma_1/\Gamma_0)$ is the $k_\perp$ dependent threshold in the slab theory, and $\Gamma_n = e^{-k_\perp^2}I_n\left(k_\perp^2\right)$. Taking $\hat{\phi} = \hat{\phi}^{(0)} + \sqrt{\epsilon_n}\hat{\phi}^{(1)}$ and $Q(\omega) = Q_r(\omega_r)/\epsilon_n + i\left[Q_i(\omega_r)+\gamma\partial Q_r(\omega_r)/\partial\omega_r\right]/\sqrt{\epsilon_n}$ allows a perturbation solution for the mode structure, frequency (lowest order), and growth rate (next order).

The WKB solution of the lowest order equation is complicated by the existence of an infinite number of turning points at intervals of about π. A detailed solution (not given here) requires matching the central solution (near $\hat{\theta}\sim\theta_{\vec{k}}$) to the asymptotically vanishing Foquet solutions (appropriate for $|\hat{\theta}-\theta_k| \gtrsim \pi$), approximately yielding the phase quantization condition

$$\left(\frac{b_\theta q^2\eta_i}{2\epsilon_n^2 p}\right)^{1/2}\int_{\theta_T}^{\theta_T} d\hat{\theta}\sqrt{\omega_r/\omega_{*i}-A/2}=\left(l+\frac{1}{2}\right)\pi \tag{4}$$

Approximating A as a quadratic yields

$$\omega_r/\omega_{*i} \simeq 2\epsilon_n \left[\left(l + \frac{1}{2} \right) \left(\frac{\epsilon_n p}{b_\theta q^2 \eta_i} \right)^{1/2} - 1 \right]. \tag{5}$$

For a bound mode of width $\Delta_{\hat{\theta}} \simeq \pi$, (the only allowable normal modes) the integer l must be in the range of $l + \frac{1}{2} \sim (b_\theta q^2 \eta_i/\epsilon_n p)^{1/2}$ (not arbitrary as in the usual WKB problem). This solution is supported by shooting code calculations.

The growth rate is obtained by multiplying the next order equation by $\hat{\phi}^{(0)}_{\vec{k}}$, and taking $\int_{-\infty}^{\infty} d\hat{\theta}$ (which annihilates the $\hat{\phi}^{(1)}$ terms), yielding

$$\gamma = -\frac{\int_{-\infty}^{\infty} d\hat{\theta} \hat{\phi}^{(0)} Q_i(\omega_r) \hat{\phi}^{(0)}}{\int_{-\infty}^{\infty} d\hat{\theta} \hat{\phi}^{(0)} (\partial Q_r(\omega_r)/\partial \omega_r) \hat{\phi}^{(0)}}$$

$$\simeq \sqrt{2\pi} \omega_{*i} (\epsilon_T/p)^{1/2} \left[\frac{\eta_i}{\eta_c} - 1 - 2\epsilon_n (p-1) \right], \tag{6}$$

where the integrals have been approximated by evaluating Q at the mode center. The threshold is thus

$$\eta_c^{\text{tor}} \simeq \eta_c \left[1 + 2\epsilon_n \left((1 + 1/\tau)/\Gamma_0 \left(k_\perp^2 \right) - 1 \right) \right]. \tag{7}$$

This theory requires that $\gamma \ll \omega_r$, leading to the restriction $\eta_i - \eta_c^{\text{tor}} \ll O(\sqrt{\epsilon_T})$.

Nonlinear Theory: In the regime where $\gamma \ll \omega_r$, a weak turbulence expansion may be performed on Eq. (1), producing a wave kinetic equation that describes saturation from two nonlinear processes.[2] First is three wave resonance, which is small since wave triplets that obey both $\vec{k} = \vec{k}' + \vec{k}''$ and $\omega_{\vec{k}} = \omega_{\vec{k}'} + \omega_{\vec{k}''}$ are rare (due to the strong dispersion of ω_r and the low level of frequency broadening in the weak turbulence regime). The second saturation process is ion Compton scattering (which occurs when an ion resonates with the beat wave between two normal modes), which can be expected to accompany the presence of strong *linear* ion resonances. This is the dominant saturation mechanism for the threshold regime.

Equation (1) shows three kinds of nonlinear coupling. The coupling of p is negligible due to the relatively narrow width of the quasi-modes. The coupling of k_r is important for giving radial structure to the fluctuations, decorrelating a fluctuation in a radial distance of $1/\hat{s} k_\theta \Delta_{\hat{\theta}} \sim \rho_i$ (where $\Delta_{\hat{\theta}}$ is the parallel width of a quasimode). This reconciles diffusive transport with the broad radial width of the linear modes (infinite to the order considered here). Finally k_θ coupling is important for transfer of energy from the unstable $k_\theta \sim 1$ modes to the stable modes at lower k_θ.

Calculation of the damping rate from Compton scattering is laborious and not presented here, but follows along the lines of Ref. 1. The calculation is facilitated by the fact that the ω_{Di} terms give only higher order contributions to resonances, given

the ordering of the linear theory. After extensive calculation, the damping rate from Compton scattering becomes, to lowest order

$$\gamma_{\vec{k}}^{C} \simeq -\frac{16\pi^{\frac{5}{2}} k_{\|}^2}{\Gamma_0 \eta_i} \sum_{k'_\theta, k'_r} \frac{\left(k_r k'_\theta - k'_r k_\theta\right)^2}{\left(\omega_{\vec{k}} k'_{\|} - \omega_{\vec{k}'} k_{\|}\right)^2} \left(G'_{k,k'} \eta_i - G_{k,k'}\right) \left|k''_{\|}\right| H\left(k''_{\|} k_{\|}\right) \left|\hat{\phi}_{\vec{k}'}\right|^2 \qquad (8)$$

where $G_{k,k'} = \int_0^\infty d(v^2/2) J_0^2(k_\theta v) J_0^2(k'_\theta v) \exp(-v^2/2)$, $G'_{k,k'} = \partial G_{k/\sqrt{\alpha},k/\sqrt{\alpha}}/\partial\alpha$, and H is the Heaviside step function. Balancing this with the linear growth rate gives an integral equation for the saturated turbulent spectrum. Solution of this will be undertaken in the future, but for the present rough scaling arguments can yield the order of magnitude of $\hat{\phi}$

$$\left\langle \hat{\phi} \right\rangle_{\text{rms}}^2 \sim \left(\eta_i - \eta_c^{\text{tor}}\right) \left(\frac{L_T}{R}\right)^2 \left(\frac{\rho_i}{L_n}\right)^2 .$$

This is smaller than the mixing length estimate[5] by roughly a factor of $L_T/R \ll 1$, implying that ion Compton scattering is a strong damping mechanism for toroidal η_i turbulence (although not as strong as in the slab model, where a factor of $(L_T/R)^2$ was found[2]). The ion thermal conductivity, χ_i, is expected to be diminished by a similar factor.

Conclusions: This work indicates that inclusion of the parallel dynamics of toroidal η_i modes produces a threshold regime similar to that of the slab η_i mode. Linear stability is determined by transit resonances ($\omega \simeq k_{\|} v_{\|}$), yielding a threshold that varies as $\eta_c^{\text{tor}} = \eta_c^{\text{slab}} + O(\epsilon_n)$. This could help correct for discrepancies between the slab theory and tokamaks with flat density profiles.[7] Note that neglecting $k_{\|}$ produces a similar threshold,[6] but predicts entirely different dynamics from those given here, especially in the nonlinear regime. Nonlinear saturation is provided by ion Compton scattering, and preliminary estimates indicate that the resulting saturated fluctuations are smaller than the mixing length level. It is not yet clear whether this level is large enough to cause significant transport on tokamaks.

For η_i above this threshold regime, resonances should be less important for the fluid-like modes,[8] but could provide a cutoff for the higher eigenmodes (which are more unstable, but also more susceptible to resonance through higher $k_{\|}$). This regime will be the subject of a future study.

References:

1. F. Tibone *et al.*, elsewhere this meeting.
2. N. Mattor and P. H. Diamond, Phys. Fluids B **1**, 1980 (1989).
3. N. Mattor, Culham Laboratory Report CLM-P872.
4. E. A. Frieman and Liu Chen, Phys. Fluids **25**, 502 (1982).
5. W. M. Tang, Nucl. Fusion **20**, 1605 (1986).
6. F. Romanelli, Phys. Fluids B **1**, 1018 (1989).
7. H. P. L. de Esch *et al.*, elsewhere this meeting.
8. S. C. Guo *et al.*, Plasma Physics and Controlled Fusion **31**, 423 (1989).

ON SELF-CONSISTENT DISTRIBUTION FUNCTION OF HIGH ENERGY ALPHA PARTICLES IN AXISYMMETRIC TOKAMAK

V.A.Yavorskij, Yu.V.Yakovenko

Institute for Nuclear Research, Ukrainian SSR
Academy of Sciences, Kiev, USSR

ABSTRACT. An influence of enhanced radial diffusion of marginally circulating fast alpha particles on their distribution function is investigated. Resulting collisional losses of fast alphas in axisymmetric tokamak-reactor are found to be of order of several percents.

1. Distribution function (f) of fast alphas in thermonuclear plasma in the case of ingnorable radial transport is well known [1]. However, according to Ref.[2] enhanced radial diffusion of marginally circulating fast alphas in tokamak reactor should essentially influence f , as the diffusion rate of these particles

$$D_{r\max}/a^2 \simeq (\Delta r_b/a)^2 \omega_b \qquad (1)$$

(where Δr_b and ω_b are banana width and bounce period of trapped alphas, a is the plasma radius) significantly exceeds slowing down (ν_s) and pitch angle ($\nu_\perp$) collision rates, as well as radial diffusion rate of the rest alphas.

The purpose of this report is the investigation of the influence of radial transport of fast alpha particles in axisymmetric tokamak on their distribution function.

2. We proceed from the following model self-consistent (taking into account radial transport) kinetic equation for fast alphas

$$\frac{\nu_s}{v^2}\frac{\partial}{\partial v} v^3 f + \frac{\partial}{\partial \chi} D_\chi \frac{\partial f}{\partial \chi} + \frac{\partial}{\partial \psi} D_\psi \frac{\partial f}{\partial \psi} + \frac{S\nu_s}{v_\alpha^2}\delta(v-v_\alpha) = 0. \qquad (2)$$

Here v and χ are the particle velocity and pitch angle cosine, respectively; ψ is the bounce averaged poloidal flux; $D_\chi = \nu_\perp(1-\chi^2)$; D_ψ is the radial diffusion coefficient;

$S\nu_s \delta(v-V_\alpha)/V_\alpha^2$ is the alpha particle source; $V_\alpha = 1.3\cdot 10^9 cm\ s^{-1}$.

To simplify our consideration we take into account the radial diffusion of marginally circulating particles only, i.e. we choose

$$D_\psi = D_{\psi max}\, U[(|\chi| - \chi_0)(\chi_0 + \Delta - |\chi|)] \qquad (3)$$

where $2U(x) = 1 + sgn(x)$, $\chi_0 \simeq \epsilon^{1/2}$, ϵ is the inverse aspect ratio, $\Delta \simeq (\nu_\perp/\omega_b)^{1/2} \ll 1$ is the χ range with enhanced transport [2]. Taking into account that $D_\psi/\psi_a^2 \ll D_\chi/\Delta^2$ Eq.(2) in the region $\chi_0 < |\chi| < \chi_0 + \Delta$ can be reduced to the following particle balance equation [3]:

$$\frac{\partial F^i}{\partial t} = \frac{1}{(1+t)^2}\frac{\partial}{\partial \xi} D_\xi \frac{\partial F^i}{\partial \xi} + \frac{2}{\bar\Delta (1+t)^{2/3}}\,\Gamma(\xi, t) \qquad (4)$$

with $F^i = v^3 f^i$; $f^i \equiv f\ (\chi_0 < |\chi| < \chi_0 + \Delta)$; $\xi = \int_0^\psi d\psi' \nu_s / \int_0^{\psi_a} d\psi' \nu_s$; $\bar\Delta = \Delta|_{v=V_\alpha}$; $D_\xi = \nu_s D_\psi v^3/[3V_\alpha^3 (\int_0^{\psi_a} d\psi' \nu_s)^2]$; $\Gamma = D_\chi v^3/(3V_\alpha^3 \nu_s)\, \partial F^e/\partial\chi\,|_{\chi=\chi_0,\chi_0+\Delta}$ the particle flow from the external region ($|\chi| > \chi_0 + \Delta$, $|\chi| < \chi_0$). One can show that in this region [3]

$$F^e \equiv v^3 f^e = S(\xi) + \int_0^t d\tau\, Z\Big(\frac{|\chi| - \chi_*|}{2\sqrt{\pi \bar D_\chi (t-\tau)^3}}\Big)[F^i(\xi,\tau) - S(\xi)], \qquad (5)$$

$$\Gamma = (\bar D_\chi/\pi)^{1/2} \int_0^t d\tau\, Y(t-\tau)[F^i(\xi,\tau) - S(\xi)],$$

where $\chi_* = \chi_0 + \Delta\, U(|\chi| - \chi_0)$, $Z(x) = x\, e^{-x^2}$, $Y(x) = \frac{d}{dx}\frac{U(x)}{\sqrt{x}}$, $\bar D_\chi = \frac{v^3 D_\chi}{3\nu_s V_\alpha^3}$. On using (5) to eliminate Γ one obtains integrodifferential equation for $F^i(\xi,t)$. Finally expanding F^i and S in the series of the eigen-functions $\varphi_j(\xi)$ of the $-\frac{\partial}{\partial\xi} D_\xi \frac{\partial}{\partial\xi}$ operator, i.e. using $F^i(\xi) = \sum_j F_j^i \varphi_j(\xi)$, $S(\xi) = \sum_j S_j \varphi_j(\xi)$ we derive the following equation for F_j^i.

$$\frac{\partial F_j^i}{\partial t} = -\frac{\lambda_j}{(1+t)^2} F_j^i - \frac{\tau_\Delta^{-1/2}}{(1+t)^{2/3}} \int_0^t d\tau\, Y(t-\tau)[F_j^i(\tau) - S_j], \quad F_j^i(0) = S_j \qquad (6)$$

where λ_j is the corresponding eigenvalue, $\tau_\Delta = \pi\bar\Delta^2/(4\bar D_\chi)$.

The solution of Eq(6) is essentially dependent on the

parameter

$$\eta_j = \tau_\Delta^{1/2} \lambda_j \qquad (7)$$

It can be easily seen that for $t > \tau_\Delta (\ll 1)$ the LHS of Eq.(6) is negligiby small. Thus on integrating (6) over t with weight $(t-t')^{-1/2}(1+t')^{2/3}$ and neglecting $\partial F/\partial t$ one obtains

$$S_j - F_j^i(t) = \pi^{-1}\eta \int_0^t d\tau F_j^i(\tau)(1+\tau)^{-4/3}(t-\tau)^{-1/2} \qquad (8)$$

For $\eta \ll 1$ ("weak" radial transport) Eq.(8) gives

$$F_j^i(t) = S_j \left[1 - \pi^{-1}\eta \int_0^t d\tau (1+\tau)^{-4/3}(t-\tau)^{-1/2}\right] \qquad (9)$$

while in the case of "strong" diffusion ($\eta \gg 1$), for $\eta^{-2} \ll t \ll \eta^{6/5}$, solution has the following form

$$F_j^i(t) = S_j \eta^{-1} t^{-1/2}(1+t)^{4/3} \qquad (10)$$

Thus "strong" radial transport results in the formation of the loss-cone in the vicinity of separatrix between trapped and circulating particles.

We now investigate f for fast alphas in the ITER-like tokamak. In the simplest case $n^{2/3} \sim T \sim 1-\psi/\psi_a$ (i.e. $\nu_s = \text{const}$, $\xi = \psi/\psi_a$ and $S = S_0(1-\xi)^5$) one can obtain

$$\lambda_k \tau_\Delta^{1/2} \equiv \eta_k \simeq \frac{\pi^2}{4}\left(\frac{\Delta r_b}{a}\right)^2 \left(\frac{\omega_b}{\nu_s}\right)^{1/2}\Bigg|_{v=v_\alpha} (2k-1)^2, \quad k = 1,2,\ldots \qquad (11)$$

As for ITER $\eta_k \gg 1$ we take into account the contribution of the fundamental ($k=1$) harmonic only. Results of the calculation based on the formulae (10) and (5) are shown in Figs.1,2. One can see that radial diffusion of alphas results in depression and peaking of the distribution function in the central region and the plasma periphery, respectively.

In conclusion we evaluate the fraction of alphas (Δ_n) lost due to the radial diffusion in the range $\mathcal{E}_{min} \le \mathcal{E} \le \mathcal{E}_\alpha$ and the corresponding alpha power loss fraction (Δ_ε). For

the reasonable parameters ($\eta_1 \gg 1$), on using (10), one can obtain provided $1.6 < \mathcal{E}_\alpha/\mathcal{E}_{min} < \eta^{0.8}$

$$L_\eta \simeq 2\sqrt{D_\chi}\sqrt{(\mathcal{E}_\alpha/\mathcal{E}_{min})^{3/2}-1}\,, \quad L_\mathcal{E} \simeq (1\div 3)\sqrt{D_\chi}\,. \tag{12}$$

It is readily seen that for ITER-like tokamak ($\eta_1 \simeq 10$)

$$L_\eta \sim (\nu_\perp/\nu_s)^{1/2}\big|_{v=v_\alpha} \sim 0.1\,, \quad L_\mathcal{E} \simeq (0.3 \div 0.5)\, L_\eta\,.$$

3. Finally we note that the fraction of collisionally lost fast alphas in an axisymmetric tokamak reactor may reach the order of several percents. The self-consistent distribution function (taking into account the influence of collisional radial transport) is essentially anisotropic which may affect plasma stability.

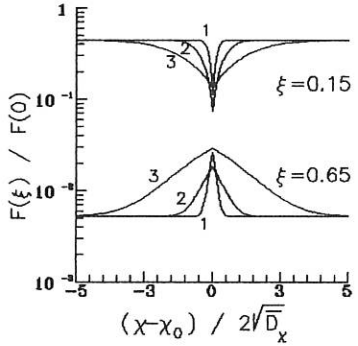

Fig.1. f versus χ;
1- $\mathcal{E}$ = 3.35 MeV;
2- $\mathcal{E}$ = 2.56 MeV;
3- $\mathcal{E}$ = 1 MeV; $\xi \simeq \frac{\psi}{\psi_a}$.

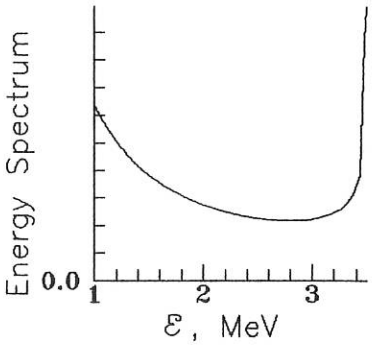

Fig.2. Energy spectrum of escaped alphas

References

1. Kolesnichenko Ya.I., Nucl.Fusion 20 (1980) 727.
2. Goloborod'ko V.Ya., Yavorskij V.A., Fusion Technology 12 (1990), to be published.
3. Yavorskij V.A., Yakovenko Yu.V., Preprint KINR (1990), to be published.

MAGNETIC ISLAND SELF-SUSTAINMENT BY FINITE LARMOR RADIUS EFFECT

M.Hugon and P.H.Rebut

JET Joint Undertaking, Abingdon, Oxon, OX14 3EA, United Kingdom

Introduction

The particle and energy transport observed in tokamaks could be explained by a turbulence resulting from a mixture of small magnetic islands and a chaotic region, where field lines link different plasma regions [1]. This paper investigates how this topology could be self-sustained by finite ion Larmor radius effect in a collisionless plasma.

Magnetic topology

Islands are in equilibrium in a chaotic zone, when the overlapping parameter γ is between 0.75 and 1.50. γ is the ratio of the virtual island width 2ε to the distance between two island chains Δ [2]. The island is defined by its poloidal extension $2\Theta_0/k_y \leq 2\pi/k_y$ and its radial width $2b(\Theta_0) \leq 2\varepsilon$; it is assumed to be thin: $k_y\, b(\Theta_0) \ll 1$. In the present model, the vector potential outside the island is calculated assuming that the chaotic region is made of nested magnetic surfaces.

The z-component of the vector potential $\mathcal{A}_z$ in a slab geometry is defined by:

$$\mathcal{A}_z(x,y,\Theta_0) = \frac{B_0'}{2}\, x^2 + \frac{\tilde{\tilde{B}}(\Theta_0)}{k_y}\, A(x,y,\Theta_0) = \left(-\frac{\tilde{\tilde{B}}(\Theta_0)}{k_y}\right)\left(\frac{2\,x^2}{b^2(\Theta_0)} - A(x,y,\Theta_0)\right) \quad (1)$$

where $B_0' = (rq'/Rq^2)B_z$ is the shear term and $\tilde{\tilde{B}}(\Theta_0)$ the amplitude of the perturbing radial field. $A(x,y,\Theta_0)$ is assumed to be an even function of y with a period $2\pi/k_y$ and to be independent of x and equal to $a(y,\Theta_0)$ inside the island. The last closed surface of the remaining island is defined by $\mathcal{A}_z(x,y,\Theta_0) = 0$ and its radial coordinates are given by:

$$\mathcal{L}(y,\Theta_0) = \mp\, b(\Theta_0)\,\sqrt{a(y,\Theta_0)/2} \quad (2)$$

Perturbed electric potential associated to a magnetic island

Imposing quasi-neutrality in the chaotic region defines the radial electric field E_0 in the reference frame rotating with the islands [1]. This condition is now extended inside the magnetic island.

The ion distribution function depends on the electric potential ψ. The

electron distribution function depends on ψ and on the vector potential A_z. The electrons are in thermodynamical equilibrium in the electric potential ψ, because their thermal velocity is much larger than the drift velocity $\mathbf{v_D} = (-\nabla\psi \times \mathbf{B}) / B^2$. In pure MHD (limit of very small Larmor radii), ψ is a function of A_z. When taking into account the finite size of their Larmor radius ρ_c ($\rho_c \simeq b(\Theta_0)$), the ions experience an average electric potential ψ_i different from ψ_e experienced by the electrons. Under these conditions, the electric potential is no longer a function of A_z.

The potential ψ_i experienced by the ions is expressed as:

$$\psi_i = - E_0 \, x + b(\Theta_0) \, E_0 \int_{-\infty}^{+\infty} G(x-x') \, \tilde{\psi}(x',y) \, dx' \qquad (3)$$

$\tilde{\psi}(x,y)$ is dimensionless and the integral containing $G(x-x')$ is the operator associated to the finite ion Larmor radius.

As the electron Larmor radius is much smaller than $b(\Theta_0)$, the electric potential ψ_e felt by the electrons is given by:

$$\psi_e = - E_0 \, x + b(\Theta_0) \, E_0 \, \tilde{\psi}(x,y) \qquad (4)$$

Imposing quasi-neutrality inside and outside the island leads to two integral equations satisfied by $\tilde{\psi}(x,y)$. They indicate that $\tilde{\psi}(x,y)$ is an odd function of x. This system of equations is solved by numerical iteration. The result of such a computation is plotted against x in Fig.1 for $y = 0$, $b(\Theta_0) = 1$, a ratio of $\rho_c/b(\Theta_0) = 1$, $\nabla x n_e / n_e = 1$ and $\nabla x T_e / T_e = 2$.

Computations show that the finite Larmor radius operator can be approximated by: $J_0^2[(\rho_c/\ell(y,\Theta_0))^2] \, \tilde{\psi}(x,y)$, where the function J_0^2 is defined by $J_0^2(u) = e^{-u} I_0(u)$, $I_0(u)$ being one of the modified Bessel functions of zeroth order. $J_0^2(u)$ is equal to 1, when u is zero ($\rho_c \ll b(\Theta_0)$), and tends toward zero for u infinite ($\rho_c \gg b(\Theta_0)$). When $\rho_c/b(\Theta_0) \geq 1$, the above approximation for the finite Larmor radius operator is used in both integral equations and $\tilde{\psi}(x,y)$ can be written as:

$$\tilde{\psi}(x,y) = \frac{\frac{1}{2}\frac{\nabla_x T_e}{T_e}}{\frac{\nabla_x n_e}{n_e}\left(1 - J_0^2\left[\left(\frac{\rho_c}{\ell(y,\Theta_0)}\right)^2\right]\right) + \frac{1}{2}\frac{\nabla_x T_e}{T_e}} \left(\frac{x}{b(\Theta_0)} - \mathcal{P}\sqrt{\frac{x^2}{b^2(\Theta_0)} - \frac{a(y,\Theta_0)}{2}} \right) \qquad (5)$$

with: $\mathcal{P} = \begin{cases} -1 \text{ for } x \leq -\ell(y,\Theta_0) \\ 0 \text{ for } -\ell(y,\Theta_0) \leq x \leq \ell(y,\Theta_0) \\ +1 \text{ for } x \geq \ell(y,\Theta_0) \end{cases}$

The relative accuracy of $\tilde{\psi}(x,y)$ given by Eq.(5) is less than 10% of the full computation. $\nabla x n_e$ and $\nabla x T_e$ are the average gradients of electron density n_e and temperature T_e.

Current density inside the island due to finite ion Larmor radius effect

In steady state, the current density conservation satisfies:

$$\nabla \cdot (J_{\parallel} \mathbf{e}_{\parallel} + n_i q_i \mathbf{v}_{Di} + n_e q_e \mathbf{v}_{De}) = 0 \qquad (6)$$

$J_{\parallel}$ is the electron current along the field lines, which is the sum of the constant plasma current and of the perturbed current sustaining the island $\delta J_{\parallel}(x,y)$. $\mathbf{v_{Di}}$ and $\mathbf{v_{De}}$ are the ion and electron drift velocities respectively.

Keeping the leading terms of Eq.(6) and after integration with respect to y, $\delta J_{\parallel}(x,y)$ can be expressed as:

$$\delta J_{\parallel}(x,y) = - \frac{q_e E_0}{B'_0} \nabla_x n_e \frac{b(\Theta_0)}{x} \left(\tilde{\psi}(x,y) - \int_{-\infty}^{+\infty} G(x-x')\, \tilde{\psi}(x',y)\, dx' \right) \qquad (7)$$

$\delta J_{\parallel}(x,y)$ results from the difference between the electric potentials experienced by the electrons and the ions. It is an even function of x. The computed values for $\delta J_{\parallel}(x,y)$ using the data of $\tilde{\psi}(x,0)$ shown in Fig.1 are plotted as a function of x in Fig.2: they indicate that the current density is nearly constant inside the island. The integral in Eq.(7) can be approximated by the function J_0^2 defined above for $\rho_c / b(\Theta_0) \geq 1$.

Magnetic island self-sustainment

In the case of thin islands ($k_y\, b(\Theta_0) \ll 1$), Ampère's law is written as:

$$\frac{\tilde{\tilde{B}}(\Theta_0)}{k_y} \nabla_x^2 A(x,y,\Theta_0) = - \mu_0\, \delta J_{\parallel}(x,y) \qquad (8)$$

Eq.(8) is integrated with respect to x across the island using the expression of the perturbed current as a function of J_0^2. This leads to an equation in y and Θ_0, which is equivalent to a non-linear eigen function equation. It is solved by computing the Fourier components of the vector potential with respect to y with an iterative code for different values of Θ_0. Eq.(8) then becomes:

$$\mu_0 \frac{n_e K T_e}{B'^2_0} \frac{1}{2} \frac{\nabla_x T_e}{T_e} \frac{\nabla_x n_e}{n_e} \frac{\left(\frac{\nabla_x n_e}{n_e} + \frac{1}{2} \frac{\nabla_x T_e}{T_e} \right) \left[1 - J_0^2 \left[\left(\frac{\rho_c}{b(\Theta_0)} \right)^2 \right] \right]}{\frac{\nabla_x n_e}{n_e} \left[1 - J_0^2 \left[\left(\frac{\rho_c}{b(\Theta_0)} \right)^2 \right] \right] + \frac{1}{2} \frac{\nabla_x T_e}{T_e}} \frac{1}{k_y \Delta} = F(\Theta_0) \qquad (9)$$

$F(\Theta_0)$ is determined from Poincaré map computation by numerical integration of the field line equations using the vector potential obtained previously. The values calculated for $F(\Theta_0)$ as a function of Θ_0 are given in Table I. This function increases, as Θ_0 decreases, that is as the island is destroyed. Its minimum value compatible with the existence of small magnetic islands embedded in a chaotic region is close to 0.12: it corresponds to $\gamma \simeq 0.75$, when the last KAM surface between island chains is destroyed. Islands are self-sustained, when the left-hand side of Eq.(9) is larger than 0.12. This result is lower by about one order of magnitude than the threshold calculated for the self-sustainment of a fully chaotic medium [3].

Conclusion

This study has proposed a possible mechanism maintaining islands in a chaotic zone. The islands are sustained by an electron current along the

field lines produced by the difference between the electric potentials experienced by the electrons and the ions. This difference is due to the finite size of the ion Larmor radius. The condition for island self-sustainment is given by the left-hand side of Eq.(9) larger than 0.12. This condition depends on the electron temperature and density gradients.

Eq.(9) can be written in terms of the non dimensional structural parameters β, Ω and additional shape factors, β representing the plasma pressure and Ω the finite Larmor radius [2]. It is proportional to $\beta\Omega$ in the limit of small ion Larmor radius and to β for large ion Larmor radius.

References
[1] P.H.Rebut et al., Plasma Physics and Controlled Nuclear Fusion Research, 1986 (Kyoto) 2, 187 (IAEA, Vienna).
[2] P.H.Rebut and M.Brusati, Plasma Phys. Control. Fusion 28, 113 (1986).
[3] X.Garbet et al., Plasma Phys. Control. Fusion 32, 131 (1990).

Table I

Numerical results for $F(\Theta_0)$ obtained from the Poincaré map computation as a function of Θ_0 and of the overlapping parameter γ.

γ	0.4	0.7	1.0	1.2	1.4
Θ_0	0.91π	0.70π	0.44π	0.32π	0.13π
$F(\Theta_0)$	0.08	0.12	0.15	0.20	0.78

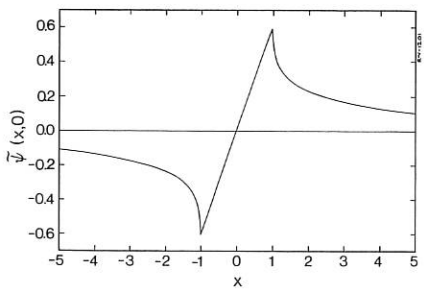

Fig.1: Computed values for the perturbed electric potential $\tilde{\psi}(x,0)$. The island lies between x = −1 and x = 1. The ion Larmor radius ρ_c to island half-width $b(\Theta_0)$ ratio is 1. $\nabla x n_e/n_e = 1$ and $\nabla x T_e/T_e = 2$.

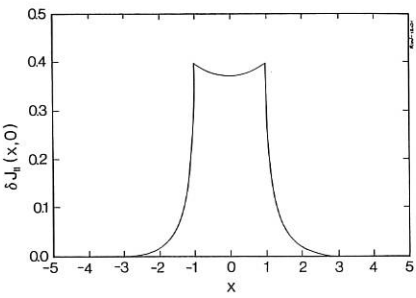

Fig.2: Result of computation of the the current density sustaining the island $\delta J_{\parallel}(x,0)$ using the data given in Fig.1.

THE LONG WAVELENGTH LIMIT OF THE ION-TEMPERATURE GRADIENT MODE IN TOKAMAK PLASMAS

L. Chen*, S. Briguglio, F. Romanelli

Associazione EURATOM-ENEA sulla Fusione,
Centro Ricerche Energia Frascati
C.P. 65 - 00044 Frascati, Rome, Italy

*Plasma Physics Laboratory, Princeton University,
Princeton, NJ 08543, U.S.A.

Abstract. The stability of the ion temperature gradient (∇T_i) mode in tokamak geometries is examined in the limit of long wavelength and flat density, retaining the nonadiabatic electron response. The existence of three unstable branches is shown.

Several experimental observations suggest that the ion temperature gradient driven mode, the so called ∇T_i-mode is a possible candidate for the explanation of anomalous ion energy transport in tokamaks. Most of the analyses of this instability have considered the short-wavelength limit $(k_\theta \rho_i)^2 \sim \varepsilon_{T_i}^{\frac{1}{2}}$, with k_θ being the poloidal wavenumber, $\rho_i = v_{T_i}/\Omega_i$ the ion Larmor radius, v_{T_i} the ion thermal velocity, $\Omega_i = eB/m_i c$ the ion cyclotron frequency, $\varepsilon_{T_i} = L_{T_i}/R$, $L_{T_i} = -(\nabla T_i/T_i)^{-1}$, T_i the ion temperature and R the major radius. In this limit the eigenfunction has a moderate ballooning structure in the outer part of the torus and can be destabilized by the combined effect of the ion temperature gradient and the local unfavourable curvature. The resulting instability has an interchange character with the growth rate γ given by $\gamma \approx (\omega_D \omega_{*T_i})^{\frac{1}{2}}$ and weakly dependent on shear. In the latter expression $\omega_D = k_\theta c T_i/eBR$ is the magnetic drift frequency, $\omega_{*T_\alpha} = k_\theta c T_\alpha / e_\alpha B L_{T_\alpha}$, $\alpha = e, i$ and B is the equilibrium magnetic field. The effect of the parallel dynamics is, in this limit, to provide a moderate ballooning structure. This, in turn, allows the use of the strong coupling approximation.

In this paper we consider the long-wavelength limit, which has received less attention in the past. In Refs. 1 and 2 it has been shown that for values of k_θ lower than $\varepsilon_{T_i}^{\frac{1}{4}} \rho_i^{-1}$ an unstable mode exists, corresponding to a broader eigenfunction: the effect of the normal curvature tends to be averaged out, while the geodesic curvature simply yields a renormalization of the inertia term through the Pfirsch-Schluter enhancement factor. Such a mode has a slab-like character.

In the present paper we show that in the long-wavelength limit, in addition to the slab-like mode another branch exists, peculiar to toroidal geometry.

For the sake of simplicity we consider here the fluid-ion limit of the eigenmode equation, which in the ballooning representation, reads

$$\frac{d^2\phi}{d\chi^2} + q^2\Omega^2 b \left[\frac{\tau\Omega(1-i\delta)}{1+\tau\Omega\varepsilon_{T_i}^{\frac{1}{2}}} + b(1+\hat{s}^2\chi^2) + \frac{2}{\Omega}(\cos\chi + \hat{s}\chi\sin\chi) \right] \phi = 0 \qquad (1)$$

where ϕ is the electrostatic potential, χ is the extended poloidal variable, $\Omega = \omega/\tau(\omega_{*T_i}\omega_D)^{\frac{1}{2}}$ is the normalized frequency, and positive Ω corresponds to wave propagating in the electron diamagnetic–drift direction, $\tau = T_e/T_i$, $b = \tau k_\theta^2 \rho_i^2/\varepsilon_{T_i}^{\frac{1}{2}}$, q is the safety factor, $\hat{s} = rq'/q$ is the shear, and the usual circular flux surfaces equilibrium has been employed. In Eq. (1) δ accounts for the nonadiabatic electron response. For dissipative trapped electron dynamics and $\omega < \omega_{*T_e}$, $\delta \approx \varepsilon^{\frac{1}{2}}\omega_{*T_e}/\nu_{\text{eff}} > 0$, where $\varepsilon = r/R$, r is the radial coordinate, $\nu_{\text{eff}} = \nu_{ei}/\varepsilon$, and ν_{ei} is the electron–ion collision frequency.

If the ordering $b \sim 1$ is considered, the strong coupling approximation $(\cos\chi + \hat{s}\chi\sin\chi \approx 1 + (\hat{s} - 1/2)\chi^2)$ can be applied. In this approximation Eq. (1) becomes a Weber equation; its lowest eigenmode is given by $\phi = \exp(-\sigma\chi^2)$, with the condition $Re\sigma > 0$ to be imposed for the existence of the ballooning transform.

In the limit $b \gg 1$, $\varepsilon_{T_i} \ll 1$, $\delta = 0$, the eigenvalue is given by

$$\Omega = -\frac{b}{\tau} + i\frac{\hat{s}\tau}{qb} \qquad (2)$$

while $Re\sigma = Re\left[-\frac{i}{2}\Omega bq\hat{s}\right] = \frac{1}{2}\hat{s}^2 = O(1)$, in accordance with the strong coupling assumption. Note that the root given by Eq. (2) has a slab like character, with the growth rate being proportional to $\hat{s}/q$.

In the limit $b \lesssim 1$, Eq. (1) has been solved, in Refs. 1 and 3, obtaining

$$\Omega \approx \left(-\frac{2}{\tau} + i\frac{\hat{s}}{q\tau}\right)^{\frac{1}{2}} \qquad (3)$$

For $\hat{s}/q \ll 2$, the mode has an interchange character.

When nonadiabatic electron dynamics is considered $(\delta \neq 0)$, the root given by Eq. (3) is weakly affected and it can be shown that no further root is destabilized by the δ term.

In the limit $b \ll 1$, the real part of σ tends to be small, $Re\sigma \approx bq\hat{s}Im\Omega$ and the eigenfunction becomes broader in χ. That is, for b sufficiently small, the strong coupling approximation becomes invalid. In this limit, due to the perturbative character of the curvature term, a multiple scale analysis can be carried out.

The eigenfunction exhibits a periodic variation over the connection length scale $\chi \sim 1$ and a secular variation over a larger scale $\chi \gg 1$. The structure of the curvature term suggests two possible forms for the eigenfunction.

One form corresponds to balancing the parallel compressibility term and the curvature term.

Eq. (1) then yields

$$\phi = \phi_0(b^{\frac{1}{2}}\chi) + 2b\hat{s}\Omega q^2 \chi\sin\chi\phi_0(b^{\frac{1}{2}}\chi) + O(b) \qquad (4)$$

with $\phi_0(b^{\frac{1}{2}}\chi)$ satisfying to

$$\phi_0'' + \left[\frac{q^2\Omega^3\tau(1-i\delta)}{1+\tau\Omega\varepsilon_{T_i}^{\frac{1}{2}}} + bq^2\Omega^2\hat{s}^2(1+2q^2)\chi^2\right]\phi_0 = 0 \tag{5}$$

with boundary conditions given by $|\phi_0| \underset{\chi\to\infty}{\longrightarrow} 0$. For $\varepsilon_{T_i} \ll 1$ Eq. (5) yields

$$\Omega \approx e^{i\frac{3}{4}\pi}\left[\frac{\hat{s}}{q\tau}\frac{(1+2q^2)^{\frac{1}{2}}}{(1-i\delta)}\right]^{\frac{1}{2}} \tag{6}$$

Note that the eigenvalue is independent of b and weakly affected by the nonadiabatic electron dynamics.

The other form for the eigenfunction corresponds to balancing the parallel compressibility and the adiabatic electron response. The two-scale analysis of Eq. (1) yields

$$\phi = C_0(b^{\frac{1}{3}}\chi)\cos\frac{\chi}{2} + S_0(b^{\frac{1}{3}}\chi)\sin\frac{\chi}{2} + O(b^{\frac{1}{3}}). \tag{7}$$

C_0 and S_0 must satisfy the conditions

$$C_0' - \left[\frac{b^{\frac{2}{3}}q^2\Omega^3\tau(1-i\delta)}{1+\tau\Omega\varepsilon_{T_i}^{\frac{1}{2}}} - \frac{1}{4b^{\frac{1}{3}}}\right]S_0 - b^{\frac{2}{3}}q^2\Omega\hat{s}\chi C_0 = 0$$

and (8)

$$S_0' + \left[\frac{b^{\frac{2}{3}}q^2\Omega^3\tau(1-i\delta)}{1+\tau\Omega\varepsilon_{T_i}^{\frac{1}{2}}} - \frac{1}{4b^{\frac{1}{3}}}\right]C_0 + b^{\frac{2}{3}}q^2\Omega\hat{s}\chi S_0 = 0$$

which again yield a Weber equation for C_0 and S_0. The eigenvalue Ω is given by

$$\Omega^3(1-i\delta) - \frac{1}{4bq^2}\left(\varepsilon_{T_i}^{\frac{1}{2}}\Omega + \frac{1}{\tau}\right) \simeq 0 \tag{9}$$

For the sake of simplicity we first consider the limit $\delta = 0$. Eq. (9) shows that, for $\varepsilon_{T_i} = 0$, an unstable mode exists for any value of b, propagating in the ion diamagnetic direction, with $\Omega = \exp(i2\pi/3)/(4bq^2\tau)^{\frac{1}{3}}$, along with a marginally stable solution $\Omega = 1/(4bq^2\tau)^{\frac{1}{3}}$, corresponding to a mode propagating in the electron diamagnetic direction. For finite ε_{T_i}, the unstable root exists only for $b > b_0 \equiv \varepsilon_{T_i}^{\frac{3}{2}}\tau^2/27q^2$. Meanwhile, for $b < b_0$, Eq. (9) yields three marginally stable solutions.

When nonadiabatic electron dynamics is retained, i.e. $\delta \neq 0$, Eq. (9) indicates that instabilities persist for $b < b_0$. Specifically, we find, for $b \ll b_0$

$$\Omega \approx -\frac{1}{\tau\varepsilon_{T_i}^{\frac{1}{2}}} + 4\frac{i\delta bq^2}{\tau^3\varepsilon_{T_i}^2}\ , \tag{10}$$

and

$$\Omega \approx \pm\frac{\varepsilon_{T_i}^{\frac{1}{4}}}{2b^{\frac{1}{2}}q}(1-i\delta)^{-\frac{1}{2}}\ . \tag{11}$$

Eq. (10) corresponds to an unstable solution. Eq. (11), meanwhile, does contain an unstable solution (the one with the positive sign), propagating in the electron diamagnetic–drift direction, only if $\delta > 0$. For nonadiabatic electron response associated to dissipative trapped electron dynamics, this is the case, as far as the condition $\omega < \omega_{*T_e}$ is satisfied, which however is not consistent with $b \ll b_0$ for usual temperature profiles, $\varepsilon_{T_e} \sim \varepsilon_{T_i}$. In any case, both Eqs. (10) and (11) indicate that $|\omega| \lesssim |\omega_{t_i} = v_{T_i}/qR|$ violating the parallel incompressibility ($|\omega| > |\omega_{t_i}|$) assumption made in deriving Eq. (1). Thus, to properly examine the $b \lesssim b_0$ regime, we need to retain ion kinetic effects such as ion transit/bounce resonances which may be expected to be further stabilizing.

On the other hand, for $1 > b > b_0$, we have the following two unstable solutions

$$\Omega \simeq \left\{ \begin{matrix} \exp(i2\pi/3) \\ 1 \end{matrix} \right\} (4bq^2\tau)^{-\frac{1}{3}}(1 - i\delta)^{-\frac{1}{3}} \tag{12}$$

From Eq. (12), we can readily show that $|\omega/\omega_{*T_e}| \sim |b_0/b| < 1$ and, hence, $\delta > 0$. Thus, Eq. (12) does contain an unstable solution propagating in the electron diamagnetic–drift direction. Also, since $|\omega| > |\omega_{t_i}|$, the fluid–ion approximation is valid in this regime.

REFERENCES

[1] F. Romanelli, Phys. Fluids B1, 1018 (1989).

[2] S.C. Guo, L. Chen, S.T. Tsai, and P.N. Gudzar, Plasma Phys. and Controlled Fusion 31, 423 (1989).

[3] W.M. Tang, G. Rewoldt, and L. Chen, Phys. Fluids. 29, 3715 (1986).

SOLITARY VORTEX SOLUTION OF NONLINEAR η_i-MODE EQUATIONS

B.G. Hong*, F. Romanelli and M. Ottaviani

Associazione EURATOM-ENEA sulla Fusione,
C.R.E. Frascati, 00044 Frascati(Roma), Italy.

I. INTRODUCTION

Drift wave instabilities driven by the ion temperature gradient (η_i) mode (η_i = d lnT_i/d lnN) play an important role in explaining the anomalous transport in tokamak experiments [1-3]. Several studies have been made in order to assess on which extent the experimentally observed anomalous transport is correlated to the properties of turbulent drift wave spectra [4]. In particular recent 2-D numerical simulations [5,6] of the η_i-mode show that long-lived, large scale coherent structures exist and considerably affect the level of magnitude of the anomalous transport. A significant reduction of the turbulent heat flux with respect to the quasilinear estimate and positive dependence on dissipations is indeed observed.

In this work, we address the question whether the η_i-mode nonlinear equations admit such a coherent solution. In the cold ion limit and slab model the nonlinear drift wave equation (Hasegawa-Mima equation[7]) have stationary solitary vortex solutions. These solutions correspond to a coherent fluid motion with vanishing anomalous thermal flux. The simplest form of these solutions is a dipolar vortex (modon) traveling in the direction perpendicular to the density gradient and first found by Larichev and Reznik [8]. Properties of this solution have been widely studied [9-11] showing that it has a high degree of stability. The anomalous transport associated with the vortex-vortex inelastic collision was studied by W.Horton [12].

II. MODEL EQUATIONS

The hydrodynamic ion equations are used to describe the toroidal η_i instability and the electrons are assumed to satisfy the Boltzmann relation, $n_e/N_o \cong e\Phi/T_e$. Two dimensional slab geometry is considered, with the gradient in the direction of the equilibrium magnetic field approximated as $\nabla_\parallel \cong x/L_s\partial/\partial y \cong ik_y x/L_s$, where L_s=qR/s is the shear length and s=rq'/q and the curvature term evaluated at the outside of the torus. For the perturbed electrostatic potential φ, the parallel ion velocity v, and the ion pressure p, the following set of nonlinear fluid equations are obtained which describes the η_i-mode dynamics.

$$(1-\nabla_\perp^2)\frac{\partial\varphi}{\partial t} = -(1-2\varepsilon_n+\frac{1+\eta_i}{\tau}-\nabla_\perp^2)\frac{\partial\varphi}{\partial y}+2\varepsilon_n\frac{\partial p}{\partial y}-Sx\frac{\partial v}{\partial y}+[\varphi,\nabla_\perp^2\varphi], \qquad (1)$$

$$\frac{\partial v}{\partial t} = -Sx\frac{\partial}{\partial y}(\varphi+p)-[\varphi,v], \qquad (2)$$

* ENEA Guest

$$\frac{\partial p}{\partial t} = -\frac{1+\eta_i}{\tau}\frac{\partial \varphi}{\partial y} - [\varphi, p], \qquad (3)$$

with $\varepsilon_n = L_n/R$, $S = L_n/L_s$, $\tau = T_e/T_i$ and $L_n^{-1} = \nabla N/N$.

In Eqs.(1)-(3), nomalized variables are used, with $(x,y) \rightarrow \rho_s(x,y)$, $z \rightarrow L_n z$ and $t \rightarrow L_n/c_s t$ with $c_s = (T_e/M_i)^{1/2}$, $\rho_s = c_s/\Omega_i$ and the fields scaled as $(e\phi/T_e, v_{||,i}/c_s, p_i/P_e) = (\phi, v, p)\rho_s/L_n$. The $\mathbf{E}\times\mathbf{B}$ convective nonlinearities are expressed in terms of the Poisson bracket operator by $\mathbf{v}_E\cdot\nabla f \equiv [\varphi, f]$.

In this work, the simplest fluid set of equations for the η_i-mode turbulence are used in order to focus the attention on the problem of the existence of the coherent solution. Therefore the compressional terms in the ion pressure equation, which give a stabilizing contribution and are important in order to determine the critical ion temperature gradient η_c and the finite Larmor radius terms are neglected in the ion pressure equation.

In the shearless limit, the ion parallel velocity equation is decoupled from the potential and pressure equation, and the resulting equations have been studied through numerical simulations [5,6]. Also, in the case of cold ion limit and no toroidicity, Eq.(1) reduces to the Hasegawa-Mima equation [7] (equivalent to the Rossby wave equation[13]).

III. STATIONARY SOLUTION

In this section, we look for the stationary solution of Eqs.(1)-(3) traveling with velocity u in the y direction, $\varphi(x,y,t) = \varphi(x,y-ut)$.

The general solution of Eq.(1) to (3) is

$$P = F(\varphi - ux) + Kx, \qquad (4)$$

$$v = G(\varphi - ux) + Sx^2(1+F')/2, \qquad (5)$$

$$\nabla_\perp^2\varphi = H(\varphi - (u+K)x) + P_0 + xP_1 + x^2P_2 + x^3P_3, \qquad (6)$$

where F,G and H are arbitrary functions, $K = (1+\eta_i)/\tau$ and $P_j(\varphi - ux)$, j=0,1,2 and 3 are determined by

$$KP_3' = -\frac{S^2}{2}F'', \quad KP_2' = -3P_3, \quad KP_1' = -2P_2 - SG',$$
$$KP_0' = u - 1 + 2\varepsilon_n + 2\varepsilon_n F' - P_1 \qquad (7)$$

F,G and H are determined by the condition that p,v and φ vanish as $|x|, |y| \rightarrow \infty$, giving

$$\nabla_\perp^2\varphi = C\varphi - \frac{S^2}{u^2}x^2\varphi - 3D(u+K)x\varphi^2 + D\varphi^3, \qquad (8).$$

where

$$A = K/u, \quad B = -\frac{S(1+A)}{2u^2}, \quad C = \frac{u - 1 + 2\varepsilon_n(1+A)}{u+K} \quad \text{and} \quad D = \frac{SB(3u+K)}{3(u+K)^3}.$$

The localized solutions of Eq.(8) are singular and the general solution is obtained by matching the solution of Eq.(8) at some boundary corresponding to a closed curve in x, y plane, with

the solution in the region inside the boundary which is nonsingular at the origin x = y = 0. In the inner region, the form of the function H can not be determined within the framework of the present analysis. In order to make further progress it is convenient to assume that H is linear. For the sake of simplicity it is better to discuss separately the shearless and the case with shear.

In the shearless case Eqs.(8) reduces to p=A ϕ, v=0 and

$$\nabla_{\perp}^2 \varphi = C\varphi, \tag{9}$$

with C > 0 for localized solution, giving the condition for the speed of the vortex u > 0 or u < -K when $(1-2\,\varepsilon_n)^2 < 8\,\varepsilon_n K$, which is easily satisfied by the unstable η_i-mode. It should be noted that C < 0 reduces to the stable linear mode, $\exp(i\mathbf{k}\cdot\mathbf{x}-i\omega t)$ with the phase velocity $u = \omega/k_y$. With a linear dependence for H, we obtain the usual dipolar vortex solution

$$\varphi = (u+K) r_0 \cos\theta \begin{cases} \dfrac{K_1(kr)}{K_1(kr_0)} & , r > r_0 \\ (1+\dfrac{k^2}{q^2})\dfrac{r}{r_0} - \dfrac{k^2}{q^2}\dfrac{J_1(qr)}{J_1(qr_0)} & , r < r_0 \end{cases} \tag{10}$$

where $k^2 = C$, $x = r\cos\theta$, $y-ut = r\sin\theta$ and q is determined by

$$\frac{K_2(kr_0)}{k\,K_1(kr_0)} = -\frac{J_2(qr_0)}{qJ_1(qr_0)}\,. \tag{11}$$

The solution (10) has two free parameters of the vortex speed u and the vortex radius r_0.

In the case with shear, we use a perturbation theory to find a stationary solution for small shear. In the lowest order in S, the solutions are given in Eqs. (9)-(11). With the simplest choice of H for the inner region and $\varphi = \varphi_0 + \varphi_1$, the following solution is obtained

$$\varphi_1 = \begin{cases} (a_1 J_1 + \varphi^i_{p,1})\cos\theta + (a_3 J_3 + \varphi^i_{p,3})\cos 3\theta & , r < r_0 \\ (b_1 K_1 + \varphi^o_{p,1})\cos\theta + (b_3 K_3 + \varphi^o_{p,3})\cos 3\theta & , r > r_0 \end{cases} \tag{12}$$

We note that the magnetic shear yields a second order contribution. The particular solutions of Eq.(12) are given by (m=1 and 3)

$$\varphi^i_{p,m} = \frac{\pi}{2} Y_m(qr) \int_0^r sG^i_m J_m(qs)\,ds + J_m(qr) \int_r^{r_0} sG^i_m Y_m(qs)\,ds - \frac{Y_m(qr_0)}{J_m(qr_0)} J_m(qr) \int_0^{r_0} sG^i_m J_m(qs)\,ds$$

and

$$\varphi^o_{p,m} = I_m(kr) \int_{\infty}^r sG^o_m K_m(ks)\,ds + K_m(kr) \int_r^{r_0} sG^o_m I_m(ks)\,ds - \frac{I_m(kr_0)}{K_m(kr_0)} K_m(kr) \int_{\infty}^{r_0} sG^o_m K_m(ks)\,ds$$

with

$$G^i_1 = 3G^i_3, \quad G^i_3 = \frac{1}{4}\left[\frac{SB(3u+K)}{3} r^3 - SBr^2\xi\right],$$

$$G^o_1 = 3G^o_3, \quad G^o_3 = \frac{1}{4}\left[-\frac{S^2}{u^2} r^2\xi - 3D(u+K) r\xi^2 + D\xi^3\right]$$

In Eqs.(12), J and Y are the Bessel functions of the first and second kind, and K and I are Modified Bessel functions. The circular boundary is changed by the effect of shear, $(r_0 + r_1(\theta))\,\mathbf{r}$. With the continuity condition of $\nabla_\perp^2 \varphi_1$ on the boundary, we obtain $r_1(\theta) = R\cos^2\theta$. The continuity condition of φ_1 and $\partial\varphi_1/\partial r$ determine the constants a_1, a_3, b_1, b_3 with R determined by the following relation

$$R = \frac{4}{3}\,\frac{1}{(u+K)\left[1 - kr_0\dfrac{K_1'(kr_0)}{K_1(kr_0)}\right]}\,\frac{\left.\dfrac{\partial\varphi^o_{p,1}}{\partial r} - \dfrac{\partial\varphi^i_{p,1}}{\partial r}\right|_{(r=r_0)}}{q\dfrac{J_1'(qr_0)}{J_1(qr_0)} - k\dfrac{K_1'(kr_0)}{K_1(kr_0)}} \qquad (13)$$

and

$$3\,\frac{q\dfrac{J_1'(qr_0)}{J_1(qr_0)} - k\dfrac{K_1'(kr_0)}{K_1(kr_0)}}{q\dfrac{J_3'(qr_0)}{J_3(qr_0)} - k\dfrac{K_3'(kr_0)}{K_3(kr_0)}} = \left.\frac{\dfrac{\partial\varphi^o_{p,1}}{\partial r} - \dfrac{\partial\varphi^i_{p,1}}{\partial r}}{\dfrac{\partial\varphi^o_{p,3}}{\partial r} - \dfrac{\partial\varphi^i_{p,3}}{\partial r}}\right|_{(r=r_0)}. \qquad (14)$$

We note the shear reduces the free parameter from two to one. For given value of the vortex speed u (or r_0), Eq.(14) determines the vortex radius r_0 (or u). The stationary solution is given by Eqs.(12)-(14). The boundary which was a circle becomes an ellipse.

IV. CONCLUSION

We have shown that a localized stationary solution exists for the nonlinear equations describing the ion temperature gradient driven turbulence with and without magnetic shear. When the magnetic shear is finite, the circular boundary of shearless modon solution becomes an ellipse and the number of free parameters reduce to one with the vortex radius r_0 (or the speed u) is determined by Eq.(14). The work of Meiss and Horton [10] contains only the linear effect of magnetic shear and shows that the shear damping is exponentially small in S. Our study include a full nonlinear effect of shear and we have shown that there exists a stationary solution.

Although it is difficult to identify the coherent structures found in η_i-mode simulations as the simplest stationary solutions found in this work, it may be a mixture of these solutions through the vortex-vortex or vortex-wave interactions.

References

1. F. Romanelli, Plasma Physics and Controlled Fusion **31**, 1535 (1989).
2. R.J. Fonck, et al. Phys. Rev. Lett. **63**, 520 (1989).
3. F.X. Soldner,et al. Phys. Rev. Lett, **61**, 1105 (1989).
4. W. Horton, Phys. Fluids **29**, 1491 (1986).
5. B.G. Hong and W. Horton, to be published in Phys. Fluids 1990.
6. M. Ottaviani, et al. Phys. Fluids **B2**,67 (1990).
7. A. Hasegawa and K.Mima, Phys. Rev. Lett. **39**, 205 (1977).
8. V.D. Larichev and G.M. Reznik, Oceanology **16**, 547 (1976).
9. G.R. Flierl, et al.,Dyn. Atmos. Oceans. **5**, 1 (1980).
10. J.D. Meiss and W. Horton, Phys. Fluids **26**, 990 (1983).
11. J. Nycander, Phys.Fluids **B1**, 1788 (1989).
12. W. Horton, Phys.Fluids **B1**, 524 (1989).
13. A. Hasegawa, C.G. Maclennan and Y. Kodama, Phys. Fluids **22**, 2122 (1979).

NEOCLASSICAL TRANSPORT CALCULATIONS FOR "LINEAR" MHD EQUILIBRIA

H. Werthmann, H. Rieser, and S. Kuhn

Institute for Theoretical Physics, University of Innsbruck
Technikerstrasse 25, A–6020 Innsbruck, Austria

1. The "linear" axisymmetric equilibria. Following the procedure given by Hohenauer /1/, the Schlüter–Grad–Shafranov (SGS) equation in quasi–toroidal coordinates (r,ϑ,φ),

$$\frac{\partial^2\psi}{\partial r^2} + \frac{R_0}{r(R_0-r\cos\vartheta)}\frac{\partial\psi}{\partial r} + \frac{1}{r^2}\frac{\partial^2\psi}{\partial\vartheta^2} - \frac{\sin\vartheta}{r(R_0-r\cos\vartheta)}\frac{\partial\psi}{\partial\vartheta} + \hat{B}_\varphi(\psi)\frac{d}{d\psi}\hat{B}_\varphi(\psi) + 4\pi(R_0-r\cos\vartheta)^2\frac{d}{d\psi}P(\psi) = 0\,, \tag{1}$$

with φ the ignorable coordinate and R_0 the major radius, is linearized by assuming the total pressure and the third covariant magnetic–field component to be of the form

$$P(\psi) = P_0 + P_1\psi + \tfrac{1}{2}P_2\psi^2 \tag{2a}$$

and

$$\hat{B}_\varphi(\psi) = B_{1,0} + B_{3,1}\psi\,, \tag{2b}$$

respectively. The resulting linear equation for ψ is then solved through first order in the inverse aspect ratio η, with the result

$$\psi = R_0\left\{A_T[J_0(\kappa_T r)-1] + \eta\cos\vartheta\left[s_1\frac{r}{a} - \frac{r}{2a}A_T J_0(\kappa_T r) + [s_2(\frac{r}{a})^2+s_4]J_1(\kappa_T r)\right]\right\}. \tag{3}$$

Hence **B** follows in the form

$$\mathbf{B} = \frac{1}{R_0-r\cos\vartheta}\left[-\frac{1}{r}\frac{\partial\psi}{\partial\vartheta}\mathbf{e}_r + \frac{\partial\psi}{\partial r}\mathbf{e}_\vartheta + \hat{B}_\varphi(\psi)\,\mathbf{e}_\varphi\right], \tag{4}$$

and by inserting (3) into (2a) we obtain an analytical expression for P as well. A weak additional magnetic field $\mathbf{B}^v = O(\eta)$, which may be applied in tokamak configurations by external vertical–magnetic–field coils, can be taken into account in the equilibrium solutions (3) by prescribing appropriate conditions at the plasma boundary (r = a) /2/; the latter affect only the constant s_4. A suitable scheme for evaluating the constants appearing in the linearizing expressions (2a) and (2b) has been developed, which permits us to relate these constants to certain physical quantities of immediate relevance – such as the safety factor q at the plasma boundary or the β–factor at r = 0 – and to thus establish a plausible connection with real experiments. With this scheme one can find low–β ($\beta \simeq 1\%$) or high–β ($\beta \simeq 5\%$) equilibria corresponding to tokamak experiments employing Ohmic or additional (e.g., neutral– beam injection) heating, respectively.

2. Neoclassical transport calculations. (a) We consider a two–component plasma satisfying the basic scaling assumption of neoclassical theory, $\epsilon \equiv \rho_L/L_H \ll 1$, with ρ_L the thermal ion Larmor radius and L_H the hydrodynamic length /3/. To lowest order in ϵ, the temperatures of both particle species are surface quantities, i.e., functions of ψ alone. By means of the plausible ansatz

$$T_a(\psi) = T_{a,0} + T_{a,1}\psi + T_{a,2}\psi^2 \tag{5}$$

(which provides us with some freedom in fitting experimental data), the expressions for P and B, and the quasineutrality condition, the two–fluid variables n_e, n_i, p_e and p_i are obtained in $O(\epsilon^0)$. These quantities are needed in neoclassical transport equations determining the surface averages of the radial components of the particle and heat fluxes.

Such transport equations governing the averaged *physical* radial components have been derived by Balescu /3/ for the special case $l_\varrho = l_\varrho(\rho)$, where $l_\varrho \equiv \sqrt{g_{\varrho\varrho}}$ is the scale factor of the orthogonal Hinton–Hazeltine coordinates (ρ,θ,ζ) /4/. Since, however, for the equilibria considered here l_ϱ is no surface function but rather depends on ρ *and* θ, we had to generalize Balescu's equations to this case.

There are two possibilities of performing this generalization. First, one can derive equations which again determine the *physical* components $\langle h_\varrho^{\alpha(n)}\rangle$, cf. (b) below. The second, much simpler possibility consists in deriving transport equations for the averaged *contravariant* radial flux components, cf. (c) below. For geometries where l_ϱ is no flux function, one usually calculates such *contravariant* flux components, although for the "figures of merit" of a confinement configuration it is the corresponding *physical* components which are of immediate relevance.

(b) For the dimensionless particle fluxes $h^{\alpha(1)}$ and heat fluxes $h^{\alpha(3)}$, the equations for the averaged *physical* radial flux components read

$$\langle h_\rho^{\alpha(n)}\rangle = \delta_{1n}\langle h_\rho^{\alpha(1)}\rangle_{DR} + \langle h_\rho^{\alpha(n)}\rangle_{CL} + \langle h_\rho^{\alpha(n)}\rangle_{NCL}^{\dagger} + \langle h_\rho^{\alpha(n)}\rangle_{geo}^{\dagger}\,, \tag{6}$$

where $\langle h_\varrho^{\alpha(1)}\rangle_{DR}$ and $\langle h_\varrho^{\alpha(n)}\rangle_{CL}$ are given by Eqs. (12.9.10) and (12.9.11) of Ref. /3/ and the neoclassical contributions are of the modified form (marked by the superscript $\dagger$)

$$\langle h_\rho^{\alpha(n)}\rangle_{NCL}^{\dagger} \equiv -\mathcal{J}(R_o\mathcal{B}_p)^{-1}\,\langle l_\rho\Omega_\alpha^{-1}\,[Q_{ll}^{\alpha(n)} + \delta_{1n}e_\alpha m_\alpha^{-\frac{1}{2}}T_\alpha^{-\frac{1}{2}}E_{ll}^{(A)}]\rangle\,. \tag{7}$$

Moreover, we find the new terms

$$\langle h_\rho^{\alpha(1)}\rangle_{geo}^{\dagger} \equiv -2^{-\frac{1}{2}}3m_\alpha^{-\frac{1}{2}}T_\alpha^{\frac{1}{2}}\,\mathcal{J}\langle(\Omega_\alpha B l_\rho l_\theta l_\zeta)^{-1}h_{ll}^{\alpha(2)}\,\frac{\partial}{\partial\theta}l_\rho\rangle \tag{8}$$

and

$$\begin{aligned}\langle h_\rho^{\alpha(3)}\rangle_{geo}^{\dagger} \equiv\; & -10^{-\frac{1}{2}}3m_\alpha^{-\frac{1}{2}}T_\alpha^{\frac{1}{2}}\,\mathcal{J}[7^{\frac{1}{2}}\langle(\Omega_\alpha B l_\rho l_\theta l_\zeta)^{-1}h_{ll}^{\alpha(4)}\,\frac{\partial}{\partial\theta}l_\rho\rangle \\ & + 2^{\frac{1}{2}}\langle(\Omega_\alpha B l_\rho l_\theta l_\zeta)^{-1}h_{ll}^{\alpha(2)}\,\frac{\partial}{\partial\theta}l_\rho\rangle]\,,\end{aligned} \tag{9}$$

which describe purely geometrical effects and are not related to any thermodynamic forces /5/.

In the short–mean–free–path regime, these relations can be shown to assume the form of transport equations, i.e., equations relating the fluxes linearly to the corresponding thermodynamic forces.In the long–mean–free–path regime, on the other hand, they in addition involve certain unknown irreducible Hermitian moments whose evaluation appears to be rather complicated. The calculation of physical particle and heat fluxes from these equations may be a worthwhile task to be tackled in the future.

(c) In our second generalization of Balescu's transport equations /3/, we have derived the following relations for the averaged *contravariant* radial flux components with respect to the coordinate system (ψ,θ,ζ):

$$\langle\Gamma^e\cdot\nabla\psi\rangle_k = L_1^k\,\mathfrak{X}_1 + L_2^k\,\mathfrak{X}_2 \tag{10a}$$

$$\langle q^e\cdot\nabla\psi\rangle_k = T_e[L_2^k\,\mathfrak{X}_1 + L_3^k\,\mathfrak{X}_2] \tag{10b}$$

$$\langle q^i\cdot\nabla\psi\rangle_k = T_i\,L_4^k\,\mathfrak{X}_3 \tag{10c}$$

where Γ^α and q^α denote the particle and heat fluxes, respectively, k equals CL for the classical and PS for the Pfirsch–Schlüter fluxes,

$$\mathfrak{X}_1 = -\frac{1}{P_e}\frac{dP}{d\psi}\,, \quad \mathfrak{X}_2 = -\frac{1}{T_e}\frac{dT_e}{d\psi}\,, \quad \mathfrak{X}_3 = -\frac{1}{T_i}\frac{dT_i}{d\psi} \tag{11}$$

are the relevant thermodynmaic forces, and

$$L_1^{CL} = \frac{c_{11}^e}{\tau_e}\frac{P_e m_e c^2}{e^2}\left\langle\frac{|\nabla\psi|^2}{B^2}\right\rangle\,, \quad L_2^{CL} = -\sqrt{5/2}\,\frac{c_{13}^e}{\tau_e}\frac{P_e m_e c^2}{e^2}\left\langle\frac{|\nabla\psi|^2}{B^2}\right\rangle\,,$$

$$L_3^{CL} = \frac{5}{2}\frac{c_{33}^e}{\tau_e}\frac{P_e m_e c^2}{e^2}\left\langle\frac{|\nabla\psi|^2}{B^2}\right\rangle\,, \quad L_4^{CL} = \frac{5}{2}\frac{c_{33}^i}{\tau_i}\frac{P_i m_i c^2}{(Ze)^2}\left\langle\frac{|\nabla\psi|^2}{B^2}\right\rangle\,, \tag{12}$$

$$L_n^{PS} = \left[\hat{B}_\varphi^2 \mathscr{B}_0^{-2}\left\langle\frac{\mathscr{B}_0^2}{B^2} - 1\right\rangle\left\langle|\nabla\psi|^2 B^{-2}\right\rangle^{-1}\right] L_n^{CL} \qquad (n = 1, \ldots, 4)$$

are the related transport coefficients. For the various other quantities appearing in these equations the reader is referred to Ref. /3/. The radial contravariant component of the ion fluxes are determined by the ambipolarity condition

$$\langle\Gamma^i\cdot\nabla\psi\rangle_k = \langle\Gamma^e\cdot\nabla\psi\rangle_k/Z\,. \tag{13}$$

Equations (10) and (13) completely determine neoclassical transport in tokamaks in the short–mean–free–path regime; in the long–mean–free–path regime, the banana fluxes will also have to be taken into account with the help of analogous equations.

(d) The main task in evaluating the transport equations (10) consists in computing the various surface averages entering the transport coefficients (12), to which end the flux–surface geometry must be known. In our case, the surfaces are determined by the transcendental equation $\psi = \text{const}$, with ψ given by Eq. (3), from which the relation $r = r(\vartheta;\psi)$ can be obtained only numerically. However, in order to still be able to proceed analytically, we have chosen to solve the equation $\psi = \text{const}$ with the help of the perturbational expansion

$$r = r_0 + \eta r_1(\vartheta;r_0) + O(\eta^2)\,, \tag{14}$$

where $0 \le r_0 \le a$ /6/. It turns out that through order η these approximate flux surfaces are non–concentric circular tori. However, a fundamental shortcoming of the expansion (14) lies in the fact that it is not applicable to those innermost magnetic surfaces whose ψ–values do not occur in $O(\eta^0)$. We have thus assumed these innermost surfaces to be circular tori as well, determined by an appropriate ansatz for $r = r(\vartheta;r_0)$, where now $-a \le r_0 < 0$. Then, the quantity $\rho = \frac{1}{2}(r_0+a)$ may be considered as a topological radius /3/ labeling *all* circular–toroidal approximate flux surfaces ($-a \le r_0 \le a$). The surface averages required for the various transport coefficients are now approximatly calculated by integrating over these circular tori.

3. First numerical results. Figure 1 shows the electron– and ion–pressure profiles (solid and dashed lines, respectively), and Fig. 2 shows the related density profile ($n_e = n_i$) for a low–β tokamak equilibrium with $R_0 = 100$ cm, $B_\varphi(r=0) = 5$ T, $\eta = 0.2$, $\beta(r=0) = 0.01$, $q(r=a) = 3.85$, and $Z = 1$, corresponding to specifically chosen electron and ion temperature profiles (5). The classical and Pfirsch–Schlüter particle fluxes (10a) for this configuration are given, in units of $cm^{-1/2}s^{-2}g^{1/2}$, in Figs. 3 and 4, respectively. Note that in each case the symmetry axis of the torus is to the right of the figure.

Comparison of classical and Pfirsch–Schlüter particle fluxes for some configurations considered by us has shown that the latter exceed the former by a factor of about $10 \div 20$. More systematic studies are under way and their results will be reported at the Conference.

Acknowledgment. This work was partly supported by Austrian Research Fund Project P7005.

References

/1/ W. Hohenauer, Diploma thesis, Institute for Theoretical Physics, University of Innsbruck, 1988.

/2/ J.P. Freidberg, *Ideal Magnetohydrodynamics* (Plenum Press, New York, 1987).

/3/ R. Balescu, *Transport Processes in Plasmas* (North–Holland, Amsterdam, 1988).

/4/ F.L. Hinton and R.D. Hazeltine, *Rev. Mod. Phys.* **48**, 239 (1976).

/5/ R. Balescu, private communication (1990).

/6/ N. Schupfer, private communication (1990).

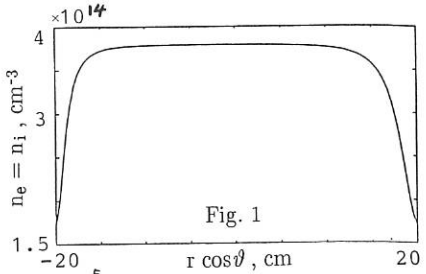

Fig. 1

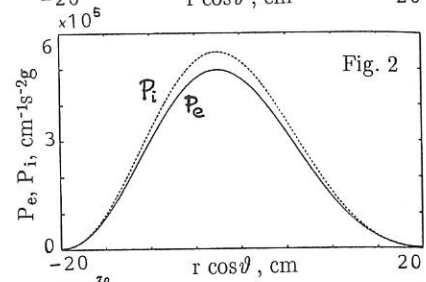

Fig. 2

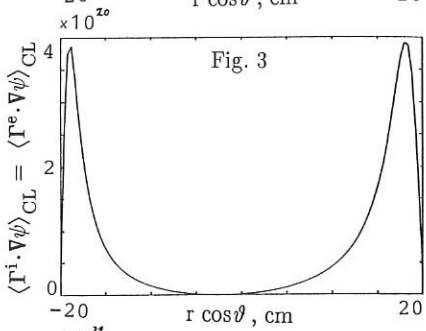

Fig. 3

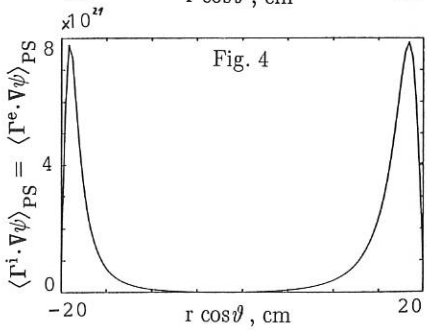

Fig. 4

DIFFUSION OF IONS IN PRESENCE OF NEARLY OVERLAPPING MAGNETIC ISLANDS

J. T. Mendonça and M. Brusati*

Instituto Superior Técnico, 1096 Lisboa Codex, Portugal

*JET Joint Undertaking, Abingdon, Oxon 0X14 3EA, U.K.

1. Introduction

The anomalous transport of energy and particles is one of the main physical problems encountered in fusion plasma research. One plausible drive of such transport is the field stochasticity arising from the interaction between magnetic islands, caused by MHD activity associated with microtearing modes.

It is accepted that, when islands overlap does occur, electrons experience a radial diffusion associated with the stochastic behaviour of magnetic field lines. This exceeds the ion diffusion, due to the larger ion mass.

However, a different situation occurs when the overlapping condition is not fulfilled or is only marginally attained. Electron diffusion is prevented by undestroyed magnetic surfaces, but ions maintain a high diffusion rate due to their finite Larmor radius. Collisions will further enhance the ion diffusivity.

In this work, ion diffusion coefficients are computed using a simple mathematical model, where magnetic islands are described by a discrete mapping and finite Larmor effects are simulated by a random force which depends on two distinct parameters.

2. Model equations

We assume that the electron and ion guiding-centres confined in a toroidal magnetic field and in presence of magnetic islands, can be conveniently described by

he following discrete mapping:

$$\bar{X}_{j+N} = [\, \bar{T}\,(\,\bar{X}_j\,)\,]^N + \bar{F} \qquad (1)$$

where $\bar{X} = (\, I, \theta)$, I representing the radial variable and θ the poloidal angle. The standard mapping, describing the magnetic field perturbations is given by:

$$\bar{T}\,(\,\bar{X}_j\,) = \left(\; I_j + K \sin\theta_j\,, \quad \theta_j + I_j \;\right) \qquad (2)$$

where K is the amplitude of the magnetic islands. Instead of K, the overlapping parameter $\gamma = 2K^{1/2}/\pi$ is commonly used. In eq.(1) we also have:

$$\bar{F} = A\left(\; \cos(2\pi R)\,, \;\; \sin(2\pi R) \;\right) \qquad (3)$$

where A is an additional parameter and R is a random variable in the domain (0,1).

When A=0 (and N=1), the above eq.(1) simply states that the electron and ion guiding centre follow the magnetic field lines along the torus. In this case, their motion will be mainly regular as long as $\gamma < \gamma_c = 2/\pi$ (or $K < 1$). For $\gamma > \gamma_c$, the particles will be allowed to diffuse radially, just by following the stochastic field lines. When $A \neq 0$, two additional diffusion mechanisms can be described by eq.(1). One is due to collisions: N represents the mean collision time and A the particle Larmor radius. The other is due to deviations on the ion cyclotron orbit which occurs when the ions cross the stochastic separatrices surrounding the islands, even if their guiding centre remains on a regular magnetic surface.

In order to calculate the various diffusion processes, we assume the following definition for the diffusion coefficient [1]: $D = \sigma/V$, where:

$$\sigma = \frac{K}{T} \Sigma\, |\sin\theta_o| \qquad V = \frac{K}{T} \Sigma\, L\, |\sin\theta_o| \qquad (4)$$

Here, T is the total number of particle trajectories, θ_o their initial angular value and L the number of iterations they take to cross one single chaine of islands (or equivalently, to cross the radial distance $\Delta I = 2\pi$). The sum in eqs.(4) is taken over all the trajectories crossing that distance, in the sense of ref. [1].

3. Numerical results

Let us assume that $\gamma \leq \gamma_c$ and that collisions can be neglected. The electrons will not diffuse, but the ions will be influenced by the stochastic magnetic fields surrounding each magnetic island, twice in each cyclotron period.

This means that, in each iteration of the mapping (1), where we should assume N=1, the ions will be acted by a random force weighted by A. The value of A can

be estimated by assuming that, in each iteration (or toroidal turn) the ions have performed a large number M of gyro-orbits and that, in each of them, two small random perturbations occured.

This means that A should be seen as a measure of the mean distance travelled by the ion guiding centre during M cyclotron periods. The result of such a diffusion process is shown in Figure 1, where D is calculated using eqs.(1) and (4), with N=1 and for two values of A: 1) A=0 illustrates the electron behaviour, where diffusion only occurs for $\gamma > 0.7$; 2) $A=\pi$ illustrates the ion behaviour, where diffision at a significant level is present even for $\gamma<\gamma_c$.

Let us now consider the influence of collisions. In this case, A is just a meassure of the ion Larmor radius ρ_i. If we assume that $\rho_i k \simeq 1$, where k is the typical wavenumber of the microtearing turbulence, we can take $A=\pi$, which means that in each collision the ion guiding centre can travel half the distance between two adjacent magnetic islands. Such a diffusion process will be negligible for the electrons, because $\rho_e \simeq A=0$.

Now, because the ions are not very collisional in high temperature plasmas they can perform a large number N of toroidal turns between two consecutive collisions. In Figure 2 we represent D as a function of N, for two values of γ, one bellow and the other above γ_c. The probability p of a given trajectory starting at $I_o=0$ to attain $I=2\pi$ is also shown. We see that D tends rapidly to zero for $N > 10$.

4. Conclusions

With the aid of a simple model we have shown that the ions can diffuse anomalously more than the electrons in the presence of non-overlapping chains of magnetic islands. These islands can eventually be associated with microtearing turbulence. Two regimes of anomalous diffusion can be envisaded, one dominated by the ions, for $\gamma < \gamma_c$, and the other dominated by the electrons, for $\gamma > \gamma_c$. The same model can also be used to estimate the enhancement of the diffusion process due to collisions, where again the ions will diffuse faster than the electrons, for moderate values of γ.

References

[1] - M. Hugon, J.T. Mendonça and P.H. Rebut, Comptes Rendus Acad. Sciences (Paris) 308 II, 1319 (1989).

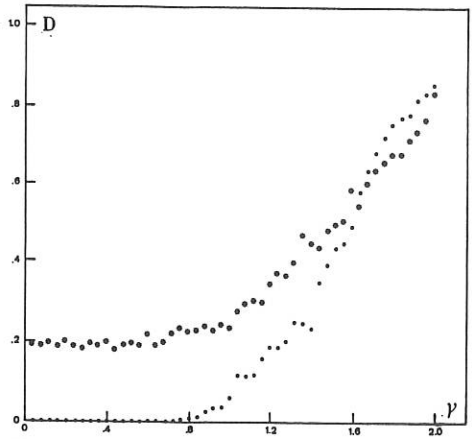

Figure 1- D as a function of the overlapping parameter γ.

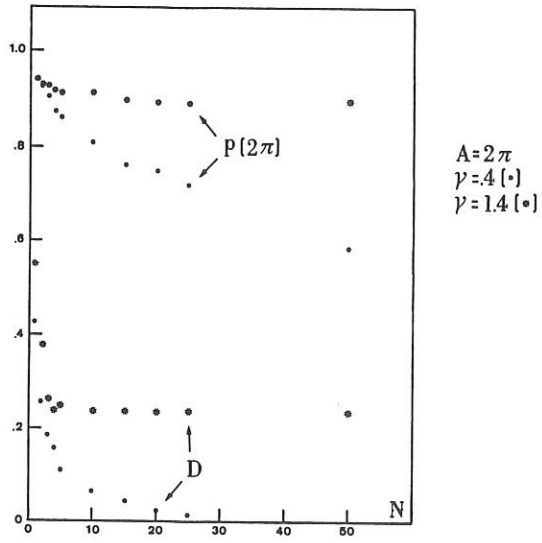

Figure 2 - D and p, as a function of the mean collision time N.

TOROIDAL η_i-MODE TURBULENCE WITH COLLISIONAL TRAPPED ELECTRON EFFECTS

A. Jarmén and H. Nordman

Inst. for Electromagnetic Field Theory and EURATOM/NFR Association
Chalmers Univ. of Technology, S-412 96 Göteborg, Sweden

Introduction

In this work the effect of dissipative trapped electrons [1] on the particle and heat transport caused by η_i-modes in Tokamaks [2] is studied. The plasma is assumed to be in the collision dominated regime. Using a toroidal fluid model for the ions [3] and a kinetic description for the trapped electrons a coupled system of nonlinear evolution equations for electric potential, particle density and temperatures is derived and solved numerically.

Transport coefficients from the numerical simulations show good agreement with coefficients obtained from quasilinear estimates. The transition from the neo-Alcator scaling of the energy confinement time with density to a saturated state is demonstrated. Contrary to the case with nondissipative trapping [4], particle and heat pinch effects (inward transport) do not seem to be possible for the modes studied here when the plasma is in the collisional regime.

Ion model

The ions are described by a toroidal fluid model [3] which includes all the curvature effects in the energy and continuity equations and where an important role is played by the ion diamagnetic heat flow. The model neglects ion motion parallel to the background magnetic field and uses localization of the particles by the magnetic field in the perpendicular direction. Comparisons with linear results of kinetic models [5] including effects of magnetic drift resonances have shown a good agreement.

Electron model

The trapped electrons are described by the Vlasov equation with an energy dependent Krook collision operator and an effective collision frequency $\nu_{ef}=\nu_{ei}/\varepsilon$ giving the rate of detrapping. The untrapped electrons are assumed

to have a Maxwellian distribution (at the potential perturbation ϕ). Assuming collision dominance, $\nu_{ef} >> |\omega|$, the total (trapped + untrapped) electron density and temperature perturbations are then given by a simple Boltzmann law slightly modified by the trapping effect, $\delta n_e/n_e=(1-i\alpha)e\phi/T_e$, where $\alpha \sim \varepsilon^{3/2}\eta_e\omega_{*e}/\nu_{ei} << 1$ is directly proportional to the fraction of trapped electrons but inversely proportional to the collision frequency.

Numerical simulations

The equations governing the evolution of the potential, temperature and density perturbations are

$$\left(\frac{\partial}{\partial t} + \vec{v}_E\cdot\nabla\right)\left(\frac{\delta n_i}{n_0} - \rho_s^2\nabla^2\frac{e\phi}{T_{0e}}\right) + \left(1+\frac{1+\eta_i}{\tau}\rho_s^2\nabla^2\right)\vec{v}_{*e}\cdot\nabla\frac{e\phi}{T_{0e}}$$

$$+ \vec{v}_{Di}\cdot\nabla\left\{\tau\frac{e\phi}{T_{0e}} + \frac{\delta n_i}{n_0} + \frac{\delta T_i}{T_{0i}}\right\} = \rho_s^2(\vec{\tilde{v}}_{*i}\cdot\nabla)\nabla^2\frac{e\phi}{T_{0e}} \qquad (1)$$

$$\left(\frac{\partial}{\partial t}+\vec{v}_E\cdot\nabla\right)\frac{\delta T_i}{T_{0e}} + \left(\frac{\eta_i}{\tau} - \frac{2}{3\tau}\right)\vec{v}_{*e}\cdot\nabla\frac{e\phi}{T_{0e}} - \frac{2}{3\tau}\left(\frac{\partial}{\partial t}+\vec{v}_E\cdot\nabla\right)\frac{\delta n_i}{n_0} + \frac{5}{3\tau}\vec{v}_{Di}\cdot\nabla\frac{\delta T_i}{T_{0e}} = 0 \qquad (2)$$

$$\frac{\delta n_i}{n_0} = \frac{\delta n_e}{n_0} = (1 - \beta\vec{v}_{*e}\cdot\nabla)\frac{e\phi}{T_{0e}} \qquad (3)$$

where quasineutrality has been assumed and "i" and "e" refer to ions and electrons respectively. The electron temperature perturbation from the kinetic electron model is given by $\delta T_e/T_e=(1/2-4\beta\vec{v}_{*e}\cdot\nabla)e\phi/T_e$. In (1, 2) both convective and FLR nonlinearities are included. The system is solved using a fully dealiased Fourier spectral method in x,y and a predictor-corrector method for the time integration. A 64x64 grid spanning $-1.8 \le \rho k_x, \rho k_y \le 1.8$ has been found appropriate. The turbulence is driven at intermediate length scales ($k^2\rho^2 \approx 0.1$) and is artificially damped at low and high mode numbers assumed to represent the effect of ion Landau damping and high-k viscosity respectively [4]. In the simulations the profiles are kept unchanged and hence only nonlinear saturation mechanisms are considered. The thermal conductivities and particle diffusion coefficient are calculated as time-space averages over the turbulent state

$$\chi_i = -\frac{L_{Ti}\,c}{T_i\,B_0} < \frac{\partial\phi}{\partial y}\,\delta T_i > \qquad (4)$$

$$\chi_e = -\frac{L_{Te}\,c}{T_e B_0} < \frac{\partial\phi}{\partial y}\,\delta T_e > \qquad (5)$$

$$D = -\frac{L_n\,c}{n_0\,B_0} < \frac{\partial\phi}{\partial y}\,\delta n > \qquad (6)$$

Quasilinear diffusion

Assuming a perturbation $\sim \exp(ik_x x+ik_y y-i\omega t)$ the linearized form of (1-3) gives the linear perturbations which substituted in (4-6) gives the quasilinear diffusion coefficients

$$\chi_i = C\frac{L_{Ti}}{\rho_s}\frac{\left[\omega_r\left(\omega_r-\frac{5}{3}\omega_{Di}\right)+\gamma^2\right]\frac{2}{3}\alpha-\gamma\omega_{*e}\left[\frac{2}{3}-\eta_i+\frac{10}{9\tau}\varepsilon_n\right]}{\left(\omega_r-\frac{5}{3}\omega_{Di}\right)^2+\gamma^2}\frac{\gamma^2}{k_x^2\,k_y c_s} \qquad (7)$$

$$\chi_e = 4\,C\frac{L_{Te}}{\rho_s}\alpha\frac{1}{k_x^2}\frac{\gamma^2}{k_y c_s} \qquad (8)$$

$$D = C\frac{L_n}{\rho_s}\alpha\frac{1}{k_x^2}\frac{\gamma^2}{k_y c_s} \qquad (9)$$

where γ is the linear growth rate ($\omega=\omega_r+i\gamma$). For the modes studied here we have in general $\gamma\leq\omega_r$, hence the weak turbulence approximation is motivated. We note that $D=\chi_e\eta_e/4$. The normalization constant C replaces the summation over k and has been chosen after comparisons with the simulations. The saturation level of the potential has been obtained by balancing the linear growth and the dominant convective nonlinearity in the energy and continuity equations which gives $e\phi/T_e=\gamma/\omega_{*e}\;1/k_xL_n$. In the saturated turbulent state the spectrum is roughly isotropic with $k_x\rho_s\approx k_y\rho_s\approx$ 0.3 which is used in the quasilinear expressions. From (8,9) it follows that χ_e and D are always positive (outward). χ_i, however, contains pinch terms proportional to ε_n and in the limit $\alpha\to 0$ it has been shown that this leads to a decrease in χ_i for large ε_n giving a radial profile of χ_i that compares favourably with experimental results [4].

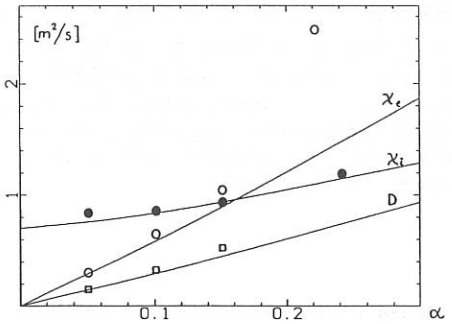

Fig 1a. Scaling of diffusion coefficients with $\alpha\sim\varepsilon^{3/2}\eta_e\omega_{*e}/\nu_{ei}$ as obtained from nonlinear simulations and quasilinear theory.

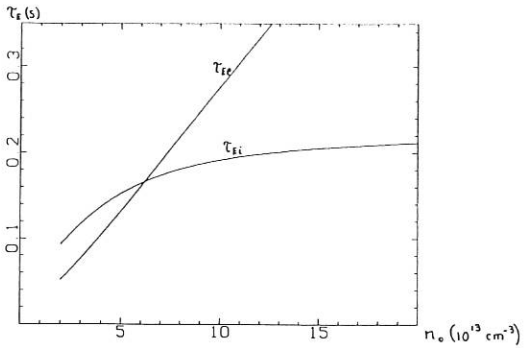

Fig 1b. Energy confinement time versus density.

Discussion

In fig 1a the scaling of the diffusion coefficients with α is given as obtained from the fully nonlinear simulations and from quasilinear theory for $k\rho_s$=0.3. The corresponding scaling of the energy confinement times τ_{Ej}= a^2/χ_j with $n \sim 1/\alpha$ is shown in fig 1b. Typical ASDEX parameters have been used with a=0.4 m, R=1.6 m, T_e=T_i=0.5 keV, η_i=η_e=2 and ε_n=1. The normalization constant here is C=14. It is obvious that there is a reasonably good agreement between the results from the quasilinear theory and the mode coupling simulations, especially for small values of α. The linear dependence of D and χ_e for small α is a consequence of the weak dependence of γ and the fluctuation level on α. The relation between D_{sim} and D_{ql} follows the χ_{esim}-χ_{eql} relation since the particle and electron energy transport is determined by the linear electrons. The disagreement for larger α-values is expected since here the expansion in α breaks down for the high-k part of the turbulent spectrum. Thus modes with $k^2\rho^2 \triangleq 1$ will give a nonnegligible contribution to the transport giving $\chi_{sim} > \chi_{ql}$. The energy confinement time in Fig 1b saturates when $n_o \geq 7 \cdot 10^{13}$ cm^{-3} corresponding to the regime where $\chi_i \geq \chi_e$. For smaller values of n_o the electron transport dominates giving the neo-Alcator scaling of the confinement time. The low n_o regime, however, has been excluded since here the assumption of collision dominance is violated ($n_o \sim 1/\alpha$).

References:

[1] Kadomtsev B B, Pogutse O P, Nucl. Fusion **11** (1971) 67.
[2] Söldner F X, Müller E R, Wagner F et al., Phys. Rev. Lett. **61** (1988) 1105.
[3] Jarmén A, Andersson P and Weiland J, Nucl.Fusion **27** (1987) 941.
[4] Weiland J, Jarmén A and Nordman H, Nucl. Fusion **29** (1989) 1810.
[5] Romanelli F, Phys. Fluids B **1** (1989) 1018.

The anomalous resistivity in the neutral sheet of the magnetotail

Jian-lin Mu
CCAST-World Lab. and Inst. of Phys., Academia Sinica, Beijing
Zu-yin Pu
Dept. of Geophys., Peking University, Beijing
Shih-tung Tsai
Inst. of Phys., Academia Sinica, Beijing

Abstract

In this paper a new kind of kinetic drift instability, crossing-axis (AC) ion diamagnetic drift instability, is proposed. Our results show that the AC ion trajectories can be expressed with an analytical expression, there are two kinds of drift motion associated with AC ions: orbit drift and diamagnetic drift, both of them can reach the order of the thermal velocity. An electrostatic instability can thus be driven by the AC ion diamagnetic drift velocity and enhanced by the orbit drift resonance with the wave. The associated anomalous resistivity reaches the order of $10^4\ m\Omega$.

Guiding center theory in the reversed magnetic geometry

Jian-lin Mu Shih-tung Tsai
CCAST-World Lab. and Inst. of Phys., Academia Sinica, Beijing

Abstract

In this paper the guiding center Hamiltonian in the current sheet of the field-reversed magnetic geometry is presented. An exact solution of the unperturbed particle orbit and guiding center position in a strong inhomogeneous magnetic model is obtained. The contribution of small normal magnetic component to the Hamiltonian is carried out by Lie transfomation method. Numerical results show that this theory can be used in the cases of magnetotail and field pinch geometry.

SPECIFIC EDGE EFFECTS ON TURBULENCE BEHAVIOUR

X.Garbet, L.Laurent , J.P. Roubin, A.Samain

Association Euratom CEA DRFC/ SPPF
CEN Cadarache 13108 St Paul lez Durance France

I. Introduction

In both divertor and limiter configurations, tokamak plasmas are surrounded by a region with open field lines, the scrape off layer. Direct measurements of plasma density or potential using Langmuir probes show that this region is highly turbulent i.e. $\tilde{n}/n \approx 100\%$, $k_\perp \rho_{thi} \approx 0.1$ (where ρ_{thi} is the ion Larmor radius). The plasma zone just inside the last magnetic surface has also been similarly observed to be unstable [1,2,3]. Theoretical models generally fail to find linearly unstable modes: the free motion of electrons along flux lines stabilizes the rippling and interchange modes; collisional drift modes are also found to be stable [4]. Several models have then been developed which include specific edge effects to explain the large level of turbulence: for example impurity radiation or ionization and charge exchange [5,6].

In this paper we take into account new effects which are shown to modify drastically the instability behaviour. In the second section the linear stability in the scrape off layer is investigated taking into account the fact that the flux lines are open. In the third section specific edge effects in the region with closed flux surfaces are investigated.

II. Stability of open flux lines

For the sake of simplicity we shall consider only the case of an axisymmetric configuration (i.e. inner wall operation, belt limiter, standard divertor). Each field line in the scrape off layer intersects the wall or the limiter at two poloidal angles θ_1, θ_2 as shown in the figure. Its length is $L = qR(\theta_2 - \theta_1)$ where q is the safety factor and R the major radius. At both extremities the sheath potential ϕ adjusts itself in such a way that the ion current neV_{thi} is balanced by the electron current $nV_{the}\, e^{-e\phi/T}$. It is interesting to study the stability of a potential perturbation $\tilde{\phi}$ in such a flux tube using a fluid model. The mass conservation provides a relation between the potential and density fluctuation $\frac{\tilde{n}}{n} = -\, e\, V_e^*/T\gamma \frac{1}{r}\frac{\partial \tilde{\phi}}{\partial \theta}$ where V_e^* is the diamagnetic velocity and γ (=-iω) the growth rate. The charge conservation in a flux tube of vanishing cross section can be expressed as :

$$\int_{\theta_1}^{\theta_2} \mathrm{div}(\tilde{J}_{curv}+\tilde{J}_{pol})qRd\theta + \tilde{J}_{//}(\theta_1) + \tilde{J}_{//}(\theta_2) = 0 \qquad (1)$$

The divergence term reflects the charge accumulation due to curvature and polarisation currents. The two last terms represent the parallel current through the sheathes at the extremities of the flux tube. The perturbation of these sheath currents results from a modification of the number of reflected electrons: $\tilde{J}_{//}(\theta) = ne^2 V_{thi} \frac{\tilde{\phi}(\theta)}{T}$. Note that $\tilde{J}_{//}(\theta)$ is generally much smaller than the standard parallel current response $k_{//}\tilde{\phi}/\eta$, by a factor $\sqrt{m_e/m_i}\, k_{//}\lambda_{coll}$. Because of the high parallel conductivity the perturbations tend to be constant along the portion of field lines. Thus a function of the form $\tilde{f}(r)\, e^{-im(q(r)\theta+\phi)}\, e^{\gamma t}$ has been chosen for the potential (since the field lines are open there are no problem of multiple determination when θ varies of 2π). Equation (1) then implies the differential equation in $\tilde{f}(r)$:

$$\frac{\partial^2 \tilde{f}}{\partial r^2} + \tilde{f}\left(\frac{\mu}{r^2}+\nu\right) = 0 \qquad (2)$$

where $\frac{\mu}{r^2} = -\frac{k_\theta^2 q^2 [G(\theta)-AH(\theta)]_{\theta_1}^{\theta_2}}{[\theta]_{\theta_1}^{\theta_2}}$, $\nu = \frac{-4\omega_{ci}^2}{q\gamma R V_{thi}[\theta]_{\theta_1}^{\theta_2}}$

with $G(\theta) = s^2\theta^3/3+\theta$, $H(\theta) = (1+s)\sin\theta - s\theta\cos\theta$, $k_\theta = m/r$ is the poloidal wavenumber and $s=\frac{rdq}{qdr}$ is the shear parameter (2 at the edge). To simplify the computation $\frac{\partial^2 q}{\partial r^2}=0$ has been assumed. The quantity $A=-4V_e^* V_{ge}/(\rho_{thi}^2\gamma^2) \approx 4V_{thi}^2/\gamma^2 R L_N$ represents the interchange effect (L_N is the characteristic length of the pressure gradient and V_{ge} is the curvature drift velocity). Since there is no resonant layer, it is reasonable to look for radial variation in the eikonal form $\tilde{f}(r) = e^{ikr}$. The dispersion equation writes, $k^2 = \mu/r^2+\nu$ or :

$$\left[[G(\theta)]_{\theta_1}^{\theta_2} + \frac{k^2[\theta]_{\theta_1}^{\theta_2}}{q^2 k_\theta^2}\right]\left(\frac{\gamma}{Vthi/qR}\right)^2 + \frac{4}{q^2 k_\theta^2 \rho_{thi}^2}\left(\frac{\gamma}{Vthi/qR}\right) - \frac{4q^2R}{L_N}[H(\theta)]_{\theta_1}^{\theta_2} = 0 \qquad (3)$$

The first term (stabilizing) contains the effect of the shear and inertia and the second (stabilizing) represents the end losses . The third term represents the curvature effect, stabilizing if $H<0$. Like in the standard interchange mode theory there are real γ values only if H is positive i.e. the average curvature is unfavorable. The maximum growth rate corresponds to $k=0$. In practice G is rather large and γ is only a weak function of k for $k \leq q^2 k_\theta$. Thus by superposing several radial modes it is possible to construct solutions localized in the SOL where this model is correct. The most unstable modes are found when the end loss term can be neglected. This happens if: $k_\theta \rho_{thi} > \left(L_N/Rq^6[H(\theta)]_{\theta_1}^{\theta_2}[G(\theta)]_{\theta_1}^{\theta_2}\right)^{\frac{1}{4}}$ ($\approx$ typically 0.1) . The corresponding

growth rate is $\gamma = \frac{V_{thi}}{R}\sqrt{2R\left[H(\theta)\right]_{\theta_1}^{\theta_2}/L_N\left[G(\theta)\right]_{\theta_1}^{\theta_2}}$. Three cases corresponding to unfavourable curvature are considered (see table). The growth rate for k=0 as been computed taking $R/L_N = 20$.

	θ_1,θ_2	$\left[G(\theta)\right]_{\theta_1}^{\theta_2}$	$\left[H(\theta)\right]_{\theta_1}^{\theta_2}$	$\gamma\frac{R}{V_{thi}}$
Inner wall	$-\pi,\pi$	90	13	2.4
Double null low field side	$-\pi/2,\pi/2$	24	6	6
Belt limiter	$\pi/12,\pi/12$	0.26	0.26	6

In conclusion, the contact of field lines with the wall cause interchange modes to be unstable when the average curvature is unfavourable i.e. in many common configurations. This could explain why the scrape off layer is unstable in inner wall operation, between two toroidal belt limiters , like in JET [7], in the external part of the scrape off layer in a double null configuration as observed in ASDEX [8]. This explains also other observations like the large radial scale of turbulence, the fact that the collisionality plays no role as observed in CALTECH [9], and the observed 90° phase shift between density and potential fluctuation . The problem is not so simple in non axisymmetric geometry (like the case of discrete limiter). There is a mixture of stable and unstable field lines. This model could explain the existence of localized turbulent spot sensitive to limiter configuration and current direction like the ones observed in TEXT [10]. One should note that the rippling modes are not expected to be more unstable within this model because the stabilizing parallel heat flux is not cancelled in open field lines.

III. Non linear effects in region with closed magnetic surfaces:

The edge is characterized by density gradient such that the mixing length fluctuation level $1/k_\perp L_N \approx \tilde{n}/n$ is of the order of 100% while in the plasma core it is rather 1%. In presence of such a level of turbulence the trajectories of particles are strongly modified and this affects the plasma response to a test mode. This effect has been investigated by considering the stability of a test mode in presence of background turbulence simulated by a large amplitude helical pump mode. The stability of an electrostatic drift test mode was studied in such a modified configuration. Two effects have been found : i) A significant number of electrons are trapped in the turbulence and this increases the power transfer to the turbulence. This provide a new energy source, ii) The ions experience large convective motion (a typical scale is 1cm $\approx L_N$). This new scale tends to replace the ion Larmor radius in the averaging operators as a radial scale of the turbulence.

Another effect of large density (or electric field) gradient is that the diamagnetic velocity may vary drastically in the width of a test mode. When this effect is introduced in a simple WKB approach [11] enhanced instability can be found since the mode reflects on a cut off layer rather than it convects its energy towards the ion Landau resonance.

For both effects the plasma parameters play an important role through the collisionality and the density, temperature, or electric field gradients which depend themselves on the transport. Such features could produce bifurcation for the turbulence level which corresponds to the L-H transition. More details can be found in [12].

IV. Conclusion

Several features of the plasma edge modify the plasma stability:

- In the scrape off layer the field lines intersect the wall. This inhibits the parallel current which tends to stabilize interchange modes. This effect makes interchange modes to appear with radial scales such as $k_\theta \rho_{thi} \approx 0.1$, and their growth rate is rather unsensitive to plasma parameters like collisionality. It is thus possible to explain the existence of turbulence in the scrape off layer and some of its characteristics in configurations where the average curvature of field lines is unfavourable. Several observations related to the in - out asymetry of the scrape-off layer are also understood.

- The strong density gradient allows large turbulence level and strong non linear effects due to electron trapping and ion convective motion are possible. This results in a better coupling of the electrons with turbulence and on the other hand in the appearance of a new non linear radial scale for the turbulence larger than the ion Larmor radius as observed in experiments.

-Unlike in the plasma core, the plasma parameters vary strongly within the scale of an eigenmode.

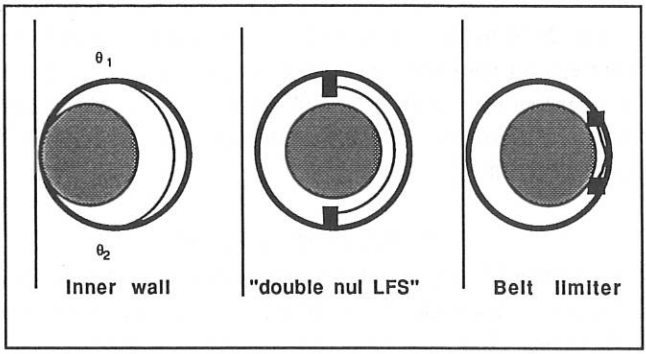

References:

[1] P.C. Liewer Nucl. Fusion **25** (1985) 543.
[2] C.Ritz, R.D. Bengston, S.J.Levinson, E.J.Powers Phys. Fluids **27** (1984) 2956.
[3] C.P. Ritz et al Phys. Rev. Lett. **62** (1989) 1844.
[4] A.Hirose, O.Ishihara Nucl.Fus. **29** (1989) 795.
[5] D.R. Thayer and P.H. Diamond Phys.Fluids **30** (1987) 3724.
[6] D.KH Morozov, M.N.Morozov, D.Sünder International Workshop on plasma edge theory in fusion devices. Augustusburg September 1989.
[7] S.Clement et al 16th European conference on controlled fusion and plasma physics. Proceedings VOLIII p.935
[8] A. Rudyj et al , 16th European conference on controlled fusion and plasma physics. Proceedings VOL I p.27
[9] S.J Zweben, R.W Gould Nucl. Fusion **23** (1983) 1625.
[10] A.J. Wooton et al 11th conference on Plasma Physics and controlled nuclear fusion research 1986 VOL I p187.
[11] L.D. Pearlstein and W.L. Berk Phys.Rev Lett **23** (1969), 220.
[12] X.Garbet et al rep. EUR CEA 1386 submitted for publication to Physics of Fluids B

RIPPLE INDUCED STOCHASTIC DIFFUSION OF TRAPPED PARTICLES IN TOKAMAK REACTORS

J-P. Roubin, P. Grua

Association EURATOM-CEA sur la Fusion Contrôlée
Centre d'Etudes Nucléaires de Cadarache B.P. n°1
13108 Saint-Paul-lez-Durance, France

INTRODUCTION

The confinement of charged fusion products in tokamaks is a key issue for thermonuclear reactors. Concerning energetic trapped ions, the important role played by the toroidal magnetic field ripple was identified several years ago [1]. The hamiltonian description of mechanics is an adequate frame to analyse the resonant interaction of such weakly collisionnal particles with a perturbating field [2],[3]. In this work, we study within this frame the particle-ripple interaction and show that the destruction of the particle adiabatic invariants can be understood through the resonance overlapping mechanism. Two different regimes are clearly identified and the associated stochastic thresholds and diffusion coefficients are derived. This analysis is applied to fusion products in ITER.

HAMILTONIAN MODEL

The unperturbed motion of a trapped particle is quasiperiodic and adequatly described by a set of conjugated action angle-variables: $\{J_1,\phi_1\}$ related to the magnetic momentum invariant μ and the cyclotronic motion, $\{J_2,\phi_2\}$and $\{J_3,\phi_3\}$ respectively associated to the bounce ($\omega_2=\omega_b$) and precession ($\omega_3=\omega_p$) motions. The angle variables (ϕ_2,ϕ_3) are related to the guiding center coordinates (r,φ,θ) by $\theta = \theta_0 \sin\phi_2$ and $\varphi - q(r)\,\theta = \phi_3$ where θ_0 is the poloidal bounce angle. Retaining the dominant n_3=N toroidal harmonic (N is the number of TF coils), the TF ripple $\delta B/B$ can be expressed as $\delta(\vec{r}) = \sum \delta_m(r) \cos m\theta \cos N\varphi$ and, expanding the resulting hamiltonian perturbation on the angle variables, we obtain (J_{n_2} are the Bessel functions):

$$\delta H = \mu B \sum_{n_2=-\infty}^{+\infty} \sum_{m=0}^{+\infty} \frac{\delta_m(r)}{2} \left[J_{n_2}((Nq+m)\theta_0)+J_{n_2}((Nq-m)\theta_0)\right] \cos(n_2\phi_2+N\phi_3)$$

The particle motion is strongly affected when a Fourier component $\delta H_n = \delta h_n \cos(n_2\phi_2+N\phi_3)$ of the perturbation is stationnary along the trajectory. The corresponding resonance condition reads $N\omega_3(J_k) + n_2\omega_2(J_k) = 0$. For 3.5 MeV trapped α-particles in a reactor sized tokamak, one typically gets $\omega_2 \approx 2\omega_3$ and several resonant surfaces ($n_2 \approx N/2$) are found inside the plasma. Retaining the low poloidal harmonics of the ripple perturbation ($m \ll Nq$), and considering that most orbits satisfy ($Nq\theta_0 \gg n_2$) we obtain using the asymptotic expression of Bessel functions:

$$\delta h_n = \mu B\, \delta_0 \sqrt{2/(\pi N q \theta_0)}\, \cos(Nq\theta_0+\xi)$$

where the ripple has to be evaluated at the banana tip ($\delta_0=\delta(r,\theta_0)$).

MOTION NEAR A RESONANT SURFACE - REGIME IDENTIFICATION

Introducing the variables (λ,Φ) defined by $\vec{J} = \vec{J_0} + \vec{n}\,\lambda$, $\Phi = \sum n_k\phi_k$, where $\vec{J_0}=(J_1,J_2,J_3)$ is a point located on the resonant surface $\vec{n}=(0,n_2,N)$, the hamilton equations of motion have the simple form:

$$\frac{d\lambda}{dt} = \delta h_n \sin\Phi \quad \text{and} \quad \frac{d\Phi}{dt} = \sum n_k\omega_k + n_k \frac{\partial(\delta h_n)}{\partial J_k}\cos\Phi \ ,$$

where the new variables (λ,Φ) are defined by $\vec{J} = \vec{J_0} + \vec{n}\,\lambda$, $\Phi = n_k\phi_k$

Defining $\alpha = n_k n_{k'} \partial^2 H_0(\vec{J})/\partial J_k \partial J_{k'} = n_k n_{k'} \partial\omega_k/\partial J_{k'}$ (α is the hamiltonian non linearity along $\vec{n}$)

$h = \mu B \delta_0 \sqrt{2/(\pi N q \theta_0)}$ (h is the resonant perturbation maximum value) and

$p = N\,\partial(Nq\theta_0)/\partial J_3 + n_2\,\partial(Nq\theta_0)/\partial J_2$ (p describes the perturbation spatial variations along $\vec{n}$), these trajectories (λ,Φ) can be described by the following reduced hamiltonian.

$$\frac{1}{2}\alpha\lambda^2 + h\cos p\lambda\cos\Phi = \text{Constant}$$

Analytical expressions for the action angle variables, for α,p can be found in [4]. For p=0, this equation describes a standard island topology of width $\lambda_{isl} = 4\,|h/\alpha|^{1/2}$ (Fig.1.a). For the general case where $p\neq 0$, it must be noticed that the topology of the trajectories strongly depends on the fact that the perturbation can or cannot vanish inside the standard island width λ_{isl} thanks to its cos(pλ) dependence. Consequently, two different regimes emerge: for low $p\lambda_{isl}$ values, the standard island shape is conserved, whereas for higher values, new separatrixes appear and a more involved structure emerges (Fig.1b). For high $p\lambda_{isl}$, the width of the whole structure (i.e. the distance between the two outermost separatrixes) is given by $\lambda_{str} = 2p.h/\alpha = p\lambda_{isl}^2/8$. A frontier between the two regimes can be determined by $\lambda_{isl}\approx\lambda_{str}$. This relation defines a critical ripple value:

$\delta_{lim} = C_{lim}(s,\theta_0)\,\dfrac{\varepsilon}{(Nq)^{3/2}}$, where C_{lim} is a function of the magnetic shear s and θ_0 and $\varepsilon=r/R$.

In the intervals $3\pi/4<\theta_0<\pi/4$, $r/a>1/2$, C_{lim} has slow variations: typically $C_{lim}\approx 4\pm 1$. For ITER, the condition $\delta(r,\theta_0)=\delta_{lim}$ divides the plasma into 2 zones: an inner one (typically corresponding to $\theta_0>\pi/2$), where $\delta<\delta_{lim}$ and an outer one, where $\delta>\delta_{lim}$.

STOCHASTIC THRESHOLDS AND DIFFUSION COEFFICIENTS

In the low ripple zone, the resonances have the classical island topology, and a standard Chirikov parameter $S_1 = \Omega_{isl}/\omega_2$ can be used to determine the stochastic threshold. We obtain

$\delta_1 = C_1(s,\theta_0)\,\dfrac{\kappa^2\varepsilon^4 R^2}{N^{3/2} q^{7/2} \rho_L^2}$ where $C_1(s,\theta_0)$ is of order 0.03 and κ is the plasma elongation

Above the stochastic threshold, the collisionless diffusion coefficient can be, in this case, obtained from the quasilinear theory. For $\theta_0 \approx \pi/2$ the radial diffusion coefficient writes:

$$D_{r1} = \frac{N}{4\sqrt{2}} \frac{\rho_L^2 v}{r\,\theta_0} \frac{q^2}{\kappa^2 \varepsilon^{3/2}} \delta^2$$

In the high ripple zone, we have to consider a more relevant S parameter that takes into account the size of the multiple islands structure (Fig 1.b): $S_2 = \Omega_{str}/\omega_2$ where $\Omega_{str} = 2$ p·h. This gives

$$\delta_2 = C_2(s,\theta_0) \left(\frac{\varepsilon}{Nq}\right)^{3/2} \frac{r}{\rho_L\, q}$$

Expressing C_2 for $\theta_0 \approx \pi/2$, one get $\delta_{2\,(\pi/2)} = 0.33 \left(\frac{\varepsilon}{Nq}\right)^{3/2} \frac{\kappa}{\rho_L\,(dq/dr)}$ which is quite similar to the stochastic threshold initially proposed by Goldston, White and Boozer in [1].

However, in this case the quasilinear approximation is no more valid. An evaluation of the diffusion coefficient can be made using the characteristic time and space steps associated to the rotation frequency $\omega_{sec.isl}$ of the particles in the secondary islands and the distance between two such islands. From the structure of the perturbation, we find $\tau_{eff} = 2\pi / \omega_{sec.island} = 2\pi / (p.h)$ and that $\Delta\lambda_2 = \pi/p$. This leads for $\theta_0 \approx \pi/2$ to the following radial diffusion coefficient:

$$D_{r2} = \sqrt{\frac{\pi}{2Nq\theta_0}} \frac{v\,\rho_L}{4\,\kappa\,s\,\theta_0} \delta$$

It must be noticed that $D_{r2}/D_{r1} = \omega_2/(p.h) = 1/(2S_2)$ where S_2 is the resonance overlap parameter corresponding to the strong perturbation regime. Consequently, an important result is that in the zone where the D_{r2} diffusion coefficient is applicable, its numerical value is always smaller that the quasilinear one.

APPLICATION TO ITER

For ITER, the case of 3.5 MeV α-particles is resumed on Fig.2 showing the upper half part of the plasma poloidal section. The curves where $\delta = \delta_1$ and $\delta = \delta_2$ (thick lines) indicate that there is an unstable domain in the outer part of the plasma (strong ripple regime) whereas the inner zone (weak ripple regime) is stable except at the very edge. The diffusion coefficients are found to be very large as soon as the stochastic regime is reached: from typically 10 $m^2 s^{-1}$ at the frontier of the stable domain up to 100 $m^2 s^{-1}$ near the plasma edge (Fig.2). As a consequence, in the major portion of the stochastic zone, the confinement time of trapped α particles is far smaller than their thermalisation time: these zones can be considered as a sink for these particles.

REFERENCES

[1] Goldston, R.J., White, R.B., Boozer, A.H., Phys.Rev.Lett. **47** (1981) 647.

[2] Samain, A., Nucl.Fusion **12** (1972) 577.

[3] Bécoulet, A., Gambier, D.J., Grua, P., Rax, J.M., Roubin, J.P., Proc. 16th Europ. Conf. on Contr. Fus. and Plasma Phys., Venise (1989), Vol. I, p 267.

[4] Grua, P., Roubin, J.P., Report EUR-CEA-FC-1382, December 1989. (Nucl.Fus. to appear)

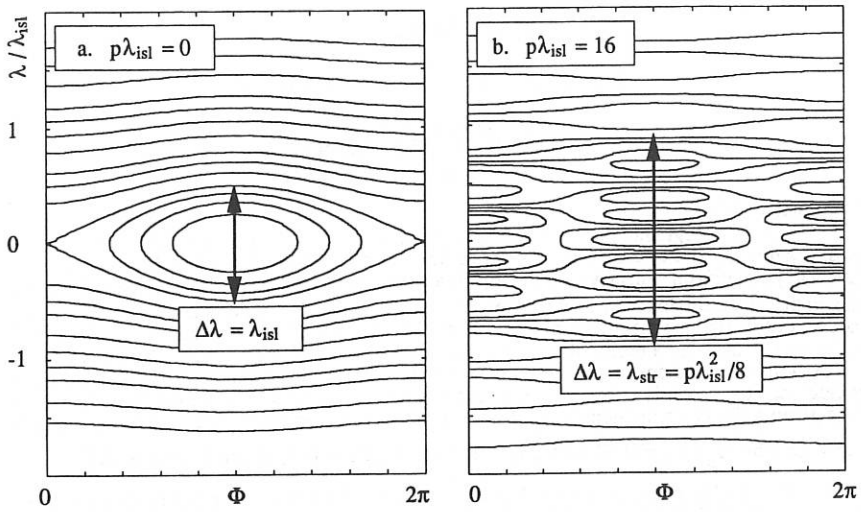

Figure 1: Motion near a resonant surface in the (λ,Φ) phase space
a: Weak perturbation regime ($\delta<\delta_{lim}$) b: Strong perturbation regime ($\delta<\delta_{lim}$)

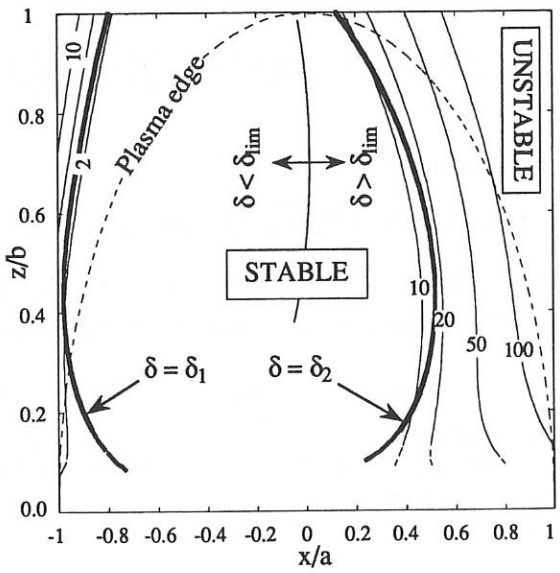

Thick lines:
limits of the stable domain

Thin lines:
radial diffusion coef. values in m^2s^{-1} and frontier between the stochastic regimes $\delta\approx\delta_{lim}$

Figure 2: Stochastic diffusion coefficients for 3.5 MeV α-particles in ITER

MICROTEARING MODES

X. Garbet, F. Mourgues, A. Samain, X. Zou

Association euratom-CEA
DRFC SPPF CEN Cadarache
13108 St Paul lez Durance

INTRODUCTION

A serious degradation of confinement with additional heating is commonly observed on most tokamaks. The microtearing modes could provide an explanation for this experimental fact. They are driven linearly unstable by diamagnetism in collisional regimes, but it may be shown that the collisions in non linear regimes provide a small diffusion coefficient [1] which can be only significant at the plasme edge . In the bulk of the plasma, the microtearing turbulence could play a basic role if it is unstable in the collisionless regime. While it is linearly stable without collisions, it could be driven unstable in realistic regimes by the radial diffusion it induces. To study this effect, we have used a model where the non linear action of the modes on a given helicity component is represented by a diffusion operator. They are found unstable for reasonable $\beta_p=2\mu_o nT/ B_p^2$,with a special radial profile of the potential vector A [2].

The problem arises the validity of this model where non linearities in the trajectories behaviour are replaced by the diffusion which broadens resonances. To test this procedure, we calculate the actual electron distribution function when it is determined by the ergodicity of the field lines. We compute the correlations of the distribution function with the magnetic perturbation and compare them with the analytical expressions derived from the resonance broadening model.

I BASIC EQUATIONS

To simplify the computations, we assume that there exists a frame of reference R rotating around the major axis where the magnetic configuration is static. The magnetic perturbation is given by:

$$\delta A = \sum_{l,m} A_{l,m}(r) \exp i\left(m\phi + l\theta + \delta(l,m)\right) \qquad (1)$$

In the frame R, there exists a static electric field $-\nabla \overline{U(r,\theta,\phi)}$ that we restrict to its average radial component $-\dfrac{\partial \overline{U}}{\partial r}$ which confines electrons. In a first approach, we neglect the corresponding electric drift velocity. Each component l,m in (1) creates an island chain near the resonant surface defined by:

$$r=r_{l,m} \quad \text{where} \quad m + \frac{l}{q(r_{l,m})} = 0. \qquad (2)$$

The magnetic surfaces are destroyed and the field lines wander stochastically when the half width δ_I of an island is greater than the distance between two neighbouring resonant surfaces d. The electron current is derived from the Vlasov equation by:

$$\delta I = \int F(r,\theta,\phi)\, e\, v_{//} \quad \text{and}$$

$$T(F) = v_{//} \nabla_{//} F - D(v^2) \Delta F = S(v^2) \left(\delta(r-r_{min}) - \delta(r-r_{max}) \right) \qquad (3)$$

where $\nabla_{//}$ is the derivative along the actual flux lines , S is the source term of particles localized at the radii r_{min} and r_{max} and $D(v^2)\,\Delta.$ is a small diffusion operator which prevents the singularities due to the stochasticity of the flux lines. The solution of (3) is expected to exhibit fluctuations from the δ_I up to the smallest scale $\delta_D=\left(\frac{DL}{v_{//}}\right)^{1/2} \ll \delta_I$ where L is the parallel correlation length of order $\frac{q^2R}{l\,\delta_I\,\frac{dq}{dr}}$. We propose to find numerically the solution of (3) at large scales of order of the width of the islands δ_I. It will be verified that this solution is independent of the exact form of the diffusion operator $D(v^2)\,\Delta.$ as long as $\delta_D \ll \delta_I$.

II NUMERICAL METHOD

The inversion of the operator T is performed by a new method based on the integration of equation (3) along the flux lines. Because the solution of (3) is independent of the exact form of the diffusion operator at large scale, we may localize the diffusion operator in a meridian plane $\phi = 0$. The source term may be also localized in the same plane. We then have:

$F(\alpha)=F(\beta)$ if $\beta= (r(\beta)\,,\,\theta(\beta)\,,\,\phi(\beta))$ is magnetically connected to $\alpha= (r(\alpha)\,,\,\theta(\alpha)\,,\,\phi(\alpha))$ and $\phi(\beta)$ is in the interval $(0, 2\pi)$. The problem is reduced to compute F in in a meridian plane $\phi= 0$.

We define an application T transforming a point α into its magnetic image in the same plane after a 2π variation of ϕ. We then build a set E of points α which is invariant by T: $T(E)=E$.. In pratice, we construct a series of loops of points α : $(\alpha_1; \alpha_2; \ldots\ldots; \alpha_n)$ such that $\alpha_2=T(\alpha_1)\,;\, \alpha_3=T(\alpha_2)\,;\;\ldots\;;\, \alpha_n$ very close to α_1. The function F will be computed at the points α of the set E ,which must be uniformly distributed over the plane $\phi = 0$. For each point α, we define a set of the neighbouring points β in order to simulate the diffusion operator in (3). Namely we replace $\left(\frac{D(v^2)}{v_{//}}\Delta F\right)(\alpha)$ by $\sum_{\beta} d_{\beta}^{\alpha}\left(F(\beta)-F(\alpha)\right)$ where $d_{\beta}^{\alpha}=d_{\alpha}^{\beta}$ is a constant related to D if the distance between α and β is smaller than δ_{neig} and d_{β}^{α} equals zero otherwise. We choose $\delta_{neig} \ll \delta_I$. The equation (3) after integration between two points α and $T(\alpha)$ then becomes:

$$F(T(\alpha)) - F(\alpha) = \sum_{\beta} d_{\beta}^{\alpha}\left(F(\beta)-F(\alpha)\right) + s(\alpha) \qquad (4)$$

where $s(\alpha)$ results from the integration of the source term. This equation is solved by the iterative procedure:

$$F^{n+1}(T(\alpha)) - F^{n}(\alpha) = \sum_{\beta} d_{\beta}^{\alpha}\left(F^{n}(\beta)-F^{n}(\alpha)\right) + s(\alpha) \qquad (5)$$

which may be shown to be convergent if all the d^{α}_{β} are positive. As the distribution function along the flux lines is a constant, we know at each point the value of the distribution function $F(r,\theta,\phi)$. The correlations with the perturbation are computed for each radial position. They are compared with those obtained from the renormalized equation [3] in order to justify the diffusive model:

$$i K_{//} F_{l,m} - \frac{v_{//}}{|v_{//}|} \sum_{l'm'} D^{l'm'}_{l,m} \frac{\partial^2 F_{l'm'}}{\partial r^2} = -i \frac{l}{r} \frac{\partial F_o}{\partial r} \frac{A_{l,m}}{B_o} \qquad (6)$$

where $F(r,\theta,\phi) = \sum_{l,m} F_{l,m}(r) \exp i(m\phi + l\theta + \delta(l,m))$

The coefficients $D^{l'm'}_{l,m}$ are expected to be of order of the quasilinear value D_{ql} for $(l',m')=(l,m)$. In the following, we test the model with a constant $l = \pm 1$ in the series of (1) by taking $D^{l'm'}_{l,m} = D_0 \delta^{l'm'}_{l,m}$ or $D^{l'm'}_{l,m} = D_0 \delta^{l'm'}_{l,m} + D_1 \delta^{l'm'}_{l,m\pm1}$ with the appropriate ratio D_0/D_{ql} and D_0/D_1.

III COMPARISON AND RESULTS

The fig 1 shows the θ and ϕ averaged value of $F(r,\theta;\phi)$ labelled by $\langle F \rangle$ for a typical case of 11 island chains obtained with $l = 1$ and m=-5 to 5 with $\delta_i = d$. The slope is approximately constant between the source and the sink . The radial flux defined by

$\Gamma = \iint \frac{\partial \delta A}{B_0 \, r \partial \theta} F(r,\theta,\phi) \frac{d\theta d\phi}{4\pi^2}$ agrees with the values of the source terms and the diffusion coefficient defined by $D_{erg} = \frac{\Gamma}{\partial \langle F \rangle / \partial r}$ is in agreement with the quasilinear value. The Fourier component $F_{l,m}(r)$ appears as a standard function of $\frac{(r-r_{l,m})}{\delta_d}$ where $\delta_d = \left(\frac{D_{erg} \, q \, R \, d}{V_{th}} \right)^{1/3}$ is the Kolmogorov scale. It may be verified that these functions are independent of the diffusion coefficient D introduced in (3). They may be compared with the values derived with the diffusive approach on fig 2. The best fit is obtained for $D_0 = D_{ql}$ and $D_1 = 1{,}1 \, D_0$

(1) X. Garbet , F. Mourgues , A. Samain ,Plasma Phys. and Cont. Fusion , 30 (1988),343
(2) X. Garbet , F. Mourgues , A. Samain ,Plasma Phys. and Cont. Fusion , 32 (1990),131
(3)P.H Diamond and M.N Rosenbluth , Phys. Fluids, 24 (1981),1641

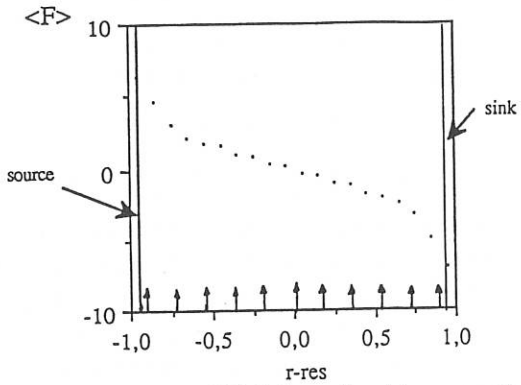

Fig 1 : Averaged value of $F(r,\theta,\phi)$ over θ and ϕ versus r. The arrows indicate the position of the islands.

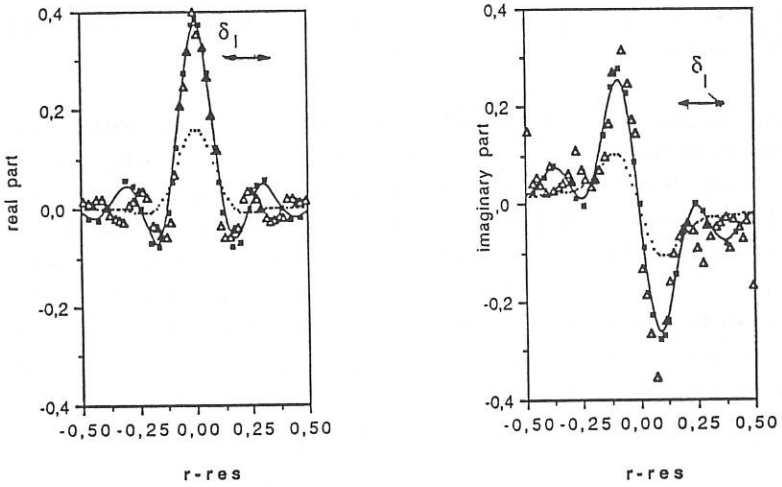

Fig 2: Real and imaginary parts of $F_{l,m}(r)$. The solid lines represent the values obtained from the diffusive model with $D_0 = D_{ql}$ and $D_1 = 1{,}1\ D_0$. The dotted lines correspond to $D_0 = D_{ql}$ and $D_1 = 0$.

Modelling of Improved Confinements in Tokamaks

[A] Peaked Density Profile and Inward Pinch

[B] Change of Transport at L/H mode Transitio

Sanae-I. Itoh and Kimitaka Itoh

National Institute for Fusion Science, Nagoya 464-01 Japan

Introduction Recently various improved modes have been found other than H-mode in tokamaks. In H-mode the steep gradient is established only near the edge region. Other improved modes are characterized by the peaked density/ion temperature profiles. In this paper, a model of peaked density profile in the core associated with sheared rotation due to E_r' and the extended model of H-mode[1] based on the bifurcation of E_r' at the edge are presented. Both confinements are related to the plasma rrotations due to E_r(E_r') in edge and core regions. If the plasma radius is large, combined structure can exist.

Peaked Profile Modes This model[2] shows that differential part of the plasma rotation due to E_r and an anomalous electron viscosity induces the inward flow of electrons. Ion viscosity differently acts on ion, so that the balance of particle diffusion and the inward pinch due to the viscous friction to the velocity shear determines the E_r structure. The ratio of the viscosity and the diffusion coefficient, namely the diffusion Prandtl number, determines the relative peakness of the rotation velosity profile and the density profile. To obtain $E_r(r)$, electron flux is assumed to be anomalous due to drift-type microturbulence of toroidal mode number n. Applying the mixing length theory,

$$\Gamma_{s,a} = -D_s n_s[\frac{n_s'}{n_s}(1+\alpha_s\eta_s) - p_{Ds}(\frac{eE_r}{T_s} - \frac{eqR\omega B_t}{ncT_s})] \qquad (1)$$

where $D_e=D_{e0}\sqrt{1+u_g/u_c}$, $u_c^2=8\sqrt{2\varepsilon}(4-u_c)$, $u_g=\rho_p E_r'/v_{Ti}B_p$, $\eta=d\ln T/d(\ln n)$, q and p_{De} denote safety factor and the ratio of anomalous electron viscosity to diffusion coefficient, i.e., electron diffusion Prandtl number. Note that the shear term of E_r/r in Eq.(1), (differential rotaion affects the particle flux.

Stationary ion flux also comes from the classical viscosity flow and the momentum loss by charge exchange in the presence of toroidal rotation, $U_\phi = (qT_iR/erB)[n_i'/n_i(1+c_in_i) - eE_r/T_i]$. They are $\Gamma_{i,v} = (qR/erB)\, n_i m_i \nabla\mu\nabla U_\phi$, $\Gamma_{i,cx} = (qR/erB) n_i m_i U_\phi n_0 \langle\sigma_{cx} v\rangle$, where μ is the viscosity. Basic equations are Poisson's equation, $\Gamma_{e,a} = \Gamma_{i,a} + \Gamma_{i,v} + \Gamma_{i,cx}$ and the continuity equation as, $-\nabla\cdot\Gamma_{e,i,tot} + S_{e,i} = 0$. Particle sources $S_{e,i}$ and $\Gamma_{i,cx}$ dictate the boundary condition for the core structure ($r<a-\Delta$, Δ is the penetration length of nuetrals), where neutral density $n_0 \simeq 0$. We assume that the n_0 is given as a parameter.

In the core we get solutions for the shear part of E ($= a^2 eE_r/rT_i$) as $p_{De}\{E\} = A_0 I_0(\sqrt{\nu_a/\nu_\mu}\, y)$, $p_{De}\{E\} = -2(\ln n)'$, $\nu_a = (1+p_{Di}/p_{De})D_i/\rho_i^2$, $\nu_\mu = (1+1/p_{De})q^2R^2\mu/a^4$, $y = r^2/a^2$, and ρ_i is the gyroradius. In this case, u_g in D_e is neglected. The peaked profile is sustained in the absence of particle source. Due to the anomalous/classical viscous effects on differential rotation in the presence of E_r, an inward pinch is caused. The ratio of ν_μ(normalized viscosity)to ν_a(normalized diffusivity), namely normalized Prandtl number, strongly affects the structures of n(r) and E. In Fig.1, we show the density profiles for various values of $\sqrt{\nu_a/\nu_\mu}$ (fixed $A_0 = a/\lambda_n - a^2\langle S\rangle/D_{e0}$). The density fall-off length of scrape-off layer(SoL), λ_n, is assumed to be determined by SoL transport. We see that the peaked density profile is obtained when the normalized Prandtl number is large. If the electron Prandtl number is also large, the more peaked profile is expected. Reduction of the edge source, $\langle S\rangle$, rises the value of A_0 and causes density peaking as well. The corresponding differential part of the electric field is shown in Fig.2. In Figs.1 and 2 , the line averaged density is kept constant. Associated with the inward drift, an anomalous heat transfer to ions due to viscous friction is predicted; the increase of ion temperature and its peaking are also expected.

H-mode The H-mode transition models based on the sudden change of E_r have been reported[3,4], and the change in edge E_r have been observed in experiments. However, neither of models could fully explain the H-mode transition. We extend our previous theory[3], including the effects of E_r'. Ion losscone rate changes in the presence of E_r'; banana width and

the minimum energy which bounds the loss cone region alter. Introducing numerics F and C, we have the ion loss flux as,

$$\Gamma_{i,NA}=(Fn_i\nu_i\rho_p/\sqrt{\varepsilon}\sqrt{|1-u_g|}+C\varepsilon)\ \exp[-\sigma|1-u_g|X^2],\ X=\rho_p eE_r/T_i$$

where $\varepsilon=a/R$ (a,R; minor, major radius) and σ indicates limiter place. The equation, $\Gamma_{e,a}=\Gamma_{i,NA}$ gives the refined condition for transition. Transition (L-H) occurs even in the case of $\sigma=0$ (limiter case). Associated with the negative jump of E_r', it takes place independent of the sign of E_r. In Fig.3, the solution of E_r', relative groth rate of the instability and the resultant flux is shown. We assume the relation, $E_r=\beta\rho_p E_r'$. In Eq.(1), the effect of E_r' on the trapped particle mode is included. Simple estimation shows that the growth rate reduces as $\gamma=\gamma_0\sqrt{1+u_g/u_c}$. Sudden reductions of fluctuations and conduction loss are predicted. Critical gradient, λ_c, of new model is close to the value obtained from previous model.

The work is partly supported by the Grant-in-Aid for Scientific Research of MoE Japan.

References

1] S.-I. Itoh and K. Itoh, NIFS(National Institute for Fusion Science) report #4 (1990).

2] S.-I. Itoh, NIFS rep. #8 (1990).

3] S.-I. Itoh and K. Itoh, PRL 60 2276 (1988); NF 29 1031 (1989).

4] K.C. Shaing and E.C.Crume,Jr., PRL 63 2369 (1989).

Fig. 1 Density profiles for various values of ν_a/ν_μ for fixed $A_0=10=(a/\lambda_n-a^2\langle S\rangle/D_{e0})$. The line averaged density is kept constant.

Fig. 2 Potential profile which corresponds to sheared rotation is shown for cases of Fig.1. $p_{De}=1$.

Fig. 3 Gradient of E_r, instability growth rate γ, and particle flux are shown as a function of the gradient parameter λ. $\beta=0.25$.

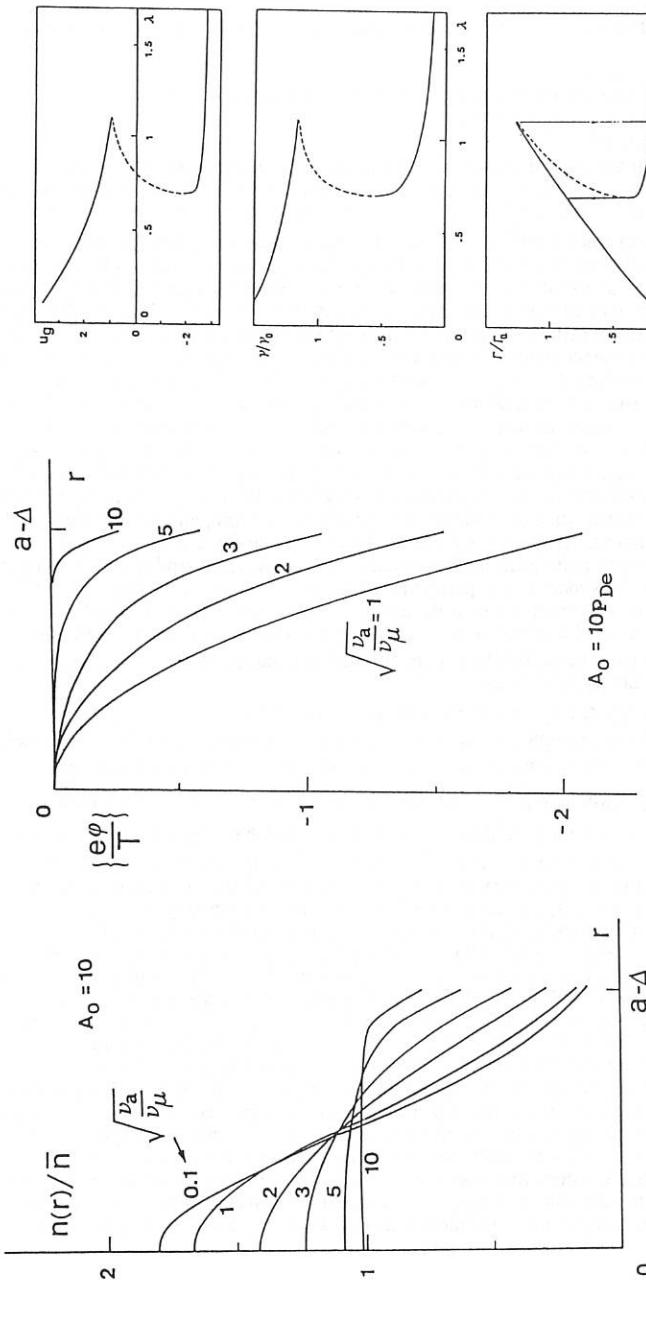

Fig. 1

Fig. 2

Fig. 3

THE EFFECT OF THE RADIAL ELECTRIC FIELD ON THE L-H MODE TRANSITION.

M.Tendler,V.Rozhansky*
Royal Institute of Technology,S-10044, Stockholm 70, Sweden
*Polytechnic Institute,Leningrad,USSR

1.INTRODUCTION

Consider the plasma in a tokamak,which is not initially in a state of equilibrium.Quasi-electrostatic electric fields usually emerge in a tokamak plasma due to varying departures from the exact local charge neutrality.In the standard neoclassical theory the particle fluxes across magnetic surfaces to order $(\rho/r)^2$ result from the toroidal component of the momentum balance.The contributions to the radial flux emerge due to the inertial,viscous and friction forces.The temporal and spatial discharge ontogeny consists of two phases.The first phase governed by the balance of the parallel inertial and viscous forces is not intrinsically ambipolar owing to the significant difference of the ion and electron inertia and viscosity.Thence the parallel viscous force associated with the magnetic field modulation in a tokamak rapidly damp the poloidal flow,producing a radial current caused by the force of inertia and proportinal to dE_r/dt.The convective derivitive of the electric field $u_r\partial E_r/\partial r$ arises.If u_r is of the order of the Pfirsch-Schluter particle flow then the poloidal rotation resulting from the radial electric field is quickly damped.However,the transport in a tokamak is notoriously anomalous and exceeds the value of the Pfirsch-Schluter particle flow by orders of magnitude. Therefore the role of this phase of the discharge is very important in reality.The intrinsically non-ambipolar phase of the discharge terminates when the mean parallel viscous force compensates exactly the inertial force.Then the radial flux is primarily governed by the friction force owing to Coulomb collisions between ions and electrons.This results in the intrinsically ambipolar fluxes across magnetic surfaces.Thus more subtle phenomena such as the shear viscosity invoke at this phase. The well-known conservation of the toroidal angular momentum by Coulomb collisions results for an arbitrary value of the electric field E_r.Therefore the ambipolar electric field at this stage is determined as a linear function of the toroidal angular momentum and the pressure-gradient -driven diamagnetic fluxes.

$$\tilde{V}_0=V_0^{NEO}=-\{cT_i[kd(\ln T_i)/dr+d(\ln n_i)/dr]\}/(eB)=V_0+\theta\tilde{U}_{\|} \qquad (1)$$

where $V_0=-cE_r/B$.For example the neoclassical theory predicts that the radial electric field vanishes due to the shear viscosity and a large value of the toroidal rotation velocity $U_{\|}=V_0^{NEO}/\theta$ emerges,where V_0^{NEO} is a neoclassical value of the poloidal rotation and $\theta=\langle B_\vartheta/B\rangle$ is the ratio of the poloidal to the total field.Nevertheless,this large value of the toroidal rotation velocity is never observed experimentally in the absence of the unbalanced neutral beam injection.Numerous experiments have shown that the toroidal rotation velocities never reach high values[2,4].The reason for this is the strong anomality of the shear viscosity.Moreover the neoclassical theory predicts that the first term at the r.h.s. in Eq.(1) vanishes due to the shear viscosity.Thus the poloidal rotation results entirely due to the second term in Eq.(1) (toroidal rotation).However,for experimentally observed values of the toroidal velocity,the second term in Eq.(1) turns out to be negligible.Thus the resulting poloidal rotation is governed by the electric field.The current driven through the periphery on the tokamak CCT resulted in the triggering of the L/H transition and the subsequent improvement of the overall confinement [5].The main idea advocated in the present work is that the polarization current resulting from the spatial variation of the electric field and the anomalous transport triggers the L/H transition and is the cause of the improved confinement.This current results from the charge separation (polarization) due to finite electron-ion displacements.There are several mechanisms which would affect the polarization current.Besides already mentioned enhancement of an anomalous transport resulting from the strong auxiliary heating or pellet injection the current turns out to be significantly modified (enhanced) due to the effective increase of the plasma mass provided there is a population of the banana-trapped ions.Then the

radial current torque is strongly amplified and the parallel viscosity is undermined to damp the poloidal rotation.This catastrophe-type transition is termed "the inertial catastrophe".

2.THE VELOCITY OF THE POLOIDAL ROTATION.

In this Section the combined effect of the inertia and the viscosity is analyzed provided the quasi-stationary electric field given by Eq.(1) is modified due to the injection of neutral beams or pellets.If an arbitrary poloidal rotation velocity V_0 differs from Eq.(1),the non-ambipolar ion fluxes emerge. From the sum of the parallel components of momentum balances for ions and electrons follows that the ambipolarity is fulfilled when

$$<nm_i du_{||i}/dt+ (\nabla \cdot \vec{\pi})_{||}>=0 \qquad (2)$$

The effect is considered in the vicinity of the separatrix where the population of banana particles is significant and $V_0 \leq \theta C_S$.The contribution of untrapped particles to the inertia flux is small. Thus we obtain for the stationary case ($\partial/\partial t=0$)

$$dV_0(r)/dr+\alpha(r)V_0(r)=\beta(r) \qquad (3)$$

Here,

$$\alpha(r)=\nu_i/u_r \qquad \beta(r)=\alpha(r)V_0^{NEO} \qquad (4)$$

Eq.(3) constitutes the main equation of the present study unfolding the effect of inertia and yielding the profile of the poloidal rotation velocity and the associated radial electric field.The first term in Eq.(3) has been omitted in previous studies.The solution for V_0 is obtained integrating by part the solution of Eq.(3)

$$V_0(r)=[V_0(a)-V_0^{NEO}(a)]\exp(\int_r^a \alpha(r')dr')+V_0^{NEO}(r) \qquad (5)$$

The governing parameter turns out to be $[V_0(a)-V_0^{NEO}(a)]$.

If $V_0(a)$ coincides with the neoclassical value $V_0^{NEO}(a)$ then the profile of the poloidal rotation velocity is determined by the neoclassical velocity profile $V_0^{NEO}(r)$ given by Eq.(1). On the other hand,if $V_0(a)$ differs from $V_0^{NEO}(a)$ then the solution does grow exponentially from the separatrix into a plasma core on the length scale of the order $\alpha(r)^{-1}$.

This exponential growth is terminated only when the poloidal rotation $V_0(r)$ approaches θC_S.This occurs due to the significant decrease of the total amount of banana particles in the inner core.Then the inertia is dominated by the untrapped particles.

We obtain for $V_0 \approx \theta C_S$

$$dV_0(r)/dr+\tilde{\alpha}(r)V_0(r)\exp(-V_0^2/\theta^2 C_S^2)=\tilde{\gamma}(r) \qquad (6)$$

where

$$\tilde{\gamma}(r)=\tilde{\alpha}(r)V_0^{NEO}-du_{pi}/dr$$

$$\tilde{\alpha}(r)=\nu_i\sqrt{\varepsilon}[u_r\theta^2(1+2q^2)]^{-1}$$

Neglecting terms of the order V_0^{NEO} compared with θC_S and accounting for $aL >>1$,we obtain from Eq.(6) with the logarithmic accuracy

$$\int_0^{\theta C_S}\exp(x^2)dx=\int_r^a \tilde{\alpha}(r)dr \qquad (7)$$

The function V_0 as a function of radius (Eq.(8)) is roughly proportional to $V_0=\theta C_S \sim\sqrt{T_i(r)}\,\theta(r)$ in agreement with [5].The crucial criterion for the exponential growth of the solution is governed both by the presence of banana particles up to a separatrix and by the magnitude of the poloidal rotation velocity at the inner side of a separatrix. As emphasized already by us in [1],a layer arises due to a discontinuity of rotational velocities in the SOL and in the inner core.The thickness of this layer is of the order of the banana width.The separatrix constitutes the outer boundary of the layer.The profile of the poloidal rotation velocity crucially depends on the boundary conditions imposed both by the conditions in the scrape-off layer,which are governed by a contact with a metal, and by the gap in the poloidal rotation ΔV_0 in this

layer.The velocity of the poloidal rotation in the SOL has been calculated by us in [1].For given temperature $T_e(r)$ and density n (r) profiles,the velocity of the poloidal rotation V_0 reads

$$V_0=\{cT_e[d(\ln T_e)/dr+d(\ln n)/dr]\}/(eB)\}<0 \qquad (8)$$

Note that this value of the poloidal rotation is sustained by the positive radial field and is therefore negative here.The change in the gap calculated from the condition for detrapping of banana ions turns out to be approximately $\sqrt{\varepsilon}\theta C_S$.Thence the resulting value of the poloidal rotation velocity at the inside of the separatrix layer employed as the boundary condition in Eqs.(3 &6) $V_0(a)$ is found out

$$V_0(a)=V_0+\sqrt{\varepsilon}\theta C_s = \{cT_e[d(\ln T_e)/dr+d(\ln n)/dr]\}/(eB)+\sqrt{\varepsilon}\theta C_S \qquad (9)$$

The two terms at the right hand side of Eq.(9) have opposite signs.If the banana width $\rho_{ci}\sqrt{\varepsilon}/\theta$ is less than h,where h is a typical scale of plasma parameters in the SOL,the second term gets dominant and the $V_0(a)$ becomes positive.This means that the resulting value of the poloidal rotation velocity at the inside of a separatrix $V_0(a)$ exceeds the neoclassical value given by Eq.(1). The solution obtained from Eqs.(5&7) is shown in Fig.1. In summary,within the framework of this model,the L/H transition occurs if $\rho_{ci}\sqrt{\varepsilon}/\theta<h$.

3.Conclusions.

The velocity of the poloidal rotation inside the separatrix turns out to be positive(note this means the inward direction of the radial electric field) and much larger than the neoclassical value provided there is a significant population of banana ions at the inner side of the separatrix and the poloidal Larmor radius is smaller than the typical scale length of plasma parameters in the SOL, $\rho_{ci}\sqrt{\varepsilon}/\theta<h$.Then the exponential solution for the profile of the velocity of the poloidal rotation inside the separatrix results due to a significant anomalous loss of particles.The gradient of this profile is predicted to be the steepest in the vicinity of the separatrix. It should be emphasized that this solution emerges entirely due to the substantial spatial inertia of banana ions originating from the salient anomalous transport.The physical phenomenon expressed by this solution can be described as " the inertial catastrophe" elucidating the suddenness and the explosive nature of this effect.These features seem to be characteristic for the L/H transition.

When the value of the poloidal rotation velocity reaches the order of $\approx \theta C_S$,then the V_0 profile follows adiabatically the radial dependence of the product θC_S(see Fig.1) in agreement with [5].The L/H transition results in our model due to the dependence of u_r on the V_0.In general the anomalous transport quantified by u_r may be either a function of the electric field or a function of the vector differential operators of the electric field.If the latter turns out to be the case our model predicts the strongest improvement in confinement to occur on the distance of the order α^{-1} inside the separatrix.For large values of $V_0\approx\theta C_S$ the rate of the particle outflux u_r decreases drastically and the density profile gets very steep,typical for the H-regime. The profiles of the velocity of the poloidal rotation inside the separatrix,as predicted by Eqs.(5&7) , are shown in Fig.1 for different regimes.It is easily seen that the profile of the velocity of the neoclassical poloidal rotation inside the separatrix decreases drastically over the length of 1 cm.On the other hand the profile of the velocity of the poloidal rotation inside the separatrix in our model grows exponentially inward over the length of a few centimeters,then more slowly up to the value $V_0 \approx\theta C_S$,and then decreases in the core of a tokamak due to the form of the $\theta(r)$ profile.

The drastic enhancement of the velocity of the poloidal rotation inside the separatrix during the L/H transition has been recently measured on D-III D[6].The direction of the electric field has been consistent with our model.The experimentally measured quantity for the V_0 is about 4.10^6 cm/sec at a distance varying within 1 and 3 cm inside the separatrix.This result also

seems to be consistent with our conclusions that V_0 is much larger than the neoclassical value V_0^{NEO} and approximately equal to $V_0 \approx \theta C_S$. Furthermore,in the H regime,the neoclassical value V_0^{NEO} turns out to be of the order θC_S in the vicinity of the separatrix due to the steep density gradient there.Thus the effect of inertia,crucial within the framework of this model,has to be very pronounced there.

In summary,it is shown that the momentum balance equation inside the separatrix in a tokamak might have two globaly different bifurcated solutions for a profile of the radial electric field.The first solution,which is shown to grow inward inside the separatrix,emerges when there is a significant population of banana particles in the inner core up to a separatrix and a sufficiently large anomalous loss.This effect results due to the anomalous particle transport and the inhomogeneity of the radial electric field.The second solution is predicted to agree with the neoclassical value.The bifurcation of these two solutions occurs inside the separatrix However,the emergence of the bifurcation of these two solutions is governed by the boundary conditions imposed on the value of the poloidal rotation velocity at the inside of the separatrix.These boundary conditions are shown to depend on the poloidal rotation both in the scrape-off layer (SOL),examined in [1],and the collisionless layer,arising due to the rotational discontinuity.The catastrophe type transition,termed " the inertial catastrophe", between the two solutions has been demostrated from this model.This newly discovered regime seems to contain many features typical for the H-mode.

In addition our theory predicts that the rapid start of an H-mode is caused by the poloidal rotation.The time scale of the transition is shown to occur on the time scale of ion-ion collisions.The plasma rotation is driven by the polarization currents.The rotation-induced negative E fields are responsible for the improved ion transport.

References.

1.M.Tendler & V.Rozhansky Comm.Plasma Phys.&Contr.Fusion **4**,191 (1990)
2.M.G.Bell Nuc.Fus.**19**,33 (1981)
3.V.I.Bugaraya et al. Nuc.Fus.**25**,1707 (1985)
4.Ch.Ritz Phys.Fluids **27**,2956 (1984)
5.R.J.Taylor et al.Phys.Rev.Lett.**63**,2365(1989)
6.R.J.Groebner ,P.Gohil,K.H.Burrell,T.H.Osborne R.P.Saraydarian,H.St.John,in Proceedings 16th Conference on Controlled Fusion and Plasma Physics ,edited by S.Segre,H.Knoepfel and E.Sindoni(European Physical Society,Venice,13-17 March ,1989)Vol.I,p.245

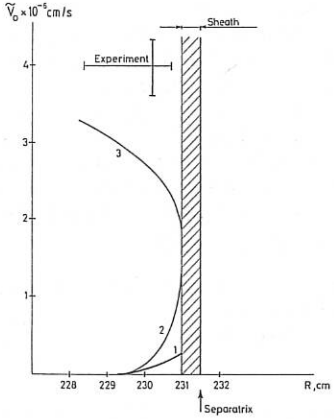

A FAST METHOD FOR SIMULATING α-PARTICLE ORBITS IN TOKAMAKS

W. D. D'haeseleer

The NET Team
c/o Max-Planck-Institut für Plasmaphysik, Garching-bei-München, FRG

1. *Introduction*

The simulation of alpha-particle trajectories, to determine their losses out off the plasma in tokamak reactors, by means of orbit-following Monte-Carlo (OFMC) codes, consumes vast amounts of computer CPU time. The order of magnitude is roughly 100 hrs Cray-CPU time for 1000 alpha particles launched with birth energy of 3.52 MeV, followed for about a slowing-down time. Since of those launched particles, only $25 - 30\%$ are non-passing particles (i.e., banana blocked and ripple trapped), which are the ones followed without time enhancement, we are talking about 300 particles in 100 hrs or 20 mins per particle (K. Tani, private communication).

To perform simulations for reactor-design purposes, it is necessary to develop faster codes. In this paper, we report on a speed-up technique, based on reasonable approximations of the physics involved, that enables us to gain roughly a factor 3 on a scalar computer. In combination with vectorization, we have obtained an additional gain factor of $6 - 7$, resulting in an overall speed-up factor of about 20.

In Section 2, we give a short overview of the physics-based approximation technique employed in the code *Alphanet*. An evaluation of the results produced by *Alphanet* is presented in Section 3. Finally, Section 4 summarizes the paper.

2. *The "Switching Procedure" in a Nutshell*

The framework of the "base-line" OFMC code *Alphanet*, is that of time integration of the particle's guiding-center equations, using a maximal time step τ to guarantee an energy conservation so that $|\triangle E|$ is less than 1 in 10^6. We integrate the guiding-center equations as derived by Boozer [1].

Inbetween time steps, the particle gets a collisional kick in energy and pitch angle (the latter is here denoted by $\lambda = v_{\|}/v$). The discretized model collision operator used has been derived by Boozer and Kuo-Petravic [2].

Since alpha-particle losses should not depend too strongly on the details of the magnetic-field structure, a model magnetic field, incorporating all the basic features of the plasma equilibrium, suffices for this computation. Using the Boozer guiding-center equations, the particle motion can be described completely if $B = |\mathbf{B}|$ and ι are known. Therefore, the only magnetic input needed are *mod* B, for example

$$B = B_0(1 + \varepsilon_t(r,\theta)\cos\theta + \delta(r,\theta)\cos N\varphi), \tag{1}$$

and a rotational-transform profile. B in Eq. (1) is expressed in flux coordinates; φ is the usual toroidal angle, θ measures the poloidal angle (θ being 0 on the *in*side of the device) and r stands for the flux variable

$$\mathrm{r} \equiv \sqrt{2\Psi/B_0}\ , \tag{2}$$

in which Ψ is the magnetic flux function. Both ε and δ are a function of r and θ. To simulate the ellipticity and triangularity, $\varepsilon(r,\theta)$ can contain higher harmonics in

2θ and 3θ, respectively: $\varepsilon(r,\theta) = \epsilon(r)(1 \pm a(r)\cos 2\theta \pm b(r)\cos 3\theta)$. Here $\epsilon(r) \equiv r/R_0$. Effects such as Shafranov shift are also easily incorporated. Below, we will assume $\varepsilon(r,\theta) \equiv \epsilon(r)$. For the ripple profile, we use the INTOR model:

$$\delta(r,\theta) = \delta_0(\frac{r+R_0}{a+R_0})^N \ \exp[\frac{(\pi-\theta)^2}{2}] \ ; \tag{3}$$

a is the minor radius, N the number of toroidal-field coils and R_0 the major radius.

Away from a banana particle's bounce points, the canonical toroidal angular momentum, p_φ, oscillates about an average value. Only close to the bounce point can it suffer a large jump. Consequently, near the bounce points, the particle must be integrated in the full ripple field of Eq. (1). Away from the bounce points, however, the average constancy of p_φ permits us to follow the particle trajectory as if it only felt the axisymmetric field, Eq. (1) without the $\cos N\varphi$ term. Since $v_\parallel = \sqrt{2(K-\mu B)/m}$, in which K is the kinetic energy of the particle, arbitrarily changing B by turning off and on the ripple term, would give rise to an artificial kick in $v_\parallel$ and thus cause an unphysical pitch-angle scattering. Therefore, we switch off (and on) the field only when the δ term is zero, i.e., at any toroidal angle φ^* for which $\cos N\varphi^* = 0$.

The mechanics of the "switching procedure" goes as follows. We construct two boundary curves which are elevated above the axisymmetric B field. The first curve, called B_ℓ (for "lower"), is determined by $B_\ell = B_0(1+\varepsilon\cos\theta+\xi\ max[\delta(r,\theta),\delta(r,\pi/2)])$. This curve is elevated by a distance $\xi\,\delta$ above B_{sym}. Since the ripple becomes small on the inside of the device, and to avoid that there B_ℓ comes too close to B, we impose a minimum on the height above B_{sym}, equal to $\xi\delta(r,\pi/2)$. For typical INTOR parameters, $R_0 = 5.2m$, $a = 1.2m$, $B_0 = 5.5T$, $N = 12$ and $\delta_0 = 0.012$, a value of $\xi = 4$ ensures that $\lambda > 0.1$, whenever "switching" happens for $B > B_\ell$. A second boundary curve is constructed, $B_u = B_\ell + \triangle$ (u for "upper"), where $\triangle = B_0\varepsilon\iota/2p$.

As long as $K/\mu < B_\ell$, the particle is followed in the full field; if $K/\mu > B_u$, the ripple term is dropped. Whenever the particle enters the "belt" between B_ℓ and B_u, $B_\ell < K/\mu < B_u$, the code starts searching for the nearest possible switching point φ^* that is still within the belt. Then, the code integrates up to the switching point. Upon reaching a toroidal angle such that $|\varphi - \varphi^*| < tolerance$, switching takes place. The tolerance in $|\triangle\varphi|$ is derived from the above mentioned energy tolerance $|\triangle E| < 10^{-6}$.

The width $\triangle$, is obtained from the requirement that at any place in the belt, the particle should be able to see at least one possible φ^* that lies still within the belt.

The CPU time gained by this switching approach derives from the fact that a longer integration time step can be used when just the axisymmetric field is used to preserve a given energy tolerance. From experience, the time steps are approximately related as $\tau_{sym} \simeq (6-7)\ \tau_{ripple}$. It is an overall characteristic of trajectory integrators that accuracy is determined by the *spatial* step. Hence, particles with large $v_\parallel$ are characterized by a small time step and vice versa. It is clear, however, that near the bounce points, where $v_\parallel$ goes to zero, an ever growing time step is not allowed; close to the bounce point, a maximum time step must be imposed. This has the consequence that, for banana particles, the code still spends a considerable amount of time ($\sim 1/3$) in the "full-field region" (where $K/\mu < B_\ell$), and therefore, one can only save CPU time in the remaining part. If one simulates all particles, including the very passing ones, this consideration does not play a great role. Then, the CPU gain is about a factor of 5. In practice, the very passing particles need not be followd, however. On the other hand, considering only banana-blocked particles, ignores some of the physics, in that detrapping and entrapping is disregarded. Therefore, we follow only the banana

particles and those passing particles whose minimum λ value does not exceed, say, $\lambda_{min} = 0.2$. To see that $\lambda_{min} = 0.2$ is a reasonable value, one should recognize that a barely-passing particle has $\lambda \simeq 0$ near $\theta = 0$, whereas, on the other side of the midplane, near $\theta \simeq \pi$, λ already takes a value of $\lambda = 0.557$ — for $r \simeq 0.9m$ and $B = B_{sym}$. A passing particle with $\lambda_{min} = 0.2$ near $\theta = 0$, does not reach a higher value than $\lambda = 0.581$ near $\theta = \pi$. So, a $\triangle\lambda$ of 0.2 near $\theta = 0$ gives a $\triangle\lambda$ of only 0.024 near $\theta = \pi$. For the Boozer pitch-angle-scattering operator, this $\triangle\lambda$ can be bridged by roughly 10^3 unidirectional kicks for $E = 3.5\ MeV$. For $\lambda_{min} = 0.2$, we obtain an overall gain factor of just over 3. When combined with vectorization, we have been able to show a combined gain factor of just under 20.

3. *Analysis of the Speed-up Technique using Poincaré Plots*

To check the validity of our "switching" technique, we have compared the statistical behavior of the orbits for particles calculated this way and with the "full field". The natural way to do this, is by means of Poincaré puncture plots, giving the intersection of the trajectory with the equatorial plane in terms of the major radius, $R = R_0 - r\cos\theta$, and the ripple phase, $N\varphi$. For 400 bounces each, with all particles launched at $\theta = \pi$, $\varphi = 0$ and $r_i = 0.2 + 0.03(i-1)$, the results for "full-field" case, with collisions disregarded, are shown in Fig. 1. In Figs. 2 and 3, the same particles are launched, but the ripple term is switched off and on as explained above. In Fig. 2, we made sure that, any time the particle was followed using the axisymmetric field, it was done so for an integer number of ripple periods, in order to average out as many effects as possible. In Fig. 3, this provision was not taken so that switching was allowed to happen at all values where $\varphi^* = \pi/p$. Both Figs. 2 and 3 agree quite well with Fig. 1. But, although the difference is not big, the second option seems to give the best agreement with Fig. 1. We believe that numerical errors are not responsible for this unexpected result. Possible explanations for this are currently being investigated.

In reality, the particles suffer pitch-angle scattering collisions. Although they are small for energetic alphas, their effect becomes noticeable after several bounces. From Fig. 4, we observe that the scattering due to pitch-angle scattering in the full-field case is considerably greater than that due to our switching procedure (for collisionless particles). The presence of collisions on top of the switching approach results in similar scatter as for the collisional full-field case, making the integer/non-integer discussion, concerning the collisionless orbits, rather academic.

4. *Summary and Conclusions*

A speed-up technique for the simulation of energetic alpha-particles via the OFMC method has been developed. A substantial CPU-gain factor can be obtained (~ 3 in a scalar code; ~ 20 if the gain due to additional vectorization is taken into account), while preserving sufficient accuracy of the orbits.

Acknowledgements

This work has been supported by the European Commission, via a Euratom Post-doctoral Fellowship.

References

1. Boozer, A. H., *Phys. Fluids* **23** (1980) 904
2. Boozer, A. H. and G. Kuo-Petravic, *Phys Fluids* **24** (1981) 857

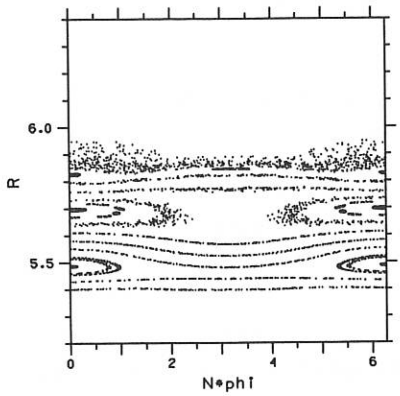

Fig. 1:
$(R, N\varphi)$ Midplane Puncture Plot.
Collisionless; full ripple field

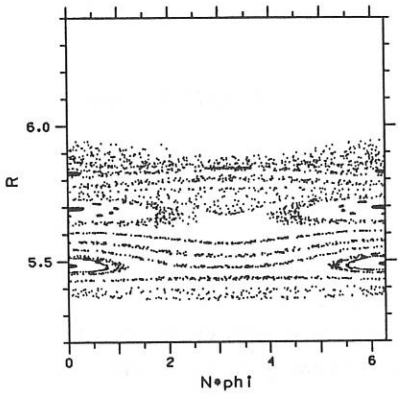

Fig. 2
$(R, N\varphi)$ Midplane Puncture Plot.
Collisionless; partly axisymmetric field
for integer number of ripple periods

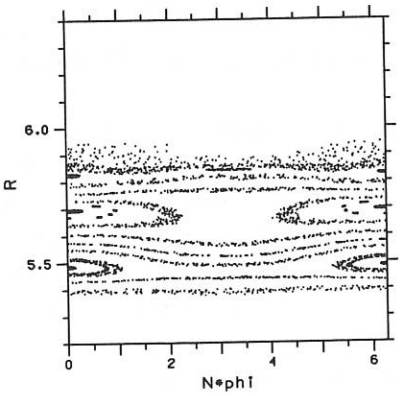

Fig. 3:
$(R, N\varphi)$ Midplane Puncture Plot.
Collisionless; partly axisymmetric field
with "integer" check removed

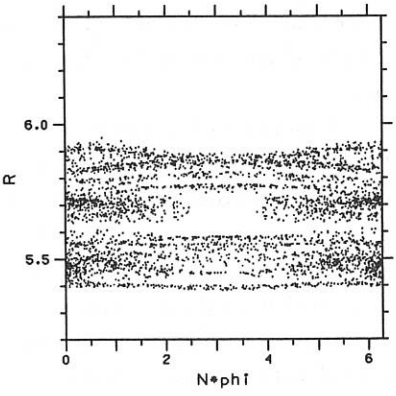

Fig. 4
$(R, N\varphi)$ Midplane Puncture Plot.
Collisional; full ripple field

The neoclassical effects on resistive MHD modes in general toroidal geometry

Yong-Ho Oh, Jang-Gyoo Yang, Duk-In Choi and *J.Y.Kim* *

Department of Physics

Korea Advanced Institute of Science and Technology

P.O.Box 150, Cheongyangni, Seoul, Korea

Introduction

The stability of resistive MHD modes is an important problem for the confinement of tokamak plasmas . Recently, with the achievement of higher temperature plasma it was recognized that the conventional MHD description applicable to the Pfirsch-Schlüter regime needs to be generalized to include the lower collisionality regime. Callen and Shaing[1] were the first ones to derive the equations describing these neoclassical resistive MHD dynamics starting from the two-fluid MHD equations in the incompressible and electrostatic limit. Later, Conor and Chen[2] also derived similar equations starting from the gyro-kinetic equations. These studies showed that a new instability can be generated by the trapped-particle effect. The destabilizing mechanism is from the bootstrap current in the Ohm's law, coupled to the flow damping term in the vorticity equation. Recently, T.S.Hahm[3] investigated this trapped-particle effect on the tearing instability deriven by Δ' .

In present work, we extend these previous studies to include the compression effect. From the two-fluid resistive MHD equations we derive the neoclassical resistive MHD equations in the compressible and electromagnetic limit utilizing the methods of the ballooning representation and flux-surface averaging. Using these equations, we study the effect of compression on the neoclassical instability. Also, we investigate the trapped-particle effect on the conventional resistive MHD instabilities of interchange, tearing, and ballooning modes by the numerical method. Our study includes the numerical method and for such numerical work we are developing a new numerical code. This is the generalized version of our previous work[4] which now includes the neoclassical effects.

Derivation of basic equations

*present address : IFS, U. of Texas at Austin, Austin, Tex. U.S.A.

We start from the two-fluid equations including the neoclassical viscosity and compression effects. Here, we restrict ourselves to the cases where the temperature gradients and thermal transports are unimportant, thus we assume the constant temperature. Then the equations for ion and electron are

$$\frac{\partial \mathbf{v}_j}{\partial t} + \nabla \cdot (n_j \mathbf{v}_j) = 0 \tag{1}$$

$$m_j n_j \frac{d\mathbf{v}_j}{dt} = n e_j (\mathbf{E} + \mathbf{v}_j \times \mathbf{B}) - \nabla p_j - \nabla \cdot \mathbf{\Pi}_j - \mathbf{R}_j \quad , \tag{2}$$

where the subscript $j = i, e$ represents the electron, ion species, respectively. Using the relation $\mathbf{E} = -\frac{\partial \mathbf{A}}{\partial t} - \nabla\phi$, $\mathbf{B} = \nabla \times \mathbf{A}$ and the assumptions of low frequency ($\omega/\Omega_i << 1$) and low β, we can derive following reduced equations.

$$\eta_{\parallel} J_{\parallel} = -\frac{\partial A_{\parallel}}{\partial t} - \mathbf{b} \cdot \nabla\phi + \frac{1}{en}\mathbf{b} \cdot \nabla p_e + \frac{1}{en}\mathbf{b} \cdot \nabla \cdot \mathbf{\Pi}_e \tag{3}$$

$$\frac{\rho}{B^2}\frac{d}{dt}\nabla_{\perp}^2(\phi + \frac{p_i}{en}) = -\mathbf{B} \cdot \nabla(\frac{\nabla_{\perp}^2 A_{\parallel}}{B}) + 2\frac{\mathbf{B} \times \kappa}{B^2}\nabla p + \nabla \cdot [\frac{\mathbf{b}}{\mathbf{B}} \times (\nabla \cdot \mathbf{\Pi}_e + \nabla \cdot \mathbf{\Pi}_i)] \tag{4}$$

$$\frac{\partial p_j}{\partial t} + \mathbf{v}_E \cdot \nabla p_j + p_j[\mathbf{B} \cdot \nabla(\frac{v_{\parallel}}{B}) + \nabla \cdot \mathbf{v}_{\perp i}] = 0 \tag{5}$$

where

$$\nabla \cdot \mathbf{v}_{\perp i} = \nabla \times (\frac{\mathbf{b}}{B}) \cdot \nabla(\phi + \frac{p_i}{en}) - \frac{1}{B\Omega_i}\frac{d}{dt}\nabla_{\perp}^2(\phi + \frac{p_i}{en}) - \frac{\eta_{\perp}}{B^2}\nabla_{\perp}^2 p + \nabla \cdot [\frac{\mathbf{b} \times \nabla \cdot \mathbf{\Pi}_i}{B}] \ .$$

We note that Eq.(3) is the parallel Ohm's law, Eq.(4) is the vorticity equation, and Eq.(5) is the ion continuity equation multiplied by T_j. Now, we linealize these equations, and if we use the ballooning representation we can obtain the ordinary differential equations with two scale lengths of the extended poloidal coordinate θ($\theta \sim 1$ and $\theta \gg 1$) in the ballooning space. Taking the flux-surface average over short scale length ($\theta \sim 1$) after some lengthy algebras, we obtain following flux-surface averaged neoclassical resistive MHD equations.

$$\partial_x(\phi + \frac{iQ_*}{Q}p) + (1 + \frac{iQ_{*e}}{Q})\psi + \frac{1}{Q}(x^2\psi - xHp) - N_e(x) = 0 \tag{6}$$

$$Q^2x^2\phi + \partial_x(x^2\psi) - Dp - Hx(\psi + \partial_x p) - \frac{Q}{iQ_*}E_1(1 + \frac{2L}{3})(N_e(x) + N_i(x)) = 0 \tag{7}$$

$$[G(1 + \frac{iQ_*}{Q}) + KF]p - (G - KE)\phi - \partial_x[\frac{1}{Q^2}(\psi + \partial_x p) - \frac{1}{iQQ_*}(N_e(x) + N_i(x))]$$
$$+ \frac{M_{\perp}}{Q}x^2 p + iKQQ_* x^2\phi + Hx\psi - \frac{L}{3}KE_1 x N_i(x) = 0 \tag{8}$$

where N_i, N_e represent the neoclassical viscosity effect and are

$$N_e = T_0[\partial_x(\phi + \frac{iQ_*}{Q}) + (1 + \frac{iQ_{*e}}{Q})\psi + \frac{1}{Q}E_1 xp] \tag{9}$$

$$N_i = M(\theta)[\frac{iQ_*}{Q}(\psi + \partial_x p) - N_e(x) + \frac{Q}{\nu i Q_*}E_1 x\phi] \tag{10}$$

with

$$T_0 = \frac{\mu_e/\nu_e}{1+\mu_e/\nu_e}, \quad M(\theta) = \frac{\hat{\mu}_i}{\hat{\mu}_i + Q} \quad (\hat{\mu}_i = \mu_i/\gamma_R)$$

$$E_1 = \frac{\langle B^2/\mid \nabla V\mid^2\rangle}{q'^2\chi'}\frac{p'}{\chi'}\frac{2\pi R B_T q'}{\langle B^2\rangle}, \qquad \nu = \frac{m_e\nu_e}{m_i\gamma_R}$$

$$E_2 = ME_1(1+\frac{2}{3}L)\,, \qquad E_3 = \frac{L}{3}ME_1\,,$$

and

$$L = \frac{\langle B^2\rangle}{\langle(\mathbf{b}\cdot\nabla\mathbf{B})^2\rangle}\cdot\langle\frac{(\mathbf{b}\cdot\nabla\mathbf{B})^2}{B^2}\rangle\,.$$

Definitions of other quantities and normalization constants are in Ref.5.

First of all, we note that the incompressible limit of Eq.(8) gives $\phi = (1 + \frac{iQ_{*i}}{Q})p$, then Eqs.(6) and (7) become

$$(1-T_0)(Q_i + Q_{*e})(\psi + \partial_x p) + x^2\psi - (H + E_1T_0)xp = 0 \tag{11}$$

$$Q(Q+iQ_{*i})(1+KE_1E_2)x^2p + \partial_x(x^2\psi) - Dp - (H+ME_2)(\psi+\partial_x p)$$
$$-\frac{Q}{iQ_*}E_2(1-M)T_0x(Q+iQ_{*e})(\psi+\partial_x p) = 0\ . \tag{12}$$

In the limit $\hat{\mu} \gg Q$, i.e M=1, we find that these equations are reduced to the form used by T.S.Hahm[3], which were derived from the gyrokinetic equations. In Eq.(8), $N_e(x)$ represents the parallel bootstrap current and is proportional to the trapped-particle fraction T_0. In Eq.(12), the neoclassical viscosity terms present two effects. One is the increase of the ion-polarization drift ($\simeq KE_1E_2$ term in Eq.(12)) and the other is the flow damping effect ($\simeq ME_2$ term in Eq(12)). These are similar to the results of Callen et al.[1], but the values are somewhat different compared with Ref.1. In Eq.(6), the neoclassical viscosity effect mainly gives contributions to the two terms of parallel ion sound and ion-polarization compressions. In particular, the ion-sound compression effect is significantly reduced in the limit of $\hat{\mu}_i \gg Q$.

Numerical analysis

As well-known, the equations of (6)-(8) can be transformed to the real space by the Fourier transform method. In Ref.4 a comprehensive numerical analysis was presented

when the neoclassical viscosity effects were absent. From Eqs.(6)-(8), we observe that the neoclassical viscosity terms do not generate any significant structure change in the equations, so that the extension of previous numerical code to this case appears to be straightfoward. With the development of this advanced code, we will be in a position to study the problems such as the compression effect on the resistive MHD instabilities of interchange , ballooning and tearing modes. These results will be reported in the conference.

Conclusion

In this work, we derived the neoclassical resistive MHD equations in the compressible and electromagnetic limit. We find that in the incompressible limit, these equations are reduced to the previous cases. We are in the process of developing a numerical code which is capable of solving these equations. The results will include the compression effect on the neoclassical instability, and the trapped-particle effect on the conventional resistive MHD modes.

Acknowledgement

This work was supported by the Korean Science and Engineering Foundation.

References

[1] J.D. Callen and K.C. Shaing, Phys. Fluids **28**,1845(1985).

[2] J.W. Connor and Liu Chen, Phys. Fluids **28**, 2201(1988).

[3] T.S. Hahm, Phys. Fluids **31**, 3709(1988).

[4] J.Y. Kim, G.S. Cho, and D.I. Choi, Phys. Fluids **31**, 2659(1988).

[5] T.S. Hahm and Liu Chen, Phys. Fluids **29**, 1891(1986).

LOW FREQUENCY ELECTROSTATIC INSTABILITIES IN A TOROIDAL PLASMA WITH A HOT ION BEAM

M. Liljeström

Institute of Electromagnetic Field Theory, Chalmers University of Technology and EURATOM. NFR Association
S- 41296 Göteborg, Sweden

Introduction

During the last years the η_i-mode has become a very strong candidate for anomalous transport in tokamaks.[1,2] Numerous works are concerned with specifying the caracteristics of the mode. In this work the influence of a hot ion beam on the η_i-mode is investigated A kinetic model[5] and an unexpanded diamagnetic heat flow fluid model[4,5] are used. The beam is characteraized by a Maxwellian distribution function whether it originates from ICR- or NBI- heating. Quasineutrality for this system yields

$$\frac{\delta n_e}{n_0} = (1-\beta)\frac{\delta n_i}{n_i} + \beta\frac{\delta n_{ih}}{n_{ih}} \qquad (1)$$

where β is the fraction of ions belonging to the beam.

1. Kinetic description

In the electrostatic limit without Larmor radius effects it is possible to write the kinetic density respons as[5]

$$\frac{\delta n_{ij}}{n_{ij}} = \frac{e\phi}{T_{ij}}\left\{-1+2\,\frac{\eta_{ij}}{\varepsilon_{nj}}\left[1-W\left(\sqrt{2\alpha_j}\right)\right]\right\} + \left[1-\frac{1}{\varepsilon_{nj}\alpha_j}-\frac{\eta_{ij}}{\varepsilon_{nj}}\left(2-\frac{1}{\alpha_j}\right)\right]\left[W\left(\sqrt{2\alpha_j}\right)-1\right]^2\Bigg\} \quad (2)$$

here $\eta_{ij}=\nabla T_{ij}/\nabla n_{ij}$, $\varepsilon_{nj}=\omega_{Dj}/\omega_{*j}$ and $\alpha=\omega/\omega_{Dj}$ and W is the plasma dispersion function. For the well-known η_i-mode the frequency is of the order of the background drift frequency and the beam drift frequency is T_{ih}/T_i times greater. We are thus allowed to expand the beam response for small argument $\alpha_h = \omega/\omega_{Dh}$. This gives

$$\frac{\delta n_{ih}}{n_{ih}} \approx \frac{e\phi}{T_{ih}}\left\{-1+\frac{\pi}{\varepsilon_{nh}}\left(1-\eta_{ih}-\frac{\omega}{\omega_{*ih}}\right)\right\} \equiv \frac{e\phi}{T_{ih}}\,P_h \qquad (3)$$

Expressing the plasma dispersion function in the Dawson integral, D, and using adiabatic electrons we obtain the dispersion relation at marginal stability as

$$[4D^2+\pi e^{-2\alpha}](1-\beta)\sqrt{\alpha}\left(\alpha-\frac{1}{\varepsilon_n}\right)=[(2\alpha-1)2D-\sqrt{\alpha}]\left[\frac{1}{\tau}+1-\beta\left(1-\frac{P_h}{\tau_h}\right)\right] \quad (4a)$$

The imaginary part gives the η_i-threshold as

$$\left(\frac{\eta_i}{\varepsilon_n}\right)_{th}=\frac{\left[\frac{1}{\tau}+1-\beta\left(1-\frac{P_h}{\tau_h}\right)\right]2D}{(1-\beta)\sqrt{\alpha}[4D^2+\pi e^{-2\alpha}]}\rightarrow\{\beta\text{ small}\}\rightarrow\frac{\left[\frac{1}{\tau}+1+\beta\left(\frac{1}{\tau}+\frac{P_h}{\tau_h}\right)\right]2D}{\sqrt{\alpha}[4D^2+\pi e^{-2\alpha}]} \quad (4b)$$

where $\alpha=\omega/\omega_D$, $\tau=T_e/T_i$, $\tau_h=T_{ih}/T_i$, $\varepsilon_n=2L_n/L_B$ and $D=e^{-\alpha}\int_0^{\sqrt{\alpha}}e^{t^2}dt$.

For $1/\tau_h+P_h/\tau_h<0$ which is usually the case, we can see that the threshold grows linearly with β which means that the beam has a stabilizing influence.

As we can observe from (4b) the strongest stabilizing dependency of β comes from the denominator. This is due to the reduction of the nonadiabatic background ion response where the instability originates. The β in the numerator is due to the reduction of the adiabatic part of the cold ion response. This effect is destabilizing. For example for ordinary $\tau\sim 1$ it iseasy to understand the stabilization mechanism as a greater reduction of the nonadiabatic cold ion response than the reduction of the sum of the adiabatic electron and ion responses. Thus a higher per cent of the particles are free to prevent phase differences between the perturbed quantities compared to the case without beam. The adiabatic beam response is also stabilizing and it is interesting to note eq. (3) that ∇T_h has a stabilizing influence while ∇n_h is destabilizing. The reason for this is that in the limit $\omega << \omega_{Dh}$ the effect of the two dimensional (double) resonance exceeds the effect of the principal part of the kinetic integral and reverses the effects of convection. For $1/\tau_h+P_h/\tau_h<0$ the threshold decreases with β and the beam is destabilizing. In eq. (4b) we observe a possibility to have zero η_i-threshold for a very steep density gradient of the beam, i.e. when

$$L_{nh}<\frac{L_B}{2}\left\{\frac{\beta\pi(\eta_{ih}-1)}{\tau_h/\tau+\tau_h+\beta(\tau_h-1)}\right\} \quad (5)$$

For a reasonable choice of parameter values $\eta_{ih}=1.5$, $\tau_h=5$, $\tau=1$, $\beta=0.2$ and $L_B=3$ we obtain $L_{nh}<3\pi/216\text{m}\sim 0.05$ m. In this limit we have a beam density interchange mode

2 Fluid model

The diamagnetic heat flow fluid model[4] has been proved to be able to accurately reproduce the characteristics of the corresponding kinetic

system[5].This fluid model is obtained by combining the equation of continuity and the equation of energy to form the ion density response

$$\frac{\delta n_{ij}}{n_{oj}} = \frac{e\phi}{T_{ij}}\,\omega_{*ij}\left[\omega(1-\varepsilon_{nj}) - \left(\frac{7}{3}-\eta_{ij}-\frac{5}{3}\varepsilon_{nj}\right)\omega_{Dij} + \right.$$

$$\left. + k^2\rho_{ij}^2\,(\omega-\omega_{*ij}(1+\eta_{ij}))\left(\frac{\omega}{\omega_{*ij}}-\frac{5}{3}\varepsilon_{nj}\right)\right]\left[\omega^2-\frac{10}{3}\,\omega\omega_{Dij}+\frac{5}{3}\,\omega_{Dij}^2\right]^{-1} \qquad (6)$$

With adiabatic electrons we form a dispersion relation by introducing (6) for the different ion species in (1). This dispersion relation is then analyzed numerically.In fig. 1 the threshold is plotted for different values of beam parameters.. For this choice of parameters the threshold is growing with increasing β as expected from (4b).

Particle and heat diffusivities

For obtaining the radial dependence of the diffusion coefficients sets of profile parameters are used[3].The diffusion coefficients are defined as

$$D_j = R_e\,\frac{\langle V_E^{*}\,\delta n_j\rangle}{|\nabla n_e|} = -\gamma^2\left(\frac{cT}{eB}\right)^{3/2}\frac{|\nabla n_i|}{n_{io}\sqrt{\Omega_{ci}k^2\rho_i^2}}\,\mathrm{Im}\left\{\frac{\delta n_j}{n_o}\,\frac{T_e}{e\phi}\right\} \qquad (7)$$

$$\chi_j = \mathrm{Re}\,\frac{\langle V_E^{*}\,\delta T_j\rangle}{|\nabla T_j|} =$$

$$= \frac{\gamma^2}{\eta_{ij}}\left(\frac{cT}{eB}\right)^{3/2}\frac{|\nabla n_i|}{n_{io}\sqrt{\Omega_{ci}k^2\rho_i^2}}\,\mathrm{Im}\left\{\frac{1}{\varpi-\frac{5}{3}\varepsilon_{nj}\tau_j}\left[\frac{2\omega}{3}\left(\frac{\delta n_{ij}}{n_j}\,\frac{T_{ij}}{e\phi}\right)+\left(\frac{2}{3}-\eta_{ij}\right)\frac{\varepsilon_n\,\tau_j}{\varepsilon_{nj}}\right]\right\} \qquad (8)$$

since

$$\frac{\delta T_j}{T_j} = \frac{\omega}{\omega-\frac{5}{3}\,\tau_j\,\varepsilon_{nj}}\left[\frac{2}{3}\left(\frac{\delta n_j}{n_j}\right)+\frac{\varepsilon_n\,\tau_j}{\varepsilon_{nj}}\left(\frac{2}{3}-\eta_{ij}\right)\frac{e\phi}{T_j}\right] \qquad (9)$$

as obtained from the equation of energy. In eq. (7)-(9) ω and γ are normalized by ω_{*i} and $\tau_j = T_j/T_i$ j = i, ih. From eq. (6) it can be seen, by expansion around a small positive imaginary part of the eigenfrequency, that the imaginary part of the background ion density response is > 0. This is consistent with outward hot particle transport. In the limit $\omega << \omega_{Dh}$ the hot fluid particle density response becomes

$$\frac{\delta n_{ih}}{n_o} = \frac{e\phi}{T_h}\left\{-1+\left(\frac{7}{5}-\eta_i\,\frac{3}{5}\right)-\frac{7}{5}\,\frac{\omega}{\omega_{Dih}}\right\} \qquad (10)$$

Here, as in eq. (3) $I_m\{\omega\} > 0$ gives $D_h > 0$. This means that the upper curve in fig. 3. corresponds to hot ion outward transport. The corresponding background ion pinch effect is consistent through the condition of quasineutrality while the electrons are adiabatic. In figures 3 and 4 we can see how the beam reduces the heat transport of the background ions whereas the hot ion heat flow remains small. This is mainly due to the maintained large difference between ω and ω_{Dh}.

The difference in magnitude of the diffusivities in the two cases is due to the difference in temperature. As we can see eqs. (8) - (9) the diffusivities have a temperature dependence to the power of 1.5. The background temperature of JET is about ten times the background temperature of TEXTOR

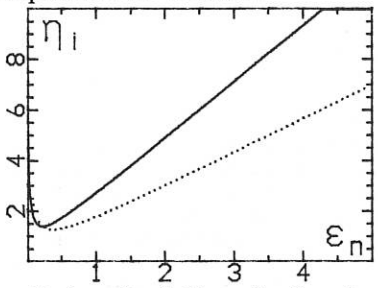

Fig.1. η_i–threshold as a function of ϵ_n,

$k^2\rho_i^2 = 0.05$,$\tau = 1$,$\eta_{ih} = 1$, $\epsilon_{nh} = 1$

— $\beta = 0.4$, $\tau_h = 5$, ··· without beam

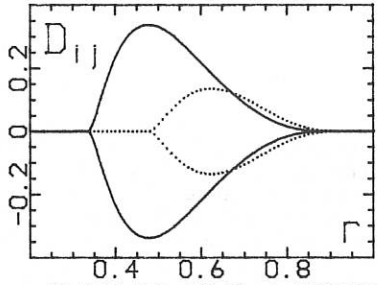

Fig.2. Particle diffusion in TEXTOR

Profile characteristics in accordens with

fig.3. $\tau_h = 5$,— $\beta = 0.2$,··· $\beta = 0.4$

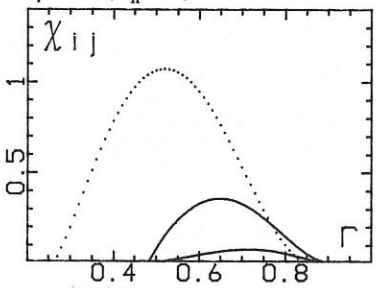

Fig. 3. Energy diffusion in TEXTOR.

$T_e=T_i=T_0(1-r^{2.3})^{1.7}$, $n=n_0(1-r^{4.64})$,

a/R = 0.26 , B ≈ 2.4T, T_0 = 1keV,

$(cT/eB)\Omega_{ci}^{-0.5}$ ~ 0.5 , ··· χ_i(no beam)

↑— $\chi_i(\beta=0.4, \tau_h=5)$, ↓— χ_{ih}

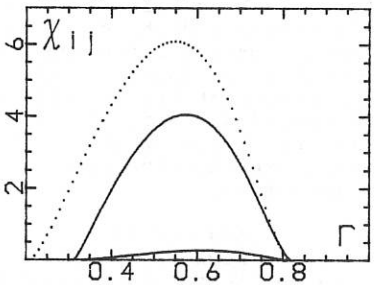

Fig.4.Energy diffusion in JET B ~ 3.45T

$T_i= T_0(1-r^{1.25})^{0.89}$, $T_e= 0.97T_0(1-r^{1.6})^{0.98}$

$n = n_0(1 - r^{5.5})$, a/R = 0.33 , T_0 = 7keV ,

$(cT/eB)\Omega_{ci}^{-0.5}$ ~ 5 , ··· χ_i(no beam),

↑—$\chi_i(\beta=0.2, \tau_h=10)$, ↓—χ_{ih}

References

1. D.L. Brower et al, Nucl. Fus.29, 1247 (1989)
2. S.D. Scott et al Phys. Rew. Lett. 64, 531 (1990)
3. A. Rogister, et. al. Nucl. Fus. 28,1053 (1988).
4. A. Jarmén, P. Andersson and J. Weiland, Nucl. Fus. 27, 941 (1987).
5. J. Nilsson, M. Liljeström and J. Weiland, Proc. 16th European Conf. on Contr. Fusion and Plasma Physics, Venice 1988, vol.IV p. 1417.

RADIATION-INDUCED η_e-MODES

P.K. Shukla & M.Y. Yu

Institut für Theoretische Physik
Ruhr-Universität Bochum
D-4630 Bochum, FRG

Impurity radiation in a plasma can cause not only static instibilities, but also dynamic instabilities related to the drift and acoustic waves. Radiative instabilities are of much interest because they are associated with relatively high frequency and short wavelength fluctuations, which have been suspected to be responsible for anomalous electron energy transport in tokamak edge plasmas. In this paper, we consider radiation-induced η_e instabilities, taking into account electrostatic effects as well as density and temperature inhomogeneities. Also included are the effects of finite gyroradius and dissipation. It is found that the latter can cause strong linear coupling between the modes of interest. The resulting instabilities can have larger growth rates than the static radiative instability [1]. Analytical expressions for the growth rates and instability regimes are given for the limiting cases of practical interest. In particular, it is shown that the η_e-mode can couple to both radiation and dissipation to cause resistive instabilities. The parameter regimes of the original radiative as well as the dissipative modes are thereby broadened and shifted because of the interaction.

We consider an inhomogeneous electron-ion plasma in an external magnetic field $B_o\hat{z}$. Within the slab model, the density and temperature gradients are taken to be in the x-direction. We shall first consider electrostatic waves of short wavelength ($k\rho_e \ll 1 \ll k\rho_i$, where $\rho_{i,e}$ are the ion and electron gyroradii, and k is the wave number). Thus, the fluctuations are in the electron acoustic wave range [2]. In this regime, the ions are in equilibrium and satisfy

$$\frac{n_{i1}}{n_o} = \frac{-e\phi}{T_{io}} , \tag{1}$$

where n_o is the unperturbed density, e is the electronic charge, T_{io} is the ion temperature, and ϕ is the electrostatic potential.

We shall further assume $\partial_t \ll \nu_e \ll \omega_{ce}$, where ν_e and ω_{ce} are the electron collision and gyro frequencies, respectively. The Braginskii equations for the electrons are

$$\partial_t \frac{n_{e1}}{n_o} + \frac{c}{B_o}\hat{z}\times\nabla\phi\cdot\nabla(\ln n_o) + \partial_z v_z = 0, \tag{2}$$

$$m\partial_t' v_z = e\partial_z\phi - T_e\partial_z\frac{n_{e1}}{n_o} - (1+\alpha)\partial_z T_{e1}, \tag{3}$$

where $\alpha = 0.71$, and

$$\left(\frac{3}{2}\partial_t - K_\parallel\partial_z^2 - K_\perp\nabla_\perp^2\right)T_{e1} + \frac{cT_{eo}}{B_o}\hat{z}\times\nabla\phi\cdot\nabla\ln\left(\frac{T_{eo}^{3/2}}{n_o}\right)$$
$$-T_{eo}\partial_t\frac{n_{e1}}{n_o} = -\frac{1}{n_o}\frac{\partial R}{\partial T_e}T_{e1} - \frac{1}{n_o}\frac{\partial R}{\partial n_e}n_{e1} - \alpha T_{eo}\partial_z v_z, \tag{4}$$

where $\partial_t' = \partial_t + \nu_e/2$, m is the electronic mass, c is the speed of light, T_{eo} is the unperturbed electron temperature, v_z and T_{e1} are the perturbation electron velocity and temperature, respectively. Note that the thermal force effects are included and we have assumed $\nu_e\rho_e^2\nabla^2 \ll \partial_t$ and $\rho_a^2\nabla^2 \ll 1$, where $\rho^2 = T_{io}/m\omega_{ce}^2$. The thermal conductivities are given by $K_\parallel = 3.2T_{eo}/m\nu_{e2}$ and $K_\perp = 4.7\nu_e T_{eo}/m\omega_{ce}^2$. The radiation rate is denoted by $R = \varepsilon n_e g(T_e)$, where ε is the impurity ratio. The diamagnetic flux yields no contribution to (2), and the diamagneitc drift convection terms have been cancelled by terms from the stress tensor and the Righi-Leduc heat flux. It is of interest to note that we are not in the ion acoustic wave regime.

Applying the usual Fourier transformation, we obtain

$$\left(\omega+\tfrac{2}{3}i\Gamma\right)\left(\omega+\omega^*+0.63i\delta R_D\right) = 1.07iR_D\left[\omega^*\left(\eta_e-1.14\right)+\tfrac{2}{3}\left(1.14\Gamma+R_n\right)\right], \tag{5}$$

where $\Gamma = R_T + R_D$, $R_D = k_z^2K_\parallel \gg k_\perp^2K_\perp$, $\omega^* = k_yV_{Dj}$, $\delta = 2.95 + \mu$, $\mu = T_i/T_e$, $R_T = \partial R/n_o\partial T_e$, and $R_n = \partial R/T_{eo}\partial n_o$.

We now discuss several special cases of interest. First, in the absence of inhomogeneity, (5) becomes

$$\omega = -\frac{iR_1}{2} \pm \frac{i}{2}\left\{R_1^2 + 4R_D\left[0.71R_n - \delta_2\left(R_T+R_D\right)\right]\right\}^{1/2}, \tag{6}$$

where $R_1 = \frac{2}{3}R_T + \delta_1 R_D$, $\delta_1 = 2.53 + 0.63\mu$, $\delta_2 = 0.42(1+\mu)$.

Thus, for small R_D, when $\omega \sim -2iR_T/3$, a new type of instability appears if $1.69\,R_n/(1+\mu) - R_T > R_D$. It is R_n-driven and is enhanced by negative R_T.

In the limit $\omega^* \neq 0$ and $\omega^* > (R_D, R_n, R_T)$, we obtain

$$\omega = \begin{cases} -\omega^* - i\,(0.64 + 0.63\mu + 1.07\eta_e)R_D, \\ -i\left[\frac{2}{3}R_T + (1.89 - 1.07\eta_e)R_D\right], \end{cases} \tag{7}$$

which describe collisional ion drift waves and a purely growing negative R_T instability. When $R_T = 0$, the latter reduces to the dissipative η_e-mode of Drake et al. [3].

Equation (5) also describes in appropriate limits the dissipative and radiative temperature gradient instabilities. For example, if $d_x n_o = 0$, and $\omega_T^* = \eta\omega^* >> (R_n, R_D, R_T)$, we get

$$\omega^2 \approx 1.07 R_D \omega_T^*, \tag{8}$$

which is a purely growing dissipative temperature gradient instability.

On the other hand, for $\Gamma >> |\omega|$, we have

$$\omega \approx (1.61\omega_T^* + 1.07 i R_n)/(1 + R_T/R_D), \tag{9}$$

which describe a radiative temperature gradient instability. Note, however, (11) is valid only if $\eta_e >> 1$ and $R_n >> \Gamma$.

Another type of radiative instabilities exists in the regime $R_T >> |\omega|$. Here, one obtains

$$\omega^2 + \omega^*\omega - k_z^2 v_{te}^2 \left\{ \delta + 1.71\left[\frac{3i\omega^*}{2R_T}(\eta_e - 1.14) - \frac{R_n}{R_T} - 1.14\right]\right\} = 0, \tag{10}$$

Thus, for $\omega^* << k_z c_a << R_T$ and $\mu >> 1$, we have

$$\omega^2 \simeq k_z^2 c_a^2 (1 - 1.71 R_n/\mu R_T), \tag{11}$$

which describes a purely growing instability of the electron-acoustic waves.

In the opposite limit, $\omega^* >> k_z c_a$, one obtains

$$\omega = \begin{cases} -\omega^* - A, \\ k_z^2 v_{te}^2 A/\omega^*, \end{cases} \tag{12}$$

where we have defined

$$A = \frac{k_z^2 v_{te}^2}{\omega^*}\left[1 + \mu + 2.57 i(\eta_e - 1.14)\frac{\omega^*}{R_T} - 1.71\frac{R_n}{R_T}\right].$$

Here, one sees that the ion drift waves are unstable if $(\eta_e - 1.14)/R_T < 0$. Coupling of ion drift waves to the electron acoustic waves (lower branch) also can lead to an instability if $(\eta_e - 1.14)/R_T > 0$.

The wellknown oscillatory instability in the large η_e limit,

$$\omega^3 = -1.71\, k_z^2\, v_{te}^2\, \omega_T^* \qquad (13)$$

can be recovered in the limit $|\omega| >> (\omega^*, \sqrt{\delta}\, k_z v_{te}, R_T)$.

We have shown that impurity radiation can cause instabilities related to the electron acoustic waves, whose frequency lies between the ion and electron gyrofrequencies. These instabilities can have quiet different characteristics as compared to the usual radiative modes.

Acknowledgments: This work was partially supported by the Deutsche Forschungsgemeinschaft through Sonderforschung sbereich 191 Niedertemperaturplasmen.

References

[1] Stringer, T., in Proceedings of the 12th European Conference on Controlled Fusion and Plasma Physics, edited by L. Pócs and A. Montvai (European Physical Society, Budapest, 1985), Pt. 1, p.86.

[2] Mikhailovskii, A. B., Theory of Plasma Instabilities (Consultants Bureau, New York, 1974), Pt. 2, p.151.

[3] Drake, J. F., Guzdar, P. N., Hassam, A. B., Phys. Rev. Lett. 61, 2205 (1988).

Ionization and charge exchange effects on dissipative drift modes in an edge tokamak plasma.

D.K.Morozov,N.N.Morozov,D.Sünder.

An edge tokamak plasma in the region, where the temperature is somewhat higher than the ionization potential of the main gas, is considered in connection with the fact that an effect of a neutral flux entering the plasma from the wall upon the level of fluctuations in the edge zone has been found in some experiments.

It is shown that ionization of a gas entering the plasma from the wall or from a limiter essentially affects the drift-dissipative mode exited by the pressure gradient. In the slab model such a mode, stable at the edge due to a large shear, is destabilized, when a critical density of neutrals is reached. It can be qualitatively explained as an effect of the ionizational instability on a drift mode in a thermodynamically-non-equilibrium plasma. In a torus, dependent on the discharge parameters and on the transversal length, the exiting waves can be slightly or strongly localized within a poloidal angle of the solution. The first ones correspond to a weak toroidal mode coupling and become unstable at the critical neutral density. The second ones correspond to a strong toroidal coupling. It is known that they are unstable at a zero density of neutrals. However, ionization can essentially increase an instability increment. he role of charge exchange is insignificant. The preliminary analytical results obtained previously (D.Kh.Morozov,N.N.Morozov,D.Sünder. International Workshop on Plasma Edge Theory in Fusion Devices, Augustusburg, German Democratic Republic, 26-30 Sept,1989) are calculated with a higher precision. An equation has been obtained in the ballooning representation for the case, when the entry of neutrals into the plasma is non-uniform within toroidal and poloidal angles that takes place in some experiments. An estimate of transport coefficients is done.

EQUILIBRIUM BETA LIMIT AND ALPHA-PARTICLE CONTAINMENT IN STELLARATORS AS A FUNCTION OF THEIR ASPECT RATIO

F. Alladio, P. Batistoni, F. Crisanti, and S. Mancuso

Associazione EURATOM-ENEA sulla Fusione, Centro Ricerche Energia Frascati, C.P. 65 - 00044 Frascati, Rome, Italy

The possibility of designing stellarator or torsatron configurations at low aspect ratio remains an ambitious goal. The advantages of such an approach are the high use of the magnetic field volume, the reduced space taken by the windings and the computed equilibrium and ideal stability high beta limit, whereas the disadvantages are the increased fast particle losses. The choice of the winding law for the helicoidal coils is certainly the most critical tool for maximizing the advantages and minimizing the disadvantages. The choice of winding the helicoidal currents on circular cross section tori with constant pitch in toroidal coordinates $(\theta,\tilde{\omega},\phi)$ [1] (θ = const; $m\tilde{\omega}+n\phi$ = const., that means a higher pitch on the outside of the torus and a lower one on the inside) has turned out to be a rewarding one [2,3]; it allows a fully analytical treatment of the 3-D vacuum fields and permits an easy access to low aspect ratio configurations.

In this paper we attempt a systematic scan in the aspect ratio of idealized stellarators, with fixed poloidal m=2 number and toroidal field B^T_0 = 5T at R = R_0=2m (concentration point of the toroidal coordinates); the helicoidal currents are surface currents flowing with constant pitch in toroidal coordinates on circular cross section tori of major and minor radius R_*, a_*:

$$J_\phi = \frac{mI}{2R^2}\left(\frac{R_*^2}{a_*^2}-1\right)\cos(m\tilde{\omega}+n\phi);\ J_{\tilde{\omega}} = \frac{nI}{2R^2}\sqrt{R_*^2/a_*^2-1}\,\cos(m\tilde{\omega}+n\phi) \qquad (1)$$

In order to have the most self similar configurations the toroidal winding number has to be varied as $n=1.57\ m\sqrt{(R_*/a_*)^2-1}$. Also the vertical axisymmetric field has to be varied in order to maximize the rotational transform t_{edge} at the edge of the configuration; it is generated by a surface current on the same torus R_*, a_*

$$J_\phi = \frac{B^T_0 R_0}{\mu_0}\,\frac{1}{3R^2}\,\frac{1}{[m^2\,R_*^2/a_*^2+n^2-m^2]^{3/4}} \qquad (2)$$

The main parameters of the four configurations are summarized in the following table.The vacuum magnetic surfaces of the four cases are shown in Fig. 1. The

R_* (m)	a_* (m)	n	I (MA)	Ψ_{edge} (mWb)	$A = R_0/\langle a\rangle$	t_{axis}	t_{edge}	$\langle\beta\rangle^{lim}$ (%)
2.26	1.05	6	4.17	1070	2.78	0.106	0.67	≥6.6
2.12	0.72	9	2.78	518	3.92	0.108	1.15	6.6
2.04	0.39	16	1.56	169	6.90	0.145	2.31	4.3
2.01	0.24	26	0.96	67	12.50	0.197	3.24	3.3

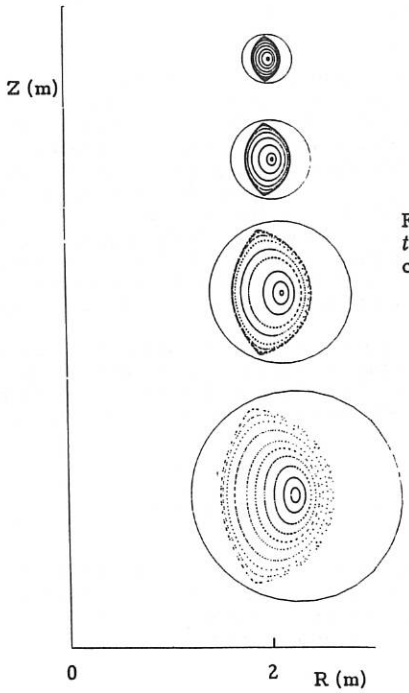

Fig. 1 Vacuum magnetic surfaces of idealized stellarators with A=2.78, 3.92, 6.90, 12.50

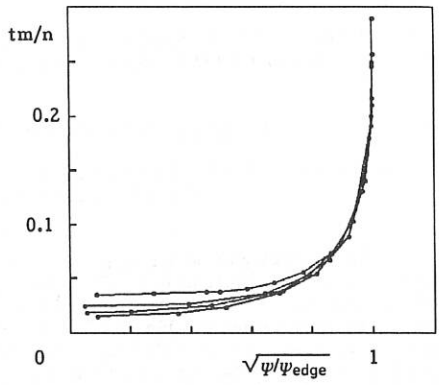

Fig. 2 Normalized rotational transforms $t \cdot m/n$ vs normalized radius for the configurations of Fig. 1

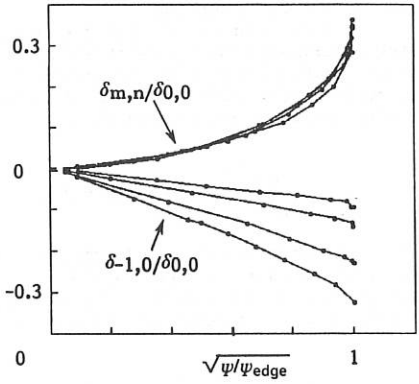

Fig. 3 Normalized main helicity $\delta_{m,n}/\delta_{0,0}$ and normalized toroidicity $\delta_{-1,0}/\delta_{0,0}$ of the field modulus vs normalized radius for the configurations of Fig. 1

profiles of the normalized rotational transforms tm/n as a function of the normalized radius $\sqrt{\psi/\psi_{edge}}$ (with ψ = toroidal flux/2π) are very similar and very steep at the edge (see Fig. 2) where they reach the value t_{edge} = 0.25 n/m and exhibit pronounced separatrix-like features that rotate once again with constant pitch in toroidal coordinates.

The slight differences in the central values of tm/n are due to the different wobbling of the magnetic axis that becomes larger at smaller aspect ratio.

A collisionless alpha-particle orbit calculation based on the Boozer formalism [4] has been performed using the ORBIT code [5]. The evaluation of the magnetic

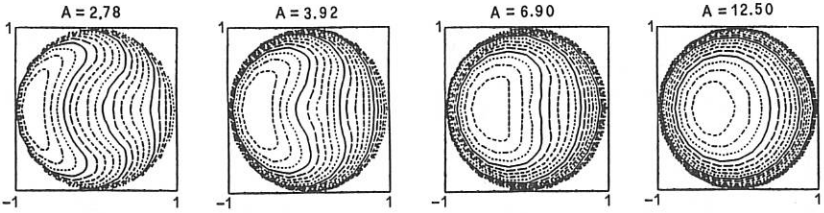

Fig. 4 - Plot of minimum |B| over $0<\phi_\psi<2\pi/n$ in the $(\sqrt{\psi/\psi_{edge}}, \theta_\psi)$ polar representation; the area where the contours are closed is shaded.

coordinates $(\psi, \theta_\psi, \phi_\psi)$ for the idealized stellarator analytical fields is particularly simple [3]. The modulus of the magnetic field is written like $B = \Sigma\, \delta_{pq}(\psi) \cos(p\theta_\psi - q\phi_\psi)$ and the two most relevant Fourier coefficients $\delta_{m,n}(\psi)/\delta_{0,0}(\psi)$, that expresses the main helicity, and $\delta_{-1,0}(\psi)/\delta_{0,0}(\psi)$, that expresses the toroidicity, are plotted in Fig. 3 versus the normalized radius $\sqrt{\psi/\psi_{edge}}$. The self similarity of the configurations is evidenced by the main helicity component being almost equal, whereas the toroidicity varies as required.

The plots of the minimum |B| along ϕ_ψ in the $(\sqrt{\psi/\psi_{edge}}, \theta_\psi)$ polar plot are shown in Fig. 4. The position of the area where the contours are closed gives an accurate idea of the fraction of the trapped alpha-particles that are contained in each configuration. To obtain a reactor relevant estimate of the alpha-particle containment capabilities of these configurations the products B°_T <a> have been rescaled to reduce the Larmor radius of the alpha-particle to 2% of the minor radius. Figure 5 shows that yet an aspect ratio A=7 is able to provide almost perfect containment capabilities $f_{cont} \approx 94\%$.

The equilibrium β limit was explored with the VMEC 3-D equilibrium code [6] used in fixed boundary conditions. A good description of the boundary ($\chi^2 \leq 1\%$) was

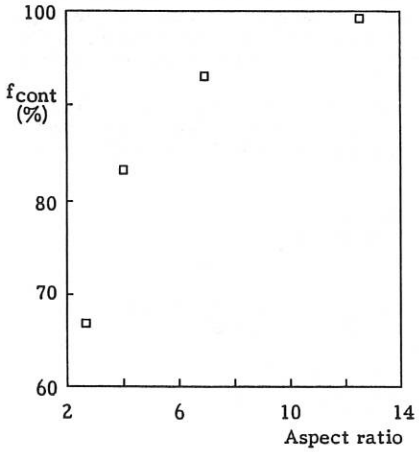

Fig. 5 - Fraction of contained α-particles vs aspect ratio for the configurations of Fig. 1

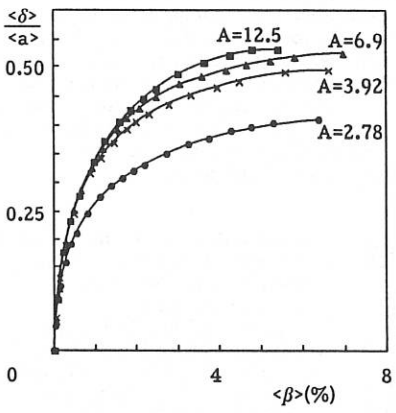

Fig. 6 - Normalized displacement of the magnetic axis <δ>/<a> vs average <β> for the configurations of Fig. 1

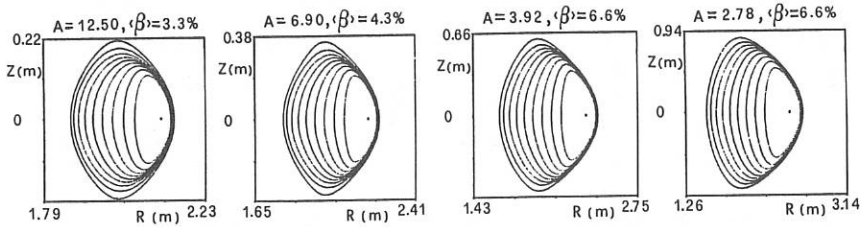

Fig. 7 - Magnetic surfaces as calculated by the VMEC code for the equilibrium β limit of the four configurations of Fig. 1

found for all four cases of Fig. 1 with 18 Fourier modes. For each configuration a mesh composed by 21 radial x 16 poloidal x 12 toroidal steps reproduced at β=0 the magnetic axis position and rotational transform and furthermore allowed a convergence $d(\ln W)/dt \leq 10^{-8}$ in 3000 iterations. The plot of the displacement of the magnetic axis normalized to the plasma minor radius $\langle\delta\rangle/\langle a\rangle$ versus $\langle\beta\rangle_{vol}$ is shown in Fig. 6. Using the conventional $\langle\delta\rangle/\langle a\rangle = 0.5$ as the equilibrium β limit, it appears that $\langle\beta\rangle_{lim} = 3.3\%$ for the A=12.5 configuration, $\langle\beta\rangle_{lim} = 4.3\%$ for A=6.9, $\langle\beta\rangle_{lim} = 6.6\%$ for A=3.92, whereas at the same $\langle\beta\rangle$ the low aspect ratio case A=2.78 has $\langle\delta\rangle/\langle a\rangle = 0.41$. However same caution must be exrcized because, as shown in Fig. 7, that displays the flux surfaces for the four configurations at their $\langle\beta\rangle_{lim}$, it appears that the A=2.78 case has an outboard compression of the magnetic flux that is relatively twice as much with respect to the A=12.5 case, and so it may be more prone to finite β destruction of the magnetic surfaces even before the conventional limit $\langle\delta\rangle/\langle a\rangle = 0.5$ is reached [7]. As a conclusion we could state that the choice of winding the helicoidal currents with constant pitch in toroidal coordinates allows a reasonably good compromise in between the equilibrium β limit and the alpha-particle containement down to plasma aspect ratio A=4 (coil aspect ratio $R_*/a_*=3$). A more refined choice of winding law is probably required to access the extremely low plasma aspect ratios in the region A=2÷3.

The authors of this paper would like to express their gratitude to the ORNL group (in particular to S. Hirshman for the use of VMEC code), to the Euratom-CIEMAT Group (in particular to A. Lopez Fraguas) and to R. White of PPPL for the use of the ORBIT code.

REFERENCES

[1] F. Alladio, F. Crisanti: Nucl. Fusion 26, 1143 (1986)
[2] F. Alladio et al.: Proc. 16th Eur. Conf. on Controlled Fusion and Plasma Physics, Venice, 1989, Part II, 579
[3] F. Alladio et al.: "Analytical Field Results for Stellarator/Torsatron Configurations" Int. Stellarator Workshop, Oad Ridge, 1989
[4] A.H. Boozer: Phys; Fluids 23,904 (1980)
[5] R.B. White, M.S. Chance: Phys. Fluids 27,2455(1984)
[6] S.P. Hirshman, J.C. Whitson: Phys. Fluids 26,3553 (1983)
[7] T. Hayashi et al.: Phys. Fluids B2, 329 (1990)

COLLISIONLESS TWO-FLUID THEORY OF TOROIDAL η_i STABILITY

J. P. Mondt

Los Alamos National Laboratory, Los Alamos, NM 87545, USA

J. Weiland

Chalmers University of Technology,
Gothenburg, S41296, SWEDEN

Introduction

A multi-moment generalization of the 'double-adiabatic' equations (Chew, Goldberger, and Low 1956) is derived, which is to be viewed as a collisionless analogue of the thirteen-moment method (Grad 1958). However, truncation is achieved by neglecting only the irreducible part of the fourth-order velocity moment, which is exact linearly within the context of the collisionless Boltzmann equation if wave-particle resonances (parallel transit and field curvature and ∇B resonances) are neglected; but is otherwise arbitrary.

The use of the present model is advocated in the study of the dynamics of reactive instabilities and the associated transport in the collisionless regime, because of the advantage of a continuum description with regard to the feasibility of mode-coupling simulations.

As an example of its utility, it is presently shown that the marginal stability condition for the "toroidal", i.e., interchange-type, branch of η_i modes (but, for simplicity without the important effects of gyroviscosity and trapped electrons) agrees well with kinetic theory, both as a function of the ratio $\epsilon_n \equiv 2L_n/R_c$ (Figure 1) of density gradient scale length divided by magnetic field curvature length, and as a function of the temperature ratio $\tau \equiv T_e/T_i$ (Figure 2).

1. Derivation of the dynamical equations

We take velocity moments of the collisionless Boltzmann equation, assuming localization of ions both perpendicular ($k^2\rho^2 \ll 1$) and parallel ($v_{th,i} \ll \omega/k_\parallel$) to the magnetic field. Parallel ion motion effects are neglected ($C_s \ll \omega/k_\parallel$). Only low fequencies are considered ($\omega \ll \omega_{ci}$), enabling the usual iterative solution of force balance in terms of drifts. A similar iterative solution is carried out for the heat flux equation. Like the pressure, due to the strong magnetic field and lack of collisions, the heat flux is anisotropic. We have to distinguish the flux of the perpendicular ($\mathbf{q}^{(\perp)}$) and parallel ($\mathbf{q}^{(\parallel)}$) parts of the peculiar kinetic energy. The former equals

$$\mathbf{q}^{(\perp)} = 2\frac{P_\perp}{m\omega_c}\mathbf{b}\times\nabla T_\perp - P_\perp \mathbf{V}_k \quad ,$$

where $\mathbf{V}_k \equiv \frac{T_\parallel}{m\omega_c}\mathbf{b}\times\mathbf{k}$, $k \equiv \mathbf{b}\cdot\nabla\mathbf{b}$ being the curvature vector; whereas

$$\mathbf{q}^{(\parallel)} \simeq \frac{1}{2}\frac{P_\perp}{m\omega_c}\mathbf{b}\times\nabla T_\parallel + P_\parallel \mathbf{V}_k \quad .$$

The (ion) pressure equations are found to be

$$d_t P_\perp + 2P_\perp \nabla\cdot\mathbf{u} + \nabla\cdot\mathbf{q}^{(\perp)} + P_\parallel \mathbf{k}\cdot\mathbf{u} + 2\mathbf{k}\cdot\mathbf{q}^{(\parallel)} = 0 \quad ,$$

and

$$d_t P_\parallel + P_\parallel \nabla\cdot\mathbf{u} + 2\nabla\cdot\mathbf{q}^{(\parallel)} - 2P_\parallel\mathbf{k}\cdot\mathbf{u} - 4\mathbf{k}\cdot\mathbf{q}^{(\parallel)} = 0.$$

Here, $d_t \equiv \partial/\partial t + \mathbf{u}\cdot\nabla$. Ion force balance yields

$$\mathbf{u} = \mathbf{V}_E + \mathbf{v}_{*i} + \frac{T_\parallel - T_i}{T_\parallel}\mathbf{V}_k \quad ,$$

where $\mathbf{v}_{*i}$ is the ion diamagnetic drift. The continuity equation completes the ion description. For the electrons, for simplicity, parallel force balance is adopted without viscosity, and the isothermal assumption is made (large thermal electron conductivity parallel to $\mathbf{B}$), leading to the Boltzmann relation $\delta n/n \simeq q\phi/T_e$ between density and electrostatic response.

2. Threshold, growth rate, frequency

In view of the close relation between the local solution and the global solution in the electrostatic regime ($\omega_H \gg \omega$) in the case of the collisional model (dissipative contributions to heat flux being neglected, but the perturbed pressure assumed isotropic due to collisions), it is of interest to consider the local solution to the present truly collisionless fluid model. Equating field curvature and ∇B drift frequencies (low beta), the increase in the order of the system due to anisotropy is compensated and a quadratic dispersion equation results. The growth rate and real frequency are found to be

$$\gamma = \omega_{*e}\left[\left(\frac{\epsilon_n}{\tau}\right)(\eta_i - \eta_{i,th})\right]^{1/2} \quad ,$$

$$\omega_r = \frac{1}{2}\omega_{*e}\left[1 - \left(1 + \frac{3}{\tau}\right)\epsilon_n\right] \quad ,$$

where ω_{*e} is the electron diamagnetic drift frequency and

$$\eta_{i,th} = \frac{\tau}{4\epsilon_n} + \frac{1}{2}(1-\tau) + \frac{1}{4}(\tau + \frac{3}{\tau} + 1)\epsilon_n$$

is the critical value of $\eta_i \equiv L_n/L_{T_i}$. The factor '3' in ω_r is 10/3 in the collisional model, whereas the expression for the growth rate is identical to that in the collisional model except through η_{ith}. Figures 1 and 2 represent comparisons between the collisional fluid model, kinetic theory, and the present model. For moderate ϵ_n and as a function of τ the present model represents an improvement, while for large ϵ_n the slopes of the marginal stability curves are 1.43, 1.36, and 1.25, respectively, for kinetic, collisional, and collisionless fluid theories.

References

1. Chew, G. F., Goldberger, M. L., and Low, F. E. 1956, *Proc. Roy, Soc.* **A236**, 112.
2. Grad, H. 1958, **"Principles of the kinetic theory of gases,"** in **"Thermodynamics of Gases,"** ("Thermodynamik der Gase"), Handbuch der Physik, Springer-Verlag, Berlin 1958, Bd. 12.
3. Mondt, J. P., and Weiland, J., LA-UR-89-3678, Los Alamos National Laboratory Report.

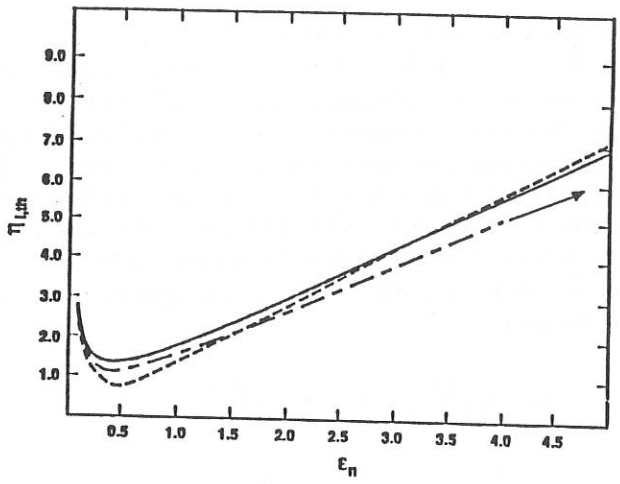

Fig. 1. Marginal stability curve in the $\eta_i - \epsilon_n$ plane for the two-fluid model with isotropic pressures (solid curve),the kinetic model (equidistant dashes) and the present model (non-equidistant dashes), for the case when $\tau = 1$ and $k_\perp^2 \rho^2 = 0$.

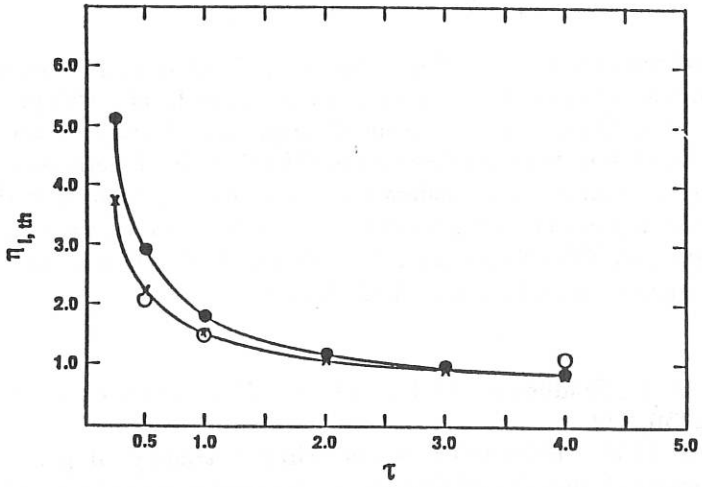

Fig. 2. Threshold $\eta_{i,th}$ for fixed $\epsilon_n = 1$ and $k^2\rho^2 = 0$ as a function of $\tau \equiv T_e/T_i$ according to the collisional (dots) and collisionless (crosses) two-fluid theories. The kinetic results are indicated with open dots.

MODELLING OF TRANSPORT IN STOCHASTIC MAGNETIC FIELD REGIONS

M.A. Hellberg, N.A. Frank, M.J. Handley, W. Feneberg[1]

University of Natal, Durban, South Africa

INTRODUCTION

We describe two studies of collisional transport in regions with perturbed magnetic surfaces, as may occur spontaneously or be externally induced in the edge-region of a tokamak.

Using Wobig's[1] mapping procedure, we have investigated test-particle transport of circulating particles in tearing mode-like structures[2] for some q-profiles.

In addition, in an extension of our earlier work[3], we have now used a fully self-consistent BGK collision term in the drift kinetic equation when calculating transport coefficients in a static perturbed region as produced by an ergodic divertor system.

TEST PARTICLE TRANSPORT

It is well-known that the equations for the field-lines in a toroidal device can be written in Hamiltonian form. Instead of solving them by integration, we use a Poincaré plot mapping technique[1] to obtain a realization of the field structure. Successive puncture points represent canonical transformations of the coordinates. The field perturbations and particle orbits are dealt with as canonical perturbations of the integrable system, and collisions introduced as a random perturbation.

The tearing mode magnetic field is modelled by a contribution[2]

$$h(\psi_1, \theta_0) = \sum_{\ell=2,3} \frac{K \psi_1^{\frac{\ell}{2}} sin\ell\theta_0}{\ell(1 + (\psi_1/\psi_{k\ell})^{\ell})}, \tag{1}$$

(where K and $\psi_{k\ell}$ are constants) to the generating function of the second kind $S(\psi_1, \theta_0)$, which yields the transformation $(\psi_0, \theta_0) \rightarrow (\psi_1, \theta_1)$. Typically we have used $\psi_{k2} = 1.0; \psi_{k3} = 0.5$.

We have carried out calculations with tokamak models having linear[2] and exponential[4] ι-profiles. In the former, we use $\iota/2\pi = 1.05 - 0.34\psi$ for $(0 < \psi < 2.5)$. The latter, modelling TOKOLOSHE over the same range, $(0.952 < q < 3.33)$, has the form $\iota/2\pi = \exp(\psi/7.26)$, with $0.357 > \psi > -8.74$.

Depending on the perturbation strength K, one may obtain islands, stochastic regions or mixed regions. Examples are shown in Figure 1. We note that, although the perturbation has $\ell = 2, 3$ only, the nonlinear tearing mode mapping gives rise to an island at $q = 1$.

The guiding centre drift orbits of passing particles are represented by an effective field $\mathbf{B}^* = \mathbf{B} + \nabla \times (\rho_{\|}\mathbf{B})$, with $\rho_{\|}$ the parallel gyroradius.

A simple collision model provides random changes in magnetic moment. Particles essentially diffuse out between the islands. Loss rates measured across a thin edge-layer are presented in Figure 2. For weakly perturbed field structures, higher collisionality δ causes an increase in loss rate, but for larger K values, enhanced collisionality reduces the diffusion rate. This anomalous behaviour was found earlier[2]. Our studies of tracer particles suggest

[1] MPI für Plasmaphysik, Association EURATOM, Garching, FRG

that collisions do not so much cause particles to be trapped in the few remaining islands, as to slow down the radial motion by preventing particles from rapidly free-streaming along the ergodic field lines.

It was found that the exponential and linear profiles gave similar results if the diffusion test-layer was defined by a range in q rather than a range in ψ. Lower loss rates were observed in weak shear regions.

The mapping has been applied, possibly beyond its nominal range of validity, to a profile including a small Shafranov shift[4], which reduces to the exponential model in the cylindrical limit. An example of field structure is shown in Figure 1(d). The loss rate was found to be lower than for the equivalent exponential model.

Recently, the mapping was modified so as to model the Ergodic Magnetic Limiter (EML) on TEXT. This includes a calibrated field perturbation, varying as r^m, with $m/n = 7/2$ predominantly. An alternative collision model has also been developed. In addition, using the relativistic form for $\rho_{\|}$, the technique may be applied to runaway electrons. Preliminary results of modelling of TEXT will be presented.

TRANSPORT COEFFICIENTS

We have earlier[3] estimated the widths of the resonances at $k_{\|} = (m-nq)/Rq = 0$ exhibited by transport coefficients calculated for a magnetically perturbed region. It was assumed that cylindrical flux surfaces were disturbed by a radial magnetic field with Fourier components $b_{\omega,m,n}$, the sole frequency being that due to the diamagnetic drift. The drift kinetic equation with a BGK collision term was solved for the perturbation distribution function $f_1(r,\theta,\phi,t)$, with a similar Fourier Ansatz. In the calculation of f_1 for the two species, it was assumed that particle number, momentum and energy were conserved in like-particle collisions, in $e-i$ collisions momentum was not conserved (friction), and $i-e$ collisions were neglected. In finding the transport coefficients themselves, however, the collision term was simplified to conserve particles only. Analytically the electron diffusion resonance width was then estimated to be given by $0 \leq \mid \beta \mid \leq \gamma^{\frac{1}{2}}$, where $\beta = k_{\|} v_{e,th}/\nu, \gamma = \omega_D/\nu$, and ν is the collision frequency.

Now using a fully self-consistent BGK model, we have found that the radial electron flux may be written as:

$$\Gamma_{r,e} = -n_e v_{e,th} \left(\frac{\lambda_e}{Rq}\right) D_M \left\{ A_1(k_{\|},\omega) \left[\frac{n'}{n} - \frac{e\phi'}{T}\right] + A_2(k_{\|},\omega) \left[\frac{T'}{T}\right] \right\}. \qquad (2)$$

Here D_M has the form of a magnetic diffusion coefficient, viz.

$$D_M = Rq \sum\sum\sum b_{\omega,m,n} b^*_{\omega,m,n},$$

and A_1 and A_2 are form factors yielding the behaviour (near $k_{\|} = 0$) of the two contributions in terms of the characteristic parameters β and γ.

Analytically, one may show that for $\beta \ll 1$, the flux reduces to the form found earlier[3], although it differs by a factor 2 in value. The halfwidths of A_1 and A_2 both scale as $\beta \propto \gamma^{\frac{1}{2}}$, but as their widths are not actually equal, one cannot simply lump the two contributions together, even if $\phi(r)$ represents an ambipolar electric field[3] .

The radial thermal flux has similar coefficients for the gradients, which we denote by $\tilde{A}_1$ and $\tilde{A}_2$. Not surprisingly, the first coefficient is found to be negligible - the heat flux is proportional to T'/T. In Figure 3 we present numerical evaluations of the form factors for the electrons, where we have chosen $\gamma = 0.1$, appropriate for TORE SUPRA.

For the ions, the form factors are all found to peak at $\beta \simeq \gamma$ and to have a width of order γ. While the particle flux coefficients tend to a δ-function of β as γ tends to zero, this is not the case for the heat flux coefficients. Numerical solutions for $\gamma = 5$ are shown in Figure 4, confirming and extending the analytical results.

Useful discussions with D.S. Sherwell, A. Wootton and P.J. Morrison are gratefully acknowledged, as are the hospitality of the University of Texas at Austin and the IPP, Garching.

1. H. Wobig *Z. Naturf.* **42a**, 1054 (1987); H. Wobig, R.H. Fowler *Pl. Phys. Cont. Fus.* 30, 721 (1988).
2. H. Sander *Report IPP 2/296; MPI für Plasmaphysik, Garching* (1988).
3. W. Feneberg, M.A. Hellberg *XV EPS Fusion Conf., Dubrovnik* **III**, 1081 (1988).
4. D.S. Sherwell *Private communication* (1988).

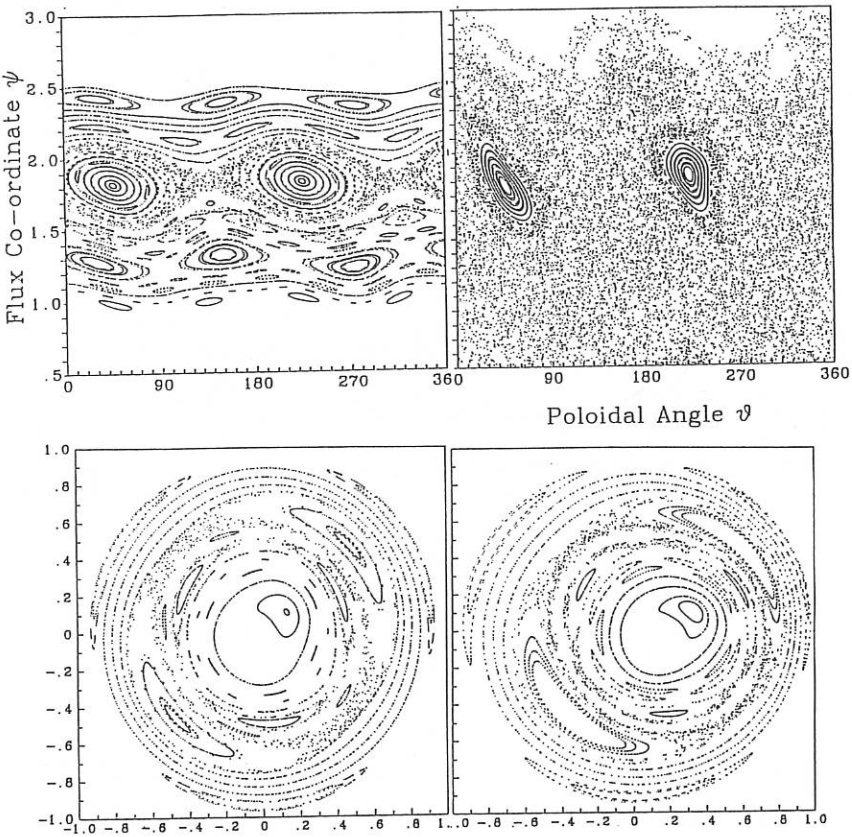

FIGURE 1. Magnetic field plots. (a) K = 0.2, linear profile; (b) K = 1.0, linear profile; (c) K = 0.2, exponential profile; (d) K = 0.2, including Shafranov shift.

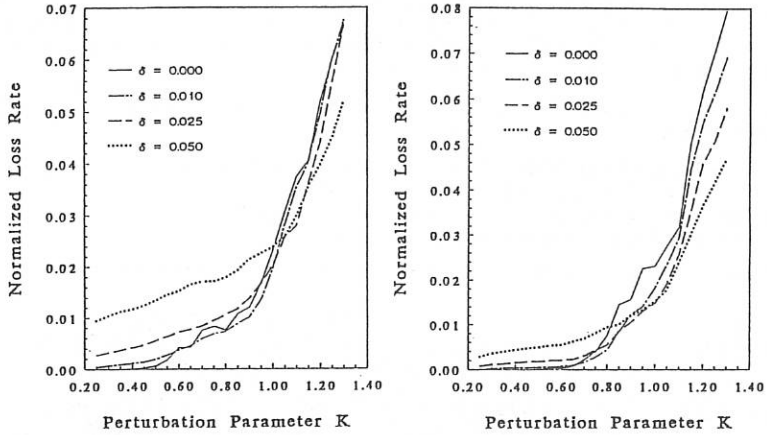

FIGURE 2. Loss rate versus perturbation, K, for various collision parameter values δ. (a) Linear ι-profile; (b) Exponential ι-profile.

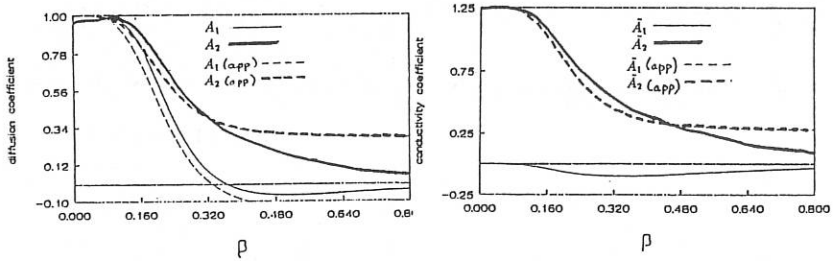

FIGURE 3. Particle and heat flux coefficients, A_1 and A_2, and $\tilde{A}_1$ and $\tilde{A}_2$, respectively, for electrons, versus $\beta = k_\parallel v_{th}/\nu$, calculated for $\gamma = \omega_D/\nu = 0.1$.

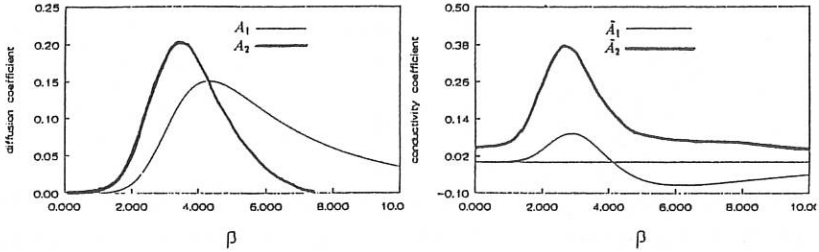

FIGURE 4. Particle and heat flux coefficients for ions as a function of β, for $\gamma = 5.0$.

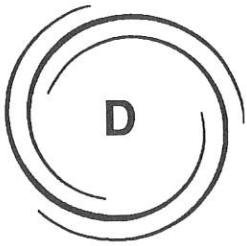

MAGNETIC CONFINEMENT THEORY AND MODELLING

D2 MODELLING

D2

SIMPLIFIED MODELS FOR RADIATIONAL LOSSES CALCULATIONIN A TOKAMAK PLASMA.

ARUTIUNOV A.B., KRASHENINNIKOV S.I., PROKHOROV D.Yu.
I.V.Kurchatov Institute, Moscow, USSR.

1. To determine the magnitudes and profiles of radiational losses in a Tokamak plasma, particularly for high plasma densities, when formation of MARFE or detached-plasma takes place [1], it is necessary to know impurity distribution over the ionizational states. Equations describing time evolution of this distribution [2-4] are rather cumbersome, besides that, transport coefficients as well as rate constants of the processes involving complex ions are known nowadays with high degree of uncertainty, thus it is believed necessary to develop simplified, half-analytical models describing time evolution of the impurities distribution over the ionizational states for more convenient analysis of physical processes taking place in a Tokamak plasma on the base of the experimental data.

Let us consider the differential analog [5] of the system of equations, describing time evolution of impurity ionizational states:

$$\frac{\partial n_k}{\partial t} = -\nabla(n_k \vec{V}) + \nabla(D\nabla n_k) + \frac{\partial}{\partial k}\left[A_k n_k + B_k \frac{\partial n_k}{\partial k}\right] + I_k, \quad (1)$$

where: n_k is the concentration of impurity in the ionizational state k; $A_k=R_{k+1}-S_k+E_{k+1}$, $B_k=(R_{k+1}+S_k+E_{k+1})/2$; S_k, R_k, E_k are, respectively, ionization, recombination and charge exchange (imp. + H/D/T atoms) rate constants for impurity ions; V, D are, respectively, pinch velocity and diffusion coefficient of impurity; I_k is the source of impurity in the ionization state k. In what follows it is assumed that $E_k=0$. It is to be noted that the results obtained below can be easily generalized for the case $E_k \neq 0$.

If impurity transport and the source only slightly influence the process and both of them can be neglected, then solution of the eq.(1) fits local corona equilibrium [2]: $n_k(\vec{r},t)=n(\vec{r},t)n_k^c \equiv n(\vec{r},t)C_* EXP\left(-\int_{k_*}^{k} \frac{A_{k'}}{B_{k'}} dk'\right)$, (2)

where: $n(\vec{r},t)=\sum n_k(\vec{r},t)$; $k_*(T_e)=\langle k \rangle_c$, C_* is a normalizing factor; T_e is the electron temperature.

2. Let us consider how corona equilibrium is established in a uniform isotropic plasma, assuming that at the time t=0 impurity (also uniform) is injected into plasma, impurity charge number distribution being localized in the vicinity of k_0. Let us seek the solution of eq.(1) in the form: $n_k(t)=\eta[k-\bar{k}(t),t]$ assuming that distribution dispersion is small during the evolution process.

Based on assumptions made and introducing new variable $i=k-\bar{k}(t)$, we obtain from (1) the following equation for $\bar{k}(t)$ [5]:

$$d\bar{k}/dt = -\bar{A} \equiv A_{\bar{k}} \quad (3)$$

and for $\eta(i,t)$:

$$\frac{\partial \eta}{\partial t} = \frac{\partial}{\partial i}\left(i\,\bar{A}'\eta + \bar{B}\,\frac{\partial \eta}{\partial i} \right), \quad (4)$$

where: $\bar{A}'=\partial A/\partial k\big|_{k=\bar{k}}$; $\bar{B}=B_{\bar{k}}$. It has been possible to solve eq.(4) in a general form, however for expressions $\langle i^{2m}\rangle$, where m is integer, recurrence relations can be obtained. Thus for dispersion (m=1) we find from (4):

$$\langle i^2\rangle=\langle i^2\rangle_o \exp(-2\tau)+2\int_0^{\tau} \frac{\bar{B}(\tau')}{\bar{A}'(\tau')}\,\mathrm{EXP}\left[-2(\tau-\tau')\right]d\tau', \quad (5)$$

where: $\tau=\int \bar{A}'(t')dt'$, $\langle i^2\rangle_o$ is the dispersion in the initial instant of time.

It is to be noted that in the process of evolution, as $\bar{k}(t)$ runs through electronic states related to filled shells drastic change of ratio $\bar{B}/\bar{A}'$ takes place, hence monotonic behaviour of $\langle i^2\rangle(t)$ is disturbed as it follows from equation (5) and has been observed in numerical calculations.

3. Thus in the case when characteristic time scale of transport processes in eq.(1) exceeds the time scale of local corona equilibrium set up (3): $t_R=-\int_{k_o}^{k\to k_*} d\bar{k}/A(\bar{k})$, then distribution $n_k(\vec{r},t)$ as a whole is close to that governed by (2), where $n(\vec{r},t)$ is described by the following equation:

$$\frac{\partial n}{\partial t} = -\nabla(n\vec{V}) + \nabla(D\nabla n) + I \quad (6)$$

where: $I=\sum_k I_k$. Deviation from (2) may be taken into account by means of successive approximation method. However this method is too cumbersome for practical use. If far tails of ions distribution over ionization states, caused for example by some source I_k, are excluded from (2) the method may be used based on Hermit polynomial series $H_l(y)$ of the function n_k:

$$n_k(\vec{r},t)= \frac{n(\vec{r},t)}{\sqrt{\pi\sigma}}\,\mathrm{EXP}\left[\frac{(k-\bar{k})^2}{\sigma} \right] \sum_{l=0}^{\infty} a_l(\vec{r},t)H_l\left(\frac{k-\bar{k}}{\sqrt{\sigma}}\right), \quad (7)$$

where: $\bar{k}(\vec{r},t)$, $\sigma(\vec{r},t)$ are the mean charge and dispersion of the distribution; $a_l(\vec{r},t)$ are the expansion factors. Assuming $a_o=1$,

$a_1=a_2=0$ and $\bar{A}_k = A_* + A'_*(k-k_*)$, where $A_* \simeq 0$, from equations (1), (7) we obtain:

$$\frac{\partial \bar{k}}{\partial t} = -\vec{V}\nabla\bar{k} + 2D\,\nabla\bar{k}\,\nabla\ln(n) + \nabla(D\nabla\bar{k}) - A'_*(\bar{k}_*-k)$$

$$\frac{\partial \sigma}{\partial t} = -\vec{V}\nabla\sigma + 2D\,\nabla\sigma\,\nabla\ln(n) + \nabla(D\nabla\sigma) + 2\left[2D(\nabla\bar{k})^2 - A'_*\sigma + 2\bar{B}\right] \qquad (8)$$

where: $B_*=B_{k_*}$. Expressions for a_l, $l>2$, are not presented here since they are rather cumbersome.

Equations (6), (8) describe the case of weak deviation from local corona equilibrium. Calculated dependencies $A_*(T_e)/n_e$ and $B_*(T_e)/n_e$ for Fe ions are shown on Fig.1 (ionization and recombination rate constants are taken from [6]). 4. Let us consider now the case of strong deviation from corona equilibrium, caused by spatial transport of the impurity at a distance x_i from the plane wall, where recombination of impurity ions takes place, $I_k=I_o\delta_{k1}\delta(x-x_i)$. We assume that plasma parameters are uniform, and that $\vec{V}=0$. Since we are interested in the case when t_R is greater then the characteristic time of spatial impurity transfer, $t_d \cong x_i^2/D \cap 6$, then in the most interesting region, - the region of strong deviation from corona equilibrium $-A_k \cong B_k$ and therefore diffusional term in k-space in eq.(1) may be neglected.

Introducing new variable $\xi=\int_1^k A_k^{-1}dk$ and denoting $N_k=-n_kA_k$, we obtain from (1):

$$\frac{\partial N}{\partial \xi} = D\frac{\partial^2 N}{\partial x^2} + I_o\delta(\xi)\delta(x-x_i) \qquad (9)$$

Solving eq.(9) with the following boundary conditions $N(x=0)=0$, $N(x\Rightarrow\infty)=0$, we find:

$$n_k = -\frac{I_o}{2A_k\sqrt{\pi D\xi(k)}}\left[\mathrm{EXP}\left(\frac{(x-x_i)^2}{4D\xi(k)}\right) + \mathrm{EXP}\left(\frac{(x+x_i)^2}{4D\xi(k)}\right)\right] \qquad (10)$$

It is of interest to determine charge composition of the ions falling at the wall $\Gamma_w=\int j_w(\xi)d\xi$:

$$j_w(\xi) = \frac{DI_o x_i}{2\sqrt{\pi}(D\xi(k))^{1.5}}\,\mathrm{EXP}\left(-\frac{x_i^2}{4D\xi(k)}\right) \qquad (11)$$

As would be expected, distribution (11) has a maximum at $\xi(k_m)\cong x_i^2/4D\cong t_D$, and a long power tail. The particles which forms

this tail accelerating under the action of wall potential up to energies $\propto k$ may contribute considerably in the plate sputtering. It is to be noted, that the expression obtained for n_k (10) may be generalized for the case accounting for the both pinch-effect and impurity flow discharge at the limiter. 5. Conclusions. a) Explanation is find of nonmonotonic character of ions distribution over charge numbers time evolution, obtained in numerical calculations; b) Simplified model is proposed for impurity behavior description in the case of small deviation from corona equilibrium; c) It is shown that charge states distribution of the ions recycling near the tokamak chamber wall has pronounced power tail, which may be the controlling factor in tokamak first wall sputtering.

REFERENCES

1. Lipschultz B., J.Nucl. Mater. V.145-147 (1987) 15.
2.Gervids V.I., et al. "Reviews of plasma physics", V.12, 1982, p.156. (in Russian)
3.Hawryluk R.J., Suckewer S., Hirshman S.P., "Low Z impurity transport in tokamaks.", Rep.PPPL-1473,1978.
4.Dnestrovskij Yu.N., Strizhov V.F. "The model of impurity diffusion in tokamaks.", Rep. IAE-1473, 1983. (in Russion)
5.Ivanov V.V., Kukushkin A.B., Lisitsa V.S., Fisika plasmy , V.13, (1987) 1341. (in Russion)
6.Post D.E.,et al., Atomic Data and Nucl. Data Tables.,V.20 (1977) 397.

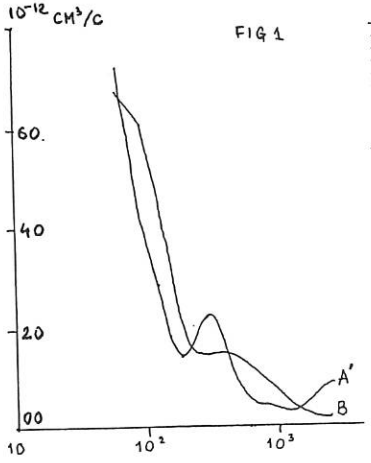

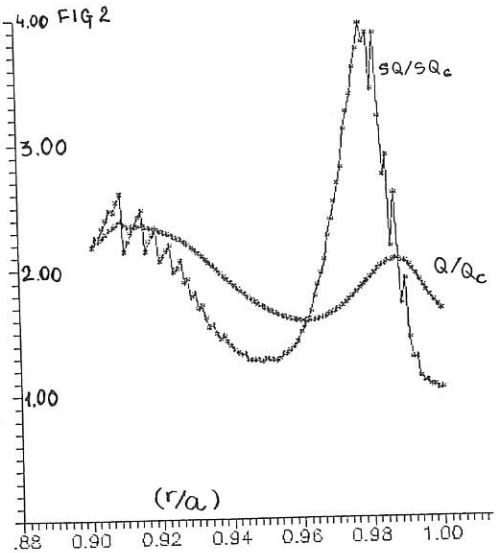

PHYSICAL ACCURACY ESTIMATE OF GLOBAL ENERGY CONFINEMENT SCALING LAWS FOR TOKAMAKS

Chudnovskij A.N., Yushmanov P.N.

I.V.Kurchatov Institute of Atomic Energy, Moscow, USSR

A reliability estimate for the derived relationships is one of the most important problems in the analysis of data on global energy confinement in tokamaks. At present the problem of accuracy estimation for the scaling laws obtained on the basis of a statistical analysis of experimental data on global energy confinement [1] is still open. The problem is in the fact that the energy confinement in tokamaks actually depends on a greater number of parameters than the set P, B, I_p, k, R, a, n, M usually used in the statistical analysis. An additional difficulty emerges due to the fact that we don't know theoretical lows of τ_E dependence on experimental parameters. By these two reasons a difference between the experimental τ_E and any scaling law expression for τ_E^{fit} is not a random quantity. Under the conditions, when $\tau_E - \tau_E^{fit}$ is not a random quantity with a zero average magnitude, the standard methods of statistical analysis turn out to be unapplicable. Unsatisfaction of this condition in practice results in a great sensitivity of statistical treatment results to the chosen set of experimental information. As a result, using samewhat different subsets of the total data base, essentially - different scaling lows have been produced. In this case, even the scaling lows of the same functional type the dependences on the experimental parameters P, B, I_p, k, R, a, n, M differ by values noticeably-exceeding the error bars for the dependences [2,3].

One of the methods for solving this problem is described in [4]. It includes the splitting of all the data into the groups, when in each of them the necessary statistical assumtions are satisfied. In [4] all the discharges in the same tokamak belong to such a group. In this case, for the scaling laws developed for each separate facility the standard method of statistical analysis are used. The global scaling law is produced by the treatment of these data.

It is easy to see that in the development of a scaling law for one facility the same problems as those in the analysis of data from a number of tokamaks emerge. Usually at each facility there are groups of regimes with various natures of confinement. The supershots, regimes with various degrees of plasma density profile peaking, H and L-modes, IDC, IOC, detached plasmas etc are the most pronounced examples. Such a physically-justified splitting is naturally realized on the basis of a whole set of experimental information, not on the

basis of a minimal data set used for the global energy confinement analysis. This confirmes the presence of hidden parameters even in the data from one separatly-taken facility that does not allow one to use the standard method of statistical analysis in this case too.

A detailed analysis of the dependences on the plasma current, I, heating power, P, average plasma density, n, and, if possible, on the magnetic field, B, for separate tokamaks on the basis of splitting all the discharges on a given facility into differently-selected groups was carried out.

Fig. 1-3 demonstrate some culculation results for large tokamaks. α_I, α_P, α_n, α_B are proper exponents in a power-type scaling law. Error bars were obtained by "physical" error estimate [3]: $\delta\alpha \approx \sqrt{N/10} \cdot \delta\alpha_s$, where $\delta\alpha_s$ is the statistical error, N is the number of shots. The numbers beside error bars indicate on a quantity of points in a group, other information conserns the splitting limits. The first left error bars correspond to the one facility all L-mode points fit.

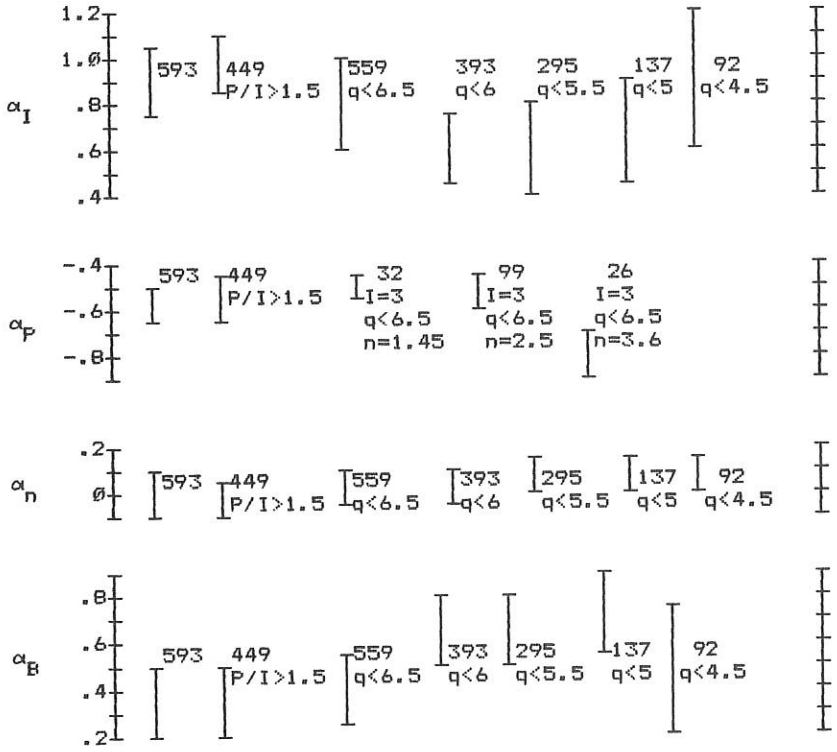

Fig.1 Examples of fitting results for JET.

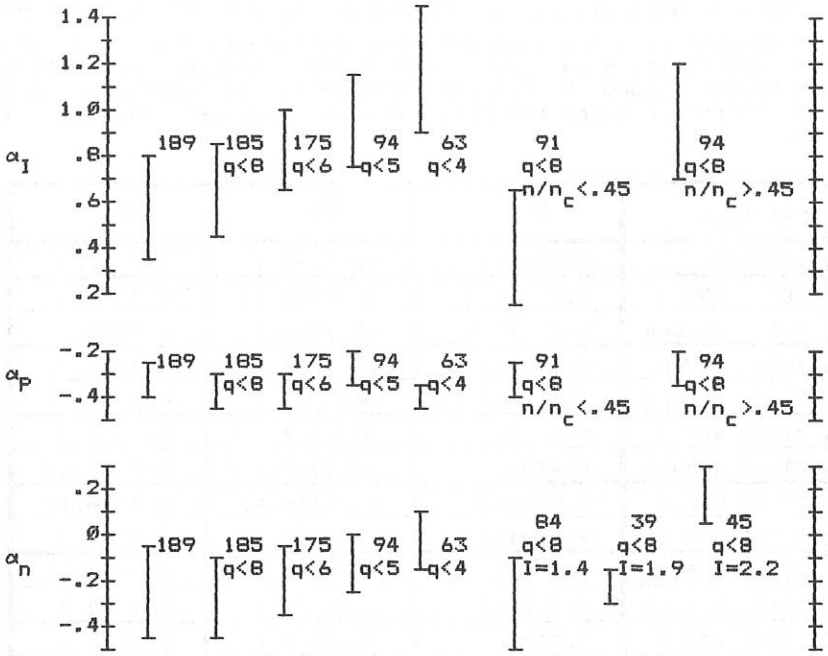

Fig.2 Examples of fitting results for TFTR.

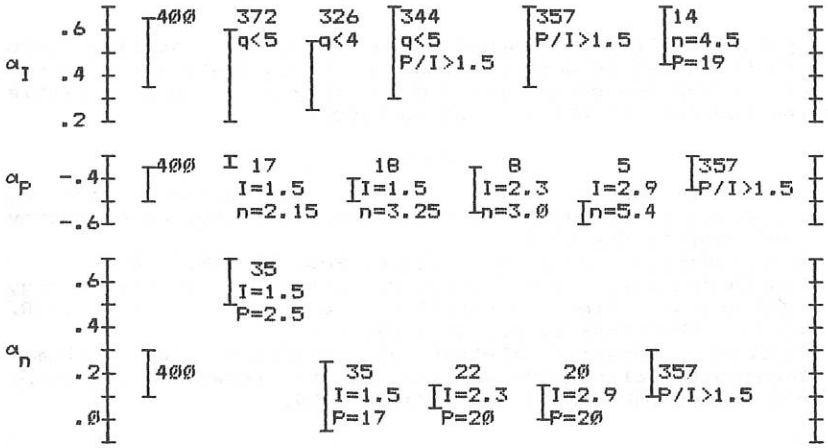

Fig.3 Examples of fitting results for JT-6Ø.

The exponents α_I, α_B for JET and α_I, α_n for TFTR culculated for different groups are distributed noticeably-exceeding the error bars of all point fit, and hence accuracy estimation ought to be changed. Preliminary estimation of exponents and their errors for large tokamaks and some other are given in a table.

Fit type	α_I	α_P	α_n
ITER-89	0.85±0.2	-0.5 ±0.1	0.1 ±0.1
JET 593 p	0.9 ±0.15	-0.62±0.07	0.0 ±0.1
JET groups	0.8 ±0.2	-0.65±0.1	0.05±0.1
TFTR 189 p	0.58±0.22	-0.3 ±0.1	-0.25±0.2
TFTR groups	0.8 ±0.4	-0.3 ±0.1	-0.1 ±0.25
JT-60 400 p	0.5 ±0.15	-0.42±0.07	0.2 ±0.1
JT-60 groups	0.45±0.2	-0.42±0.1	0.1 ±0.15
D-III 216 p	0.95±0.2	-0.77±0.12	0.2 ±0.15
D-III groups	0.95±0.3	-0.77±0.12	0.2 ±0.2
DITE 205 p	1.25±0.2	-0.9 ±0.2	0.42±0.12
DITE groups	1.4 ±0.3	-0.9 ±0.4	0.3 ±0.3
ISXB 108 p	1.37±0.17	-0.65±0.1	0.15±0.1
ISXB groups	1.3 ±0.2	-0.65±0.15	-0.15±0.25
T-10 28 p	0.55±0.05	-0.55±0.05	0.68±0.05
T-10 groups	0.55±0.1	-0.55±0.15	0.65±0.1

Splitting all the discharges on a given facility into differently-selected groups allows one to estimate a real error in the scaling law parameters and to obtain a more reliable scaling low for all the facilities later.

References

1. S.M.Kaye. Survay of energy confinement scaling expressions. Presented at ITER specialist meeting on energy confinement, May 1988.
2. R.J.Goldston. Plasma Phys. Contr. Fus. 26 (1984) 87.
3. A.N.Chudnovskij, P.N.Yushmanov. Estimate of the energy confinement time prediction accuracy for ITER. ITER-IL-PH-4-9-S-11, August 1989.
4. K.Riedel. Advanced statistical analysis for tokamak transport. Colinearity and tokamak to tokamak variation. NYU Report DOE/ER/53223-98, March 1989.

TRANSPORT MODEL OF CANONIC PROFILES FOR ION AND ELECTRON TEMPERATURES IN TOKAMAKS

E.L. Berezovskij, Yu.N. Dnestrovskij, S.E. Lysenko, A.A. Pivinskij and K.N. Tarasyan

I.V. Kurchatov Institute of Atomic Energy, Moscow, USSR

Abstract . The transport model of power balance for ions and electrons, using an idea of canonic temperature profiles is developed. The comparison with experiments on T-10, TFTR, ASDEX and JET allowed to derive the transport scaling for L-regime. The predictions for fusion reactor ITER are given.

1. Model. In our previous works [1-2] the canonic profile model was used to describe the evolution of electron temperature $T_e(r)$. It was shown that this model can describe the behavior of T_e in many experiments on T-10, JET and DIII-D. In this report we try to extend this idea for description of the ion temperature $T_i(r,t)$ also. We suppose:

$$T_{ic}(r)=[T_{ec}(r)]^{2/3}, \quad T_{ec}(r)/T_{ec}(0)=(1+r^2/a_j^2)^{-1}, \quad a_j= a/\sqrt{q_a-1} \qquad (1)$$

Here $T_{ec}(r)$ and $T_{ic}(r)$ are canonic profiles of temperatures.

The model contains 3 equations for T_e, T_i and poloidal field:

$$\frac{3}{2}\frac{\partial}{\partial t}(nT_e) = \frac{1}{r}\frac{\partial}{\partial r}(r\Gamma_e)+P_{OH}-P_{ei}+P^e_{aux}+P_{rad}+P^e_{ion},$$

$$\frac{3}{2}\frac{\partial}{\partial t}(nT_i) = -\frac{1}{r}\frac{\partial}{\partial r}(r\Gamma_i)+P_{ei}+P^i_{aux}+P^i_{ion}+P_{cx}, \qquad (2)$$

$$\frac{\partial \mu}{\partial t} = \frac{c^2}{4\pi}\frac{\partial}{\partial r}\left[\frac{1}{r\sigma}\frac{\partial}{\partial r}(r^2\mu)\right], \qquad \mu = 1/q.$$

The distributions of density n and radiation power P_{rad} are supposed to be known from the experiments. In (2) P_{aux} is the additional heating power, P_{cx}, $P^{e,i}_{ion}$ are charge-exchange and ionization losses. For heat fluxes $\Gamma_{e,i}$ we suppose:

$$\Gamma_e= \Gamma_e^{neo}+\Gamma_e^{con}+\Gamma_e^{T-11}+\Gamma_e^{PC}+\Gamma_e^{mix}, \quad \Gamma_i = \Gamma_i^{neo}+\Gamma_i^{con}+\Gamma_i^{T-11}+\Gamma_i^{PC}+\Gamma_i^{mix}, \qquad (3)$$

where $\Gamma^{neo}_{e,i}$ are neoclassical fluxes, $\Gamma^{con}_{e,i} = 5/2\ \Gamma_n T_{e,i}$, Γ_n is the particle flux known from the experiment,

$$\Gamma_e^{T-11} = -\alpha_e^{T-11}\, \text{æ}_e^{T-11}\, \partial T_e/\partial r, \quad \alpha_e^{T-11} = 0.2,$$

$$\text{æ}_{e,i}^{T-11} = \hat{\text{æ}}_e^{T-11}/q = 0.5 \times 10^{20}(r/R)^{1.75}\sqrt{T_{e,i}(eV)}/R(cm)q,$$

$\Gamma_{e,i}^{PC}$ are correspond to heat fluxes invoked by the deviation of $T_e(r)$ and $T_i(r)$ from $T_{ec}(r)$ and $T_{ic}(r)$. Here we consider only L-regimes in discharges with additional heating. Thus we suppose

$$\Gamma_{e,i}^{PC} = -\alpha_{e,i}^{PC}\ \hat{\text{æ}}_{e,i}^{T-11}(a/4)\ q(a/2)\ g\ L_T(T_{e,i}), \tag{4}$$

$$L_T(T_{e,i}) = \frac{\partial T_{e,i}}{\partial r} - \frac{T'_{ec,ic}}{T_{ec,ic}}\ T_{e,i}, \quad g = 10[a(m)^2]\ \frac{\langle n(10^{13}cm^{-3})\rangle}{I(MA)} \tag{5}$$

is stiffness of canonic profiles, a and R are minor and major radii. As a usual the stiffness parameter g is high (g ~ 5-20), and the set of equations (2) is a stiff system. If $q_a \leq 3$ then in the central zone the $T_{e,i}(r)$ profiles are perturbed by sawteeth mixing, that is described by fluxes

$\Gamma_{e,i}^{mix} = -\text{æ}_{e,i}^{mix}\, \partial T_{e,i}/\partial r$ when $r \leq r_{mix}$, and $\Gamma_{e,i}^{mix} = 0$ when $r > r_{mix}$, $\text{æ}_{e,i}^{mix} = 3\text{-}5 \times 10^{17}\ cm^{-1}s^{-1}$, $r_{mix} = a/q_a$, $\alpha_{e,i}^{PC}$ have to be determined from comparison of calculations with the experiment.

2. ECRH on T-10. The calculated vs measured values of total energy content $W = 3/2\int n(T_e + T_i)dV$ are displayed in Fig.1. We used experimental database described in [2]. The crosses are correspond to OH-regimes, the circles to ECRH one for Δt = 40-50 ms and Δt = =80-100 ms after start of heating with power Q_{EC}= 1.6-1.8 MW. The lines connect the points for the same discharge. The calculations was performed with α_e^{PC}= 0.5, α_i^{PC}= 0.8. The calculated and the measured ion energy contents $W_i = 3/2\int nT_i dV$ are displayed in Fig. 2. Note that ion temperature decreases during ECRH.

3. NBI on TFTR. The experimental [3] (solid lines) and calculated (dashed lines) energy contents as a function of total input power Q_{tot} in L-regime are given in Fig.3. Here α_e^{PC}= 0.3, α_i^{PC}= 0.45. In experiment the density increases with power and current. W_{th} is the thermal part of energy content for I=1.4 MA, $\bar{n}=3.5\times10^{13}\ cm^{-3}$. In the regime with I = 2.2 MA and $\bar{n} = 4.7 \times 10^{13}\ cm^{-3}$ the fraction of hot particles from neutral beam is small.

4. ICRH on JET. The model of "equivalent" tokamak that has the same major radius R and circular cross-section with minor radius $a^* = a\sqrt{k}$, where k=b/a, used to model the elongated JET plasma. The experimental [4] and calculated dependencies of W vs total power Q_{tot} are shown in Fig. 4. In calculations we supposed I = 3 MA, $\bar{n} = 4 \times 10^{13}$ cm^{-3}, or I = 5 MA, $\bar{n}$ = 4 and 5 $\times 10^{13}$cm^{-3} and fitted $\alpha_e^{PC} = 0.2$, $\alpha_i^{PC} = 0.37$.

5. NBI on ASDEX. The experimental [5] and calculated energy content vs plasma current for NBI power Q_{NBI}= 0.4-1.2 MW are shown in Fig. 5. Here we fitted $\alpha_e^{PC} = 0.45$, $\alpha_i^{PC} = 0.75$.

6. TRANSPORT COEFFICIENTS SCALING. The fitted above coefficients $\alpha_{e,i}^{PC}$ are deposited in Fig. 6 as a function of aspect ratio R/a for each device. The best fits are the linear functions:

$$\alpha_i^{PC} = 1.5\ \alpha_e^{PC} = 0.18\ R/a. \qquad (6)$$

After substituting (6) in (4) we have:

$$\Gamma_{e,i}^{PC} = -\varkappa_{e,i}^{PC}\ L_T(T_{e,i}), \qquad (7)$$

$$\varkappa_{e,i}^{PC} = (0.34_e,\ 0.5_i) \times 10^{19} \left[\frac{a}{R}\right]^{0.75} q(a/2)\ q(a)\frac{\sqrt{T_{e,i}(a/4)}\langle n\rangle}{B}, \qquad (8)$$

$T_{e,i}$(keV), n(10^{13} cm^{-3}), B(T), $\varkappa_{e,i}^{PC}$(cm^{-1}s^{-1}). Note, that $\varkappa_{e,i}^{PC}$ is independent on r.

7. PREDICTIONS FOR ITER. The expressions (7)-(8) allow us to perform the calculations for ITER. The results of calculations are very sensitive to deposition profile of heating power. If $P_{aux}^{e,i}$ is located in the central region (r/a < 0.5) then in regime with $\bar{n}$ = = 9 $\times 10^{13}$cm^{-3}, Q_{aux}= 70 MW we have τ_E = 3.6 s, $T_i(0)$ = 16.7 keV, $T_e(0)$ = 21 keV and Lawson criterion is fulfilled: $n\tau_E$= 3.2 $\times 10^{14}$ cm^{-3}s. If $P_{aux}^{e,i}$ has the flat profile then τ_E decreases in 2 times.

REFERENCES

[1] Yu.N.Dnestrovskij, G.V.Pereverzev. Plasma Physics Contr. Fusion 30 (1988) 1417.

[2] Yu.N.Dnestrovskij, et al. Fizika Plasmy, 16, 2 (1990) 216.

[3] D.Johnson., et al. Bul. Amer. Phys. Soc. 32, 9 (1987) 1741.

[4] JET Team. Preprint JET P(88)40.

[5] F.Wagner. Preprint IPP III/131 (1988).

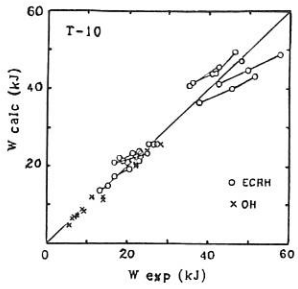

Fig.1

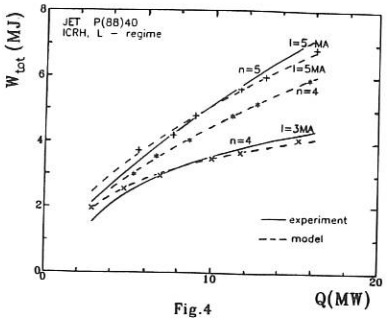

Fig.4

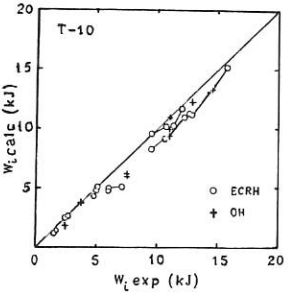

Fig.2

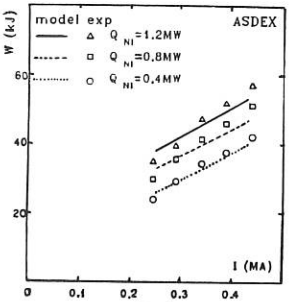

Fig.5

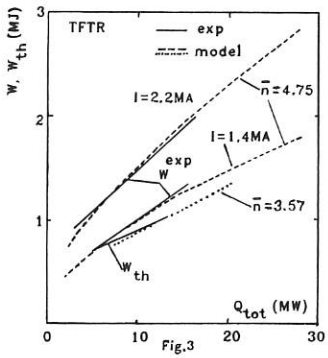

Fig.3

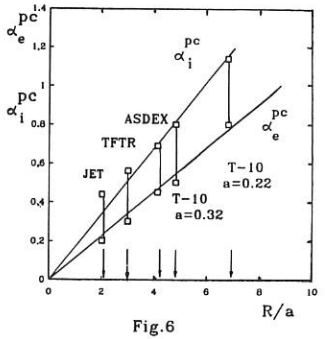

Fig.6

PLASMA PERIPHERY INFLUENCE ON PLASMA CORE CONFINEMENT UNDER AUXILIARY HEATING.

S. I. Krasheninnikov, A. Yu. Dnestrovskii, P. N. Yushmanov

I. V. Kurchatov Institute of Atomic Energy, Moscow, USSR

INTRODUCTION. Simulation of tokamak discharges by the self-consistent description of transport in the main plasma and in the SOL has been done. The values of electron temperature T_s and density n_s are set to be boundary conditions for the main plasma. Using these quantities and transport equations for the main plasma, the heat and particle fluxes Q_s and Γ_s are calculated. They are used by the SOL-model [1]to calculate T_s, n_s and neutral flux Γ_n. In such an approach all the properties of the SOL are reduced to the dependencies T_s, n_s, Γ_n on Q_s and Γ_s. To represent the processes occurring in the SOL the integral zero dimensional relationships, taking into account the main effects on the periphery (neutral ionization, radiation, longitudinal and cross field heat conduction and convective transports), are used.

The self-consistent representation is especially important to describe phenomena having a bifurcational nature, for which a smooth change in one set of parameters results in stepwise jumps in others. For examples, some discharges in T-10 with gas puffing and with the ECRH [2], as well as IDC-operating conditions in JT-60 with the strong radiation in the SOL [3], are considered.

MAIN PLASMA MODEL. The heat conductivity coefficient well-determined in the discharged on T-10, represents by the sum of

$$\chi^{st} = C^{st}\ \varepsilon\ \frac{c^2 \nu_e}{\omega_{pe}^2 qR} \sim \frac{T^{1/2}}{n} \qquad (1)$$

(the transport provided by stochastic diffusion due to drift waves [4]) and

$$\chi^{dce} = C^{dce}\ \frac{\omega_*^2\ \nu_e}{k^2 \omega_{te}^2} \sim \nu_e \rho_e^2\ q^2\ \frac{R^2}{l_n^2} \sim \frac{n}{T^{1/2}} \qquad (2)$$

(the transport provided by the dissipative mode due to passing

electrons [5]) In this expressions $\omega_* = kv_e^2/\omega_c l_n$, v_e is the electron velocity, $\omega_{te} = v_e/qR$, ω_c is the cyclotron frequency $l_n = n/\nabla n$, ρ_e is the electron Larmor radius, ν_e is the electron collision frequency, C^{st} and C^{dce} are the fitting factors of the order of unity. The first of these coefficients represents the plasma core, the second one becomes essential near by the periphery. For matching with heat conduction inside the SOL, which is assumed to be Bohm's one, the total heat conduction is represented:

$$\chi_e = \left[\frac{1}{\chi^{st} + \chi^{dce}} + \frac{1}{D_{\text{Bohm}}} \right]^{-1} \qquad (3)$$

The diffusion coefficient, which mainly determines the intensity of the particle exchange with the SOL, is assumed to be equal to a half of the heat conduction coefficient, $D = \chi_e/2$.

T-10 DENSITY LIMIT DISCHARGE [2]. Let us consider first the discharge behavior in T-10 under gas puffing, when density limit is approached. The trajectory of discharge parameter motion upon the plane (Q_s, Γ_s) is given in Fig.1b, the time evolution of the main parameters determining the periphery behavior is given in Fig.1a. At the Ohmic stage, the discharge places at the point $Q_s \sim 100$kW, $\Gamma_s \sim 2.5\ 10^{21} s^{-1}$ which corresponds to $n_s \sim 5\ 10^{18} m^{-3}$, $T_s \sim 25$eV, which close to the experimental data. After "switching on" the ECRH the energy flux from the plasma, Q_s, starts to rise in time during a time interval of the order of energy confinement time, being stabilized at the level of about 750kW. The gas puffing simultaneous with the ECRH leads to gradual growth of n_s, volume average density $\langle n \rangle$, and Γ_s. Until n_s remains below its critical value corresponding to the $n_s(\Gamma_s)$ dependence saturation, the flux Γ_s rises not very intensively ($\Gamma_s \leq 10^{22} s^{-1}$). The dependencies $n_s(\Gamma_s)$, approaching the critical value, becomes more flat and for further increase in n_s one needs in considerable flux growth.

Thus, when the maximum density is approached, the discharge becomes unstable and rapidly transits into the state with high circulation of particles at the periphery ($\Gamma_s \sim 4\ 10^{22} s^{-1}$)

which is limited by the transport processes in the main plasma. This transition results in a strong rise in radiation losses, periphery cooling, current profile rearrangement and, probably, in the discharge disruption [6].

JT-60 IDC DISCHARGE [3]. Characteristic feature of this IDC regime (I_p=1MA, B_o=4.5T, $\langle n_e \rangle$=(3-4)$10^{19}m^{-3}$, NBI heating power 25MW, $T_e(0)$~6keV, T_s~50-100eV) was a smooth transition to a higher SOL radiation and lower central radiation, accompanied by a slight τ_e increase. Such a regime existence also can be considered as a transition to a regime with higher edge particle flux Γ_s. As one can see from the Fig.1c (the time evolution of the main parameters for JT-60 IDC discharge), this regime corresponds to higher SOL radiation P_r. The transition to the regime with high fluxes is concerned with the saturation of dependence $n_s(\Gamma_s)$ as well as in T-10 case which was discussed above. This effect is demonstrated on Fig.1d (trajectory of the discharge).

CONCLUSIONS. Simulation of T-10 and JT-60 discharges have shown that the developed model gives not only qualitative but quantitative agreement with experimental data. It has been established that the periphery behavior is determined by the transport in the SOL and by that in the edge plasma. We have managed to represent the dynamics of the parameters in the edge plasma for the T-10 discharge under ECRH and under density rise and for JT-60 IDC discharge under NBI heating.

REFERENCES.

1. KRASHENINNIKOV S.I., YUSHMANOV P.N. Self-consistent description of the tokamak plasma periphery for 1.5-D transport modeling. ITER report ITER-IL-PH-13-9-S-6, March 1989.
2. ALIKAEV V.V. et.al. 12th Int. Conf. on Plasma Phys. and Contr. Nuc. Fus. Res. Nice, v.I,p.513,1988.
3. JT-60 team presented by M.NAGAMI 12th Int. Conf. on Plasma Phys. and Contr. Nuc. Fus. Res. Nice, v.I,p.265,1988.
4. W.HORTON,D.-I.CHOI,P.N.YUSHMANOV,V.V.PARAIL Plasma Phys. and Contr. Fus. 29, No 7,(1987)
5. WALTS R.E., DOMINGUES R.R., WONG S.K. 11th Int. Conf. on Plasma Phys.and Contr. Fus. Res. Kyoto, 1986, A-VI-1-3-
6. DRAKE J.F.,KLEVA G.R. Preprint UMLPR 89-039, May 1989.

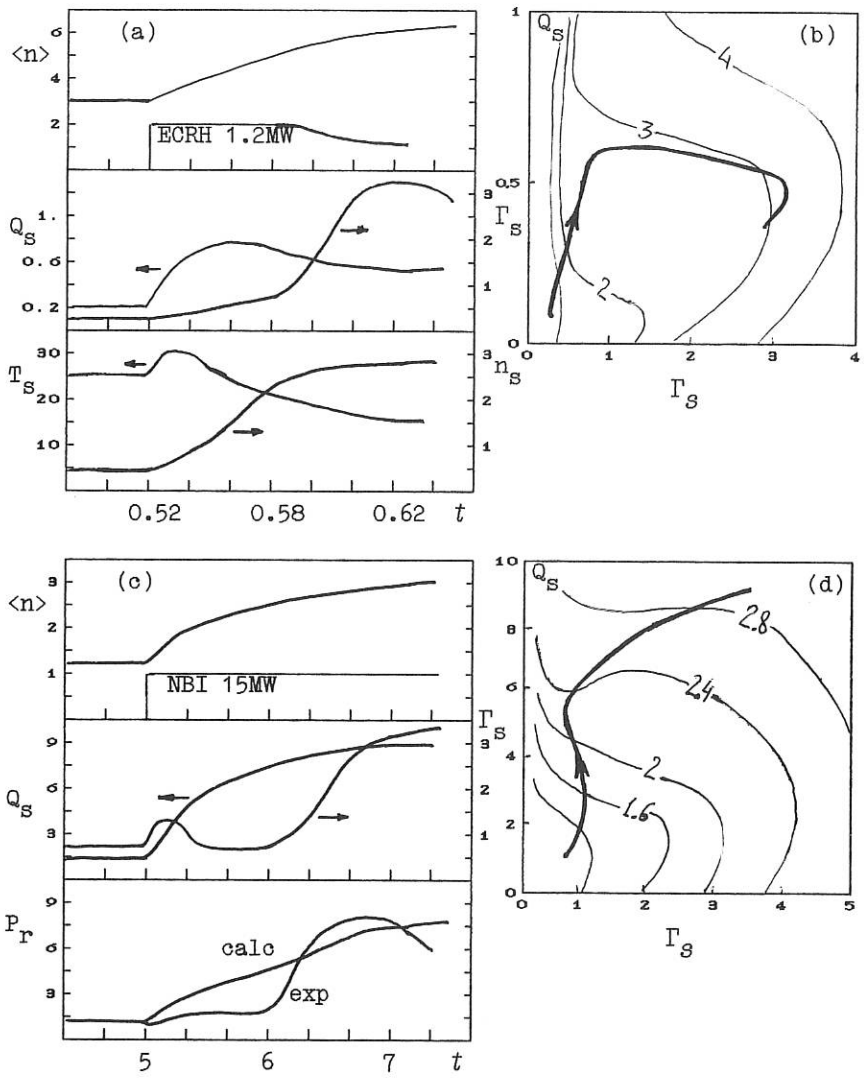

Fig.1.The main parameters of edge plasma for T-10 (a,b) and JT-60 (c,d). (a,c) - time evolution of some parameters. (b,d) - level lines of boundary density n_s, obtained by the model [1]. Thick lines describe the discharge trajectories.
Here P_r,Q_s-MW,Γ_s-$10^{22}s^{-1}$,n_s,<n>-$10^{19}m^{-3}$,T_s-eV,t-s.

CURRENT DENSITY AND ENERGY TRANSPORT IN HIGH TEMPERATURE PLASMAS

B. Coppi and F. Pegoraro
Massachusetts Institute of Technology, Cambridge, Mass. USA
Scuola Normale Superiore di Pisa, Italy

The relationship between the steady state current density and electron temperature profiles is considered for high plasma temperature regimes. A formalism is adopted in which gradients of both the electron temperature and plasma current density determine the electron heat flux in the energy balance equation, while diffusion-like terms in both the temperature and the plasma current appear in the electron longitudinal momentum balance equation. Proper constraints on the resulting matrix diffusion equation are formulated on the basis of symmetry properties and of realistic radial profiles.

Understanding the mechanisms that, in a high temperature toroidal plasma determine the stationary (time asymptotic) form of the profile of the plasma current density is important as it provides a reference case on which to evaluate the ohmic power density produced in a given experiment by the plasma current. It is equally needed when predictions are sought on the plasma stability against global (resistive) MHD modes whose excitation depends on the current density distribution. Furthermore a growing body of experimental information on the current density profiles is presently becoming available.

A starting point for the present analysis is the observation that in a high temperature toroidal plasma, magnetically trapped electrons affect the plasma resistivity in such a way as to cause a current density distribution with a cusp at the magnetic axis in the case of the well behaved ("canonical") temperature profiles that are observed under stationary conditions. Such a spatial feature seems unlikely to occur in real experiments, although presently available current profile determinations would not be sufficiently accurate to resolve it. On the other hand it is generally thought that the time scale for the *global* momentum transfer from electrons to ions is consistent in present experiments with the estimates based on neoclassical resistivity.

We propose that the temperature and current profiles are determined by a system of two coupled diffusion equations which generalise the electron thermal balance equation and ohm's law. This model is based on the assumption of common microscopic anomalous machanisms that link the temperature and current transport, and which are subject to a global constraint such that, under stationary conditions, the current and temperature profiles do not differ significantly form the "canonical" one that would be realised in ohmic discharges in the absence of neoclassical modifications of the resistivity. Not explicitly included in this formulation are the effects of global resistive modes with low toroidal mode numbers, such as in particular the temperature relaxations that are associated to the onset of the m=1, n=1 instability. In a

toroidal plasma this instability is driven by the plasma pressure gradient and can be expected to lead mainly to a rearrangement of the central pressure profile. As higher plasma temperature regimes are reached, the microscopic plasma properties become important and, in combination with the contribution of a minority population of energetic particles such as fusion produced α–particles, may retard the onset and reduce the growth rate of the m=1, n=1 instability and eventually suppress it. These effects are not expected to count for the m=1, n=2 instability so that 1/2 can be taken as a "hard " lower bound on the value of the winding parameter q on the magnetic axis, thus providing an additional constraint on the maximum value of the current density.

In particular we adopt the following set of transport equations [1] to be applied to steady state ohmic plasmas:

$$EJ = -\nabla\cdot\left\{\kappa\nabla T-(\alpha-1)LJ\left[\nabla J-\alpha\left(\frac{J}{T}\right)\nabla T\right]\right\}\ , \tag{1}$$

$$E-\eta J = -\nabla\cdot\left\{L\left[\nabla J-\alpha\left(\frac{J}{T}\right)\nabla T\right]\right\}\ , \tag{2}$$

where E is the toroidal electric field, J is the toroidal current, T is the electron temperature, κ is the (anomalous) electron thermal conductivity and L is a thermal-viscous diffusion coefficient acting both on the temperature and the current density gradients. In writing Eqs (1) and (2) we have been guided by the following arguments:

i) the additional diffusive terms in ohm's law have been related in such a way that, if the parameter α is chosen equal to 3/2, their contribution vanishes identically in the limit where the resistivity η reduces to its Spitzer form and $J\propto T^{3/2}$.

ii) the additional terms in the energy balance equations have been chosen so that the system (1), (2) exhibits Onsager-type symmetry relations when the energy equation is expressed in terms of the entropy production. This is apparent when the system (1), (2) is rewritten in the matrix form

$$-\nabla\left[\cdot\begin{vmatrix}\frac{\kappa}{T}+\frac{\alpha^2LJ^2}{T^2} & -\frac{\alpha LJ}{T}\\ -\frac{\alpha LJ}{T} & L\end{vmatrix}\nabla\begin{vmatrix}T\\ J\end{vmatrix}\right]=\begin{vmatrix}\frac{\eta J^2}{T}+\kappa\left(\frac{\nabla T}{T}\right)^2+\left(\frac{LJ^2}{T}\right)\left[\left(\frac{\nabla J}{J}\right)-\alpha\left(\frac{\nabla T}{T}\right)\right]^2\\ E-\eta J\end{vmatrix} \tag{3}$$

Again, if $J\propto T^{3/2}$ and α=3/2 , the contribution of the additional terms in the energy equation vanishes identically Further we assume that the microscopic processes and the global constraints that shape the temperature profile are related to those that cause the diffusive terms in ohm's law. We express this assumption through the relationship

$$\frac{LJ^2}{T} = \frac{\lambda}{\alpha(\alpha-1)}\,\kappa = \frac{\hat{\lambda}E}{\alpha(\alpha-1)E^*}\,\kappa \quad , \tag{4}$$

where the constant λ is chosen to be proportional to the ratio between the applied electric field and a reference field E^*. The latter is assumed to be determined by the microscopic processes that cause the anomalous electron energy transport. Assumption (4) allows us to obtain from Eqn (2) a direct relationship between the temperature and the current profiles

$$\lambda\left[\frac{\alpha}{T}\frac{dT}{dx} - \frac{1}{J}\frac{dJ}{dx}\right] = -\alpha\left[\frac{1}{T}\frac{dT}{dx} + \frac{E\int_0^x J(x')\,dx'}{T\hat{\kappa}x}\right] , \tag{5}$$

where, for the sake of simplicity, we are referring to a large aspect ratio toroidal configuration with circular cross section, $x \equiv r^2/a^2$, with a the plasma minor radius, and $\hat{\kappa} = 4\kappa/a^2$. Furthermore, we assume that the anomalous thermal conductivity κ has a CMG functional dependence [2] of the type

$$\kappa \propto \frac{E^*}{Tx}\int_0^x J(x')\,dx' \quad . \tag{6}$$

Then the second term on the right of (5) reduces to a constant, which we denote by $\alpha_T = \hat{\alpha}_T E/E^*$, while from (5) we derive the parametrization

$$\hat{T} = F(x)\exp\left(-\alpha_T x\right), \quad \hat{J} = H(x)\exp\left(-\alpha_j x\right) \quad , \tag{7}$$

where $\alpha_j \equiv \alpha\,\alpha_T$, $\hat{T} = T/T_0$, $\hat{J} = J/J_0$, $F(0) = H(0) = 1$, and

$$H(x) = F(x)^{\alpha(1+1/\lambda)} \quad . \tag{8}$$

The functions F and H describe the profile modifications introduced, in the considered stationary ohmic plasma regime, by the neoclassical corrections to the electrical resistivity and reduce to unity for $\eta = \eta_{sp}$, where η_{sp} is Spitzer's resistivity. They are determined by the integrodifferential equation which is obtained from Eqn (2)

$$\frac{1}{H}\frac{dH}{dx} = -\alpha_j(\alpha-1)\left(1+\frac{1}{\lambda}\right)\left[\frac{1}{G}\frac{dG}{dx}\right]\int_0^x\left(1-\frac{\eta J}{E}\right)dx \ , \qquad (9)$$

where $G(x) \equiv \int_0^x \exp\left(-\alpha_j x'\right) H(x')\, dx'$, with the global condition

$$\int_0^1 (E-\eta J)\, dx = 0 \ . \qquad (10)$$

In Eqs (9) and (10) the term ηJ is to be expressed in the form

$$\frac{\eta J}{E} = \left(\frac{E_{sp}}{E}\right)\Sigma(x)\, H^{1/(1+\lambda)} \ , \qquad (11)$$

where $E_{sp} \equiv \eta_{sp}(T_0)\, J_0$, and $\Sigma(x)$ is the neoclassical trapping factor such that $\eta = \eta_{sp}\,\Sigma(x)$. Condition (10) determines the value of the ratio between E and the reference Spitzer's field E_{sp}, that is compatible with the envisaged stationary regime, and can be expressed as the additional boundary condition $\left[\left(\frac{1}{G}\frac{dG}{dx}\right)^{-1}\left(\frac{1}{H}\frac{dH}{dx}\right)\right]_{x=1} = 0$. It ensures that, on average, the relationship between the electric field and the plasma current is determined by the neoclassical resistivity, as is consistent with the observation on the global current time scale made at the beginning.

Numerical solutions of Eqn (9) are presently being investigated.

In the presence of sources of additional heating, we conjecture that the constraints which we have imposed on the transport matrix in Eqn (3), and which reflect the intrinsic relationship between the heating source and the current which confines the plasma, are violated. We express the degradation of the electron energy transport in the presence of additional heating in terms of a new contribution κ' which is added to the ohmic thermal conductivity κ. This new contribution has no counterpart in the generalised ohm's law, and is taken to have a form dictated by the relevant microinstabilities [3]. This additional transport coefficient, together with the simultaneous reduction of the electric field, tends to decouple the thermal energy transport from that of the current.

REFERENCES

[1] B. Coppi and F. Pegoraro, MIT/RLE Report PTP-90/2 (Cambridge, MA, 1990)

[2] B. Coppi, Phys. Letters **128**, 193 (1988)

[3] B. Coppi, Comm. Plasma Phys. Cont. Fus. **12**, 319 (1989)

UNIFIED PHYSICAL SCALING LAWS FOR TOKAMAK CONFINEMENT

J.P. Christiansen, J.G. Cordey, O. Kardaun*, K. Thomsen

JET Joint Undertaking, Abingdon, Oxfordshire, OX14 3EA, England.
*IPP Garching, BRD.

1. Introduction The scaling of plasma energy confinement in JET has been studied in a recent paper [1]. The form of the scaling expressions used in the study satisfy the constraints imposed by a particular theoretical model of thermal transport. It was shown that both the JET L and H-mode data satisfy the constraints of the short wavelength gyro kinetic model. In this paper we extend the study in [1] by using data from the ITER L-mode data base and we also consider other theoretical transport models.

The ITER data base will be fitted to an expression for the thermal energy confinement time of the form,

$$\tau_E = (\tau_{model})^x \, g \qquad (1)$$

in which x denotes an exponent which, for a model that describes the data well, will be unity. The function g will be represented in this paper by

$$g = \nu_*^{x1} \, \beta^{x2} \, q^{x3} \, \varepsilon^{x4} \, \kappa^{x5} \, A^{x6} \qquad (2)$$

where the arguments, defined below, are dimensionless variables.

An alternative approach, often pursued, is to use a power law scaling for τ_E in the form

$$\tau_E = C \, a^{y1} \, \kappa^{y2} \, \varepsilon^{y3} \, n^{y4} \, I^{y5} \, P^{y6} \, q^{y7} \, A^{y8} \qquad (3)$$

where the "engineering" variables are minor radius a, elongation κ, density n, current I, power P, safety factor q, aspect ratio $\varepsilon = a/R$, atomic mass A. We will show though that just as a good fit can be obtained with the more physical form Eq. (1) - (2) which contains less free parameters.

In section 2 we describe the selection of the ITER L-mode data, in section 3 formulas for τ_{model} and the parameters of g are presented.

2. The ITER L-mode data The ITER L-mode data base contains 1431 sets of data from JET, TRTR, IT60, DIII-D and JFT2. We restrict our data analysis to NBI heated plasmas labelled "L" and this eliminates 457 data sets half of which are TFTR supershots, the other half being ECRH, ICRH, or LH plasmas. In addition, to only include shots with an accurate thermal energy content $W = W_{total} - W_f$ we apply the following condition

$$W_f / W_{total} < \frac{1}{3} \qquad (4)$$

where W_f is the fast ion energy content and W_{total} the total energy determined from MHD fits. The fast ion energy is calculated from

$$W_f = P_{abs}\,\tau_s/2, \quad \tau_s = \frac{1}{3}\,0.117\,\frac{T^{3/2}A_b}{n}\log\left(1 + \left(\frac{E_b}{E_c}\right)^{3/2}\right) \qquad (5)$$

P_{abs} is the absorbed NBI power and in the expression for the slowing down time τ_s the average temperature T is in keV, density n in units of 10^{19} m^{-3}; A_b is the beam atomic mass, E_b the beam energy in keV and the critical energy is $E_c = 14.8\ T\ A_b / A^{2/3}$. The average temperature T is not generally available in the data base and it is therefore defined as

$$T = W_{total} / (2.1\ V\ e\ n) \qquad (6)$$

The factor 2.1 arises from a fit to existing data on T. The restriction [4] yields 680 obserations distributed as follows:- 353 (JET), 67 (TFTR), 209 (JT60), 5 (DIII-D) and 46 (JFT 2).

3. Confinement models The following theoretical models for τ_E are considered; short and long wavelength gyro-kinetic turbulence model denoted by τ_{ES}, τ_{EL} respectively, ideal MHD τ_{EI}, resistive MHD τ_{ER} [2]. The leading terms are expressed as follows (a numerical constant C' is dropped)

$$\tau_{ES} \sim a\, I^{4/5} \left(\frac{aknR}{P}\right)^{3/5} \left(\frac{q}{\varepsilon^3}\right)^{2/5} A^{-1/5}$$

$$\tau_{EL} \sim a\, I^{1/2} \left(\frac{aknR}{P}\right)^{1/2} \varepsilon^{1/2} \qquad (7)$$

$$\tau_{EI} \sim \tau_{ER} \sim I^{-1}\, n^{1/2}\, a^2\, A^{1/2}$$

For τ_{EI} $x1 \equiv 0$ in g and for τ_{ER} the collisionality is $\nu_* \rho^2 / a^2$.

Each variable used in the fit is standardised as follows

$$\log n \rightarrow \log n - \log \bar{n}\ , \quad \log \bar{n} = \frac{1}{N} \sum \log n_j$$

In Fig. 1-3 the results are displayed in these standardised variables.

An extensive series of regression analyses have been carried out, for each Tokamak individually and for the data as a whole. The results from the latter ones for the scaling with the leading term in Eq. (1), i.e. the exponent x, is 1.1,

1.45, 1.3, 1.7 for τ_{ES}, τ_{EL}, τ_{ER}, τ_{Ei} resp. The r.m.s. errors in the fits in % are respectively 4.4, 4.1, 12, 17. Thus only the short wavelength gyrokinetic turbulence scaling provides a good fit to the data and this is shown in Figure 1. An essential feature of Eq. (1) is that the leading term by definition must explain the major variation in the τ_E data. We illustrate the contrast between models in Figure 2 which shows τ_{ER} versus τ_{ES}. The variation by a factor 40 of τ_E in the ITER data can be explained by τ_{ES} but not by τ_{ER} or τ_{EI}. A fit to the "engineering" expression (4) gives an r.m.s. error of 4%, i.e., marginally better than that of τ_{ES}. However, all 8 parameters are needed. It is a nice feature that this fit can be already described by the short wavelength leading term. We emphasize this point, since the selected ITER data exhibits some collinearity in ν_*, and β as is shown in Figure 3. Thus the best and simplest fit and physically most plausible description of the data is in our opinion offered by

$$\tau_E \text{ (ITER L-mode)} = \tau_{ES}\, \nu_*^{-0.13}\, \frac{\kappa A^{1/2}}{\varepsilon} \qquad (8)$$

This expression has <u>one</u> free parameter only rather than the 8 parameters of Eq. 3. The r.m.s. error of (8) is only 4.7%. Presently we have no physical argument explaining the geometric term in (8).

Expression (8) can be used to predict the energy confinement time in ITER or any other reactor device. A better approach though which avoids making a particular choice of the functional form for g is the similarity method [1]. In this technique the data is grouped in ν^*, β and q and then displayed versus the leading term of the theoretical model of interest. In Fig. 4 this is done for the short wavelength gyro-kinetic model, the grouping of the data into parallel lines with a slope close to unity for each range of ν^*, indicates that the model is a good representation of the ITER data base. By choosing a particular discharge from Fig. 4 with the same ν^*, β and q as in ITER one can then by using Eq. (1) accurately predict the energy confinement.

4. <u>Conclusion</u> It has been shown that the ITER L-mode data base can be fitted to a physically meaningfull scaling law which satisfies the constraints of the short wavelength gyro-kinetic model.

<u>References</u>

[1] Christiansen, J.P., Cordey, J.G., Thomsen, K., A unified physical scaling low for Tokamak confinement. To appear in Nucl. Fusion.

[2] Connor, J.W., Plasma Physics and Controlled Fusion <u>30</u> 619 (1988).

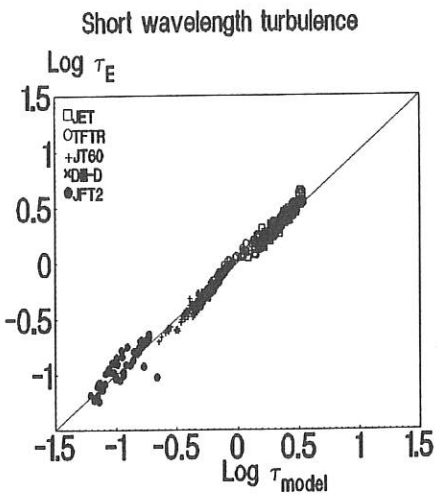

FIG. 1. ITER L-mode data fitted to the short wavelength scaling including collisionality, beta, safety factor, aspect ratio, elongation and mass number.

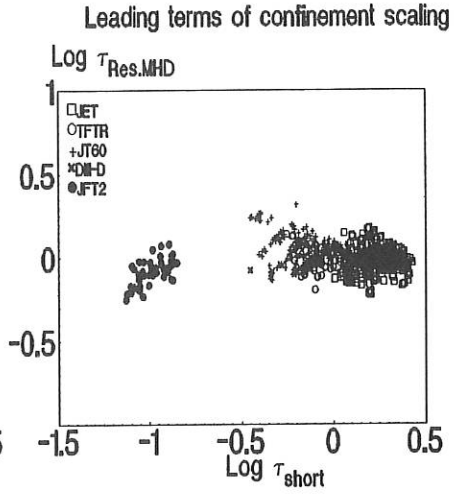

FIG. 2. The leading term of resistive MHD does not span the data range of the ITER L-mode data base. That of the short wavelength turbulence scaling does.

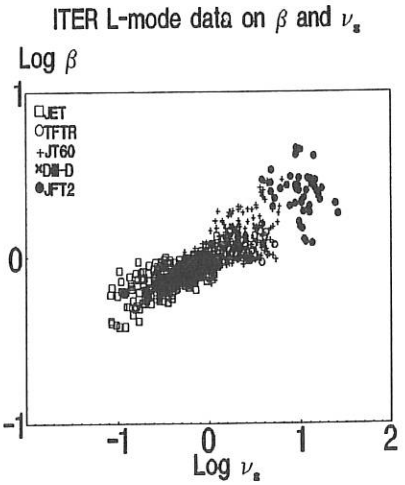

FIG. 3. There is some correlation between the plasma beta and the normalised collisionality in the ITER L-mode data set.

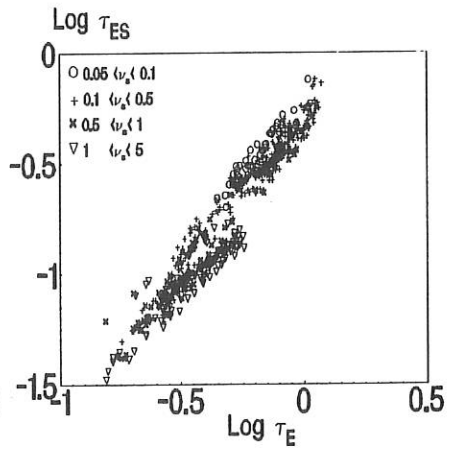

FIG. 4. The main variation in the ITER L-mode confinement data can be explained by the short wavelength turbulence scaling. Data points are marked by collisionality and selected with β<0.5

ASSESSMENT OF TRANSPORT MODELS ON THE BASIS OF JET OHMIC AND L-MODE DISCHARGES

G. Corrigan, D.F. Düchs, A. Nocentini*, Ch. Sack, E. Springmann, T.E. Stringer, A. Taroni, F. Tibone

JET Joint Undertaking, Abingdon, Oxon., OX14 3EA, UK
*NET Team, Garching, FRG

1. Introduction

Transport codes for the prediction of performance of next step tokamak devices require "complete" transport models. This means that such models must represent the local plasma properties from core to boundary in the ignition relevant regimes for a given device. However, most transport models derived from theory are known not to be valid in the external region of tokamak plasmas and in many cases also in the plasma core, where sawtooth activity often masks local transport effects.

For this reason, the existing models have to be completed by adding empirical prescriptions, and need to be tested against experimental results. In particular, it is important to clarify the role and relative importance of theoretical and empirical assumptions in a model.

This kind of analysis is being carried out at JET for various models. We report here on the results obtained for those models the main empirical assumption of which is "Profile Consistency" (PC in the following [1-3]). We refer to ohmic and L-mode regimes, which are the only ones getting close to steady state conditions, for which PC has been introduced.

2. The Models

It has been observed in many tokamak devices that the electron temperature profile in quasi-steady state condition of ohmic and centrally heated discharges is usually well represented, outside the sawtooth region, by an exponential of the form:

$$T_e = T_{ea} e^{\alpha(1-\rho^\beta)} \qquad (1)$$

Here ρ is a flux coordinate ($\rho \propto \sqrt{\phi}$, ϕ being the toroidal flux) normalised at a, the plasma boundary. In JET, for example, one finds $\alpha = 2.8$ ($\pm$ 15%), $\beta = 1.5$-2 without any clear relationship between these parameters and physical quantities such as q_a, the value of the safety factor at the plasma boundary. The central idea of PC related transport models is to use Eq. (1) to derive a profile form factor in an expression of the thermal conductivity χ_e (defining the heat flux $q_e = -n_e \chi_e \nabla T_e$) that implies steady state temperature profiles given by Eq. (1). The model of χ_e is completed by a scaling law for T_{ea} or, equivalently, if sawtooth activity is not too important, for any of these quantities: the central value T_{eo}, the volume average value $\langle T_e \rangle$, the electron energy content W_e or, in the case of ohmic discharges, the loop voltage V_L. Any theoretical consideration is restricted to the derivation of a scaling law, the form factor in χ_e being entirely empirical and theoretically unjustified. The general form of such χ_e is, in flux surface coordinates:

$$\chi_e^{PC} = \frac{\int_o^{V(\rho)} (P_{in}^e - P_{out}^e) dV}{\alpha\beta\rho^{\beta-1} n_e T_{ea} e^{\alpha(1-\rho^\beta)} \langle |\nabla\rho|^2 \rangle \frac{dV}{d\rho}} \qquad (2)$$

Here $V(\rho)$ is the volume inside ρ, P_{in}^{e} and P_{out}^{e} are the source and loss terms in the electron energy balance equation and $< >$ is a flux surface average.

From Eq(2) various forms of χ_e^{PC} are obtained by: the possible replacement of $T_{ea}e^{\alpha(1-\rho^{\beta})}$ by T_e; different choices of the scaling law determining the absolute value of T_e; different choices of α and β.

Deviations from strict PC are introduced by dropping terms in (P_{in}^{e} - P_{out}^{e}) and/or models of sawtooth activity and different models of q_e in the boundary region.

The Tang-Redi (T-R) model of χ_e [2] is obtained from Eq(2) with: $\alpha=2/3(q_a + 0.5)$, $\beta=2$. The scaling of T_{eo} is obtained, with some approximations, from the theory of transport based on microinstabilities related to trapped electron modes. In [2] exactly the same procedure is used also to derive an expression of χ_i assuming the same shape for T_i and T_e.

The Coppi-Mazzucato-Gruber (CMG) model in its most recent form [4], intended to cover ohmic and L-mode discharges, is obtained from Eq(2) with: $\beta = 2$, T_e in place of $T_{ea}e^{\alpha(1-\rho^{\beta})}$ and replacing the numerator by I_pV_L*:

$$V_L^* = \alpha_v \bar{n}^{1/5} R/a \left[1+\gamma <\beta_p> \left(P_{in} - P_{OH}\right)^2 / P_{in}^2\right] \qquad (3)$$

Here γ is a constant (≈ 9 for L-modes), $<\beta_p>$ is the average value of the poloidal β on the plasma cross-section, P_{in} and P_{OH} are the total plasma input power and the ohmic input power. V_L* reduces to V_L in ohmic discharges. In the ohmic case PC is obtained by neglecting the ohmic radiation losses, but it can be shown that while α_v/α is prescribed, the separate values of α_v and α depend on the boundary condition T_{ea}. This implies that results are sensitive to the choice of T_{ea} or, equivalently, to the transport model assumed for the boundary region. PC may be strongly violated when non-ohmic heating is present.

3. Comparison With Experimental Result

It is clear from the discussion in the previous section that empirical assumptions play a very important role in any PC related model such as the CMG and T-R models. In particular, their use in time dependent simulations is expected to lead to reasonable results only if the time scale of the evolution of T_e is comparable or longer than τ_E, the energy confinement time. In order to check the range of validity of such models we have carried out extensive tests against experimental findings for a variety of ohmically and additionally heated JET discharges. For the CMG and T-R model the results of our tests are summarised in the following. The scaling (3) of V_L with constant α_v is not found in JET (Fig. 1). Nevertheless JET ohmic discharges are generally well simulated (see e.g. Fig. 3) by the CMG model if α_v/α is increased by about 40% with respect to the value given in [5] and T_{ea} is taken in agreement with experimental observations. In addition $\chi_i \geq \chi_e$ has to be assumed. The model fails to simulate non-ohmic centrally heated discharges (see Fig. 4): the allowed deviation from PC is too strong.

JET low current (1MA) discharges indicate that the q_a dependence assumed for α in the T-R model is too strong. At 3 and 5MA the model is usually somewhat optimistic, leading to a total energy content 20-50% in excess of the observed one. The numerical values of χ_i and χ_e are usually very close. One would expect larger values of χ_i when the η_i modes (on which the theoretical part of χ_i is based) are destabilised. The T-R model, however, contains an arbitrary empirical reduction in the theoretically expected χ_i [5]. An example of application of the model in comparison to measurements of a typical 5MA JET discharge is given in Figs. 3-5.

These results show that the validity of the CMG and the T-R models as predictive tools is rather questionable. However, we find that the combination of a PC shape factor and a scaling

law, working for a wide range of tokamak parameters such as the one proposed in [6], may produce an effective χ_e that "works" in transport codes on the same range of devices as suggested in [2] (see e.g. PC + Lackner-Gottardi scaling (PCLG) in Figs. 3-5). This latter version of PC allows transport code studies of other aspects of transport, such as ion energy and particle transport in slow transients. It can also be used for predictive studies, provided these are confined to slowly evolving situations and to the assessment of the sensitivity of results against the assumptions in the adopted model.

References

[1] Coppi, B. and Mazzucato, E., Phys. Lett. 71A, 337 (1979)
[2] Redi, M.H. et al., Nucl. Fus., 27, 2001 (1987)
[3] Taroni, A. and Tibone, F., Proc. of the 13th EPS Conference, Schliersee, 1986, Vol. I, p. 160; see also: Düchs, D.F. et al., II European Theory Meeting, Varenna, 7-9 Dec. 1987
[4] Englade, R.C., Nucl. Fus., 29, 999 (1989)
[5] Stringer, T.E. and Tibone, F., private communication
[6] Lackner, K. and Gottardi, N., JET-P(88)77
[7] Rebut, P.H. et al., (Proc. 12th Int. Conf., Nice, 1988). Paper IAEA-CN-50/D-4-1, IAEA, Vienna

Figure Captions

Fig. 1 Measured ohmic loop voltage vs loop voltage from CMG model (see Eq(3)) for three different plasma currents: x: 1MA; o: 3MA; $\overline{V}$: 5MA

Fig. 2 $|\nabla T_e/T_e|$ from ECE profiles at $\rho = 0.7$ vs $2\alpha\ (T-R)\rho/a$, $\alpha(T\text{-}R) = 2/3(q_a + 0.5)$ for the same currents as in Fig. 1

Fig. 3 Comparison of calculated and measured electron and ion temperature profiles vs normalised ρ at the end of the ohmic phase; $I_p = 5.1$MA, $B_T = 3.1$T. As a reference for a non-PC model the temperature profiles resulting from the Rebut-Lallia model (R-L) [7] are shown as well.

Fig. 4 Same as Fig. 3 but end of the additional heated phase; $P_{NBI} = 6.3$MW, $P_{RF} = 5.1$MW

Fig. 5 Comparison of calculated and measured total energy content vs time between the end of the ohmic and the end of the additional heated phase.

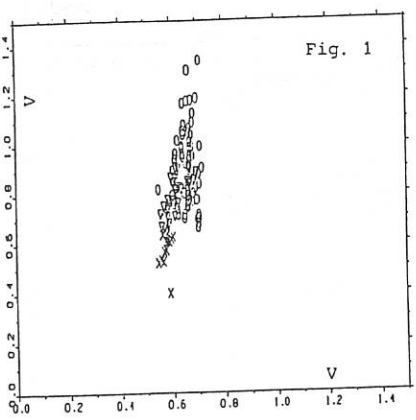

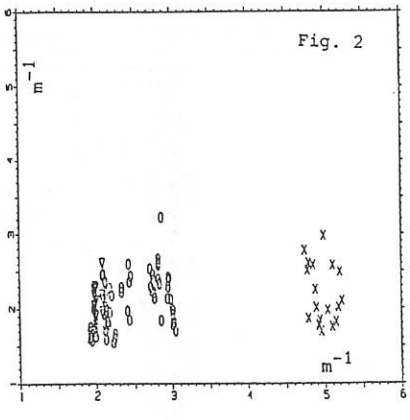

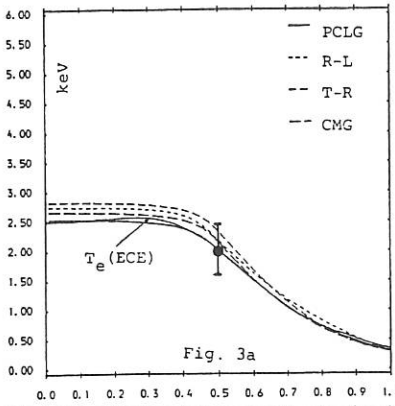

Fig. 3a

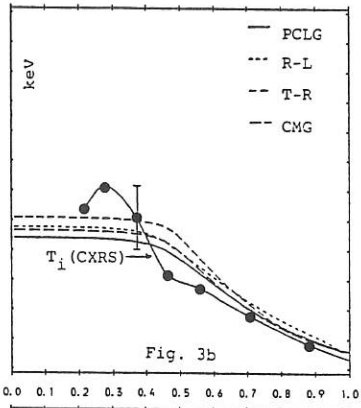

Fig. 3b

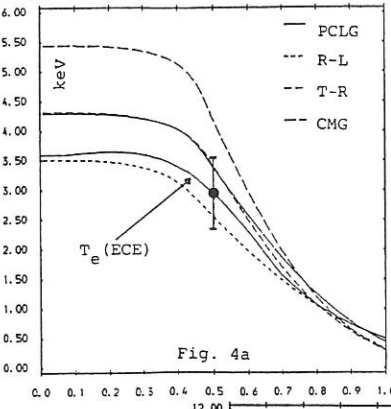

Fig. 4a

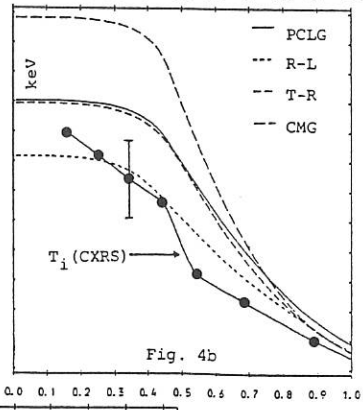

Fig. 4b

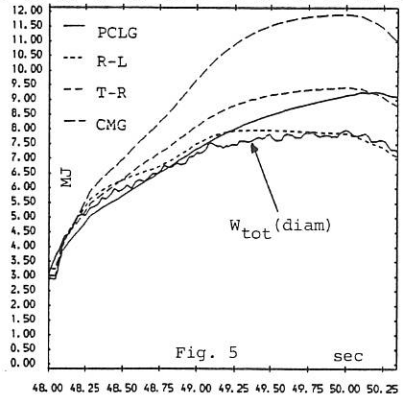

Fig. 5

A QUANTITATIVE ASSESSMENT OF ∇T_i - DRIVEN TURBULENCE THEORY BASED ON JET EXPERIMENTAL DATA

F Tibone, G Corrigan and T E Stringer

JET Joint Undertaking, Culham OX14 3EA, U.K.

Introduction

The discovery of a "pellet-enhanced" confinement regime in JET experiments [1] has revived interest in the theory of ∇T_i -driven turbulence (*ITGDT*) as a candidate for the explanation of anomalous transport in tokamaks.

The apparent improvement in central energy confinement following pellet injection qualitatively agrees with the theoretical prediction of a correlation between density profile peaking and reduced anomalous energy transport.

However the expectation that, in the absence of density peaking, ∇T_i -driven modes can account for the observed anomalous transport has not been confirmed. Comparisons with early JET data [2] showed large discrepancies with theoretical prediction. A systematic investigation, based on a more complete set of measurements, is now possible.

In this paper we aim for a quantitative assessment of the capability of existing models based on *ITGDT* theory to reproduce the level of anomalous transport observed in JET. To this end, we compare theoretically predicted heat fluxes with those inferred from measured data (taking into account the uncertainties in both) for representative L-mode plasmas in a variety of conditions.

Experimental data

We consider a database of 35 L-mode plasmas with a plasma current of 3 MA, for which spatially resolved measurements of the electron density (from *LIDAR* Thomson scattering) and of the ion temperature (from charge-exchange recombination spectroscopy) are available.

All these plasmas are in quasi-steady-state conditions: in particular, $dW/dt \lesssim 0.2\, P_{TOT}$ (W being the total stored energy, with P_{TOT} the power input) and sawtooth effects are absent, *ie* the time slices considered belong either to a "monster sawtooth", or to the saturated phase of ordinary sawteeth. Thus the measured profile shapes can be regarded as determined by transport effects only.

The additional heating scheme varies from dominant *ICRH* for monster sawteeth to exclusive *NBI* heating for plasmas in the so-called "hot-ion" regime (central ion temperature T_{io} significantly larger than the peak electron temperature T_{eo}). The total auxiliary power varies between 2 and 20 MW.

With the volume-averaged electron density ranging between 0.7 and 4.0 (in units of $10^{19} m^{-3}$), a variation in T_{io} from 3 to 16 keV is explored. The electron density profile is never significantly more peaked than parabolic, which is typical of JET L-modes fuelled by edge recycling and neutral beam injection.

Comparison between theory and experiment

Various quasilinear estimates of the anomalous ion energy transport due to the excitation of ∇T_i -driven modes are available in the literature. We have performed detailed comparisons using the formulations of Lee and Diamond [3] (with Connor's [4] correction for large L_n), Mattor [5] and Romanelli [6]:

$$\chi_\eta(\eta > 1) = \chi_\eta^{LD} \simeq \frac{(1+\eta)^2 \, v_{ti} \, \rho_i^{\,2}}{2 \, L_s \, \tau^{1/2}} \quad , \quad \text{but} \quad \chi_\eta(L_n \gtrsim \sqrt{L_s L_{T_i}}) = \chi_\eta^{C} \simeq \frac{v_{ti} \, \rho_i^{\,2} \, \tau^{3/4}}{L_s^{\,1/4} \, L_{T_i}^{\,3/4}} \quad ;$$

$$\chi_\eta^{M} \simeq 0.03 \left(\frac{L_s}{L_{T_i}} \right)^2 \frac{v_{ti} \, \rho_i^{\,2}}{L_{T_i}} \, \frac{\tau^3}{(1+\tau)^{3/2}} \left[1 - \frac{\eta_{cr}}{\eta} \right]^3 \qquad \text{with} \qquad \eta_{cr} \simeq 1.2 \quad ;$$

$$\chi_\eta^{R} \simeq \frac{3 \, v_{ti} \, \rho_i^{\,2}}{(R L_{T_i})^{1/2}} \left[1 - \frac{\eta_{cr}}{\eta} \right]^{1/2} \qquad \text{with} \qquad \eta_{cr} = 0.5 + \left[0.5 \, , \; 2.5 \, \frac{L_n}{R} \right]_{\max} .$$

Here v_{ti} and ρ_i are ion thermal velocity and gyroradius, $\tau \equiv T_e / T_i$ and R is the plasma major radius. η_{cr} is the threshold value above which the transition from neoclassical to turbulent transport takes place.

These anomalous thermal conductivities have different functional dependences on the plasma parameters, but their magnitude is similar for typical JET regimes, when all uncertainties are taken into account. Concerning their radial variation, the common $T_i^{3/2}$ dependence is at least in part compensated by the radial decrease of L_{T_i} and L_s.

An important difference between the models lies in the predicted behaviour for vanishing density gradients: according to Connor and Mattor, the transport will saturate at a level determined only by L_{T_i}; for Romanelli, the instability might be suppressed even in the limit $\nabla n \to 0$.

In practice, however, we find that the JET profiles correspond to values of η well in excess of the theoretical threshold, even when the L_n-dependence of η_{cr} predicted by Romanelli is taken into account (Figure 2). The degree of departure from marginal stability also appears to be independent from the temperature ratio τ. A comparison of the predicted ion heat flux induced by strongly turbulent transport with the observed total flux (upper bound on the actual ion transport) is illustrated in Figure 3.

While there is no definite inconsistency between theory and experiment in low-temperature plasmas, the predicted transport is clearly too strong for high-T_i regimes. Given that the departure from marginal stability is rather uniform in all cases, this result may be interpreted as questioning the theoretical prediction of a $T^{3/2}$-dependence of the turbulent thermal conductivity. Figure 3 was obtained using Romanelli's formulation, but analogous results are obtained with the other models, with larger "error bars" due to the additional uncertainty in L_s.

If the ∇T_i -driven transport is an overestimate in the hot core of the plasma, in the cool outer region it generally accounts for only a minor part of the observed heat flux, indicating that other transport mechanisms should be dominant there. In the outer plasma, however, the effect of experimental uncertainties tends to become overwhelming, and this often makes a proper quantitative assessment impossible.

Analysis technique

We use the methods of interpretive transport analysis to infer local "experimental" heat fluxes $q^{EXP}(\rho)$ from the measured plasma profiles and from physics modelling assumptions (*eg* for the evaluation of power deposition profiles). These are then compared with the local ion heat fluxes $q_i^{THEORY}(\rho) = -n_i \chi_\eta \nabla T_i$ predicted by various versions of *ITGDT* theory.

Ideally, the comparison should involve the measured *ion* heat flux. This is, however, generally difficult to determine because of large uncertainties in the separation of the local electron and ion power balances.

Instead, we shall consider the total $(e + i)$ local heat flux, which can typically be determined to an accuracy of $\pm$ 20 %, and check what part of it can be accounted for by the predictions of *ITGDT* theory.

Since q_i^{THEORY} is a sensitive function of the plasma parameters and their gradients, and is evaluated using experimental data, estimating the uncertainties associated with the predicted fluxes is an important part of the assessment.

We construct density and temperature profiles by least-squares fitting the measured radial points with a polynomial form with three fitting parameters. The experimental error bars are then propagated to any given function of the profiles through the covariance matrix of the best fit parameters.

This procedure leads, for example, to an estimate of the uncertainty on the local scale lengths $L_n \equiv n/|\nabla n|$ and $L_T \equiv T/|\nabla T|$. The values shown in Figure 1 correspond to the radial plasma region characterized by maximum temperature gradient. The parameter $\eta \equiv L_{n_e}/L_{T_i}$ can reach values well in excess of 2 there. In the outer plasma, lower values of η (and affected by larger fractional uncertainties) are generally found.

The local shear length $L_s \equiv Rq_\psi^2/r\nabla q_\psi$, also an important parameter in the context of theory, is not directly measured. We estimate it using q_ψ-profiles from the mhd equilibrium reconstruction code IDENTC; the uncertainty on L_s is assigned arbitrarily.

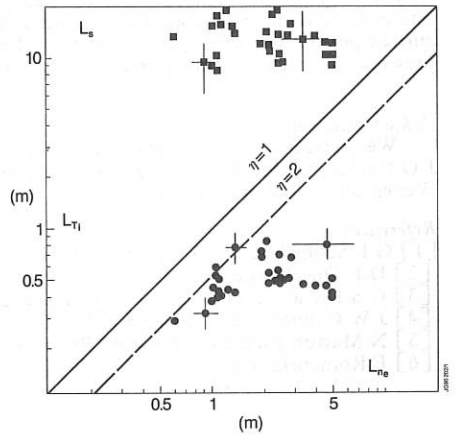

Figure 1 - *Profile scale lengths at $\rho = 0.4$ for 3 MA JET L-modes. ρ is a normalized flux surface label*

Figure 2 - *Ratio of* η_{EXP} $(\rho = 0.4)$ *to the predicted threshold value* [6] *as a function of* τ

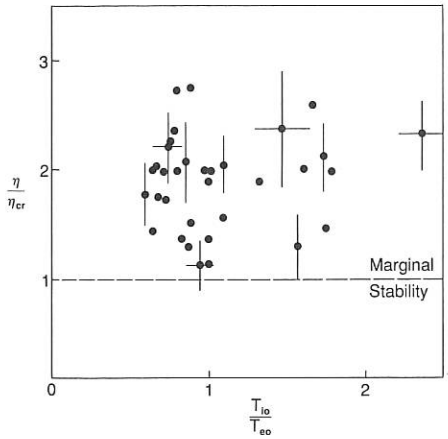

Figure 3 - *Ratio of the predicted* ion *heat flux to the* total *measured heat flux at* $\rho = 0.4$ *, as a function of* T_{io}

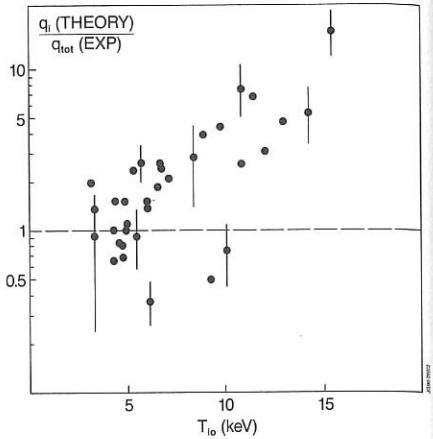

Conclusions

Existing models based on *ITGDT* theory are inadequate to describe the transport properties of JET L-mode plasmas. The measured density and temperature profiles indicate that the theoretical threshold for onset of strong turbulence can be significantly exceeded, without inducing the dramatic deterioration of local confinement predicted by theory. In order to be reconciled with the experimental evidence, the models considered here require rather radical modifications, such as a two-fold increase in the instability threshold and/or a significant reduction in the strength of the turbulent transport.

These findings suggest that the "pellet-enhanced" regime may not be a result of the stabilization of ∇T_i -driven modes. It seems therefore advisable to explore alternative interpretations; in particular, the possible influence on transport of the dynamics of current penetration when pellets are injected at the end of the current rise, and in the presence of large bootstrap currents, deserve further investigation.

Acknowledgments

We gratefully acknowledge discussions with N Mattor, A Taroni, G L Schmidt and J G Cordey, and helpful advice from C Gowers, P Nielsen, M von Hellerman and H Weisen on the use of their data.

References

[1] G L Schmidt *et al* / A Taroni *et al*, *Proc* 12th *IAEA Conf* (1988) **Vol I** p 215/367
[2] D F Duechs *et al*, *Proc* 11th *IAEA Conference* (1986) **Vol I** p 325
[3] G S Lee and P H Diamond, *Phys Fluids* **29** (1986) 3291
[4] J W Connor, *Nucl Fusion* **26** (1986) 193
[5] N Mattor, Culham Laboratory Report *CLM-P872* (1990)
[6] F Romanelli, *Phys Fluids B1* (1989) 1018

Transport of Scrape-off Layer Plasma in Toroidal Helical System

K. Itoh*, S.-I. Itoh*, N. Ueda+, K. Nagasaki**, A. Fukuyama++

* National Institute for Fusion Science, Nagoya, Japan
+ Mitsubishi Atomic Power Industries, Inc., Tokyo, Japan
** Faculty of Engineering, Kyoto University, Kyoto, Japan
++ Faculty of Engineering, Okayama University, Okayama, Japan

Abstract

Plasma transport in the scrape-off layer of the toroidal helical system is investigated. Braided magnetic field is studied and two-dimensional transport model is presented. Analytic forms of the edge temperature and heat channel width are obtained. Numer-ical simulation (UEDA code) is applied and the condition to have the dense and cold divertor plasma is studied.

1. Introduction

The plasma transport in the scrape-off layer(SOL) in toroidal helical devices is a key issue because the stationary operation in these devices depends on the proper control of the heat, particles and impurities. The nature of the plasma in SOL of helical systems has not been so far understood well, at least compared to tokamaks. This is partly because of the lack of the experimental data but also due to the complexity of the magnetic field in the SOL region. The magnetic surface is destroyed in the SOL region of the helical systems[1]. As a first step to analyse the SOL plasma, we present a two-dimensional modelling of the transport based on the fluid picture of the plasma. The structure of the magnetic field is taken into account. Applying the analytic as well as numerical calculations, we study the condition to establish the divertor function in torsatron heliotron configurations.

2. Connection Length of the Field Line to the Wall

The two-dimensional structure of the plasma is determined by the competition between the fast parallel flow and cross-field diffusion. The distance along the field line from the SOL region to the wall, L, as a function of the radial distance δ from the outermost magnetic surface is calculated[2,3]. Figure 1 shows the result for the case of m=19 and ℓ=2 (m is the pitch number and ℓ is the multipolarity of the field). The logarythmic dependence is found as

$$L(\delta) = \frac{\ell}{m}\frac{R}{\lambda_1}\ln\frac{b-a}{\delta\lambda_2} \qquad (1)$$

where R is the majour radius, a is the minor radius and $\lambda_{1,2}$ are numerical constants of the order of unity. The parameter dependence of λ_1 is studied, and is found that λ_1 has weak dependence on m. The control of the vertical magnetic field is known to be effective in reducing the ergodicity of the edge magnetic field. The increment of the plasma volume by this control does not change the formula (1) nor the value of λ_1.

3. Two-dimensional Transport Model

Based on the result (1), the two-dimensional model of plasma transport is proposed. The parallel loss is assumed to be classical and the heat diffusivity is given by $\kappa_{//}=\kappa_0 T^{2.5}$. The perpendicular one is assuemd to be Bohm-like, $\kappa_\perp=\kappa_B T$. The diffusion equation is given as

$$\pi a \frac{d}{dr}\kappa_\perp\frac{dT}{dr} = \frac{\kappa_0}{7L}\frac{\langle B_p\rangle}{B}T^{3.5} \qquad (2)$$

under the condition $T_b >> T_d$ (the suffix b and d stand for the plasma boundary and divertor, respectively). Solving Eq.(2), we obtain that $T_b \simeq 1.5T_0$ and the heat channel width $\Delta \simeq 2\Delta_1$, where

$$T_0 = \left(\frac{7}{2m^2\pi^4\lambda_1^2}\frac{P^2}{a^2\kappa_0\kappa_B}\right)^{2/11} \qquad (3)$$

$$\Delta_1 = 2\pi^2 a R \kappa_B T_0^2 P^{-1} \qquad (4)$$

The result shows only a small dependence on λ_2. This result shows a similar depndence on the cases of tokamaks, but the absolute value of T_b is smaller by a factor, owing to the shorter connection length of the field line to the wall.

4. Numerical Simulation

Numerical simulation of the plasma and neutral particles in a straight helical configuration is performed using the UEDA code, which solves the time-dependent fluid equation coupled with the Monte-Carlo code for neutral particles[4,5]. Because of the short field line compared to tokamaks, the establishment of the dense and cold divertor plasma is more difficult to obtain. Several models of the buffle plates are examined.

Numerical simulation is performed for the parameters; R=4m, B=4T at axis, m=10, total heat out flux Q_T=20MW, and the total particle outflux $\Gamma=8\times10^{20}$/s (which corresponds to $n_e=4\times10^{19}/m^3$). Figure 2 shows the neutral particle density showing the increase of recycling near the divertor plate. In this case, the power flux density to the plate reaches 5MW/m² and the erosion rate is 1.2m/year for carbon. The sputtered carbon flows to the core plasma by the thermal force. For this case, the electron temeprature is still too high near the divertor plate. In order to reduce it, the additional buffle plate is tested (see Fig.3). In this case, T_d reduces to 4eV allowing the low erosion rate (less than 0.1m/year). This shows the importance of the design of the divertor configuration for the toroidal helical systems.

This work is partly supported by the Grant-in-Aid for Scientific Research of MoE Japan.

References

[1] N.N. Filomenko, et al., Nucl. Fusion 7 (1967) 253.
[2] K. Itoh, et al., Nucl. Fusion 29 (1989) 1299.
[3] K. Nagasaki and K. Ioth, Research Report NIFS-17 (1990).
[4] N. Ueda, K. Itoh, S.-I. Itoh, Nucl. Fusion 29 (1989) 173.
[5] N. Ueda, K. Ioth, S.-I. Itoh, Jpn. J. Appl. Phys. 28 (1989) 2597.

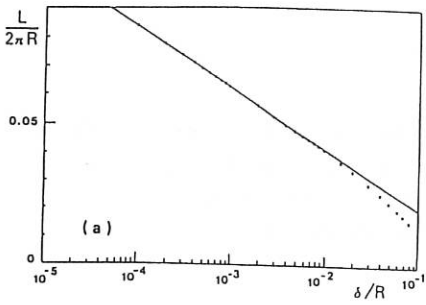

Fig.1

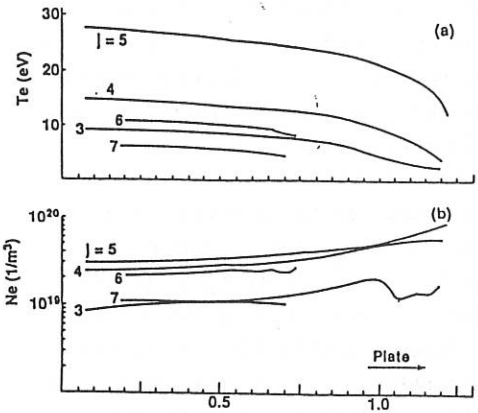

Fig.2

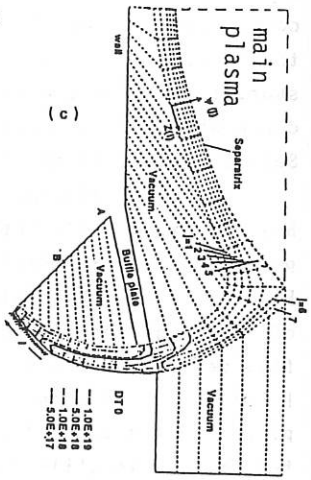

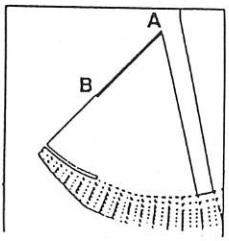

Fig. 3

Fig.1 Connection length of the field line to the wall, L, as a function of δ (δ being the radial distance fron the outermost magnetic surface).

Fig.2 Poloidal cross section and the contour of the neutral particle distribution. One quarter is shown.

Fig.3 Design of the buffle plate which allows good divertor functioning. The area A-B indicates the pumping duct. Fin structure is added.

SENSITIVITY OF IGNITION CONDITIONS TO PLASMA PARAMETERS FOR A COMPACT TOKAMAK

A.Airoldi *, G.Cenacchi **

* Istituto di Fisica del Plasma, Associazione EURATOM-ENEA-CNR, Milano, Italy
** CRE "E.Clementel", ENEA - Bologna, Italy

Summary - The 1 1/2-dimensional equilibrium-transport code JETTO has been used for simulating the achieving of ignition in Ignitor. Different sets of magnetic field and plasma current specifications have been considered. The time evolution for all scenarios has been simulated during the current plateau lasting about 3.5 seconds. The transport models adopted for electrons and ions, based on the 'profile consistency' concept, present the power dependent degradation observed in present-day auxiliary heated experiments. The influence of the machine parameters and transport assumptions on ignition has been investigated. The results show that, for a machine which can sustain a plasma current from 10 to 12 MA and a toroidal field from 11 to 13 tesla, ignition should be guaranteed for wide operating ranges in the plasma parameters.

Simulations - Ignitor has a highly elongated and triangular plasma shape /1/, therefore, as it was already shown /2/, it is necessary to use the real equilibrium configurations in performing predictive simulations. The present analysis has been carried out employing the 1 1/2-dimensional equilibrium-transport code JETTO /3/. A description of the transport models /4/ and of the main assumptions adopted is given in Ref.5. The changes included with respect to the previous simulations are given here. The parallel electrical resistivity has the neoclassical expression taking into account the trapped particle correction /6/. We recall that we defined the central region by the condition $q < q_{min}$. In this region an effective value for the electrical resistivity is defined, in the poloidal magnetic field diffusion equation, so as to keep the q value close to q_{min}. However the resistivity used for calculating the ohmic heating maintains its neoclassical formulation. The neoclassical contribution to χ_i has been corrected following Ref.7 and including the impurity Z values. The initial temperature for electrons and ions is assumed to have a parabolic form with a peak value of 4 keV.

Previous results showed that the density profile influences the ignition achieving because higher peaking factor $n_e(0)/\langle n_e \rangle$, obtained by assigning a higher value to α_{inw}, pinch coefficient for particle diffusion, give lower ignition times /8/. Moreover, for each set of assumptions, such as transport coefficients, central region extension, $\langle Z_{eff} \rangle$, it is possible to obtain in the plane *(average density,ignition time)* an "ignition curve" exhibiting a minimum which defines the optimum density value. The present investigation refers to the displacements and deformations of this curve due to changes in

plasma configurations or transport modelling. The examined scenarios (Table I) refer to the Ignitor machine presented to EURATOM and to an extended parameters version of the project.

Table I - Design parameters and density limits

Case	1	2	3	4
$R_o(m)$	1.175	1.175	1.265	1.265
$a(m)$	.433	.433	.455	.455
$b(m)$	.78	.78	.825	.825
δ	.33	.33	.36	.36
$I_p(MA)$	10.	11.	11.	12.
$B_t(T)$	11.0	12.0	12.0	13.
q_{cyl}	2.11	2.09	2.18	2.18
$<n_{Mu}>(10^{20}m^{-3})$	6.75	7.3	6.5	7.1
$<n_{Gr}>(10^{20}m^{-3})$	10.0	11.2	10.1	11.1

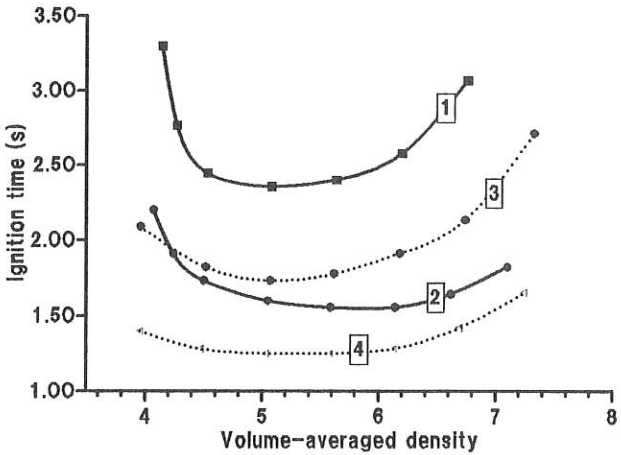

Fig.1 - Ignition time (s) vs. volume-averaged density ($10^{20}m^{-3}$). The numbers on the curves refer to the cases in Table I.

Analysis of the results - The standard assumptions for the presented simulations are: $q_{min} = .7$; $\alpha_{inw} = 2.5$; $<Z_{eff}> \simeq 1.17$. Fig.1 shows the "ignition curves" obtained under these hypotheses. The peaking factors $n_e(0)/<n_e>$ obtained at ignition in these simulations are in the range 2.4-2.6. The broadening and lowering of the ignition curve when plasma current increases is a characterizing feature for both geometric configurations. The performances at 11 MA, 12 T are better for case 2 with respect to case 3, however, taking into account the major operation margins /9/ of the extended parameters version, the influence on ignition of the main assumptions has been investigated for cases 3 and 4. The effect of assuming χ_i in a form proportional to χ_e has been analyzed and Fig.2 shows the ignition curves obtained with $\chi_i = \chi_e$ It should be noted that the standard χ_i model roughly corresponds to $\chi_i = .5\ \chi_e$

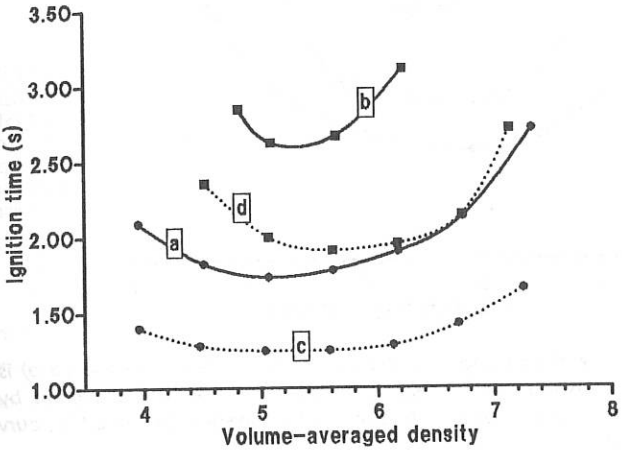

Fig.2 - Effect of $\chi_i = \chi_e$ on ignition curves. Full lines refer to plasma configuration 3 in Table I; curve a) is obtained under standard assumptions; curve b) refers to $\chi_i = \chi_e$. Dotted lines refer to plasma configuration 4 in Table I; curve c) is for standard assumptions and curve d) refers to $\chi_i = \chi_e$

The influence of pessimistic assumptions as a higher impurity content ($<Z_{eff}> \simeq 1.33$), a global increase of the thermal diffusivity coefficients by 20 %, and a broadening of the central region by assuming $q_{min} = .9$, has also been investigated for case 3 of Table I. The relevant results are shown in Fig.3. The general trend of the ignition curve, when degrading hypotheses are assumed, is a shrinking in the density range together with a shifting to higher values of the optimum density and this effect is presumably independent on the chosen transport model.

The depletion of D and T ions due to fusion has been roughly estimated by varying the relevant percentage in the D-T mixture. The results show that, for percentages between 40 and 60, no significant variations are to be expected in the performance of the machine.

The simulations carried out show that, even when degrading hypotheses tend to shrink and raise the ignition curve, the parameters planned for Ignitor should guarantee ignition to be reached within the flat-top of the plasma current.

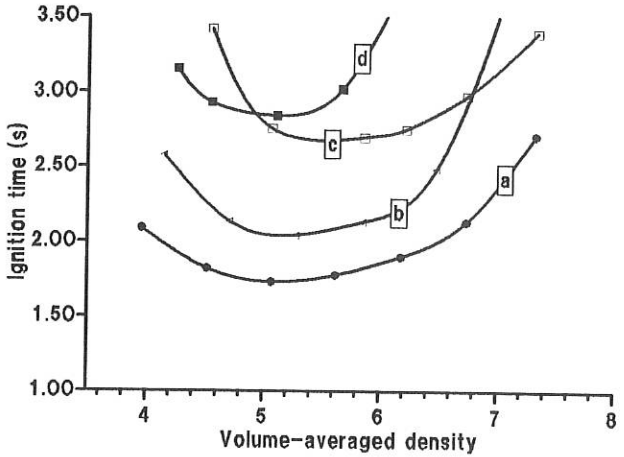

Fig.3 - Effect of some degrading hypotheses on the ignition time. Curve a) is the reference corresponding to case 3 in Table I; curve b) is obtained by assuming $\langle Z_{eff} \rangle = 1.33$; *curve c) refers to* χ_i *and* χ_e *enhanced by 20 % ; curve d) is for* $q_{min} = .9$.

References

1 - B.Coppi - Vuoto **XVIII** , 153 (1988)
2 - A.Airoldi and G.Cenacchi - Proc. 16th European Conf. Contr. Fusion and Plasma Physics, Venice, 1989, ECA, Vol.**13B** , Part I, 367
3 - G.Cenacchi and A.Taroni - Report JET-IR(88)03, (1988)
4 - M.H.Redi, W.M.Tang, P.C.Efthimion, D.R.Mikkelsen and G.L.Schmidt - Nucl. Fusion **27** , 2001 (1987)
5 - A.Airoldi, G.Cenacchi - IFP Report FP89/9 Milano, Italy (1989)
6 - S.P.Hirshman, R.J.Hawryluk and B.Birge - Nucl. Fusion **17** , 611 (1977)
7 - C.S.Chang and F.L.Hinton - Phys. Fluids **29** , 3314 (1986)
8 - A.Airoldi and G.Cenacchi - The 3rd Eur. Fus. Theory Conf., Oxford, 1989, paper C4
9 - B.Coppi - Private Communication (1990)

STUDIES OF BURN CONTROL FOR ITER/NET

D. Anderson[1], T. Elevant[2], H. Hamnén[1], M. Lisak[1], J. Lorenzen[3], and H. Persson[3,4]

1) Chalmers University of Technology, Institute for Electromagnetic Field Theory and Plasma Physics, S - 412 96 Göteborg, Sweden.

2) Royal Institute of Technology, Plasma Physics and Fusion Research, S - 100 44 Stockholm, Sweden.

3) Studsvik Nuclear, S - 611 82 Nyköping, Sweden.

4) Also with Group of Theoretical Electrotechnics, Department of Technology, Uppsala University, Box 534, S - 751 21 Uppsala, Sweden.

We have put the approximation procedure involved in the transition from 1-D to 0-D models for fusion burn on a formal basis. Simple approximations of the equilibrium temperature profiles have been derived for a class of nonlinear transport and heating models. These approximations should be useful when investigating various schemes for feedback control of the equilibrium. The stability of the 1-D equilibrium is also investigated and is shown to be the same as that derived from the simplest 0-D space averaged model. (Cf. Ref 1.). The energy balance equation can be written

$$\frac{\partial T}{\partial t} = \frac{1}{r}\frac{\partial}{\partial r}\left(r\frac{\kappa}{3}\frac{\partial T}{\partial r}\right) + S$$

where T is the plasma its temperature. The reaction rate is modelled by $S = S_o T^p$; the exponent p is typically 2-3, and decreases with increasing temperature. The heat conductivity κ is also modelled by a power law: $\kappa = K_o T^\delta$. The density n is first assumed to be constant in time as well as in space. The boundary conditions are

$$\partial T / \partial r\,(0,t) = 0; \qquad T(a,t) = 0$$

where a denotes the plasma minor radius.

To formally carry out the space-averaging procedure, an assumption about the temperature must be made. A convenient model compatible with the boundary conditions is

$$T = T(0)\,(1 - r^2/a^2)^\alpha$$

Averaging of the diffusion yields a finite result only if $\alpha = 1 / (\delta+1)$. This implies that the thermal conductivity has a dominating influence on the temperature profile, much stronger than the heating term. Note in particular that the profile peaking factor, R, is determined solely by the power law exponent of the thermal conductivity, viz. $R = T(0) / \langle T \rangle = (\delta+2)/(\delta+1)$. The confinement time becomes

$$\tau_E = \frac{a^2}{4K_o \langle T \rangle^\delta}\,\frac{(\delta+1)^{\delta+2}}{(\delta+2)^{\delta+1}}$$

The first equation is also used for studying profile characteristics of the equilibrium solution, formulated as a nonlinear eigenvalue problem. It turns out that an efficient variational procedure for its solution can be obtained, as is shown in Fig. 1. The averaging procedure and the approximate profile analysis can be generalized to include a fixed density radial profile, as well as to incorporate a density dependent thermal conductivity.

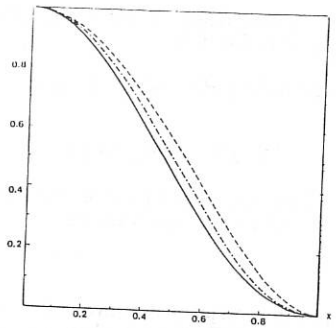

Fig. 1 Comparison between numerically obtained solution (-----) and approximate solutions according to $\alpha = 1/(\delta+1)$ (---) and the variationally determined α (-.-.-) respectively for the case $p = 0.5$ and $\delta = -0.5$ ($p = 1+\delta$).

In subignited operation, with actively controlled auxiliary heating, the limited NBI swing, $0 \le P_{aux} \le P_{max}$, introduces a limitation on the interventions possible against thermal runaway. In particular, with a working-point close to ignition -- high Q -- , the control margin becomes small, and systematic or random errors in temperature measurements might cause a major thermal excursion. This has been analyzed in detail by Bromberg et al.[2]. We have derived the essential features qualitatively, by simple means. One obtains

$$Q_{max} \cong \frac{5}{\varepsilon} \frac{1}{p-1-\delta}$$

where $\varepsilon = \delta T_{max} / T_o$. The quantity δT_{max} is the maximum allowable temperature perturbation. As before, δ is the scaling exponent of the thermal conductivity with temperature and p is the local value of the exponent in $\langle\sigma v\rangle \sim T^p$. The thermal runaway time becomes $\tau_{runaway} \approx \tau_E / (p-1-\delta)$. The achievable Q_{max} depends strongly on δ. With $\varepsilon \approx 0.2$, one finds $Q_{max} \approx 10\text{-}15$, which would be inconveniently low from a reactor point of view.

Several cases of the nonlinear, 0-D, coupled n and T variations with time of uncontrolled and controlled plasmas have been analyzed numerically, using an efficient ODE solver [3]. Here, we only wish to illuminate the question of maximum allowable Q. Fig.2 corresponds to a case with $n_o = 10^{20}/m^3$; $T_o = 18$ keV; $Z_{eff} = 2$; $Q_o = 50$; $\tau_E \sim n\, T^{0.1}$. The uncontrolled plasma is unstable; it is stabilized by state-space feedback, which would give the phase portrait shown in the figure, if the limited NBI swing could be disregarded. The corresponding picture, with this limitation included, is shown in Fig. 3. Clearly, there is a thermal runaway for high enough density and temperature. An initial point with $\delta T = 0.2\, T_o$ does give a temperature rise initially, but the system is then stably attracted towards the working point, in spite of the high Q_o-value (Curve A in the figure). On the other hand, (curve B), $\delta T = 0.25\, T_o$ produces a more significant temperature rise.

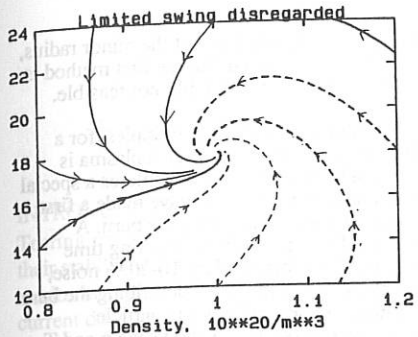

Fig. 2 Phase portrait of feedback stabilized plasma, neglecting limited NBI swing.

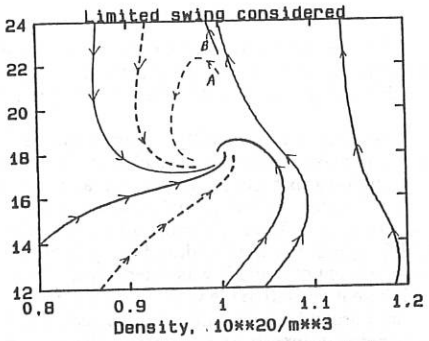

Fig. 3 Same as Fig. 1, but considering limited NBI swing.

We have considered the question whether a perturbed temperature profile, with a hotter kernel than the equilibrium profile, will develop towards self-heating or quenching. The answer to this question obviously determines which control action to take. Fig. 4. shows the evolution in time of two profiles, initially with the same profile shape, but with slightly different axial values.As can be seen, for both cases the axial temperature initially decreases, but at later timesone case self-heats and the other is quenched. One finds that the thermal runaway is determined by whether or not the momentaneous thermal energy content is more or less than the equilibrium content. However, it turns out that one then has to consider the change in thermal

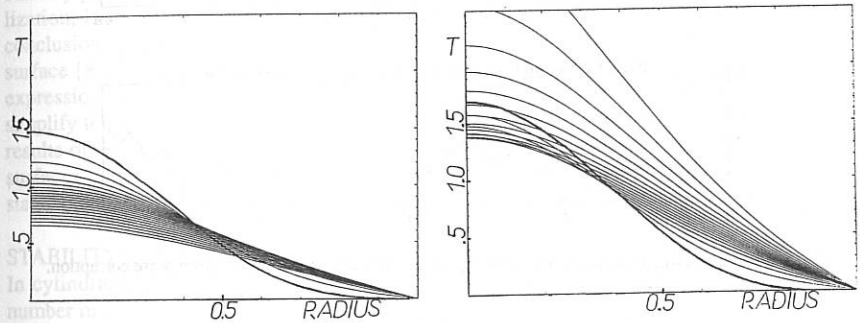

Fig. 4 Time development of two similar profiles, giving quench and runaway, respectively.

content during the first phase of the temperature profile development, during which a central peak spreads out, after which the profile during its subsequent growth or decay will remain similar in shape to the equilibrium profile.

The presence of sawteeth complicates the active feedback control of an unstable equilibrium temperature profile. We have tentatively analyzed this problem from two aspects: (i) the profile changes involved in the sawtooth process complicates the interpretation of neutron emission signals if these are used to infer central ion temperatures and (ii) the sawtooth temperature variation implies an inherent Q-limitation for subignited scenarii, as discussed above.

The feasibility of control by a couple of alternative schemes, variation of the minor radius, and dynamic stabilization, has been tentatively analyzed. It is concluded that the first method is worth looking into more closely, but it appears that the second one is probably not feasible.

As long as no generally accepted scaling laws, based on first physical principles, for a tokamak plasma have been found, they should be determined empirically when a plasma is brought towards high Q, in order that a proper control can be exerted. This constitutes a special case of "system identification", widely used in science and technology. We have made a first, numerical simulation of identification, using the 0-D equations characterizing the burn. A PRBS-signal (Pseudo Random Binary Sequence) was used as input and the resulting time development of n and T was determined. These data were then corrupted by 10-20 % noise, and thereafter used to identify one of the matrix elements of the local matrix describing the burn linearly around the working point. Essentially, this amounts to determining the particle confinement time, from noisy data. The agreement was very good; Fig. 5 shows the n and T curves -- before any noise was added -- and the curves reconstructed by identification, using a program package due to L. Ljung[4], using the prediction error method.

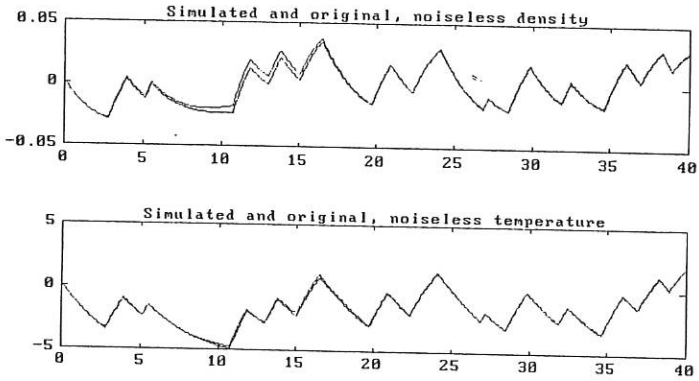

Fig. 5 System identification: Simulated and original density and temperature, before noise corruption.

References: 1. D. Anderson, T. Elevant, H. Hamnén, M. Lisak, J. Lorenzen, H. Persson, "Prestudy of burn control in NET.", Second Intermediate Report, February 1990, CTH-IEFT/PP-1990-03.

2. L. Bromberg, J. L. Fisher, D. R. Cohn, Nucl. Fus. 20 (1980) 203.

3. G. Dahlqvist and S. Littmarck, private communication.

4. L. Ljung and S. Littmarck, private communication.

ON TEARING MODE STABILIZATION BY LOCAL CURRENT DENSITY PERTURBATIONS

E. Westerhof
Association EURATOM-FOM, FOM Instituut voor Plasmafysica 'Rijnhuizen'
Nieuwegein, The Netherlands

INTRODUCTION

Tearing modes play a crucial role in the stability and performance of tokamaks [1-5]. Hence, their stabilization will be of great importance for future tokamak reactors. The stability of tearing modes is very sensitive to the details of the current density profile and, in particular, to the current density gradient around the mode rational surface. In this light, it has been proposed to stabilize the mode by a small current perturbation at the mode rational surface [6]. The most direct way to generate such a perturbation is by means of non-inductive current drive.

In a previous paper, an analyses of the requirements on the localization and amount of non-inductively driven current to stabilize the m=2, n=1 tearing mode has been presented [7]. Simple criteria for stability were presented, based on intuitive arguments, and subsequently confirmed by parameter scans. However, the influence of the strength of the instability in the absence of the additional current, the role of the shear at the mode resonant surface, and the differences in effectiveness for mode stabilization of co- and counter-driven currents remained unclear. Some conclusions on these points can be drawn from a recent report by L.E. Zakharov and A.A. Subbotin, in which the effect of an additional, block-shaped, current layer on the stability parameter Δ' is calculated perturbatively [8]. The additional current required for stabilization, is shown to be proportional to the square width of the current layer, confirming the conclusion of Ref. [7], to the strength of the instability, and to the shear at the mode resonant surface [8]. In this paper, the analyses of Ref. [8] is extended, and a particularly illustrative expression for Δ' is obtained for the case of a Gaussian profile of the additional current. To simplify the stability calculations, we use the cylindrical approximation. A comparison with the results of Ref. [8], which do include effects due to toroidicity and non-circularity of the flux surfaces, shows that these effects do not change the scaling of the current required for stabilization, but only lead to an additional geometrical factor of order unity.

STABILITY CRITERION WITH A LOCAL CURRENT DENSITY PERTURBATION

In cylindrical geometry, the stability of the tearing mode with poloidal and toroidal mode number m and n, respectively, is determined by the parameter Δ' [9]

$$\Delta' \equiv \lim_{\varepsilon \downarrow 0} \left(\frac{\partial \psi}{\partial r}(r_s+\varepsilon) - \frac{\partial \psi}{\partial r}(r_s-\varepsilon) \right) / \psi(r_s) , \qquad (1)$$

$\Delta' > 0$ meaning instability. Here, r_s denotes the mode rational surface where $q(r_s) = m/n$, and ψ is the perturbed helical flux. This flux satisfies

$$\frac{d^2\psi}{dr^2} + \frac{d\psi}{r\,dr} - \left(\frac{m^2}{r^2} + \frac{2\pi}{r} \frac{\partial j}{\partial r} / \left(\frac{1}{q} - \frac{n}{m} \right) \right) \psi = 0. \qquad (2)$$

Here, the following normalizations are used. The minor radius r is normalized to 1 at the plasma edge and the current density is normalized by the factor $2\pi B_T/\mu_o R_o$.

Following the treatment of Ref. [8], a small, well localized current density perturbation is assumed to affect only $\psi'(r_s)$ and to leave $\psi(r_s)$ unchanged. In that case, one obtains

$$\Delta' = \Delta'_0 + P \int_{-\infty}^{+\infty} dx \, \frac{2\pi}{x} \frac{\partial \delta j}{\partial x} \left[\frac{r}{q^2} \frac{dq}{dr} \right]^{-1}_{r=r_s}, \qquad (3)$$

where Δ'_0 is the stability parameter in the absence of the current perturbation, δj is the current density perturbation, and $x \equiv r - r_s$ is the normalized distance to the rational surface. The current perturbation is now assumed to have a Gaussian profile: $\delta j = e^{-\beta(x-x_0)^2} I_{CD} / 2\pi r_s \sqrt{\pi/\beta}$, where $\beta^{-1/2}$ is a measure of its width and $x_0 = r_{CD} - r_s$ is the position of the centre of the current perturbation with respect to the rational surface. Then, the integration in Eq. (3) can be carried out to obtain

$$\Delta' = \Delta'_0 - I_{CD} \left[\frac{r^2}{q^2} \frac{dq}{dr} \right]^{-1}_{r=r_s} 2\beta \left[1 + \sqrt{\beta} x_0 \, \mathrm{Re} \, Z(\sqrt{\beta} x_0) \right], \qquad (4)$$

where $Z(z)$ is the plasma dispersion function. The profile function, $F(z) \equiv 1 + z \, \mathrm{Re} \, Z(z)$ is given in Fig. 1. A criterion for the integrated current perturbation I_{CD} required for stabilization can be derived from Eq. (4). Assuming that the mode is located close to the plasma edge, the total plasma current I_p may be approximated by the current inside the mode rational surface surface, i.e. $I_p \approx r_s^2/q_s$. Then, one obtains the following requirement for stability ($\Delta' \leq 0$)

$$\frac{I_{CD} F(\sqrt{\beta} x_0)}{I_p} \geq \frac{\left[\frac{1}{q} \frac{dq}{dr} \right]_{r=r_s} \Delta'_0}{2\beta}. \qquad (5)$$

From these results it can be concluded that the current required for stabilization is proportional to Δ'_0 [8], the shear at r_s [8], and to the square width β^{-1} of the current perturbation [7,8]. A co-driven current should be centred within the interval $r_s \pm \sqrt{1/\beta}$, while a counter-driven current should be localized around $r_s \pm \sqrt{2/\beta}$ [7]. A co-driven current is about 3 times as effective in stabilizing tearing modes as a counter-driven current. The effect of an appropriately localized current on other (low m) modes than the mode that is to be stabilized, is negligible.

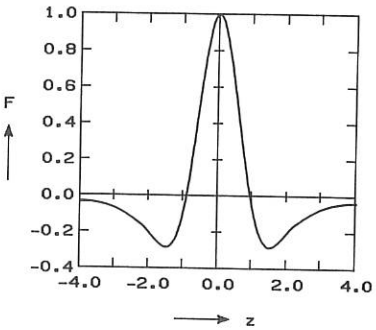

Fig. 1. The profile function $F(z) \equiv 1 + z \, \mathrm{Re} \, Z(z)$.

APPLICATION TO A GAUSSIAN EQUILIBRIUM CURRENT PROFILE

For a quantitative comparison with the results of Ref. [7], we concentrate on the m=2, n=1 tearing mode, and consider an equilibrium with a Gaussian current profile: $j(r) = j(o) \, e^{-1.5\lambda r^2}$. Typical current profiles as considered for future tokamaks (e.g. NET, ITER) would be relatively broad (i.e. $\lambda = 1$ to 2) with the $q = 2$ surface close to the plasma edge. Such a profile is well within the unstable parameter regime for the m=2 mode [7]. Assuming e.g. $\lambda = 1$ and $r_{q=2} = 0.85$, we obtain a strongly unstable profile with $\Delta'_0 = 6.2$. For this profile, the value of q on axis is $q_o = 1.22$ and q at the edge is $q_a = 2.36$. The shear at q=2 is $[rdq/qdr]_{r=r_{q=2}} = 0.9$. After substitution of these values into Eq. (5), one obtains the minimum requirement

$$\frac{I_{CD}}{I_p} \gtrsim \frac{2.5}{\beta}, \tag{6}$$

in excellent agreement with the results presented in Ref. [7]. As a further check, the effect on the instability of a current perturbation with peaking factor $\beta = 400$ is calculated for a scan in the driven current I_{CD} and its position r_{CD}, using the full Eqs. (1) and (2). The results are given in Fig. 2 as level curves of Δ' in the I_{CD}~r_{CD} plane. These results clearly confirm, both qualitatively and quantitatively, the criteria for stabilization given above.

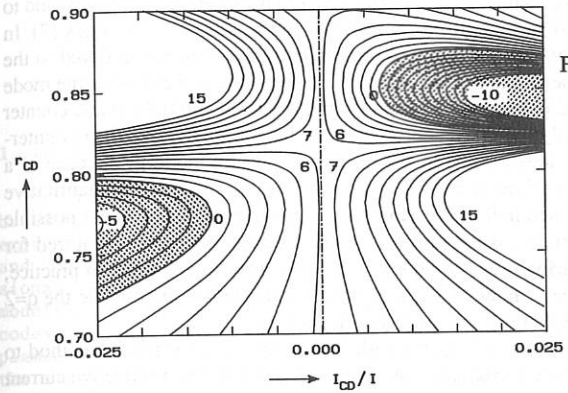

Fig. 2. Results of stability calculations for $\lambda = 1$ and $\beta = 400$. Contours of constant Δ' are given. The shaded area indicates the stable parameter regime.

APPLICATION TO A BLOCK SHAPED EQUILIBRIUM CURRENT PROFILE

Of course, the Gaussian equilibrium current profile used above, is only one special case of all possible current density profiles. An alternative model for a broad current density profile, is a block profile with a constant and finite current inside a radius r_c and zero current outside this radius (cf. Ref [6]). For such a current profile, the tearing mode with mode numbers m and n is unstable in the range $0 < m - nq_0 < 1$ [6]. Here, the lower limit is due to the absence of a rational surface with $q = m/n$ in case $q_0 > m/n$, while at the upper limit, when q_0 approaches m/n from below, Δ' becomes arbitrary large. For example, the stability parameter Δ' of the m=2, n=1 mode becomes

$$\Delta'_0 = \frac{-4\,(1 - q_0)}{r_s\left(1 - \frac{1}{2}q_0\right)^2}. \tag{7}$$

Already for $q_0 \gtrsim 1.2$, Δ'_0 becomes so large, that the current required to stabilize the m=2 mode is larger than $8 I_p/\beta$, which is more than three times the minimum required current as estimated above on the basis of a Gaussian current density profile. As pointed out in Ref. [6], however, the stability of tearing modes is significantly improved, when a modest pedestal is present in the current profile. In the present case, such a pedestal not only helps to reduce Δ'_0, but also reduces the shear at the rational surface and, thereby, the current required for stabilization. In a tokamak reactor such a pedestal may well be provided by the bootstrap current, which will be largest towards the outer region of the plasma where the density gradient is expected to be relatively steep. Nevertheless, the requirements to stabilize the m=2, n=1 tearing mode may well become prohibitively large in the case of broad current density profiles with high q_0 (≈ 1.5

or larger) but with very little or no current outside the q = 2 surface. It seems advisable to avoid such current profiles in a tokamak reactor.

CONCLUSIONS

We have derived an expression (Eq. (4)) for the tearing mode stability parameter Δ' in a plasma with an additional current that is localized near the mode rational surface. The stability requirement $\Delta' > 0$ then leads to a criterion on the additional current (Eq. (5)). This criterion shows that the current required for stabilization is proportional to the total plasma current and to the square width of the additional current profile, confirming the results of earlier work [7]. In agreement with the results of Ref. [8], the required current is found to be proportional to the strength of the instability Δ'_0 in the absence of the additional current and to the shear at the mode rational surface. In addition, the different effectiveness for mode stabilization of co- and counter driven currents is shown explicitly: co-driven currents being far more effective than counter-driven currents. Application of these results to the m=2, n=1 tearing mode in the case of a relatively broad Gaussian equilibrium current density profile also provides a quantitative confirmation of the results presented in Ref. [7]. However, very large values of Δ'_0 are possible in case of block shaped equilibrium current profiles. In such a case, the current required for stabilization of the m=2, n=1 tearing mode could well become prohibitively large. In practice, such profiles are not likely to occur. In any case, a significant current density outside the q=2 surface, which has a stabilizing effect [6], is expected to be present.

A practical application of this method of mode stabilization requires an efficient method to generate the required current density perturbation. As shown in Ref. [10], non-inductive current drive by electron cyclotron waves is a prime candidate to generate such a current. Because of the good localization of the wave-particle interaction in the electron cyclotron range of frequencies, narrow current profiles with peaking factors of $\beta \approx 400$ can easily be generated around the q = 2 surface without excessive demands on the wave launching system. A detailed analyses of this application to NET is presented in Ref. [10].

ACKNOWLEDGEMENTS

Stimulating discussions with Drs. T.J. Schep and F. Engelmann are gratefully acknowledged. This work was performed under NET contract Nº NET/88-151 and under the Euratom-FOM association agreement with financial support from NWO and Euratom.

REFERENCES

[1] WADDELL, B.V., et al., Phys. Rev. Lett. **41** (1978) 1386.
[2] TURNER, M.F., WESSON, J.A., Nucl. Fusion **22** (1982) 1069.
[3] HOLMES, J.A., et al., Nucl. Fusion **19** (1979) 1333.
[4] FURTH, H.P., Phys. Fluids **28** (1985) 1595 (and references therein).
[5] FURTH, H.P., Plasma Phys. and Contr. Fusion **28** (1986) 1305.
[6] GLASSER, A.H., FURTH, H.P., RUTHERFORD, P.H., Phys. Rev. Letters **38** (1977) 234.
[7] WESTERHOF, E., Nucl. Fusion **27** (1987) 1929.
[8] ZAKHAROV, L.E., SUBBOTIN, A.A., 'Tearing-mode stabilization by generation of an additional current layer in tokamaks', ITER Internal Note Nº ITER-IL-PH-11-9-S-2, 1989.
[9] FURTH, H.P., RUTHERFORD, P.H., SELBERG, H., Phys. Fluids **16** (1973) 1054.
[10] GIRUZZI, G., SCHEP, T.J., WESTERHOF, E., Current drive and profile control in NET plasmas, NET Report no. EUR-FU/80/89-96 (1990).

IMPLEMENTATION OF SCALING LAWS IN 1-1/2-D TRANSPORT CODES AND APPLICATIONS TO THE IGNITION SPHERICAL TORUS

A. Nicolai, Y.-K.M. Peng*), J.T. Hogan*)

Institut für Plasmaphysik des Forschungszentrums Jülich GmbH,
Association EURATOM-KFA, P.O. Box 1913, D-5170 Jülich, FRG

*)Oak Ridge National Laboratory, Oak Ridge, Tennessee 37831, USA

1. Introduction

Predictions of future ignition experiments often use scaling laws based on the experimental data of the energy confinement time τ_E. Various expressions for these laws had been proposed by different authors /1,2/ and applied directly in systems tradeoff studies /3/ that use zerodimensional approximations to the plasma transport. In the 1-1/2-d transport modeling which uses 2d MHD equilibrium codes coupled to 1-d transport codes, radially resolved transport are needed. Here we report on the implementation of selected scaling laws in an 1-1/2-d transport code, and the results of its application ot the spherical torus regime /4/ of very small aspect ratios (A).

2. Transport models based on scaling laws

A recipe is developed to obtain one-dimensional diffusivity profiles for particle and energy transport from the scaling expressions. This process involve two unavoidable ambiguities that require additional assumptions to proceed:

Firstly, the power flux associated with the scaling laws must be attributed to the major non-radiative loss channels, i.e., the electron and ion heat conduction and convection. The radiation and atomic loss channels, i.e., line radiation, bremsstrahlung, synchrontron, and charge exchange, need to be excluded from the definition of τ_E in using empirically derived scaling laws.

Secondly, ambiguity arises because of the uncertainties in the radial dependence of the heat and particle diffusivities. Here we make use of the experimentally deduced profiles of the electron heat diffusivity as a guide to formulate relatively simple approximations to the profiles of electron and ion heat conduction.

Interpretative calculations show that the electron heat diffusivity increases towards the plasma boundary /5/. This may be reflected by a diffusivity proportional to /6/

$$g(\rho) = 1 + 4 \ (\rho/\rho_p)^2 \qquad (1)$$

Since the computed confinement time depends on the power fluxes of all loss channels which may have a complicated time dependence, a correction factor C(t) is introduced so that

$$\frac{\tau_e - \tau_c}{\tau_e} \quad 2\ \% \tag{2}$$

τ_c is the computed confinement time given by

$$\tau_c = \frac{E_e + E_i}{P_{net}} \tag{3}$$

P_{net} is the "net heating" power

$$P_{net} = P_\alpha + P_{OH} + P_{AUX} - P_{RAD} \tag{4}$$

E_e and E_i are the electron and ion energy contents, respectively. $\chi_e(\rho)$ may than be written as

$$\chi_e(r) = G\ C(t)\ g(\rho)\ /\tau_E \tag{5}$$

The constant G is chosen such that C(t) is of the order unity. The solution of the diffusion problem in a cylindrical medium with elongation κ, constant diffusivity and minor effective radius a_o indicates the choice /6/

$$G = 0.95\ a_o^2\ \ 2\ \kappa^2/(1 + \kappa^2) \tag{6}$$

We note that this choice of G is of minor principal importance and the introduction of the correction factor C(t) ensures that (2) holds.

A feedback control of C(t) is introduced by means of the expression

$$C(t) = \left(1 + \frac{\int_o^t \left[\left(1 - \frac{\tau_c}{\tau_E}\right) \Theta_b\ (\tau_E - \tau_c)\ dt'\right]}{t_r}\right)^{-1} \tag{7}$$

The function Θ_b differs from zero only if the difference between τ_E and τ_c is larger than b = 10 msec. The introduction of Θ_b into (7) ensures that the control is well damped such that minor oscillations are excluded.

As scaling laws for τ_E which are to be inserted into equation (5) the KAYE-BIG /1/ and the REBUT-LALLIA law /2/ are envisioned because they emanate from data belonging to large devices. They have the unfavourable scaling with the heating power in common.

The convective loss channels and the diffusion of the particle species are determined by the assumption

$$D = \delta\ \chi_e \tag{11}$$

The ion heat diffusivity χ_i is assumed to be given by

$$\chi_i = \chi_{neo} + f_\chi \chi_e \qquad (12)$$

The constants δ and f_χ are to be determined by experimental indications ($\delta = 0.25$, $f_\chi = 0.2$). χ_{neo} is the neoclassical ion heat diffusivity /7/.

3. Temperature control during the ignition phase

Since the α-particle heating power in general causes an instability of the plasma temperatures it is assumed here that during the burn phase the temperature are feedback stabilized either by additional heating or by energy unloading processes, as adiabatic compression and decompression or enhanced ripple losses. These heating or unloading processes are modelled by power gain or loss terms which are switched on, if the temperatures exceed or drop below prescribed space dependent limits. Ignition is achieved if the total control power

$$\bar{P}_{CON} = 4\,\pi^2 \int (P_{CON_e} + P_{CON_i})\,\rho\,d\rho$$

is negative ($\bar{P}_{CON} = 0$ means "marginal" ignition). P_{CONe} and P_{CONi} are the control power densities deposited into the electron or ions. For $P_{CON} \geq 0$ ignition is not achieved, because additional heating is needed.

4. Results

The calculation had been based on the data of the ignition spherical torus (IST) /8/: minor half axis $a = 87.5$ cm, major radius $R_o = 134$ cm, elongation $\kappa = 2$, plasma current $I_p = 14$ MA. The operation scenario includes the current rise drive, the density rump up, the temperature ramp up phase with a heating power $P_{LH} \approx 15$ MW and the ignition phase. The results presented here concern the ignition phase and they are devoted to the following questions.

(1) Does IST ignite, if a specific scaling law is applied?
(2) How are the parameters of IST to be modified, if ignition is not achieved?

During the ignition phase the modelling based on the REBUT-LALLIA scaling law, yields the total control power $P_{con} = -1.86$ MW i.e. ignition is achieved. The power balance for the electrons shows that the power deposited into the electrons (predominantly α-particle heating power $P_\alpha = 16.3$ MW) is mainly lost by electron heat conduction $P_{CDe} = -9.9$ MW, and radiation $P_{RAD} = -2.4$ MW.

If the KAYE-BIG scaling law is used, the total control power during the ignition phase is $P_{con} = 1.7$ MW i.e. additional heating is required to maintain the maximum plasma temperature at 20 keV; ignition is not achieved. The control power, however, is only 15 % of the total α-particle heating power. Because of the unfavourable scaling of τ_E with the heating power a density or temperature increase does not move IST into the ignition regime. However, an increase $\Delta\rho$ of the minor radius ρ at constant aspect ratio and a corresponding current increase yields

ignition for $\Delta\rho/\rho = 1.3$. The α-particle power is $P_\alpha = 30$ MW.

5. Conclusion and discussion

Implementation of the scaling laws into 1-1/2-d transport codes in manners consistent with the confinement data is an important step in modeling of the plasma transport behavior in tokamaks. By using free-boundary divertor MHD equilibria, most of the geometric and transport mechanisms can be incorporated in the modeling. Our work can be improved by inclusion of the effects of enhanced transport related to the Mirnov oscillations and the ELMs /9/. The H-mode confinement enhancement can be modeled with a local reduction of χ_e in flux surfaces just within the separatrix. The presence of saw-tooth oscillations, which prevent the safety factor q_o to drop below unity near the magnetic axis, can be modeled by local transport enhancements when q_o becomes less than 1.

The results of the IST simulations serve to provide a severe test of the ability of the code, and involve a significant extrapolation from the present tokamak data base upon which the scaling laws are deduced. The results suggest that a D-T ignition experiment using the spherical torus configuration is potentially a viable and cost-effective approach to advance fusion research, since the size and performance requirements of the IST ($R = 1.3$ m, $A \sim 1.5$, $B_o = 1.5$ T, $I_p = 14$ MA, and a fusion power of about 100 MW) are modest when compared with conventional tokamak approaches /10,11/. The required auxiliary heating power to maintain burn at high fusion multiplications is found to range from 0 to 10 MW, the latter occurs in the case of the Kaye-Big scaling /1/. A relatively small increase in the size and current of the IST would insure its ignition capability.

References

/1/ S.M. Kaye, "Survey of Energy Confinement Scaling Expressions", ITER Specialists Meeting on Energy Confinement, 24-27 May 1988, Garching, Federal Republic of Germany.

/2/ P.H. Rebut et al., "Chaotic Magnetic Topology and Heat Transport in Tokamaks", JET Report, JET-P(88)05, January 1988.

/3/ R.L. Reid, ETR/ITER Systems Code Report ORNL/FEDC-87/7 (1988).

/4/ Y.-K. M. Peng, D.J. Strickler, Nucl. Fusion, 26, 769 (1986).

/5/ A. Nicolai, P. Börner, Proceedings of the 14th European Conference on Controlled Fusion and Plasma Physics, Madrid 22.-26.6. (1987) p. 1168.

/6/ W. Houlberg, Proceedings of the 11th Symposium on Fusion Engineering, Vol. 1, p. 50, Austin, Texas (1985).

/7/ F.L. Hinton, R.D. Hazeltine, Rev. Mod. Phys. 48, 239 (1976).

/8/ Y.-K.M. Peng, S.K. Borowski, G.R. Dalton, G.E. Gorker et al., Initial Assessments of Ignition Spherical Torus, Report ORNL/FEDC-85/5.

/9/ K.H. Burrell et al., in Plasma Phys. Cont. Nucl. Fusion Research, 1988, Vol. 1, p. 193, (IAEA, 1989).

/10/ R. Parker et al., in Plasma Phys. Cont. Nucl. Fusion Research, 1988, Vol. 3, p. 341, (IAEA, 1989).

/11/ P.H. Rebut, in Plasma Phys. Cont. Nucl. Fusion Research, 1988, Vol. 3, p. 403 (IAEA, 1989).

SIMULATION OF DENSITY PROFILE PEAKING AND ENERGY AND PARTICLE TRANSPORT IN THE IOC REGIME

G. BECKER

(Max-Planck-Institut für Plasmaphysik,
Euratom-IPP Association, Garching bei München,
Federal Republic of Germany)

ABSTRACT. The evolution of the density profile in improved Ohmic confinement (IOC) discharges of ASDEX and its correlation with the local particle and energy transport are investigated by computer simulations. Electron and ion heat diffusivities χ_e and χ_i, diffusion coefficient D and inward drift velocity v_{in} and their scalings in different confinement regimes are presented. The observed better energy and particle confinement is explained by a 2 to 3 times reduction of χ_e and D correlated with the density scale length. This agrees with the measured diffusion coefficient and with χ_e being coupled to D which has been found in all confinement regimes. The existence of lower limits for these diffusivities is shown. The enhancement factor for χ_i in relation to the neoclassical value is found to be 1.4 and constant in time. Simulation of the measured density profiles yields a time-independent v_{in}/D and requires a feedback-controlled fuelling rate. One pre-requisite for density profile peaking is the reduction of the particle source. Simulations with constant gas feed and particle source yield no profile peaking during the density plateau. At a given line averaged density, two steady-state solutions for the density profile are obtained corresponding to high and low refuelling rates.

INTRODUCTION: In many tokamaks saturation of the Ohmic energy confinement time τ_E with density has been observed. In ASDEX, improved Ohmic confinement with gas puffing was achieved by optimizing the external gas feed /1-3/. The linear scaling $\tau_E \propto \bar{n}_e$ could be extended up to the density limit. The improved energy and particle transport in the IOC regime was found to be correlated with the observed density profile peaking.

In this paper, energy and particle transport and density profile peaking are explored with modified versions of the BALDUR transport code /4,5/ which also model the scrape-off plasma of the divertor tokamak. Transport is described by empirical scalings for χ_e, χ_i, D and v_{in}. This study aims at determining these coefficients and their scalings in the SOC (saturated Ohmic confinement), IOC and LOC (linear Ohmic confinement) regimes. One objective is to clarify whether a reduction of χ_e or of χ_i causes the better IOC confinement. This question is crucial for developing a theoretical model. Another topic is the role of the gas feed and particle source in the triggering process and density profile peaking mechanism.

PARTICLE AND ENERGY TRANSPORT: A series of deuterium discharges in the IOC regime /1/ is explored. During the density ramp-up phase, the plasma is in the saturated regime. The gas influx at the valve is reduced at $t^* = 1.17$s by feedback control, and the density profile starts to peak gradually. τ_E rises from 85 to 125 ms. The simulations are carried out in the period up to 1.6s, which is relatively little affected by sawteeth. Various computer models were developed and checked against the experimental data. Only the successful one (called IOC transport scaling) is presented in detail. The following coefficients are applied for simulating the measured density and electron and ion temperature profiles:

$$D(r) = 0.4\,\chi_e(r) \qquad (cm^2 \cdot s^{-1}) \qquad (1)$$

$$v_{in}(r) = 0.1\,D(r)\left(\frac{r}{a}\right)^2 \qquad (cm \cdot s^{-1}) \qquad (2)$$

$$\chi_i(r) = 1.4\,\chi_{ineo}(r) \qquad (cm^2 \cdot s^{-1}) \qquad (3)$$

During the SOC phase ($t \leq t^*$)

$$\chi_e^{SOC}(r) = 4.1 \times 10^3 \quad T_{e,keV}(r)^{-1} \quad q(r)^{-1} \quad (cm^2 \cdot s^{-1}) \tag{4}$$

during the IOC phase ($t > t^*$)

$$\chi_e^{IOC}(r) = 1.4 \times 10^4 \left(\frac{r_n\,(2a/3)}{a}\right)^3 \quad T_{e,keV}(r)^{-1} \quad q(r)^{-1} \quad (cm^2 \cdot s^{-1}) \tag{5}$$

and during the LOC phase

$$\chi_e^{LOC}(r) = 5.8 \times 10^{16} \quad n_e(r)^{-1} \quad T_{e,keV}(r)^{-1} \quad q(r)^{-1} \quad (cm^2 \cdot s^{-1}) \tag{6}$$

are used. Here, a = 40 cm is the minor plasma radius or separatrix radius and χ_{ineo} is the neoclassical ion heat diffusivity according to Ref. /6/ (with $Z_{eff} = 2.1$ as measured). This corresponds to an enhancement factor of 2.2 with respect to Z_{eff} times the neoclassical value given in Ref. /7/, which agrees with the coefficients applied in the past /8/. Note that the enhancement factor depends on the neoclassical theory for χ_i used as a reference and does not necessarily express the contribution due to an anomalous ion heat conduction.

The inward drift velocity given by Eq. (2) is almost identical to $v_{in}(r) = 0.5\, D(r) / r_{Te}(r)$ with $r_{Te} = -T_e / (\partial Te / \partial r)$ which was found to be valid in the Ohmic, L and H regimes /9/. Owing to the very small temporal variation of $r_{Te}(r)$, which will be shown later, v_{in}/D is constant in time in agreement with Eq. (2). The coupling between χ_e and D and the v_{in} scaling are supported by theoretical coefficients based on assumed electrostatic or magnetic fluctuations /10/. Without specifying the driving instabilities, $D/\chi_e = 0.3$ and $v_{in} = 0.5\, D/r_{Te}$ are predicted in agreement with the simulations. The same D/χ_e ratio was also obtained for trapped electron modes in Ref. /11/.

A scaling like $\chi_e \propto r_n^3$ is needed for a smooth transition between SOC and LOC coefficients correlated with density profile peaking. Here, r_n is the density scale length given by $r_n = -n_e / (\partial n_e / \partial r)$. As simulations with $r_n(r)^3$ are numerically unstable, $r_n(r)$ is replaced by the value in the middle of the confinement zone at $r = 2a/3$. This is a good approximation because r_n varies at all radii by about the same amount. In principle, r_n can be replaced by $\eta_e = r_n / r_{Te}$ since the T_e profile shape remains almost unchanged. The lower limit for χ_e is found to be the LOC value.

The losses due to impurity radiation and charge exchange as measured by bolometry amount to about 50% of the Ohmic input power /2/. The radiation profiles are well simulated by non-corona modelling /12/ of oxygen and iron with stationary influx rates. The coefficients D and v_{in} applied for the impurities are identical to those of the main plasma.

The success of the IOC transport scaling is documented by Figs. 1 and 2. Agreement is also obtained with the measured ion temperature profiles and the poloidal beta and loop voltage as functions of time. During the density ramp-up at the beginning, Fig. 1 shows $\partial n_e / \partial t > 0$ for all radii. Extensive computer experimetns have revealed that v_{in} / D is constant in time during density profile peaking. Increasing v_{in} / D with time yields density profiles which are more peaked than those measured and vice versa. Figure 2 shows that the measured and computed T_e profiles agree and that the profile shape is almost conserved. The diagram illustrates that the $\chi_e^{IOC} \propto r_n^3$ or η_e^3 scaling yields the right $\chi_e(r,t)$. For fixed $\chi_i / \chi_{ineo} = 1.4$, χ_e decreases by a factor of about 2 to 3 between the SOC (1.14s) and LOC (1.50s) phases (see Fig. 3). The T_i profiles measured by active CX diagnostic /13/ can be simulated with a time-independent ratio $\chi_i / \chi_{ineo} = 1.4$.

The D and v_{in} profiles presented in Fig. 4 agree with measurements by the gas oscillation technique /14/. In addition, the amount of D improvement in the IOC phase is consistent with the observed three times higher impurity confinement time /1/. One advantage of the IOC transport scaling is that it can explain the observed particle and energy confinement with D being coupled to χ_e. With the χ_e scaling presented there is no room left for improvement of the ion heat diffusivity in the IOC regime.

The lower limit χ_e^{LOC} according to Eq. (6) agrees with the result that the maximum τ_E^{IOC} values do not exceed the $\tau_E^{LOC} \propto \bar{n}_e$ line extended to higher densities. In addition, there is a lower limit for D and, via feedback control, for the particle source.

Computer experiments were also used to explore the role of the gas feed in the peaking process. Even under steady-state conditions and for a fixed v_{in} / D ratio, two different density scale lengths are possible. They exist at the same line averaged density for different refuelling rates.

References

/ 1/ Söldner, F.X., Müller, E.R., Wagner, F., et al., Phys. Rev. Lett. 61 (1988) 1105.

/ 2/ Müller, E.R., Söldner, F.X., Janeschitz, G., et al., in Controlled Fusion and Plasma Heating 1988 (Proc. 15th Europ. Conf. Dubrovnik, 1988), Part I, European Physical Society (1988) 19.

/ 3/ Fussmann, G., Gruber, O., Niedermeyer, H., et al., in Plasma Physics and Controlled Nuclear Fusion Research 1988 (Proc. 12th Int. Conf. Nice, 1988), Vol. 1, IAEA, Vienna (1989) 145.

/ 4/ Becker, G., ASDEX Team, Neutral Injection Team, Analysis of Local Transport in Neutral-beam-heated L and H Plasmas of ASDEX, Rep. IPP III/98, Max-Planck-Institut für Plasmaphysik, Garching (1984).

/ 5/ Singer, C.E., Post, D.E., Mikkelsen, D.R., et al., Comp. Phys. Commun. 49 (1988) 275.

/ 6/ Chang, C.S., Hinton, F.L., Phys. Fluids 29 (1986) 3314.

/ 7/ Chang, C.S., Hinton, F.L., Phys. Fluids 25 (1982) 1493.

/ 8/ Becker, G., Nucl. Fusion 28 (1988) 1458.

/ 9/ Becker, G., Nucl. Fusion 27 (1987) 11.

/10/ Shaing, K.C., Phys. Fluids 31 (1988) 2249.

/11/ Adam, J.C., Tang, W.M., Rutherford, P.H., Phys. Fluids 19 (1976) 561.

/12/ Lackner, K., Behringer, K., Engelhardt, W., Wunderlich, R., Zeitschr. Naturforsch. 37a (1982) 931.

/13/ Fahrbach, H.U., Herrmann, W., Mayer, H.M., in Controlled Fusion and Plasma Physics 1989 (Proc. 16th Europ. Conf. Venice, 1989), Part IV, European Physical Society (1989) 1537.

/14/ Gehre, O., Fussmann, G., Gentle, K.W., Krieger, K., in Controlled Fusion and Plasma Physics 1989 (Proc. 16th Europ. Conf. Venice, 1989), Part I, European Physical Society (1989) 167.

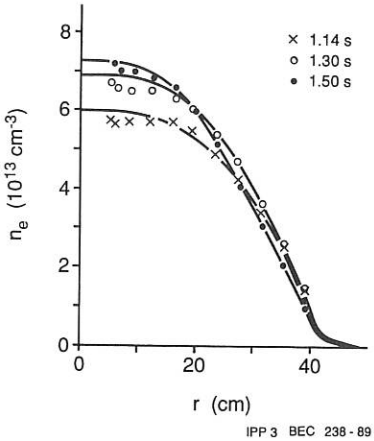

Fig. 1:
Evolution of electron density profiles measured by periodic multichannel Thomson scattering and computed (solid curves).

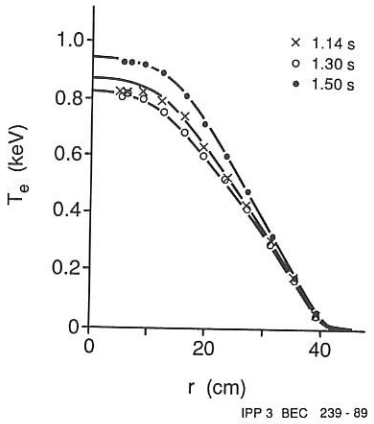

Fig. 2:
As in Fig. 1, but electron temperature profiles.

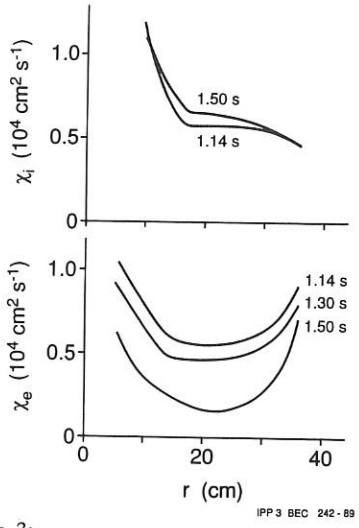

Fig. 3:
Time developments of corresponding χ_e and χ_i profiles with $\chi_i / \chi_{ineo} = 1.4$. The higher diffusivities in the inner plasma take into account the enhanced losses due to sawteeth.

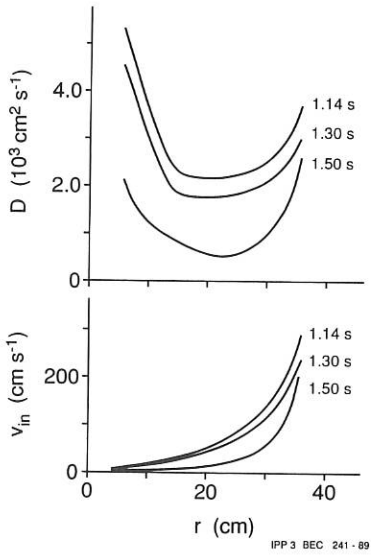

Fig. 4:
As in Fig. 3, but D and v_{in} profiles.

UNIFIED χ_e SCALING FOR THE OHMIC, L AND INTERMEDIATE REGIMES OF ASDEX

G. BECKER

(Max-Planck-Institut für Plasmaphysik,
Euratom-IPP Association, Garching bei München,
Federal Republic of Germany)

ABSTRACT. Dimensional analysis is applied to derive a unified scaling relation for the electron heat diffusivity χ_e from empirical scaling laws for Ohmically heated and auxiliary-heated plasmas. It is found that particle orbit, collisionality and finite pressure effects enter and that the different scalings in the various regimes are due to changes in the finite beta contribution. The χ_e scaling law for the intermediate region between OH and L confinement leads to a new global expression for the energy confinement time. The results are compared with microturbulence-induced transport.

Flux surface averaged cross-field transport has been determined by local transport analysis of many series of Ohmically heated (OH) and auxiliary-heated (L and H) discharges in the ASDEX divertor tokamak /1,2/.The following empirical scaling relations for the electron heat diffusivity and the diffusion coefficient were obtained:

$$\chi_e^{OH}(r) \propto A_i^{-\frac{1}{2}} B_t\, n_e(r)^{-1}\, T_e(r)^{-1}\, q(r)^{-1} \tag{1}$$

$$\chi_e^{L,H}(r) \propto A_i^{-\frac{1}{2}} B_t^{-1}\, q(r) \tag{2}$$

where A_i is the ion mass number and B_t is the toroidal magnetic field taken at the major radius R. The L and H scalings exhibit different numerical factors /2/. Relation (2) holds for heating powers much higher than the Ohmic input prior to the auxiliary heating ($P_{AUX} / P_{OH} >> 1$). Out-standing features of the L and H scalings in the asymptotic limit are the lack of density and temperature dependences and the inverse B_p scaling ($qB_t^{-1} = r(B_pR)^{-1}$, $\tau_E^{L,H} \propto I_p$).

The thermal diffusivities are expressed in dimensionless form by the ansatz

$$\frac{\chi_e}{D_B} \propto \left(\frac{\rho_e}{a}\right)^{\alpha_1} \left(\frac{a}{\lambda_e}\right)^{\alpha_2} \beta_e^{\alpha_3}\, q^{\alpha_4} \left(\frac{m_e}{m_i}\right)^{\alpha_5} \tag{3}$$

with

$$D_B = \frac{c\,T_e}{16\,e\,B_t}, \quad \frac{\rho_e}{a} = \frac{c\,m_e^{\frac{1}{2}}\,T_e^{\frac{1}{2}}}{e\,B_t\,a}, \quad \frac{a}{\lambda_e} = \frac{a}{v_{Te}\tau_{ee}}, \quad \beta_e = \frac{8\pi n_e T_e}{B_t^2}, \tag{4}$$

where a is the plasma radius, D_B is the Bohm diffusion coefficient, ρ_e is the electron gyroradius, λ_e is the mean free path for electron-electron collisions,and β_e is the beta value due to the electron pressure. The empirical scalings can be represented by

$$\frac{\chi_e^{OH}}{D_B} \propto \frac{\rho_e}{a}\left(\frac{a}{\lambda_e}\right)^{\frac{1}{2}} \beta_e^{-\frac{3}{2}}\ q^{-1}\left(\frac{m_e}{m_i}\right)^{\frac{1}{2}} \tag{5}$$

$$\frac{\chi_e^{L,H}}{D_B} \propto \frac{\rho_e}{a}\left(\frac{a}{\lambda_e}\right)^{\frac{1}{2}} \beta_e^{-\frac{1}{2}}\ q\left(\frac{m_e}{m_i}\right)^{\frac{1}{2}} \tag{6}$$

They differ only in their dependence on β_e and q. Particle orbit, collisional and finite β contributions are important in all regimes. Equations (5) and (6) can be combined by writing

$$\frac{\chi_e}{D_B} \propto \left(\frac{m_e}{m_i}\right)^{\frac{1}{2}} \frac{\rho_e}{a}\left(\frac{a}{\lambda_e}\right)^{\frac{1}{2}} \beta_e^{-1}\ (\beta_e q^2)^{\alpha} \tag{7}$$

with $\alpha = -\frac{1}{2}$ in the Ohmic and $\alpha = \frac{1}{2}$ in the L, H case. The change in scaling is merely due to the factor $(\beta_e q^2)^{\alpha}$. The exponent rises with the auxiliary heating power and beta (starting from $\alpha = -\frac{1}{2}$ for $P_{AUX}/P_{OH} = 0$) and saturates at $\alpha = \frac{1}{2}$ for $P_{AUX}/P_{OH} \approx 4$. The different scalings in the OH and L, H regimes thus result from changes in the finite pressure contribution.From Eq. (7) the following unified scaling law is obtained:

$$\chi_e(r) \propto a^{-\frac{1}{2}} A_i^{-\frac{1}{2}}\, n_e(r)^{\alpha-\frac{1}{2}}\, T_e(r)^{\alpha-\frac{1}{2}} \left(\frac{q(r)}{B_t}\right)^{2\alpha} \tag{8}$$

with $-\frac{1}{2} \le \alpha \le \frac{1}{2}$. It holds for the OH $\left(\alpha = -\frac{1}{2}\right)$ and L, H regimes $\left(\alpha = \frac{1}{2}\right)$ and for the intermediate region between OH and L confinement $\left(-\frac{1}{2} < \alpha < \frac{1}{2}\right)$. With increasing α the density and temperature dependences become weaker and finally disappear in the L and H regimes. Simultaneously, the inverse B_p scaling is approached. The smooth transition from OH to L confinement agrees with experimental findings /3/ when α is approximated by the expression $\alpha = 0.25\ P_{AUX}/P_{OH} - 0.5$ for $P_{AUX}/P_{OH} \le 4$. It is obvious that χ_e does not simply result from the superposition of Ohmic and pure L scalings.

The global scaling law proposed (without proof) in Ref. /4/

$$\frac{1}{\tau_E} = \left[\left(\frac{1}{\tau_E^{OH}}\right)^2 + \left(\frac{1}{\tau_E^{AUX}}\right)^2\right]^{\frac{1}{2}} \tag{9}$$

corresponds to $\chi_e = \left[(\chi_e^{OH})^2 + (\chi_e^{AUX})^2\right]^{\frac{1}{2}}$

with $\chi_e^{AUX} = C^{AUX} f(r)\, \beta_e\, q^2$. It is interesting that this term appears also in Eq. (7), but it enters in a different way

$$\chi_e \propto \chi_e^{OH}\left(\frac{\chi_e^{AUX}}{C^{AUX} f}\right)^{\alpha+\frac{1}{2}} \tag{10}$$

The global energy confinement time in the intermediate region thus scales as

$$\tau_E \propto \tau_E^{OH} \left(\frac{\tau_E^{AUX}}{\tau_n} \right)^{\alpha + \frac{1}{2}} \qquad (11)$$

with $\tau_n \propto a^2 / C^{AUX}$, which is different from Eq. (9).

Turning now to microinstability-based transport models, we focus on the question whether drift wave turbulence can be responsible for the empirical diffusivities in Eqs. (1) and (2) and the particle orbit, collisional and finite beta contributions (see Eq. (7)). From gyrokinetic models which neglect collisions and finite pressure effects it follows that

$$\chi_e \propto \frac{T_e}{B_t r_n} \frac{1}{k_\perp} \qquad (12)$$

with the density scale length $r_n = |d \ln n_e / dr|^{-1}$ and the wave number $k_\perp$. Replacing $k_\perp$ by the fastest growing wave number of most drift instabilities given by $k_\perp \rho_s \cong 0.3$, where $\rho_s = m_i^{\frac{1}{2}} c T_e^{\frac{1}{2}} / (eB_t)$ is the ion gyroradius evaluated at the electron temperature, then yields

$$\chi_e \propto A_i^{\frac{1}{2}} \frac{T_e^{\frac{3}{2}}}{B_t^2 r_n} \qquad (13)$$

Compared with the empirical scaling laws, this formula has the wrong dependence on B_t, T_e and A_i. Taking into account only particle orbit effects is thus totally insufficient. If collisions are included, a υ_{ei}-dependent factor appears, which, however, does not remove the B_t^{-2} scaling. Note that the different B_t laws cannot be reconciled either by a factor q^2 since this would introduce a wrong B_p variation. It is thus concluded that purely electrostatic drift wave turbulence is not consistent with the empirical scalings in the OH, L and H regimes. Electromagnetic effects have to be included. Taking into account the fluctuations of the parallel vector potential $\tilde{A}_\parallel$ can introduce a β dependence.

The OH regime and intermediate region between OH and L confinement of ASDEX are characterized by $P_{AUX} / P_{OH} = 0$ to 4.0, $\beta = 0.3$ to 0.6 % and $\beta_p = 0.3$ to 0.6 (for $I_p = 380$ kA). In this beta range the growth rate and k spectrum of drift instabilities are just slightly modified by the electromagnetic terms /5/. The anomalous transport due to electrostatic fluctuations $(\tilde{\Phi})$ does not differ much from that in the $\beta = 0$ limit. A substantial change can occur, however, in the electron heat diffusivity owing to the magnetic fluctuations $(\tilde{A}_\parallel)$. Incorporating both Φ and $\tilde{A}_\parallel$ induced by drift instabilities and applying $\rho_e^2 \omega_{pe}^2 \propto \beta_e$ yields a scaling as $\chi_e / D_B \propto \beta_e^{-1}$ /6, 7/. Consequently, the inverse β_e dependence in Eq. (7) can be explained by drift wave turbulence if electromagnetic effects are included. It should be mentioned that the β_e^{-1} scaling is also obtained from microtearing /8, 9/ and drift-tearing modes /10/.

It seems to be impossible to reconcile the factor $(\beta_e q^2)^\alpha$ in the empirical scaling law with the theoretical diffusivities inferred from drift wave turbulence alone. The dependence on $\beta_e q^2$ with positive exponent α is indicative of pressure-driven modes, since a similar factor $[\beta q^2 R / (r_p s)]^\mu$ appears in the diffusivities derived from resistive ballooning /11/ or interchange instabilities /5/.

Here, $r_p = |d \ln p/dr|^{-1}$ is the pressure scale length and $s = (r/q)\, \partial q / \partial r$ is the dimensionless shear.

For the Ohmic case, a factor close to $(\beta_e q^2)^{-\frac{1}{2}}$ was deduced from a model based on drift-tearing instabilities and magnetic reconnection /10/. These modes are driven by the current density gradient. It is likely that the α increase with heating power and beta in the intermediate region reflects the growing contribution of pressure-driven modes, e.g. resistive ballooning modes, to magnetic turbulence induced transport.

It is concluded that the empirical χ_e scalings in the OH, L and H regimes are incompatible with purely electrostatic drift wave turbulence. Inclusion of electromagnetic effects yields the β_e^{-1} scaling but fails to explain the factor $(\beta_e q^2)^{\alpha}$ which is indicative of resistive ballooning or interchange instabilities. The different scalings in the OH and L, H regimes result from changes in this finite pressure contribution and thus in magnetic turbulence induced transport.

References

/1/ Becker, G., Nucl. Fusion 24 (1984) 1364.

/2/ Becker, G., Nucl. Fusion 28 (1988) 1458.

/3/ Wagner, F., Gruber, O., Bartiromo, R., Becker, G., Bosch, H.S., et al., in Controlled Fusion and Plasma Physics 1985 (Proc. 12th Europ. Conf. Budapest, 1985) Part I, European Physical Society (1985) 335.

/4/ Goldston, R.J., Plasma Phys. Controll. Fusion 26 (1984) 87.

/5/ Waltz, R.E., Phys. Fluids 28 (1985) 577.

/6/ Molvig, K., Hirshman, S.P., Whitson, J.C., Phys. Rev. Lett. 43 (1979) 582.

/7/ Parail, V.V., Pogutse, O.P., in Plasma Physics and Controlled Nuclear Fusion Research 1980 (Proc. 8th Int. Conf. Brussels, 1980), Vol. 1, IAEA, Vienna 1981, 67.

/8/ Ohkawa, T., Phys. Lett. 67A (1978) 35.

/9/ Drake, J.F., Gladd, N.T., Liu, C.S., Chang, C.L., Phys. Rev. Lett. 44 (1980) 944.

/10/ Coppi, B., Mazzucato, E., Phys. Lett. 71A (1979) 337.

/11/ Carreras, B.A., Diamond, P.H., Murakami, M., Dunlap, J.L., Bell, J.D., et al., Phys. Rev. Lett. 50 (1983) 503.

CHANGES IN THE DENSITY PROFILE DUE TO THE m=2 TEARING MODE IN ASDEX

M. E. Manso, A. Silva, F. Serra, J. Matias, J. Mendonça
Instituto Superior Tecnico, Lisboa, Portugal

H. Zohm, O. Klüber, F. X.- Söldner
Max-Planck-Institut fur Plasmaphysik, Garching, F.R.G.

1 - Introduction

Resistive MHD tearing modes can develop magnetic islands near the rational magnetic surfaces, where q=m/n. In some situations, depending on the shape of the current profile and on the radial position of the q=2 surface, the (m=2,n=1) rotating structure of growing islands can come to rest ("mode locking"); in ASDEX, the so-called locked modes can be found for several plasma scenarios, and generally they are precursor to disruptions /1/.The magnetic structure of rotating tearing modes in a tokamak plasma is quite well known from the measurements of the modulations of the poloidal magnetic field. We have studied the effects on plasma density of large amplitude m=2, n=1 modes in ASDEX, using broadband microwave reflectometry.

2 - Density profile deformations

Reflectometric measurements were performed with the ASDEX O-mode reflectometric system, described in an acompanying paper /2/. Signals were obtained with two reflectometers (covering respectively the ranges 18-26.5 and 26.5-40 GHz), during Lower Hybrid Current Drive (LHCD) discharges. Results are shown concerning the shot 29285 where a locked mode occured between 1577 and 1585 ms, refering to: (a) magnetic island rotation at t=1565 ms, (sweep time t=2 ms), and (b) mode locking at t=1580 ms.

Before locking, the signals show both amplitude and phase modulations /2/ with the periodicity T of the tearing mode measured with the Mirnov coils, $T^{-1} = f_{rot} \simeq 1.4$ KHz. The spectrum exhibits several high amplitude peaks, related to the observed modulations (Fig.1a), showing the strong effect of the magnetic islands on the plasma profile. The phase shift, $\Delta\Phi/\Delta F$, of the plasma reflected microwaves (18-40 GHz) is presented in Fig.2a. It exhibits two disturbed regions: the beat frequency f ($f \propto \Delta\Phi/\Delta F$) decreases followed by an increase, corresponding respectively to outward and inward movements of the plasma layers, occuring during the 2ms (0.5 KHz) measuring time. The corresponding deformations can be seen on the evaluated profile (Fig.3a).

During mode locking, the signal at 26.5-40 GHz presents an abrupt increase in the beat frequency for microwaves with F>F'~31.2 GHz. The spectra exhibit two single peaks respectively at $f_1 \sim 22$ KHz and $f_2 \sim 40$ KHz (Fig.1b); the peak at f_2 can clearly be seen by performing a partial spectral analysis from F' to 40 GHz. The non existence of secondary peaks,

(as observed in the frequency spectra before the locking), confirms that these are due to density perturbations induced by the rotating magnetic island m=2. The phase shift $\Delta\Phi/\Delta F$ (18-40 GHz) presents two abrupt jumps, (see Fig. 2b), revealing the displacement inwards of the reflecting layers with those densities. The density profile (Fig. 3b), presents two density plateaus, (corresponding to the phase shift jumps) respectively for: (1) r = 29-32.5 cm, and (2) r=39-40.5 cm.

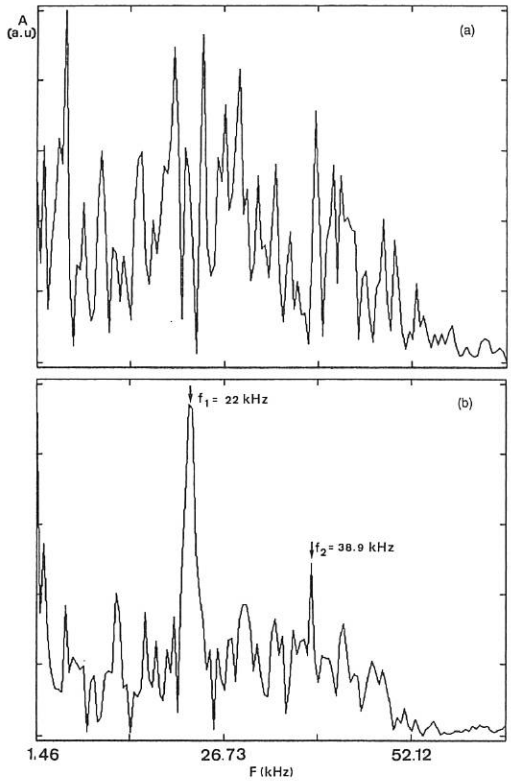

Fig. 1

The density outside (inside) the plateaus increases (decreases) and the density gradient decreases (increase) as compared to the profile measured before the magnetic islands develop. So it seems that the profile undergo a periodic deformation (T^{-1}) that is not limited to the regions where the plateaus occur. The reflectometric antennae are located in the mid-plane, such that for the magnetic island with m=2 the toroidal angular distance to "O" point is ~ 150°, so the first measured plateau should roughly correspond to only 30% of the island width; this yields an island width of about 10 cm, centered at r ~ 30-31 cm, which is in agreement with the results derived from the magnetic data for the m=2 mode. The second plateau must likely be located near another rational surface and it will be the subject of further investigation.

3 - Numerical modelling

In order to have some insight about the characteristics of the perturbation originating the deformations of the profile during the island rotation a numerical study was performed, by considering a profile of parabolic shape with neo=$2.5*10^{13}$ cm^{-3}. The density effects due to the tearing mode with m=2 (n=1) were simulated by assuming a density plateau in

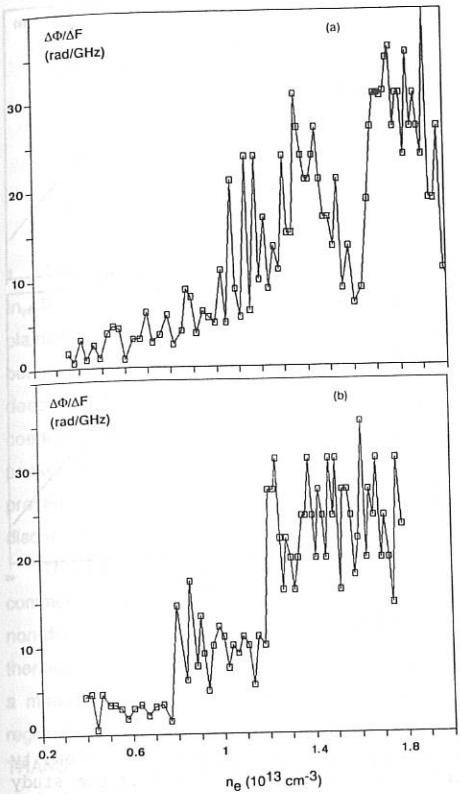

Fig. 2

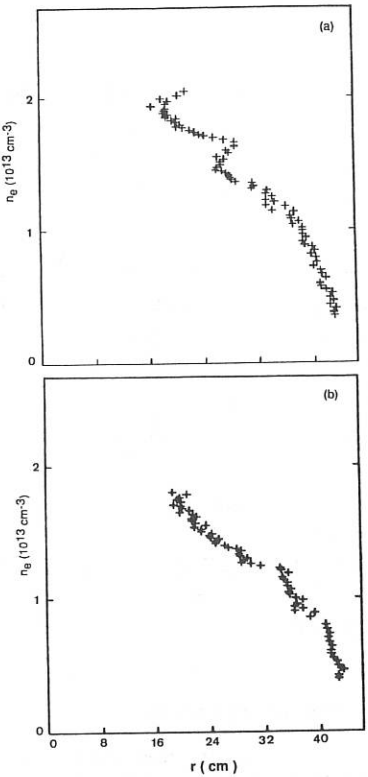

Fig.3

the profile (q=2, near r ~ 30 cm) whose width can vary as the width of a rotating magnetic island observed in a fixed position (θ=0, in the mid-plane), i.e. $w^*((1 + \cos(m\theta + \omega_{rot} t + \phi))/2)$. When the mode is locked, f_{rot} =0, ϕ =150°, and w(1580ms)=10 cm as concluded before; for frot=1.4 kHz, we consider w(1565ms)=8 cm, that takes into account the growing of the island before locking as evaluated from magnetic measurements. Fig.4 shows the numerically estimated microwave shifts for: (a) f_{rot} =1.4 KHz, (b) f_{rot} =0 KHz, and the corresponding profiles, Fig.5 (a) and (b), evaluated using the simulated phase shifts. Good agreement with the reflectometric measurements is obtained, namely in the observed perturbation when the island is rotating. From the observed deformation of the profile at t=1565 ms, it can therefore be concluded that a density plateau within the island structure (observed after mode locking, at 1580 ms) should already exist before mode locking occurs, rotating with the magnetic perturbation.

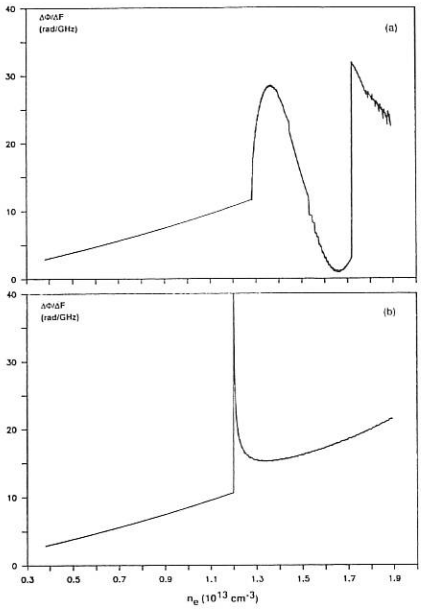

Fig. 4

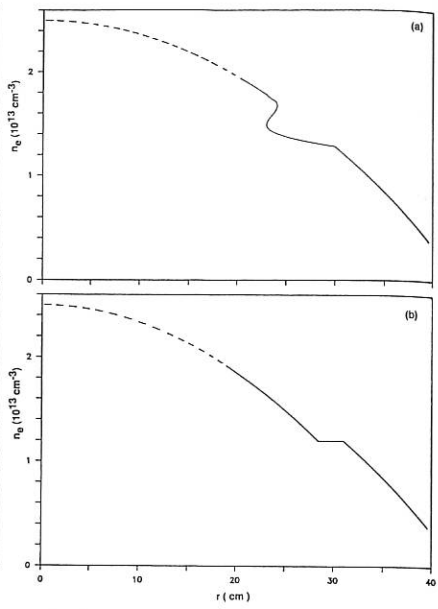

Fig.5

4 - Concluding remarks

The use of microwave reflectometry provided localized density measurements with good spatial and temporal resolution enabling the study of density perturbations due to m=2 tearing mode; the experimental results also indicates the existence of other density perturbations. Further work will aim at the study of the effect on density of the islands developed in other magnetic surfaces (namely q=3/2, q=5/2 and q=3), in order to have insight about the modifications caused by LHCD on the q-profile as compared with the ohmic regime. Experiments that will enable the obtention of a sequence of profiles during mode locking are foreseen; the study of the profile evolution might provide a tool to estimate the (nonlinear) growth of the magnetic islands, and therefore contribute to have insight about the behaviour of the plasma before disruption.

References

/1/ H. Zohm, A. Kallenbach, H. Bruhns, G. Fussmann, O. Kluber, to be published in Europhys. Lett (1990).
/2/ M. E. Manso, F. Serra et al. This Conference.

DETERMINATION OF OFF-DIAGONAL TRANSPORT COEFFICIENTS FROM PARTICLE AND POWER BALANCE ANALYSIS

O. Gruber, W. Schneider, K. Lackner

Max-Planck-Institut für Plasmaphysik, EURATOM Association, D-8046 Garching, FRG

1. Introduction

In ASDEX pellet injection and IOC discharges give rise to density peaking which cannot be explained by changes in the charged particle deposition profile. Besides a particular plasma boundary behaviour distinct changes in the bulk particle transport are necessary and can be described by an increase of $-v_p/D$ (the ratio of the inward drift velocity and the diffusion coefficient used to describe formally the particle transport) /1/. Common to all cases with peaked density profiles - having $\eta = (\nabla T/T)/(\nabla n/n) = L_n/L_T < 1$ - is that they show an improvement in energy and impurity particle confinement compared with flat density profile discharges ($\eta > 1$).

These related changes of the bulk energy and particle transport properties point towards a common change of the transport coefficients and may be interpreted in terms of a generalized non-diagonal model of particle and energy transport connecting the fluxes with the driving thermodynamic forces, namely the gradients of pressure (p) and temperature(T). Using such a model we look for a consistent set of transport coefficients in the different confinement regimes on ASDEX taking the fluxes from radial particle and power balance analysis using the TRANSP code. The numerical procedure to calculate the coefficients and results for L- and H-mode discharges are presented in this paper.

2. Transport equations and numerical procedure

Using non-equilibrium thermodynamics linear relations between the fluxes of particles (Γ_p) and energy (Q) and the true thermodynamic forces, i.e. the gradients of 1/T and μ/T for both electrons and ions (with the chemical potential μ), can be derived satisfying the Onsager symmetry for the off-diagonal coefficients. Subtracting the convective energy flux from the total energy flux Q to get the conductive heat flux $q = Q - 2.5\,kT\,\Gamma_p$ and normalizing the energy flux equation by kT one obtains relations between Γ_p, $\Gamma_{q,e}$ and $\Gamma_{q,i}$ ($\Gamma_q = q/kT$) and the recalculated forces ($\nabla T_e / T_e$, $(1+T_i / T_e)\,\nabla p/p$ and $(T_i / T_e)\,\nabla p_i/p_i$) still satisfying the Onsager symmetry for off-diagonal coefficients. Assuming $n_i \approx n_e$, $T_i \approx T_e$ and a plausible relation between off-diagonal elements the following radial electron transport model results

$$\Gamma_p = n\,D(1+\eta)(-\nabla n/n) - n\,\alpha(-\nabla T/T)$$
$$\Gamma_q = -n\,\alpha(1+\eta)(-\nabla n/n) + n\,\chi(-\nabla T/T), \qquad \leftarrow\ -\nabla p/p = (1+\eta)(-\nabla n/n) \qquad (1)$$

differing from those proposed in Ref. /2/ (the index e is omitted here and in the following). It has to be noted that we have neglected the contribution of ExB drift motions, whereas the Ware pinch contribution to the particle flux is taken into account in calculating Γ_p (see sect. 3). Connections to the often used ansatz $\Gamma_p = n\,D(-\nabla n/n) + n\,v_p$ and the simplified diagonal ansatz $\chi_{eff} = q/(nk\,\nabla T)$ will be given in sect. 3. Taking the rate of change of the entropy density for each specie

$$\partial s/\partial t = -\,\Gamma_p\,\nabla\,(\mu/T) + Q\,\nabla(1/T)$$

the requirement of increasing entropy implies a restriction on α. If we introduce $\mu = D/\chi$ and $\alpha = \sqrt{\mu}\,\chi\,\varepsilon$ the entropy production will be positive definite if the condition $\varepsilon \leq 1$ is fulfilled.

The numerical procedure for solving the above equations determines spline fits (up to third order in r) for the transport coefficients χ, μ and ε between several knots by minimization of the deviations of the calculated fluxes from the input values at the grid points used. The fit functions have a vanishing first derivitive at r = 0 and are continuous differentiable yielding the corresponding boundary conditions at the knots. With the present notation of the transport coefficients an upper bound for one of them (ε) can be given, but they enter non-linearly into the fluxes which may produce numerical problems.

The procedure has been tested first, therefore, by calculating input profiles for the fluxes and driving forces with a simulation code and assumed transport coefficients. A comparison between given and fitted coefficients is shown in Fig.1a for $\chi = (1.2\text{-}r^2/a^2)^{-1}$, $\mu = .2$ and $\varepsilon = .5 + .1\cos(2\pi r/a)$. All three quantities are recovered within 10 % nearly independent from the number of knots (3-6), while the fluxes are fitted within 10^{-3}. This result is corroberated by error analyses using modified T and n profiles obtained from the simulated ones by changing their gradients by ±10% while keeping the pressure profile p = nkT constant. One gets reasonable recalculated coefficients for χ and - for r/a > .4 - μ and ε as shown in Fig.1a too. Even a non-symmteric profile of $\varepsilon = .5 + .3\sin(2\pi r/a)$ is fitted quite well for r/a > .2 using the same error analysis (Fig.1b). We can now look for transport coefficients (including radial profiles) fulfilling the equations above and want to improve our model in a second step to find different solutions for $\eta \gtrless 1$ confinement regimes.

3. Transport coefficients in L- and H-mode plasmas

First experimental results are obtained for two L-mode discharges with 1.3 MW and 4 MW NBI heating power,respect., and a H-mode phase for the higher power. For the high power L-mode case Fig.2a schows the analysed transport coefficients χ, D and α and the ratio $\mu = D/\chi$ using the error analysis described above. The calculated χ's are in the outer plasma regions by about a factor of two larger than the χ_{eff} shown for the unmodified measured profiles used in TRANSP. This is the influence of the off-diagonal term on the heat transport amounting to about 50 % of the ∇T-term in the energy flux equation for r/a > .6. A ratio of $\mu = D/\chi = .15\text{-}.25$ is found as derived from simulations of density ramp-up scenarioes. The particle velocity v_p as

defined above increases strongly outside of a/2 and is inward directed. The Ware pinch contributes significantly only inside a/4 to Γ_p and leads even to a small outward anomalous particle velocity due to the D η ($-\nabla n$) term. The determined values of ε increase from values near zero in the plasma center to about 0.7 near the boundary.

In the H-mode phase of the 4 MW heated discharge Γ_p and Γ_q are strongly reduced, as is χ in the outer plasma regions (see Fig.3b), compared with the corresponding L-mode values . The χ reduction is enhanced relative to the χ_{eff} change considered recently /3/. Due to the even more reduced values of α (note the different scale in Fig.3b) the off-diagonal contribution to the energy flux is negligible yielding $\chi \approx \chi_{eff}$. Additionally the anomalous particle velocity is smaller than the Ware pinch velocity up to r/a $\leq$ .8 which may be an ingredient to the extremely flat density profiles observed in ELM-free H-mode plasmas. The fact that the Ware pinch alone can be responsible for the particle flux for r/a< .6 may also explain the increase of μ (and, accordingly, D and α) towards r = 0 due to larger errors in our fit procedure.

The low power L-mode case confirms the L-mode results at the high power level showing less deteriorated heat and particle diffusivities (χ, D) and also a smaller influence of the off-diagonal terms (i.e. reduced α values). The increasing transport coefficients near the center may again be explained by the Ware pinch dominating up to r/a $\leq$.4. The other reason might be the circumstance that our n and T profiles used in the TRANSP analysis are sawteeth averaged and the enhanced transport coefficients describe the action of the strong sawteeth on the fluxes at q_a = 2.5 of this discharge.

4. Summary

Using a non-diagonal linear model for the particle and energy fluxes as functions of ∇p and ∇T we have analyzed the transport coefficients χ, D and α for L- and H-mode plasmas. In the L-mode the off-diagonal term can be substantial also for the energy transport. Moreover, the respective coefficient α has a radial profile very similar to those of χ and D, respect., pointing to the existence of a common driving mechanism for electron heat and particle transport.

References

/1/ O. Gruber, et al., Plasma Phys. and Contr. Fusion 30 (1988)1611
/2/ J. O'Rourke, Nucl. Fusion 27 (1987) 2075
/3/ O. Gruber, et al., Proc.12th Europ. Conf. on Contr. Fus. and Pl. Phys., 9F (1985) I,18

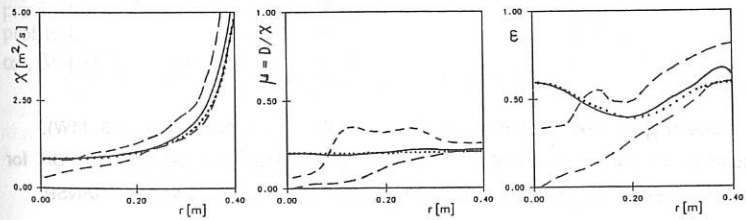

Fig. 1a

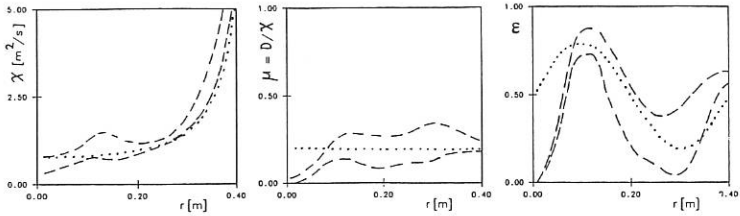

Fig. 1b

Fig.1 Comparison between given (····) and fitted (—) coefficients solving equ. (1). Results for modified n,T profiles (gradients are varried by ±10%) lie between the dashed lines.

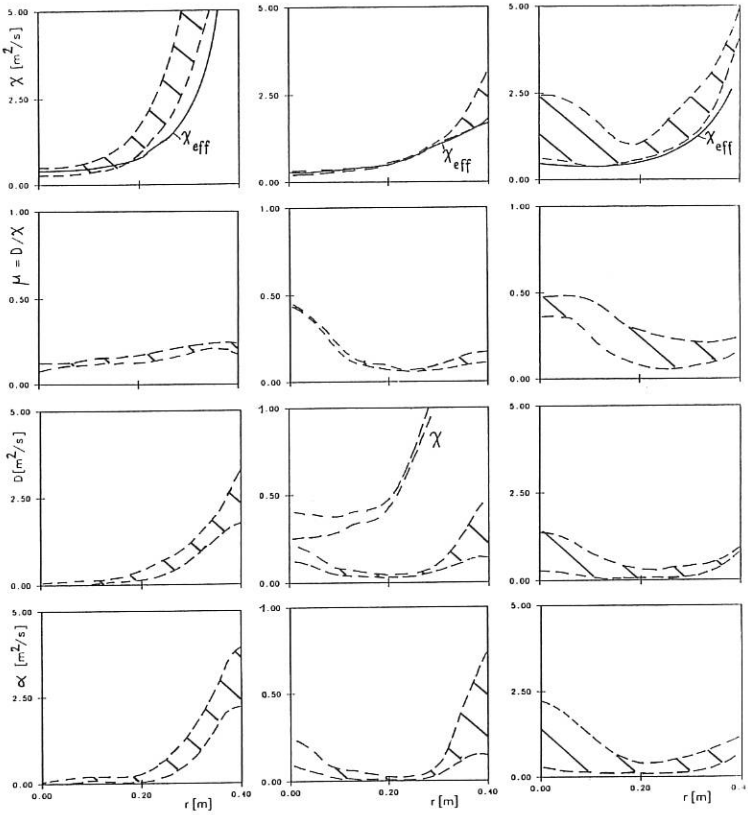

a) L-mode (P_{NI}=4 MW) b) H-mode (P_{NI}=4 MW) c) L-mode (P_{NI}=1.3 MW)

Fig.3 Calculated transport coefficients χ, D and α (off-diagonal) and the ratio $\mu = D/\chi$ for ASDEX discharges using measured n_e and T_e profiles and fluxes analysed by TRANSP.

THERMAL BIFURCATION AND STABILITY OF AN EDGE DIVERTED PLASMA

H. CAPES, PH. GHENDRIH, A. SAMAIN, J.P. MORERA

Association EURATOM-CEA sur la Fusion Contrôlée
CEN Cadarache, F-13108 - Saint Paul lez Durance, Cedex, France

ABSTRACT

In a previous paper [1] the authors have found several thermal equilibria for a 1D radiating layer at constant pressure profile. The stability of such equilibria is now discussed in connection with the radiative condensation instability [2]. The influence of the impurity density profile as the deviation to the constant pressure profile approximation is investigated numerically.

I - INTRODUCTION

We start from the heat equation in slab geometry :

$$\frac{d}{dx}\phi(x) = -\, n_e\, n_Z\, F_R(T) \quad , \quad \phi(x) = -\, K\, \frac{dT}{dx} \qquad (1)$$

where $\phi(x)$ is the heat flux, n_e and n_z are respectively the electron and impurity density, $F_R(T)$ is the plasma cooling rate function, K is the thermal conduction coefficient. In the case of the axisymmetric divertor (A.D) $K = K_{//} = 2.10^{22}\, T_e v^{5/2}$ ($m^{-1}\, s^{-1}$) and x is the abscissa along the flux line. For the ergodic divertor (E.D), x is the radial coordinate and we use the following expression for K which includes perpendicular transport effect [3] $K = K_{//}\, D$ where $D = 2\pi\, (\delta B/B)^2$.($\delta B$ is the magnetic perturbation created by the E.D coils). The boundary conditions first consist of a given heat flux from the plasma core ($x = x_1$) : $\phi\,(x = x_1) = \phi_1$. Next at the wall ($x = x_0$) we use the sheath conditions $\phi\,(x = x_0) = \phi_0 = \gamma \Gamma_0 T_0$, $\Gamma_0 = MD' n_0 v_0$ where $n_0 = n\,(x = x_0)$, $T_0 = T(x = x_0)$ and Γ_0 is the particle flux at the edge ; $v_0^2 = 2T_0/m$, m is the ion mass and γ the sheath potential ; $D' = 1$ in the A.D case while $D' = \delta B/B$ for E.D configuration - M is the Mach number.

Eq. (1) has been previously solved assuming a prescribed value for Γ_0. We are now concerned by the thermal stability of steady solutions for perturbations such that the growth rate is much smaller than the sound wave frequency so that the pressure perturbation is negligible. In that case the more convenient way to proceed is first to determine all the steady solutions of Eq. (1) for a prescribed pressure value $P_0 = n_0 T_0$. Using technics similar to the one presented previously [1], Eq. (1) is solved numerically with arbitrary pressure and impurity density profile. It can be shown that all the equilibria can be labelled in terms of only three parameters α^*, β^* and T^* with :

$$\alpha^* = \frac{C_R(\%)}{(M\gamma)^2\, A} \quad , \quad \beta^* = LA \quad , \quad T^* = \frac{\phi_1^2}{A^2\, \overline{\phi}^2} \qquad (2)$$

where C_R (%) is the impurity concentration, $A = P_0 / \bar{n}\,\bar{T}$, L the width of the radiating layer, $\bar{\phi} = M\gamma\,\bar{n}\,\bar{T}\,(2\bar{T}/m)^{1/2}\,(\delta B / B)$; here $\bar{n}$ and $\bar{T}$ are arbitrarily density and temperature normalization values. The first parameter α^*, is linked to the impurity concentration, the second β^* to the length of the radiative layer and the third T^* to the incident power. If there were no radiation losses $T^* = T_0$. Numerical solution of Eq. (1) are given in the next sections, assuming oxygen impurity only and the coronal expression for $F_R(T)$.

II - BIFURCATION AND THERMAL STABILITY

We first investigate the case where $F_R(T(x = x_1)) = 0$ so that only two parameters α^* and T^* are needed to characterize the steady solutions. A constant pressure profile is assumed and we take $n_z \sim n_e$. The results are discussed in term of the temperature at the wall T_0. For a given value of α^*, the solutions are plotted on Fig. 1. Two bifurcation points for instance $T^* = 33.6$ eV and $T^* = 50.4$ eV for $\alpha^* = 0.15$, which have infinite derivative (dT_0 / dT^*) are found. Between these two T^* values, three solutions are found for $T^* > 44.$ eV. For $T^* < 33.6$ eV no equilibrium exists. The two bifurcation points and the points where $T_0 = 0$ depend on α^*, and are plotted in the parameter space (α^*, T^*) in Fig. 2. The plane is divided in four regions I, II, III, IV with respectively 0, 1, 2, 3 solutions. In particular the region IV exhibits one steady solution with a low temperature at the wall even for high T^* values.

Let us now consider the stability of the existing equilibria for pertubations such that δP is negligible. For such thermal condensation instability it can be shown that the associated linearized equation for the temperature perturbation is hermitian. In that case the sign of the growth rate perturbation (ω) is given by sign (ω) = - sign (dT_0 / dT^*). As a consequence the low temperature solution of the region IV is stable.

III - EFFECT OF THE PRESSURE AND IMPURITY DENSITY PROFILE

The following cases have been computed for E.D configuration in TORE-SUPRA with $L = 0.1$ m, $\bar{n} = 10^{19}$ m^{-3} and $\bar{T} = 10$ eV. A constant impurity density in the layer is first assumed. In order to investigate the effect of the pressure profile variation due to neutral penetration, the pressure has been assumed to vary as $P / P_0 = 5. - 4. \exp - (x_0 - x) / \lambda L$ with $\lambda = 0.05$ and 0.3. The main effect shown on Fig. 3 is a shift of the low temperature domain in the plane (α^*, T^*) toward higher α^* and lower T^* values due to pressure variation.

Assuming a constant pressure profile, the influence of the impurity density profile is now investigated. In addition to the constant density case, two different density profiles, with the same average value have been used successively :

$$n_z = (5. - 4.\,(x_0 - x)\,/\,L)\,/\,3. \text{ and } n_z = (1 + 4.\,(x_0 - x)\,/\,L)\,/\,3.$$

The curves shown on Fig. 4 illustrate the influence of the impurity profile on the low temperature solution. For instance with an impurity density decreasing at the wall the domain in T^* where the low temperature solution can be reached is vanishing. This is also seen on Fig. 5 where n_z has been assumed to decrease to the wall.

IV - CONCLUSION

The number of equilibrium solutions of the heat equation has been studied and the stability of these solutions to the radiative condensation has been investigated. The main result is the existence at high power of a stable solution with a low edge temperature. The calculation shows that this solution becomes accessible at high power only if a strong impurity accumulation occurs at the plasma wall.

REFERENCES

[1] H. CAPES, PH. GHENDRIH, A. SAMAIN, A. GROSMAN and J.P. MORERA, Plasma Phys. and Controlled Nuclear Fusion (1990), 32, 103.

[2] J.F. DRAKE, Phys. Fluids (1987), 30, 2429.

[3] A. SAMAIN et al. (1984) J. Nucl. Mater 128-129, 185.

FIGURE CAPTIONS :

Fig. 1 : Variation of T_0 (T*) for $\alpha^* = 0.15$

Fig. 2 : Number of steady solutions in the plane (α^*, T*) for a constant pressure and impurity density profile :

Region			
	I	0	steady solution
	II	1	steady solution
	III	2	steady solutions
	IV	3	steady solutions.

Fig. 3 : Number of steady solutions in the plane (α^*, T*) for a constant impurity density profile and for two pressure profiles :

$$P / P_0 = 5. - 4. \exp - (x_0 - x) / \lambda L \quad \text{with } \lambda = 0.3 , 0.05$$

Fig. 4 : Variation of T_0 (T*) for different impurity densities ($\alpha^* = 0.03$)

---------- $n_Z = (1. + 4. (x_0 - x)/L) /3.$

..... $n_Z =$ Cte

_____ $n_Z = (5. - 4. (x_0 - x)/L) /3.$

Fig. 5 : Number of steady solution in the plane (α^*, T*) for $n_z \sim (1. + 4. (x_0 - x)/L)/3.$ and for a constant pressure profile.

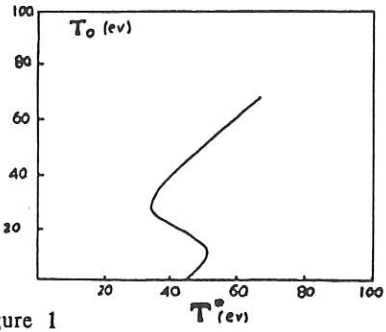

Figure 1

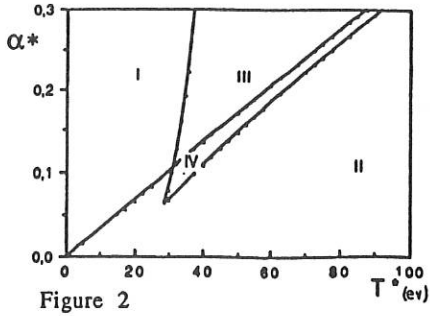

Figure 2

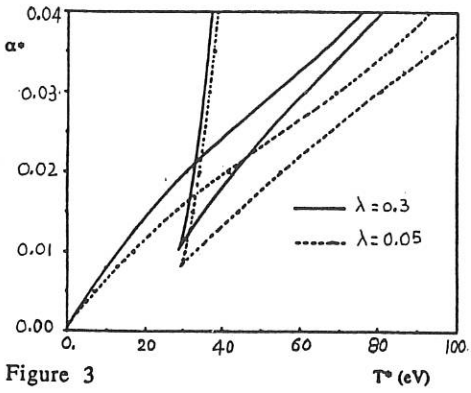

Figure 3

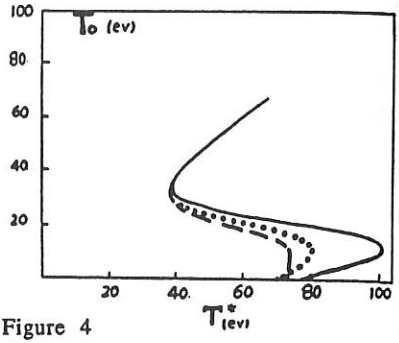

Figure 4

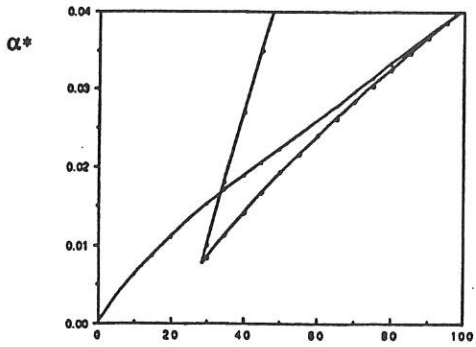

Figure 5

ON BOOTSTRAP CURRENT ENHANCEMENT BY ANOMALOUS ELECTRON-ELECTRON COLLISIONS

Aldo Nocentini

Dipartimento di Scienze Matematiche dell'Università, 34127 Trieste (Italy)
and The NET Team, c/o Max-Planck-Institut für Plasmaphysik, 8046 Garching (FRG)

Abstract: The effect on the tokamak current of an anomalous enhancement of $e-e$ collisions is considered. Its impact on tokamak reactor scenarios is discussed.

1. Introduction

Current drive in tokamaks by the bootstrap effect has attracted the attention of many authors. Recently /1/, it was noted that an enhancement (uniform in velocity space) of the $e-e$ collision frequency by anomalous effects could locally enhance the bootstrap current above its neoclassical value by a factor of the order of the square root of the local value of the inverse aspect ratio. This is attractive from the point of view of realizing long-burn tokamak reactors.

To examine this point in detail, we have considered a general expression for the current density in a tokamak, which has been recently derived within the framework of a "pseudoneoclassical" theory allowing for an "anomalous" enhancement (uniform in velocity space) of particle collisions /2/. The expression applies in all tokamak "regimes", for any shape of the (closed) magnetic surfaces and for any plasma composition. Here, for the sake of simplicity, we consider the particular case of a two-species tokamak plasma with magnetic surfaces having circular, concentric cross sections. The numerical results we present are obtained in this case, but the trends they show are generally valid. In §2 the expression of the toroidal component of the tokamak current is recalled. In §3 the influence of an anomalous enhancement of $e-e$ collisions is discussed. In §4 conclusions are presented.

2. The tokamak current

We consider the usual axisymmetric tokamak geometry, with circular, concentric cross sections of the magnetic surfaces. We use the right-handed, orthogonal coordinate system φ, r, ϑ, with φ the toroidal and ϑ the poloidal angle The external electric field is toroidal, $\underline{E}^{ext} = E_\varphi \underline{e}_\varphi$. In the plasma the components B_φ, B_ϑ and E_φ are positive throughout.

The toroidal component of the current density $\underline{j}$ can be written

$$j_\varphi = -\frac{c}{B_\vartheta}\Big(1 - \frac{B_\varphi^2}{< B^2 >}\Big)\frac{dP}{dr} + B_\varphi \frac{< \underline{B} \cdot \underline{j} >}{< B^2 >}, \tag{1}$$

where c denotes the speed of light, P the plasma pressure and the average $< A >$ of a quantity A is defined by $< A > = (\oint d\vartheta\, rA/B_\vartheta)/(\oint d\vartheta\, r/B_\vartheta)$.

Generally, the first term on the right-hand side of eq.(1) gives a negligible contribution to the current. Hence, we concentrate on the second term, which, in the case of a two-species tokamak plasma (electrons e and much heavier, $m_i \gg m_e$, singly ionized ions i) with equal temperatures, $T_e = T_i = T$, by neglecting terms of relative order $\sqrt{m_e/m_i}$, can be written /2/

$$< \underline{B} \cdot \underline{j} > = \sigma_{sp} K_\sigma < E_\varphi B_\varphi > \; - \; c\,\frac{B_\varphi}{B_\vartheta}\Big\{K_N T \frac{dN}{dr} + K_T N \frac{dT}{dr}\Big\}, \tag{3}$$

where $\sigma_{sp} = e^2 N \tau_{ee}/m_e$ is the Spitzer conductivity ($\tau_{ee} = 3\sqrt{\pi} m_e^2 v_{th,e}^3/16\pi N e^4 \Lambda$, where Λ denotes the Coulomb logarithm and m_e, $v_{th,e} = \sqrt{2T/m_e}$ and N denote respectively the mass, the thermal speed and the number density of electrons, is the classical electron collision time),

$$K_\sigma = \frac{1}{A}\big\{Y + 2.30 + x\big(0.98Y + 2.30\big)\big\}, \tag{4}$$

$$K_N = \frac{2x}{A}\big\{0.53Y^2 + 1.56Y + 0.71 + x\big(0.25Y^2 + 0.88Y + 0.71\big)\big\}, \tag{5}$$

$$K_T = K_N\,\frac{0.83 + 1.28x}{2.0 + 1.28x} - \frac{x}{A}\big(0.62Y^2 + 1.47Y\big), \tag{6}$$

$$A = Y + 0.71 + x\big(0.53Y^2 + 1.88Y + 1.41\big) \; + \; x^2\big(0.25Y^2 + 0.88Y + 1.41\big), \tag{7}$$

$$x = \frac{1.46\sqrt{\varepsilon} - 0.46\varepsilon}{1 - 1.46\sqrt{\varepsilon} - 0.46\varepsilon}\Big(1 + \frac{Y v_{th,e}}{\tau_{ee} q R_0 \varepsilon^{3/2}}\Big)^{-1}\Big(1 + \frac{Y v_{th,e}}{\tau_{ee} q R_0}\Big)^{-1}, \tag{8}$$

where q is the safety factor of the magnetic surface under consideration, R_0 the radius of the magnetic axis and $\varepsilon = r/R_0$. The enhancement factor for $e - e$ collisions is denoted by Y. Classical $e-i$ and $i-i$ collision frequencies are assumed. In the banana regime, x denotes the ratio of the numbers of trapped and untrapped particles. In the plateau regime (defined by $\varepsilon^{3/2} \ll Y v_{th,e}/\tau_{ee} q R_0 \ll 1$) it is inversely proportional to Y. In the Pfirsch-Schlüter regime (defined by $Y v_{th,e}/\tau_{ee} q R_0 \gg 1$ it is inversely proportional to Y^2.

3. Resistivity and bootstrap current

In general, the effect on the parallel conductivity and on the bootstrap current of an anomalous increase of the $e - e$ collision frequency depends on the value of x. Let

us consider the typical case of a magnetic surface on which the plasma is, for $Y = 1$, in the banana regime, and a substantial fraction of particles is trapped, i.e. $x \approx 1$. In this case, when Y increases, the parallel conductivity decreases (initially inversely proportional to Y) and reaches its minimum when the plateau regime (which is a very narrow region in this case) is reached. The amount by which the parallel conductivity decreases depends on (is proportional to) how deep in the banana regime the plasma is for $Y = 1$. Then, as Y continues to increase, it increases and eventually saturates (by becoming equal, deep in the Pfirsch-Schlüter regime, to the classical perpendicular conductivity). This holds when we start, for $Y = 1$, with x of the order or larger than 1. If we start with a value of x which is much smaller than 1, an increase of Y has only a negligible effect on the parallel conductivity and, if the starting value of x is sufficiently small, this holds throughout all regimes, so that by increasing Y the value of the parallel conductivity goes smoothly into the value of the perpendicular one, without strong variations. The reason for this behaviour can easily be explained by recalling that the electrical resistivity of a tokamak plasma in the banana regime is due to two effects: collisions of the circulating electrons with the ions and with the trapped electrons. The two effects are proportional to, respectively, the $e - i$ and the $e - e$ collision frequencies. If the number of trapped particles is not negligible with respect to the number of the circulating ones ($x \geq 1$), the first effect is at least comparable to the second one. Hence, within the banana regime the resistivity increases linearly with Y. On the other hand, for x very small the relative number of trapped particles is very small too, so that the value of the resistivity is dominated by $e - i$ collisions. In this case, the resistivity is affected by an increase of Y to a smaller extent.

As far as the bootstrap current is concerned, the dependence on Y is comparatively weaker. We consider again the typical case of a magnetic surface on which the plasma is, for $Y = 1$, in the banana regime. As Y increases, the bootstrap current increases and sets to a level which is by a factor of up to $1/x$ larger then its initial value (Connor and Taylor, 1987), up to when the Pfirsch-Schlüter regime is reached. If Y continues to increase, the bootstrap current decreases and eventually vanishes. Hence, in the case in which x is larger than, or of the order of 1, the value of the bootstrap current is not strongly affected by the enhancement of $e - e$ collisions (provided the Pfirsch-Schlüter regime is not entered too deeply). All three components of the bootstrap current (which are proportional to the gradients of, respectively, the pressure, the electron temperature and the ion temperature) have the same behaviour.

This is illustrated in the four figures, where x, K_σ, K_N and K_T are plotted. Two cases are considered. The first one (full line) refers to an inner magnetic surface ($\varepsilon = 0.1$, for $a/R_0 = 1/3$) and a plasma deep in the banana regime (the banana-plateau transition being at $Y = 100$, the plateau-PS one at $Y = 3162$). The second case (dashed line) refers to a magnetic surface near the wall ($\varepsilon = 0.25$ for $a/R_0 = 1/3$) and a plasma in the banana regime, but not so far from the banana-plateau transition (which is at $Y = 10$, while the plateau-PS transition is at $Y = 80$).

4. Conclusions

The presence of an anomalous increase of the $e - e$ collision frequency has been shown to lead locally, in a typical case, to a proportional increase of electrical resistivity, while the amount of bootstrap current does not increase very much. As a consequence, anomalous effects of this kind are favourable in the case of a steady-state tokamak equilibrium completely based on the bootstrap current effect and a non-inductive method to drive the necessary "seed current" in the center /3/. On the other hand, in the case where a non negligible fraction of the current is driven inductively, they tend to be unfavourable from the point of view of current shaping and loop voltage consumption, because the enhancement of the bootstrap effect is easily overcompensated by the increase of the electrical resistivity.

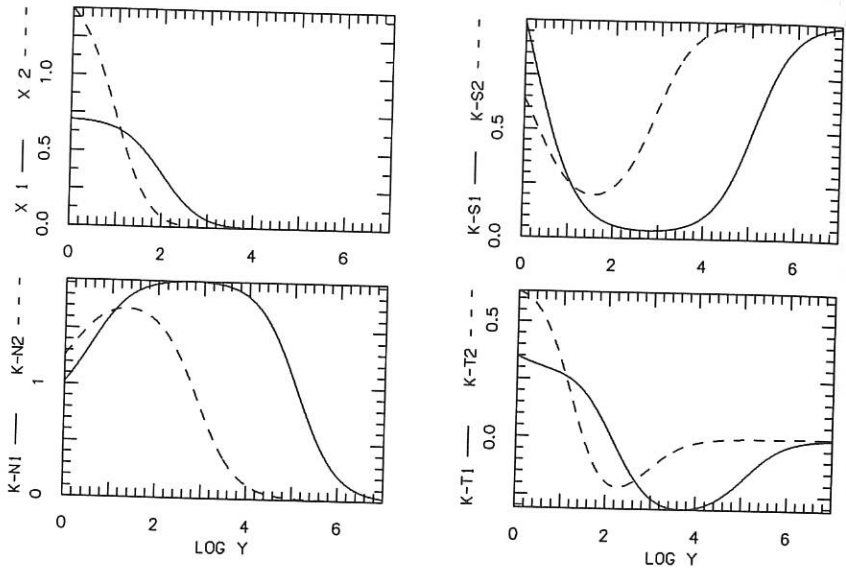

References

/1/ Connor J. W. and Taylor J. B., Comments Plasma Phys. Controlled Fusion 11, 37 (1987).

/2/ Nocentini A., to be published.

/3/ Bickerton R. J., Connor J. W. and Taylor J. B., Nature Phys. Science 229, 110 (1971).

DIRECT DERIVATION OF NEOCLASSICAL VISCOSITY COEFFICIENTS IN TOKAMAKS*

J.D. Callen, Z. Chang and J.P. Wang

University of Wisconsin, Madison, WI 53706-1687 U.S.A.

Abstract

All "banana-plateau" neoclassical transport effects stem from the parallel force due to the viscous stress along a magnetic field line[1]. The neoclassical viscosity coefficients in the low collisionality regime are usually derived somewhat indirectly[1,2]. Recently, we have developed[3] a Chapman-Enskog-like procedure for determining a kinetic equation for the distribution function distortions from which the viscous stress can be calculated directly. Both the more direct method of solution and the results for the viscosity coefficients in the banana collisionality regime are presented here.

Introduction

In the small gyroradius approximation, we have derived a drift kinetic version of the recast kinetic equation via a Chapman-Enskog-like procedure[3]. Under the customary incompressibility assumptions, i.e. $\nabla\cdot\vec{V}=0$ and $\nabla\cdot\vec{q}=0$, the drift kinetic Chapman-Enskog-like equation can be written for an axisymmetric tokamak plasma as

$$\frac{\partial\overline{F}}{\partial t}+v'_{\|}\vec{b}\cdot\nabla\overline{F}-\overline{C_R(F)}=\left[\frac{v'_{\|}}{p}\vec{b}\cdot(L_0^{(3/2)}\nabla\cdot\Pi+\frac{2}{5}L_1^{(3/2)}\nabla\cdot\Theta)-(v_{\|}'^2-v_{\perp}'^2/2)G\right]f_M \qquad (1)$$

where

$$G\equiv\frac{m}{T}[u_\theta L_0^{(3/2)}-\frac{2}{5p}q_\theta L_1^{(3/2)}]\vec{B}\cdot\nabla\ln B \qquad (2)$$

$$\overline{C_R(F)}=\frac{\nu_\perp}{2}\pounds\overline{F}+v'_{\|}(\nu_0 L_0^{(3/2)}+\nu_1 L_1^{(3/2)})f_M \qquad (3)$$

$$\nu_0\equiv-\frac{m}{p}\left[\frac{2q_{\|}}{5p}\int\frac{\nu_\perp}{3}\frac{v^2}{v_T^2}L_1^{(3/2)}f_M\,d^3v+\int\frac{\nu_\perp}{2}v_{\|}L_0^{(3/2)}\pounds F\,d^3v\right] \qquad (4)$$

$$\nu_1\equiv\frac{2q_{\|}}{5p}\frac{\nu_\perp}{v}-\frac{2m}{5p}\left[\frac{2q_{\|}}{5p}\int\frac{\nu_\perp}{3}\frac{v^2}{v_T^2}(L_1^{(3/2)})^2 f_M d^3v+\int\frac{\nu_\perp}{2}v_{\|}L_1^{(3/2)}\pounds F d^3v\right] \qquad (5)$$

$$u_\theta(\psi)\equiv\frac{\vec{V}\cdot\nabla\theta}{\vec{B}\cdot\nabla\theta}=\frac{V_{\|}}{B}+\frac{cI}{B^2}(\frac{\partial\phi}{\partial\psi}+\frac{1}{ne}\frac{\partial p}{\partial\psi}) \qquad (6)$$

$$q_\theta(\psi)\equiv\frac{\vec{q}\cdot\nabla\theta}{\vec{B}\cdot\nabla\theta}=\frac{q_{\|}}{B}+\frac{5cIp}{2eB^2}\frac{\partial T}{\partial\psi} \qquad (7)$$

and $\vec{v}'\equiv\vec{v}-\vec{V}$, $L_0^{(3/2)}=1$, $L_1^{(3/2)}=\frac{5}{2}-\frac{mv'^2}{2T}$, I is the poloidal current and $\pounds$ represents the Lorentz scattering operator. For simplicity, in the rest of this paper the prime (for coordinate system moving with $\vec{V}$) and the bar (gyromotion average) over F will be dropped.

Direct Calculation of Parallel Viscous Forces

Noting that

$$v_{\|}\vec{b}\cdot\nabla(v_{\|}B) = (v_{\|}^2 - v_{\perp}^2/2)\vec{B}\cdot\nabla\ln B,$$

where $(t, \vec{x}, v, \mu)$ are independent variables, the equilibrium drift kinetic equation can be cast into the following form

$$v_{\|}\vec{b}\cdot\nabla\left[F + v_{\|}B\frac{m}{T}(u_\theta L_0^{(3/2)} - \frac{2}{5p}q_\theta L_1^{(3/2)})f_M\right] - \frac{\nu_\perp}{2}\pounds F =$$
$$v_{\|}\left[(\nu_0 + \frac{1}{p}\vec{b}\cdot\nabla\cdot\Pi)L_0^{(3/2)} + (\nu_1 + \frac{2}{5p}\vec{b}\cdot\nabla\cdot\Theta)L_1^{(3/2)}\right]f_M. \tag{8}$$

Introducing a subsidiary ordering scheme ($\Delta \equiv \nu/\omega_b \ll 1$, where ω_b is the bounce frequency) valid in the banana collisionality regime, the distribution function distortion can be expanded as

$$F = F_0 + \Delta F_1 + \cdots \tag{9}$$

To the lowest order (Δ^0), the drift kinetic equation becomes

$$v_{\|}\vec{b}\cdot\nabla\left[F_0 + v_{\|}B\frac{m}{T}(u_\theta L_0^{(3/2)} - \frac{2}{5p}q_\theta L_1^{(3/2)})f_M\right] = 0, \tag{10}$$

whose general solution is

$$F_0 = v_{\|}B\frac{m}{T}(u_\theta L_0^{(3/2)} - \frac{2}{5p}q_\theta L_1^{(3/2)})f_M + g(v, \mu, \psi) \tag{11}$$

The constant of integration g must be determined from the next order (Δ^1) equation:

$$v_{\|}\vec{b}\cdot\nabla F_1 - \frac{\nu_\perp}{2}\pounds g = \frac{\nu_\perp}{2}v_{\|}B\frac{m}{T}(u_\theta L_0^{(3/2)} - \frac{2}{5p}q_\theta L_1^{(3/2)})f_M +$$
$$v_{\|}\left[(\nu_0 + \frac{1}{p}\vec{b}\cdot\nabla\cdot\Pi)L_0^{(3/2)} + (\nu_1 + \frac{2}{5p}\vec{b}\cdot\nabla\cdot\Theta)L_1^{(3/2)}\right]f_M \tag{12}$$

Taking the bounce average of the above equation, using

$$\oint\frac{dl}{v_{\|}} \equiv \begin{cases} \int_0^{2\pi}\frac{d\theta}{v_{\|}\vec{b}\cdot\nabla\theta}, & \text{circulating particles} \\ \sum_\sigma\int_{-\theta_c}^{+\theta_c}\frac{d\theta}{|v_{\|}|\vec{b}\cdot\nabla\theta}, & \text{trapped particles} \end{cases} \tag{13}$$

while the first term is anihilated, it is easy to show that

$$g_t = 0 \quad \text{for trapped particles}$$
$$g_{ut} \sim \int_\mu^{\mu_c}\frac{d\mu}{\langle v_{\|}\rangle} \quad \text{for untrapped particles}$$

with $\mu_c = \frac{1}{2}v^2/B_{max}$. Using the constraints $\int d^3v_{\|}L_i^{(3/2)}F_0 = 0$, with $i = 0$ or 1, we find

$$g = \frac{\langle B^2\rangle}{f_c}\frac{m}{T}(u_\theta L_0^{(3/2)} - \frac{2q_\theta}{5p}L_1^{(3/2)})f_M \frac{\sigma v}{2}\int_\lambda^{\lambda_c}\frac{d\lambda'}{\langle\sqrt{1-\lambda' B}\rangle}H(\lambda_c-\lambda), \tag{14}$$

where $\lambda = 2\mu/v^2$, $\lambda_c = 1/B_{max}$, $\sigma = \text{sign}(v_\parallel)$, $\langle\cdots\rangle$ represents a flux surface average, and H is a unit step function

$$H(\lambda_c-\lambda) = \begin{cases} 1, & \lambda \le \lambda_c, \quad \text{circulating} \\ 0, & \lambda > \lambda_c, \quad \text{trapped.} \end{cases}$$

Substituting the solution for g into the bounce-averaged first order drift kinetic equation, we obtain

$$\begin{aligned} &-\frac{\nu_\perp}{2}\langle\frac{B}{v_\parallel}\pounds g\rangle + (\tilde\nu_0 L_0^{(3/2)} + \tilde\nu_1 L_1^{(3/2)})f_M = \\ &\quad\Big[\Big(\langle B\int\frac{\nu_\perp}{2}v_\parallel L_0^{(3/2)}\pounds g\, d^3v\rangle + \frac{1}{p}\langle\vec B\cdot\nabla\cdot\mathbf{\Pi}\rangle\Big)L_0^{(3/2)} + \\ &\quad\Big(\langle B\int\frac{\nu_\perp}{2}v_\parallel L_1^{(3/2)}\pounds g\, d^3v\rangle + \frac{2}{5p}\langle\vec B\cdot\nabla\cdot\Theta\rangle\Big)L_1^{(3/2)}\Big]f_M. \end{aligned} \tag{15}$$

Defining a velocity-like variable [1]

$$u_\parallel \equiv \frac{\sigma v}{2}\int_\lambda^{\lambda_c}\frac{d\lambda'\langle B^2\rangle^{1/2}}{\langle\sqrt{1-\lambda' B}\rangle},$$

and taking the "proper"moments, $\int d^3v\, v_\parallel u_\parallel L_i^{(3/2)}H(\lambda_c-\lambda)$ of the bounce-averaged DKE we obtain the flux-surface-averaged viscous forces directly:

$$\begin{aligned} \langle\vec B\cdot\nabla\cdot\mathbf{\Pi}\rangle &= \frac{f_t}{f_c}\langle B^2\rangle\int d^3v\nu_\perp\frac{mv^2}{3v_T^2}L_0^{(3/2)}(u_\theta L_0^{(3/2)} - \frac{2q_\theta}{5p}L_1^{(3/2)})f_M \\ &\equiv mn(\mu_{00}u_\theta - \mu_{01}\frac{2q_\theta}{5p})\langle B^2\rangle \end{aligned} \tag{16}$$

$$\begin{aligned} \langle\vec B\cdot\nabla\cdot\Theta\rangle &= \frac{f_t}{f_c}\langle B^2\rangle\int d^3v\nu_\perp\frac{mv^2}{3v_T^2}L_1^{(3/2)}(u_\theta L_0^{(3/2)} - \frac{2q_\theta}{5p}L_1^{(3/2)})f_M \\ &\equiv mn(\mu_{10}u_\theta - \mu_{11}\frac{2q_\theta}{5p})\langle B^2\rangle \end{aligned} \tag{17}$$

$$f_c \equiv \frac{3}{4}\langle B^2\rangle\int_0^{\lambda_c}\frac{\lambda d\lambda}{\langle\sqrt{1-\lambda' B}\rangle}, \tag{18}$$

$$f_t \equiv 1 - f_c \simeq 1.46\sqrt{\varepsilon} + O(\varepsilon^{3/2}) \text{ for large aspect ratio tokamaks[4].} \tag{19}$$

The $\tilde\nu_0$, and $\tilde\nu_1$ terms in Eq.(15) are momentum-restoring type terms that do not contribute to Eqs.(16), (17) because the "proper" moments of them vanish.

Viscosity Coefficients

Carrying out the integrals above, we obtain for the viscosity coefficients in the banana collisionality regime[1]

$$\mu_{00} = \frac{f_t}{f_c}\frac{8}{3\sqrt{\pi}}\int_0^\infty \frac{v^4 dv}{v_T^5}\frac{\nu_\perp}{2}\exp(-v^2/v_T^2)[L_0^{(3/2)}]^2 \tag{20}$$

$$\mu_{01} = \frac{f_t}{f_c}\frac{8}{3\sqrt{\pi}}\int_0^\infty \frac{v^4 dv}{v_T^5}\frac{\nu_\perp}{2}\exp(-v^2/v_T^2)L_0^{(3/2)}L_1^{(3/2)} \tag{21}$$

$$\mu_{10} = \mu_{01} \tag{22}$$

$$\mu_{11} = \frac{f_t}{f_c}\frac{8}{3\sqrt{\pi}}\int_0^\infty \frac{v^4 dv}{v_T^5}\frac{\nu_\perp}{2}\exp(-v^2/v_T^2)[L_1^{(3/2)}]^2 \tag{23}$$

$$\tag{24}$$

For electrons and ions, these become

$$\mu_{00}^e = \frac{f_t}{f_c\tau_{ee}}\{Z+\sqrt{2}-\ln(1+\sqrt{2})\} \stackrel{Z\equiv 1}{=} 1.533\frac{f_t}{f_c\tau_{ee}} \tag{25}$$

$$\mu_{01}^e = \frac{f_t}{f_c\tau_{ee}}\{\frac{3}{2}Z+\frac{4}{\sqrt{2}}-\frac{5}{2}\ln(1+\sqrt{2})\} \stackrel{Z\equiv 1}{=} 2.125\frac{f_t}{f_c\tau_{ee}} \tag{26}$$

$$\mu_{11}^e = \frac{f_t}{f_c\tau_{ee}}\{\frac{13}{4}Z+\frac{39}{4\sqrt{2}}-\frac{25}{4}\ln(1+\sqrt{2})\} \stackrel{Z\equiv 1}{=} 4.636\frac{f_t}{f_c\tau_{ee}} \tag{27}$$

$$\mu_{00}^i = \frac{f_t}{f_c\tau_{ii}}\{\sqrt{2}-\ln(1+\sqrt{2})\} \stackrel{Z\equiv 1}{=} 0.533\frac{f_t}{f_c\tau_{ii}} \tag{28}$$

$$\mu_{01}^i = \frac{f_t}{f_c\tau_{ii}}\{\frac{4}{\sqrt{2}}-\frac{5}{2}\ln(1+\sqrt{2})\} \stackrel{Z\equiv 1}{=} 0.625\frac{f_t}{f_c\tau_{ii}} \tag{29}$$

$$\mu_{11}^i = \frac{f_t}{f_c\tau_{ii}}\{\frac{39}{4\sqrt{2}}-\frac{25}{4}\ln(1+\sqrt{2})\} \stackrel{Z\equiv 1}{=} 1.386\frac{f_t}{f_c\tau_{ii}} \tag{30}$$

Conclusions

The drift kinetic Chapman-Enskog-like equation utilized in this paper has proper momentum conserving properties. It is this property which enabled us to directly derive the neoclassical viscosity coefficients. Previous derivations [1,2,4] have had to use subtle procedures to cancel various momentum-conserving terms and thereby infer the neoclassical viscous forces.

[1] S.P. Hirshman and D.J. Sigmar, Nuclear Fusion 21, 1079(1981).

[2] K.C. Shaing and J.D. Callen, Phys. Fluids 26, 1526(1983).

[3] J.P. Wang, J.D. Callen and Z. Chang, Bull. Am. Phys. Soc. 34, 2043(1989).

[4] M.N. Rosenbluth, R.D. Hazeltine and F.L. Hinton, Phys. Fluids 15, 116(1972).

* Research supported by the U.S. DOE under grant DE-FG02-86ER53218.

TOKAMAK DENSITY PROFILES ASSOCIATED WITH VANISHING ENTROPY PRODUCTION

E. Minardi

Istituto di Fisica del Plasma, Ass. EUR-ENEA-CNR
Via Bassini, 15, 20133 Milano, Italy

Heat and particle flux coefficients involving non diagonal terms were recently considered in empirical attempts to fit the data on the radial transport in tokamaks (Capes, 1982, O'Rourke, 1987, Gruber, 1988). These terms provide a tool for the phenomenological description of the inward transport of nondiffusive nature, whose existence seems to be suggested by the observations in large tokamaks (Coppi, 1978; Behringer, 1980; Tubbing, 1987; Frederickson, 1986). In analogy with the Onsager formalism of the reciprocal relations (O'Rourke, 1987), we consider the following form for the equations of the radial heat and particle transport in a one fluid cylindrical approximation (neglecting the heat transported by particle diffusion):

$$\frac{3}{2}\frac{\partial}{\partial t}(nT)=\frac{1}{r}\frac{\partial}{\partial r}\left(r\alpha_{qq}\frac{\partial T}{\partial r}\right)+\frac{1}{r}\frac{\partial}{\partial r}\left(r\alpha_{pq}\frac{T}{n}\frac{\partial n}{\partial r}\right)+Ej+p_A=0 \qquad (1)$$

$$\frac{\partial n}{\partial t}=\frac{1}{r}\frac{\partial}{\partial r}\left(r\alpha_{pp}\frac{1}{n}\frac{\partial n}{\partial r}\right)+\frac{1}{r}\frac{\partial}{\partial r}\left(r\alpha_{pq}\frac{1}{T}\frac{\partial T}{\partial r}\right)+S(r,t) \qquad (2)$$

Here Ej is the ohmic power density, p_A is the auxiliary power density and S is the particle source.

One would expect that the physical meaning underlying the "ansatz" above could be related to a basic thermodynamic property of the plasma. It is then worthwhile, from this point of view, to investigate the relation between this form and the recently introduced concept of configurational entropy, based on the information theory (Minardi, 1988a). Recently the information entropy was applied to describe the canonical current and temperature profiles of the ohmically relaxed states of the tokamak (Minardi, 1989b). In the present work we shall investigate which conditions are imposed on the coefficient α_{pq} and on the density profile by the requirement that the configurational entropy is stationary, in other words that the steady state of the tokamak is associated with a vanishing entropy production.

The configurational entropy is constructed by operating in a suitably defined coarse-grained configuration space Γ (Minardi, 1988a, 1989a). The probability distribution P of the coarse grained current density and the entropy of the collective configuration $S_{coll}=-\int P\ln P d\Gamma$ are calculated in a statistical framework under suitable constraints which express on one hand the random character of the current density related to the particle structure and on the other the existence of collective Vlasov equilibria.

The Γ-integration implies an average over the background of free particle fluctuations so that S_{coll} is a functional of the collective part only of the current density and of the related vector potential. Its time derivative or entropy production calculated in accordance with the Maxwell equations and taking into account the heating rate due to p_A, has the form (1989b)

$$\frac{dS_{coll}}{dt} = \frac{1}{\tau} \int \left[p_A + \frac{E}{\mu^2} (\nabla^2 j + \mu^2 j) \right] dV \qquad (3)$$

Here j is the axial current density and τ is a constant which plays the formal role of the temperature in the statistical procedure and is related to the fluctuating background; μ^2 is a parameter characteristic of the equilibrium (μ^2 is arbitrary "a priori", and is related to the choice of the gauge).

In the confinement region delimited by the values $q(a) \gtrsim 2$ and $q(\lambda a) \approx 1$ of the safety factor (this is the only region of the tokamak discharge where our entropy consideration should hold) we assume ohmic relaxation, i.e. $j = E\, T^{3/2}/A$, where A is related to the Spitzer resistivity and is taken as uniform. At first we consider a situation in which α_{pq} is negligible. It turns out that by taking

$$\alpha_{qq} \equiv n\chi = \hat{n}\hat{\chi} \left(\frac{T}{\hat{T}}\right)^{1/2} \qquad (\lambda a \leq r \leq a) \qquad (4)$$

(where $\hat{n}$, $\hat{\chi}$, $\hat{T}$ are values at $r=\lambda a$ and $\hat{\chi}$ may depend on $\hat{T}$) one obtains from (3) and from the energy balance (1) the following meaningful expression for the entropy production:

$$\frac{dS_{coll}}{dt} = \frac{1}{\tau} \frac{3}{2} \int \frac{\partial}{\partial t} (nT) dV \qquad (5)$$

where we have fixed the parameter μ^2 as $\mu^2 = 3\, E^2\, \hat{T}^{1/2}/2\hat{\chi}A$. Thus the assumption of a vanishing entropy production in the plasma implies on one hand a constant plasma energy and on the other, recalling (3), a current density profile satisfying the equation

$$\nabla^2 j + \mu^2 j = -\mu^2 \frac{p_A}{E} \qquad (6)$$

We take now $\alpha_{pq} \neq 0$ together with the assumption that the configurational entropy remains stationary as in the case $\alpha_{pq} = 0$. This is tantamount to assume implicitly that the magnetic configuration is not changed essentially by the nondiagonal terms and is still described by an equation with the general form (6). On the other hand the stationary solution of (2) takes the form (S is taken as uniform for simplicity)

$$n(r) = C \exp -\left[\int \alpha_{pq}(T) dT / \alpha_{pp} T + \gamma r^2 \right] / r^m \qquad (7)$$

where $\gamma = S/4\alpha_{pp}$ and m is arbitrary at present. Substitution into (1), recalling (4), gives an equation of the form (6) for $j \propto T^{3/2}$ if the following conditions hold:

$$\alpha_{pq} = \frac{\alpha}{T}\ ,\ (\alpha_{pq})^2 << \alpha_{pp}\alpha_{qq} \qquad (8)$$

Indeed one obtains

$$\nabla^2 j + \mu^2 j = -\frac{\mu^2}{E}(p_A - 4\gamma\alpha) \qquad (9)$$

from which one recovers the same profiles predicted by equation (6), in view of the fact that they are essentially independent of the magnitude of the inhomogeneous term for given boundary values of the safety factor, a fact which was related in our previous work (1988a, 1989b) to the so called profile resiliency of j(r) (or T(r)) with respect to the auxiliary power p_A. This profile resiliency is now extended also with respect to the form of the density profile described by γ and is related to the assumed stationarity of the entropy.

The vanishing of the entropy production in an open system is not a universal law, of course, but it is useful for characterizing the natural tendency of the open system to keep the same maximum entropy of the closed system, provided that the external interaction is weak. A situation of this kind may occur in the confinement region of the tokamak, which is open to the heat flux across the inner and the outer boundaries. An extra heat flux, besides the diffusive heat flux α_{qq}, is necessary for compensating the energy unbalance across the mixing radius λa related to the fact that the solution $j \propto T^{3/2}$ of (6) involves a critical temperature gradient at $r=\lambda a$. The related diffusive heat flux $q_h(\lambda a)=-(n\chi dT/dr)_{\lambda a}=-E(dj/dr)_{\lambda a}/\mu^2$ cannot satisfy in general the energy balance across $r=\lambda a$. Assuming a flat current density profile in the core ($j=\hat{j}$), the extra flux q_{ext} necessary for energy balance in the region $r \leq \lambda\alpha$, is given by the relation

$$(E\hat{j} + p_A)\frac{\lambda a}{2} = q_h(\lambda a) + q_{ext}(\lambda a) \qquad (10)$$

The identification of q_{ext} with the nondiagonal part of the heat flux $-\alpha(dn/dr)/n$ allows the determination of the exponent m of (7). One has indeed, putting $\nu^2 \equiv -(dj(dr)_{\lambda a}(2/\hat{j}\lambda a)$, $p \equiv (p_A - 4\alpha\gamma)/E\hat{j}$:

$$m = \frac{(\lambda a)^2}{2\alpha} E\hat{j}\left[1+p-\left(\frac{\nu}{\mu}\right)^2\right] - \frac{\lambda a \alpha}{T^2 \alpha_{pp}}\left(\frac{dT}{dr}\right)_{\lambda a} \qquad (11)$$

The parameter $\beta = 1+p-(\nu/\mu)^2$ characterizes the form of the current density profile, as we know from our previous work (1989b). So we obtain a connection between the density and the current density profiles. Let us consider first the case $\beta<0$. This corresponds to a concave current density profile in the confinement region and to a large positive diffusive flux q_h, so that q_{ext} is large and negative (heat pinch). According to(1989b) this situation is typical of low values of $1/q(a)$ and of the mixing radius λa, or also of purely ohmic discharges ($p_A=0$, see figs. 2 and 3 of (1989b)).

A negative slope of the density profile implies a negative α. Then the exponent m can be seen to be positive with a magnitude of order 1. The resulting density profile is peaked.

In the case $\beta \geq 0$ the current density (or temperature) profile is broad, q_{ext} is small, as well as q_h, and can be positive. This situation can occur (but not necessarily) for large values of 1/q(a) (1989b). The exponent m is negative (see (11)) and near zero. Inspection of the sign of $(dn/dr)_{\lambda a}$ shows that, when the source of particles is sufficiently weak ($S < \alpha_{pp} E\hat{j}\beta/\alpha_{pq} T$) the shape of the density profile becomes hollow. This prediction agrees with the observations in the case of the broad temperature profiles related to the H-modes (Smeulders, 1988; Lazzaro, 1989). At the contrary, in the presence of an intense particle source (pellet injection) the density profile can be peaked (γ is large, see (7)) even when the temperature profile is broad.

Finally, it should be underlined that the condition of stationary entropy holds only in the ideal situations of an ohmically relaxed plasma not subject to strong external action (e.g. intense heating implying strong time dependence of the plasma energy, important multifluids effects, important noninductive currents and so on). Moreover the meaning of a negative coefficient α_{pq} from the point of view of the basic transport theory, is still to be seen (but in this respect see Stringer, 1989).

References

Behringer, K., Engelhardt, W., Feneberg, W. et al. (1986) Bull. Am. Phys. Soc. 25, 875.

Capes, R., Mercier, C. (1982) Plasma Phys. Contr. Nuclear Fusion Research (Proc. 9th Int. Conf., Baltimore) Vol. 1, IAEA, Vienna 337.

Coppi, B., Sharky, N. Proc. 1978 Varenna Course in Plasma Physics, Vol. 1, EUR FU BRU/XII/476/80, CEC Brussels (1980) 47.

Frederickson E.D. et al. (1986) Nucl. Fusion 26, 849,

Gruber, O. et al. (1988) Plasma Phys. Contr. Fusion 30, 1611.

Lazzaro, E., Avinash, K., Gottardi, N., Smeulders, P. (1989) Plasma Phys. Contr. Fusion 31, 1199.

Minardi, E. (1988a) Theory of Fusion Plasma, joint Varenna-Lausanne Workshop (Vaclavic J., Troyon F., Sindoni E. Editors) p. 25.

Minardi, E. (1988b) Plasma Phys. Contr. Fusion 30, 1701.

Minardi, E. (1989a) Plasma Phys. Contr. Fusion 31, 227.

Minardi, E., Lampis, G. (1989b) Maximum entropy tokamak configurations, JET-R (89) 10 (to be published).

O'Rourke, J. (1987) Nucl. Fusion 27, 2075.

Smeulders, P., Gottardi, N., Lazzaro, E., Brusati, M., Keagan, B., Nowak, S., Pasini, D., Rimini, F. (1988) Hollow profiles and high-β effects during H-mode in JET, JET-IR (88) 11.

Stringer, T.E. (1989) Comparison of predicted and measured heat transport in JET, JET-P (89) 01.

Tubbing, B.J., Lopes Cardozo, N., van der Wiel, M. (1987) Nucl. Fusion 27, 1843.

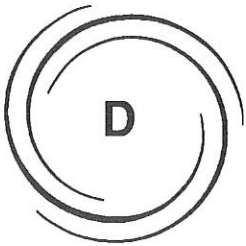

MAGNETIC CONFINEMENT THEORY AND MODELLING

D3 GENERAL THEORY

DISCRETE ALFVÉN WAVES IN CYLINDRICAL PLASMA: ARBITRARY BETA AND MAGNETIC TWIST

H. Shigueoka[1], P.H. Sakanaka[3], C.A. de Azevedo[1,4], A.S. de Assis[2]

[1]Instituto de Física, Universidade Federal Fluminense, 24024, Niterói, RJ, Brazil, e-mail: HISA@LNCCVM

[2]Instituto de Matemática

[3]Instituto de Física, Universidade Estadual de Campinas 13081, Campinas, SP, Brazil, e-mail: SAKANAKA@BRUC.ANSP

[4]Instituto de Física, Universidade do Estado do Rio de Janeiro 20550, Rio de Janeiro, RJ, Brazil, e-mail: CAUP@LNCCVM

ABSTRACT

Discrete Alfvén modes in diffuse, current-carrying, cylindrical plasma is studied numerically. Discrete Alfvén continuum in the magnetohydrodynamic spectrum of straight tokamaks. The lowest discrete Alfvén frequencies, for a fixed azimuthal mode number m and an axial mode number k, are calculated as function of the plasma current. We present the results for TCA and NET eigenfrequencies.

1. INTRODUCTION

The spectrum of the ideal magnetohydrodynamics for cylindrical plasma sistems with diffuse profile has two continua, known as SLOW WAVE and ALFVÉN WAVE continuum, due to the singularities of the eigenvalue equation, and two non-Sturmian regions intercalated by continua (Goedbloed. 1979). In between these four regions there exist discrete eigenvalues (Goedbloed. 1975). Evidences of the existence of discrete Alfvén modes, which lies just below the Alfvén continuum, are being reported by De Chambrier et al. (1981) and Ross et al. (1982). The study of discrete Alfvén modes is important for the purpose of investigating the Alfvén wave heating and current drive for tokamaks (Appert et al. 1982).

The objective of this paper is to study the effect of the equilibrium current on the discrete Alfvén eigenfrequencies. This study is applied to TCA and NET tokamaks. In Section 2 we describe the basic equations, in Section 3 the results.

2. BASIC EQUATIONS

Discrete Alfvén modes are calculated from the linearized ideal magnetohydrodynamic equation for straight or toroidal plasma, by taking positive eigenvalues, $\omega^2>0$ (stable side of the spectrum). We introduce the time and space dependence of the perturbation quanties as $f(r)\exp\{i[m\theta+kz-\omega t]\}$, where m and k (=n/R) are the azimuthal and axial wavenumbers, respectively. The equilibrium field $\vec{B}$ is given by $B_r(r)=0$, $B_\theta(r)$, $B_z(r)$. Hain and Lüst (1958) derived the second-order differential equation for the radial component of the plasma displacement vector $\vec{\zeta}$, for the straight tokamak

model, given by

$$\frac{d}{dr}\frac{(\rho\omega^2-F^2)}{N}\left[\rho\omega^2(\gamma p+B^2)-\gamma pF^2\right]\frac{1}{r}\frac{d}{dr}(r\zeta_r)\}+\{\rho\omega^2-F^2$$

$$-2B_\theta\frac{d}{dr}\left(\frac{B_\theta}{r}\right)-\frac{4k^2}{N}\frac{B^2_\theta}{r^2}(\rho\omega^2B^2-\gamma pF^2)+r\frac{d}{dr}\left[\frac{2kB_\theta}{Nr^2}\left(\frac{m}{r}B_z-kB_\theta\right)\right.$$

$$\left.(\rho\omega^2(\gamma p+B^2)-\gamma pF^2)\right]\}\zeta_r=0 \qquad (1)$$

where $$N=\rho^2\omega^4-\rho\omega^2H(\gamma p+B^2)+\gamma pHF^2 \quad , \qquad (2)$$

$$F=\frac{m}{r}B_\theta+kB_z=(\vec{k}.\vec{B}) \quad , \qquad (3)$$

$$H=m^2/r^2+k^2 \qquad (4)$$

The quantities γ, p and ρ are the adiabatic constant, plasma pressure and mass density, respectively.

Equations $\rho\omega^2-F^2=0$ and $\rho\omega^2(\gamma p+B^2)-\gamma pF^2=0$ define the Alfvén and the slow wave continua, respectively, and N = 0 gives two non-Sturmian regions on ω-space. We can deduce from equation (1) that if we use the low-β, low twist ($B_\theta/B_z \ll 1$) approximation we recover the result given by Appert et al. (1982). The eigenfrequency ω_N and the corresponding eigenmode $\zeta_r(r)$, for a given k = n/R and m, can be obtained by solving equation (1) with the following boundary conditions: $r\zeta_r = 0$ at r = 0 and r = a.

The profiles for p, B_z and B_θ obey the equilibrium equation. Two of these profiles can be chosen arbitrarily. We choose for pressure $p(r) = p_o\exp(\alpha_{p^2}r^2+\alpha_{p^4}r^4)$, where p_o, α_{p^2} and α_{p^4} are constants. The B_θ profile is obtained by solving the Ampère's law with a given J_z profile. We take for current density $J_z = J_{oN}(1-(r/a_N)^{\alpha_{j1}})^{\alpha_{j2}}$ and for density $\rho = \rho_{oN}(1-0.95(r/a_N)^2)$, where α_{j1} and α_{j2} are free parameters. The shooting method is used to obtain the eigenvalue ω_N^2 which satisfies the boundary condition at r = a. We choose the following parameters:

$$B_{zN}=1, \quad \rho_{oN}=1, \quad \alpha_{p^2}/a^2_N=-4, \quad \alpha_{p^4}/a^4_N=-6, \quad a_N=1.$$

3. NUMERICAL RESULTS AND CONCLUSIONS

We have taken parameters for TCA: R_0 = 0.61 m, a = 0.18 m, B_{z0} = 1.6 T, $n_{e0} = 10.\ 10^{19}m^{-3}$, and for NET: R_0 = 5.18 m, a = 2.17 m, B_{z0} = 5.0 T, $n_{e0} = 18.\ 10^{19}m^{-3}$.

The equation $\omega=[\rho_{0N}/(\mu_0\rho_0)^{1/2}]\left[B_{z0}/B_{zN}\right]\left[R_N/R_0\right]\omega_N$ recovers the frequency in S^{-1}. The dependence of the eigenfrequencies on current, in terms of q at the wall, is shown in Figure 1, for both TCA and NET. We find 2.3 MHz and 0.8 MHz for TCA and NET, respectively, showing a good agreement with experimental values given by De Chambrier (1983) for TCA and predicted values for NET given by Borg et al. (1989).

The toroidal effect on eigenfrequency was also studied by using the Copenhaver equation reported by Galvão et al. (1978). The main effect comes from the fact that the effective major radius $R = R_0 + \zeta$, where ζ is the displacement of the axis of the magnetic surface, affects the value of k = n/R.

ACKNOWLEDGEMENTS

This work was supported by CAPES, CNPq, FAPERJ and FAPESP.

REFERENCES

- Appert, K. et al. Plasma Phys., 24, 1142 (1982).
- Borg, G.G. et al., Centre de Recherches en Physiqye des Plasmas, Lausanne, Report LRP 374/89, Feb. 1989.
- De Chambrier, A. et al., Plasma Physics 24, 893 (1981).
- De Chambrier, A. et al., Plasma Physics 25, 1021 (1983).
- Goedbloed, J.P., Phys. Fl. 18, 1258-1276, (1975).
- Goedbloed, J.P., In Lecture Notes on Magnetohydrodynamics, Universidade Estadual de Campinas, Campinas, Brazil, 1979.
- Hain, K. and Lüst, R., Z. Naturforsch., 13a, 936 (1958).
- Ross, D.W. et al., Phys. Fluids 25, 652 (1982).
- Galvão, R.M.O., Sakanaka, P.H., Shigueoka, H., Phys. Rev. Lett., 41, 870 (1978).

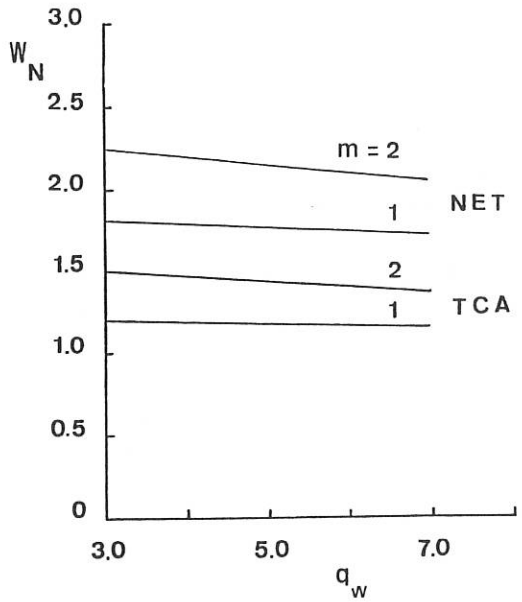

Fig. 1. - Normalized eigenfrequencies, ω_N, with the azimuthal wavenumbers m = 1 and 2, for NET and TCA, as function of $q_{wall} \sim 1/I$. The following parameters were used: NET: $R/a = 2.2$, $J_{ON} = 0.9$, $q_0 = 1$, n = 3, and $\beta = 0.05$; TCA: $R/a = 3.3$, $J_{ON} = 0.6$, $q_0 = 1$, n = 3, and $\beta = 0.01$.

THREE WAVE INTERACTIONS IN DISSIPATIVE SYSTEMS

J. Teichmann* and P. Winternitz**

Université de Montréal. * Département de Physique. ** Centre de Recherches Mathématiques. C.P. 6128-A. Montréal, Québec, H3C 3J7. Canada

The theory of interactions of coherent waves, which describes the basic processes in many schemes of plasma heating, plasma diagnostic and weak turbulence has been developed in the past for weakly dissipative systems, e.g. [1] . The purpose of this study is to apply Lie group theory to obtain exact analytical solutions of the three wave interaction equations in a dissipative systems. We write the evolution equations in the form:

$$w_{j,x_j} + a_j w_j = \varepsilon b_j w_k^* w_\ell^* \quad , \quad a_j, b_j \in \mathbb{R}, \; w_j \in \mathbb{C} \tag{1}$$

$$j,k,\ell = 1,2,3 \text{ (cyclic)},$$

where x_1, x_2, x_3 are the three characteristic coordinates assumed to be linearly independent. The subscript x_j denotes a partial derivative.

Eq.(1) describes the propagation and interaction of weakly nonlinear and dispersive waves with complex amplitudes $w_j(x_j)$. In the absence of dissipation, i.e. for $a_1 = a_2 = a_3 = 0$, the system (1) is integrable by inverse scattering techniques [2, 3] and allows multi-soliton solutions. Moreover for $a_j \neq 0$ the system has been shown to have an infinite dimensional symmetry group, the Lie algebra of which has a Kac-Moody-Virasoro structure [4] typical for integrable multidimensional systems.

When dissipation is present, the integrability is lost, however group theory can be used to obtain particular solutions.

We apply a known algorithm [5] using the MACSYMA program [6] to calculate the Lie algebra of the symmetry group when all a_j and b_j are nonzero. The result is an infinite dimensional Lie algebra with the following basis

$$X_j = \frac{\partial}{\partial x_j} \quad , \quad Y_j(f_j) = f_j(x_j)\left(-\frac{\partial}{\partial \alpha_k} + \frac{\partial}{\partial \alpha_\ell}\right) \tag{2}$$

$$j, k, \ell = 1,2,3 \text{ (cyclic)}.$$

Here $f_j(x_j)$ are arbitrary real functions (of the variable x_j). We have introduced the wave moduli $\rho_j(x_j)$ and phases $\alpha_j(x_j)$, $w_j = \rho_j \exp(i\alpha_j)$.

The operators X_j generate translations, the operators Y_j generate an infinite dimensional group of local coordinate dependent gauge transformations. The sought for Lie algebra is the direct sum of three indecomposable Lie algebras, each of them with non-zero commutation relations :

$$[X_j, Y_j(f_j)] = Y_j(f_j')$$

where the prime denotes a derivative with respect to x_j.

In order to obtain particular solutions we shall apply the method of symmetry reduction. More specifically, we shall reduce Eq.(1) to a system of ordinary differential equations by requesting that the solutions be invariant under a two-dimensional subgroup of the symmetry group. Methods for clarifying subalgebras of finite and infinite dimensional Lie algebras are described e.g. in [7]. For the algebra (2) the result is that every two-dimensional subalgebra is conjugate under the symmetry group of Eq.(1) to precisely one of the following algebras:

$$L_{2,1}^{ab}(f_3, g_3) = \{ X = X_1 + aY_2(1) + Y_3(f_3),\ Y = X_2 + bY_1(1) + Y_3(g_3) \} \tag{3}$$

$$L_{2,2}^{abc} = \{ X = X_1 + Y_2(bx_2 + c) + Y_3\left(\frac{bx_3}{a}\right),\ Y = X_2 + aX_3 + Y_1(-bx_1),\ a \neq 0 \} \tag{4}$$

For $b \neq 0$ we can transform c into $c = 0$.

$$L_{2,3}^{abcd} = \{ X = X_1 + aX_2 + Y_3\left(-\frac{cx_3}{b}\right);\ Y = X_2 + bX_3 + Y_1(cx_1) + Y_2\left(\frac{cx_2}{a} + d\right),\ a \neq 0,\ b \neq 0 \} \tag{5}$$

For $c \neq 0$ we can transform d into $d = 0$.

The a, b, c, and d above are constants, $f_3(x_3)$ and $g_3(x_3)$ are arbitrary functions of x_3.

Solutions invariant under the group corresponding to $L_{2,1}^{ab}(f_3, g_3)$ will have the form:

$$\begin{aligned} w_1 &= \rho_1(x_3) \exp\{ i[(a - f_3)x_1 - g_3 x_2 + \varphi_1(x_3)] \} \\ w_2 &= \rho_2(x_3) \exp\{ i[f_3 x_1 + (g_3 - b)x_2 + \varphi_2(x_3)] \} \\ w_3 &= \rho_3(x_3) \exp\{ i[-ax_1 + bx_2 + \varphi_3(x_3)] \} \end{aligned} \tag{6}$$

where the functions ρ_i and φ_i satisfy a system of ordinary differential

equations obtained by substituting (6) into (1) and separating real and imaginary parts. The system obtained can be separated and solved in all generality. The resulting amplitudes and phases are:

$$\rho_1^2 = \varepsilon_1\varepsilon_2 \frac{a_2 b_1}{a_1 b_2}\,\rho_2^2 = \frac{a_2 a_3}{a_1^2 b_3^2}\left\{\frac{1}{a_3} h_3 h_{3,x_3} + (a_1^2 + h_3^2)\right\}$$

$$\rho_3^2 = \varepsilon_1\varepsilon_2 (a_1^2 + h_3^2)\frac{a_2}{a_1 b_1 b_2}\,, \qquad h_3 = f_3(x_3) - a,$$

$$\varphi_1 + \varphi_2 = \operatorname{atan}\left(-a_1 h_3^{-1}\right) - \varphi_3$$

$$\varphi_3 = -\frac{a_3 b_2}{a_1 b_3}\int dx_3 \left\{ h_3 + \frac{1}{a_3}\frac{h_3^2}{h_3^2 + a_1^2} h_{3,x_3}\right\}, \qquad a_i \neq 0,$$

where $f_3(x_3)$ and $\varphi_1(x_3)$ are arbitrary functions of x_3, $\varepsilon_1 = \operatorname{sgn}(a_2 a_3 b_2 b_3)$ $\varepsilon_2 = \operatorname{sgn}(a_1 a_3 b_1 b_3)$.

The algebra $L_{2,2}^{abc}$ is related to invariant solutions of the form:

$$w_1 = \rho_1(\xi)\exp\left\{i\left[\left(\frac{b}{a}\xi + c\right)x_1 + \varphi_1(\xi)\right]\right\}$$

$$w_2 = \rho_2(\xi)\exp\left\{i\left[\left(\frac{b}{a}x_3 + d\right)x_1 + \varphi_2(\xi)\right]\right\}$$

$$w_3 = \rho_3(\xi)\exp\left\{i\left[-(bx_2 + c)x_1 + \varphi_3(\xi)\right]\right\} \qquad (7)$$

where a,b,c are constants, $\xi = ax_2 - x_3$. Again the corresponding system of ODE's can be separated. The equation for the amplitude ρ_2^2 is a second order differential equation which can be transformed by the Möbius transform into the canonical equation- Painlevé XV - provided $a = -a_2/a_3$. This condition can be always satisfied. Then:

$$\rho_2^2(x_2, x_3) = -\frac{C_1}{2a_1 b_1 b_3}\exp\left[-2(a_2 x_2 + a_3 x_3)\right]\left\{1 + C_2\exp\left[C_3 z(x_2, x_3)\right]\right\}^{-1}$$

with $$z(x_2, x_3) = -\frac{C_1}{b}\frac{a_2}{a_1 a_3}\exp\left[2c\frac{a_2}{b}\right].$$

$$\cdot\,\mathrm{Im}\left\{\exp\left[-2i\frac{a_1 a_2}{b}\right] E_i\left[-2\frac{ca_2}{b} - 2(a_2 x_2 + a_3 x_3) + 2i\frac{a_1 a_2}{b}\right]\right\} + C_4$$

where $E_i()$ is the exponential- integral function and C_j are the integration constants determined by initial conditions. Similar solution is obtained for $b = 0$. Once the amplitude ρ_2 is known, the remaining amplitudes ρ_1 and ρ_3 and corresponding phases φ_j are obtained from the system (1) .

The two-dimensional algebra $L_{2,3}^{abcd}$ leads to invariant solutions :

$$w_1 = \rho_1(\xi)\exp\left\{ i\left[\frac{c}{b} x_1 x_3 + \frac{c}{2a}(ax_1 - x_2)^2 - d(ax_1 - x_2) + \varphi_1(\xi)\right]\right\}$$
$$w_2 = \rho_2(\xi)\exp\left\{ i\left[-\frac{c}{b} x_1 x_3 + \varphi_2(\xi)\right]\right\}$$
$$w_3 = \rho_3(\xi)\exp\left\{ i\left[-\frac{c}{2a}(ax_1 - x_2)^2 + d(ax_1 - x_2) + \varphi_3(\xi)\right]\right\} \qquad (8)$$

with $\xi = x_3 + b(ax_1 - x_2)$. a,b,c and d are arbitrary constants. The corresponding system of ODE's cannot be solved in a closed form. However some approximative solutions can be constructed. For example one obtains under the assumption that $c = 0$, $ab^2 \gg b_1 b_2$ for the aplitude $\rho_3(\xi)$:

$$\rho_3^2(\xi) \doteq C_1 \exp(-2a_3\xi) + C_2 \exp\left\{ -\left[\left(\frac{a_1}{ab} - \frac{a_2}{b} + a_3 \right) + i\frac{d}{b} \right]\xi \right\}$$
$$+ C_3 \exp\left\{ -\left[\left(\frac{a_1}{ab} - \frac{a_2}{b} + a_3 \right) - i\frac{d}{b} \right]\xi \right\} + O\left(\frac{b_1 b_2}{ab^2} \right)$$

Here C_j are constants.

In contrast to the integrable case where $a_j = 0$, the number of exact solutions is substantially reduced if all the damping coefficients $a_j \neq 0$. For systems, in which one or two dissipation constants a_j are zero, new families of exact solutions appear, similarly to [4] .

References:

[1] J.Weiland and H.Wilhelmsson :" Coherent Non-Linear Interaction of Waves in Plasmas ", Pergamon Press , (1977).

[2] H.Cornille, J. Math. Phys. 20, (1979), 1653.

[3] D.J.Kaup, Physica D1, (1980), 5.

[4] L.Martina and P.Winternitz, Ann. Phys. 196, (1989), 231.

[5] P.J.Olver :" Application of Lie Groups to Differential Equations ", Springer, New York, (1986).

[6] B.Champagne and P.Winternitz, Preprint CRM-1278, (1985).

[7] P.Winternitz in " Partially Integrable Nonlinear Evolution Equations and their Physical Applications", Kluwer (1990).

STATIONARY STATES WITH INCOMPRESSIBLE MASS FLOW IN IDEAL MHD

U. Gebhardt and M. Kiessling*

Institut für theor. Physik IV, Ruhr-Universität, D-4630 Bochum 1, FRG

Abstract

The equations of stationary incompressible ideal MHD are known to be reducible to (1) a scalar elliptic equation for helically invariant systems (provided $\mathbf{E} \cdot \hat{\mathbf{e}}_{inv} = 0$); (2) two coupled scalar equations for arbitrary nontoroidal geometries (provided $\mathbf{E} = 0 \iff \mathbf{v} \parallel \mathbf{B}$). We show that these scalar equations can be transformed into simpler equations. Thereby we find a classification scheme for stationary states. Our procedure yields information for treating certain free boundary problems. To illustrate the practical value of our transformation technique we construct some simple analytical solutions. The question of a possible generalization of our method to compressible MHD is also addressed.

1. Introduction

The general solution properties of the ideal version of the stationary MHD equations is the object of our interest here. The governing equations, in SI units and standard notation, read

$$\nabla \cdot \mathbf{B} = 0 \tag{1}$$

$$\nabla \times \mathbf{B} = \mu_0 \mathbf{j} \tag{2}$$

$$\nabla \cdot (\rho \mathbf{v}) = 0 \tag{3}$$

$$\nabla \times (\mathbf{v} \times \mathbf{B}) = 0 \tag{4}$$

$$\rho(\mathbf{v} \cdot \nabla)\mathbf{v} = -\nabla p + \mathbf{j} \times \mathbf{B} \tag{5}$$

We restrict ourselves to incompressible flow, with

$$\nabla \cdot \mathbf{v} = 0 \tag{6}$$

as closure equation for the system (1)-(5). The subject of finding general solutions using free integrals of (1)-(5) plus closure equation has been pursued for quite some time. The net outcome of an integration in terms of free integrals is, generally speaking, the reduction of the

* Present address: Courant Institute of Mathematical Sciences, New - York University, New York, N.Y. 10012

set (1)-(5) to either one or two scalar partial differential equation(s) for certain flux function(s), depending on whether some symmetry assumption, like rotational invariance, is made or not. The reduced, scalar equations contain the free integrals, which are arbitrary functions of the flux functions. For that reason the reduced equations are in general nonlinear. To the best of our knowledge, explicit solutions for nonlinear choices of the free integrals have so far been obtained only in the special cases where either $\mathbf{B}$ (=SHM) or $\mathbf{v}$ (=MHS) vanishes identically, and this only for the continuously symmetric situations. Special choices of all free integrals, such that only linear terms in the flux function occur, render the scalar equation a linear equation. These special cases have been discussed extensively in the literature. It is, however, hardly imaginable that nature ''chooses'' the linear version of the free integrals as well, although occasionally such a standpoint might result in a good approximation. Therefore one has to investigate the structure and solution properties of the MHD equations, admitting large classes of nonlinear free integrals. In view of this it is interesting to realize that the known reduced equations are not yet representing the ''most convenient'' approach to tackle the problem of finding solutions of (1)-(6). We inquire into this problem. We reconsider the structure of the reduced, scalar form of the set of equations (1)-(6) in the well known cases for which a reduction to one or two scalar equations has been carried through in the literature: (i) helically symmetric systems; (ii) systems without symmetry assumption, but then with field aligned flow ($\mathbf{B} \| \mathbf{v}$). We show that for a wide class of problems the involved nonlinear partial differential operators allow a smooth mapping to simpler operators (linear in the symmetrical cases) by a suitable application of the chain rule of partial derivation. Our transformation technique applies also to a generalized version of the known reduced equations, which allows to solve some problems in closed form which otherwise would lead to nonlinear free boundary problems.

2. Nonhelical systems

We impose the condition that $\mathbf{B}$ and $\mathbf{v}$ are parallel. Reduced equations have been derived by Zwingmann (1984) and read

$$\big(1 - M^2(\alpha,\beta)\big)\nabla\beta \cdot \nabla \times (\nabla\alpha \times \nabla\beta) + \frac{1}{2}(\nabla\alpha \times \nabla\beta)^2 \frac{\partial}{\partial\alpha} M^2(\alpha,\beta) = \frac{\partial \tilde{\Pi}}{\partial\alpha} \qquad (7a)$$

$$\big(1 - M^2(\alpha,\beta)\big)\nabla\alpha \cdot \nabla \times (\nabla\alpha \times \nabla\beta) - \frac{1}{2}(\nabla\alpha \times \nabla\beta)^2 \frac{\partial}{\partial\beta} M^2(\alpha,\beta) = -\frac{\partial \tilde{\Pi}}{\partial\beta} \qquad (7b)$$

where $\alpha(\mathbf{r})$ and $\beta(\mathbf{r})$ are the Euler potentials of the magnetic field, $\tilde{\Pi} \equiv \mu_o(p + (1/2)\rho\mathbf{v}^2)$ denotes the Bernoulli integral, essentially, and $|M(\alpha,\beta)|$ is the local Alfvén Mach number. $M^2(\alpha,\beta)$ and $\tilde{\Pi}(\alpha,\beta)$ are positive free integrals of the problem and may be prescribed arbitrarily, together with suitable boundary conditions for α and β. Because of the

complicated structure of (7a/b) a satisfactory solution theory is not yet available. Zwingmann (1984) pointed out that for $M^2 \equiv const \neq 1$ the solution theory of the so simplified equations (7a/b) reduces to the one of MHS/SHM. We prove that the solution theory for (7a/b) and the reduced equations of MHS/SHM will be the same, essentially, for all choices of $M^2(\alpha,\beta)$. The ratio of kinetic to magnetic energy density (Alfvén Mach number) plays the role of a classification parameter. In case of subalfvénic flow, that is, $M^2 < 1$ we define new potentials via $[f,g]_{a,b} = \sqrt{1-M^2(\alpha,\beta)}$. Similarly for $M^2 > 1$, via $[f,g]_{a,b} = \sqrt{M^2(\alpha,\beta)-1}$. Eq.(7a/b) then take a considerably simpler form when expressed in terms of the two new potentials $f(\mathbf{r})$ and $g(\mathbf{r})$. It turns out that for the latter case the equations become identical to those obtained for stationary hydromechanics (SHM) by Yih (1967), whereas for the former they get the form of MHS ($M^2 \equiv 0$) given by Grad and Rubin (1958). If $M^2 \equiv 1$ the Bernoulli integral is a constant all over the considered domain. Any choice of independent α and β and the prescription of a positive $\rho(\alpha,\beta)$ then gives a solution of the original set (1)-(6). This set of solutions generalizes Chandrasekhar's equipartition solution (1956) where $\rho \equiv const$. The situation where M^2 crosses 1 may yield generic free boundary problems, which require separate treatment. However, we show that (7a/b) and our transformation technique can be generalized to situations where the free integrals define smooth manifolds (not functions) in α,β space. This allows to circumvent the nongeneric free boundary problems enforced by (7a/b).

3. Helical systems

A reduced equation for helically symmetric systems has been derived by Solov'ev (1961) and reads

$$(\Lambda_A^2 - \Psi_A^2)\mathcal{L}A - \frac{1}{2}(\nabla A)^2 \frac{d}{dA}\left(\Lambda_A^2 - \Psi_A^2\right) = \frac{\partial Q(A,r)}{\partial A} \tag{8}$$

with

$$\frac{\partial Q(A,r)}{\partial A} = \frac{\partial}{\partial A}\left[(n^2+k^2r^2)\tilde{\Pi} - \frac{\widehat{g}^2 - \widehat{f}^2}{2} - \frac{2kn\int \eta(A)dA}{n^2+k^2r^2}\right] \tag{9}$$

where $\Lambda(A)$ and $\Psi(A)$ denote the flux function and stream function of $\mathbf{B}$ and $\mathbf{w} \equiv \sqrt{\mu_0\rho}\,\mathbf{v}$, respectively. The operator $\mathcal{L}$ is defined as $\mathcal{L} := -\Delta + \nabla\ln(n^2+k^2r^2)\cdot\nabla$, and $\hat{f}$ and $\hat{g}$ are the components of $\mathbf{B}$ and $\mathbf{w}$ in the local invariant direction $\mathbf{s} = n\mathbf{e}_z + k\mathbf{e}_z \times \mathbf{r}$. $\eta(A) = \Lambda_A\widehat{f} - \Psi_A\widehat{g}$ is a free integral of the problem. We remark that $\hat{f}$, $\hat{g}$, and $\tilde{\Pi}$ may be represented in terms of polynomials of $n^2+k^2r^2$, the coefficients being functions of A. In Solov'ev's treatment one assumes the free integrals to be such that A could be eliminated. This is too restrictive and can, in fact, be overcome. Thereby the type (8) of the reduced equation is not changed but its interpretation as well as its range of validity is. In order to

transform (8) in a simpler equation we denote by σ the sign of $\Lambda_A^2 - \Psi_A^2$, and we set $G(A) := |\Lambda_A^2 - \Psi_A^2| \geq 0$. We define a new function via

$$\chi(r, u = n\varphi - kz) = g(A(r,u)) := \int^{A(r,u)} \sqrt{|\Lambda_A^2(\alpha) - \Psi_A^2(\alpha)|}\, d\alpha \qquad (10)$$

where r, φ, z are cylindrical coordinates. The resulting equation for χ is considerably less complicated. It yields analogies to simpler MHD states which depend on the geometry of the system. For translationally invariant systems essentially the same classification as for nonhelical systems with field-aligned flow holds. The only difference is that the Alfvén Mach number has to be replaced by the poloidal Alfvén Mach number. Rotationally and helically symmetric systems can be mapped to simpler MHD states where either ($\sigma = 1$) the velocity field or ($\sigma = -1$) the magnetic field has only a component in the local invariant direction. If $G = 0$ somewhere in the domain the classification is more subtle (note that $G = 0$ does not imply $M^2 = 1$). If all free integrals are assumed invertible our method can be shown to be equivalent to one introduced by Tkalich (1959) and Solov'ev (1961). Tkalich's method leads to some non-generic free boundary problems, however, and it excludes situations with $G = 0$.

4. Applications

The obtained simplification of the equations allows us to construct explicitly some solutions of the nonlinear equation (8) with both $\mathbf{B}$ and $\mathbf{v}$ playing nontrivial roles from known solutions of simpler MHS/SHM equations. In principle this is true for (7a/b) as well; however, no explicit solutions are known so far for this system. Our examples have translational symmetry. They include a simple z pinch, field reversed pinch and a 2D magnetosphere model, all with flow. We have also started with a generalization of our method to cover some compressible flows.

Acknowledgement

Work supported by SFB 162 and DOE Grant No. DE-FG02-86ER53223. The authors wish to thank K. Schindler for helpful discussions.

References

S. Chandrasekhar, (1956), Astrophys. J. **124**, 232.

H. Grad and H. Rubin, (1958), in Proceedings of the Second International Conference on the Peaceful Uses of Atomic Energy (United Nations, Geneva, 1958), Vol. 31, p. 190.

L. S. Solov'ev, (1961), Zh. Tekh. Fiz. **31**, 407. [Sov. Phys. Tech. Phys. **6**, 294.]

V. S. Tkalich, (1959), Bull. Acad. Sci. USSR, **4**, 134; ibid. **5**, 122.

C.-S. Yih, (1967), J. Fluid Mech. **29**, 539.

W. Zwingmann, (1984), Dissertation, Ruhr-Universität.

DETERMINATION OF THE PLASMA CURRENT DENSITY PROFILE IN A TOKAMAK FROM MAGNETIC AND POLARIMETRIC MEASUREMENTS

J. BLUM ; Y. STEPHAN

BP 53 X 38041 Grenoble CEDEX
France

The purpose of this work is to reconstruct the plasma current density profile j (r,ψ) and the electronic density n_e (ψ) in a Tokamak by using the external magnetic measurements on the vacuum vessel (poloidal flux ψ and field B), the Faraday rotation angles α_i obtained by polarimetry along several vertical chords and the integrals N_j of the electronic density obtained by interferometry along the same chords. This determination of n_e and j is achieved by minimizing a cost-fuction, representing the sum of the quadratic differences between the measured and calculated values of B, α_i, N_j ,the axisymmetric equilibrium equation being considered as a constraint. This inverse problem is made stable by the use of a Tichonoff regularization.

The numerical test-cases have been run on the geometry of JET (elongated DEE shape), with the real number and location of magnetic probes and vertical chords. Smooth profiles of j have first been studied ; they can be reconstructed from exact magnetic measurements but small differences on the magnetic measurements might induce large errors of the value of the safety factor at the magnetic axis ; the use of Faraday rotation makes then the problem of reconstruction stable.

Non-smooth profiles of j have also been studied, for example a staircase profile. It has been shown numerically that this profile cannot be reconstructed from the magnetic measurements alone, but that the use of the Faraday rotation enables us to obtain the correct profile, which remains stable with respect to small perturbations or errors on the angles α_i. Profiles of j with flat regions in rational q zones have also been studied. It is clear that the two functions p (ψ) and ff' (ψ) of the current profile cannot be indentified separately, but that the average of j over each flux line, as a function of ψ, can be determined if the errors on the measurements are not too large.

Finally experimental cases for JET with be presented, with a particular emphasis on H-mode discharges.

NEW EVALUATION OF THE FUSION CROSS-SECTIONS

H.-S. Bosch, G. M. Hale[1]

Max-Planck-Institut für Plasmaphysik, EURATOM-IPP Association D-8046 Garching, FRG,
[1]Los Alamos National Laboratory, Los Alamos, NM, USA

1. Introduction

The fusion cross-sections have always been of great interest to plasma physics since they are needed for predicting as well as for interpretating fusion rates. Especially for predicting the fusion rate and power gain Q in future deuterium-tritium plasmas it is important to know the fusion cross-sections as accurately as possible. Therefore, since 1945 a lot of measurements have been made for the reactions D(d,n)^{3}He, D(d,p)T, D(t,n)α, and D(^{3}He,p)α. For most applications, however, it is necessary to have analytical approximation formulas for the cross-sections, as derived by B. H. Duane in 1972[1], and by A. Peres in 1979[2]. M. Hively calculated a formula for the reactivity $< \sigma \cdot v >$ based on Duane's formula[3], as did Peres for his formula[2]. With new measurements, however, it becomes clear that these formulas do not describe σ as accurately as needed. Especially at the low energies Duane's formula is a factor of 10 too low, while Peres' formula is up to 20 % too low. This is shown in a comparison of the data available with the formulas mentioned. New experimental data and the results of R-matrix fits result in a much better fit, for which an analytical formula will be given.

2. Basic remarks

Over the energy range 1 – 500 keV[1] the cross-section varies over 14 orders of magnitude. This makes it more convenient to consider instead the astrophysical S-function[4], which separates the barrier penetration probability, as derived by Gamov in 1928 :

$$\sigma = S \cdot \frac{1}{E_s \cdot e^{(G/\sqrt{E_s})}} \qquad (1)$$

with $G = e^2\pi/\hbar Z_1 Z_2 \sqrt{2m_r}$, whem m_r is the reduced mass of the reacting particles. This separation of the penetration probability is strictly correct only as long as the particle energy is well below the Coulomb barrier, but here we want to consider this simply as a convenient parametrization[5].

The S-function now contains only the nuclear physics of the compound nucleus, and the following figures show that it is rather flat for the non-resonant DD-reactions and has a distinct resonance peak for the two resonant reactions (with also much higher values of S).

A. Peres used a similiar parameterization and calculated a polynomial for the S-function from the experimental data. A. H. Duane, however, also considered the "constant" G as a fit parameter and therefore had to fit the σ-values over many orders of magnitude, which is likely to give a very bad fit at the low energies, where σ is small and the contribution to χ^2 (which is minimized in the fit) is extremely small. For this reason the Duane-formula is very bad at low energies (where it has been used all the time), as we shall see later.

R-matrix theory[6,7] describes several reactions possible in one compound nucleus with a single parameter set and therefore allows one to use a much larger data set to determine these

[1]Energy here always means energy in the centre-of-mass frame E_s. For a particle A with mass m_A hitting the particle B at rest the relation $E_A = E_s \cdot (m_A + m_B)/m_B$ holds.

parameters, resulting inimproved statistical reliability. The fusion cross-section can then be calculated from these R-matrix parameters. Due to the much larger data set used for the fit this method is much better than simply using the total cross-section measurements to calculate an analytical fit formula.

3. Comparison of the data

A detailed review of the data and a comparison with the old fit formulas will be given elsewhere[5]. Here we restrict ourselves to a short overview. In Figure 1 the error bars of the experimental data have been left out for simplicity, but the data are divided into two groups, one with a large error bar and one with a small error (for the DT-reaction this border is 10%, and for the other reactions it is 5 %).

D(t,n)α : Figure 1a shows the S-function for the D(t,n)α reaction as derived from experimental data, from the fit-formulas of Duane and Peres and from the final R-matrix fit by G. Hale[8]. The R-matrix data are 20 % above Peres' data for low energies and 4 % at the maximum of the S-function. It can be clearly seen that Duane's fit is systematically low at small energies (60 %), and about 8 % too low near the maximum, as was assumed before on the basis of his method to fit the data.

D(^{3}He,p)α : For this reaction only a preliminary R-matrix evaluation exists as yet (not containing all data shown in this plot), and also the amount of experimental data is much smaller, as seen in Figure 1b. Because the discrepancies between the data are quite large and the R-matrix evaluation has not been finished, we did not try to give an analytical fit for this reaction.

D(d,n)^{3}He and D(d,p)T : The two DD-reactions shown in Fig. 1c and 1d are non-resonant and their S-functions are expected to be rather flat (if not constant). Duane's fits, however, show completely different behaviour because they decrease rapidly at low energies, as expected before from his fitting procedure. However, also at higher energies the discrepancy between the old fit formulas and the R-matrix evaluation is quite large.

4. New analytical fit formulas

Using eq. 1, we fitted the S-function (calculated with eq. 1 from the cross-section data derived from the R-matrix parameters) with a polynomial in Padé expansion :

$$S = \frac{A1 + E_s \cdot (A2 + E_s \cdot (A3 + E_s \cdot (A4 + E_s \cdot A5))}{1 + E_s \cdot (B1 + E_s \cdot (B2 + E_s \cdot (B3 + E_s \cdot B4)))} \qquad (2)$$

where S is in units of keV·millibarn, and E_s in keV.

Coefficient	D(t,n)α	D(d,n)^{3}He	D(d,p)T
A1	6.927E4	5.5576E+4	5.3701E+4
A2	7.454E8	2.1054E+2	3.3027E+2
A3	2.05E6	-3.264E-2	-1.276E-1
A4	5.2002E4	1.4987E-6	2.9327E-5
A5	–	1.8181E-10	-2.5151E-9
B1	63.8	–	–
B2	-0.995	–	–
B3	6.981E-5	–	–
B4	-1.728E-4	–	–
G [$\sqrt{keV}$]	34.3827	31.3970	31.3970
E_{max}	600	5000	5000
d S	5.0	2.0	2.0

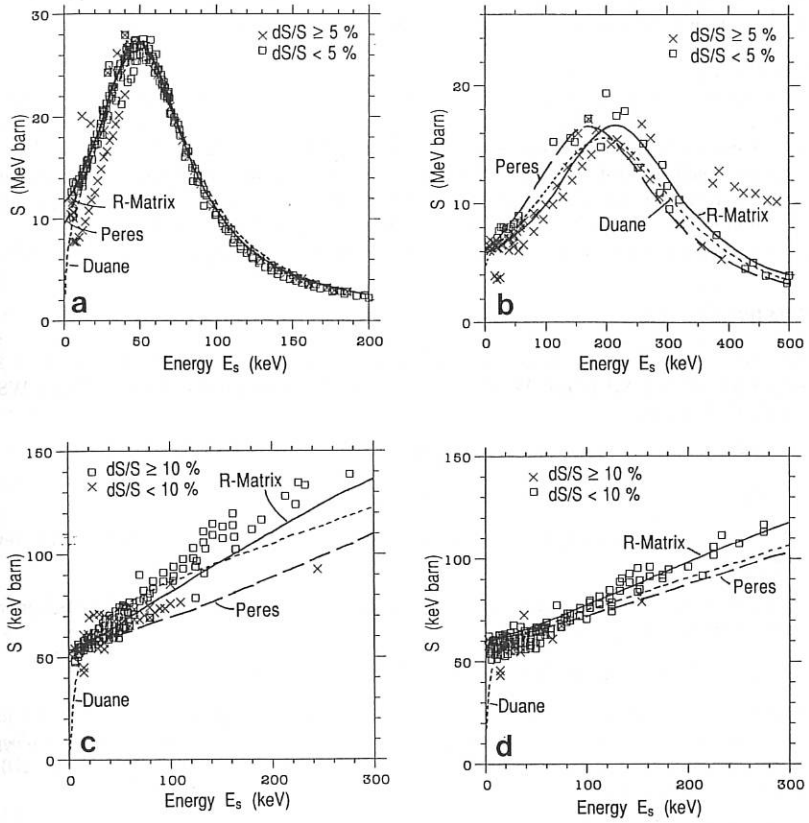

Figure 1: S-functions derived from experimental data, from analytical fit formulas (by B. H. Duane and A. Peres) and from R-matrix calculations. **a** shows the data for the D(t,n)α reaction, **b** those for the D(^{3}He,p)α, **c** the D(d,n)^{3}He reaction, and **d** the data for the D(d,p)T reaction. The experimental data in all case have been divided into two groups with small and large errors (as indicated in the figures).

This is a procedure similiar to that used by Sadler et al.[9] for a preliminary R-matrix evaluation for the D(t,n)α-reaction. The results from our fits are summarized in the table, where G is the constant in the penetration probability function (in $\sqrt{keV}$), and E_{max} and dS indicate the quality of the fit in the sense that for $E \leq E_{max}$ (in keV) the deviation of the fit from the R-matrix results is smaller than dS (in %).
The approximation for the D(t,n)α-reaction is good enough (i. e. the deviation from the original data is smaller than 5 %) for energies E_s below 600 keV, that is triton energies $E_t \approx$ 1500 keV, which includes the energy range needed for triton burnup calculations.

5. Conclusions

For the reactions D(t,n)α, D(d,n)^{3}He, and D(d,p)T the fusion cross-sections from R-matrix evaluations have been used to calculate an analytical formula which approximates σ over a very large energy range with deviations smaller than 5 % (for the DT-reaction) and 2 % (for the DD-reactions). respectively. Since these formulas are based on a much larger data set than previous formulas, they should resemble the true cross-section data with much higher reliability and we propose that the fusion community use these approximation formulas.
Analytical formulas for $< \sigma v >$ will be presented (for Maxwellian energy distributions) shortly.

References

[1] DUANE, B. H., Fusion cross section theory, in *Annual Report on CTR Technology 1972*, edited by WOLKENHAUER, W. C., Batelle Pacific Northwest Laboratory, Richland, WS, 1972, BNWL-1685.

[2] PERES, A., J. Appl. Phys. **50** (1979) 5569.

[3] HIVELY, L. M., Nucl. Fusion **17** (1977) 873.

[4] CLAYTON, D. D., *Principles of Stellar Evolution and Nucleosynthesis*, McGraw-Hill, New York, 1968.

[5] BOSCH, H.-S., Review of data and formulas for fusion cross-sections, Technical Report I/252, IPP, Garching, FRG, 1990.

[6] LANE, A. M. and THOMAS, R. G., Rev. Mod. Phys. **30** (1958) 257.

[7] HALE, G. M. and DODDER, D. C., R-matrix analyses of light-element reactions for fusion applications, in *Proc. of the Int. Conf. on Nuclear Cross Sections for Technology, Knoxville, 1979*, edited by FOWLER, J. L., pages 650–658, Washington, 1980, NBS, NBS special publication 594.

[8] HALE, G. M., BROWN, R. E., and JARMIE, N., Phys. Rev. Lett. **59** (1987) 763.

[9] SADLER, G. and VAN BELLE, P., An improved formulation of the D(t,n)^{4}He reaction cross-section, Technical Report JET-IR(87)08, JET, Culham, 1987.

THE RELAXATION IN TWO TEMPERATURE PLASMA

Bobylev A.V., Potapenko I.F.
The Keldysh Institute of Applied Mathematics
Ac. of Sci. USSR, Moscow

The problem of relaxation of space-homogeneous plasma, consisting of electrons and a sort of ions, the oldest problem of plasma physics, firstly was considered in [1]. There is exist the voluminous literature devoted to solving the problem where the standard approach is usually used. The electron and ion functions are assumed to be Maxwell's distributions with the time-dependent temperatures and thus the task is reduced to the calculation of the second momentum of the collisional integral for such functions. It is known that this approach is not quite good, because it works with the hard restrictions imposed upon the initial temperatures

$$T_e^\circ \gg \rho^{1/3} T_i^\circ, \quad \rho = m_e/m_i \qquad (1)$$

Besides, an error in approximation differential equation for $T_e(t)$ and $T_i(t)$

$$\frac{dT_e}{dt} = \frac{c}{T_e^{3/2}} (T_e - T_i) \qquad (2)$$

remains uncertain (c is a normalizing constant).

We investigated analytically and numerically the asymptotic properties of the problem solutions ($\rho \ll 1$) for different initial temperatures. We did not use the standard approach when the distribution functions of plasma components are assumed to be Maxwellian. The emphasis is made on the difference between the relaxation process under consideration and the classical case that is characterized

by the weakly nonisothermic situation (1).

We came to a closer approximation of the applicability condition for equation (2)

$$\varepsilon = \rho\, T_i \,/\, T_e \ll 1 \,. \qquad (3)$$

Inequality (1) permit us to consider the plasma with $T_i^\circ / T_e^\circ \approx 2 - 3$, and the condition (3) extends the operational range formula (2) by a factor of 100 .

The cold electrons $v < v_{T_e}$ basically interact with the ions owing to the well known collision cross-section dependence on the velocity. The deviation of the electron distribution from the quasi-equalibrium Maxwell function is more significante then a corresponding value for the ion distribution. The perturbation of the electron function $f_e(v,t)$ is great within the narrow region of the phase space $0 \le v / v_{T_e} \le \varepsilon^{2/3}$. In this case we can speak about the existence of a boundary layer near the point $v \approx 0$ with the width $\Delta \approx \varepsilon^{2/3}$. The maximum deviation of the function $f_e(v,t)$ at the point $v = 0$ is

$$f_e(0,t) \approx 2 / \sqrt{\pi} \left\{ 1 + 2.9\ \varepsilon^{2/3} \left(T_e - T_i \right) / T_i \right\} \qquad (5)$$

Now we describe in brief the process of relaxation. The most interesting is the case of strongly heated ions: $\varepsilon = \rho T_i / T_e \approx 1$, when at the initial time the heat velocities of electrons and ions are equal. The initial distributions which are far from the quasi-equlibrium case such as δ-type functions are considered too. This case, for example, corresponds to that of neutral injection into the mirror trap, neutral current drive, etc., when the usual approach is inapplicable.

1. The electrons relaxation is the fast stage. During this stage ε decreases to the value 0.1 - 0.2, i.e. T_e rises 10 times. The behaviour of the $f_e(v,t)$, $\varepsilon(t)$ depends on the initial conditions essentially.

2. At the second stage the electron function $f_e(v,t)$ "forgets" the initial conditions, conserves its quasi-equalibrium form ,depends on time only through the $\varepsilon(t)$ and it is suitable to use the evaluation (5). The electron temperature increases 100 times. The ion distribution does not in fact change. Beginning from this stage the temperatures satisfy the equation

$$\frac{dT_e}{dt} = \frac{c}{T_e^{3/2}} (T_e - T_i) \lambda(\varepsilon). \qquad (6)$$

For the initial Maxwell distributions $\lambda_1(\varepsilon) = 1 - A\,\varepsilon^{-2/3}$, $A = \frac{4\pi}{3\sqrt{3}} (3\sqrt{\pi}/4)^{2/3} \approx 2.9$, for the initial functions as $\delta(v-v_0)$ we have $\lambda_2(\varepsilon) = (1 + A\,\varepsilon)^{-2/3}$, and $\lambda_1 \approx \lambda_2$ for $\varepsilon(t) < 0.2$.

3. The peculiarity of the third stage is the simultaneity of the ion maxwellization and temperature equalization. For the real $\rho \le 10^{-3}$ this stage ends (i.e. the ion function acquires of the quasi-equalybrium form), when the ratio $T_i/T_e \approx 4$.

4. The last stage - the stage of temperature equalization is usual. Formula (6) is defined more exactly than the famous formula of Spitzer with

$$\lambda_S(\varepsilon) = (1 + \varepsilon)^{-3/2}.$$

The figs.1 and 2 show the comparison of $\lambda_1(\varepsilon), \lambda_2(\varepsilon), \lambda_S(\varepsilon)$ obtained analytically and $\lambda(\varepsilon)$ obtained numerically (dash line) for the two types of initial distributions $f_{e,i}^{\circ}(v,0)$ and different $\varepsilon(0)$.

The analytical results are confirmed by the numerical calculations carried out on the basis the completely conservative difference schemes for the nonlinear kinetic Fokker - Planck equation [2].

1. L.D.Landau, J.theor. and exper. phys., v.7 (1937), p.203.
2. A.V.Bobylev, I.F.Potapenko, preprint Inst. of Appl. Math., N 171 (1981).

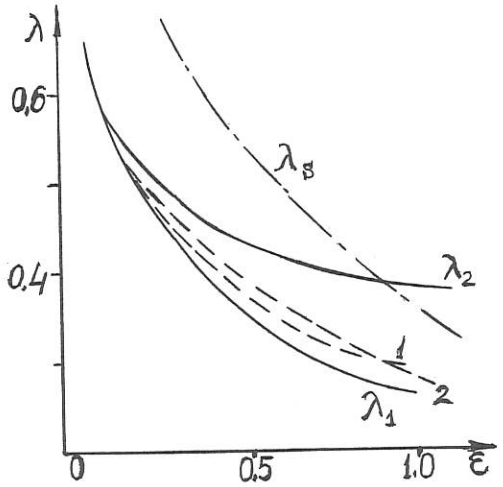

FIG. 1

The initial functions are Maxwell distributions, 1- $\varepsilon(0)=1.0$, 2- $\varepsilon(0)=1.5$.

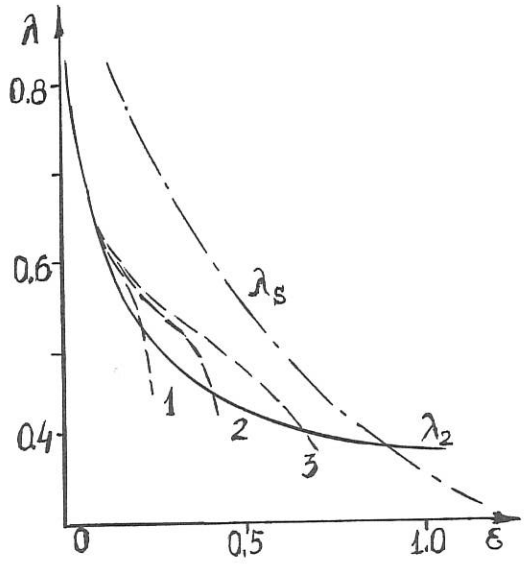

FIG. 2

The initial functions $f^{\circ}_{e,i} \approx \delta(v-v^{\circ}_{e,i})$, 1- $\varepsilon(0)=0.25$, 2- $\varepsilon(0)=0.5$, 3 - $\varepsilon(0)=0.8$.

A MULTIPLE TIMESCALE DERIVATIVE EXPANSION METHOD APPLIED TO THE FOKKER–PLANCK EQUATION FOR THE DESCRIPTION OF PLASMA RELAXATION AND TURBULENT TRANSPORT

J.W. Edenstrasser

Institute for Theoretical Physics, University of Innsbruck, Austria

ABSTRACT

A multiple timescale derivative expansion is applied to the dimensionless Fokker–Planck equation. The four timescales considered are those of Larmor gyration, particle transit, collisions, and transport. The expansion parameter is the ratio Larmor radius to plasma radius. First the zero order equations are solved leading to force–free magnetic fields. The solution of the first order equations leads to a modified MHD equilibrium equation.

1. INTRODUCTION

To make progress in understanding and describing the behaviour of a Tokamak or RFP plasma near reactor conditions, one must be fully aware of the timescales involved and of the nature of the phenomena occuring on each timescale. The fact that the natural timescales involved span from the picosecond period of electron gyration over more than 12 orders of magnitude up to the several second period of current penetration naturally suggests a multiple timescale approach to treat the various processes separately.

Whereas a huge amount of literature is concerned with the processes of the two limiting timescales of ideal MHD and resistive diffusion, only little is known from the processes occurring on intermediate timescales between them. To suggest a new approach for the investigation of such phenomena like plasma relaxation, profile consistency, turbulent and anomalous transport is the the aim of this paper. Within MHD theory several multiple timescale expansions have been applied to the transport equations, as e.g. in /1/. However, since these transport equations are valid only for the slow timescales of classical or neoclassical transport, such a procedure cannot be expected to yield the correct description on intermediate timescales. Therefore one has to perform the multiple timescale ordering already within kinetic theory, starting with the Fokker–Planck equation, so that each timescale has its own collision operator. After performing the velocity moments, one obtains for each timescale the corresponding transport equations. To initiate this rather extensive program is the object of this paper. The actual treatment of plasma relaxation and turbulent transport is then the subject of forthcoming publications.

2. THE DIMENSIONLESS FOKKER–PLANCK EQUATION

Most of the literature on kinetic plasma theory is based on the assumption of the validity of the Fokker–Planck equation, which we first bring in a dimensionless form. The dimensionless physical quantities Q, written without tilde, we obtain by normalizing the dimensional quantities $\tilde{Q}$ with respect to some characteristic values

$$t = \tilde{t}/\Omega^{-1}, \qquad f = \tilde{f}_\alpha/\bar{f}_\alpha, \qquad \vec{B} = \tilde{\vec{B}}/\bar{B}, \qquad \vec{E} = \tilde{\vec{E}}c/v_a\bar{B}$$

$$\vec{v} = \tilde{\vec{v}}/v^\alpha_{th}, \qquad \vec{\nabla} = l\tilde{\vec{\nabla}}, \qquad C = \tilde{C}_\alpha/\bar{C}_\alpha, \qquad \bar{f}_\alpha = \bar{n}_\alpha/v^{\alpha 3}_{th} \qquad (2.1)$$

Ω_α is the gyrofrequency, v_a is the Alfvén velocity, $\bar{n}_\alpha$ is the particle density, $\bar{B}$ is the magnetic field, and v^α_{th} the thermal velocity, all five values taken at the magnetic axis for a characteristic instant. l is the characteristic length over which the macroscopic quanti-

ties change and which we take as the plasma radius a. $\bar{C}_\alpha$ we choose in such a way that the leading term in C_α is of the order unity. Note, that the normalization of t and $\vec{v}$ depends on the species α, where for convenience the indices have been omitted. This fact has to be taken into account in the collision operator, in Maxwell's equations and in the transport equations.

With the normalization (2.1) we obtain the Fokker–Planck equation in the dimensionless form

$$\partial f_\alpha/\partial t + \delta_\alpha \vec{v}\cdot\vec{\nabla} f_\alpha + \sigma(q_\alpha)\,(a_\alpha \vec{E} + \vec{v}\times\vec{B})\cdot \partial f_\alpha/\partial \vec{v} = \Gamma_\alpha C_\alpha \qquad \text{with} \tag{2.2}$$

$$C_i(f,f) = \frac{\sqrt{\pi}}{2}\sum_{j,k}\frac{\partial}{\partial v_j}\int d^3v\cdot\Big\{f_i(\vec{v})\,\partial f_i(\vec{v}')/\partial v_k' - f_i(\vec{v}')\,\partial f_i(\vec{v})/\partial v_k +$$

$$\frac{A\sqrt{\gamma A}}{Z}\Big[f_i(\vec{v})\,\partial f_e(\vec{v}'\sqrt{\gamma A})/\partial v_k' - \gamma f_e(\vec{v}'\sqrt{\gamma A})\,\partial f_i(\vec{v})/\partial v_k\Big]\Big\}\,U_{jk}(\vec{v}-\vec{v}') \quad \text{and} \tag{2.2.a}$$

$$C_e(f,f) = \frac{\sqrt{\pi}}{2}\sum_{j,k}\frac{\partial}{\partial v_j}\int d^3v\cdot\Big\{\frac{1}{Z}\Big[f_e(\vec{v})\,\partial f_e(\vec{v}')/\partial v_k' - f_e(\vec{v}')\,\partial f_e(\vec{v})/\partial v_k\Big] +$$

$$(\gamma A)^{-3/2}\Big[\gamma f_e(\vec{v})\,\partial f_i(\vec{v}'/\sqrt{\gamma A})/\partial v_k' - f_i(\vec{v}'/\sqrt{\gamma A})\,\partial f_e(\vec{v})/\partial v_k\Big]\Big\}U_{jk}(\vec{v}-\vec{v}'), \tag{2.2.b}$$

where the dimensionless factors Γ_α in front of the collision operators are given by

$$\Gamma_i := -\frac{3}{2\sqrt{2}}\left[\frac{\nu_i\Omega_i}{\omega_i\omega_i}\right]\delta_i^2 \tag{2.2.c}$$

$$\Gamma_e := -\frac{3}{4}\left[\frac{\nu_e\Omega_e}{\omega_e\omega_e}\right]\delta_e^2 \tag{2.2.d}$$

and the tensor U_{jk} is defined by

$$U_{jk}(\vec{x}) = (\delta_{jk}\vec{x}^2 - x_j x_k)\,|\vec{x}|^{-3} \tag{2.2.e}$$

$$a_\alpha := \frac{v_a}{v_{th}^\alpha},\quad \delta_\alpha := \frac{\omega_\alpha}{\Omega_\alpha} = \frac{r_{l\alpha}}{l},\quad \sigma(q_\alpha) := \mathrm{sign}(q_\alpha),\quad A := \frac{\bar{T}_i}{\bar{T}_e},\quad \gamma := \frac{m_e}{m_i} \tag{2.2.f}$$

Z is the charge number of the ions, ν_α are the collision rates, ω_α are the transit frequencies $\omega_\alpha = v_{th}^\alpha/l$, $r_{l\alpha}$ are the Larmor radii.

For present magnetic fusion devices δ_α is a small parameter and is in the neoclassical transport theory used as expansion parameter. In our multiple timescale approach δ_α naturally enters as expansion parameter.

3. THE MULTIPLE TIME SCALE APPROACH

First we ask for the physical processes which lead to a change of the distribution functions. The Larmor gyration leads in connection with collisions and field inhomogenities to the neoclassical transport. As fastest timescale we thus choose the Larmor time $\tau_{\alpha 0} = \Omega_\alpha^{-1}$. Second, the distribution functions will change due to the transit of particles from regions with different temperatures and velocities, wherefore we choose the transit time as second timescale $\tau_{\alpha 1} = \omega_\alpha^{-1}$. Since the f_α's essentially change also due to collisions, we choose as third timescale the inverse collision rate, i.e., the collision time $\tau_{\alpha 2} = \nu_\alpha^{-1}$. Finally, the f_α's will change on account of transport and diffusion processes,

so that we choose the transport timescale as forth timescale $\tau_{\alpha 3}$.

For a present day Tokamak or RFP we have the following timescale ordering

$$\tau_{\alpha 0} = \Omega_\alpha^{-1} \ll \tau_{\alpha 1} = \omega_\alpha^{-1} \ll \tau_{\alpha 2} = \nu_\alpha^{-1} \ll \tau_{\alpha 3} \tag{3.1}$$

From the definitions in (2.2.f) follows $\tau_{\alpha 0}/\tau_{\alpha 1} = \delta_\alpha$. For the ratio $\tau_{\alpha 0}/\tau_{\alpha 2}$ we obtain $\tau_{\alpha 0}/\tau_{\alpha 2} = (\nu_\alpha \Omega_\alpha/\omega_\alpha^2)\delta_\alpha^2 = O(\delta^0)\delta^2$. Instead of ν_α^{-1} we therefore choose as third timescale for convenience $\tau_{\alpha 2} = \tau_{\alpha 0}\delta^{-2}$. According to the neoclassical transport theory we choose for the transport timescale $\tau_{\alpha 3} = \tau_{\alpha 0}\delta^{-3}$. In standardized form we thus arrive at

$$\tau_{\alpha n} = \tau_{\alpha 0}\delta^{-n} \text{ with } \tau_{\alpha 0} = \Omega_\alpha^{-1} \text{ and } n = 0,1,2,3. \tag{3.2}$$

We now extend the unique time variable $\tilde{t}$ into four formally independent time variables $\tilde{t}_0$, $\tilde{t}_1$, $\tilde{t}_2$ and $\tilde{t}_3$ with $\tilde{t}_n = \tau_{\alpha n} t = \tau_{\alpha 0}\delta^{-n} t$, perform for the f_α's a Taylor expansion in the smallness parameter δ_α and finally arrive at the following multiple timescale formalism

$$f_\alpha = \sum_{n=0} \delta^n f_{\alpha n}(\vec{x},\vec{v};t_0,t_1,t_2,t_3) \text{ and } \frac{\partial}{\partial t} = \sum_{n=0} \delta^n \frac{\partial}{\partial t_n}. \tag{3.3}$$

This formalism is now applied to the dimensionless Fokker–Planck equation leading to the zero and first order equations

$$\delta_\alpha^0: \frac{\partial f_{\alpha 0}}{\partial t_0} + \sigma(q_\alpha)(a_\alpha \vec{E}_0 + \vec{v}\times\vec{B}_0)\cdot\frac{\partial f_{\alpha 0}}{\partial \vec{v}} = 0 \quad \text{and} \tag{3.4}$$

$$\delta_\alpha^1: \frac{\partial f_{\alpha 0}}{\partial t_1} + \frac{\partial f_{\alpha 1}}{\partial t_0} + \vec{v}\cdot\nabla f_{\alpha 0} + \sigma(q_\alpha)(a_\alpha \vec{E}_0 + \vec{v}\times\vec{B}_0)\cdot\frac{\partial f_{\alpha 1}}{\partial \vec{v}} + \sigma(q_\alpha)\frac{\delta_i}{\delta_\alpha}(a_\alpha \vec{E}_1 + \vec{v}\times\vec{B}_1)\cdot\frac{\partial f_{\alpha 0}}{\partial \vec{v}} = 0 \tag{3.5}$$

4. THE ZERO ORDER EQUILIBRIUM

In solving the zero order equation (3.4) we are only interested in the stationary case, i.e., in the solution for the asymptotic limit $t_0 \longrightarrow \infty$. From statistical mechanics it follows that $f_{\alpha 0}$ approaches a local Maxwellian, i.e.,

$$f_{\alpha 0}(\vec{x},\vec{v};t_1,t_2,t_3) = \pi^{-3/2} n_{\alpha 0} T_{\alpha 0}^{-3/2} \exp[-(\vec{v}-\vec{u}_{\alpha 0})^2/T_{\alpha 0}] \tag{4.1}$$

with $n_{\alpha 0}$, $T_{\alpha 0}$, $\vec{u}_{\alpha 0} = n_{\alpha 0}$, $T_{\alpha 0}$, $\vec{u}_{\alpha 0}(\vec{x},t_1,t_2,t_3)$. $n_{\alpha 0}$ and $T_{\alpha 0}$ are the zero order densities and temperatures, both normalized with respect to some characteristic values $\bar{n}_\alpha$ and $\bar{T}_\alpha$ on the magnetic axis. The zero order fluid velocity $\vec{u}_{\alpha 0}$ is normalized with respect to the thermal velocity on axis. However, in order that Eq. (3.4) can be satisfied for the Maxwellian from Eq. (4.1) it follows $\vec{E}_0 = 0$, and $\vec{u}_{\alpha 0} \uparrow\uparrow \vec{B}_0$, i.e., $\vec{u}_{\alpha 0} = g_\alpha \vec{B}_0$. From Maxwell's equations $\nabla\cdot\vec{B} = 0$, $\text{curl}\,\vec{B} = \mu_0\vec{j}$ and $\vec{j} = e(Zn_i\vec{u}_i - n_e\vec{u}_e)$ we immediately conclude, that $\vec{B}_0$ must be a force–free field, satisfying $\text{curl}\,\vec{B}_0 = \lambda(\Psi_0)\vec{B}_0$. Furthermore, it may be

shown that $n_{\alpha 0}$, $T_{\alpha 0}$, g_α, and λ are flux functions of the zero order flux Ψ_0. Hence, the zero order equilibrium obtained is characterized by

$$\vec{u}_{\alpha 0} = g_\alpha \vec{B}_0, \qquad \vec{E}_0 = 0, \qquad \text{curl } \vec{B}_0 = \lambda(\Psi_0)\vec{B}_0 \quad \text{and}$$

$$n_{\alpha 0},\ T_{\alpha 0},\ g_\alpha,\ \lambda = n_{\alpha 0},\ T_{\alpha 0},\ g_\alpha,\ \lambda\{\Psi_0(\vec{x}, t_1, t_2, t_3); t_1, t_2, t_3\} \tag{4.2}$$

If we assume $\vec{u}_{\alpha 0} = 0$, then we obtain for $\vec{B}_0$ just the vacuum field. This assumption may be justified for stellarators, but usually not for Tokamaks and RFP's where rotation velocities close to the ion thermal velocity are observed.

5. THE FIRST ORDER EQUILIBIRUM

After performing for $f_{\alpha 0}$ in the zero order equation the limit $t_0 \longrightarrow \infty$, it turns out that $f_{\alpha 1}$ in the first order equation (3.5) cannot depend on t_0. The zero, first, and second order velocity moments of Eq. (3.5) lead to the normalized two–fluid equations

$$\frac{\partial n_{\alpha 0}}{\partial t_1} + \nabla(n_{\alpha 0}\vec{u}_{\alpha 0}) = 0 \tag{5.1}$$

$$\frac{\partial}{\partial t_1}(n_{\alpha 0}\vec{u}_{\alpha 0}) + \nabla\cdot(n_{\alpha 0}\vec{u}_{\alpha 0} \oplus \vec{u}_{\alpha 0}) + \frac{1}{2}\nabla(n_{\alpha 0}T_{\alpha 0}) - \sigma(q_\alpha)(n_\alpha \vec{u}_\alpha)_1 \times \vec{B}_0 -$$

$$\sigma(q_\alpha) n_{\alpha 0}\delta_i/\delta_\alpha(a_\alpha \vec{E}_1 + \vec{u}_{\alpha 0}\times\vec{B}_1) = 0 \tag{5.2}$$

$$\frac{\partial}{\partial t_1}\left\{\frac{3}{4}n_{\alpha 0}T_{\alpha 0} + \frac{n_{\alpha 0}u_{\alpha 0}^2}{2}\right\} + \nabla\cdot\left\{\left[\frac{5}{4}n_{\alpha 0}T_{\alpha 0} + \frac{n_{\alpha 0}u_{\alpha 0}^2}{2}\right]\vec{u}_{\alpha 0}\right\} = \frac{a_\alpha n_{\alpha 0}\delta_i}{\sigma(q_\alpha)\delta_\alpha}\vec{u}_{\alpha 0}\vec{E}_1 \tag{5.3}$$

The difference to the usual two–fluid equations consists in the fact that the Lorentz–force term contains zero and first order particle fluxes and zero and first order fields. With the usual simplifying assumptions changing to the one–fluid description we obtain the first order equilibrium equation

$$\rho(\vec{v}\cdot\nabla)\vec{v} = -\nabla p + \delta_i(\vec{j}_1\times\vec{B}_0 + \vec{j}_0\times\vec{B}_1) \qquad \text{with}$$

$$\vec{B} = \bar{B}(\vec{B}_0 + \delta_i\vec{B}_1),\ \vec{j} = \bar{j}(\vec{j}_0 + \delta_i\vec{j}_1),\ \text{curl } \vec{B}_0 = \lambda(\Psi_0)\vec{B}_0,\ \vec{v} \uparrow\uparrow \vec{B}_0 \tag{5.4}$$

The corresponding stellarator equilibrium equation reads

$$\nabla p = \delta_i \text{ curl } \vec{B}_1\times\vec{B}_0 \quad \text{with} \quad \vec{B} = \bar{B}(\vec{B}_0 + \delta_i\vec{B}_1) \text{ and } \vec{B}_{vac} = \bar{B}\vec{B}_0 \tag{5.5}$$

Note that $\vec{B}_1$ and $\vec{j}_1$ are not arbitrary but arise from the solution of Eq. (3.5) for $f_{\alpha 1}$.

/1/ Edenstrasser J.W., XII–th Int.Conf.Plasma Phys.Contr.Nucl.Fus.Res., Nice (1988), Paper CN 50/D–4–13

Work supported by the Austrian Research Funds, contract P7005.

EQUILIBRIA AND DYNAMICS OF A FUSION REACTOR PLASMA

Hans Wilhelmsson

Institute for Electromagnetic Field Theory and Plasma Physics
Chalmers University of Technology
S-412 96 Göteborg, Sweden

Model descriptions of the behaviour of a fusion reactor plasma are based on systems of partial differential equations, accounting for the processes occurring in the plasma as well as for the effects of boundaries. It is the purpose of the present contribution to introduce a new technique of analysis based on a central expansion in the spatial variable for a bounded state of a fusion plasma. The technique considerably simplifies the description of the dynamics as well as the determination of equilibria. For particular cases of practical interest, combining effects of alpha particle heating, external heating, ohmic heating and bremsstrahlung, explicit analytic results are obtained for equilibrium distributions. The analytic results are complementary to those of extensive direct computer calculations and useful as check-points or for interpretation.

The problem of studying nonlinear partial differential equations of a reaction-diffusion type is transformed to a description in terms of three characteristic dynamic variables which depend only on time and which are governed by three coupled nonlinear first order differential equations. The three variables are (i): a central value A, (ii): a width £, and (iii): a form function η. These quantities define at any moment a certain spatial temperature or density profile. A unified description is given in one, two and three spatial dimensions and assumes radial symmetry for 2-D and 3-D cases. The technique, which implies a central expansion in the spatial variable, allows for an analytic description which includes the influence of an external boundary.

As a result profiles of equilibria can be calculated in a simple way with high accuracy. It is described how such equilibria may be approached from initial states, which even deviate appreciably from the equilibrium state. It is furthermore demonstrated how, in the presence of diffusion, and provided an external boundary exists, the competition between the effects of a source term and a loss term may lead to situations where several equilibria are possible, i.e. to bifurcated states. Applications of the new technique are found in many fields of science, notably in plasma physics. One specific application is to the problem of thermal stability and control of a burning fusion plasma.

Consider the following form of the nonlinear heat equation with a sink term

$$\frac{\partial u}{\partial t} = x^{-\gamma}\frac{\partial}{\partial x}\left(x^{\gamma} D(u)\frac{\partial u}{\partial x}\right) + S(u,x) \qquad (1)$$

where the diffusion coefficient

$$D(u) = a\, u^{\delta}\,, \tag{2}$$

where a and δ are constants.

The source and sink terms are included in the expression

$$S(u,x) = (1 - x^2/b^2)^{\beta}\,(c\, u^{p} - e\, u^{q})\,, \tag{3}$$

where β, p and q are constants, and b defines the position of the external boundary at x = b, where S(u,b) = 0 for all times.

In Eq. (1) the quantity γ is related to the space dimension under consideration by γ = d-1. Radially symmetric situations are assumed for d = 2 and d = 3.

In the expression (3) the form factor $(1\text{-}x^2/b^2)^{\beta}$ may represent, e.g. the variation of a density and the variable u correspondingly a temperature. As an example one may, for a burning fusion plasma, choose c and e (c > 0; e > 0) proportional to the density values and $p \equiv 2.2 - 2.5$ to model the effects of alpha particle burning and q = 0.5 in order to describe bremsstrahlung losses. Simultaneously one may choose δ in expression (2) as δ = 3/2 to represent diffusion caused by drift wave turbulence.

In order to describe the dynamic evolution governed by the Eq. (1) and the boundary condition for u(x,t), namely

$$u(b, t) = 0\,, \tag{4}$$

for all t, the following form is assumed for u, namely

$$u = A\, G(x/£)\,, \tag{5}$$

where A and £, the central value and the width are functions of time, and only time, A = A(t) and £ = £(t), and where

$$G = (1 - x^2/b^2)^{\alpha}\,[1 - (x/£)^2 + \eta(x/£)^4 - \xi(x/£)^6] \tag{6}$$

where for dimensions d = 2 and d = 3 and radially symmetric situations γ = 1,2, respectively.

For the coefficients η and ξ in the expansion (6) $\eta = \eta(t)$ and $\xi = \xi(t)$ one may in the process of truncation choose ξ as a constant ξ_o.

The condition for finite, non-zero flux

$$D\,\frac{\partial u}{\partial x} = a\, u^{\delta}\,\frac{\partial u}{\partial x} = \frac{a}{1+\delta}\,\frac{\partial u^{\delta+1}}{\partial x} \tag{7}$$

for x = b uniquely determines the quantity α as

$$\alpha = (1+\delta)^{-1}\,,\quad \delta \neq -1 \tag{8}$$

Introducing the form (5) in the Eq. (1) and matching terms which depend on x^0, x^2 and x^4 separately, assuming $\xi = \xi_0$, a constant value, but $\eta = \eta(t)$, one obtains three coupled equations in A, $\pounds^2$ and η, namely

$$\frac{dA}{dt} = -2a(1+\gamma)\left(\frac{1}{B^2}+\frac{1}{\pounds^2}\right)A^{\delta+1} + c\,A^p - e\,A^q\,, \tag{9}$$

$$\frac{d\pounds^2}{dt} = -2a\,A^{\delta}\left[(1+\gamma)\frac{\pounds^4}{B^4} - 2\Omega\frac{\pounds^2}{B^2} - \Gamma\right]$$

$$- c\,A^{p-1}\pounds^2\left[(p-1)\left(\frac{\pounds^2}{B^2}+1\right) + \beta\frac{\pounds^2}{B^2}(1+\delta)\right]$$

$$+ e\,A^{q-1}\pounds^2\left[(q-1)\left(\frac{\pounds^2}{B^2}+1\right) + \beta\frac{\pounds^2}{B^2}(1+\delta)\right], \tag{10}$$

and a similar equation for $d\eta/dt$, where in Eqs. (9) and (10) $B^2 = b^2(1+\delta)$, $\Gamma = (\delta+2\eta)(\gamma+3)-(\gamma+1)$ and $\Omega = (1+\delta)(\gamma+3)-(\gamma+1)$.

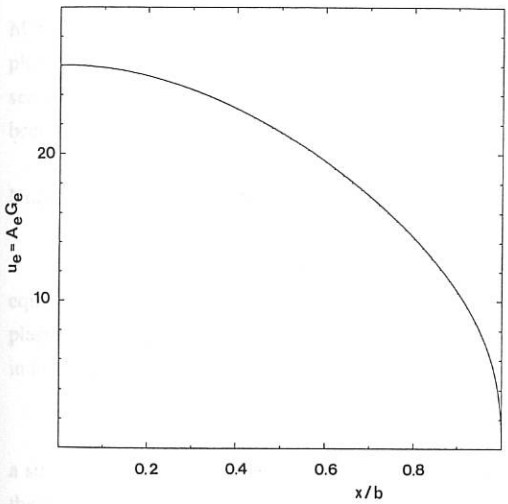

Fig. 1. Equilibrium distribution $u_e = A_e\,G_e$ for p = 2.4, δ = 1.5, η = 0.8, β = 1, γ = 1 with a = 0.25, b = 1, c = 1 and e = 0, (no decay term), obtained by the analytic approach of central expansion, which determines the form G_e from (6) and A_e from (9) with dA/dt = 0 and e = 0, (dotted line). For comparison the corresponding distribution obtained by computer calculations directly from the Eq. (1) with $\partial u/\partial t = 0$ is plotted in the same graph (full line). As can be seen the difference is hardly distinguishable.

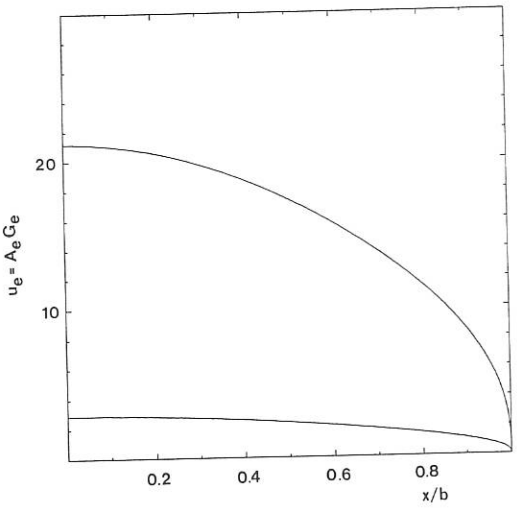

Fig. 2. Two equilibrium distributions $u_e = A_e\ G_e$ for the same parameter values as in figure one, except that e = 1 (including a decay term), obtained by the central expansion technique.

NUMERICAL SIMULATION OF THE INTERNAL KINK m = 1 IN TOKAMAK

H. Baty, M.N. Bussac, J.F. Luciani

Centre de Physique Théorique - Ecole Polytechnique - 91128 Palaiseau.

In a resistive plasma, $S = 10^6$, when $\beta_p = 1$ the internal kink exhibits a strong ballooning structure which modifies the usual picture of the "Kadomtsev" reconnection.

A full 3-D non-linear evolution code has been developped in order to study non-linear MHD instabilities [Ref. 1]. Hence it has to ensure a very good precision during the linear phase and has to avoid large slowing down of the dynamic in the resonnant layers. A new semi-implicit scheme which does not slow-down the dynamic within the resonnant layers, has been implemented in our 3D non-linear evolution code.

Non-linear evolution of an Internal kink in a resistive Tokamak

The evolution of the internal m = n = 1 kink is followed starting from a toroïdal equilibrium with $\beta_p = 1$ and a safety factor profile $q(r) = 0.8\ [1 + (2r/a)^4]^{1/2}$ where a is the plasma radius, and the aspect ratio R/a = 5. For such an equilibrium the ideal kink is unstable in toroïdal as well as in cylindrical geometry.

In cylindrical geometry the ideal mode non linearly evolves towards a configuration with a singular current layer near q = 1, where the plasma is compressed by the instability. But if the resistivity is finite, the current layer tends to diffuse and thereby drives the reconnection of

the magnetic surfaces. Along with the magnetic flux, the hot plasma core is expelled outside the surface q = 1. The reconnection stops when the central flux reconnects to the flux at the mixing radius, leaving a symetric plasma state with q larger than 1 on the magnetic axis.

In toroîdal geometry the linear ideal kink perturbation is mainly an m = n = 1 mode i.e rigide displacement of the plasma core where the safety.factor q is less that one. But it has also an m = 2, n = 1 component (where m is the poloïdal wave-number) which extends beyond the q = 1 magnetic surface (till the plasma edge). Moreover the m = 2, n = 1 component of the velocity expells the plasma outside q = 1 in the region where the displacement pushed the plasma core towards the low toroïdal magnetic field region (outer part of the torus). On the opposite in the region where the main component m = n = 1 of the displacement pushed the plasma towards the high toroïdal magnetic field (inner part of the torus), the m = 2, n = 1 component of the velocity expells the plasma *inside* q = 1, towards the plasma core.

Hence, the non-linear evolution of the internal kink in toroïdal geometry yields a current layer which is localised in the inner part of the torus. (The current sheet is broadened on the other part of the torus). [see Fig. 1 - a - b]. Then in toroïdal geometry reconnection of flux mainly occurs on the inner part of the torus, where the plasma is compressed by the ideal kink. On the other hand, at the same time the plasma pressure is also expelled in the part of the bad curvature region (outer part of the torus) where the plasma is pushed by the m = n = 1, lowering the available energy of the ideal mode, independantly of the reconnection process [see Fig. 2 - a - b].

Hence the cylindrical picture of the Kadomsev reconnection could be modified by this toroïdal effect. The reconnection, which is driven by the ideal mode, could stops when the plasma pressure gradient is flat enough inside the plasma core for the ideal kink to be stable. That is before the central flux is reconnected to the mixing radius.

Reference

[1] K. Lerbinger, J.F. Luciani "Transition between resistive Kink and Kadomsev reconnection ,this conference .

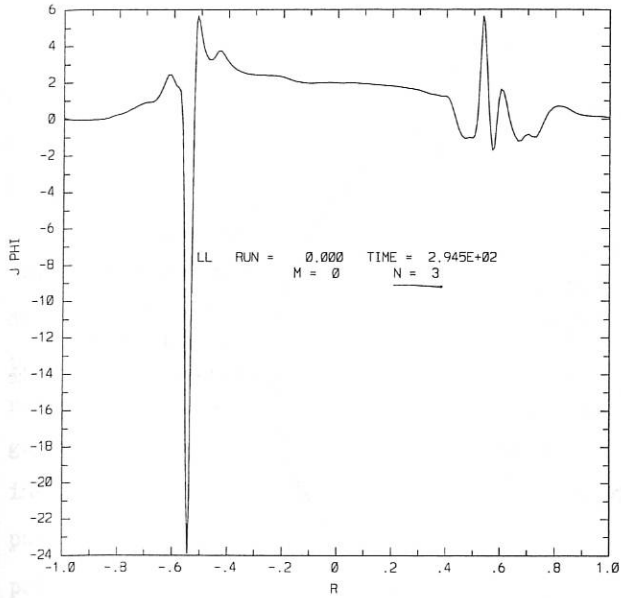

Fig. 1. A
Toroïdal current in the meridian plane $\phi = \pi$.

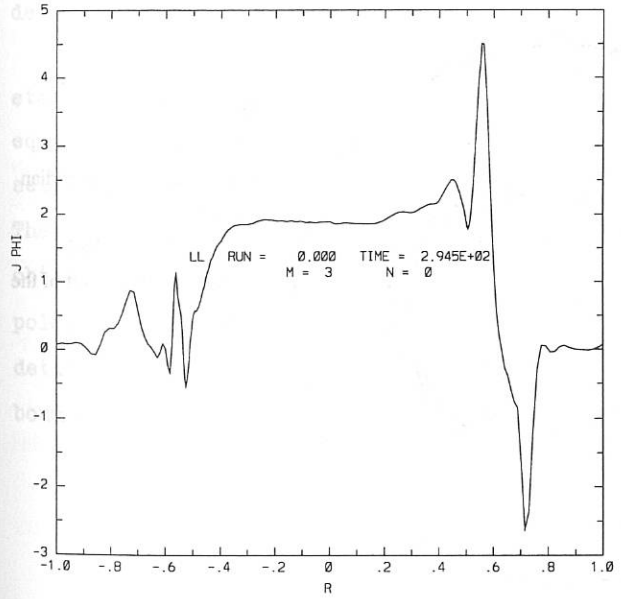

Fig. 1 - B
Toroïdal current in the meridian plane $\phi = \pi/2$.

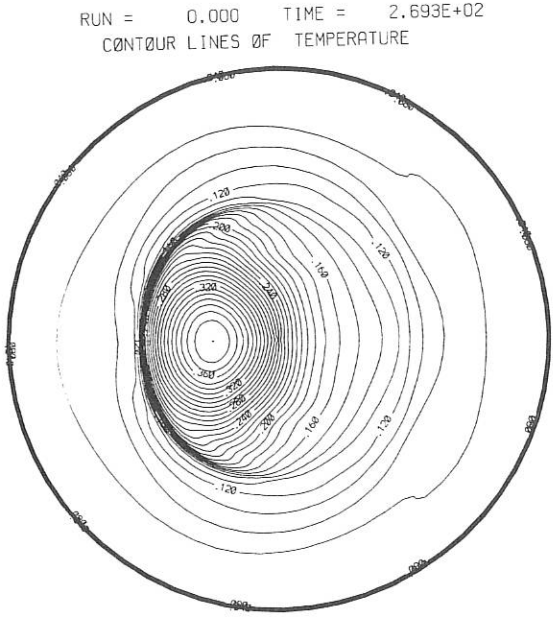

Fig. 2 - A
Contour lines of temperature in the meridian plane $\phi = \pi$.
The plasma is pushed towards the inner part of the torus.

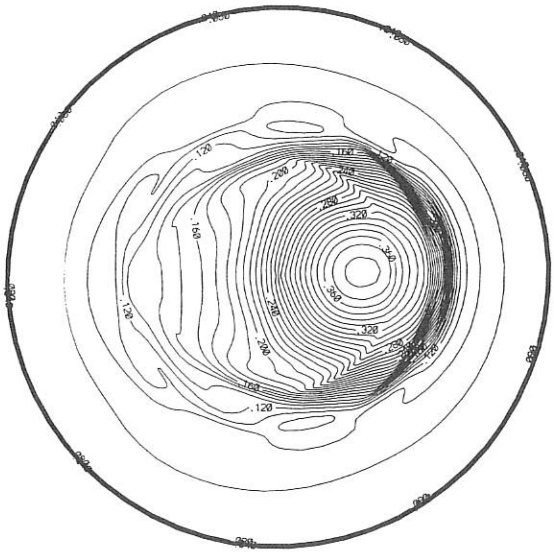

Fig. 2 - B
Contour lines of temperature in the meridian plane $\phi = 0$.
The plasma is pushed towards the outer part of the torus.

THERMAL PLASMA CORE INSTABILITY

Arutiunov A.B., Krasheninnikov S.I.
I.V.Kurchatov Institute of Atomic Energy, Moscow, 123182, USSR

As far as we know the emergence of marfe and detached-plasma can to a great extent be explained by the thermal plasma core instability that is predetermined by radiative energy losses on impurities. However, there is no general theory describing even a linear stage of such an instability. A limit of short waves lengths was studied in papers by Neihauser and Stringer . A conclusion on poloidal-symmetric perturbations stability was done by Drake recently . Yet it does not explain the emergence of detached-plasma.

In the given paper, in contrast, the analysis of the stationary solutions of the particles and energy balance equations stability is presented with due account of the self-consistent edge conditions on the plasma core periphery. The criteria of the thermal plasma core instability were obtained in two cases: 1) poloidal-non-symmetrical (marfe); 2) poloidal-symmetrical (detached-plasma). It was shown that the detached-plasma-type instability is closely connected with the boundary conditions at the plasma edge periphery.

NUMERICAL SIMULATION OF THE TEARING MODE IN TOKAMAK WITH NONCIRCULAR CROSS-SECTION. NEW APPROACH TO STUDY NON-LINEAR EVOLUTION OF RESISTIVE HELICAL MODES.

E.V. Andreeva, Yu.N. Dnestrovskij*, D.P. Kostomarov, V.V. Nefedov, A.V. Pedorenko, A.M. Popov.

M.V.Lomonosov Moscow State University, Moscow, USSR
*I.V.Kurchatov Institute of Atomic Energy, Moscow, USSR

ABSTRACT.The effective numerical code to study the tearing modes in toroidal geometry for noncircular cross-section plasmas is proposed. It is found that the stabilization of n=1 mode for particular q profile with q'=0 on the q=1 surface depends on the elongation of q=2 resonant surface. A new effective method is proposed for study of the non-linear plasma evolution in tokamak.

1.INTRODUCTION.The main accent of this report is the study of linear instability of the lowest helical modes m/n. The possibility of stabilization of these modes with special equilibrium current profile was presented in [1].The stabilization occures because of the satellite harmonics influence in toroidal and shaped geometry. In particular we obtain some conditions of 1/1 mode stabilization for q profile with $q'(\rho_{s1})=0$ which occures because of m=1 and m=2 harmonics connection and the effect of plasma cross-section shaping of the q=2 surface placed near the plasma boundary.

In this report a new effective approach for study of non-linear resistive MHD equations of tokamak plasma is suggested. It has been shown that in cylindrical geometry the non-linear interaction of resistive modes with different helicities leads in some cases to stationary states with magnetic islands.

2.REDUCED MHD-EQUATIONS IN TOROIDAL GEOMETRY.The tearing-instability model is 3D and includes three unknown functions: the longitudinal components of velocity and magnetic field vector potentials u,ψ and the pressure P. The reduced equations in toroidal geometry are the following [2]:

$$\frac{\partial \Delta_\perp u}{\partial t} = J(\Delta\psi,\psi) - \frac{1}{r}\frac{\partial}{\partial\varphi}\Delta^*\psi + \frac{1}{r}\varepsilon\beta_p J(P,X) + J(u,\Delta u),$$
$$\frac{\partial\psi}{\partial t} = J(u,\psi) - \frac{1}{r}\frac{\partial u}{\partial\varphi} + (\eta/S)\Delta^*\psi , \qquad (1)$$
$$\frac{\partial P}{\partial t} = J(u,P) ,$$

where $X=(r/R-1)$, $J(u,v) = ([\nabla_\perp u,\nabla_\perp v]\cdot\vec{e}_\varphi)$, $S=\tau_R/\tau_{H_p}$. The problem is represented in a straight-field-line magnetic flux coordinate system (ρ,θ,φ) where ρ is a flux surface label. The solution of (1) is expanded as follows:

$$\psi(\rho,\theta,\varphi,t)=\psi_{eq}(\rho) + \sum_{m,n}\psi_{mn}(\rho,t)\exp(i(m\theta-n\varphi)) . \qquad (2)$$

The metric tensor components $g^{ik}(\rho,\theta)$ are expanded in series too.

3.METHOD.The one-dimensional set for Fourier components is solved by the new effective finite-difference method based on using of the special coefficients near the second derivatives in (1).These coefficients take into account the asymptotical behaviour of solution in the neighbourhood of the resonant surfaces. The method is uniformly converged on parameter S and allows us to reproduce all of the solution peculiarities on sparse grid.

4.RESISTIVE MODE m=1 STABILITY FOR $q_o<1$. The calculations were devoted to investigate the current profile and shaping effects on m/n=1 mode linear tearing instability.The destabilizing effect of triangularity is more weak than the stabilizing role of elongation. The main stabilizing effect was obtained for q profile with an inflection point $q(\rho_{S1})=1$, $q'(\rho_{S1})=0$, $q''(\rho_{S1})=0$. Fig.1 gives the set of radial profiles $q(\rho)$ and $j(\rho)$, which are corresponded to the fixed value $q_a=2.45$, various shear values on a rational surface ρ_{S2} ($q(\rho_{S2})=2$) and inflection point $\rho_{S1}=0.46$. Fig.2 gives linear growth rates of n=1 mode versus elongation k_a for the equilibrium set, presented in Fig.1, $\varepsilon=1/3$, $S=10^5$. The stabilization is possible even if $k_a= 1.4$. The calculations show that the n=1 mode stabilization is occured due to increase of satellite harmonics m=2, m=3 influenced through elongation.

5.METHOD OF PROJECTIONS ON THE UNSTABLE MANIFOLD. In cylindrical case we introduce the non-linear solution of (1) as $\vec{Y}(\vec{r},t)$ =

$\vec{Y}_{eq}(\vec{r})+\tilde{\vec{Y}}(\vec{r},t)$ and then the set (1) in terms of perturbation $\tilde{\vec{Y}}$ will look as:

$$\frac{\partial}{\partial t} M \tilde{\vec{Y}} = L \tilde{\vec{Y}} + B[\tilde{\vec{Y}},\tilde{\vec{Y}}], \qquad (3)$$

where M,L are the linear operators and $B[\vec{X},\vec{Y}]$ is bilinear operator. The main idea of this approach consists of the decomposition of non-linear MHD solution in asymptotic series of amplitudes received by the projections of unknown solution on the unstable manifold. At first, we have to consider a linear problem $\lambda \cdot M\vec{Y}^{(1)}=L\vec{Y}^{(1)}$ and adjoint problem $\bar{\lambda} \cdot M^*\vec{\chi}^{(1)}=L^*\vec{\chi}^{(1)}$. From the solution of these problems we choose all eigenfunctions with $Re\lambda>0$. Then we define the non-linear solution amplitudes by the projection of solution on the unstable manifold formed by all of unstable eigenfunctions:

$$x_{mn}(t) = \int_{V_p} \left(M\tilde{\vec{Y}}(\vec{r},t) \, , \, \vec{\chi}^{(1)}_{mn}(r) \cdot exp(i \cdot (m \cdot \varphi + n \cdot s)) \right) dV \, , \qquad (4)$$

where (m,n) are the poloidal and toroidal wave numbers respectively. We search the solution of (3) in terms of formal power series in amplitudes $x_{mn}(t)$:

$$\tilde{\vec{Y}}(\vec{r},t) = \sum_{\substack{m,n: \\ \lambda_{mn}>0}} x_{mn}(t) \cdot \vec{Y}^{(1)}_{mn}(r) \cdot exp(i \cdot (m \cdot \varphi + n \cdot s)) +$$

$$\sum_{m_1,n_1} x_{m_1 n_1}(t) \cdot x_{m_2 n_2}(t) \cdot \vec{Y}^{(2)}_{m_0 n_0}(r) \cdot exp(i \cdot (m_0 \cdot \varphi + n_0 \cdot s)) + \dots \, ,$$

where $m_0=m_1 \pm m_2$, $n_0=n_1 \pm n_2$.

Let the following orthogonality conditions are fulfilled:

$$\int_{V_p} \left(M\vec{Y}^{(k)}(\vec{r}), \vec{\chi}^{(1)}_{mn}(r) \cdot exp(i \cdot (m \cdot \varphi + n \cdot s)) \right) dV = 0 \, , \quad k \geqslant 2. \qquad (5)$$

Multiplying (3) on $\vec{\chi}^{(1)}_{mn}$ and using (4)-(5) we obtain:

$$\frac{d\, x_{mn}}{dt} = \lambda_{mn} \cdot x_{mn} + \sum_{\substack{m_1,n_1; \\ m_2,n_2}} a_{mn}[m_1,n_1;m_2,n_2] \cdot x_{m_1 n_1} \cdot x_{m_2 n_2} +$$

$$\sum_{m_i,n_i} b_{mn}[m_1,n_1;m_2,n_2;m_3,n_3] \cdot x_{m_1 n_1} \cdot x_{m_2 n_2} \cdot x_{m_3 n_3} + \dots \, . \qquad (6)$$

It is very simple to show that $a_{mn}[\dots]=0$ due to the symmetry of

cylindrical model,so the type of bifurcation in (3) is defined by a set of $b[...]$ coefficients. For the determination of high order functions $\vec{Y}^{(k)}_{mn}$ we have to solve the set of linear ordinary differential equations. As example, in case k=2, we have:

$$(\lambda_{m_1n_1}+\lambda_{m_2n_2})\cdot M_{m_0n_0}\vec{Y}^{(2)}_{m_0n_0} = L_{m_0n_0}\vec{Y}^{(2)}_{m_0n_0} + B_{m_0n_0}[\vec{Y}^{(1)}_{m_1n_1},\vec{Y}^{(1)}_{m_2n_2}] +$$

$$B_{m_0n_0}[\vec{Y}^{(1)}_{m_2n_2},\vec{Y}^{(1)}_{m_1n_1}] \text{ , where } m_0=m_1\pm m_2, n_0=n_1\pm n_2 \text{ .} \qquad (7)$$

So the initial problem (3) separates into the system of non-linear amplitude equations (6) and a set of linear equations of type (7). We have a code for the solution of (6)-(7) in general case. But if the dimension of the unstable manifold is equal 1 or 2 it is possible to research the system (6) analytically.

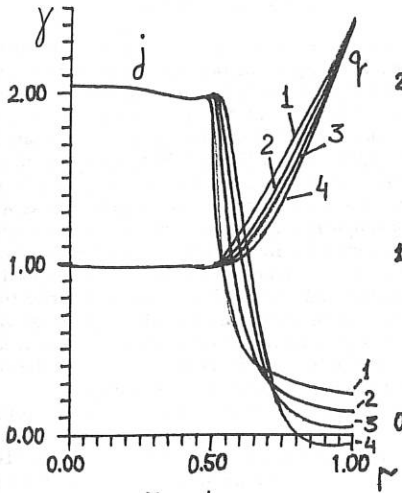

Fig. 1

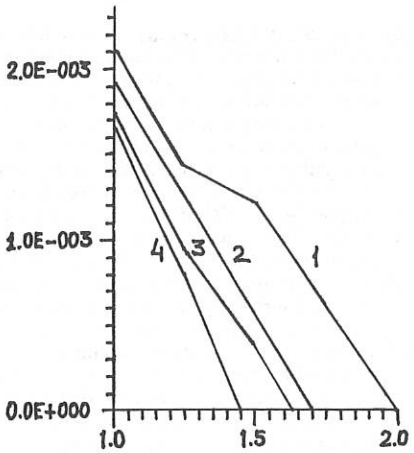

Fig. 2

REFERENCES

1. Iliyna E.V., Pedorenko A.V., Popov A.M.// Fiz. plazmy, 1989, V.15, P.926.
2. Dnestrovskij Yu.N., Kostomarov D.P. Numerical simulation of plasma. Springer-Verlag. 1986.

STABILISATION OF DRIFT-TEARING MODES AT THE BREAKDOWN OF THE CONSTANT-ψ APPROXIMATION

F. Porcelli, S. Migliuolo* and F. Pegoraro+

JET Joint Undertaking, Abingdon, Oxfordshire, OX14 3EA, U.K.
*Massachusetts Institute of Technology, Cambridge, MA, USA
+Scuola Normale Superiore, Pisa, Italy

Abstract. The growth rate of the linearised drift-tearing mode is found to be a nonmonotonic function of the stability parameter Δ'. It reaches a maximum for $\Delta' \sim 0.5\ \Delta'_1 > 0$ and becomes negative for $\Delta' \gtrsim \Delta'_1$, corresponding to the regime where the constant-ψ approximation breaks down. A second mode, identified as the diamagnetic modification of the $\eta^{1/3}$-mode near the condition for ideal MHD marginal stability, becomes unstable for $\Delta' \gtrsim \Delta'_2 > \Delta'_1$, leaving a stable window of values of Δ'. Applications to m = 1 mode stability are presented.

Introduction and main results. As is well known[1], within the resistive MHD model tearing modes are excited when the parameter Δ' (the logarithmic jump of the poloidal magnetic flux across the resonant layer $q(r_s) = m/n$, with m and n the poloidal and toroidal mode numbers, respectively) is positive. The tearing mode growth rate is $\gamma_T \approx 0.5\ m^{2/5}\ \varepsilon_\eta^{3/5}(\Delta')^{4/5}\omega_A$, where $\varepsilon_\eta \equiv \eta c^2/(4\pi r_s^2\omega_A)$, $\omega_A \equiv sv_A/R_0$ and $s \equiv r_s q'(r_s)$. When Hall effects and thermal force corrections to Ohm's law become important, i.e. when $\omega_{*e} \equiv -\ (m/r_s)\ (T_e/eBrn_e)[dn_e/dr + 1.71(n_e/T_e)dT_e/dr] > \gamma_T$, the tearing mode significantly changes its character. In this so-called drift-tearing regime[2] the mode becomes overstable with an oscillation frequency $\omega = \omega_{*e}$ and a significantly reduced growth rate, $\gamma_{DT} \approx 0.1\ m^{2/3}\varepsilon_\eta(\omega_A/\omega_{*e})^{2/3}(\Delta')^{4/3}\omega_A$ (we assume for simplicity $\omega_{*e} = -\ \omega_{di}$, with ω_{di} the ion diamagnetic frequency). The magnetic energy released by reconnection around $r = r_s$ ceases to be the main energy source available to the mode. The energy balance is dominated by the energy released by the electron pressure[3]. This energy is propagated and absorbed at a finite distance from the reconnecting surface by dissipation processes such as electron thermal conductivity or ion viscosity, which, if sufficiently small, do not perturb the eigen-frequency significantly. These results are obtained using the so-called constant-ψ approximation, ($|r_s d\ell n\psi/dr| < 1$ within the resistive layer around $r = r_s$), whose validity is restricted to values of $\Delta' << \Delta'_1 = m\omega_A/\omega_{*e}$.

Adopting a more general dispersion relation which does not rely on the constant-ψ approximation[4], we find that, when $\omega_{*e} > m^{2/3}\varepsilon_\eta^{1/3}\omega_A$, the drift-tearing growth rate has a nonmonotonic behaviour as a function of Δ'. It reaches a maximum for $\Delta' \sim 0.5\ \Delta'_1$ and becomes negative for $\Delta' > \Delta'_1$. A second mode becomes unstable with a frequency $|\omega| << \omega_{*e}$ and a growth rate $\gamma_{R*} \approx m^2\varepsilon_\eta\omega_A{}^3/\omega_{*e}{}^2$ for $\Delta' > \Delta'_2 = (\omega_{*e}/\omega_A\varepsilon_\eta)^{1/2}$. This low-frequency mode corresponds to the diamagnetic modification of the $\varepsilon_\eta^{1/3}$-mode found near the condition of ideal-MHD marginal stability. For the m = 1 case, this mode is well known under the name of resistive internal kink. A stable window is thus found when[5]

$$m\,\omega_A/\omega_{*e} < \Delta' < (\omega_{*e}/\omega_A\,\varepsilon_\eta)^{1/2} \qquad (1)$$

The existence of a stable window for positive values of Δ' was noted in Ref. 6. However, the behaviour of the two roots approaching the stable window from either sides, and the extent of the stable domain, were not discussed. It was also known that electron thermal conductivity and ion viscosity can suppress the drift-tearing and resistive internal kink modes, respectively. We find

that a stable window persists even when these additional dissipation processes are vanishingly small.

Dispersion relation. Consider the dispersion relation for tearing modes in a resistive MHD plasma with diamagnetic effects[4]:

$$\Delta'\delta = -\frac{m\pi}{8} Q \frac{\Gamma[(Q-1)/4]}{\Gamma[(Q+5)/4]}, \tag{2}$$

where $Q = -i\delta^2(\omega-\omega_{*e})/(m^2\varepsilon_\eta\omega_A)$ and $\delta^4 = -im^2\varepsilon_\eta\omega(\omega-\omega_{di})/[(\omega-\omega_{*e})\omega_A]$. The constant-$\psi$ approximation corresponds to the limit $|Q| << 1$. Acceptable solutions of (2) must satisfy the condition $\mathrm{Re}\,\delta^2 > 0$ in order for the corresponding eigenfunction to be spatially localised. This condition is violated for the drift-tearing root and for the $\varepsilon_\eta^{1/3}$-root at large values of ω_{*e}. However, as mentioned previously, for these roots the eigenfunction is regularised in the presence of electron thermal conductivity and/or ion viscosity.

The stable window is found for values of $|Q| \lesssim 1$. Then, we rewrite (2) in the form

$$C_o\Delta'\delta = mH(Q)\, Q/(1-Q) \tag{3}$$

where $C_o = (2/\pi)\Gamma(5/4)/\Gamma(3/4) \approx 0.47$ and $H(Q) = \{\Gamma[(Q+3)/4]/\Gamma(3/4)\}\{\Gamma(5/4)/\Gamma[(Q+5)/4]\}$. Now we approximate $H(Q) \approx 1$, yielding

$$-i(\omega-\omega_{*e})\delta = C_o(\Delta'/m)[m^2\varepsilon_\eta\omega_A + i\delta^2(\omega-\omega_{*e})] \tag{4}$$

The standard drift-tearing solution is recovered from (4) for $m^2\varepsilon_\eta\omega_A >> \delta^2(\omega-\omega_{*e})$, while as $\Delta' \to \infty$ the relevant dispersion relation becomes $m^2\varepsilon_\eta\omega_A + i\delta^2(\omega-\omega_{*e}) = 0$, with unstable solution corresponding to the $\varepsilon_\eta^{1/3}$-root. Solving Eq. (4) perturbatively around $\omega = \omega_{*e}$ leads to the approximate growth rate for the drift-tearing branch

$$\gamma \equiv Im\ \omega \approx \gamma_{DT}\,[1 - (8C_o^{4/3}/3)(\Delta'/\Delta'_1)^{2/3}], \tag{5}$$

yielding stabilisation for $\Delta' > \Delta'_1$. On the low frequency branch we approximate $\omega-\omega_{*e} \approx -\omega_{*e}$. Eq. (4) reduces to a quadratic equation for $\delta \approx (im^2\varepsilon_\eta\omega/\omega_A)^{1/4}$, with solution

$$(-i\omega)^{1/4} \approx (\gamma_{R*})^{1/4}\left\{\left[1+i\left(\frac{\Delta'_2}{2C_o\Delta'}\right)^2\right]^{1/2} - \frac{(i)^{1/2}\Delta'_2}{2C_o\Delta'}\right\}, \tag{6}$$

yielding stabilisation for $\Delta' < \Delta'_2$,

Numerical solution and applications to m = 1 modes. The relatively high values of Δ' needed to satisfy the inequalities in (1) make this analysis relevant to global, low-m mode. In this section we specialise to the m = n = 1 case. For a toroidal plasma with finite magnetic shear in the region where $q(r) \lesssim 1$, we can relate $\Delta' = -\pi/\lambda_H$, where the parameter λ_H is proportional to the negative of the MHD energy functional δW. Thus, $\lambda_H > 0$ is the instability condition for the ideal internal kink mode. We introduce the normalised parameters

$$\hat{\lambda}_H \equiv -\frac{\pi}{\Delta'\varepsilon_\eta^{1/3}}; \qquad \hat{\omega}_{*e} \equiv \frac{\omega_{*e}}{\gamma_R}, \tag{7}$$

where $\gamma_R \equiv \omega_A \varepsilon_\eta^{1/3}$. A numerical investigation of the dispersion relation (2) leads to the stability diagram in Fig. 1 (with $\omega_{*e} = -\omega_{di}$). For $\hat{\omega}_{*e} = 0$, the growth rate increases going from the tearing regime, $\gamma \approx \gamma_T$, in region IV, to the resistive internal kink regime, $\gamma \approx \gamma_R$, in region II, to the ideal internal kink regime, $\gamma \approx \lambda_H \omega_A$, in region I. The transition from the tearing to the resistive kink growth rate is shown in Fig. 2, where $\hat{\gamma} \equiv \gamma/\gamma_R$. The transition from the tearing to the drift-tearing regimes (region V), where $\gamma \approx \gamma_{DT}$, and to complete stability (region VI) as $\hat{\omega}_{*e}$ increases, can be observed at large negative values of $\hat{\lambda}_H$ in Fig. 3. In the same figure, the intermediate drift-tearing regime disappears for $\hat{\lambda}_H = -3$, while the mode remains unstable for $\hat{\lambda}_H = 0$. The non-monotonic behaviour of the drift-tearing growth rate as $\hat{\lambda}_H$ increases can be seen in Fig. 4, together with the stable window for two different values of $\hat{\omega}_{*e}$. Also note in this figure the difference in magnitude between the growth rates of the two different modes (the drift-tearing growth rate is multiplied by a factor 10^2 in Fig. 4 for graphic comparison with the growth rate of the resistive internal kink).

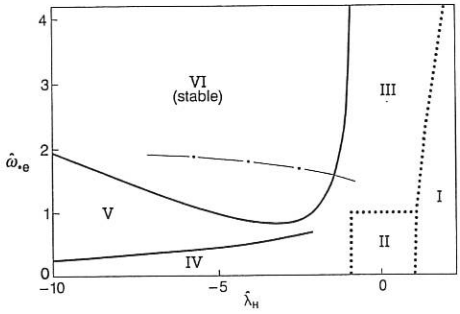

Fig. 1

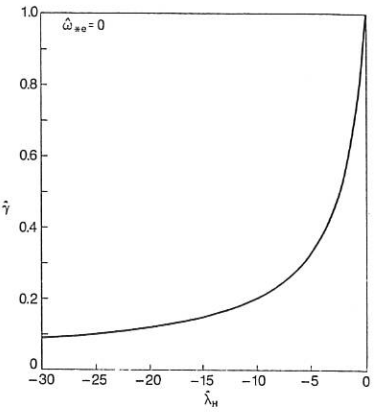

Fig. 2

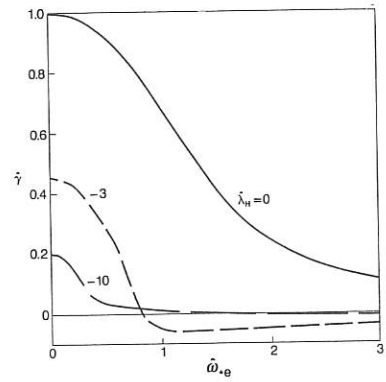

Fig. 3

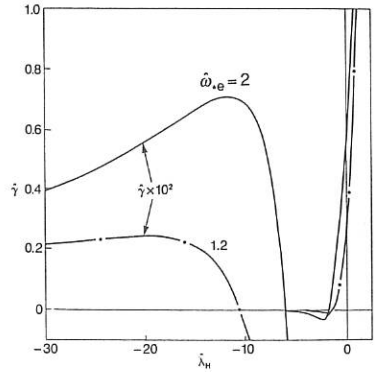

Fig. 4

By order of magnitude, $\lambda_H \sim \varepsilon_s^2(\beta_p^2 - \beta_{p,cr}^2)$ (where $\varepsilon_s \equiv r_s/R_o$, $\beta_p = [8\pi/B_p^2(r_s)][\langle p\rangle - p(r_s)]$, with $\langle p\rangle$ the average pressure within the $q \le 1$ volume, $\beta_{p,cr} \sim 0.1$ - 0.2) and $\varepsilon_\eta^{1/3} \lesssim 10^{-2}$. From inspection of the analytic form[7] of δW, an approximate scaling of $\hat{\lambda}_H$ with the local shear at the $q = 1$ surface, $s \equiv r_s q'(r_s)$, with $\Delta q = 1 - q_o$, and with the beta poloidal, β_p, can be given:

$$\lambda_H \propto \varepsilon_s^2(\Delta q)s^{-5/3}(\beta_p^2 - \beta_{p,cr}^2) \qquad (8)$$

On the other hand, $\hat{\omega}_{*e} \propto \hat{s}^{-2/3}T_e^{3/2}$. Stability against resistive $m = 1$ modes can be found even with q_o (q on axis) significantly below unity, provided $\hat{\lambda}_H$ is negative and sufficiently large and $\hat{\omega}_{*e} \gtrsim 1$. These conditions can be obtained for typical JET ohmic temperatures, for instance if β_p is low and the local magnetic shear is reduced (i.e. $q_o \sim 0.7$ - 0.9 and $s \sim 0.1$ - 0.3; note that $s = 2\Delta q$ for a parabolic q profile). Such a q profile may result from sawtooth crashes with incomplete (as opposed to Kadomtsev's) reconnection, leaving $q_o < 1$. The local flattening of q near the $q = 1$ surface diffuses away during the sawtooth ramp, and the ensuing variations of $\hat{\lambda}_H$ and $\hat{\omega}_{*e}$ yield a trajectory exemplified by the dashed-dotted curve in Fig. 1. More examples of this kind computed for sawtooth ramps of JET discharges can be found in Ref. 8.

A summary of the asymptotic regions of Fig. 1 is given in the Table below. The scalings of the growth rates with Δq, s and η are also given. We have assumed the approximate scaling[7] $\lambda_H \equiv \gamma_{mhd}/\omega_A \propto (\Delta q)s^{-1}$, while $\varepsilon_\eta \propto s^2\eta$. Therefore, $\gamma = \gamma[(\Delta q/s), s^2\eta]$. Note that the limit $s \to 0$ is outside the range of validity of the present model.

Instability regime		Normalised growth rate γ/ω_A	Scalings of γ with s, Δq, η
I	Ideal Kink	λ_H	$\gamma \sim (\Delta q)s^{-1}$
II	Resistive Kink	$\varepsilon_\eta^{1/3}$	$\gamma \sim s^{2/3}\eta^{1/3}$
III	Partially Stabilised Kink	$\varepsilon_\eta(\omega_A/\omega_{*e})^2$	$\gamma \sim s^2\eta$
IV	m = 1 tearing	$\varepsilon_\eta^{3/5}\lvert\lambda_H\rvert^{-4/5}$	$\gamma \sim s^2(\Delta q)^{-4/5}\eta^{3/5}$
V	m = 1 drift tearing	$\varepsilon_\eta\lvert\lambda_H\rvert^{-4/3}(\omega_A/\omega_{*e})^{2/3}$	$\gamma \sim s^{10/3}(\Delta q)^{-4/3}\eta$
VI	STABLE		

One question that needs to be investigated further is the nonlinear stability of region VI, i.e. whether the diamagnetic stabilisation holds in the presence of a small m = 1 island. Preliminary indications are that diamagnetic effects become ineffective for an island size, w, exceeding a critical width w_c, but just exactly how large is w_c in regimes of interest remains to be determined. Let us assume that (i) w_c is finite, so as to guarantee the stability of region VI, and (ii) w_c is below the observable level (i.e. $w_c \sim 1$ cm). Then, once the instability threshold of the resistive internal kink is crossed (region III), the mode growth rate could reach a level $\gamma \sim \gamma_R$ ($\sim 10^4 s^{-1}$ in JET) as soon as the growing island size exceeds w_c. This may help to understand the observed sudden displacement of the magnetic axis for precursorless sawtooth relaxations in JET.

References.
[1] H.P. Furth, J. Killeen and M.N. Rosenbluth, Phys. Fluids 6, 439 (1963). [2] P.H. Rutherford and H.P. Furth, PPPL Report MATT-872, 1971. [3] F. Pegoraro and T.J. Schep, Phys. Fluids 30, 3506 (1987). [4] G. Ara, et al., Ann. Phys. 112, 443 (1978). [5] S. Migliuolo, F. Pegoraro and F. Porcelli, JET Report JET-P(90)08, submitted to Phys. Fluids B. [6] M.N. Bussac, et al., in Plasma Physics and Controlled Nuclear Fusion Research 1976 (IAEA, Vienna, 1977), Vol. 1, p. 607. [7] M.N. Bussac, et al., Phys. Rev. Lett. 35, 1638 (1975). [8] R. Gill, et al., in Proc. 15th EPS Conference (Dubrovnik, 1988), Vol. I, p. 350; F. Porcelli, et al., JET Report JET-IR(88)16.

ON THE EXISTENCE OF A BENARD-LIKE CONVECTIVE INSTABILITY IN THE SAWTOOTH EVOLUTION

F. Spineanu, M. Vlad

Institute of Atomic Physics
P.O.Box MG-7, Măgurele, Bucharest, Romania

In recent years, the analysis of the sawtooth oscillations started from the assumption that the precursors, the crash and the succesors observed experimentally correspond to the development of a m=1 resistive tearing mode appearing at the resonance surface q=1 and invading the central region of the plasma. The analysis then concentrated mainly on various aspects of the stability and on the possible influences on the growth rate of this mode. The theories fail to explain some features of the magnetic instability, e.g.: (1) the very fast increase of the growth rate of the tearing mode which appears at the transition from the rise phase to the collapse; (2) the stability of the magnetic mode observed in some discharges even for $q < 1$; (3) the presence of large convective motions in the hot core. We note that the sawtooth is more likely a threshold process rather than the development of a fast growing mode.

Some of these features may have an explanation which consists basically in the identification of a second process which competes and eventually drives the fast growth of the m=1 resistive mode.

The basic (unperturbed) state consists of the ohmically heated plasma which losses energy through radially symmetric thermal conduction. Leaving for the moment the cylindrical symmetry, it is useful to imagine the analogy with the classical example of a fluid between two horizontal plates, heated from below. (In our case, a small radius cylinder centered on the magnetic axis plays the task of the lower plate.) When the temperature gradient reaches high values, the conduction of energy across the fluid slab is replaced by the more efficient convective transport. The transition is connected with a threshold condition, due to the dissipative mechanisms. Using this analogy, we may expect a family of states in which the convection governs the transport of heat from the central hot core of the plasma toward the external cold regions. The convective rolls should have helical symmetry and, in the cross section, the plasma core should be divided into an even number of lobes (since a convection cell has two rolls with oposite vorticities). Due to the fact that the states with higher symmetry are less stable to perturbations, we expect the stationary convective pattern to consist of two lobes with reflection symmetry across the median line.

Let us consider a test plasma tube at r_1, close to the magnetic axis, having helical symmetry. If it is displaced radially outward, the convected temperature $T_0(r_1)$ is greater than that of the surrounding plasma, $T_0(r_2)$. In the absence of ma gnetic effects, the current density $J_0(r_2)$ will remain constant and electric charges will accumulate on the sides of the plasma tube, creating an electric field :

$$\tilde{E}_z = \tilde{\eta}\, J_o = \tilde{\eta}\, E_o/\eta \qquad (1)$$

Combined with the magnetic field, this gives a drift velocity directed radially :

$$\delta v(r) = -\frac{3}{2}\frac{E_o B_\theta}{B_o^2}\frac{1}{T_o}\delta r\,\left(\frac{dT_o}{dr}\right) \qquad (2)$$

which determines a further increase of the initial perturbation. The inhomogenity of the drift velocity leads to the acceleration :

$$\vec{a}_E = -\frac{3}{2}\frac{E_o B_\theta}{B_o^2}\frac{1}{T_o}\,(\vec{v}\nabla)\,T_o\,\hat{e}_r \qquad (3)$$

The corresponding force is similar with the Archimedean force which drives the Benard-Rayleigh fluid convection. It can be calculated if an estimation of the plasma velocity $\vec{v}$ is obtained. From the sign of the product $\vec{E}_z x \vec{B}$, we observe that the displacements with increasing R (the distance to the major axis) along the lines of symmetry between the lobes are unstable and growing. Integrating (3) with respect to time, we can approximate the velocity with :

$$v = \frac{E_o}{B_o}\frac{r_s^2}{Rq}\frac{\Delta T_o}{T_o} \qquad (4)$$

where $\Delta T_o = T_o(r_s) - T_o(0)$ and r_s is the radial extension of the convection pattern. From this force f, the convection time of the plasma element along the distance r_s can be estimated as :

$$\tau_e = (r_s/a_E)^{1/2} \qquad (5)$$

Two dissipative processes are opposed to this motion. First, the temperature of the test element decreses during the motion due to the conductive losses. The time for the diffusion of heat is given by :

$$\tau_\chi = r_s^2\left[\chi_\perp(1 + (r_s/R)^2\,(\chi_\parallel/\chi_\perp))\right]^{-1} \qquad (6)$$

where $\chi_\parallel$, $\chi_\perp$ are the parallel and perpendicular thermal conductivities. The second process is the friction which produces the viscous diffusion of the vorticity in a characteristic time :

$$\tau_\nu = r_s^2/\nu \qquad (7)$$

where ν is the kinematic viscosity.
The analogy with the Rayleigh-Benard instability suggests the introduction of the nondimensional parameter $R = \tau_\chi \cdot \tau_\nu/\tau_e^2$. In this case :

$$R = \frac{E_o^2}{B_o^2}\frac{r_s^5}{R^2}\frac{1}{q^2}\frac{1}{L_\eta}\frac{1}{\chi_\perp \nu}\frac{\Delta T_o}{T_o}\left[1 + (r_s/R)^2\,\chi_\parallel/\chi_\perp\right]^{-1} \qquad (8)$$

The purely conductive solution is replaced by a stationary convective pattern when this parameter exceeds a threshold value.

A rigurous analysis of this phenomenon should start from the equations describing the momentum and heat balance in a fixed magnetic con-

figuration. For the Rayleigh-Benard effect, linearising the nondimensional form of the corresponding equations around the conductive solution, the Rayleigh number appears and the algebraic connection between this number and the wave length of the perturbation readly gives the threshold condition /1/. In our case, the essential nonlinear character of the problem does not permit such a simple determination of the critical R and, even more, does not offer a rigurous definition of the nondimensional parameter R. However, we obtain from the condition of stationary convection the same conclusions about the role of the plasma parameters as indicated by Eq.(8). In this situation, the distributions of $T(r,\theta)$, v_r and v_θ have been established and the motion is mentained through the equilibrium between the electric driving forces and the dissipative processes : thermal conduction and viscosity. A careful analysis is necessary when calculating the supplementary electric field felt by each plasma element. Since the neighbouring elements have different temperatures, one could expect to find an electric field arising from the difference in η on the vicinity of the test element. Actually, the fields due to all plasma elements crossed by the current line and having temperatures (and resistivities) different from the background plasma have to be added /2/.

The local difference in the drift velocity at (r,θ) comes from the difference in the temperature between two plasma tubes placed on the cylinder of radius r at θ and $\theta+\delta\theta$:

$$\delta v(r,\theta) = -\frac{3}{2}\frac{E_o B_\theta}{B_o^2}\frac{1}{T}\frac{\partial T}{\partial \theta}\delta\theta \qquad (9)$$

This expression must be integrated with constant r, from the point with zero radial velocity :

$$\vec{v}(r,\theta) = -\frac{3}{2}\frac{E_o B_\theta(r)}{B_o^2}\ln\left(\frac{T}{T_o}\right)\hat{e}_r(\theta) = -\frac{3}{2}\frac{E_o B_\theta(r)}{B_o^2}\frac{\tilde{T}}{T_o}\hat{e}_r(\theta) \qquad (10)$$

where $\tilde{T}(r,\theta)=T(r,\theta)-T_o(r)$ and $\hat{e}_r$ is the radial versor.
A plasma element moving in the time interval $d\tau$ from (r_1,θ_1) to (r_2,θ_2) is accelerated with :

$$\frac{d\vec{v}}{d\tau} = -\frac{3}{2}\frac{E_o}{B_o^2}\left[\left(v_r\frac{\tilde{T}}{T_o}\left(\frac{dB_\theta}{dr}-B_\theta\frac{1}{T_o}\frac{dT_o}{dr}\right)+B_\theta\frac{1}{T_o}(\vec{v}\nabla)\tilde{T}\right)\hat{e}_r + \right.$$

$$\left. + \left(\frac{v_\theta}{r}B_\theta\frac{\tilde{T}}{T_o}\right)\hat{e}_\theta\right] \qquad (11)$$

The displacement of the fluid elements along a closed flow line Γ must at least fulfill the periodicity condition :

$$\oint_\Gamma \left(d\vec{v}/d\tau + \nu\,\Delta\vec{v}\right)d\tau \geqslant 0 \quad . \qquad (12)$$

The thermal transport is given by :

$$(\vec{v}\nabla)T = \chi\,\Delta\tilde{T} = (\chi_\perp\Delta_\perp - \chi_\parallel k_\parallel^2)\tilde{T}(r,\theta) \qquad (13)$$

where $1/k_\parallel$ is the wave length of the perturbation in the direction of $\vec{B}$.

The integration along the symmetry line (plasma diameter) gives the most important driving contribution, while on the marginal line of Γ which is close to a semicircle, the heat exchange processes dominate. The friction force contribution is important on the whole flow line Γ. This integral can only be approximated analytically. The resulting qualitative conclusions are in agreement with the phenomenological analysis represented by Eq.(8).

The above model reveals from a new perspective the direct influence of the plasma parameters on the sawtooth characteristics. It appears that some of the observations made in experiments or in computer simulations can be explain on this basis :

-1- The collapse of the sawtooth may be regarded as arising from a threshold condition. When this condition is attained, the convection begins by a displacement of the hot plasma core as a whole, followed by a spliting in two opposite streams. Such a large scale plasma flow was experimentally observed /3/.

-2- For very good thermal conductivity along the magnetic field (large $\chi_{\parallel}$), any temperature perturbation caused by convection is rapidly damped and the driving force is small. The parameter R (Eq.8) vanishes when $\chi_{\parallel} \rightarrow \infty$ and cannot exceed the critical value. As seen also in the numerical simulations presented in /4/, the convection cannot develop.

-3- For higher $\chi_{\perp}$, the thermal conduction is efficient and the system needs not to resort to convection. Accordingly, we observe that R is small, i.e. far from the critical value.

-4- Complex numerical simulations /5/ showed that the sawtooth period increases for higher viscosity. We may explain this by the decrease of the actual value of R. The plasma parameters appearing in Eq.(8) needs longer time to evolve in the quiet phase before reaching critical conditions.

The convection is not related to the existence of the q=1 resonant surface and is independent on the magnetic perturbation. However, in most experimental conditions, the tendency to set up a regular Benard type convection is superposed with, and cannot be separated of the growth of the m=1 resistive mode.

REFERENCES

/1/ S. Chandrasekhar, "Hydrodynamic and hydromagnetic stability", Clarendon, Oxford, 1961;

/2/ B.B. Kadomtsev, in "Reviews of Plasma Physics", ed. M.A. Leontovich, Consultants Bureau New York, 1966, page 193;

/3/ E. Westerhof, P. Smeulders, N. Lopes Cardozo, Nucl. Fusion 29 (1989) 1056;

/4/ R.E. Denton, J.F. Drake, R.G. Kleva, Phys. Fluids 30(1987) 1448;

/5/ G. Vlad, A. Bonderson, Nucl. Fusion 29(1989) 1139.

GLOBAL, RESISTIVE STABILITY ANALYSIS IN AXISYMMETRIC SYSTEMS

A. Bondeson[a], G. Vlad[b], and H. Lütjens[a]

[a]Centre de Recherches en Physique des Plasmas, Ass. Euratom-Confédération Suisse Ecole Polytechnique Fédérale de Lausanne, 21 Av. des Bains CH-1007 Lausanne, Switzerland.

[b]Associazione Euratom-ENEA sulla Fusione, C.R.E. Frascati, C.P. 65 - 00044 - Frascati, Rome, Italy.

1.INTRODUCTION

Numerical codes such as ERATO [1] and PEST [2] have played an important role in developing the understanding of ideal-MHD stability for tokamaks. These codes solve the linearized ideal-MHD eigenvalue problem without any ordering assumptions. For resistive MHD, similar codes have been developed only recently [3]. Under a collaboration between the CRPP Lausanne and ENEA Frascati, we have developed a resistive spectral code, MARS (MAgnetohydrodynamic Resistive Spectrum), for the full compressional MHD equations in two-dimensional geometry. Axisymmetric equilibria are computed by the cubic Hermite element code CHEASE, which allows specification of the pressure p and toroidal field, $T = RB_\phi$, or the surface averaged toroidal current, $I' = \langle J_\phi \rangle$, as functions of the poloidal flux ψ. The two codes use flux coordinates (s, χ, ϕ), where $s = (\psi/\psi_{edge})^{1/2}$ is the radial variable, ϕ the geometrical toroidal angle, and χ the poloidal angle, specified by choosing the Jacobian, J. MARS Fourier decomposes the components of v and B in χ and uses a finite difference scheme in the radial direction.

Here, we present results for a number of resistive instabilities where toroidal effects play an important role. All calculations are made with a fixed, and except where explicitly stated otherwise, circular boundary.

2. INTERNAL KINK

The properties of the n=1, internal kink mode differ strongly between a torus and a cylinder. For $q_0 < 1$, $q_{edge} > 1$, a finite aspect ratio cylinder is ideally unstable, independent of pressure, while the torus is *ideally* stable for $\beta_{pol} < \beta_{pcrit}$. At large aspect ratio, β_{pcrit} is independent of $A = R/a$, but depends on equilibrium profiles [4]. It has been shown recently [5,6] that at tight aspect ratio, even the *resistive* internal kink mode can be stable if the shear at the q=1 surface is sufficiently low. In Fig. 1 we show the growth-rate of the resistive internal n=1 mode as a function of aspect ratio for two different sequences of equilibria at zero β. The two sequences have different current profiles $I'(\psi)$ (both smooth functions of ψ) which are kept fixed, while the aspect ratio is varied. For Fig.1a, $I'(\psi)$ is monotonic, the q=1 radius is kept fixed at $r_{q=1} = 0.44a$, the central q is about 0.90 and the shear, $\hat{s} = r\, dq/dr$ at q=1, increases slightly with $\varepsilon_{q=1} = r_{q=1}/R$ from 0.20 to 0.25. Although the resistive growth-rate decreases with increasing ε, the resistive modes remain unstable down to very tight aspect ratio, $\varepsilon_{q=1} = 0.3$. The second sequence of equilibria (Fig. 1b) has less shear in the $q \leq 1$ region and $dI'/d\psi = 0$ at the q=1 surface. Here $r_{q=1} = 0.62a$, $q_0 \approx 0.93$ and s ranges from 0.09 to 0.12, depending on aspect ratio. These equilibria are resistively stable for $\varepsilon_{q=1} > 0.25$. For $\eta < 10^{-6}$ and $\varepsilon_{q=1} < 0.15$, the growth-rates both in Fig. 1a and 1b follow the large-aspect-ratio scaling [6] for n=1 "m=1" tearing, $\gamma \propto \eta^{3/5} \varepsilon^{-8/5}$. For large η and small ε, the scaling is closer to that of the cylindrical resistive kink, $\gamma \propto \eta^{1/3} \varepsilon^{0}$. Triangularity, up to $\delta = 0.4$, has a negligible effect on the growth rates in the high-shear case, Fig.1a. In the case of lower shear (1b), triangularity is weakly stabilizing; $\delta = 0.3$ reduces the $\varepsilon_{q=1}$ needed for resistive stability from 0.25 to 0.21.

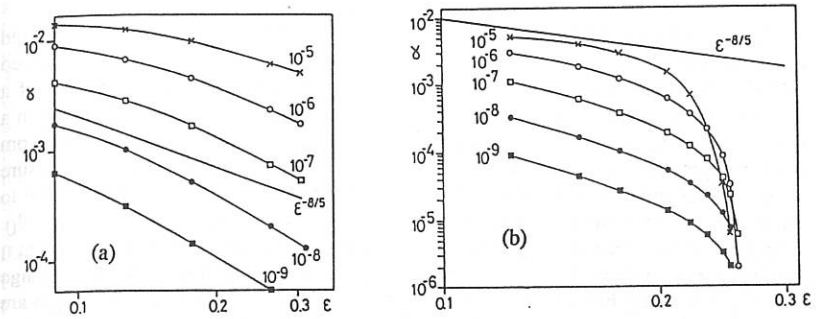

Fig. 1. Growth-rates of resistive internal kink mode as functions of aspect ratio for $\eta = 10^{-5}, 10^{-6}, 10^{-7}, 10^{-8}$,and 10^{-9}. (a) $\hat{s}_{q=1} \approx 0.2$, (b) $\hat{s}_{q=1} \approx 0.1$.

Generally, in tokamaks, $\varepsilon_{q=1} < 0.25$, and, from TEXTOR, q_0 as low as 0.7 has been reported [5]. Under such conditions, resistive stability requires a local reduction of the shear at the q=1 surface [5] and a non-monotonic current profile. Figure 2 shows resistive growth-rates for an equilibrium with finite pressure and where the shear has a local minimum near the q=1 surface. For these equilibria, R/a = 2.5, $q_0 \approx 0.7$, $q_{edge} \approx 2.4$, and $r_{q=1} \approx 0.51a$. We used a non-monotonic current profile I'(ψ), and the shear profile for $\beta_{pol} = 0.13$ is shown in Fig. 2b. Figure 2a gives contours of equal growth-rate for $\eta = 10^{-7}$ as a function of β_{pol}, measured at the q=1 surface, and $q_i \equiv q(s=0.607)$, near the inflection point of q(s). Fig. 2a shows that the stable window in q_i is narrow and eventually shrinks to zero as β increases. Furthermore, the stable values of q_i increase with increasing β, which means that the q=1 surface moves inward into a region of somewhat higher shear. The apparent reason for this is that the ideal pressure driven mode is stabilized by global shear, and this effect competes with the requirement of low local shear for resistive stability. The resistive β-limit is therefore somewhat lower than the ideal one. The maximum value of $\beta_{pol}(q=1)$ reached with our profiles is 0.2, to be compared with the ideal limit of 0.3 for a parabolic q-profile [4].

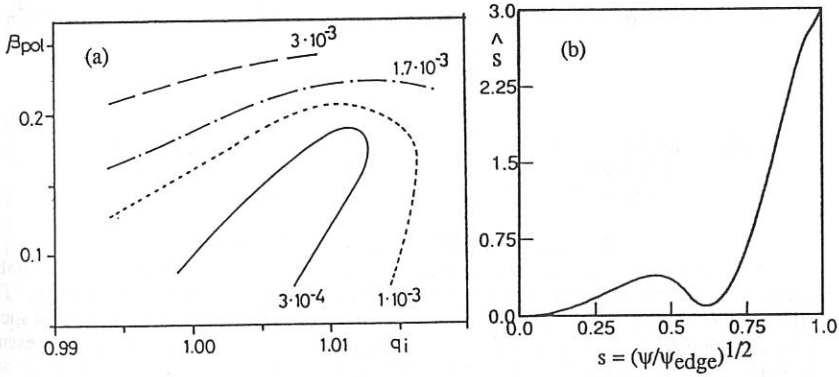

Fig. 2. (a) Growth-rate for resistive internal kink as a function of β_{pol} at q=1 and $q_i \equiv q(s=0.607)$, for a non-monotonic current profile with shear profile (b).

3. M ≥ 2 TEARING MODES AT FINITE BETA

Glasser, Greene and Johnson [7] showed analytically that the tearing mode is stabilized by favourable average curvature when β and $S = 1/\eta$ are sufficiently large. We have studied finite-β effects on the n=1 "m=2" tearing mode, using a current profile in the form of a rounded-off step-function, fixing A=2.5 and $q_0 = 1.5$ (strongly unstable to m=2 tearing in a cylinder) and varying the central β between 0.35 % and 2.45 %. (This made q_{edge} vary from 4.8 to 6.) The pressure at the edge was taken to be finite, at about 6 % of the central pressure p_0, while $p \approx 0.33\ p_0$ at the q=2 surface. The resistivity profile was inversely proportional to p. Figure 3a shows the real part of the growth rate as a function of central η for different β_0. Note that, for η above some value η_1,there are two purely growing modes which coalesce at $\eta = \eta_1$ and split into a pair with complex conjugate growth rates, which is unstable in a range $\eta_2 < \eta < \eta_1$, and finally becomes stable for $\eta < \eta_2$. The curves for different β in Fig 3 are almost identical if γ is scaled as $\beta^{3/2}$ and η as $\beta^{5/2}$, consistent with the simplified dispersion relation (88) for H = 0 in Ref.7. (For our equilibrium with $\beta_0 = 2.45$ %, in the notation of [7], $D_R \approx -0.16$ and $H \approx 0.08$ at the q=2 surface.) Clearly, high β is strongly stabilizing for resistive modes when the average curvature is favourable. Figure 3b shows the Fourier components of the perturbed magnetic field (with straight field-line Jacobian $J \propto R^2$)

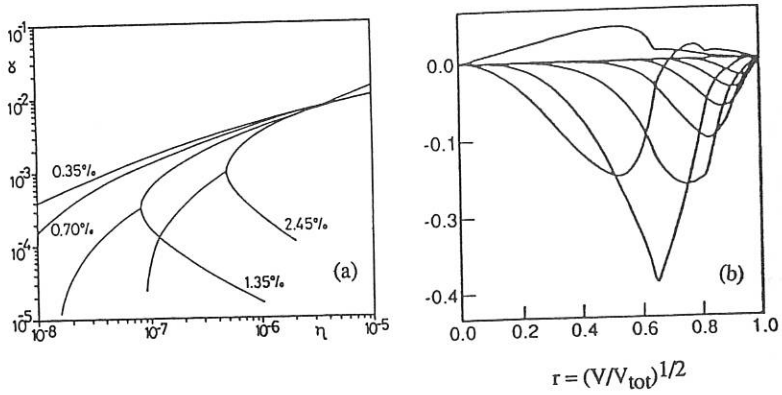

Fig.3 (a) Real part of growth-rate for "m=2", n=1 tearing mode for finite-β equilibria described in text. (b) Fourier components of $J \nabla s \cdot b$ for the near marginal mode at $\eta = 1 \times 10^{-7}$ and $\beta_0 = 2.45$ %.

4. LOW-N RESISTIVE BALLOONING

Resistive ballooning modes are driven by pressure gradients in regions of unfavourable local curvature, and the ideal stabilization by field bending is reduced by resistivity. The resistive ballooning modes are, however, stabilized at sufficiently high S and large sound speed by fluid compression [8,9]. From the analytical theory of Ref. 9, we find that the pressure necessary for stabilization of high-n resistive ballooning modes scales with resistivity and pressure gradients as $\Gamma p_{stab} \propto \eta^{1/2}\ (dp/dr)^2$, where Γ is the adiabatic index (usually set to 5/3). We have verified with MARS that this scaling holds also for n=1 and n=2 modes. The

scaling implies that resistive ballooning modes will generally be unstable near the plasma boundary, where p is small and η large, unless dp/dr goes sufficiently rapidly to zero. (This is why we added a base pressure of $0.06p_0$ to separate tearing from resistive ballooning in Sec. 3.) It should be noted that resistive ballooning is stabilized in incompressible calculations where $\Gamma = \infty$. Fig. 4 shows the Fourier components of the velocity and magnetic field for an n = 2 resistive ballooning mode. The equilibrium has $q_0 = 1.02$, $q_{edge} = 2.5$, $\langle\beta\rangle = 2$ %, and a finite pressure gradient at the edge. The pressure at the edge has been raised to the point where the mode is marginally stable, $\beta_{edge} = 1.2 \times 10^{-3}$ with $\Gamma = 1$. The resistivity profile is given by $\eta(\psi) / \eta_0 = p_0 / p(\psi)$, with $\eta_0 = 1 \times 10^{-7}$, and the real frequency of the mode is about $9 \times 10^{-3}\ \omega_A$. Figure 4 shows that the velocity perturbations have a short radial wave-length, and are confined to the edge region. It is noteworthy, however, that the magnetic perturbations penetrate with a long radial wave-length to the centre of the plasma. Another interesting property, that can be seen from the radial variation of the complex amplitudes, is that near the plasma edge, the perturbations propagate radially outward. The mode involves a large number of different poloidal Fourier components and is thus strongly ballooning. It appears justified to speculate that modes of this type are responsible for transport in the edge region of tokamaks, and that their magnetic perturbations may contribute to transport also in the interior.

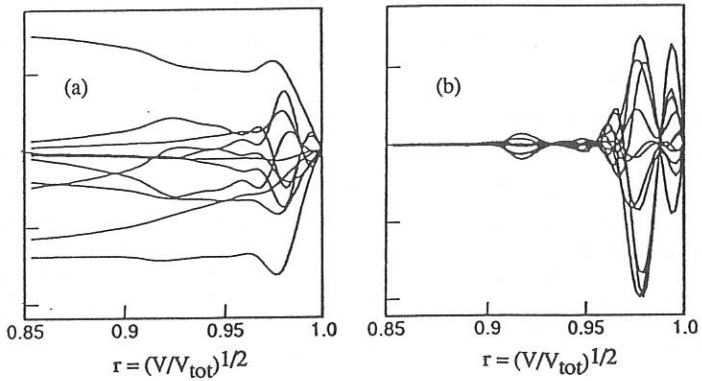

Fig. 4 Fourier components of radial magnetic field and velocity.
(a) $J \nabla s \cdot \mathbf{b}$ and (b) $\nabla s \cdot v$ over outer 8 % of the minor radius.

REFERENCES

1. R. Gruber, F. Troyon, D. Berger, et al, Comp. Phys. Comm. **21**, 323 (1981).
2. R.C. Grimm, J.M. Greene, and J.L. Johnson, Meth. Comp. Phys. **16**, 253 (1976): J. Manickam, R.C. Grimm, and R.L. Dewar, Comp. Phys. Comm. **24**, 355 (1981).
3. L.A. Charlton, J.A. Holmes, H.R. Hicks, et al, J. Comp. Phys. **63**, 107 (1986).
4. M.N. Bussac, R. Pellat, D. Edery and J.L. Soule, Phys. Rev. Lett. **35**, 1638 (1975).
5. H. Soltwish, W. Stodiek, J. Manickam, et al , IAEA Kyoto (1986),Vol I, p. 263.
6. J.A. Holmes, B.A. Carreras, and L.A. Charlton, Phys. Fluids B **1**, 788 (1989).
7. A.H. Glasser, J.M. Greene, and J.L. Johnson, Phys. Fluids **19**, 567 (1976).
8. T.C. Hender, B.A. Carreras, W.A. Cooper, et al. Phys. Fluids **27**, 1439 (1984).
9. J.F. Drake and T.M. Antonsen, Jr., Phys. Fluids **28**, 544 (1985).

ALPHA-PARTICLE DRIVEN MHD INSTABILITIES IN IGNITED TOKAMAKS*

C. Z. Cheng
Princeton Plasma Physics Laboratory, Princeton University, Princeton, NJ 08543 USA

1. Introduction and Formulation

The tokamak fusion reactors will involve significant amount of alpha (a) particles. Two types of MHD modes, the internal kink modes and the toroidicity-induced Alfven eigenmodes (TAE) are shown to be destabilized by alpha particles for the TFTR, CIT, and ITER equilibria. For the low frequency MHD modes with $\omega << \omega_d$ (ω_d is the α-particle magnetic drift frequency), the α-particle dynamics are no longer governed by the $(\vec{E} \times \vec{B})/B^2$ drift, but rather by the magnetic (∇B and curvature) drifts. The sign of the trapped α-particle potential energy is proportional to (ω_*/ω_d) (ω_* is the α-particle diamagnetic drift frequency) and the trapped α-particles have a stabilizing effect if $(\omega_*/\omega_d) > 0$ and vice versa. When ω_d is not too large, the trapped α-particles can resonantly excite a new branch of internal mode with a real frequency comparable to ω_d and the growth rates are of the same order as the ideal internal kink values[1]. For the high frequency shear Alfven waves with $\omega \approx \omega_b$, ω_t ($\omega_{b,t}$ is the α-particle bounce or transit frequency), the ideal MHD stable global Alfven modes can be driven unstable by the α-particles through bounce or transit resonances with the background waves. Alpha particles can destabilize the toroidicity-induced shear Alfven eigenmodes (TAE) [2-4] through circulating or bounce resonances by tapping the free energy associated with the α-particle pressure nouniformity. A stability criterion for the alpha particle driven TAE modes that takes into account of the stabilizing electron Landau damping is given.

We will consider an axisymmetric toroidal plasma consisting of the core electrons and ions and alpha components with $n_\alpha << n_c$ and $T_\alpha >> T_c$ so that $\beta_\alpha < \beta_c$. Summing the collisionless equations of motion for each species, we obtain the linear momentum equation. The Maxwell equations and Ohm's law hold with $\vec{b} = \nabla \times (\vec{\xi}_\perp \times \vec{B})$, and $\delta\vec{E} = i\omega \vec{\xi} \times \vec{B}$, where $\delta\vec{E}$ is the perturbed electric field. The gyrokinetic description neglecting the Finite-Larmor-radius correction is employed for all species. $\delta\overleftrightarrow{p}$ can be expressed as $\delta\overleftrightarrow{p} = -\vec{\xi} \cdot \nabla P + (\delta\hat{p}_{||} - \delta\hat{p}_\perp)\hat{b}\hat{b}$, where $\delta\hat{p}_{||}$ and $\delta\hat{p}_\perp$ are the nonadiabatic particle pressures. Note that this model of the perturbed partcle pressure takes into account of the kinetic effects due to both the core ions and electrons. The nonadiabatic perturbed pressures and the particle distribution function $\hat{g}$ for all species are given by

$$\begin{pmatrix} \delta\hat{p}_{\parallel} \\ \delta\hat{p}_{\perp} \end{pmatrix} = M\int d^3v\, \hat{g} \begin{pmatrix} 2(\varepsilon - \mu B) \\ \mu B \end{pmatrix}, \quad \hat{g} = \int_{-\infty}^{t} dt' \left(-\frac{ieF}{T}\right)\left(\tilde{\omega} - \omega_*^T\right)\left[\frac{i\,\vec{v}_d \cdot \delta\vec{E}_{\perp}}{\omega} + \frac{M_H \mu b_{\parallel}}{e}\right],$$

where $\tilde{\omega} = -(T\omega/M)\partial \ln F/\partial\varepsilon$, $\omega_*^T = -i\,(T/M\omega_c)\,(\hat{b} \times \nabla \ln F \cdot \nabla)$ only operates on the perturbed quantities, $\vec{v}_d$ is the magnetic drift velocity, T is the average temperature, ω_c is the cyclotron frequency. The kinetic-MHD equations can be cast into a set of non-Hermitian integro-differential eigenmode equations which are solved by a nonvariational kinetic-MHD stability code (NOVA-K)[5]. By taking an inner product of the momentum equation with $\vec{\xi}^*$ and integrating over the all plasma volume, we obtain from a quadratic form $D(\omega) = \delta W_f + \delta W_k - \delta K = 0$, where δK is the inertial energy, δW_f is the total fluid potential energy due to both the core and hot components, and δW_k is the kinetic potential energy. The quadratic form is useful in providing the stability properties of the system in certain limits.

2. Trapped Alpha-Particle Effects on the Internal Kink Mode

The stabilization of the n=1 internal kink mode by trapped α-particles had been reported by several authors [6] who studied the analytic dispersion relations by employing large aspect ratio tokamak plasmas with circular, concentric magnetic surfaces and other unrealistic approximations such as $(\omega_*/\omega_d) > 0$. The bounce-averaged magnetic drift frequency w_d is a function of minor radius and pitch angle, for a radial position, ω_d may change from being negative to positive as the pitch angle variable decreases, which means that (ω_*/ω_d) also varies from being positive to negative. As r increases, the pitch angle domain of negative (ω_*/ω_d) widens. These behavior also are strongly influenced by the plasma shapes and current profiles.

Figure 1 shows the stability boundaries in the $(\beta, q(0))$ space for the n=1 internal mode obtained from the NOVA-K code. The α-particle pressure is taken to be proportional to $[P(r)/P_o]^{7/2}$. From the ideal MHD stability boundary curve(no α-particle cases), the critical beta has a sharp transition as q(0) reaches 1. For $q(0) < 0.95$ the solution behaves like an internal kink mode, for $0.95 < q(0) < 1$ the solution becomes more localized near q=1 surface and is a quasi-interchange type, and for $q(0) > 1$ the solution resembles the infernal mode. The effects of α-particles on the n=1 internal modes can be studied by varying β_α but keeping the total β fixed. For unstable equilibria above the ideal MHD stability boundary, the ideal internal modes are only weakly modified by the α-particles even with $\beta_\alpha = 0.3\beta$. This can be understood from the quadratic form and the nonadiabatic trapped α-particle potential energy δW_k. Since $\omega_r << \gamma << \omega_d$, δW_k is approximately proportional to radial and pitch angle averages of (ω_*/ω_d) which can be very small, and thus has negligible effect on the stability

of the n=1 internal kink mode for small β_α. For unstable equilibria near the ideal MHD stability boundary, the ideal internal modes are first stabilized by the α-particles for small β_α but turn into resonant internal modes as β_α increases. For β below the ideal MHD critical beta, the stability is determined either by the resonant modes or by the ideal kink destabilized by the α-particles due to drift reversal.

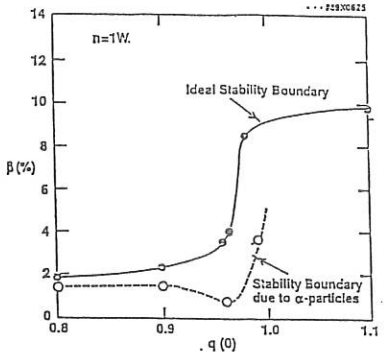

Fig. 1

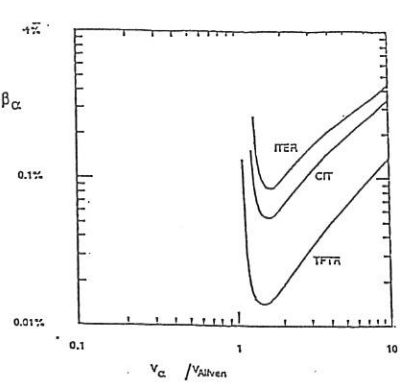

Fig. 2

3. Alpha-Particle Destabilization of Toroidicity-Induced Alfven Eigenmodes

For typical ignition tokamaks, the transiting α-particles can destabilize shear Alfven waves by the expansion free energy associated with the spatial gradient of the α-particle pressure via inverse Landau damping through the $\omega = k_{||}v_{||}$ wave-particle resonance. There are two conditions for the destabilization of the global Alfven modes. To satisfy the resonance condition, it requires that $V_\alpha > V_A$. To overcome the Landau damping by the inverse Landau damping associated with $\omega_{*\alpha}$, it requires that $\omega_{*\alpha} > \omega_A = V_A/qR$. The existence of the so-called Toroidicity-Induced Alfven Eigenmode (TAE) was shown in the ideal MHD limit[2]. The TAE mode exists inside gaps, due to toroidal coupling, in the shear Alfven continuum spectrum. For example, modes (n,m) and (n,m+1) couple at radial location ro, where $q(r_o) = (m + 1/2)/n$, to form a gap. For typical ignited tokamaks $\omega_{*\alpha}$ is large enough to overcome the usual Landau damping when $\omega_{*\alpha}/\omega_A \geq 1$ and that beyond this threshold the growth rate γ is approximately linearly proportional to $\omega_{*\alpha}$. The growth rate of the n=1 TAE mode can be of the order of 10^{-2} of the real frequency.

The NOVA-K results of the TAE mode can be interpretated from the quadratic form. For the mode frequency, we write $\omega = \omega_r + i\gamma$ and assume that the growth rate is small ($|\gamma| << |\omega_r|$). Then we have $\omega_r^2 \approx \{ \delta W_f + \text{Prin}[\delta W_k] \} / \delta K$, and $\gamma \approx \text{Res}[\delta W_k] / 2 i \omega_r \delta K$, where Prin $[\delta W_k]$ and Res $[\delta W_k]$ are the principal part and resonance contribution, respectively. The wave particle resonances are retained in Res $[\delta W_k]$. An analytical local instability criterion of the TAE mode can be obtained by integrating over the velocity space in Res $[\delta W_k]$:

$$\beta_\alpha \left\{ \frac{\left(\frac{4\,\omega_{*\alpha}}{3\,\omega_A}\right)}{x^2 \hat{v}_A^2} \left[\frac{\left(1 + 8\,\hat{v}_A^2 + 4\,\hat{v}_A^4\right)}{\left(1+\hat{v}_A^2\right)^{1/2}} - 4\,\hat{v}_A^3 \right] - \left[4\,\hat{v}_A + \frac{\left(3 - 4\hat{v}_A^2\right)}{\left(1+\hat{v}_A^2\right)^{3/2}} \right] \right\} \geq \left[8\,x^3 \hat{v}_A / 3\,\pi^{3/2} \right] \left(\frac{v_e\, m_e}{v_\alpha\, m_i} \right),$$

where $x = v_\alpha / v_A$, $\hat{v}_A^2 = [x^2 - 1]^{-1}$, $v_e = (2Te/me)^{1/2}$, v_α is the alpha birth velocity, $(\omega_{*\alpha}/\omega_A) = (mqR\rho_\alpha / 2rL_\alpha)x$, ρ_α is the alpha particle gyroradius, and L_α is the alpha pressure scale length. The first term on the left hand-side is due to the α-particle destabilizing inverse Landau damping associated with its pressure gradient and the second term is asoociated with the α-particle velocity Landau damping. The right-hand side contribution is due to the stabilizing electron Landau damping. The β_α vs. x stability curves are shown in Fig. 2 for the TFTR, CIT, and ITER D-T ignition parameters with very small critical β_α. Therefore, primary attention - especially experimental - should be focused on the TAE mode, which can be strongly destabilized by α-particles.

1. L. Chen, R.B. White, and M.N. Rosenbluth, Phys. Rev. Lett 52 (1984), 1122.
2. C.Z. Cheng and M.S. Chance, Phys. Fluids 29 (1986), 3695; C.Z. Cheng, L.Chen and M.S. Chance, Ann. Phys. (NY) 161 (1984), 21; G. Y. Fu and C. Z. Cheng, University of Texas Report IFSR #385 (1989), to appear in Phys. Fluids B (1990).
3. C. Z. Cheng, G. Y. Fu, and J. W. Van Dam, in Proceedings of Workshop on Theory of Fusion Plasmas, Chexbres, Swizerland, 1988 (Societa Italiana di Fisica), p. 259.
4. G. Y. Fu and J. W. Van Dam, Phys. Fluids B 1 (1989), 1949.
5. C.Z. Cheng, PPPL-2668(1989), to appear in Phys. Fluids B (1990).
6. B. Coppi, R. J. Hastie, S. Migliuolo, F. Pegararo, and F. Porcelli, Phys. Lett. A132 (1988), 267; B. Coppi, S. Migliuolo, F. Pegoraro, and F. Porcelli, Massachusetts Institute of technology Report # PTP-88/4 (1988).

*This work was supported by U.S. Department of Energy Contract No. DE-ACO2-76-CHO3073.

TO THE QUESTION OF ADIABATIC R-COMPRESSION IN TOKAMAK

Gorelenkov N.N., Romannikov A.N.

Branch of I.V. Kurchatov Institute of atomic energy

One of the possible methods of the auxiliary plasma heating in tokamak is the method of adiabatic R-compression (R - major radius) [1]. On the TSP tokamak (known as T-14) in USSR the plasma temperature in such way is expected to grow from 3 keV to 10 keV and plasma density up to 10^{15} cm^{-3}. At these plasma parameters τ_{ii}, $\tau_{ee} >> \tau_b$ (where τ_{ii}, τ_{ee} - times between electron-electron and ion-ion collisions, τ_b-"bounce" time). Therefore the usual laws of adiabatic compression:

$$n \sim 1/R^2; T_{i,e} \sim 1/R^{4/3} \quad (1)$$

(n-plasma density, $T_{i,e}$-ion, electron temperature) should be improved because they are the result of MHD equations [2].

More adequate model is the quasi-MHD system of guiding center approximation [3] (averaging over the Larmor circulation). In this model plasma density grows like in the origin MHD, but "transverse" and "longitudinal" components of the plasma temperature change like:

$$T_\perp \sim 1/R; T_{//} \sim 1/R^2 . \quad (2)$$

These relations can be obtained from the Vlasov equation if to assume conservating of transverse and longitudinal adiabatic invariants in form [3]:

$$\mu = \frac{V_\perp^2}{2B}; J = V_{//}R . \quad (3)$$

But collisions will lead to the isotropy distribution function of particles of interest and at collision frequencies exceeding τ_c^{-1} (τ_c -the time of R-compression) the law of temperature growth will turn into (1).

It is known from the neoclassical approach the particle motion to be determined in "quiet" plasma by the longitudinal invariant in the form (in opposite (3)):

$$J = \frac{e_\alpha \Psi(R,Z)}{2\pi m_\alpha c} - V_{//} R \ . \tag{4}$$

In this way from the point of view of a single particle heating of its longitudinal velocity component in the rested frame of reference is connected with the toroidal electric field appearing due to the change of the poloidal magnetic flux at the R-compression [4]. The value of such field is determined by the expression:

$$E_\phi = (\partial\Psi/\partial t)/2\pi Rc \ , \tag{5}$$

where Ψ- poloidal magnetic flux, c- speed of light, ϕ- asimuthal angle. The vectors of fields in a cross section of the tokamak vessel are presented in Fig. 1. Because of radial excursions of particles along the minor radius at the motion, during the τ_b it appears the uncompensated additional quantity to the longitudinal component of the velocity which couldn't be expressed by (3). The relation (3) gives the equation for the absolute value of the velocity-V:

$$\frac{dV}{dt} = \frac{V}{R_0} \left|\frac{dR_0}{dt}\right| \left[- \frac{V_{//}^2}{V^2} + \frac{V_\perp^2}{2V^2} \right] . \tag{6}$$

The neoclassical consideration based on the integral (4) results in

$$\frac{dV}{dt} = < \frac{V_{//}}{VR} \left[\frac{\partial \bar{\Psi}}{\partial t} \right] > + < \frac{V}{R_0} \left| \frac{dR_0}{dt} \right| \frac{V_\perp^2}{2V^2} > \ , \tag{7}$$

where $\bar{\Psi} = \Psi\, e_\alpha/(2\pi m_\alpha\, c)$, taken into account that for the tokamak $V_\phi = V_{//}\, B_\phi/B \simeq V_{//}$, $<...> = \int d\theta(...)\, qR_0/V_{//}\tau_b)$. After the averaging over drift trajectories we obtain the following expression for the change of the longitudinal velocity at small radial excursions of particles:

$$\left(\frac{dV}{dt}\right)_{//} = \frac{\omega_{B\alpha} R_0}{\tau_b V} \left|\frac{dR_0}{dt}\right| \oint d\theta \left[(R - R_0)/R + \rho^2/2R_0 R \right] \ , \tag{8}$$

where $\omega_{B\alpha} = e_\alpha B_0/m_\alpha c$, $\tau_b = \int d\theta \frac{qR_0}{V_{//}}$, q- safety factor, ρ- minor radius. From the conservation of the integral (4) one can to result in

$$\rho = \rho_0 + \left(\frac{V_{//} q}{\omega_{B\alpha} \varepsilon} \right)_\rho \ , \tag{9}$$

where $\varepsilon = \rho/R_0$, the second term describes the radial excursions of particles as a function of θ, $V_{//} = \sqrt{2\mu B_0 \varepsilon(2\chi^2 - 1 - \cos\theta)}$, $\chi^2 = (V^2/2 - \mu B_0 + \mu B_0\varepsilon)/2\mu B_0\varepsilon$. For passing particles $\chi > 1$, for trapped $1 > \chi > 0$. The estimation of the change of the velocity of strongly trapped particles ($\chi << 1$) is:

$$\left(\frac{dV}{dt}\right) = \frac{\chi^2 V}{R_0}\left|\frac{dR_0}{dt}\right| + \frac{V}{R_0}\left|\frac{dR_0}{dt}\right| , \qquad (10)$$

and for the well passing particles ($\chi >> 1$) is:

$$\left(\frac{dV}{dt}\right) = \frac{V}{R_0}\left|\frac{dR_0}{dt}\right| + \frac{V_\perp}{2VR_0}\left|\frac{dR_0}{dt}\right| . \qquad (11)$$

Because of $\tau_{\alpha\alpha}(\alpha=i,e) << \tau_c$ in TSP, the change of a temperature at the compression can be found by averaging the expression (8) over the maxwellian distribution function of particles of interest. The law of the density growth remains of course in form (1), but for T we obtain:

$$T \sim 1/R^{5/3}, \qquad (12)$$

by the numerical calculation. This fashion could be explained by Fig. 2 where curves according to the expressions $(d\ln(V)/dt)_{//}$ /$(d\ln(R_0)/dt)$ (dashed lined) and $(d\ln(V)/dt)/(d\ln(R_0)/dt)$ (solid line) are shown. So that the quasi MHD fits into a curve 1. The neoclassical consideration presented here fits into a curve 2 in equatorial plane at $R = R_0 + \rho$ and into the curve 3 at $R = R_0 - \rho$. The consideration of the poloidal magnetic flux in the longitudinal invariant is seen to result in heating of longitudinal velocity component exceeding one in quasi-MHD approach. In particular, it is seen for the unstrongly trapped particles (dashed curve 2).

The power of the temperature growth at the compression $\gamma = (d\ln(T)/dt)\ /(d\ln(R_0)/dt)$ as a result of numerical calculations averaged over the magnetic surface is shown in Fig. 3 as a function of ρ/R_0 for TSP. This parameter is slowly increased on the plasma edge. It can lead to the slowly flattening of the temperature profile.

Our consideration, first of all, concerns the ions. Basing on the idea about the destruction of magnetic surfaces along the inner scale length c/ω_{pe}), the longitudinal invariant for electrons in form (4) appears to be not conserved [6]. Therefore MHD should be considered as a more adequate approximation for electrons, assuming that the anomalous transport is invariable at the compression.

Summarizing our report we note that for TSP where τ_c is comparable with τ_E the electron component is expected to be heated at best in accordance with the expression (1). As for ions component in accordance with the expression (12) its temperature will increase more than the original MHD value by ~ 35%.

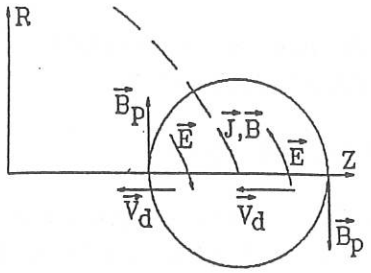

fig.1.

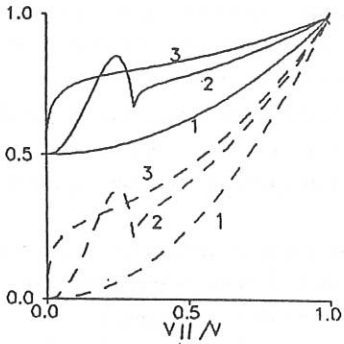

fig.2

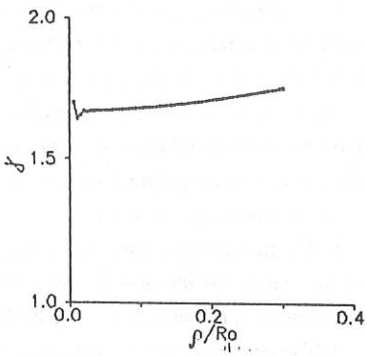

fig.3.

REFERENCES

1. Azizov E.A., Alekseev Yu.A., Brevnov N.N., et al., in Plasma Physics and Controlled Nuclear Fusion Research (Proc. 8th Int. Conf. Brussels, 1980) IAEA, Vienna, 1981, V.2, p. 599.
2. Dnestrovskij Ju.N., Kostomarov D.P., in Matematitcheskoe modelirovanie plasmy. (in Russian) M.: Nauka, 1982, s. 258-260.
3. Rudakov L.I., Sagdeev R.Z. - in: Fizika plasmy i problema UTR., (in Russian), t.3, 1958, s. 268.

   Kalsrud R.-in: Osnovy fiziki plasmy (in Russian), t.1,M.: Energo-atomizdat, 1983, s. 122.
4. Gorelenkov N.N., Fizika Plasmy, 1990. T.16.
5. Kadomtsev B.B., Pogutse O.P., in: Voprosy teorii plasmy, pod red. Leontovitcha M.A. (in Russian), M: Atomizdat, 1967, vyp. 5, s. 209.
6. Kadomtsev B.B., Pogutse O.P. VII Intern. Conf. on Plasma Phys. and Contr. Nucl. Fus. Innsbruck, 1978, IAEA, Vienna, 1979, v. 1, 649.

MAGNETIC FIELD STRUCTURE AT THE ONSET OF SAWTOOTH RELAXATIONS

J.T. Mendonça and F. Porcelli*

GFN, Instituto Superior Tecnico, 1096 Lisboa Codex, Portugal
*JET Joint Undertaking, Abingdon, Oxfordshire, OX14 3EA, UK

The main difficulty with a theoretical interpretation of the sawtooth phenomenon lies with the very fast rearrangement of the plasma core. It is thus quite important to understand the details of the magnetic field structure at the onset of the sawtooth relaxations.

In this work we consider the topological change of the magnetic configuration resulting from the nonlinear coupling between the dominant m=1, n=1 mode component and the m/n≠1, where m and n are the poloidal and toroidal mode numbers. Our model is semi-analytical and includes the following new features:

1) The radial dependence of the m=1 component is retained self-consistently with the nonlinear Ohm's law $\partial\Psi/\partial t + \vec{v}.\nabla\psi = \eta J$, where Ψ is the poloidal flux, $\vec{v}$ is the nonlinear perturbation flow, η is the resistivity and J is the parallel current density;

2) The coupling term is assumed to vanish as a linear power of the distance from the shifted magnetic axis; this boundary condition, appropriated to a mode dominated by the m=2, n=1 component near the q=2 surface, leeds to a poloidal structure whose Fourier components and radial profiles in the region where $q \leq 1$ are determinated by geometric consideration.

The resulting magnetic structure, and in particular its dependence on the island width and on the magnetic shear, has been obtained numerically. This structure is compared with previous 3-D nonlinear simulations and with experimental observations.

THE m=1 KINK MODE IN A ROTATING TOKAMAK PLASMA WITH ANISOTROPIC PRESSURE

H.J. DE BLANK

FOM-Instituut voor Plasmafysica Rijnhuizen, Association Euratom-FOM, P.O. Box 1207, 3430 BE Nieuwegein, The Netherlands

Abstract. The $m = 1$ internal kink mode is investigated in axisymmetric toroidal plasmas with poloidal and toroidal plasma flow and anisotropic pressure. The guiding centre model of the plasma is used to derive a dispersion relation that contains the full guiding centre distribution of the equilibrium. Due to kinetic damping, smaller growth rates are found than predicted by fluid theory. Pressure anisotropy $p_\perp > p_\parallel$ is found to reduce the growth rate too, while toroidal rotation contributes to the destabilizing effect of the pressure gradient.

Introduction. Neutral beam injection can cause plasma rotation frequencies that are comparable with the sawtooth collapse time. If the rotational energy is a significant fraction of the total kinetic energy, or if the centrifugal force significantly contributes to the Shafranov shift of the plasma centre, the rotation is expected to affect the stability of the $m = 1$ mode. In JET, sawtooth stabilization has been observed during intense heating with ICRH and neutral beams [1]. These heating methods may produce a population of trapped high energy ions with very anisotropic pressure that might be the cause of sawtooth stabilization.

In this paper, the effects of plasma rotation and pressure anisotropy on the internal $m = 1$ kink mode are considered. Firstly, the MHD energy principle in the presence of pressure anisotropy is used to derive the mode eigenfunctions and the dispersion relation to the required order in the inverse aspect ratio ε. In this derivation the equations of state, which determine $\dot{p}_\perp$ and $\dot{p}_\parallel$, are left unspecified. Subsequently, the evolution of $p_{\parallel,\perp}$ is calculated from the guiding centre equations for the $m = 0$, 1, 2 harmonics of the mode.

Equilibrium. We consider a stationarily rotating axisymmetric tokamak plasma with low-β ordering of $p_\perp$, $p_\parallel - p_\perp$, and ρU^2. Plasma rotation and pressure anisotropy give rise to poloidal variations of the mass density and the pressure components over a flux surface, and to a radial component of the current density. The axisymmetric magnetic field and the rotation velocity, which satisfy the equilibrium fluid equations, are

$$\boldsymbol{B} = \nabla\psi \times \nabla\phi + F\nabla\phi\,, \qquad \boldsymbol{U} = f(\psi)\boldsymbol{B}/\rho + R^2\Omega(\psi)\nabla\phi\,,$$

where ϕ is the toroidal angle and where $R = |\nabla\phi|^{-1}$. The flux quantities f and Ω represent field-aligned flow and a rigid toroidal rotation of each flux surface, respectively. We use Grad's guiding centre description [2] of the equilibrium, which allows for arbitrary (non-thermal) axisymmetric particle velocity distributions.

Ordering of the mode In a large aspect ratio torus, the toroidal and poloidal mode numbers $m = n = 1$ are special because the associated perturbation of the magnetic energy can be very small, $\mathcal{O}(\varepsilon^4)$. We divide the mode vector $\boldsymbol{\xi}$ into a component α parallel to $\boldsymbol{B}$, a poloidal component χ and a radial component ξ. Because $\delta B = \mathcal{O}(\varepsilon^2)$, these components are related through $(\partial/\partial r)(r\xi) + \partial\chi/\partial\theta = \mathcal{O}(\varepsilon^2)$. Since $\nabla\cdot\boldsymbol{\xi} = \mathcal{O}(\varepsilon)$, and because the mode is taken to be dominantly an $m = 1$ harmonic in the poloidal plane, it follows that the density perturbations and the parallel displacement α are dominated by $m = 0$, 2 harmonics. Therefore, the components of $\boldsymbol{\xi}$ can be written as

$$(\xi,\, \chi,\, \alpha) = \big(\xi_1(r)e^{i\theta},\, \chi_1(r)e^{i\theta},\, \alpha_0(r) + \alpha_2(r)e^{2i\theta}\big)e^{i(\omega t - \phi)} + \mathcal{O}(\varepsilon)\,. \tag{1}$$

Further minimization of the magnetic energy yields $(q-1)^2\xi_1' = \mathcal{O}(\varepsilon^2)$. This relation, when applied to equilibria with a single $q \approx 1$-region $[r_-, r_+]$ that may or may not be broad, leads to the following ordering schemes in different parts of the plasma [3]. In the central plasma ($r < r_-$), where $q - 1$ is finite, we have $\xi_1' = \mathcal{O}(\varepsilon^2)$ so that ξ_1 is constant to leading order. Similarly, $\xi_1 = 0$ to leading order in the exterior region ($r > r_+$). In the region where $q - 1 = \mathcal{O}(\varepsilon)$, however, ξ_1' is unrestricted. Therefore, $\xi_1(r)$ is a step-function if the magnetic shear at $q = 1$ is finite, while it is a smooth radial function (quasi-interchange mode) in the case of a broad layer, where $q - 1 = \mathcal{O}(\varepsilon)$ and where the shear is small. With this ordering, the energy functional of the mode becomes $\mathcal{O}(\varepsilon^4)$. To this order in the energy, all $\mathcal{O}(\varepsilon^0)$ components in Eq. (1) contribute, as well as the $m = 0$, 2 harmonics of ξ and χ, which are $\mathcal{O}(\varepsilon)$. The ideal MHD computation for the case of a thin $q - 1 = \mathcal{O}(\varepsilon)$ layer is given in Ref. [4] and is generalised to plasmas with a broad $q - 1 = \mathcal{O}(\varepsilon)$ region in Ref. [3].

Guiding centre theory In the guiding centre approximation of the Vlasov equation, the pressure tensor is diagonal, $\boldsymbol{P} = p_\perp(\boldsymbol{I} - \boldsymbol{bb}) + p_\parallel \boldsymbol{bb}$, where $\boldsymbol{b} = \boldsymbol{B}/B$. We will formally express changes $\dot{p}_{\parallel,\perp}$ in the pressure components in terms of combinations of the parallel and perpendicular plasma compression, introducing four coefficients with a relation which expresses that the motion is non-dissipative,

$$\dot{p}_{\parallel,\perp} = \dot{\rho}\frac{\partial p_{\parallel,\perp}}{\partial\rho} + \dot{B}\frac{\partial p_{\parallel,\perp}}{\partial B}\,, \qquad B\frac{\partial p_\parallel}{\partial B} = \rho\frac{\partial}{\partial\rho}\Big(\frac{p_\parallel - p_\perp}{\rho}\Big)\,. \tag{2}$$

Here a dot denotes $d/dt = \partial/\partial t + \boldsymbol{U}\cdot\nabla$. The coefficients $\partial p_{\parallel,\perp}/\partial\rho$ and $\partial p_{\parallel,\perp}/\partial B$ generally depend on the plasma motion. In the case of the $m = 1$ mode in a large aspect ratio, rotating plasma, however, the quantities $\dot{\rho}$ and $\dot{B}$ each can be decomposed into three poloidal harmonics, for which the coefficients in (2) can be specified. To each of these

three harmonics a resonant velocity V can be assigned such that $d/dt = (U_\parallel - V)\boldsymbol{b}\cdot\nabla$. The three contributions arise from

(a) the toroidal rotation of the equilibrium. Since $d/dt = \boldsymbol{U}\cdot\nabla$ in this case, the resonant velocity is $V = \Omega F/B$.

(b) the $m = 0$ parallel component of the displacement, $\alpha_0(r)\boldsymbol{B}$, which contributes to $\dot{p}_{\parallel,\perp}$ with a resonant velocity $V = \omega R$.

(c) the $m = 2$ parallel component $\alpha_2(r)e^{2i\theta}\boldsymbol{B}$, which corresponds to a resonant velocity $V = R(2\Omega - q\omega)/(2-q)$.

These contributions are derived from the guiding centre equations

$$\frac{\partial f_s}{\partial t} + (\boldsymbol{U}_\perp + v_\parallel \boldsymbol{b})\cdot\nabla f_s + \left[v_\parallel \boldsymbol{U}_\perp\cdot(\boldsymbol{b}\cdot\nabla\boldsymbol{b}) - \boldsymbol{b}\cdot\nabla E_s\right]\frac{\partial f_s}{\partial v_\parallel} = 0\,, \tag{3}$$

where $E_s \equiv \mu B + \Phi e_s/m_s - \frac{1}{2}U_\perp^2$ and where $v_\parallel$, μ, m_s, e_s, and $f_s(\boldsymbol{x}, t, \mu, v_\parallel)$ are the parallel velocity, magnetic moment, mass, electrical charge, and distribution function of the particle species s. It has been shown in Ref. [5] that in an axisymmetric, rotating equilibrium, the distributions can be written as $f_s(\psi, \varepsilon_s, \mu)$, with $\varepsilon_s \equiv \frac{1}{2}v_\parallel^2 - v_\parallel \Omega F/B + E_s$. From the expressions for $\nabla p_\parallel$, $\nabla p_\perp$ and $\nabla\rho$ in Ref. [5], the equilibrium contributions (a) to Eq. (2) can be derived. The contributions (b) and (c) to Eq. (2) of the mode components α_0 and α_2 are determined by linearizing the guiding centre equation (3) and taking the $m = 0$, 2 harmonics. Because all three contributions satisfy the second equation in (2), an energy principle for $\boldsymbol{\xi}$ can be applied.

The dispersion relation. By minimizing the mode energy over the entire plasma volume, a dispersion relation is obtained which resembles the MHD result in Ref. [3],

$$\begin{aligned} &-1/S_0 + \tfrac{9}{16}A(r_-) - \tfrac{1}{2}r_-^4 s(r_-) - \tfrac{1}{2}R^2\int_0^{r_-} dr\, r^2 K_2'/B_0^2 \\ &\quad = \left[-S_1/S_0 + \tfrac{3}{4}A(r_-)\right]^2 \Big/ \left[S_2 - S_1^2/S_0 - A(r_+) + A(r_-)\right]. \end{aligned} \tag{4}$$

The quantities S_i, $(i = 0, 1, 2)$ are integrals over the layer where $q - 1 = \mathcal{O}(\varepsilon)$,

$$S_i \equiv R^{-2}\int_{r_-}^{r_+} dr\, r^{-3}\left\{r^4\left[\beta_g(r) + s(r)\right]\right\}^i \Big/ \left[\left(\frac{1}{q} - 1\right)^2 - K_1/B_0^2\right].$$

Here we have defined

$$\beta_g(r) \equiv -r^{-4}\frac{R^2}{B_0^2}\int_0^r dr\, r^2\langle p_\perp + p_\parallel + \rho U^2\rangle' \quad \text{and} \quad s(r) \equiv r^{-4}\int_0^r dr\, r^3\left(\frac{1}{q^2} - 1\right).$$

The flux function β_g is a generalization of the poloidal beta. The quantities $A(r_\pm)$ are the boundary values of $A(r) \equiv r^4(1-a)/(3+a)$, where $a(r) \equiv (1-2/q)^2 r\zeta'/\zeta$ and where $\zeta(r)$ is the solution of the usual "cylindrical" $m = 2$ Euler equation in the regions $[0, r_-]$

and $[r_+, r_2]$, where the constant-ξ_1 approximation applies [3, 4]. All kinetic effects are in the two quantities K_1 and K_2,

$$K_1(r) = \rho(\omega + \omega_p - \omega_t)^2 R_0^2 + \tfrac{1}{4} C(\omega R_0) + \tfrac{1}{4} C\big(\frac{2\Omega - q\omega}{2-q} R_0\big) - \tfrac{1}{2} C(\Omega R_0)\,,$$

$$K_2(r) = p_\perp + p_\parallel - \frac{4}{q}\big(\frac{1}{q} - 1\big) p_{\rm an} - 2\rho\omega_p^2 R_0^2 + 4\rho\omega_t^2 R_0^2 - 2\rho(\omega + \omega_p - \omega_t)^2 R_0^2 - C(\omega R_0)\,,$$

where $\omega_p \equiv \langle fB/\rho q R\rangle$, $\omega_t \equiv q\omega_p + \Omega$, and where C(V) depends on the equilibrium guiding centre distribution and on the resonant velocity V, which takes the three values corresponding to the contributions (a), (b), and (c),

$$C(V) \equiv \rho(V + U_\parallel)^2 - \textstyle\sum_s m_s C_{2,s} + \big[\sum_s e_s C_{1,s}\big]^2 \,/\, \big[\sum_s \frac{e_s^2}{m_s} C_{0,s}\big]\,,$$

$$C_{i,s}(V) \equiv \int d\mu\, B(\mu B + V^2)^i \int \frac{dv_\parallel}{v_\parallel - V} \frac{\partial f_s}{\partial v_\parallel}\,.$$

For monotonic profiles, K_2 is a decreasing function of r and therefore slightly destabilizing. The growth rate depends more strongly on $K_1(r)$, which occurs in the denominators of the integrals S_i. As an example, we consider K_1 for cases where the equilibrium distribution functions are of the form $f_s(\psi, \varepsilon_s, \mu) = f_s(\psi) \exp\big[-\mu/\mu_{s,0}(\psi) - \varepsilon_s/\varepsilon_{s,0}(\psi)\big]$, with $\mu_{s,0}$ and $\varepsilon_{s,0}$ chosen such that $p_{e\parallel} = p_{i\parallel}$ and $p_{e\perp} = p_{i\perp}$, and where ωR and ΩR are much smaller than the thermal velocities. Writing $\omega = \Omega - i\gamma$, with $\mathrm{Re}(\gamma) > 0$ for a positive growth rate, we obtain

$$K_1 = -\rho\gamma^2 R^2 \Big[\frac{3}{2} + \frac{p_\perp}{p_\parallel} + \big(\frac{\pi}{8} - 1\big)\frac{p_\perp^2}{p_\parallel^2}\Big] - \frac{1}{2}\gamma R \frac{p_\perp^2}{p_\parallel^2}\sqrt{\pi\rho p_\parallel} + \mathcal{O}(\gamma, \Omega)^3\,. \tag{5}$$

Compared to the value $K_1 = -3\rho\gamma^2 R^2 + \mathcal{O}(\gamma^4)$ obtained from ideal MHD, the growth rate is strongly reduced due to the damping term (linear in γ). For higher growth rates, this effect is compensated because the inertia term (quadratic in γ) is smaller than in ideal MHD. Since Ω enters Eq. (5) only in higher orders, the dominant effect of toroidal rotation is the contribution of the rotation energy to β_g, which is destabilizing.

Acknowledgement. This work was performed under the Euratom-FOM association agreement with financial support from NWO and Euratom. The author thanks Dr. T.J. Schep for for many useful suggestions.

References.

[1] D. Campbell, D.F.H. Start, J.A. Wesson, *et al.*, Phys. Rev. Lett. **60** (1988) 2148.
[2] H. Grad, in *Magneto-Fluid and Plasma Dynamics*, edited by H. Grad (American Mathematical Society, Providence, RI, 1967), p. 162.
[3] H.J. de Blank, T.J. Schep, in *Proceedings of the 15th European Conference on Controlled Fusion and Plasma Heating*, Dubrovnik (EPS, 1988), Vol. 1, p. 421.
[4] M.N. Bussac, R. Pellat, D. Edery, J.L. Soulé, Phys. Rev. Lett. **35** (1975) 1638.
[5] D. Dobrott, J.M. Greene, Phys. Fluids **13** (1970) 2391.

INTERACTION OF RESONANT MAGNETIC PERTURBATIONS WITH ROTATING PLASMAS

T.C.Hender and R.Fitzpatrick.
UKAEA/EURATOM Fusion Association, Culham Laboratory, Abingdon, OX143DB, UK.

1 Introduction

In several tokamak experiments, resonant magnetic perturbations have been applied using coils external to the plasma (eg TOSCA [1], PULSATOR [2], and recently COMPASS [3]). Such perturbations have been used to control and influence the internal MHD activity. Generally this activity has a finite frequency, whilst the applied perturbations are static [1–3]. To theoretically understand such experiments it is thus necessary to study the effect of external perturbations on modes rotating, due to diamagnetic or $\vec{E} \times \vec{B}$ drifts, with frequencies significantly different to that of the applied perturbation. Analytic linear and nonlinear theories describing this situation are outlined in the next Section. In Section 3, linear and nonlinear numerical simulations which support and extend the analytic theory are presented. Finally, in Section 4 the relationship of the results to experiment are discussed, and some conclusions are drawn.

2 Analytic Theory

Suppose a helical magnetic perturbation, resonant at $r = r_s$, is applied to the edge of the plasma with an $e^{-i\Omega t}$ time-dependence. It can be demonstrated that the final amount of reconnected flux at the rational surface Ψ is given by

$$\frac{\Psi}{\Psi_c} = \frac{1}{1 + \Delta(\Omega)/(-\Delta_0')}. \tag{1}$$

Here, Δ_0' (assumed negative) is the delta-primed of the mode in the unperturbed equilibrium, $\Delta(\Omega)$ is the usual integral of the parallel current across the resistive layer calculated assuming an $e^{-i\Omega t}$ time-dependence, and Ψ_c is the final amount of reconnnected flux obtained when there is complete resonance between the applied signal and one of the natural modes.

Equation (1) is completely general. However, as an illustrative example we consider the simple dispersion relation of Ara et al [4] valid for a collisional, diamagnetic plasma. Fig. 1 shows $|\Psi/\Psi_c|$ calculated in accordance with Eq(1) for this type of dispersion relation. The quantity Ω' is the Doppler shifted applied frequency as seen in the local $\vec{E} \times \vec{B}$ frame at the resonant surface, $r = r_s$. It can be seen that there are three sharp resonances, at the electron diamagnetic frequency(ω_{*e}), zero frequency (in the local frame), and the ion diamagnetic frequency(ω_{*i}). The widths of these resonances are the typical linear damping rates of the natural electron, low frequency, and ion modes, respectively, evaluated at $\Delta' = \Delta_0'$. Between the resonances $|\Psi/\Psi_c|$ typically falls to a value $1/Q$, where $Q \sim [\omega_* \tau_c]^{5/4}$. Here, ω_* is a typical diamagnetic frequency, and τ_c is

the typical time-scale of a drift-tearing mode ($\tau_c = S^{3/5}\tau_H$). In modern tokamaks $Q \gg 1$ (e.g. for COMPASS $Q \sim 60$ assuming $f \sim 15$kHz). It follows, therefore, in the linear regime, that unless the applied frequency lies very close to one of the Doppler shifted natural mode frequencies, the amount of reconnection induced in a realistic plasma by a resonant external magnetic perturbation is likely to be substantially smaller than that obtained in a strictly non-rotating, non-diamgnetic plasma.

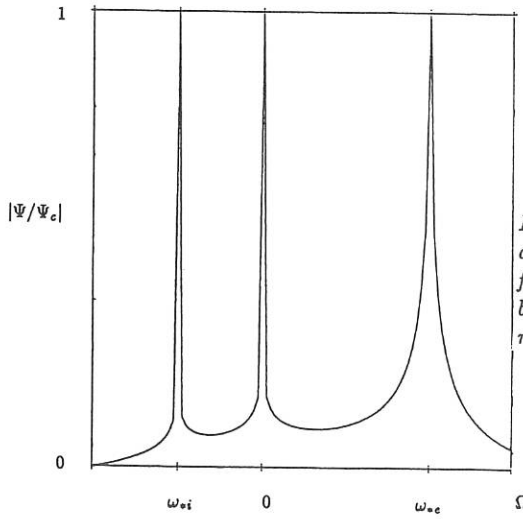

Fig 1 Schematic figure of the final amount of normalised reconnected flux induced by a resonant perturbation of frequency Ω', in the linear regime.

A non-linear theory of reconnecting modes in the presence of stong flows has also been developed. This theory, which is based on a set of reduced MHD equations similar to those of Biskamp [5], is valid when **i)** the island width W is much greater than any microscopic scale-length or linear layer width, and **ii)** purely resistive flows are negligible compared with diamagnetic or $\vec{E} \times \vec{B}$ flows. The key to the correct formulation of this theory is the requirement that the flow patterns inside and outside the island seperatrix be linked together smoothly. The island width is found to evolve as

$$I_1 \tau_R \frac{d}{dt}\left(\frac{W}{r_s}\right) = Re(r_s\Delta') - I_2\,(\Omega'\tau_H)^2\left(\frac{r_s}{W}\right)^3, \qquad (2)$$

where τ_R is the resistive timescale and τ_H the hydromagnetic timescale. The quantities I_1 and $I_2(\Omega)$ are $O(1)$ integrals over the flow-patterns around the magnetic island. The last term in Eq.(2) represents a non-linear rotational suppression of island formation, which is rapidly weakened as the island width increases ($\propto W^{-3}$). An equation which describes the time evolution of the island frequency (Ω') has also been obtained from the $Im(r_s\Delta')$.

3 Numerical Simulations

A set of nonlinear reduced MHD equations [5], including diamagnetic and $\vec{E} \times \vec{B}$ flows, is solved using a semi–implicit numerical scheme. These equations are identical to those solved analytically.

In the linear regime (where direct evaluation of the analytic results is possible) there is reasonable agreement between the analytic and numerical predictions. Figure 2 shows how the reconnected flux changes as the relative frequency (Ω'), between a poloidally rotating plasma and a static $m = 2$, $n = 1$ applied perturbation, is varied. The equilibrium in this case, $q = 0.7(1 + 2.75r^2)$, is tearing stable ($\Delta'_{2,1} = -0.7$). It can be seen from Fig 2 how the reconnected flux is strongly reduced by the plasma rotation. Comparisons with the analytic predictions for diamagnetic rotation also show similarly good agreement in the linear regime.

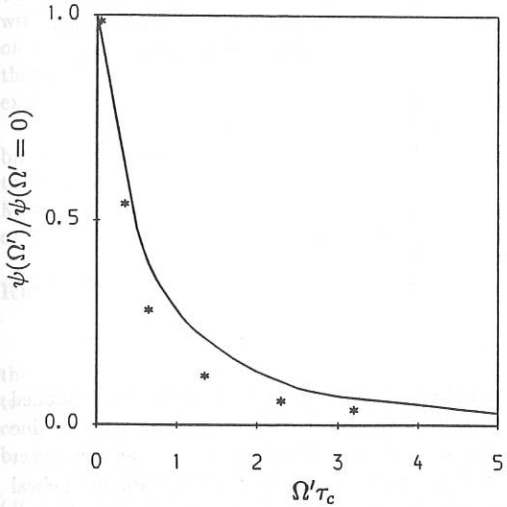

*Fig 2 Normalised reconnected flux versus applied frequency. The line is analytic result and the * are from linear simulations.*

A full evaluation of the terms in the nonlinear analytic theory is still in progress. The qualitative features of this theory are however borne out by the numerical simulations. From Eq(2) we have noted that the rotation suppression of island growth is rapidly weakened ($\propto W^{-3}$) as the island width increases. Figure 3 shows the nonlinear evolution of the $m = 2$ island width for two applied currents ($I_c = 10^{-5}$ and 8×10^{-4}) and various relative frequencies. It can be seen for the larger applied current (and island widths) that the suppression of tearing by relative rotation ($\Omega' \neq 0$) is substantially reduced. In steady state at small currents ($I_c \sim 10^{-6}$) the nonlinear results limit to the linear regime (Fig 2), but as the current is increased the suppression of tearing (by $\Omega' \neq 0$) is weakened. Associated with this weakening of tearing suppression there is a torque applied within the island, which acts to reduce the relative plasma to mode frequency. This effect is described by the anlaytic theory and is observed in the simulations as a reduction of plasma velocity near the resonant surface ($q = 2$).

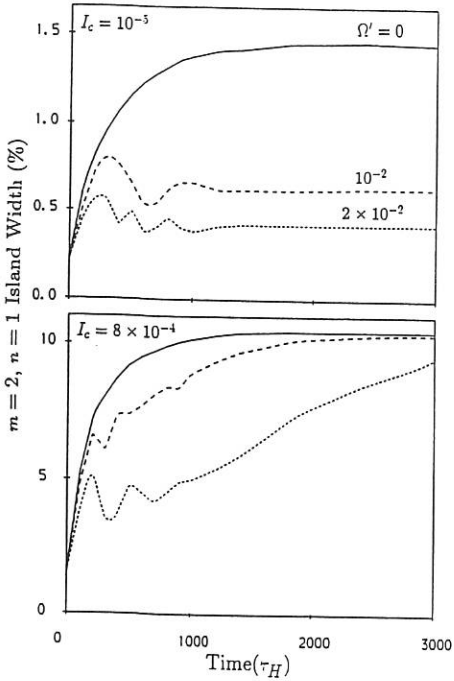

Fig 3 Evolution of $m = 2$, $n = 1$ island widths for various relative plasma to coil frequencies (Ω') and two applied $m = 2$, $n = 1$ currents (I_c which is normalised to the toroidal field and minor radius).

4 Summary and Discussion

The analytic and numerical results show that tearing at the surface at which an appplied helical perturbation is resonant, is strongly inhibited by relative plasma motion (due to diamagnetic drift and/or fluid plasma rotation). Nonlinearly however this effect is ameliorated and essentially full tearing occurs for sufficiently large applied helical perturbations. For COMPASS parameters ($S \sim 10^6$, $\Omega' \sim 15$kHz, $q_\psi \sim 3$) we find that full tearing occurs for applied $m = 2$, $n = 1$ islands with $W > 15\%$. Such island widths are also typical of those required to stimulate disruptions in low–q ($q_\psi \sim 3$) discharges [3]. Thus it may be that the threshold in applied field to stimulate disruptions is given by that required for the rotation inhibition of tearing to be overcome.

References

[1] J.J.Ellis et al, IAEA Conf Lodon 1984, IAEA **1** (1985) 363.
[2] F.Karger et al, IAEA Conf Tokyo 1974, IAEA **1** (1975) 207.
[3] A.W.Morris et al, 'Resonant Magnetic Perturbation and Disruption Studies on COMPASS-C', this Conf.
[4] G.Ara et al, Anals of Phys **112** (1978) 1059.
[5] D.Biskamp, Nucl Fusion **18** (1978) 443.

THE EFFECT OF THE PLASMA SHAPE ON THE ACCESSIBILITY OF THE SECOND STABILITY REGIME

O. J. Kwon and T. C. Hender

UKAEA/EURATOM Fusion Association
Culham Laboratory, Abingdon Oxon, OX14 3DB, U.K.

INTRODUCTION

The limit on β in the tokamak set by the high–n (n being toroidal mode number) ballooning mode and $n = 1$ kink mode [1,2] has been shown to agree well with that is found experimentally. The ballooning β–limit can be improved or avoided with stable access to the ballooning second stable regime, by raising the safety factor on axis (q_0) [3], by indentation [4], or by using energetic particles [5]. It is also known that in some geometries, a second stable region for the $n = 1$ internal mode may also exist depending on the pressure and safety factor profiles [6].

Here, we investigate the effect of the plasma boundary shape on the accessibility to the ideal second stable regime. We concentrate on the technique of raising q_0 to enhance the magnetic well and to give a direct access to the second stable regime. Most shapes and parameters are chosen such that they can be experimentally realizable on COMPASS, which has a flexible poloidal shaping system.

RESULTS

In this study, three numerical codes have been used; a code which examines the stability to the high–n ballooning mode, the *ERATO* code [7] which has been used to investigate the stability to high–n ballooning, and $n = 1$ ideal modes, and the *FAR* code [8] which has been used to test the stability to low–n (mainly n =1,2,3) fixed boundary modes including the infernal modes [9].

In the ballooning code, the diamagnetic term (RB_T) and the pressure gradient (P') may be specified as:

$$FF' = A_f \psi^{\lambda_f} + \sum_{i=1}^{3} A_i \psi^i - R_0^2 \sum_{i=1}^{2} C_i \psi^{\lambda_i},$$

$$P' = B_{p'} \psi^{\lambda_p} + \sum_{i=0}^{3} B_i \psi^i + \sum_{i=1}^{2} C_i \psi^{\lambda_i},$$

or the pressure gradient may be increased until the marginal limit is reached on all surfaces. Therefore, we can find the marginal pressure profile for a given q–profile and poloidal beta (β_p), where β_p is defined as $8\pi \oint P dV / \oint B_p^2 dV$.

The accessibility of a globally stable route to the second ballooning stable regime has been tested for for various shapes with different elongations (E) and triangularities (Δ). For $E = 0.65$, 1.0, and 1.9, triangularities in the range $-0.72 < \Delta < 0.49$

have been chosen. For $E = 0.65$, shapes with a negative and positive triangularity, resemble a comet shape with inboard and outboard separatrices, respectively. The former is of particular interest because it allows the direct access to the ballooning second stability on the outermost flux surface [10] and is also favorable for Mercier stability. However, here we are interested in the global access to the second stable region.

Figure 1 shows the global ballooning stability boundaries in the $\beta_p - q_0$ plane for various shapes. We have fixed $q_a(\sim 3.3)$ and a flux conserving sequences is used. The pressure profile is optimized such that every flux surface is marginally ballooning unstable. As shown in Fig. 1, only certain group of the boundary shapes (for $E = 1$, $\Delta = 0.2$, 0.0, and for $E = 1.9$, $\Delta = 0.39$) allow the global access to the ballooning second stability region. For these shapes, there is no unstable region as β_p is increased with fixed q–profile when $q_0 > q_{0,c}$. Circular shape has the lowest critical $\beta_{p,c}(\sim 2.7)$ and D–shape has the lowest critical $q_{0,c}(\sim 1.55)$.

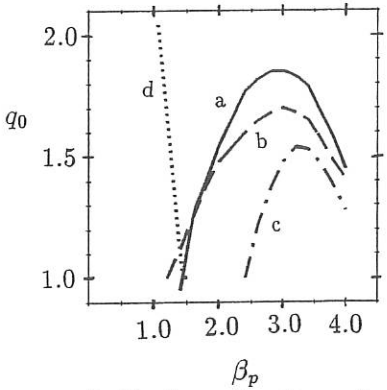

Fig. 1 Global ballooning stability boundaries in the $\beta_p - q_0$ plane for shapes with (a) $E = 1.0$, $\Delta = 0.0$, (b) $E = 1.0$, $\Delta = 0.2$, (c) $E = 1.9$, $\Delta = 0.39$; areas under these lines are unstable to the high–n ballooning mode, and (d) $E = 1.0$, $\Delta = -0.72$; right hand side of this dotted line is unstable to the high–n ballooning mode, other shapes without realistic access to the ballooning second stability have similar boundaries to (d).

In Fig. 2, we show flux surfaces for the circular boundary shape, along with the zero curvature boundary (dotted line) and negative local shear region (shaded area), for β's in the first (a) and second (b) stability region. In the second stability region, flux surfaces are strongly deformed, which acts to shorten the connection length, strengthen the stabilizing line bending, and weaken the destabilizing normal curvature. The negative local shear region and the favorable curvature region becomes wider as β_p is increased and in some cases they overlap (Fig. 2(b)). We find that in general the overlapping is a necessary, but not sufficient condition for second stability access.

For shapes which allow the access to the ballooning second stability, the low core shear (due to high q_0 value for access) is unfavorable for the low–n infernal mode [9], which can become unstable below the ballooning limit. Therefore, high–q_a, high shear operation as in Ref. [11] might be needed to stabilize the infernal mode. We have examined the global ballooning second stability access for a case ($q_a \simeq 7.5$). It is found that the boundary shapes that permit the access remain the same as those in low shear sequences. For a circular boundary, $\beta_{p,c} \simeq 1.9$ and $q_{0,c} \simeq 2.3$ have been found in the sequences where the profiles are not fully optimized. Typically when optimized, $q_{0,c}$ decreases and $\beta_{p,c}$ increases. With $q_0 \simeq 2.3$, a direct access to the second ballooning stable regime has been found for the D–shape.

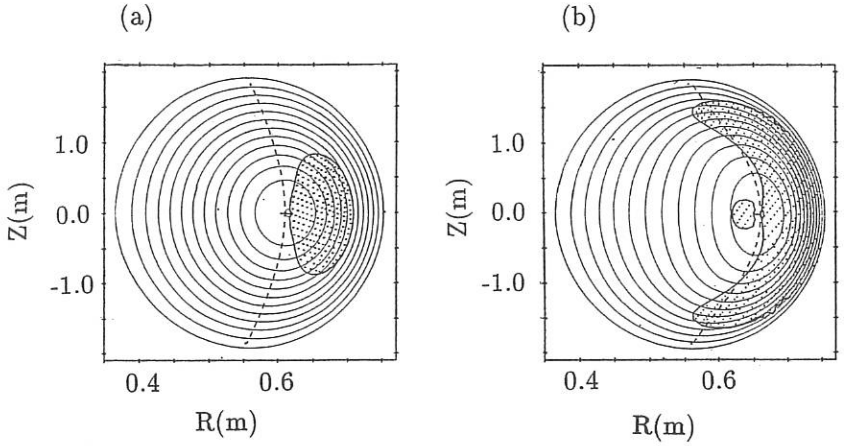

Fig. 2 Equilibrium poloidal flux surfaces (thin solid line), negative local shear region (shaded region surrounded by thick solid line), and favorable curvature region (left hand side of the broken line) for (a) low-β_p (~ 1.6, in the ballooning first stability region, $\beta_0 \simeq 2.8\%$) and (b) high-β_p (~ 4.4, in the ballooning second stability region, $\beta_0 \simeq 8.1\%$). Both are from the high shear sequence ($q_0 \simeq 2.3$ and $q_a \simeq 7.5$).

The stability of these high shear sequences ($q_a \simeq 7.5$) to the $n = 1$ mode has been investigated using the ERATO code. It should be noted that the results on the ballooning stability from the ERATO code, agree well with those above. For the circular shape, the $n = 1$ mode is stable with a wall at infinity when β_p is low ($\beta_p \lessapprox 1.4$). As β_p is increased, an $n = 1$ ballooning–like mode appears with the dominant flows located in the unfavorable curvature region. The vortex sturctures in the flow show a dominant poloidal mode number (m) of 4 or 5. Figure 3 shows how γ^2 (γ is the growth rate for $n = 1$ mode) changes with the position of the conducting wall for $\beta_p \sim 2.1$ and $q_0 \simeq 2.3$ (which is in the ballooning second stable regime, $\beta_{p,c} \simeq 1.9$). It is clear that a tight-fitting conducting wall is needed to completely stabilize the $n = 1$ ideal mode. Finally, calculations with the resistive stability code FAR indicate that these sequences which access the second ballooning stable regime, are stable to the low-n (n=1,2,3) resistive fixed boundary modes for a magnetic Reynolds number, $S_M > 10^6$.

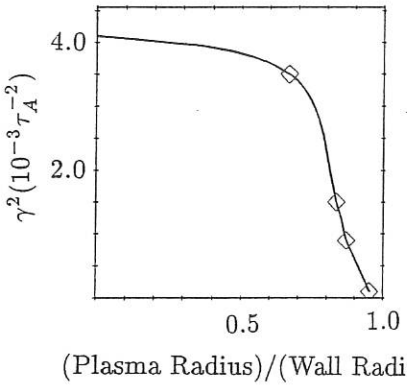

Fig. 3 Effect of the position of the conducting wall on the $n = 1$ growth rate from the ERATO code (for $q_0 \simeq 2.3$, $q_a \simeq 7.5$, $\beta_p \simeq 2.1$).

CONCLUSIONS

It has been shown that the plasma boundary shape has a strong effect on the accessibility to the second ballooning stable regime. For circular boundary and D–shapes, access to the second stability is possible by control of the current profile (i.e., raising q_0). The shapes with a high shear ($q_a \simeq 7.5$), which remain stable to both ballooning and infernal modes as β_p is increased, are found to be the same as those with the low shear ($q_a \simeq 3.3$). At high–β_p ($\beta_p \sim \beta_{p,c}$), an $n = 1$ ideal ballooning–like mode becomes destabilized and can only be suppressed with a close–fitting, stabilizing wall. Low–n, fixed boundary modes are stable in these sequences. Therefore, high–β tokamak operation in the second stable regime appears to be possible, although the $n = 1$ free boundary modes require a close–fitting shell for stability.

REFERENCES

[1] Troyon, F., et al., Plasma Phys. Controll. Fusion **26** (1983) 209.
[2] Wesson, J. A., Sykes, A., Nucl. Fusion **25** (1985) 85.
[3] Sykes, A., Turner, M. F., EPS Meeting Oxford 1979; Coppi, B., Crew, G. B., Ramos, J. J., Comments Plasma Physics Controlled Fusion **8** (1983) 11.
[4] Grimm, R.C., et al., Nucl. Fusion **25** (1985) 805.
[5] Rosenbluth, M. N., et al., Phys. Rev. Lett. **51** (1983) 1967.
[6] Manickam, J., Nucl. Fusion **24** (1984) 595.
[7] Gruber, R. et al.,, Comp. Phys. Communications **21** (1981) 323.
[8] Charlton, L. A., et al., Jrnl., Comp. Phys. **63** (1983) 107.
[9] Manickam, J., Pomphrey, N., Todd, A.M.M., Nuclear Fusion **27** (1987) 1461.
[10] Bishop, C. M., Nucl. Fusion **26** (1986) 1063.
[11] Gerver, M.J., Kesner, J., Ramos, J.J., Phys. Fluids **31** (1988) 2674.

GLOBAL IDEAL MHD STABILITY OF 3D PLASMAS WITH PSEUDO-VACUUM TREATMENT FOR FREE-BOUNDARY MODES

U. SCHWENN, D.V. ANDERSON*, W.A. COOPER**, R. GRUBER**, S. MERAZZI**
Max-Planck-Institut für Plasmaphysik
IPP-EURATOM Association, D-8046 Garching
**NERSC Livermore, USA*
***EPFL Lausanne, Switzerland*

The determination of the ideal MHD stability properties of plasma containment devices is never complete without the investigation of the impact that can be had by the class of instability that can displace the plasma-vacuum interface. These free-boundary modes impose in many cases the severest restrictions on the plasma beta that a configuration can achieve and/or the toroidal plasma current that can flow within it. In order to examine the free-boundary stability of a plasma, the potential energy contribution of the vacuum region that surrounds the plasma must be added to the internal contribution of the plasma itself. In two-dimensional (2D) plasmas, two methods have been developed to tackle the vacuum contribution to the energy principle. One scheme uses a Green's function technique which is particularly convenient when the conducting wall is placed at infinity. An alternative scheme is to treat the vacuum region as a pressureless and shearless pseudo-plasma. The main advantage of this scheme is that the structure of the problem in the vacuum region is identical to that in the plasma region. A detailed analysis and comparison of the two methods in 2D axisymmetric and helically symmetric geometry has been discussed by Gruber and Rappaz (1985) /1/ and by Gruber et al. (1981)/2/.

We have generalized the vacuum treatment as a pseudo-plasma to three dimensional (3D) geometry and implemented it in the TERPSICHORE ideal MHD stability code, which was previously limited only to the study of internal structures /3/. For this purpose, we identify (s,θ,ϕ) as the Boozer magnetic flux coordinate system within the plasma domain and introduce the coordinate system (s_v,θ_v,ϕ_v) in the vacuum domain subject to the constraints that $s_v = s = 1$, $\theta_v = \theta$ and $\phi_v = \phi$ at the plasma-vacuum interface. Furthermore, we introduce a pseudo-magnetic field $\mathbf{T}$ that satisfies $\nabla\cdot\mathbf{T} = \mathbf{T}\cdot\nabla s_v = 0$, which in most general form can be written as

$$\mathbf{T} = \frac{\mathrm{d}\Phi_v}{\mathrm{d}s_v}\left[\left(\frac{\mathrm{d}\Psi_v}{\mathrm{d}\Phi_v} - \frac{\partial\lambda_v}{\partial\phi_v}\right)\nabla\phi_v\times\nabla s_v + (1+\frac{\partial\lambda_v}{\partial\theta_v})\nabla s_v\times\nabla\theta_v\right] .$$

Invoking as a gauge condition that the perturbed magnetic field vector potential $\mathbf{A}$ have no components aligned with $\mathbf{T}$, we can introduce a pseudo-displacement vector $\boldsymbol{\xi}_v$ that we express in a form that is quite similar to that in the plasma such that $\mathbf{A} = \boldsymbol{\xi}_v\times\mathbf{T}$.

$$\boldsymbol{\xi}_v = \sqrt{g_v}\frac{\Phi'(1)X_v}{(\mathrm{d}\Phi_v/\mathrm{d}s_v)}\nabla\theta_v\times\nabla\phi_v + \frac{\mathbf{T}\times\nabla s_v}{T^2}Y_v ,$$

The vacuum energy thus becomes

$$\delta W_{\mathrm{v}} = \frac{1}{2} \int_{1}^{s_{\mathrm{v}\max}} \mathrm{d}s \int_{0}^{2\pi/L_s} \mathrm{d}\phi_{\mathrm{v}} \int_{0}^{2\pi} \mathrm{d}\theta_{\mathrm{v}} \sqrt{g_{\mathrm{v}}} \left[\nabla \times (\boldsymbol{\xi}_{\mathrm{v}} \times \mathbf{T})\right]^2$$

where L_s is the number of periods of the instability structure in one toroidal transit and $s_{\mathrm{v}\max}$ is the value of s_{v} at the conducting wall.

The boundary condition at the plasma-vacuum interface $\nabla s \times \mathbf{A} = -(\boldsymbol{\xi} \cdot \nabla s)\mathbf{B}$ reduces to $(\boldsymbol{\xi}_{\mathrm{v}} \cdot \nabla s)\mathbf{T} = (\boldsymbol{\xi} \cdot \nabla s)\mathbf{B}$, where $\mathbf{B}$ is the equilibrium magnetic field and $\boldsymbol{\xi}$ is the perturbed displacement vector from the plasma side, from which we obtain

$$\frac{\mathrm{d}\Psi_{\mathrm{v}}}{\mathrm{d}\Phi_{\mathrm{v}}} = \frac{\Psi'(1)}{\Phi'(1)}$$

$$\lambda_{\mathrm{v}}(1, \theta_{\mathrm{v}}, \phi_{\mathrm{v}}) = 0 \text{ and}$$

$$X_{\mathrm{v}}(1, \theta_{\mathrm{v}}, \phi_{\mathrm{v}}) = \xi^s(1, \theta, \phi)$$

where $\xi^s \equiv \boldsymbol{\xi} \cdot \nabla s$. To avoid introducing fictitious resonances in the vacuum region, we impose that $\mathrm{d}\Psi_{\mathrm{v}}/\mathrm{d}\Phi_{\mathrm{v}} = \Psi'(1)/\Phi'(1)$ everywhere. Furthermore, for simplicity, it is convenient also to choose $\lambda_{\mathrm{v}}(s_{\mathrm{v}}, \theta_{\mathrm{v}}, \phi_{\mathrm{v}}) = 0$. The boundary condition at a conducting wall $\nabla s_{\mathrm{v}} \times \mathbf{A} = 0$ reduces to $X_{\mathrm{v}}(s_{\mathrm{v}\max}, \theta_{\mathrm{v}}, \phi_{\mathrm{v}}) = 0$.

To construct the geometry of the vacuum region in order to apply a pseudo-plasma treatment, we have developed a procedure that guarantees that the Jacobian and the metric elements, and thus the geometry, vary smoothly across the plasma-vacuum interface into the vacuum region. Within this procedure, the shape of the conducting wall can be arbitrarily prescribed or is dictated by the shape of the plasma-vacuum interface subject to the conditions that the radial derivatives of R, the distance from the major axis, of v, the geometric toroidal angle, and of Z, the distance from the horizontal midplane, be constant throughout the vacuum domain. In either case, the shape of the conducting wall does not coincide in general with that of the plasma-vacuum interface, and therefore the approach we have followed differs from that in the ERATO code. Two important constraints are imposed in the development of the vacuum region. These are that the vacuum pseudo-surfaces remain always nested and that the conducting wall should not intersect the major axis. The nestedness constraint precludes, in general, that a prescribed conducting wall can approach the plasma-vacuum interface too closely. The alternative scheme for describing a conducting wall, however, will not violate the nestedness constraint even for a wall arbitrarily close to the plasma-vacuum interface.

The vacuum energy acquires a structure that is similar to that obtained from the internal plasma energy with a Fourier decomposition of the perturbations like that undertaken in the plasma. The bulk of the computational effort in the vacuum region concentrates on the calculation of 6 double Fourier flux tube integrals. As the integrals involved here are of the same type as those evaluated inside the plasma, the very efficient MULFI technique can be applied which transforms the discretized integrations into MXM operations /4/.

Applying finite hybrid elements for the radial discretisation of the vacuum energy, we recover the special block pentadiagnonal structure of the matrix equation that was a feature of the formulation of the internal plasma problem in the TERPSICHORE code. Thus, the internal plasma potential energy principle can be straightforwardly combined with the vacuum potential energy principle so that the ideal MHD stability to global modes can be evaluated in a single step. Furthermore, the efficient computational tools previously developed to solve for the eigenvalues of the system in the fixed-boundary problem are applied to the free-boundary problem with virtually no additional effort.

The pressureless and shearless pseudo-plasma treatment of the vacuum region that we have described has been implemented in the TERPSICHORE code. Benchmark studies of analytic Solove'v equilibria have been carried out and compared with results obtained with ERATO /5/. Because the right-hand side matrix in TERPSICHORE is basically the unity matrix rather than derived from the physical kinetic energy as in ERATO, a direct comparison of the magnitude of the eigenvalues is not possible except at points of marginal stability. In Solove'v equilibria, the most unstable free-boundary mode computed by both codes never crosses a marginal point, remaining always unstable. The second most unstable mode, which closely tracks the most unstable fixed-boundary mode, is shown in both codes to become critical when the q-value at the magnetic axis approaches 0.59 for $n = 2$ instabilities in a case with a circular aspect ratio of 3.

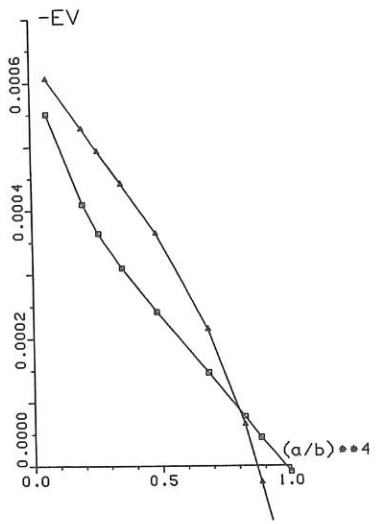

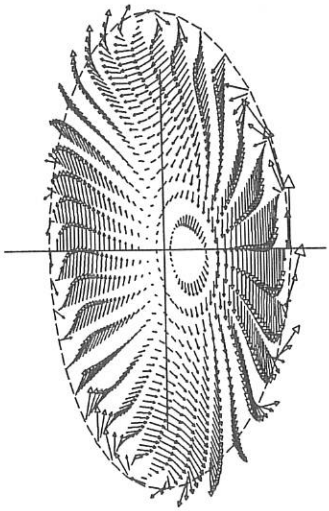

Fig. 1: (left) Eigenvalues as functions of (a/b) for $n = 1$ ($\square$), $n = 2$ ($\triangle$) free-boundary modes in an $\ell = 2$ stellarator with $A = 10$, $\iota = 0.43 \ldots 0.49$ and $\beta_0 = 1.9\%$.

Fig. 2: (right) Eigenfunction of an $n = 1$, $m = 2$ free-boundary mode, data as in Fig. 1, $b/a = 6$, 24 radial, 36 poloidal and 12 toroidal intervals.

A real 3D test was performed by reproducing former results obtained with the STEP code for toroidal $\ell = 2$ stellarators /6/. We chose an $A = 10$ configuration where ι varies from 0.43 to 0.49, a parabolic pressure profile with $\beta_0 = 1.9\%$, and five periods on the torus. This configuration proved to be stable to internal resonant modes due to the finite toroidal aspect ratio. Displacing the conducting wall away from the plasma-vacuum interface led to unstable external modes resonant with $m_{\text{res}} = 2n$. The equilibrium for the TERPSICHORE input was produced with the most recent VMEC code in the fixed-boundary mode /7/. Figure 1 shows the dependence of the eigenvalues for $n = 1$ and $n = 2$ modes on the fourth power of the ratio between the mean radii of the conducting wall b and of the plasma-vacuum interface a. The marginal points found with STEP could easily be reproduced with an accuracy mostly determined by the completely different equilibrium input. Figure 2 shows a typical displacement pattern for an $n = 2$, $m = 1$ mode. As in the former TERPSICHORE results for fixed-boundary global modes, extrapolation studies proved to be mostly unnecessary.

In summary, we have described a method to evaluate free-boundary ideal MHD instabilities in 3D equilibria with nested flux surfaces which has been successfully implemented in the TERPSICHORE code and tested against the results obtained with ERATO for Solove'v equilibria and with STEP for toroidal $\ell = 2$ stellarator equilibria.

REFERENCES

1. R. Gruber, J. Rappaz, Finite Element Methods in Linear Ideal MHD (Springer Verlag, Heidelberg 1985).
2. R. Gruber, S. Semenzato, F. Troyon, T. Tsunematsu, W. Kerner, P. Merkel, W. Schneider, Comput. Phys. Commun.**24** (1981) 363.
3. D.V. Anderson, W.A. Cooper, R. Gruber, U. Schwenn, Theory of Fusion Plasmas (Bologna, 1989) 93.
4. D.V. Anderson, W.A. Cooper, R. Gruber, S. Merazzi, U. Schwenn, International Journal for Supercomputer Applications 1990 (to be published).
5. D. Berger, L.C. Bernard, R. Gruber, F. Troyon, ZAMP **31** (1980) 113.
6. F. Herrnegger, Proc. Workshop on Wendelstein VII-X , Schloss Ringberg 1987, EUR 11058 EN (1987) 49.
7. S.P. Hirshman, J. Nührenberg, U. Schwenn, J. of Comput. Phys.**87** (1990) (to be published).
   O. Betancourt, S.P. Hirshman, private communication.

Transition between resistive Kink and Kadomstev reconnection

K. Lerbinger, J.F. Luciani

Centre de Physique Théorique - Ecole Polytechnique - 91128 Palaiseau

A - Description of the numerical code

A full 3.D toroïdal non linear evolution code has been developped in order to study MHD instabilities. The numerical scheme [1] used here is a semi-implicit predictor-corrector scheme where numerical stability is ensured by replacing the equation of velocity $dV/dt = F$ by

$$(1 - (\Delta t)^2 L_0 - c\Delta)\, dv/dt = F$$

Here, L_0 is the linearized MHD operator, obtained by linearizing the MHD equations around the equilibrium (i.e, the $n = 0$ harmonic, where n is the toroïdal wave-number).

The elliptic operator $c\Delta$, in this scheme, dominates only the perturbation of the equilibrium (i.e, the non linear $n \neq 0$ modes).

The constant c is arbitrary choosen ; for c large, and dropping the L_0 term, one recovers the semi-implicit scheme proposed by Harned and Kerner [2], where the $c\Delta$ term stabilizes as well the linear waves. Here, on the contrary, the scheme is linearly unconditionnally stable, without distorsion of the linear dynamics even for large time steps, and the non-linear numerical stability is ensured by :

$$\Delta t \leq \sqrt{c} / \delta B$$

where δB is the magnitude of non-linear ($n \neq 0$) modes. Thus, cloosing $c \sim 10^{-4}$ (that is, a very small "smoothing") enables to work with precision at large time steps, since a typical value for δB is 10^{-2} in non-linear phases.

The major advantage of this scheme is that it enables to work with large time-step, even in very non-linear situations, without a slowing of the dynamics of resonnant layers.

B - Kadomstev cylindrical reconnection

Toroïdal results obtained with this code are presented elsewhere [3]. Here, we present a study of cylindrical Kadomstev reconnection.

We have taken a "standard" profile, $q = 0.9\left[1 + \left(\frac{2r}{a}\right)^4\right]^{1/2}$, with a poloïdal β $\beta_p = 0.2$. This provides an ideally unstable kink with a rather large linear layer. Then we study the resistive reconnection. On fig (1) is plotted the displacement of the magnetic axis versus time, for several values of S ranging from 10^4 to 10^7.

The result can be summarized by stating that if the reconnection layer is larger than the ideal layer ($S < 10^5$ in this case), we see a resistive kink. On the contrary, if the reconnection layer is smaller than the ideal layer ($S > 10^5$ in this case), we see a Kadomstev reconnection : the first phase is the saturation of the ideal kink, which is not modified by resistivity ; then we observe the reconnection itself, on a time scale $S^{1/2}$ as predicted by Kadomstev.

C - Conclusion

This cylindrical study is certainly academic, though it is, at our knowledge, the first simulation of this kind (reduced MHD equations cannot lead to this scaling as they do not support an ideal kink). But it confirms the fact that, in devices with $S \approx 10^8$, the sawteeth time crash is not compatible with an MHD reconnection, within a factor 10 at least.

References

[1] K. Lerbinger, J.F. Luciani, submitted to Journal of Computionnal Physics.

[2] D.S. Harned, W. Kerner, J. Comput. Phys. 59, 108 (1085).

[3] H. Baty, M.N. Bussac, J.F. Luciani, Poster in this conference.

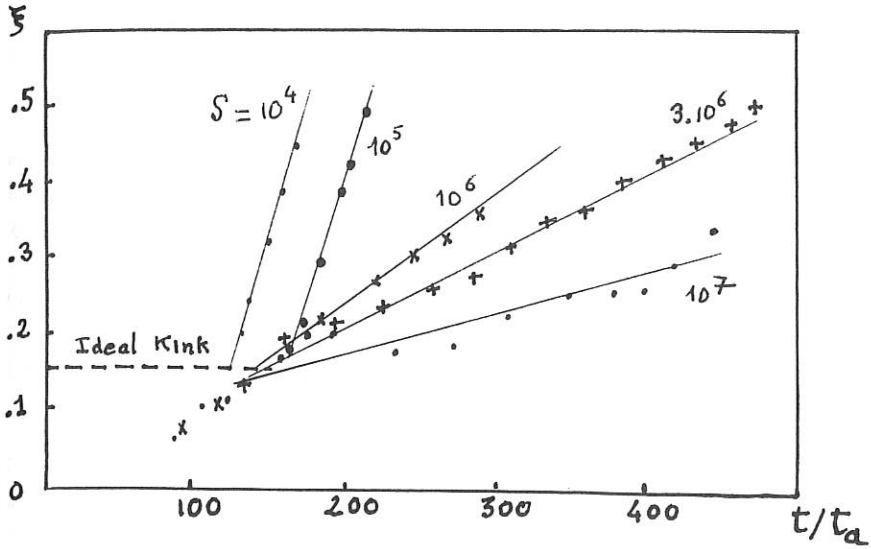

Fig. 1 : The displacement of the magnetic axis is plotted versus time for different values of S. The displacement corresponding to the saturation of the ideal kink is indicated.

TEARING MODE STABILIZATION BY ENERGETIC TRAPPED IONS

D.Edery, X.Garbet, J-M. Rax, J-P. Roubin, A. Samain

Association EURATOM-CEA sur la Fusion Contrôlée
Centre d'Etudes Nucléaires de Cadarache B.P. n°1
13108 Saint-Paul-lez-Durance, France

INTRODUCTION

The access to the so-called "monster sawteeth" regime during additional heating in JET [1] is related to the creation of energetic trapped ions inside the plasma. Several models have been put forward to explain the behaviour of the central part of the discharge [2,3]. These studies mainly analyse the influence of the fast ion population on the ideal internal kink mode destabilized by the thermal pressure gradient. However, the stability of the associated reconnecting mode is to be considered. Along this line, in this paper, we investigate a new stabilization criterion expressing that the fast trapped ions (by balancing the effect of the current density gradient) provide a negative Δ' to that mode.

MODEL

To account for the effect of a suprathermal population, we extend the usual variational formulation of MHD through a more general Lagrangian formalism. Both Maxwell equations and plasma gyrokinetics equations are consistently accounted for when the functional [4]:

$$\mathcal{L}(\vec{A},U,\vec{A}^*,U^*) = \mathcal{L}_{MHD} + \mathcal{L}_{res} \qquad (1)$$

is extremal with respect to the variations of the electromagnetic potentials $\vec{A}^*$ and U^*. $\mathcal{L}_{MHD}$ describes the usual adiabatic fluid/field coupling whereas $\mathcal{L}_{res}$ displays the trajectory and resonance effects. For a n=1,m=1 tearing mode ($A=A_{//}\neq 0$ on the surface $r=r_1$ where q=1), the contribution of the resistive layer to $\mathcal{L}_{res}$ imposes a low frequency ω of thermal diamagnetic type. We introduce a maxwellian hot ion population (pressure $p_H=\beta_H \cdot B_\varphi^2/2\mu_0$), localized inside the domain $r=r_1$, whose trapped part (the only to be active in the stabilization) exhibits precession frequency $\omega_p >> \omega$. We then obtain from (1), ignoring the inertia, thermal pressure and toroidal effects, the following Euler equation outside the resistive layer near the q=1 surface

$$\left(\frac{1}{r}\frac{\partial}{\partial r} r \frac{\partial}{\partial r} - \frac{1}{r^2} + \frac{2}{q_0 r}\frac{\partial (j/j_0)/\partial r}{1-1/q} + \beta_{H0}\frac{R^{1/2}}{2r^{3/2}}\frac{\partial (p_H/p_{H0})/\partial r}{(1-1/q)^2} \right) . A(r) = 0 \qquad (2)$$

where the index 0 refers to r=0. For $p_H=0$, the solution A(r) of equation (2) which is regular at r=0 cancels at $r=r_1$. This means that the n=1,m=1 mode is marginally unstable under the MHD

constraint $A_{//}(r_1)=0$. On the other hand, the mode exhibits a large positive Δ' and is strongly unstable as a tearing mode. At this point, two routes are possible:

The first one, considered in [2] [3], is based on the fact that the introduction of the thermal pressure gradient effect in (2) destabilizes the MHD mode [5]: The regular solution A(r) now cancels at $r<r_1$ and one may ask the fast ions to balance this effect, and to restitute a marginally MHD unstable situation with $A(r_1)=0$.

The second one, considered here, is to ask the fast ions to transform the mode into a traditional stable tearing mode. This means that the solutions of (2) regular at r=0 and $r=\infty$ must have a finite value $A(r_1)$ and $\Delta' = [\partial \mathrm{Log}(A)/\partial \mathrm{Log}(r)] \leq 0$.

RESULTS

In the case of a step pressure profile ($p_H=p_0$ for $r<r_H<r_1$, $p_H=0$ for $r>r_H$), an exact solution of (2) can be constructed as a superposition of the two independent solutions A_1, A_2 in the three intervals $0<r<r_H$, $r_H<r<r_1$ and $r_1<r$:

$$A_1 = -\,r\,(\,1 - 1/q\,) \quad \text{and} \quad A_2 = A_1\,F \ \text{with}\ F(r) = \int_{+\infty}^{r} \frac{du}{u^3}\,\frac{1}{(1-1/q)^2}$$

A_1 corresponds to the usual internal kink displacement $\xi=Cte$, and, for $r<r_1$ we choose the continuation of F that insures the continuity of A_2 and $\partial A_2/\partial r$ at $r=r_1$ (Fig.1). The actual solution A(r) can be obtained by requiring the continuity of A(r) and discontinuities of $\partial A/\partial r$ at $r=r_H$ and $r=r_1$ respectively associated with the localized gradient $\partial p_H/\partial r$ and the desired Δ' value. Such a set of conditions leads to:

$$\Delta' = s_1^{\,2}\left(\bar{\beta}_H^{\,-1} - \beta_{crit}^{\,-1} \right) \qquad (3)$$

$$\text{where} \quad \bar{\beta}_H = \beta_{H0}\,R^{1/2} r_H^{\,3/2} / 2r_1^{\,2} \quad \text{and} \quad \beta_{crit}^{\,-1} = r_1^{\,2}\,F(r_H) \qquad (4)$$

(s_1 is the magnetic shear parameter $\partial \mathrm{Log}(q)/\partial \mathrm{Log}(r)$ at $r=r_1$).

In a more general case, considering an arbitrary fast ion profile localized inside the q=1 surface and developing the solution to first order in β_H, the equation (3) is still valid with:

$$\bar{\beta}_H = \frac{\beta_{H0}R^{1/2}}{2r_1^{\,2}} \int_0^{r_1} -\frac{\partial}{\partial r}\left(\frac{p_H}{p_{H0}}\right) r^{3/2} dr \quad \text{and} \quad \beta_{crit}^{\,-1} = r_1^{\,2} \int_0^{r_1} \frac{\partial}{\partial r}\left(\frac{p_H}{p_{H0}}\right) F(r) r^{3/2} dr \;\Big/\; \int_0^{r_1} \frac{\partial}{\partial r}\left(\frac{p_H}{p_{H0}}\right) r^{3/2} dr \qquad (4')$$

For a step pressure profile, these relations are equivalent to (4). Both expressions of β_{crit} clearly indicate that the radial localisation of the hot ion pressure gradient plays a major role through the variations of the function F(r).

For a parabolic q profile, $q=q_0+(1-q_0)(r/r_1)^2$, the following expression for F(r) is obtained:

$$F(r) = -\frac{1}{(1-q_0)^2}\left(\frac{q_0^{\,2}}{2r^2} + \frac{1}{r^2-r_1^{\,2}} + \frac{q_0}{r_1^{\,2}} \mathrm{Log}\left| \frac{r^2}{r_1^{\,2}} - 1 \right| \right) \qquad (5)$$

DISCUSSION

The function F(r) monotonically increases from $-\infty$ to $+\infty$ and has a zero at r^* in the interval $[0,r_1]$. In the case (5), F(r)=0 for $r = r^* \approx 2r_1/3$ (Fig.1). For the sake of simplicity, the

discussion is done for a step pressure profile but all the results can be easily extended to any profile thanks to (4'). According to the stabilisation criterion equations $\Delta'<0$ where Δ' is given by (4) the position of the localized hot ion pressure gradient r_H is to be compared to r^*:

- If $r_H<r^*$, β_{crit} is negative and the hot ion pressure gradient is unable to achieve a complete stabilization: Δ' decreases as β increases but never cancels.

- If $r_H>r^*$, β_{crit} is positive and a complete stabilisation can be obtained if $\bar{\beta}_H > \beta_{crit}$. The function A(r) for such a stable case is depicted on figure 2. When the hot ion pressure gradient approaches the resonant surface, the balance between the destabilizing current gradient term and the stabilizing hot ion pressure term becomes favorable owing to their respective radial scalings $(1-q)^{-1}$ and $(1-q)^{-2}$. This result is not restricted to a localized gradient and parabolic q profiles, and is confirmed with fairly general q and p profiles by the analysis of equations (4') as well as by direct numerical integration of the equation (1).

Under the condition $r_H>r^*$, the critical β_{H0} value corresponding to marginally stable modes ($\bar{\beta}_H=\beta_{crit}$) is plotted on figure 3. Three zones clearly appear. For $r_H \approx r^*$, the critical β_{H0} is too high with respect to the usual equilibrium limits. For $r^* < r_H < r_1$, the critical β_{H0} is found in the range 10^{-3}-10^{-2}. Such values can be easily reached during additionnal heating in JET and thus, tearing stabilization can be achieved. We have approximately $\beta_{H0} \approx 4\,(r_H/R)^{1/2}(1-q_0)(1-q)$. This scaling clearly indicates that stability dramatically depends on the precise value of q_0. For $r_H \approx r_1$, it appears that very small values of β_H leads to stabilization. Obviously, this result is to be revisited, because in this zone, the resonant layer near the surface q=1 and its reconnecting dynamics plays a major role. In this layer, the equation (1) must be complemented by a U coupled equation arising through the breakdown of the ideal MHD constraint. We have also investigated the effect of a conducting wall at finite distance. As expected, a weak stabilizing effect is observed when the mode amplitude is peaked near the q=1 surface.

CONCLUSION

The n=1, m=1 mode, considered as a tearing mode, can be stabilized by energetic trapped ions. The negative pressure gradient $\partial p_H/\partial r$ of this population must be localized beyond a critical radius r^* ($r^*/r_1 \approx 2/3$ for a parabolic q profile) and the corresponding critical β_H scales as $(1-q_0)^2$. This result is different from the scaling of the critical β that is required for the ideal internal kink stabilisation [2,3]. On this basis, experiments should allow to distinguish which mechanism is at work during sawtooth stabilisation.

REFERENCES

[1] D.J. Campbell et al., Phys. Rev. Lett. **60**, 2148 (1988)
[2] R.B. White, M.N. Bussac, F. Romanelli, Phys. Rev. Lett. **62**, 539 (1989)
[3] B. Coppi, P. Dedragiache, S. Migliuolo, F. Pegoraro, F. Porcelli, Phys. Rev. Lett. **63**, 2733 (1989)
[4] D.Edery, X.Garbet, J-M. Rax, J-P. Roubin, A. Samain, EUR-CEA-FC-1393 Report, 1990.
[5] M.N. Bussac, R. Pellat, D. Edery, et J.L. Soulé, Phys. Rev. Lett. **35**, 1638 (1975)

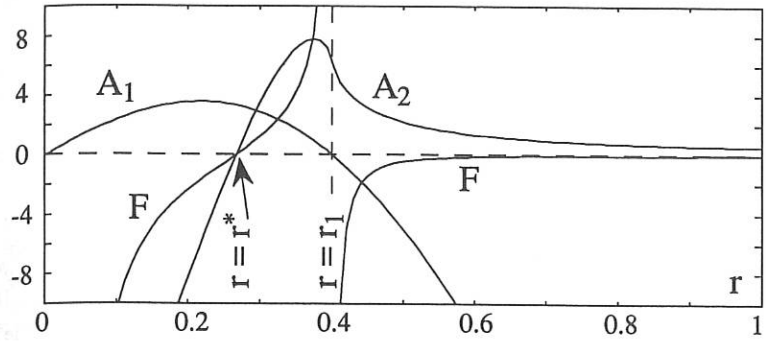

Figure 1: A_1 (the internal kink), A_2 and F, q_0=0.8, q(0.4)=1.

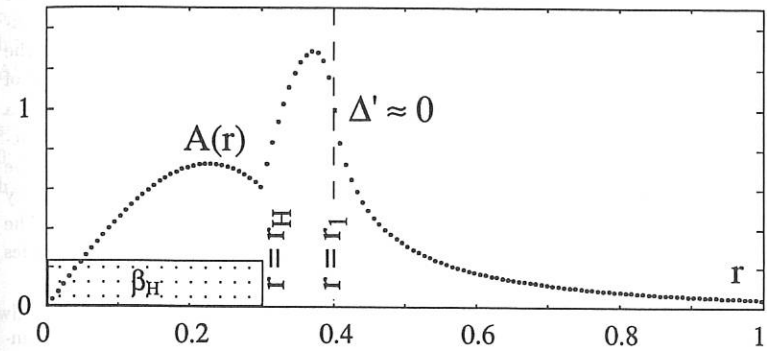

Figure 2: Stable mode with step p profile, q_0=0.9, r_H=0.3, β_H =1.5%

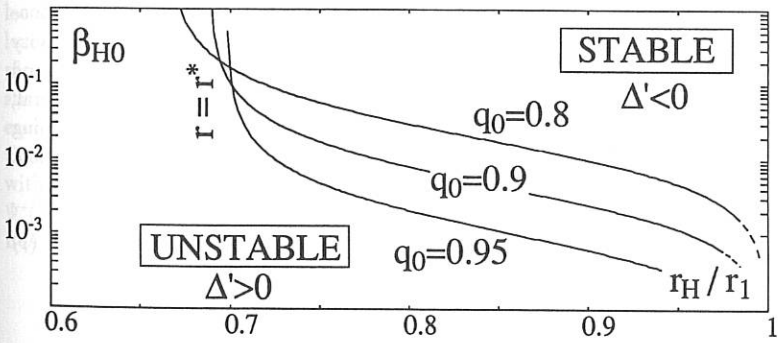

Figure 3: Critical beta as function of q_0 and r_H

Asymptotic Theory of the Non-linearly Saturated $m = 1$ Mode in Tokamaks with $q(0) < 1$

A. Thyagaraja and F.A. Haas

Culham Lab./Euratom Fusion Assoc. Abingdon, OX14 3DB, UK

1. Introduction: In this paper the necessary and sufficient conditions required for the existence of a non-linearly saturated $m = 1$ tearing mode in tokamaks with $q_0 < 1$ are considered in cylindrical tokamak ordering using the asymptotic techniques developed by one of the authors in an earlier paper[1]. The outer equations for the helical perturbation amplitude $\psi_1(r)$ can be solved exactly, in closed form for an arbitrary mean profile $\psi_0(r)$ in leading order. This results in a "no disturbance" theorem: the $m = 1$ perturbation must be confined to within the radius r_i such that $q(r_i) = 1$. The bifurcation relation for the non-dimensional perturbation amplitude is then constructed by solving the non-linear inner critical layer equations using an ordered iterative technique. For monotonically increasing q-profiles, the equation has a solution if and only if the longitudinal current density of the unperturbed equilibrium has a maximum within r_i and the parameter $\frac{d\log q(r)}{d\log \eta(r)}$ (where, $\eta(r)$ is the resistivity profile consistent with the q-profile of the unperturbed equilibrium) is sufficiently small at r_i. When the conditions are met, a non-linearly saturated $m = 1$ tearing mode is shown to exist with a novel island structure, quite different to those obtained from the usual Δ' analysis, which is shown to be inappropriate to the present problem. The relevance of the results of the present theory to sawtooth phenomena reported in JET and other tokamaks is briefly discussed. The solution constitutes a novel, analytically solved test case for numerical simulation codes to leading orders in a/R and the shear parameter $\frac{d\log q}{d\log \eta}$.

2. The Mathematical Formulation and Results: We consider the single-fluid, incompressible, resistive MHD equations in cylindrical tokamak ordering. The set of equations used is identical with (they are some times called RMHD equations) the steady-state forms of those used by previous workers apart from trivial notational differences. As is well-known, these equations are derived under the assumptions $B_z \to \infty$, $\frac{a}{R} \to 0$, keeping $q(r) \equiv \frac{rB_z}{RB_\theta}$ fixed. The equilibrium q-profile is assumed to have $q_0 < 1$ and to be monotonically increasing[2,3], with small shear at the $q = 1$ radius[4]. We assume that the resistivity is a specified function of r, as in earlier work[1], where it was shown to produce good agreement with numerical work and experiment. Parts of our analysis are more general, enabling qualitative deductions to be made about saturation properties. Thus, defining a helical variable $u \equiv \theta - \frac{z}{R}$, and introducing the corresponding helical flux function, $\psi(r,u)$, and electrostatic potential $\Phi(r,u)$, the following equations are obtained:

$$\frac{1}{r}\frac{\partial(\psi, j_z)}{\partial(r,u)} = 0 \tag{1}$$

where, the current density j_z is given by $j_z = -\nabla^2\psi + \frac{2B_z}{R}$ and

$$E_z - \eta(r) j_z(\psi) = \frac{1}{r}\frac{\partial(\psi,\Phi)}{\partial(r,u)}. \tag{2}$$

E_z is uniform and constant. The above equations admit an "unperturbed equilibrium", $\psi_0(r), \Phi_0 \equiv 0$. For general profiles ψ_0, assuming a small perturbation of the form $\psi_1(r)\cos u$ for the $m = 1$ mode, it is clear that ψ_1 satisfies the ordinary differential equation (away from $r = r_i$, where $q(r_i) = 1$),

$$\frac{1}{r}\frac{d}{dr}(r\frac{d\psi_1}{dr}) - \frac{\psi_1}{r^2} + \left(\frac{dj_0}{dr}/\frac{d\psi_0}{dr}\right)\psi_1 = 0, \tag{3}$$

where, $j_0 = -\nabla^2\psi_0 + \frac{2B_z}{R}$. It is easily shown that the "outer" solution to the above equations for $0 < r < r_i$ is of the form, $\psi_0(r) + \lambda r_i \frac{d\psi_0(r)}{dr}\cos u$, where λ is a non-dimensional small parameter to be determined by a suitable matching in the inner region. Interestingly, the perturbation vanishes identically for $r > r_i$. This behaviour is specific to the $m = 1$ mode in the present approximation and is related to the ideal MHD "flat top" displacement. It is more important to note that this outer solution implies an island structure in the inner region, and (in its inner limit) determines the approximate topology, whilst the inner solution fixes the saturation conditions for a helically symmetric bifurcated state. It is clear that the present outer solution does not have a determinate Δ'.

Plainly, the correct scaling in the inner region requires that $\psi_0(r) \simeq \lambda r_i \frac{d\psi_0}{dr}$. Thus, setting $Y \equiv \frac{r-r_i}{\lambda r_i}$ and $\psi_0(r) = \psi_0(r_i) - \lambda^2 r_i^2 \psi_0''(r_i)\Psi_0^*(Y)$ (we assume explicitly that $\psi_0''(r_i) \neq 0$; this is equivalent to the generic assumption, $q'(r_i) \neq 0$), we obtain the equation satisfied by $\Psi_0^*(Y,\lambda)$:

$$\frac{d^2\Psi_0^*}{dY^2} = -\left[\frac{\frac{2B_z}{R} - \frac{E_z}{\eta(0)}}{\psi_0''(r_i)}\right] - \alpha\left[1 - \frac{1}{H(Y,\lambda)}\right] \tag{4}$$

where the relations, $\psi_0''(r_i) \equiv \left(\frac{2B_z}{R} - \frac{E_z}{\eta(0)}\right)$ and $\alpha \equiv \frac{1}{(\frac{2B_z\eta(0)}{RE_z} - 1)}$ hold. The non-dimensional resistivity profile is described by the function, $H(Y,\lambda) = \frac{\eta(Y,\lambda)}{\eta(r_i)}$. The parameter α is related to the slope of the q-profile at resonance through the equation, $\alpha = \frac{2 - r_i q'(r_i)}{r_i q'(r_i)}$. For monotonic q-profiles, the Taylor expansion co-efficients of H must satisfy, $h_2 > \alpha h_1^2$. This is equivalent to the relation $q''(r_i)^2 < 2q'(r_i)q'''(r_i)$ which must hold if the q-profile is locally monotonic near r_i. The inner limit of the outer solution takes the following form in leading (formal) order in λ (for $Y < 0$): $\Psi^*_{outer}(Y,u) = -\frac{Y^2}{2} - Y\cos u$. In Fig. 1 we have plotted this function showing the approximate topology of the inner region and the island structure implied by it. The problem of finding bifurcating solutions to the governing equations reduces to finding a function $\Psi^*(Y,u)$ which satisfies the inner limiting forms of the equations, has the correct boundary conditions imposed at $Y = 0$ and which matches with Ψ^*_{outer} as $Y \to -\infty$ in the usual sense of asymptotic matching theory. The functions $\Psi^*(Y,u), \Phi^*(Y,u)$ must satisfy the non-linear partial differential equations derived from Eqs.(1,2) in the inner limit. Thus,

$$\frac{\partial^2\Psi^*}{\partial Y^2}(Y,u) = -1 - \alpha[1 - J^*(\Psi^*)] \tag{5}$$

holds, together with the inner version of Eq.(2).

These formidable equations cannot be solved exactly, but a lengthy analysis (Thyagaraja and Haas, 1990, to be published) using the iteration scheme of Thyagaraja[1] starting with the first approximation to the island given above, leads to the following general bifurcation relation: $2\alpha \int_0^{\frac{1}{2}} \left[J_+^*(\sigma;\lambda,h_1,h_2) - 1\right] d\sigma = 1$, where J_+^* is the current density within the island and the constants h_1, h_2 are non-dimensional derivatives of the resistivity at r_i. Assuming, $\alpha \gg 1$ (ie. $r_i q'(r_i) \ll 1$) we obtain the result,

$$\frac{Islandwidth}{r_i} \equiv \lambda = \frac{\alpha^*}{2} \frac{d\log q(r_i)}{d\log \eta(r_i)} \tag{6}$$

where, α is approximated by, $\alpha \simeq \frac{2}{r_i q'(r_i)}$. The numerical constant α^* satisfies the inequality $1 < \alpha^* < \frac{3}{2}$.It follows that the island width is small compared to r_i if the conditions $h_2 > \alpha h_1^2$, $h_1 > 0$ and $\frac{d\log q(r_i)}{d\log \eta(r_i)} \ll \frac{4}{3}$ hold simultaneously. Simple examples of q profiles satisfying the required conditions are easily constructed. In Fig.2 we give a schematic sketch of such a profile. Our model can be further generalized to include the possibility that $J_+^*(\Psi^*)$ (or rather the resistivity within the island) is actually determined by solving an appropriate energy equation within the island. Making very general assumptions, it is possible to derive conditions for the existence or otherwise of bifurcated equilibria with $m = 1$ helical symmetry. We have presented the theory for the case of monotonic q-profiles with a single $q = 1$ resonant point. It is of interest to note that the analysis applies *mutatis mutandis* to non-monotonic profiles with multiple resonances when it is the outermost resonance which determines saturation.

3. Discussion: The purpose of this section is to discuss the significance and possible relevance to experiment of the analytical model presented. The solution reveals that the perturbation due to the $m = 1$ non-linear tearing mode is confined entirely within the q=1 surface ($0 < r < r_i$). Furthermore, while there is an island interior to this radius, it differs from the "symmetrical" islands for higher values of m in non-linear tearing mode theory. The saturation of the mode depends upon the properties of the mean q-profile at the resonant point, rather than globally, as is the case for higher - m tearing modes. Our theoretical results can be viewed in three ways. Firstly, they constitute a "proof of principle" model based on certain assumptions, and demonstrate the conditions necessary for an $m = 1$ neighbouring equilibrium solution of the RMHD equations. The relationship of this novel result to those of Hazeltine et al[5] and others will be discussed more fully in our forthcoming publication. Secondly, the model described could be used as an analytic test case for numerical simulations of sawtooth phenomena. Thirdly, we examine the possible relevance of our model to sawtooth phenomena observed in Tokamaks. The neighbouring equilibria found in this paper could be relevant both to sawtooth-free discharges (eg. "monsters" in JET[3]) with $q_0 < 1$, and for the ramp phase of sawteeth when q_0 is known to be less than unity [2]. Several experiments have been reported[2,3] which appear to show that generic q-profiles of the type assumed by us in this paper do exist. The measurements of Gill et al.[4] appear to suggest that the shear near the $q = 1$ resonance may indeed be rather small. Our theory shows that in the cylindrical limit the main $m = 1$ disturbance

to the equilibrium is always confined to within the $q = 1$ radius. This analytic fact is consistent with observations under sawtoothing conditions in several tokamaks, provided one accepts the effect of linear toroidal coupling to other modes as a correction. We also note that our island structure gives a simple description of the "snake" seen in JET[4]. It is of interest to remark that our theory also suggests that an increased current density within the island aids in saturation at lower island widths. This result is in qualitative agreement with the experimental results summarized by Soldner[6] on the lower hybrid stabilization of both sawteeth and the $m = 1$ indicating that only currents driven in the same sense as the Ohmic current lead to stabilization when $q(0) < 1$. Finally, it should be clear that although in principle the theory could describe the slow growth of the $m = 1$ islands, the later stages of this growth, and the crash, can only be obtained numerically. The cause of the crash itself could possibly be due to a fast, ideal instability of a finite amplitude island as suggested by Dubois and Samain[7]. Alternatively, it could be caused by a failure of equilibrium at the end of the ramp phase as suggested by Thyagaraja[1]. Further work is required to elucidate these questions.

4. References

[1] *A. Thyagaraja*, Phys. Fluids, **24**, 1716, (1981).

[2] *F.M. Levinton et al*, Phys. Rev. Letts.**61**, 2060,(1989).

[3] *D.J. Campbell et al* in Proc. 12th International Conf. on Plasma Physics and Controlled Fusion Research (International Atomic Energy Agency, Vienna, 1989), Vol. I, p. 377.

[4] *R.D. Gill et al.* Proc. 16^{th} European Conf. on Controlled Fusion and Plasma Heating, Venice (European Physical Soc. Geneva, 1989) Vol. 13B, Part II, p. 469.

[5] *R.D. Hazeltine, J.D. Meiss, and P.J. Morrison*, Phys. Fluids, **29**, 1633, (1986).

[6] *F.X. Soldner*, Proc. Seventh Topical Conf. Kissimmee, Florida (American Institute of Physics, New York, 1987) Vol. 159, p. 102.

[7] *M. Dubois and A. Samain*, Nucl. Fusion, **20**, (9),(10), 1101, (1980).

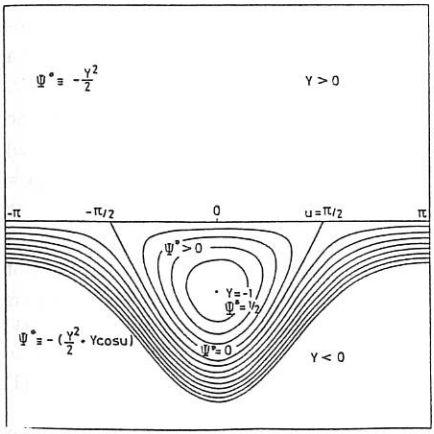

Fig.1: Approximate Island Structure

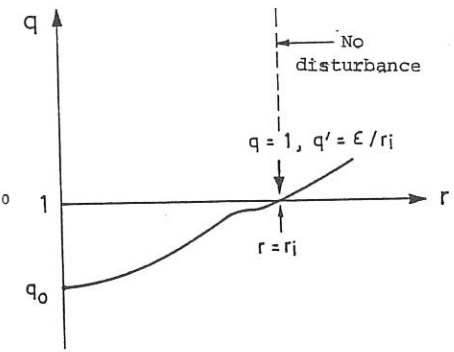

Fig.2: Schematic q-profile

LARGE GYRORADIUS m = 1 ALFVÉN MODES AND ENERGETIC PARTICLES

F. Pegoraro*, F. Porcelli, T.J. Schep+

JET Joint Undertaking, Abingdon, Oxon. OX14 3EA, UK.
*Scuola Normale Superiore, Pisa, Italy.
+FOM Instituut voor Plasmafysica, Rijnhuizen, Nieuwegein, The Netherlands.

In the large gyroradius regime, where the width of the transition layer is determined by the gyroradius of the main ions, the m=1 mode couples to a discrete spectrum of resistively damped Alfvén-type modes [1], characterized by frequencies of the order of $\omega_\rho = [\omega_{di}^2 + \frac{1}{2}(s_o\rho_i\omega_A/r_o)^2]^{1/2}$. A population of energetic ions can resonantly destabilize these modes (fish-bone oscillations). On the other hand the reactive response of the energetic ions has been shown [2] to improve the plasma stability against m=1 modes. We show that the enhanced stability found in the fluid ion regime is partly reduced in the ion kinetic regime.

We refer to the results of [3] where a detailed investigation of internal m=1 modes in the ion kinetic regime has been presented based on the analysis of resistive modes in the so-called semi-collisional regime [4]. We consider modes [1] with frequencies larger than the bulk ion diamagnetic frequency ω_{di} (m=1 Alfvén modes) and include the effect of an energetic ion population with magnetic precession frequency ω_{Dh} much larger than ω_{di}, as is the case in an ignited plasma. We are interested in plasma regimes such that $\varepsilon_\eta^{1/3} < \rho_i/r_o < \omega_{Dh}/\omega_A$, where $\rho_i = c(T_i m_i)^{1/2}/eB$, r_o is the radius of the q=1 surface, ε_η is the inverse magnetic Reynolds' number, $\omega_A = V_A/(R_o\sqrt{3})$, $V_A = (B^2/4\pi\rho_m)^{1/2}$, ρ_m is the mass density and R_o is the torus major radius.

Inside the transition layer around $r=r_o$ resistivity and parallel compressibility are taken into account in the electron response, and the ion response is calculated to all orders in the ion gyroradius. The plasma response in the ideal region outside the transition layer is represented by a single parameter denoted by λ_H [5], proportional to the negative of the energy functional δW. The modification of this response due to the energetic ion population is accounted for by the substitution $\lambda_H \to \lambda_{HK} \equiv \lambda_H + \lambda_K(\omega)$. For an isotropic distribution the complex function $\lambda_K(\omega)$ can be written as [2] $\lambda_K(\omega) = (\varepsilon_o^{3/2}\beta_{ph}/s_o)\Lambda_K(\omega)$, where $\varepsilon_o = r_o/R_o$, $s_o = r_o(dq/dr)_{r_o}$, $\beta_{ph} = -8\pi B_p^{-2}(r_o)\int_o^1 dx\, x^{3/2}\, dp_h/dx$, p_h is the hot particle pressure and $\Lambda_K(\omega)$ is a form factor. The real part of $\Lambda_K(\omega)$ represents the reactive response of the energetic ions and is negative (stabilizing) for lower frequencies and positive for higher frequencies. The imaginary part of $\Lambda_K(\omega)$ represents the velocity dependent resonant interaction with the precessing energetic ions and is negative (destabilizing) for $\omega/\omega_{Dh} > 0$. The resulting dispersion relation has the form [1]

$$\frac{L(\lambda_{HK},\omega) + iF(-\nu)}{L(\lambda_{HK},\omega) + iF(\nu)} = \frac{H(\nu)}{H(-\nu)}\,(i/\varepsilon)^\nu\,, \qquad (1)$$

where $L(\lambda_{HK},\omega) = \omega_A[\lambda_H + \lambda_K(\omega)][\omega(\omega-\omega_{di})]^{-1/2}$ with $\omega_{di} = -[(c/eBrn)(dp_i/dr)]_{r_o}$, and $F(\nu)$ is defined by $iF(\nu) = 8(\frac{1}{4}-\nu^2)^{-3/2}\Gamma^2(\frac{5}{4}+\frac{1}{2}\nu)/\Gamma^2(-\frac{1}{4}+\frac{1}{2}\nu)$ with $\nu^2 = (\omega_\rho^2-\omega^2)/2(\rho_i s_o\omega_A/r_o)^2$.

The electron and ion temperatures are taken to be equal. In the right-hand side of Eq. (1), $H(\nu) = 2^{\nu}\Gamma^2(\nu)\Gamma^2(\frac{5}{4} - \frac{1}{2}\nu)$, and

$$\varepsilon(\omega) = \varepsilon_\eta\,(\omega^2 - \omega_{di}^2)\,[4\omega\,\omega_A(s_o\rho_i/r_o)^4]^{-1}\,, \tag{2}$$

with $\varepsilon_\eta = \eta s_o^2 c^2/(4\pi r_o^2\omega_A)$ the inverse magnetic Reynolds' number, and η the parallel resistivity. In the semi-collisional regime under consideration, $|\varepsilon| << 1$.
For ion modes with real frequencies in the range $\omega_{di} \le \omega \le \omega_\rho$, we have $0 \le \nu \le \frac{1}{2}$. In this range $F(\nu)$ is purely imaginary. For larger real frequencies ν becomes imaginary and $F(\nu)$ is complex, while for purely growing modes, $\nu^2 > \frac{1}{4}$ and $F(\nu)$ is real. In the limit of large frequencies, $|\nu| \to \infty$ and $F(\nu) \to 1$.

If the right-hand side of (1) is large, the dispersion equation reduces to

$$L(\lambda_{HK},\omega) = -iF(\nu)\,. \tag{3}$$

The ideal MHD growth rate, $\gamma_{mhd} \equiv \lambda_H\omega_A$, is obtained from (3) in the limit $\omega_\rho/\gamma_{mhd} \to 0$ and $\lambda_K = 0$. Due to the smallness of ε, the dispersion equation (3) is obtained from (1) for finite and positive values of Re ν (with $\nu \to -\nu$, for negative values). On these modes resistivity leads to corrections proportional to powers of ε_η. For real positive values of ν in the range $\nu < \frac{1}{2}$ and not too close to zero, marginally stable modes can be found with $\omega_{di} < \omega < \omega_\rho$ if λ_{HK} is real and larger than the negative value $\lambda_{H\,min} \equiv -2\sqrt{2}[\Gamma^2(1/4)/\Gamma^2(-1/4)][\omega_\rho(\omega_\rho + \omega_{di})]^{1/2}(\rho_i/r_o)$. These modes are destabilized by the resonant interaction with energetic ions, i.e. by Im λ_K. However, the stabilizing effect of resistivity cannot be neglected as ν approaches zero.

In the high-frequency limit in which $\nu \propto -i\omega$ the right-hand side of Eq. (1) is a fast oscillating function of the frequency. Its amplitude is finite for modes with almost real frequencies such that $\mathrm{Re}[\nu ln(16|\nu|^2/\varepsilon) + i\nu\pi/2] = 0(1)$. This balance corresponds to high-frequency Alfvén modes [3]. If this balance is not satisfied, i.e. for larger damping or growth rates and for purely oscillatory modes, the dispersion relation (3) is recovered. Modes similar to the high-frequency Alfvén type modes are also found for intermediate values of ν close to the imaginary axis and for small values of ν. For these values $H(\nu)/H(-\nu)$ is a finite quantity so that the magnitude of the right-hand side of (1) is determined by the factor $(i/\varepsilon)^\nu$ which is finite for $\mathrm{Re}(\nu ln\,\varepsilon) = 0(1)$. The MHD boundary conditions play an increasingly important role for decreasing ν because the right-hand side of Eq. (1) oscillates more slowly and all contributions to the dispersion relation become of the same order of magnitude.

We are interested in the marginal stability conditions for modes with frequencies near ω_ρ. For these frequencies ν is small and the full dispersion relation has to be considered. In order to treat these modes analytically we consider the ordering $\nu\ ln\ 1/\varepsilon = 0(1)$. With this ordering the dispersion relation (1) becomes

$$\frac{x - \bar{\nu}}{x + \bar{\nu}} = (1 + \bar{\alpha}_1\bar{\nu})\exp[\bar{\nu}(1 + i\bar{\alpha}_2)]\,, \tag{4}$$

where we have used the variables $x = [(L(\lambda_{HK},\omega_\rho) + iF(0))/iF'(0)]ln(1/\varepsilon)$, $\bar{\nu} = \nu\, ln(1/\varepsilon)$, $\bar{\alpha}_1 = \alpha/ln(1/\varepsilon)$, $\bar{\alpha}_2 = (\pi/2)/ln(1/\varepsilon)$, ε is evaluated at $\omega = \omega_\rho$ and $\alpha = 2[ln2 + 2\psi(1) - \psi(5/4)]$. In the absence of energetic ions $L(\lambda_{HK},\omega_\rho)$ is real. To leading order in $(ln\ 1/\varepsilon)^{-1}$, Eq. (4) gives, for fixed real x, a discrete spectrum of m=1 Alfvén modes with frequencies $\mathrm{Re}\,\omega = \omega_\rho + O[(ln\ 1/\varepsilon)^{-2}]$, that accumulate at $\omega = \omega_\rho$, and $\mathrm{Im}\,\omega = O[(ln\ 1/\varepsilon)^{-3}]$. This spectrum of damped modes is destabilized by the resonant interaction with the energetic ions. According to (4) the marginal stability curve is a spiral in the complex x-plane. The radius of the spiral is very large on the normalized x-scale due to modes with $\bar{\nu} \simeq -2n\pi i$. This implies that along the marginal stability curve $\mathrm{Re}\,\lambda_{HK}$ and $\mathrm{Im}\,\lambda_{HK}$ undergo excursions that are of order one and are independent of resistivity to leading order in $1/ln(1/\varepsilon)$. Thus the relevant zero resistivity limit is obtained by first setting the mode growth rate equal to zero and by taking subsequently the limit of vanishing resistivity.

For realistic values of the magnetic Reynolds' number, $ln\ (1/\varepsilon)$ is large but still finite so that the dispersion relation (1) has to be solved numerically. The resulting marginal stability curve is shown in Fig. 1 in the complex λ_{HK} plane for $\omega_{di}/\omega_{Dh} = 0.07$, $\omega_\rho/\omega_{Dh} = 0.12$ and $\omega_\rho/(\omega_A \varepsilon_\eta^{1/3}) = 8.5$, corresponding to $\varepsilon(\omega=\omega_\rho) \simeq 1.5\times10^{-4}$. This marginal stability curve translates into the solid curve in the $(\hat{\gamma}_{mhd}, \hat{\beta}_{ph})$-plane of Fig. 2, where $\hat{\gamma}_{mhd} \equiv \gamma_{mhd}/\omega_{Dh}$ and $\hat{\beta}_{ph} \equiv (\varepsilon_o^{3/2}\beta_{ph}/s_o)\omega_A/\omega_{Dh}$. The latter curve starts for ω near ω_{di}, where $\nu \sim \frac{1}{2}$. For these frequencies $F(\nu) \to 0$ and resistivity plays an essential role leading to semi-collisional tearing and resistive m=1 internal modes as discussed in [3] and [4]. The stable domain lies below and to the left of the solid line of Fig. 2. For unrealistic low values of ε_η, the spiral curve will extend to negative values of $\hat{\gamma}_{mhd}$ at small values of $\hat{\beta}_{ph}$. Inside the loops more than one mode can be unstable with $\mathrm{Re}\,\omega \simeq \omega_\rho$, while elsewhere only one mode with $\omega_{Dh} \gtrsim \mathrm{Re}\,\omega \gtrsim \omega_\rho$ is unstable. The boundary of the stable domain at large $\hat{\beta}_{ph}$ corresponds to large negative values of $\nu^2(\omega \sim \omega_{Dh})$ and therefore depends very weakly on resistivity. On the other hand, the portion of the boundary at low values of $\hat{\beta}_{ph}$ (not drawn in Fig. 2), beyond the point where the solid curve in the figure starts, is determined by modes with $\mathrm{Re}\,\omega \lesssim \omega_{di}$. This frequency range has been studied with the two-fluid model for the plasma bulk [2] and leads to the threshold indicated by the part of the dashed line adjoining $\hat{\beta}_{ph} = 0$ in Fig. 2. This line intercepts a second dashed curve corresponding to the two-fluid marginal stability at higher frequency ($\omega > \omega_{di}$). We expect a similar stability boundary for $\mathrm{Re}\,\omega < \omega_{di}$ in the main-ion kinetic regime. In fact, in this regime, similarly to the two-fluid case, the growth rates in the absence of energetic ions scale as a linear power of resistivity [3] at sufficiently large diamagnetic frequencies $\omega_{di}/(\omega_A \varepsilon_\eta^{1/3}) > (\rho_i/(r_o \varepsilon_\eta^{1/3}))^{4/7}$. The dotted curve in Fig. 2 corresponds to marginal stability from Eq. (3) for $\omega_{di}/\omega_{Dh} = 0.07$, $\omega_\rho/\omega_{Dh} = 0.12$, $\varepsilon_\eta = 0$ and growth rate $\gamma/\omega_\rho \to 0$.

In conclusion we have shown that modes with frequencies in the ω_ρ range exist as localised modes in the presence of resistivity, even for negative values of λ_H. The resistive damping of these modes is relatively strong in that case and, being proportional to $(ln\ 1/\varepsilon)^{-3}$, is weakly dependent on the value of the magnetic Reynolds' number. Thus, for realistic parameters unstable fishbone oscillations do not occur for negative values of λ_H. Nonetheless, the new frequency ω_ρ ensures the existence of a low frequency fishbone regime even when ω_{di} is

negligible, as the mode remains oscillatory and therefore subject to a resonance with the energetic ion motion. For the lower values of $\hat{\beta}_{ph}$ the enhanced stability as found in the fluid regime is partly reduced in the ion-kinetic regime. For modes with frequencies $\omega > \omega_\rho$ the stability boundary obtained in the large gyroradius regime does not differ significantly from that obtained from a two-fluid approach [2], provided $\rho_i/r_o << \omega_{Dh}/\varepsilon_o\, \omega_A$. In particular, the two boundaries practically coincide for modes with $\omega \sim \omega_{Dh}$.

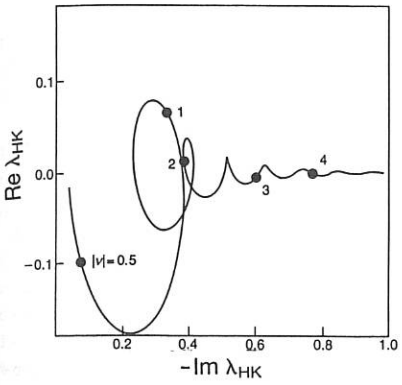

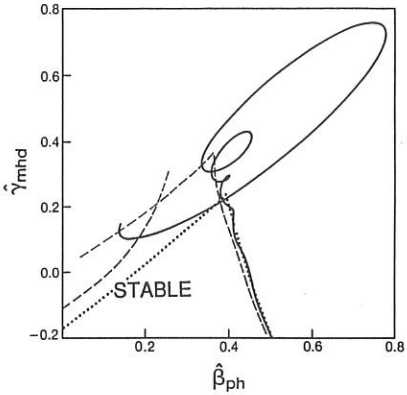

Fig. 1. Re λ_{HK} versus Im λ_K along the marginal stability curve for the following parameter values: $\omega_{di}/\omega_{Dh} = 0.07$; $\omega_\rho/\omega_{Dh} = 0.12$ and $\omega_\rho/(\omega_A\, \varepsilon_\eta^{1/3}) = 8.5$ corresponding to $\varepsilon(\omega_\rho) \simeq 1.5\times10^{-4}$.

Fig. 2. Marginal stability curves in the $(\hat{\gamma}_{mhd}, \hat{\beta}_{ph})$-plane. The solid line corresponds to marginal stability from the dispersion relation (1) for Re $\omega > \omega_{di}$. The stable domain lies below and to the left of this line. Parameter values are the same as in Fig. 1. The dotted curve corresponds to marginal stability from Eq. (4) for $\omega_{di}/\omega_{Dh} = 0.07$, $\omega_\rho/\omega_{Dh} = 0.12$, $\varepsilon_\eta \equiv 0$ and growth rate $\omega_\rho \to 0$. The dashed curves correspond to the fluid limit of Ref. [2], with $\omega_{di}/\omega_{Dh} = 0.07$.

[1] F. Pegoraro, F. Porcelli and T.J. Schep, Report JET-P(90)13, submitted to Phys. Fluids.
[2] B. Coppi, P. Detragiache, S. Migliuoli, F. Pegoraro and F. Porcelli, Phys. Rev. Lett. **63** (1989) 2733; B. Coppi, S. Migliuoli, F. Pegoraro and F. Porcelli, Phys. Fluids, in press.
[3] F. Pegoraro, F. Porcelli and T.J. Schep, Phys. Fluids **B1** (1989) 364.
[4] F. Pegoraro, T.J. Schep, Plasma Phys. Contr. Fusion **28** (1986) 647.
[5] B. Coppi, R. Galvão, R. Pellat, M.N. Rosenbluth and P. Rutherford, Fiz. Plazmy **6** (1976) 961 [Sov. J. Plasma Phys. **2** (1976) 533].

TEARING MODES IN HIGH-S PLASMAS

A. VOGE

Institut für theor. Physik IV, Ruhr-Universität, D-4630 Bochum 1, FRG

Abstract

I Introduction

The behaviour of tearing instabilities in plasmas with large magnetic Reynold-numbers ($S \approx 10^8$) is analysed. Being primilary interested in basical physical effects we restricted our analysis to two-dimensional plane geometries, although the sawtooth-crash is addressed. The central point of our work is the investigation of the dynamics near the neutral sheet *prior to the onset of a tearing instability.* Here we found that the profile of the current density developes toward structures that fundamentally differ from those of the starting equilibrium and that these structures are finally dominated by a singular current sheet at the neutral line (in the limit of vanishing resistivity). We further point out that these dynamics are not necessarily due to an instability and consequently will occure even if the equilibrium is stable. In section II we describe these structures and the concerning dynamics. In section III we discuss the consequences for the tearing instability.

II Description of the current density profiles

We carried out numerical simulations of an initially perturbed Harris-sheet. Being interested in high-S plasmas ($S \approx 10^8$) we used IMHD as long as reconnection can be excluded and switched on resistivity later. (Assumeing ideality for the first part of the evolution seems to be reasonable because the diffusion time- scale is widely seperated from the Alfvén time-scale for the parameter ranges of interest. Furthermore (in view of tokamak applications) this procedure simulates the stability against tearing instabilities during the ramp phase.) Fig.1 shows the central current density profile at t=250 (in units of Alfvén times). The equilibrium profile was $j_z = (\cosh z)^{-2}$. The energy of the perturbation was 6 orders of magnitude smaller than the total energy of the system. Nontheless the energy of the perturbation is the only energy source of the dynamics so that there is no contradiction to the (ideal) stability of the Harris-sheet. This can be seen by calculating the energy of the perturbation and comparing it with the kinetic energy related to the dynamics. The simulations further show, that the distance between the sheets decreases in time. (A quite similair (linear) problem has been

investigated analytically by *Hahm and Kulsrud* who predicted structures as shown in Fig.1. Although they considered the process to be externally driven by appropiate boundary conditions it can be easily shown that the kinetic energy in their solution decays as $1/t^2$ so that the driving energy can be replaced by an initial perturbation because they did not solve the boundary-value problem but only calculated an approximate solution for the inner region.)

III Application to tearing modes

Looking at Fig.1 it is obivious that the shown structures are likely to change the growth rate of a tearing instability fundamentally. There are two aspects that have to be discussed in this context:

1. The width of the current sheet decreases dramatically. Although the common theory of tearing instabilities does not apply to complicated structures as shown in Fig.1 it seems reasonable to assume an enhanced growth rate due to this effect.

2. The configuration is characterized by parallel current sheets that move toward the neutral line. We modelled this situation by a current density that consits from an infinite number of aequidistant δ - distributions, all of them carrying the same current density in altering direction and calculated the growth rate as a function of the distance between two sheets (using a procedure of *Otto, Birk and Jamitzky*.) Fig.2 shows the result for k=0.1 and $S = 10^8$. It is clearly seen, that the growth rate becomes highly sensitive to the distance of the sheet at small distances.

Both these points indicate that the spontaneous formation of current sheets in highly conducting plasmas may be an important effect to explain the growth rates of tearing modes connected with the sawtooth crash. Calculations in more realistic geometries are required for a quantitative test of this model.

Figure captions

Fig.1 The central current density of a pertubed Harris-sheet at t=250.

Fig.2 The groth rate of a tearing instability in a system of parallel current sheets as a function of the distance of the sheets.

References

1.Hahm and Kulsrud, Phys.Fluids 28 (1985) 2412

2.Otto,Birk and Jamitzky, to be published

FIG. 1

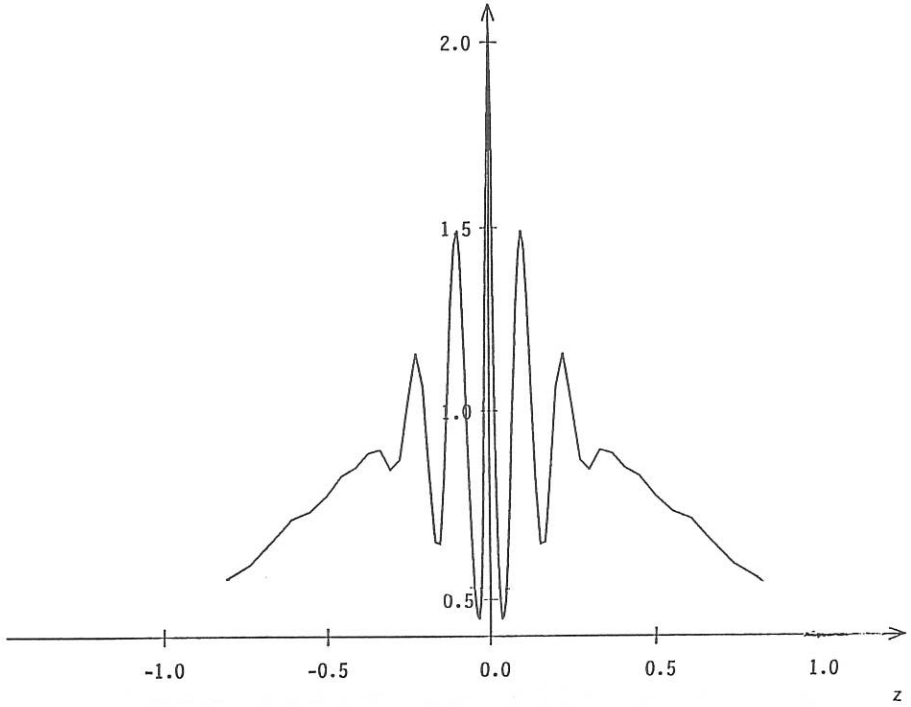

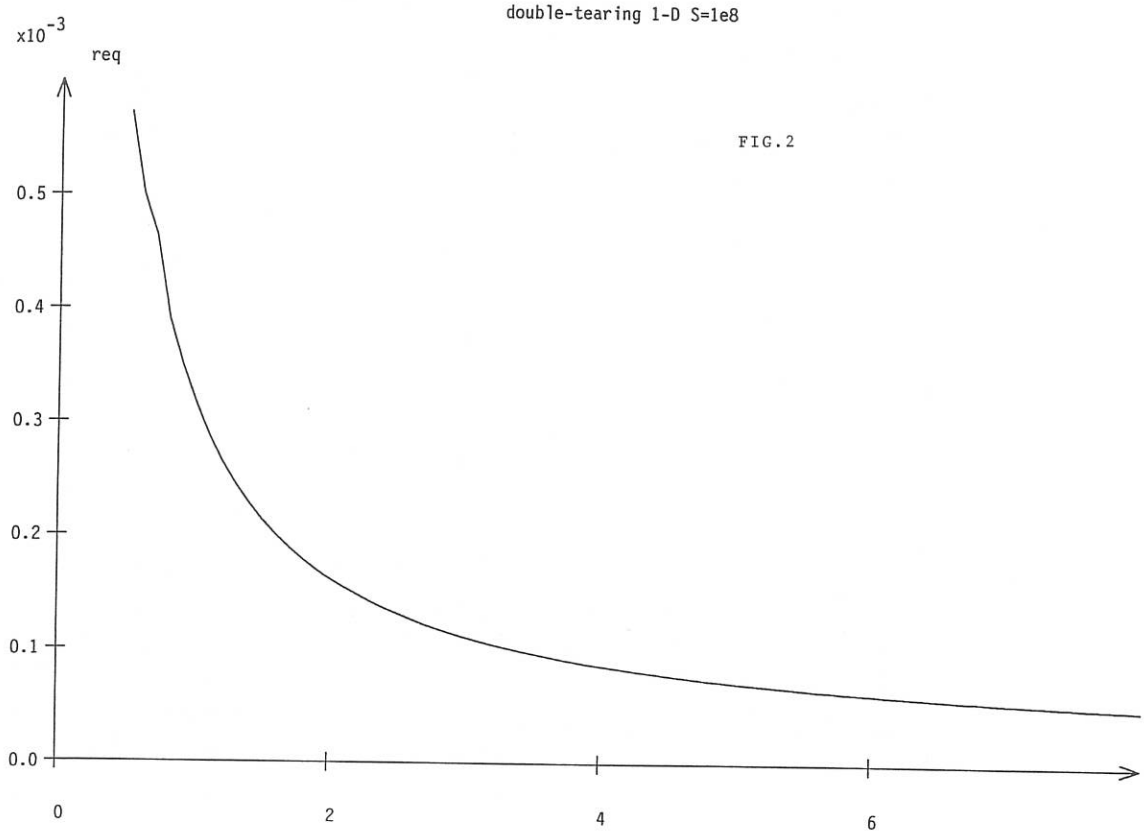

FIG.2

INFLUENCE OF TRIANGULARITY AND PROFILES ON IDEAL-MHD BETA LIMITS FOR NET

G. Schultz, A. Bondeson, F. Troyon, and A. Roy

Centre de Recherches en Physique des Plasmas
Association Euratom - Confédération Suisse
Ecole Polytechnique Fédérale de Lausanne
Av. des Bains, CH-1007 Lausanne, Switzerland

1. INTRODUCTION Ideal-MHD stability calculations are presented to show the effect of triangularity δ on the beta-limit for plasmas of NET/ITER type with ellipticity $\kappa = 2$ and aspect ratio $A = 3.7$. The optimum betas are achieved as a tradeoff between n=1 ideal kink stability and stability against Mercier and ballooning ($n=\infty$) modes. Two different types of beta-optimisations have been made to study the influence of equilibrium profiles.

In one set of optimisations, the *current* profile is prescribed and the pressure profile is optimised. We impose current profiles that are flat in the central region and decrease monotonically to zero at the edge. For such current profiles, maximum beta is obtained for broad pressure profiles, in particular, for low q_s and small triangularity. The beta-limit is independent of triangularity up to $\delta = 0.4$, but increases slightly for high triangularity, $\delta = 0.6$.

In the other set of optimisations, we specify a more *peaked pressure* profile and optimise the current profile. Peaked pressure profiles, when combined with standard current profiles, for which the central q is flat and near unity, tend to be unstable to localised, pressure driven modes. Therefore, careful tailoring of the central current profile is required. After optimisation of the current profile the n=1 and $n = \infty$ modes give a beta-limit for peaked pressure profiles that is almost unchanged from that for broad profiles, if the cross-section is *sufficiently triangular*, $\delta \geq 0.4$. By contrast, in an *elliptical* cross-section, $\delta = 0.0$, the maximum beta decreases significantly for the peaked profiles.

2. CENTRALLY FLAT CURRENT, OPTIMISED PRESSURE Here we have fixed the profile for the surface averaged toroidal current: it is flat in the central region, zero at the edge, and a cubic polynomial in between with zero derivative at the end points. The pressure profile is optimised. The safety factor at the edge q_s has been varied from 2 to 6.5 and four values of triangularity have been considered: $\delta = 0.0$, 0.2, 0.4, and 0.6. The beta-limit is rather insensitive to q_0 ($1.02 < q_0 < 1.12$) and we give results for only one value, $q_0 = 1.07$. Figure 1 shows β_{max} as a function of the normalised current, I_N.

Figure 1 shows that, for the broad profiles, the beta-limit is almost independent of triangularity for $0 \leq \delta \leq 0.4$, where $\beta_{max} \approx 4.6$ %. A certain gain results from increasing δ to 0.6, which gives $\beta_{max} \approx 5.6$%. However, triangularity has a stronger effect on the maximum normalised current $I_N = \mu_0 I/aB_0$, which increases from about 2.35 at $\delta = 0$ to about 3 at $\delta = 0.6$. As a consequence, $g = \beta_{max}/I_N$ decreases with triangularity. With q_0 held fixed at 1.07, the beta-limit is usually set by ballooning/Mercier modes, except for large triangularity and high current $q_s < 3$, where the limit is set by the n = 1 kink mode.

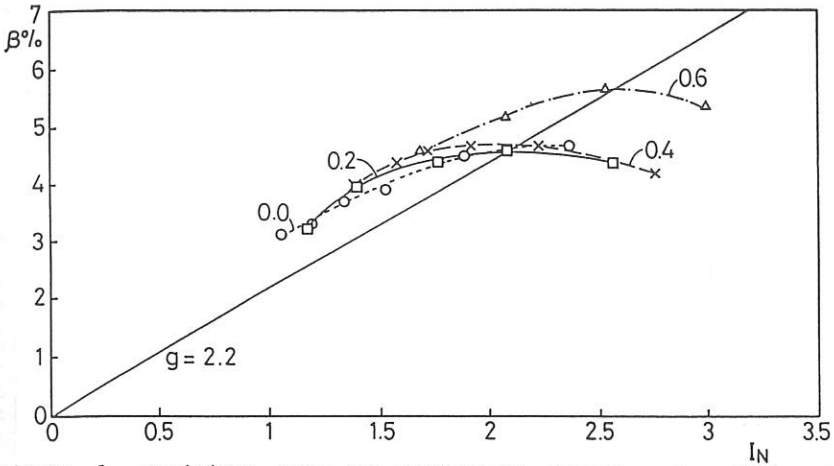

Figure 1. Optimised beta vs normalised current, for different triangularities. The straight line shown is $g = \beta/I_N = 2.2$.

β_{max} does not degrade significantly for $q_s < 3$. Such degradation as well as the so-called ravines in β_{max} for q_s just below integer values have been reported in other studies[2], in which $\langle J_\phi \rangle$ was not kept sufficiently small at the edge. With our choice for $\langle J_\phi \rangle$ which goes quadratically to zero at the edge, such ravines do not occur.

3. PEAKED PRESSURE PROFILES Pressure profiles observed in most tokamaks are more peaked than those found to give the highest beta in ideal-MHD stability studies. Therefore, we have studied the beta-limit for a prescribed peaked pressure profile where $dp/dr \approx$ constant for $|r-R| > 0.1a$. (r is the major radius in the mid-plane z=0, and R is the major radius of the magnetic axis.)

To test the sensitivity of the results to the choice of current profile, we have applied two different classes of current profiles with the peaked pressure profile, corresponding to two different strategies for improving Mercier stability in the central region. The first class of profiles have a rounded step in the current density near the centre and, outside this step, a monotonically decaying $\langle J_\phi \rangle$ to increase the shear. The second class has a reduced central current density or, equivalently, an increased q_0. For both these types of current profiles, the cases with $\delta \geq 0.4$ give beta-limits for $n = 1$ and $n = \infty$ stability close to those for the broad pressure profile. For small triangularity, $\delta = 0.2$, and even more so for $\delta = 0.0$, the beta-limit for strongly peaked pressure is substantially lower than for the broad profiles.

Figure 2 shows the beta-limits for strongly peaked pressure, obtained with the high-shear current profile and q_0 held fixed at 1.02. For high triangularity, there are relatively minor differences from the results obtained for the broad profiles. Notably, β_{max} for $\delta = 0.6$ drops slightly from 5.6 % to 5.1 %, while for $\delta = 0.4$, the peaked pressure plus optimised current profile even improves the maximum beta from about 4.6% to 5.2 %. Figure 2 shows that beta as a function of current is almost the

same for δ = 0.4 and δ = 0.6. The two curves in Fig. (2) show broad maxima of $\beta_{max} \approx 5.1$ % at $I_N \approx 2.2$, where q_s is about 3.1 and 3.7, respectively. For lower triangularities δ= 0.0 and 0.2 the beta-limit with peaked pressure profiles (Fig. 2) is clearly lower than for the broad profiles (Fig. 1).

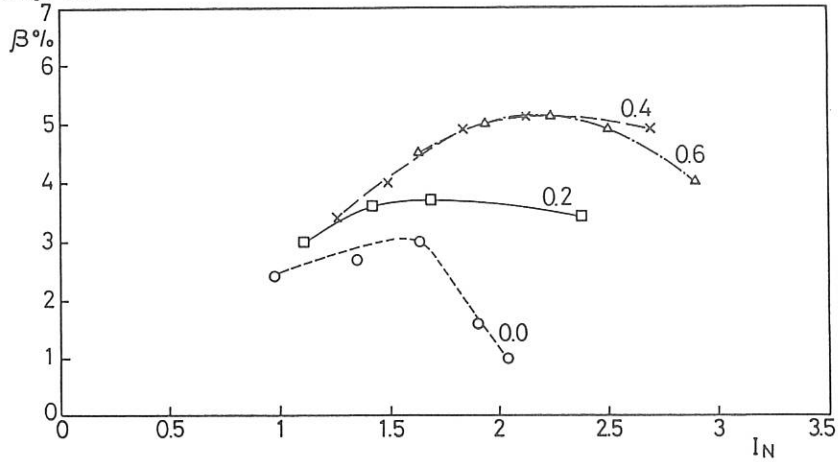

Figure 2. Optimised beta vs normalised current for different triangularities. A peaked pressure profile is prescribed and the current profile has been optimised, using a central step

To indicate what current profiles are required to give sufficient central shear for a strongly peaked pressure profile and q_0 = 1.02, we show in Fig. 3 optimised equilibria with (a) δ = 0.6, q_s = 3.65 and (b) δ = 0.0, q_s = 3.31. The height of the step is about 10 % for the triangular

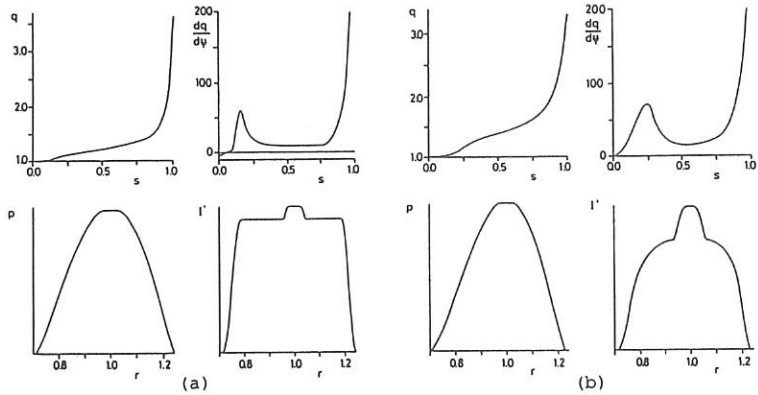

Figure 3. Equilibria with strongly peaked pressure profile and optimised, high-shear current profile. In (a) δ= 0.6, q_s= 3.65, β= 5.2%, β*= 6.5%, β_0= 14.7%, and l_i= 0.58. In (b) δ= 0.0, q_s= 3.31, β= 2.9%, β*= 3.6%, β_0= 8.0%, and l_i= 0.72.

equilibrium and 30 % for the ellipse. As expected, triangularity reduces the amount of shear needed for Mercier stability in the centre. The optimal height of the step increases with q_s.

Stability to n =1 and n = ∞ modes can also be achieved, even for a centrally flat current distribution, by increasing q_0. The resulting beta-limit for high triangularity δ = 0.4 and 0.6 is very similar to that of the high-shear current profile (Fig. 2). For small triangularity, δ = 0.2 and 0.0, the limit is inferior to that in Fig. 2. For the optimised equilibria with raised q_0, q_0 increases with q_s and decreases with triangularity from 1.02 at q_s = 2.0 for δ = 0.6, to 1.57 at q_s = 6.5 for δ = 0.0. The highest beta is reached for δ = 0.4, where β = 5.4%, β^* = 6.8%, and β_0 = 15.0%.

An important difference between the high-shear equilibria and those with a raised q_0 lies in the stability to intermediate-n modes. We have made spot checks of the n = 2, 3, and 4 stability of the two sets of equilibria with peaked pressure profile, optimised for n =1 and n = ∞ stability. We find that, whereas the the high-shear profiles are generally stable, the low-shear profiles with a raised q_0 tend to be unstable to the so-called infernal modes[3]. However, it appears that the beta-limit set by infernal modes for these profiles is only slightly lower than the n = 1, n = ∞ limit.

In summary, optimisations with prescribed, *peaked* pressure profiles show clearly advantageous effects of triangularity, and for $\delta \geq 0.4$, high beta can still be confined by an optimised current profile. For the strongly peaked pressure profile, we find a maximum beta of about 5.1 % both for δ = 0.4 and δ = 0.6, with β^* = 6.4 % and a central beta β_0 = 14.5 %. For the ellipse, these values are considerably lower, β_{max}= 3.0%, β^*= 3.7% and β_0= 8.3%.

4. CONCLUSION The main conclusions of the present study are easy to formulate. For *broad* pressure profiles, triangularity has little effect on the beta-limit. For *peaked* pressure profiles, triangularity has a clear positive effect, and $\delta \geq 0.4$ is highly favourable. To confine strongly peaked pressure profiles with high beta, the q-profile must have sufficient shear in the central region for local stability. The necessary central current gradients decrease with increasing triangularity. The current profiles for highly triangular cross-sections with $q_0 \geq 1$ and low q_s are considerably flatter than those maintained at steady-state in ohmic discharges, and will require non-inductive current drive.

ACKNOWLEDGEMENT This work was supported by NET under contract 310/88-7 FU CH NET and by the Swiss National Science Foundation.

REFERENCES

[1] TROYON, F., GRUBER, R., SAURENMANN, H., SEMENZATO, S., SUCCI, S., Plasma Phys. Controlled Fusion **26** (1984) 209.
[2] PHILLIPS, M.W., TODD, A.M.M., HUGHES, M.H., MANICKAM, J., JOHNSON, J.L., PARKER, R.R., Nucl. Fusion, **28** (1988) 1499.
[3] MANICKAM, J., POMPHREY, N., TODD, A.M.M., Nucl. Fusion **27** (1987) 1461

INFLUENCE OF AN X-POINT AND ITS POLOIDAL LOCATION ON THE IDEAL MHD STABILITY OF A QUASI-CIRCULAR TOKAMAK.

A.Roy and F.Troyon

Centre de Recherches en Physique des Plasmas
Association Euratom - Confédération Suisse
Ecole Polytechnique Fédérale de Lausanne
21, Av. des Bains, CH-1007 Lausanne/Switzerland

ABSTRACT

The effect of a divertor on the ideal MHD stability of a quasi-circular single-null tokamak is investigated. Five different poloidal positions of the X-point are studied (inside and outside the torus, on the top of the section and two intermediate positions), and compared to an equivalent reference circular case. For low β plasmas, we compute the current limit imposed by the n=1 kink. The stable operating window, in the (q_o,q_{cyl}) plane, is also determined. The lower bound on q_{cyl} is found to be ~1.2 for the divertor configuration. Then the β-limit at different values of the total current is considered. The maximum value of β set by the n=1 mode is comparable for each configuration, except when the X-point points upwards, in which case the maximum is roughly doubled. The results of the ballooning optimization are also presented for the five divertor configurations and for the reference circular case.

1. Introduction.

Experimental results and β optimization studies show that ideal MHD stability imposes a limit on the value of β in tokamaks. Theoretically it was found [1] that the critical β is proportional to the normalized current: $\beta_c=g\, I_N$, with $I_N=\mu_o I(A)/a(m)B(T)$ and $a=(r_{max}-r_{min})/2$, where r_{max} and r_{min} are the maximum and the minimum distance of the plasma surface to the torus axis. Only limiter configurations have been considered. The object of this work is to extend these results to divertor configurations which offer the possibility of reaching a high confinement regime [2].

The most dangerous instabilities are the n=1 free-boundary kink and the ballooning modes, imposing a limit on β, β_k and β_b respectively. The n=1 kink also restricts the total current at low β. The influence of an X-point and its location has already been studied in the case of ballooning modes [3], and Ozeki et al. [4] have computed the axisymmetric stability of divertor configurations for the JT-60 tokamak. They have also investigated the n=1 stability of some cases at low and high β. Our approach is similar to theirs in the sense that the equilibria we are using with ERATO have as plasma boundary, a flux surface just inside the separatrix, but in our study the safety factor at the edge q_s is always kept high (>4-6) and is not a relevant parameter. Only single-null and quasi-circular cross-sections are considered. The angle between the horizontal and the X-point is α_o, $\alpha_o=0$ meaning that it points outward the torus. With $\alpha_o=\pi$ the inverse aspect ratio ε is 0.274, ε being defined as follows: $\varepsilon=(r_{max}-r_{min})/(r_{max}+r_{min})$. The area of the cross-section, normalized to $(R_c)^2=((r_{max}+r_{min})/2)^2$, is always kept constant, and with $\alpha_o=3\pi/4$(fig.1), $\pi/2$, $\pi/4$, 0 the values of ε are 0.2261, 0.2124, 0.2261, 0.274. The reference circular case with the same area has ε=0.2273. An equilibrium is computed by specifying the pressure gradient $P'(\psi)$ and the surface average current density $J(\psi)$ in two sections:

a) Between the edge and the flux surface where $\psi/\psi_s=a_J$, P' and J are cubic functions of (ψ/ψ_s)

with zero derivative at both ends; $J(\psi=\psi_s)=0$ and $P'(\psi=a_J\,\psi_s)=0$. P' is therefore maximum at $\psi=\psi_s$ (ψ is the poloïdal flux and ψ_s its value at the edge).

b) P'=0 and J constant between $\psi=a_J\,\psi_s$ and the magnetic axis. a_J is determined by the total current I_N and the value of q_o. If $a_J=0$ and q_o is still too high, the derivative of J on the axis is adjusted.

2. Low β stability.

The operating space at low β has been determined for six configurations: the reference circular case, $\alpha_o=\pi$, $3\pi/4$, $\pi/2$, $\pi/4$ and 0. We are looking for the domain in the (q_o, q_{cyl}) plane, where the equilibria are stable to the n=1 free-boundary kink (q_o is always larger than 1). The results of the circular case is well-known; the stable window is limited by $q_s>2$, which corresponds here to $q_{cyl}>1.93$. At a given value of q_{cyl}, the highest q_o is constrained by the fact that one singular surface is necessary and sufficient to have stability. With an X-point the lower limit on q_{cyl} is now about 1.2. At constant current the highest stable q_o value is always obtained with a J profile having $a_J=0.75$-0.8. The operational diagram obtained with $\alpha_o=3\pi/4$ is shown on fig.2, and with other α_o the stable domain has the same shape. Table 1 shows the minimum value of q_{cyl} and the corresponding current limit ($q_o\simeq1$) for the six configurations considered. The current limit indicated in the last column is computed for B=1.5T and R_c=0.875m. Notice that the divertor configurations can carry a total current about 50% higher than the circular case.

α_o	q_{cyl} min.	I_N max.	I_{phys}(kA) max.
π	1.28	0.880	252
$3\pi/4$	1.26	1.128	267
$\pi/2$	1.19	1.295	287
$\pi/4$	1.25	1.125	266
0	1.24	0.942	270
circ.	1.93	0.737	175

Table1: Current and q_{cyl} limits.

3. β-limit imposed by the n=1 free-boundary kink.

β_k has been computed for the reference circular case and for the divertor configurations. Fig.3 shows the result when $\alpha_o=3\pi/4$, fig.4 when $\alpha_o=\pi/2$ and the six curves of β_k vs. I_N are superposed in fig.5. When $\alpha_o=\pi/2$ (fig.4), β_k is strongly enhanced, reaching a maximum value which is roughly twic that for other positions of the X-point. The g factor ($\beta_k=gI_N$) is larger than that for the reference circular case if $\alpha_o\geq\pi/2$ and lower if $\alpha_o<\pi/2$. For all the divertor cases (except $\alpha_o=\pi/2$), in contrast to the circular cross-section, β_k varies little over a wide range of current.

In order to clarify the dependence of β_k on α_o, additional runs have been made around $\alpha_o=\pi/2$, for a fixed value of the current $I_N=0.84$. The results are on fig.6, where we see that β_k is peaked around $\alpha_o=\pi/2$. In all cross-sections, when β increases, the poloidal field B_p is reinforced outside the torus and weakened inside. For $\alpha_o=\pi$, this increases further the shear in the peripheral region, already large because of the X-point. But for $\alpha_o=0$, this effect reduces the shear at the edge. For $\alpha_o=\pi/2$ there are two poloidal locations where B_p is weak and this seems to be stabilizing.

4. β-limit imposed by ballooning modes.

For a given J profile, β_b is computed by optimizing the pressure gradient on each surface [5]. q_o is kept around 1 as for the computation of β_k and therefore the second stability regime is not accessible [6]. With $\alpha_o=\pi/2$ (fig.4), β_b is lower than β_k, but for all other configurations (fig.3), including the circular one, β_b is higher. The six curves of β_b are superposed in fig.7. Nothing special at $\alpha_o=\pi/2$ is observed and if $\alpha_o\geq\pi/2$ ($\alpha_o<\pi/2$) the g factor of β_b is higher (lower) than the one of the reference circular case. When α_o is varied (fig.6) β_k and β_b do not have their maximum at the same

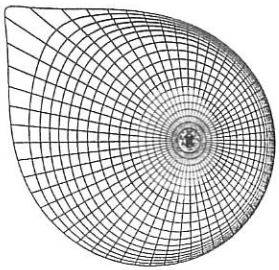

Fig.1: Divertor configuration with $\alpha_o=3\pi/4$.

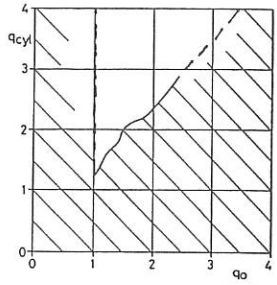

Fig.2: Operational diagram of a divertor configuration with $\alpha_o=3\pi/4$. The dashed region is unstable to the n=1 kink.

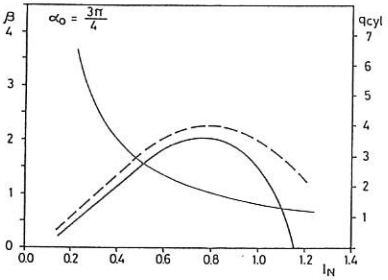

Fig.3: β_k (continuous line),β_b (broken line) and q_{cyl} (thin line) obtained with $\alpha_o=3\pi/4$.

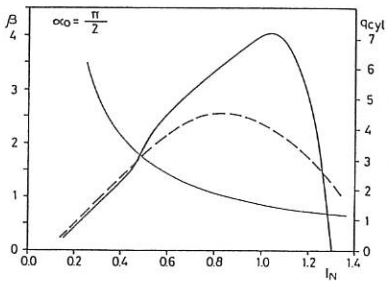

Fig.4: β_k (continuous line),β_b (broken line) and q_{cyl} (thin line) obtained with $\alpha_o=\pi/2$.

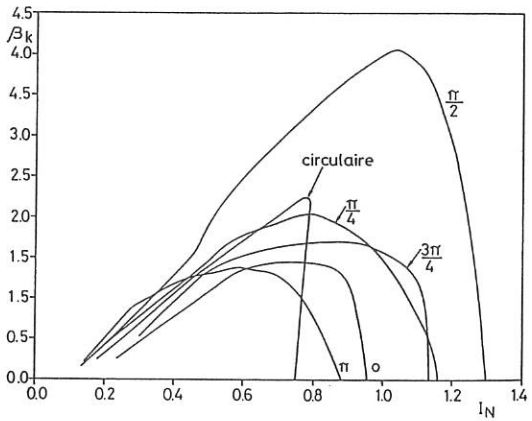

Fig.5: β_k obtained with $\alpha_o=\pi$, $3\pi/4$, $\pi/2$, $\pi/4$, 0 and a circular section.

value of α_o. For β_b the maximum is at $\alpha_o=3\pi/8$, where the poloidal extension of the bad curvature region is minimum [5]. Moreover, the X-point is in the bad curvature region for $\alpha_o<3\pi/8$. This may be the explanation of the "strange" position of the maximum of β_b.

5. Conclusion.

Adding an X-point to a quasi-circular cross-section strongly increases the current limit at low β, just as increasing elongation or triangularity. But the β limit does not follow the linear law up to the maximum current. For $\alpha_o=\pi/2$, β_k is enhanced and the β limit is set by ballooning modes. For all other five configurations the kink limit is more constraining and the g factor is larger for $\alpha_o>\pi/2$ than for $\alpha_o<\pi/2$. These results suggest that operation at high β should be possible in a wide range of current. This would favor divertor configurations over limiter ones. We are not aware of experimental results supporting these predictions.

6. References.

[1] F. Troyon et al, Plasma Phys. **26** (1984) 209.

[2] F. Wagner et al., Phys. Rev. Lett. **49** (1982) 1408.

[3] C.M. Bishop, Nucl. Fusion **26** (1986) 1063.

[4] T. Ozeki et al., Nucl. Fusion **28** (1988) 1859.

[5] A. Roy, EPF-Lausanne Thesis (1990).

[6] A. Roy, F. Troyon, in Theory of Fusion Plasmas (Proc. Workshop held at Varenna, Italy, August 1987),Editrice Compositori, Bologna (1988) p143.

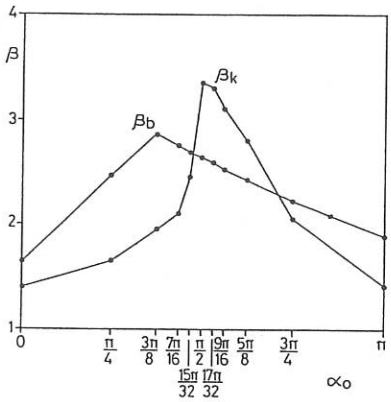

Fig.6: β_k and β_k vs. α_o at $I_N=0.84$.

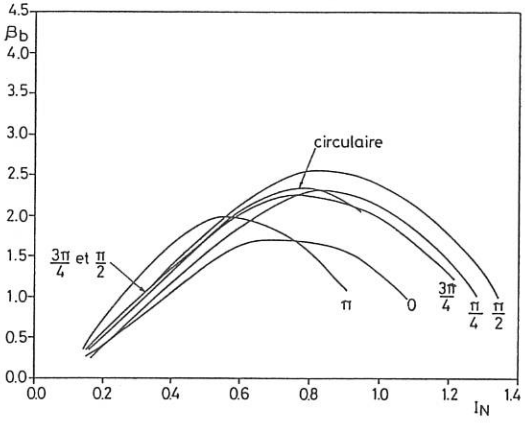

Fig.7: β_b obtained with $\alpha_o=\pi$, $3\pi/4$, $\pi/2$, $\pi/4$, 0 and a circular section.

SIMULATION OF MHD ACTIVITY DURING DENSITY LIMIT DISRUPTIONS IN JET

R. Parker, A. Bondeson, and M. Hugon*

Centre de Recherches en Physique des Plasmas, Ass. Euratom - Confédération Suisse
Ecole Polytechnique Fédérale de Lausanne
21 Av. des Bains, CH-1007 Lausanne, Switzerland

*) JET Joint Undertaking, Abingdon, Oxfordshire, United Kingdom

1. INTRODUCTION

The operation of tokamaks is limited to densities below some threshold value which, in ohmic discharges, is proportional to the plasma current. When the density limit is exceeded, the discharge usually disrupts, because the profile contracts and becomes MHD unstable when the radiation losses equal, or exceed, the input power [1,2]. (However, recent experiments performed with beryllium coating or boronisation have shown non-disruptive behaviour at the density limit.) Here, we report on a simulation study of density limit disruptions, in which radiation losses were specified according to experimental data from a disruption in JET [2]. The MHD activity was simulated by a reduced-MHD code with a simple transport model [3]. The simulations reproduce the sequence of events observed during density limit disruptions in JET, starting with m=3/n=1 activity, followed by strong growth of the m=2/n=1 mode, a sequence of minor disruptions, and finally a major disruption, in which the current profile flattens over almost the entire plasma, leading to a large drop in internal inductance, and an accompanying negative voltage spike.

It is well known that the m=2/n=1 resistive tearing mode plays a key role in the disruption process, and this is recognised by existing mode-coupling [4] and quasi-linear [5] models of disruptions, and is also very clearly seen in our simulations. However, the simulations presented here give a scenario, different from that of previous theories [4,5], for the final phase of the disruption, including the so far ill-understood phase where the current profile broadens. In our simulations, the major disruption occurs in two steps, in agreement with observations on JET [2]. First, a large fraction of the central temperature is lost in an "energy quench", which occurs as a sawtooth modified by the large amplitude 2/1 mode. At the end of the energy quench, the magnetic field in the central $q \approx 1$ region becomes stochastic because of the simultaneous presence of modes with different helicities, notably 2/1, 1/1, and 3/2. In a major disruption, good flux surfaces are never restored again, the kinetic energy of several modes continues to grow, and in the final phase, the activity is dominated by the 2/1 and a rapidly growing 3/1 mode.

2. NUMERICAL MODEL

The basic model adopted here is three-dimensional resistive reduced MHD including anisotropic heat conduction, with $\chi_\perp \ll \chi_\parallel$ [3]. The model of Ref. [3] has been upgraded by including radiation losses in the temperature evolution equation. These losses are introduced as a front moving inward from the edge of the plasma. The amplitude, width, and position of the front are prescribed as functions of time in accordance with measurements on JET [2]. Moreover, we use neoclassical resistivity [6], which gives rise to rather peaked current profiles that are strongly Δ'-stable in the absence of radiation losses. The resistivity is taken as a function of the temperature, and our model thus includes the thermal instability discussed in Ref. [7]. To make nonlinear simulation possible, it is necessary to reduce the Lundquist

number S from the very high values in JET (close to 10^9). To accomplish this, we multiply all dissipative terms (such as $\chi_\perp$, resistivity η and viscosity ν) by the same factor E, and shorten the time-scale for variation of the prescribed radiation by the same factor.

3. TIME HISTORY OF ONE RUN

In Fig. 1, we show the time-evolution during one entire run of (a) electron temperature in the centre, r=0.54a and r=0.75a, (b) internal inductance l_i and loop voltage V_l, and (c) the m=2/n=1, m=3/n=2, and m=3/n=1 components of the radial magnetic field at the wall. The enhancement factor E was 2000 in this run, 16 different m/n Fourier components were used and the radial resolution was 150 grid points. The profile for $\chi_\perp$ was adjusted to give a steady-state temperature profile (without radiation) in agreement with that of JET shot #11051, and was then kept fixed in time, and the radiation losses were prescribed according to the same shot. The radiation is turned on at time t=0, but no mode activity is observed in the simulation until $t=2000\tau_A$. At this time the radiation front has reached $q \approx 3$, and the m=3/n=1 resistive tearing mode reaches sufficient amplitude to be visible in the B_r signal (Fig. 1c). With the radiation time-scale sped up by a factor E=2000, the m=3 mode does not have time to saturate before the radiation front has moved inside the q=3 surface. It should be noted that the m=3 mode is stable, or at most marginal from a Δ' analysis, but the resistivity perturbations destabilize a mode that is partly "rippling". As the current profile contracts further, and the radiation front approaches the q=2 surface, the m=2/n=1 mode becomes unstable at $t = 2900\tau_A$. There follows a phase of several minor disruptions, during which the B_r signal at the wall reaches about 14 G. The minor disruptions are triggered by increases in the 2/1 amplitude, and disturbances leading to field stochasticity propagate inward from the q=2 surface. During each minor disruption a sawtooth-like relaxation occurs in the $q \approx 1$ region. The standard m=1/n=1 sawtooth mode is modified by the large amplitude 2/1 perturbation and involves large components m=3/n=2 and m=1/n=0, all coupled by the m=2/n=1.

4. THE MAJOR DISRUPTION

As seen from Fig. 1b, the internal inductance first rises during the contraction phase, and then drops somewhat during the minor disruptions. The final major disruption, in which l_i drops by almost unity and the current profile becomes almost flat, occurs at about $t=6200\tau_A$.In Fig. 2 we show details from such a major disruption, simulated with 25 Fourier components, to improve on numerical resolution. The major disruption involves a sequence of events, the first of which is the "energy quench". This starts similar to a sawtooth. The m=1/n=1 mode is modified by the m=2/n=1 mode, as described in Sec. 3 for the minor disruptions. Furthermore, at the beginning of the modified sawtooth, the temperature is almost flat in the centre and falls off quickly outside the $q \approx 1$ region. Figure 2a is a contour plot of the electron temperature and a Poincaré plot of the magnetic field lines during the first phase of the energy quench. The region around the original q=2 and q=3/2 surfaces is stochastic, while the $q \approx 1$ region has good flux surfaces and shows a standard q=1 reconnection pattern. The modified sawtooth has a large content of m=3/n=2 magnetic perturbation, and at the end of the reconnection, the whole central region becomes stochastic over a short time (see Fig. 2b), by the simultaneous presence of high amplitude modes of different helicities. After this, there is a partial recovery of good flux surfaces in the centre, interrupted by another event similar to that in Fig. 2b. This time, q_0 rises sharply, and the m=2 mode continues to grow. The current profile now broadens quickly under the combined action of the m=2 mode and fine-scale turbulence. When the current profile becomes sufficiently broad, the m=3/n=1 mode grows

more or less on the Alfvén time-scale, and the internal inductance rapidly falls close to 1. During this phase, the negative voltage spike appears. Figure 2c shows a cross-section of the current profile and completely stochastic magnetic fields at this time.

Acknowledgement. This work was supported by JET under contract JW8/9007 and by the Swiss National Science Foundation.

REFERENCES

1. P.H. Rebut and B.J. Greene, IAEA Berchtesgaden 1976, Vol 2, 3.
2. J.A. Wesson, R.D. Gill, M. Hugon, et al, Nucl. Fusion **29**, 641 (1989).
3. A. Bondeson, Nucl. Fusion, Nucl. Fusion **26**, 929 (1986).
4. B.V. Waddell, B. Carreras, H.R. Hicks, et al, Phys. Rev. Lett. **41**, 1386 (1978).
5. M.F. Turner and J.A. Wesson, Nucl. Fusion **22**, 1069 (1982); K.I. Hopcraft and M.F. Turner, Phys. Rev. Lett. **56**, 2372 (1986).
6. S.P. Hirshman, R.J. Hawryluk, and B. Birge, Nucl. Fusion **17**, 611 (1977).
7. P.H. Rebut and M. Hugon, IAEA London 1984, Vol 2, 197.

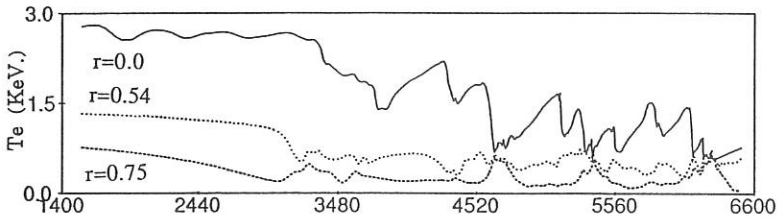

Figure1a. Time evolution of electron temperature at different radii.

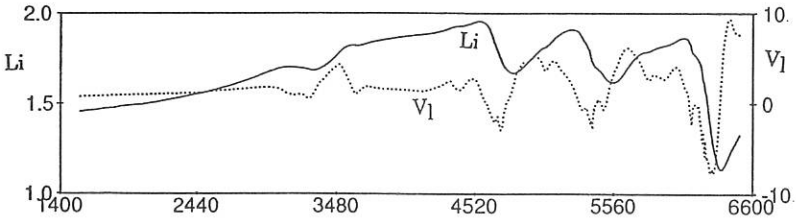

Figure 1b. Time evolution of internal inductance and loop voltage.

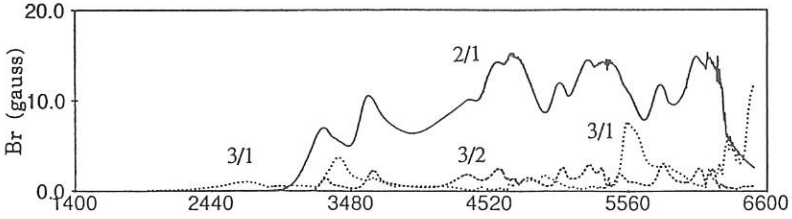

Figure 1c. Radial magnetic field at the wall; m=2/n=1, m=3/n=2, and m=3/n=1.

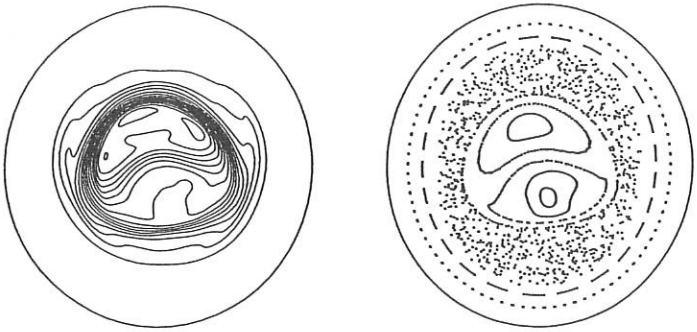

Figure 2a. Electron temperature and field lines during first stage of energy quench.

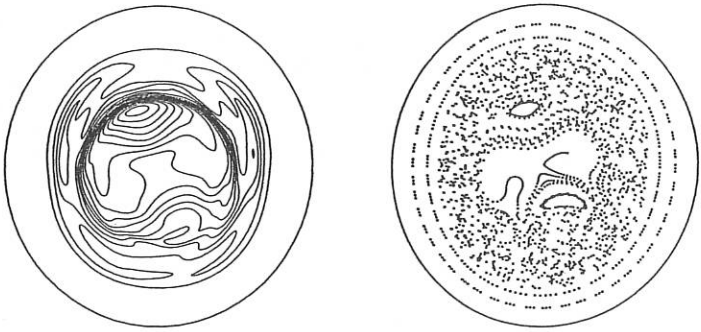

Figure 2b. Electron temperature and field lines at end of energy quench ($70\tau_A$ after 2a).

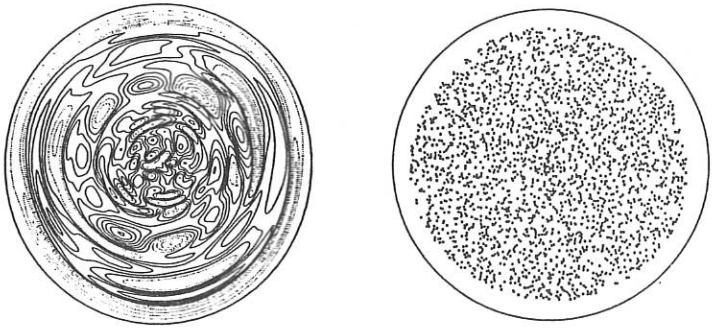

Figure 2c. Current density and field lines during voltage spike ($370\tau_A$ after 2a)

EFFECT OF SHEARED TOROIDAL PLASMA FLOWS ON EQUILIBRIUM AND STABILITY OF TOKAMAKS

A. Sen, A.K. Agarwal, S.N. Bhattacharyya and P.K. Kaw

Institute for Plasma Research,
Bhat, Gandhinagar 382 424 INDIA

The equilibrium of a toroidally rotating axisymmetric plasma was studied theoretically by Maschke and Perrin [1]. They showed that the Grad-Shafranov equation can be generalised to include the effect of rotation if either the temperature or the entropy is assumed to be constant on the magnetic surfaces. They also obtained analytical solutions for certain simple cases. Some more analytical solutions were obtained by Throumoulopoulos and Pantis [2]. However all these solutions are for rigid rotation only. In this work we investigate the effect of velocity shear on the toroidal equilibrium and stability both numerically and analytically. We consider an isothermal plasma obeying ideal MHD equations confined in a perfectly conducting shell with a circular cross section. The generalised equilibrium equation [1] in cylindrical coordinates (R, ϕ, Z) is

$$\Delta^* \psi = -R^2 \left[\frac{d\bar{p}}{d\psi} + R^2 \bar{p} \frac{d}{d\psi} \left(\frac{\omega^2}{2\bar{R}T} \right) \right] \exp\left(\frac{\omega^2 R^2}{2\bar{R}T} \right) - I \frac{dI}{d\psi} \qquad (1)$$

where Δ^* is the usual Grad Shafranov operator, $\bar{R}$ is the gas constant, $\bar{p} = p \exp(-R^2\omega^2/2\bar{R}T)$ where p is the plasma pressure, and I is the poloidal current function. The solution of this equation depends on the choice of four arbitrary flux functions $\bar{p}(\psi)$, $I(\psi)$, $\omega(\psi)$ and $T(\psi)$, and of course on the boundary conditions. We choose the following forms of the flux functions for the numerical work

$$\bar{p} = p_o \psi_n^{\alpha} \qquad (2)$$

$$I = R_o B_o \left(1 - \gamma \psi_n^{\beta} \right) \qquad (3)$$

$$\frac{\omega^2}{\bar{R}T} = \frac{\lambda \psi_n + \Omega^2}{R_o^2} \qquad (4)$$

where $\psi_n = (\psi - \psi_s)/(\psi_a - \psi_s)$ is the normalised ψ, ψ_a is the flux on the magnetic axis, ψ_s is the flux on the plasma surface,

B_o is the externally imposed vacuum toroidal field at the major radius R_o , $p_o, \alpha, \bar{\beta}, \lambda$ and Ω are the input parameters. The value of γ is adjusted in each iteration to keep the toroidal current constant. The parameters Ω and λ characterize the rigid rotation and the velocity shear respectively. Eq. (1) is now solved numerically with the boundary condition that $\psi = 0$ on the circular plasma boundary. Contours of the solution $\psi(R,Z)$ for the parameter values $p_o = 10^4$ N/m^2, $\alpha = 1.8$, $\bar{\beta} = 1.8$, $R_o = 0.75$ m, minor radius a = 0.25 m, $B_o = 1$ Tesla and $I_p = 200$ KA are shown in figs (a),(b),(c) for different values of Ω and λ . Figure (d) corresponds to a high beta equilibrium with $p_o = 10^5$ N/m^2 It is observed that both rigid rotation and velocity shear cause an outward shift of the magnetic axis However the effect of λ is smaller than Ω on the position of magnetic axis. Ellipticity of the flux surfaces are also found to be influenced by shear.

To understand these numerical results we next carry out a perturbative analysis of eqn(1) in terms of the inverse aspect ratio $\varepsilon = a/R$. Approximate analytical solutions are obtained for both low β and high β tokamak orderings. For the low-β tokamak ordering, for example, an expression for the shift of the magnetic axis is given by

$$\Delta = \frac{8\pi r^3}{9 B_p^2 R_o} \left[\frac{d\bar{p}}{dr} + 2 \lambda R_o B_p \bar{p} \psi_a^{-4} \right] (1 + \frac{\Omega^2}{2}) \exp(\Omega^2/2) \quad (5)$$

The contributions to the outward shift of the magnetic axis now include rigid rotation effects as well as those arising from shear (in addition to the usual finite β term). We have neglected the hoop force term in deriving (5). It is seen that both rigid rotation and shear enhance the outward shift. For the high β tokamak ordering similar trends are observed. The results of the approximate analytical solution are in reasonable agreement with the results of the numerical solution.

We have next carried out a linear stability analysis for ideal ballooning modes in the presence of velocity shear. As is well known [3] the presence of equilibrium flows makes the eigenmodal formulation nonself-adjoint and thereby precludes the application of energy principle methods. In the presence of shear the problem is further complicated by the appearance of explicit time dependence in the coefficients of the evolution equations and one cannot speak in terms of normal eigenmodes. It is more appropriate to solve an initial value problem [4]. We have carried out such an analysis on the following equation obtained by applying a modified eikonal ansatz on the perturbed ideal MHD equations

$$\frac{\rho}{B^2}\frac{\partial}{\partial t}\left[\,|\nabla S|^2\frac{\partial \xi}{\partial t}\,\right]=\frac{(B\cdot\nabla)\left[\,|\nabla S|^2(B\cdot\nabla)\xi\,\right]}{B^2}+$$

$$\frac{2(B\times\nabla S\cdot\kappa)(B\times\nabla S\cdot\nabla p)\xi}{B^4}+\frac{[B\times\nabla S\cdot(V\cdot\nabla)V](B\times\nabla S\cdot\nabla\rho)\xi}{B^4} \qquad (6)$$

where the eikonal S is chosen to be $S = \phi - q(\psi)\theta - \omega(\psi)t$ and the other notations are standard [5]. We have obtained an approximate analytical solution to equation (6) in the strong ballooning limit. The solution displays temporal growth of an initial perturbation with average growth rates comparable to the usual static growth rates. Shear is found to have a stabilizing influence and the perturbations are found to be peaked around $\theta = 0$. The solution also displays periodic bursting behaviour observed in previous numerical investigations [4].

REFERENCES

[1]Maschke, E.K. and Perrin, H., Plasma Physics 22 (1980) 579

[2]Throumoulopoulos, G.N. and Pantis, G., Phys. Fluids B 1 (1989) 1827.

[3]Frieman, E. and Rotenberg, M., Rev. Mod. Phys. 32 (1960) 898.

[4]Cooper, W.A., Plasma Physics and Contr. Fusion 30 (1988) 1805.

[5]Sen, A. and Sundaram, A.K., Nucl. Fusion 29 (1989) 1161

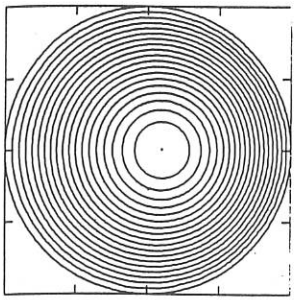

(a)

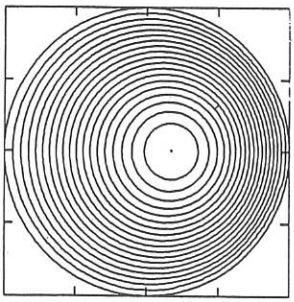

(b)

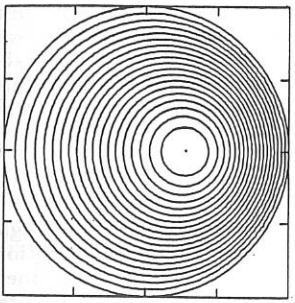

(c)

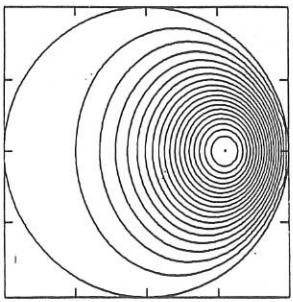

(d)

Contour plots of poloidal magnetic flux for (a) no toroidal rotation, p= 1000.0 N/m^2 (b) rigid rotation with Ω = 1.0, (c) sheared flow with λ = 1.0, Ω = 1.0. (d) high β plasma with p = 10000.0 N/m^2, Ω = 1.0, λ = 1.0.

ALPHA CONTAINMENT, HEATING, AND STABILITY IN THE IGNITEX EXPERIMENT

Z. Guo[1], *R. Carrera*, *G. Y. Fu*[2], *L. M. Hively*[3], *G. H. Miley*[4], *E. Montalvo*, *M. N. Rosenbluth*[5], *S. Tamor*, and *J. W. Van Dam*

The University of Texas at Austin, Austin, TX 78712, *U. S. A.*
(1) *Institute of Physics, Academia Sinica, Beijing, P. R. China.*
(2) *CRPP, Lausanne, Switzerland.*
(3) *Oak Ridge National Laboratory, Oak Ridge, Tennessee.*
(4) *University of Illinois, Urbana, Illinois.*
(5) *University of California, San Diego, California.*

INTRODUTION

The fusion ignition experiment IGNITEX has recently been proposed by M. N. Rosenbluth, W. F. Weldon, and H. H. Woodson[1] on the basis of B. Coppi's idea for a compact, thermonuclear experiment and recent technology advances on pulsed-power systems. The basic idea is to utilize the best-estabilished fusion regime of operation, ohmically-heated tokamaks to produce a self-sustained fusion reaction. The basic elements of fusion-product alpha particle behavior in IGNITEX are analyzed in this paper on the basis of present understanding. It is shown that the IGNITEX experiment permits fairly high alpha particle containment, heating, and stability in the proposed ignition regime. Other ignition regimes in which alpha modes can be destabilized are accessible. The IGNITEX experiment can be a feasible, simple, and relatively inexpensive way to produce and control ignited plasmas for scientific study.

IGNITEX EXPERIMENT

The basic idea of the IGNITEX experiment is to use a 20-Tesla, single-turn-coil tokamak to ohmically heat a plasma to thermonuclear conditions and thus, produce and control an ignited plasma. The IGNITEX experiment should reach ignition with ohmic heating alone and produce a stable ignited phase during the flat top of the discharge. Typically ramping of the currents and fields will be done in 3 seconds, the flat top will last 5 seconds and the plasma will be shut down in 2 seconds.

The ohmic regime and L-mode of operation proposed for IGNITEX have the most immediate prospects for ignition. They have a large database, have produced clean discharges, have sufficient energy confinement time, and offer the possibility of design simplicity and reduced maintenance requirements. The low-beta mode of operation proposed for IGNITEX permits an ample stability margin in the non-ignited and ignited phases of operation. Low-beta allows operation with the required high plasma currents and thus, with high probability of ignition.

Initial calculations for the IGNITEX experiment indicate that the predicted margin for ignition is high[2] and ignition can be reached far below stability limits, i.e. the ignited phase of the discharge can be maintained passively by the plasma itself without exceeding disruptive limits.

The IGNITEX experiment permits access to ignition conditions throughout a wide range of densities and temperature. Typically, densities from 3. to 15. $\times 10^{14} cm^{-3}$ and temperature from 5. to 15. keV are possible. These regimes are alpha-heating dominated and produce high-power-density, ignited plasmas.

ALPHA PARTICLE CONTAINMENT

Alpha containment is found to be rather high even in the assumption of significant levels of toroidal asymmetries. The small alpha Larmor radius and the large alpha containment factor (ratio of the plasma current to the minimum plasma current for confinement of most alpha particles according to neoclassical orbit theory) justify the high alpha containment in IGNITEX. Alpha transport simulations using the code DESORB indicate[3] negligible alpha losses with high-n-ripple levels up to 4%. Threshold levels of low-n-ripple losses are even higher.

Some of the good characteristics of the IGNITEX experiment with respect to alpha containment are: high plasma current (12MA), elongated plasma cross section ($\kappa = 1.6$), small alpha-Larmor radius ($\rho_\alpha / a = 0.027$), low safety factor ($q_{cyl}(a) = 2.2$, $q_\psi(a) = 2.72$), high alpha particle containment factor (3.2), negligible high-n ripple (single-turn, compact toroidal field magnet), moderate low-n ripple ($n = 2$ due to poloidal magnet leads and $n = 1$ due to generator failure), and high threshold value of ripple for stochastic losses calculated by using the code RIPLOS (specifically for $n = 1,\ 2$ ripple sources).

These characteristic are possible because of the magnet system to be used in the IGNITEX: Single-turn-coil TF system (minimizes high-n ripple, minimizes gyroradius, provides stable (low beta) low-q_a operation, and support a high plasma current) and internal PF system (maximizes plasma current) with low-n ripple. The accommodation of a high plasma current in the compact design creates a flat safety factor profile which basically makes the alpha losses negligible by significantly increasing the threshold value of the ripple for stochastic diffusion fast losses.

ALPHA PARTICLE HEATING

As a single-turn-coil tokamak with high fields, IGNITEX permits a suitable path to ignition from the ohmic-dominated regime (up to 4 keV average plasma temperature) to the alpha-dominated regime (from 5 to 15 keV average plasma temperature). The intrinsic ohmic heating of tokamak operation is sufficient to heat the plasma to temperatures at which alpha heating is significant and enough to produce ignition. At the ignition point the temperature dependence of the fusion power can be stronger than the temperature dependence of the power losses and the plasma could experience a thermal runaway that may cause the plasma to reach MHD stability limits and the plasma will disrupt.

Thermally stable ignited plasma can be produced in the IGNITEX ex-

periment. In the IGNITEX design the plasma thermal runaway associated with plasma ignition is stabilized by the plasma's own radiation emission. Simulation with the STIC and TDIC codes (steady state and time dependent, volume-average codes) show that electron cyclotron emission, which have been calculated by using analytic formula by Trubnikhov, Engelman and Curatolo and by the cyclotron radiation transport code SNECTR[4], can damp the thermal runaway. The low-beta operation proposed for IGNITEX permits a discharge that will evolve far below from disruptive limits. This gives the possibility of production of thermally stable plasmas and then facilitates control of the thermal runaway associated with ignition conditions.

ALPHA PARTICLE INDUCED MHD MODES

The stability of internal kink modes, high-n ballooning modes, and shear Alfven modes have been investigated in the presence of fusion alpha-particles in ignited plasmas. These modes can be either stable or unstable depending on the parameter regime of the ignition phase. The stability of these MHD modes favors high field and low beta tokamak experiments.

The "sawtooth" and "fishbone" oscillations, which may occur in the central part of the plasma column, are associated with the $m = 1, n = 1$ internal kink modes and considered to be a potential threat to the attainment of ignition. The energetic trapped particles are thought to be responsible for destabilizing /stabilizing the internal kink mode and to cause "fishbone" instabilities and/or "sawtooth" suppression. It appears that the fusion-product trapped alpha particles can open a stability window where both sawtooth and fishbone oscillations are suppressed in burning D-T plasmas. The actual width of this window depends on the characteristics of the alpha particles, bulk plasma profiles, and the model used to describe the $m = 1$ internal kink "inner" layer dynamics. It will be desirable that the alpha's beta value be high enough to stabilize sawtooth but low enough that fishbone modes are not resonantly excited. The stability window may be attained in IGNITEX since the major radius is relatively small and its magnetic field is high.

The trapped alpha particles can also interact through their precession drift with high-n ballooning modes. Instabilities can be excited if the alpha beta exceeds a critical value[5] which is formally the same as the "fishbone" mode's but now considering radially localized modes with $n \gg 1$. The IGNITEX plasma can separate far below the ideal ballooning stability limit. Thus high-n ballooning modes should be stable in the IGNITEX experiment owing to its high magnetic field and possible low beta operation.

Shear Alfven waves may be destabilized via alpha particles transit and magnetic drift frequency resonances. The high energy alpha particles are born with a radially peaked profile. The expansion free energy associated with the alpha particle density gradient can drive Shear Alfven Modes instabilities efficiently. The Kinetic Alfven Waves (KAW) and Global Alfven Eigenmodes (GAE) experience strong electron damping so that they are not to be destabilized by alpha particles. The Toroidicity-Induced Alfven Eigenmodes (TAE), which can exist only in toroidal geometry with frequencies lies within gaps in the Shear Alfven Continuum, may be destabilized by alpha particles. An ig-

nited tokamak plasma with high magnetic field requires a large alpha particle density gradient to destabilize the TAE modes. The high-n TAE are easier to excite by alpha particles and have higher growth rate than the low-n TAE. The latter should be stable in IGNITEX. It should be noted that high-n TAE may not exist in the central part of the plasma column since finite bulk plasma pressure will force the high-n TAE into the continuum accumulation point at the edge of gaps at low shear case. Thus, there may be no TAE mode to be destabilized by alpha particles whose density is highly peaked at the (low shear) center of the ignition plasma. An investigation of these question with detailed $P_0(r)$, $\omega_A(r)$ radial profiles in IGNITEX experiment is underway. The various excitation mechanisms that correspond to different free energy sources and resonance channels are also under consideration.

The IGNITEX experiment should provide a research tool to explore the problem of alpha-particle stability of thermonuclear plasmas. IGNITEX is capable to access relatively high-beta operation in the ignition phase so that MHD modes could be resonantly excited by fusion alpha particles, and then permit the study of their effects on the alpha particle confinement and heating.

CONCLUSION

A preliminary analysis of alpha particles effects in the fusion ignition experiment IGNITEX has been presented. It is argued here that, according to present understanding, the ohmic heating, L-mode, low-beta mode of operation is a regime of operation favorable for a magnetic fusion ignition experiment. Initial calculations indicate that the IGNITEX concept offers favorable characteristics for a magnetic fusion ignition experiment and provides a simple, theoretically reliable means of producing ignited plasma for scientific study at a relatively low cost. Specifically, it has been shown that high alpha containment is possible in a single-turn-coil tokamak, that thermally stable ignited plasmas can be produced, and that alpha-stabilized and non-alpha-stabilized modes of operation are feasible in IGNITEX.

REFERENCES

[1] M. N. Rosenbluth, W. F. Weldon, and H. H. Woodson, "Basic Design Report of the Fusion Ignition Experiment IGNITEX", Center for Fusion Engineering Report (March 1987)

[2] R. Carrera and E. Montalvo, "Fusion Ignition Experiment", Nuclear Fusion 30, 00 (1990)

[3] L M. Hively, Nuclear Fusion 24, 779 (1984); also R. B. White, and H. E. Mynick, Phys. Fluids B 1, 980 (1989)

[4] S. Tamor, Nuclear Technology/Fusion 3, 293 (1983)

[5] J. W. Van Dam *et al.* "Plasma Physics and Controlled Nuclear Fusion Research 1986", (IAEA, Vienna 1987), Vol.2, p. 135.

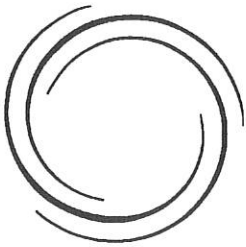

INDEX OF ALL AUTHORS

INDEX